MESOSCALE INTERACTIONS IN POROUS ELECTRODES

by

Aashutosh N. Mistry

A Dissertation

Submitted to the Faculty of Purdue University

In Partial Fulfillment of the Requirements for the degree of

Doctor of Philosophy

School of Mechanical Engineering

West Lafayette, Indiana

May 2019

THE PURDUE UNIVERSITY GRADUATE SCHOOL
STATEMENT OF COMMITTEE APPROVAL

Prof. Partha P. Mukherjee, Chair

School of Mechanical Engineering

Prof. Xiulin Ruan

School of Mechanical Engineering

Prof. Vilas Pol

Davidson School of Chemical Engineering

Prof. Vikas Tomar

School of Aeronautics and Astronautics

Approved by:

Prof. Jay Gore

Head of the Graduate Program

Dedicated to my mummy and pappa,

whose unconditional love constantly reminds me of God's glory…

"Peace is the beauty of life. It is sunshine. It is the smile of a child, the love of a mother, the joy of a father, the togetherness of a family. It is the advancement of man, the victory of a just cause, the triumph of truth."

- Menachem Begin (1913 – 1992)

ACKNOWLEDGMENTS

Doctoral studies, despite its academic affiliation, is uniquely challenging as it lacks the structure and certainty associated with other formal pedagogical ranks. Quite curiously, such conditions create an opportunity for exploring unknowns, which in turn demands singular focus and sacrifices. Given the abnormal requirements, success is contingent on having a support structure. I feel privileged to have a *glocal* network of mentors, friends, and family that constantly encouraged me to pursue my passion for science.

I am sincerely grateful to *Prof. Mukherjee* (thesis advisor) for being a strong influence on my research journey. Be it providing scientific inputs or creating opportunities for holistic growth, he has always believed in my abilities, even during the first half of my Ph.D. when I was a below mediocre candidate. Continued interactions with national lab researchers, namely, *Dr. Kandler Smith* (NREL), *Dr. Scott Roberts* (SNL), *Dr. Venkat Srinivasan* (ANL) and *Dr. Corey Love* (NRL) have shaped my approach to different facets of electrochemistry. I am also thankful to the thesis committee members, *Prof. Ruan*, *Prof. Pol*, and *Prof. Tomar*, for coaching me to present my findings to a broader audience.

As a *side effect* of my inquisitive nature, I am often overflowing with thoughts. Fortunately, I have friends like *Ankit*, *Arjun*, *Daniel*, *Justin*, *Rakesh*, and *Vyas* who offer the strongest critiques to my whims. My labmates have been *a family away from family*, and the conducive ecology for personal and professional advancement.

I have always been indebted to my parents for their unconditional love and support. However, the past few years have been overly taxing due to the *spatiotemporal* separation and my *unconventional* decisions, and I feel eternally grateful to their unwavering trust in me.

TABLE OF CONTENTS

LIST OF TABLES

LIST OF FIGURES

GLOSSARY

In the order or appearance…

Term	***Description***	***Remark***
Electrode	Solid phase responsible for electrochemical reactions; it can be made up of an energy storing phase (*e.g.*, intercalating graphite) or provide a structural backbone for active phase to deposit (*e.g.*, carbon in sulfur based conversion) or be the active phase (*e.g.*, metal anodes) or merely provide a conducting surface to host reactions (*e.g.*, platinum in fuel cell or traditional solution electrochemistry)	Here composite electrodes are primarily discussed
Active Phase	In a composite electrode, (solid) material phase responsible for electrochemical energy storage	
Electrolyte	Medium responsible for ionic conduction	Here liquid organic electrolytes are discussed
Active Area	Interfacial area contributing to electrochemical reaction(s)	
Porosity	Volume fraction of pore (electrolyte) phase	
Tortuosity	A descriptor for convolutedness of the pore-network	
Effective Property/ Microstructural Property	Relevant material property of a composite system that is a combination of (bulk) material property and geometrical arrangement of various phases in the composite	
Morphology	Classification of geometrical shapes, not always quantitative	
Conductivity	A measure of current flow for a prescribed potential gradient; there are two common charge carriers – electrons and ions, and in turn there are electronic and ionic conductivities	
Performance	Electrochemical response of the battery; often implies voltage *vs.* capacity (or time) characteristics	
C-rate	A dimensionless measure of current – an xC operation implies theoretical operation time to be (60/x) minutes	
Overpotential	Voltage departure from an equilibrium value when finite current being passed	
Kinetic	Related to reactions	
Ohmic	Related to transport, *e.g.*, species diffusion or electron conduction	
Butler-Volmer	Functional (analytical) form of electrochemical kinetics; assuming Arrhenius-type thermally active	

	reaction and elemental (not necessarily reversible) steps	
Ion Blockage	A phenomenon where not all the solid – electrolyte interface area is available for reaction given the presence of inactive solids	Quantified by N_r or N_k
Impedance	A measure of temporal voltage fluctuation for a given current fluctuation (or vice versa)	
Dilute Solution Theory	Electrolyte transport representation at low salt concentrations – interspecies interactions are neglected	Relies on NP
Concentration Solution Theory	Transport description in concentrated electrolytes – accounting for the full range of inter- and intra-species interactions	Relies on OSM
Double Layer	Small spatial region close to an electrode-electrolyte interface which exhibits charge separation given the interfacial effects such as adsorption	Debye length is a measure of double layer thickness
Degradation	Deterioration in performance over repeated use	
Self-heating	Heat generated during an electrochemical operation in response to finite resistance of transport processes	
Abuse-heating	Heat generated due to exothermic chemical reactions between electrode materials; manifests at elevated temperatures	Root cause for thermal runaway
Plating	Metallic deposition	
Diffusion	Species flux in response to a concentration gradient	
Migration	Species flux in response to a potential gradient	
Intercalation Length	Effective distance for intercalation in a solid host; often the smallest dimension, *e.g.*, radius for a spherical particle, while thickness of a platelet	
Stochasticity	Spatial variability as opposed to a homogeneous picture; often manifests at multiple length scales and leads to inhomogeneity and anisotropy in effective properties	
Inhomogeneity	Spatial dependence of properties	
Anisotropy	Directional dependence of properties	
Calendaring	An electrode fabrication stage where electrode porosity is reduced *via* compression, *e.g.*, typical NMC electrode porosity is around 50-55% after evaporation-based preparation, and it is calendared to increase energy density	
Surface Passivation	Gradual reduction in active area given the precipitation of insulating solids	Quantified by $N_{passivation}$
Pore Blockage	Gradual constriction of electrolyte pore network given the precipitation of secondary solids	Quantified by $N_{blockage}$
Oxygen Starvation	Local unavailability of dissolved oxygen to sustain the electrochemical reaction	

Reactant Starvation	Generalized situation similar to *Oxygen Starvation* with respect to a particular reactant; the limiting reactant can be either in solid, liquid or gaseous phase	
Solubility	Equilibrium maximum concentration of a given solute in a given solution at a given temperature and pressure	
Pristine Electrode	Devoid of presence of any secondary solids, *e.g.*, at the onset of first discharge in Li-oxygen and before sulfur impregnation in Li-sulfur	
Short-range Conduction	Local availability of electrons to participate in electrochemical reactions	
Speciation	Continuous evolution of local concentration field due to production/consumption and transport of species; fast nonlinear dynamics makes it a challenging aspect to control	

LIST OF ABBREVIATIONS

In the order of appearance…

Abbreviation	***Description***
LIB	Lithium-Ion Battery
AM	Active Material
FIB-SEM	Focused Ion Beam – Scanning Electron Microscopy
XRT/ XCT	X-ray (Computed) Tomography
CBD	Carbon Binder Domain
REV	Representative Elementary Volume
RVE	Representative Volume Element
NMC/ NCM	lithium Nickel Manganese Cobalt oxide
PVDF	polyvinylidine difluoride
BET	Bruanuer Emmett Teller
DNS	Direct Numerical Simulation
EIS	Electrochemical Impedance Spectroscopy
NP	Nernst-Planck equation
OSM	Onsager-Stefan-Maxwell
OCP	Open Circuit Potential (electrode *vs.* reference)
OCV	Open Circuit Voltage (electrode couple)
SEI	Solid Electrolyte Interphase
SVD	Singular Value Decomposition
PCA	Principal Component Analysis
LIS	Lithium-Sulfur Cell
SEM	Scanning Electron Microscope

ABSTRACT

Author: Mistry, Aashutosh, N. PhD
Institution: Purdue University
Degree Received: May 2019
Title: Mesoscale Interactions in Porous Electrodes
Committee Chair: Partha P. Mukherjee

Despite the central importance of *porous electrodes* to any advanced electrochemical system, there is no clear answer to "*How to make the best electrode?*". The source of ambiguity lies in the incomplete understanding of convoluted material interactions at smaller – difficult to observe length and timescales. Such *mesoscopic interactions*, however, abide by the fundamental physical principles such as mass conservation. The porous electrodes are investigated in such a physics-based setting to comprehend the interplay among structural arrangement and off-equilibrium processes. As a result, a synergistic approach exploiting the complementary characteristics of controlled experiments and theoretical analysis emerges to allow *mechanistic insights* into the associated mesoscopic phenomena. The potential of this philosophy is presented by investigating three distinct electrochemical systems with their unique peculiarities.

1. INTRODUCTION

Electrodes are the most essential (and often the least understood) aspect of any advanced electrochemical device. The state-of-the-art practice is to employ porous composite electrodes. The porous nature is expected to ensure an increased electrode – electrolyte contact that is necessary for improved kinetic response. Since the overall electrochemical behavior is composed of various transport processes, spanning across multiple length and timescales, the composite structure is meant to facilitate these different interactions (*e.g.*, Figure 1). However, when combined together, each of these materials does not necessarily act synergistically, giving rise to technological bottlenecks.

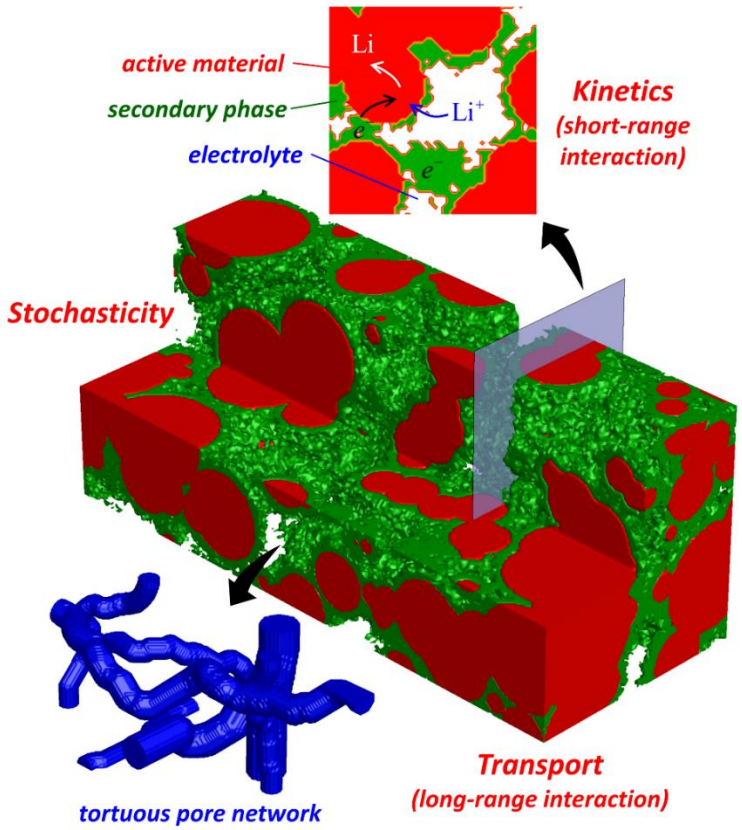

Figure 1. The electrochemical response of a composite porous electrode is composed of different short- and long-range physicochemical processes. The schematic outlines the interactions in a porous composite intercalation electrode.

The conventional interpretation of the porous electrode response is about three to five decades old and dates back to Newman's research[1-3]. With the advancements in energy-storage materials and porous architectures, the understanding of porous electrode response needs to evolve to account for the associated peculiarities. Despite the apparent need for fundamental investigations, directed efforts have been stymied due to the lack of observability at the smaller physical dimensions where relevant interactions take place (Figure 2). Such intermediate length-scales are most suitable for mesoscopic investigations to elucidate fundamental materials – microstructure correlation.

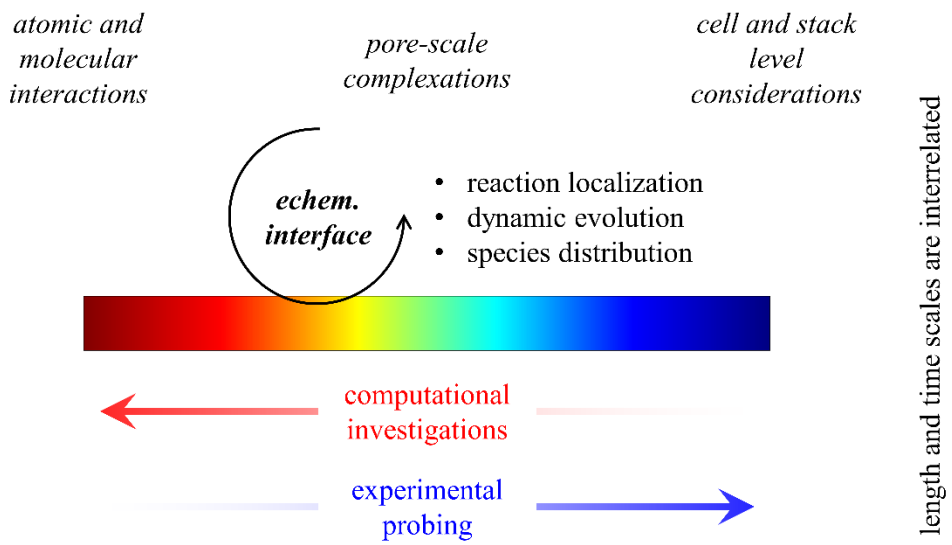

Figure 2. The scope of mesoscopic investigations lies at intermediate length-scales where computations and experiments complement each other.

1.1 Mesoscale Interactions

In general, as the dimensions shrink, interfacial effects become more prominent as compared to bulk (macroscale) response of the materials[4]. For example, stable liquid drops could be formed due to surface tension (an interfacial character) in contrast to the bulk tendency which acts to form horizontal surfaces[5, 6]. These lengths are however much larger than atomistic or molecular dimensions, thus representing continua[7]. Such intermediate scales, also referred to as mesoscale, has an additional characteristic of stochasticity. Thus, the salient aspects of mesoscopic interactions are:

- Interfacial effects
- Stochasticity

The associated dimensions are smaller than the optical limit, and any form of explicit probing relies on higher energy (in turn smaller wavelength) waves such as x-rays or electrons. Such approaches require specialized specimen preparation and equivalently not all the relevant physicochemical fields can be observed.

The physical principles governing behavior such a mass and energy conversion hold true at the mesoscale. Subsequently, there exists an opportunity for combining these fundamental principles and experimental information to reconstruct the description of electrode physics.

1.2 Outline of the Dissertation

In this dissertation, a general approach has been proposed to understand the convoluted interactions in composite porous electrodes. The material responses, specifically, kinetic and transport characteristics, have been defined through non-equilibrium thermodynamics[8]. The microstructural effects have been abstracted based on theories of random heterogeneous media[9, 10]. The experimental information is obtained through past studies, collaborations or new techniques developed to probe a particular behavior. In what follows, three distinct electrode systems have been studied:

i. Intercalation electrodes, *i.e.*, Li-ion, where electrochemical energy is stored in active particles in the form of intercalated lithium: Chapter 2 discusses the correlation between electrode microstructure and the electrochemical response, especially focused on the arrangement of the secondary solids. Chapter 3 explores the relevance of such structure-functionality interplay with conjugate modes such as thermal response (related to safety) and chemical degradation (defines life). Chapter 4 investigates the relevance of small-scale inhomogeneities to the electrode-scale performance.

ii. Conversion electrodes, *i.e.*, Li-oxygen and Li-sulfur systems where energy is stored in a precipitating phase at the solid-electrolyte interface: Chapter 5 explores electrochemical complexations in Li-oxygen chemistry, while Chapter 6 delves into the evolving nature of electrode geometry and chemical speciation in the Li-sulfur system.

This following discussion proffers the basic description of Li-ion (LIB) and Li-sulfur (LiS) batteries. Their operationality along with standard descriptors of their electrochemical response have been discussed. An overview of the related literature, with an emphasis on microstructure-scale probing, is also presented.

1.3 Lithium-Ion Batteries (LIBs)

Since its inception about four decades ago, lithium-ion technology has improved substantially. They have successfully replaced their predecessors given their compact size, better performance (voltage and capacity), reversibility and cyclability. They have surmounted the consumer electronics market and are actively being pursued for automobile and grid-storage applications. With this shifted focus on high energy and power applications, the advances in the lithium batteries are going to be measured differently. For example, earlier research that led to LIBs for small electronics was focused on descriptors like reversibility and cell voltage, which are closely tied to electrode materials. On the other hand, future research is to focus on the efficient utilization of these materials when they form a working cell[11-17].

Consider Figure 3 which schematically shows an LIB unit cell. The cell is made up of porous electrodes (anode and cathode) sandwiching a separator. The pore-network spanning across the thickness of the cell houses electrolyte. The electrolyte primarily facilitates ionic transport. The separator is a polymeric material (*e.g.*, polyethylene) whose function is to electronically isolate the two electrodes. Both the electrodes have Li storing solids, also referred to as active material. State-of-the-art LIBs employ graphite as active material at the anode (negative electrode) and transition metal oxides like lithium cobalt oxide ($LiCoO_2$), lithium manganese oxide ($LiMnO_2$) and nickel manganese cobalt oxide ($LiNiMnCoO_2$) at the cathode (positive electrode). Given the presence of electronically insulating separator, electrons cannot reach from anode to cathode internally and have to traverse via an external circuit, thus, in turn, supplying electricity (during discharge) operation. During a discharge operation, Li gets deintercalated at anode, at the active material – electrolyte interface (electrochemically active surface) it converts to electron and Li^+, electron traverses to external circuit while Li^+ ion transports in the electrolyte, both of them reach cathode (via electronic and ionic pathways, respectively) and undergo another electrochemical reaction at cathode which stores energy in the form of intercalated Li at cathode. During charging the reverse dynamics take place internally. During discharging, the electrochemical energy stored in the active

materials translates to electrical energy in the external circuit. During charging this process reverses and external electrical energy gets converted to electrochemical energy.

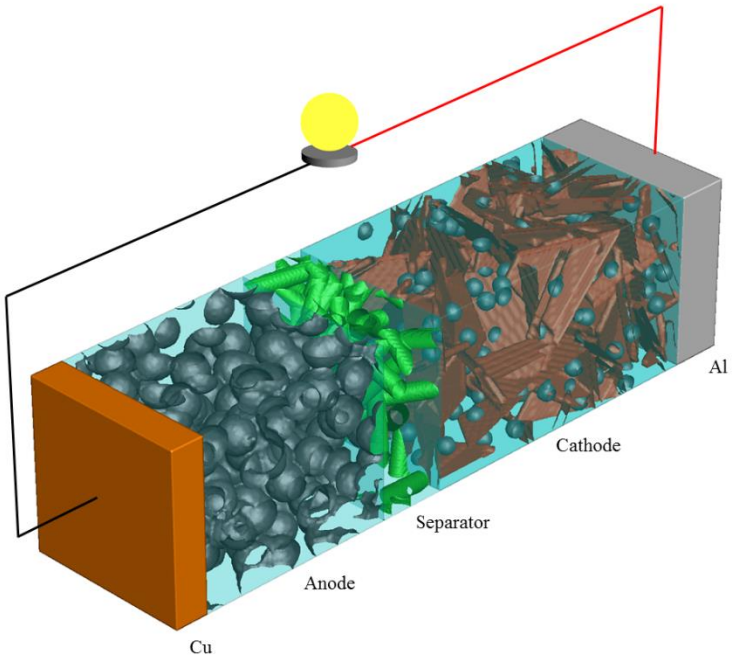

Figure 3: A schematic diagram showing various components of a typical Li-ion unit cell [18].

Note that the porous electrodes simultaneously serve as a reaction zone and reservoir for Li as well as facilitate ionic and electronic transport [18-20]. Each of these functionalities is related to the presence of different material phases. The active material stores Li, pore-network filled with electrolyte conducts ions, active interface sustains electrochemical reactions, conductive additives and binder are responsible for electronic conduction as well as mechanical rigidity. This poses a very curious dilemma as electrochemical energy storage is only related to the presence of active material, but the functionality (finite-rate performance) requires the presence of all the different phases. This arrangement of multiple phases is referred to as electrode microstructure and is the focus of the present work.

1.4 Basic Concepts related to LIBs

LIB electrodes are composed of multiple materials, thence their material behavior should be understood as a first step to propose modifications. This material scale description can be categorized in terms of

i. Thermodynamic properties

ii. Transport properties

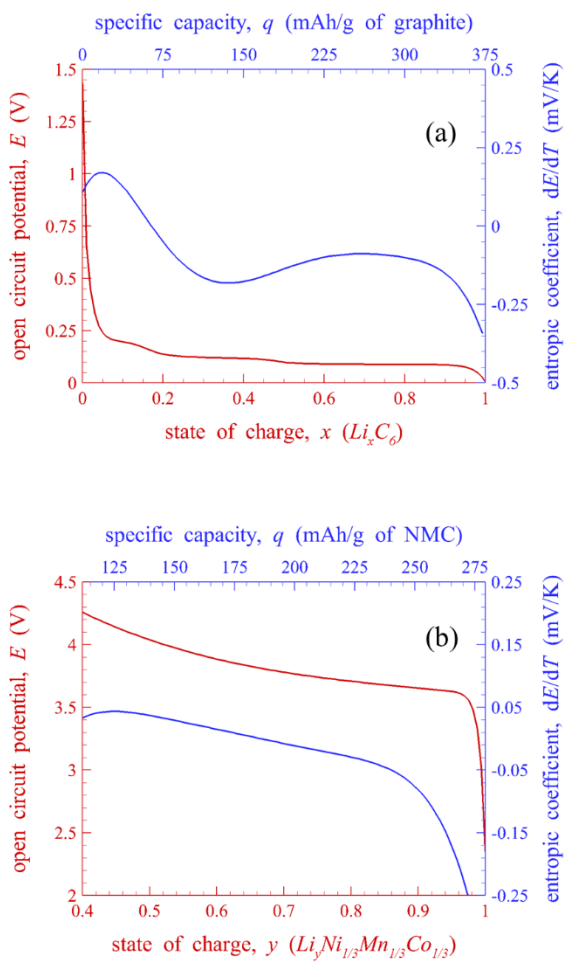

Figure 4: Variation of open circuit potential for (a) graphite and (b) NMC materials as a function of lithiation. Corresponding entropic coefficients are also shown [18].

1.4.1 Thermodynamic Properties

Imagine an active material being lithiated at an infinitesimal rate. If the operation is carried out so slowly, the system undergoes reversible transitions (*i.e.*, the direction of the change can be easily reversed by changing the sign of the efforts) and is close to its equilibrium (or thermodynamic) state. The electrode voltage measured under such conditions is referred to as open circuit potential (OCP). Note that for Li based chemistries, all the voltages are measured with respect to Li/Li^+ couple. Such OCP values are often characterized as a function of the state of lithiation. Two such plots have been shown for graphite and NMC in Figure 4. OCP values measured for any electrode is essentially the thermodynamic behavior of corresponding active materials. The OCP directly correlates to free energy exchanges related to associated intercalation/deintercalation reaction. The second law of thermodynamics dictates that heat of reaction, ΔH , cannot be completely converted to corresponding free-energy change, ΔG , and a part of it converts to heat, $T\Delta S$. This is a source of heat generation as cells are being operated and is characterized in terms of the entropic coefficient for each of the electrode materials. Instead of making such measurements for individual electrodes, full cells can be characterized in a similar fashion. This gives rise to open circuit voltage (OCV) and is the difference of OCP of cathode and OCP of the anode. Note that here degrees of lithiation for both the electrodes need not be the same.

$$\mathrm{OCV} = \mathrm{OCP}_{cathode} - \mathrm{OCP}_{anode} \tag{1}$$

Note that the OCP relations for these intercalation based materials do not conform to the Nernst relation for liquid phase electrochemistry, as intercalation takes place in the solid phase and the corresponding concentrations are very high, thus leading to strongly varying activity coefficients.

1.4.2 Transport Properties

During a finite rate operation of these electrodes, various transport and interfacial resistances come into play. Each of these resistances is associated with a flow of charge (electronic or ionic) and in turn, manifests as voltage difference. This voltage difference is often referred to as overpotential. A cell with high overpotential has higher irreversibilities and poorer performance when compared with the ideal (thermodynamic) limit.

1.4.2.1 Butler-Volmer Kinetics

Electrochemical reactions take place at the active interface. The electrochemical reactions essentially refer to change in the identity of charge carriers (electronic to ionic and vice versa). For LIBs, the rate of electrochemical reaction is quantified by the expression (also referred to as the Butler-Volmer kinetics):

$$i = k\sqrt{C_s C_e \left(C_s^{max} - C_s\right)}\left\{e^{F\eta/2RT} - e^{-F\eta/2RT}\right\} \tag{2}$$

$$\eta = \phi_s - \phi_e - U\left(C_s\right) \tag{3}$$

Here i is the rate of electrochemical reaction in A/m^2 of active interface, k is reaction rate constant, C_s is the concentration of Li in solid phase, C_e is the concentration of Li^+ in the electrolyte phase, η is overpotential at the active interface, F is Faraday's constant (96 487 C/mol), R is universal gas constant (8.314 J/mol·K) and T is the temperature of the interface. The overpotential at the electrode-electrolyte interface refers to the penalty to be paid for finite current flow in either direction and is related to potentials of solid (active material) and electrolyte phases as well as the corresponding OCP. Note that the concentrations (C_s, C_e) used in the above relations (2) and (3) are phase concentrations at the interface.

In porous electrodes, electrochemically interface is distributed in space and the area of this active surface leads to corresponding volumetric (electrochemical) reaction rate, as described by Equation (4), where j is reaction rate in A/m^3.

$$j = ai = ak\sqrt{C_s C_e \left(C_s^{max} - C_s\right)}\left\{e^{F\eta/2RT} - e^{-F\eta/2RT}\right\} \tag{4}$$

1.4.2.2 Li-diffusion in Active Material

Intercalation dynamics in LIBs is mathematically quantified as a combination of two processes:

i. Electrochemical reactions at active material – electrolyte interface
ii. Li diffusion in active material particles

This diffusion process is described by Fick's second law (Equation (5))

$$\frac{\partial C_s}{\partial t} = \nabla \cdot \left(D_s \nabla C_s\right) \tag{5}$$

This diffusion process is characterized by the diffusivity of Li in the active material phase. Often it is found that this solid-state diffusion is a function of local concentration, *i.e.*, $D_s = D_s\left(C_s\right)$. Solid state diffusivity exhibits an Arrhenius dependence on temperature.

1.4.2.3 Electrolyte Phase Transport

Electrolytes in LIBs are a combination of suitable Li salt dissolved in organic solvents. As Li is a highly reactive metal, especially in the presence of water, organic solvents are used (in contradiction to aqueous electrolytes). One most commonly used LIB electrolyte is $LiPF_6$ (salt) in three equivolume solvents PC (propylene carbonate)/ EC (ethylene carbonate) / DMC (dimethyl carbonate). $LiPF_6$ dissolves in the solvents to give Li^+ and PF_6^- ions which are responsible for the passage of the ionic current. Given the presence of charged species, the ionic flux is essentially a combination of two distinct transport modes: diffusion and migration (advection is assumed to be absent). Diffusion describes the flow of ions in response to their concentration gradients, while migration is the flux of ions in response to a potential gradient in the electrolyte phase. The migrational component is zero for a charge-less species. Mathematically the electrolyte phase transport for an LIB electrolyte is expressed by the following set of governing equations[21-23]:

$$J = -D\nabla C_e + \frac{t_+}{F} I \tag{6}$$

$$I = -\kappa\nabla\phi_e - \kappa_D \nabla \ln C_e \tag{7}$$

Here J is the flux of Li^+ ions (expressed as mol/m^2/s) and I is total ionic current. D is electrolyte phase diffusivity, κ is ionic conductivity and κ_D is diffusional conductivity. In expression (7), the first term describes the contribution of migrational current, while the second term being the contribution of diffusional current to total ionic current. The variation of these three electrolyte phase transport properties is presented in Figure 5. All three properties demonstrate a strong dependence on electrolyte phase concentration as well as temperature. Note that ionic conductivity exhibits a non-monotonic dependence on salt concentration. At lower salt concentrations, with more salt, the number density of ionic charge carriers increases, which in turn enhances the electrolyte conductivity. After a certain salt concentration (here 1.0-1.2 M) the boundary layers of various ions start interacting which in turn hinder each other's mobility. Essentially at this stage with the addition of more salt, the ionic number density is too high for each of them to move freely (as was possible for dilute solutions) and ionic conductivity starts decreasing with salt concentration. This concentrated solution effect is quite relevant for practical cells as it quantifies the maximum ionic conduction possible from a given electrolyte and what should be corresponding salt concentration.

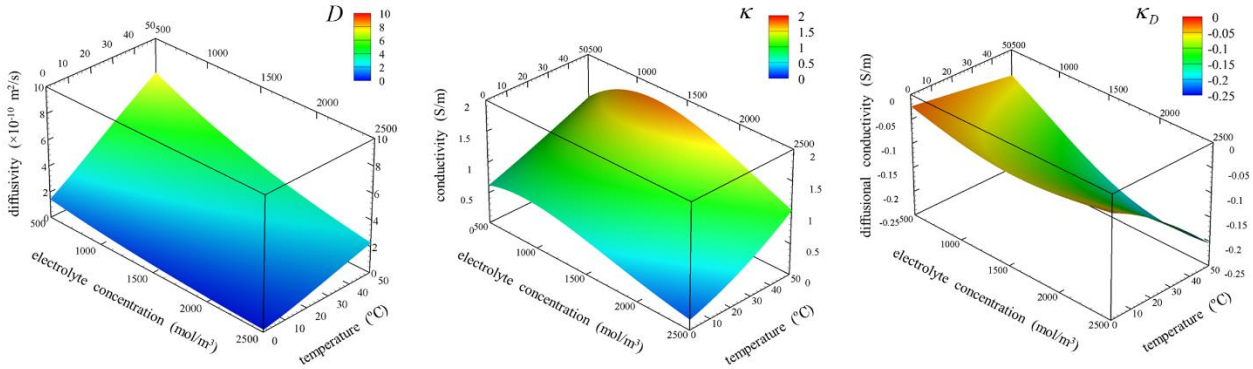

Figure 5: Electrolyte properties strongly depend on salt concentration and temperature [24].

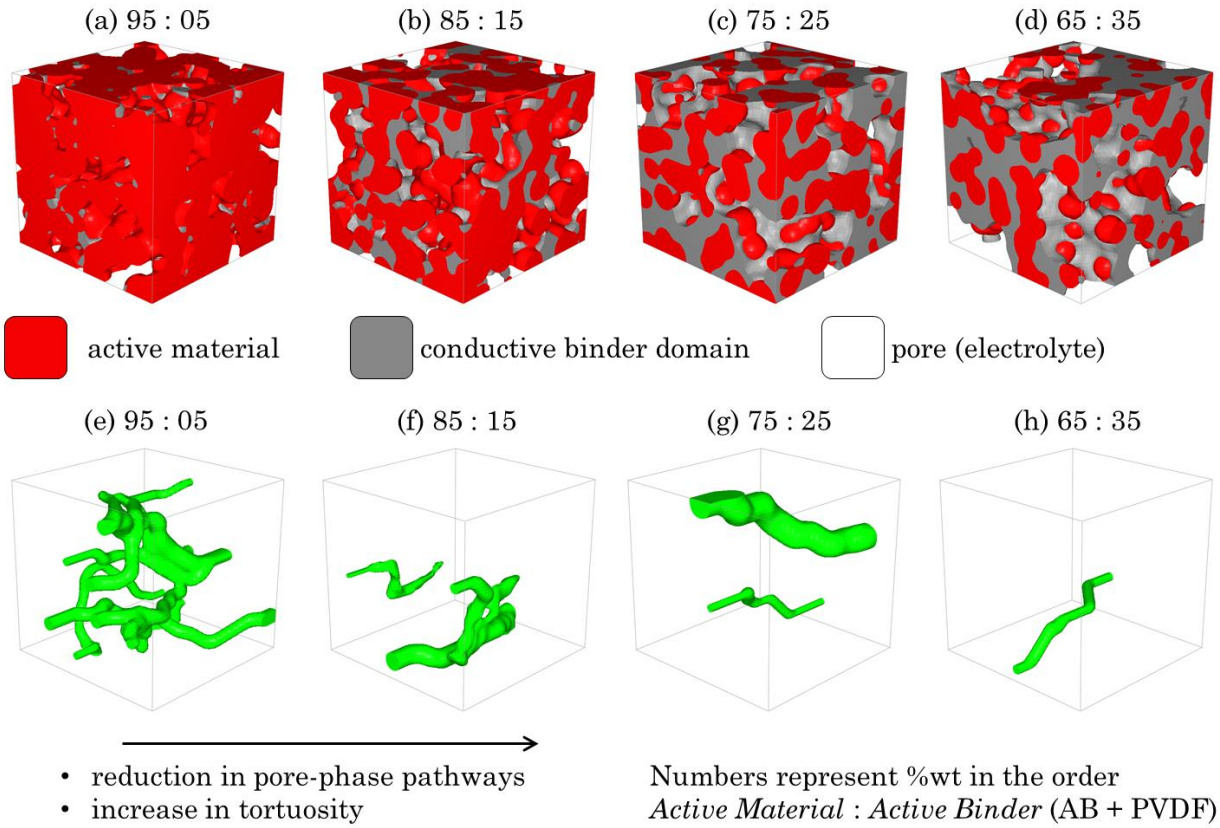

Figure 6: Schematic representation of composite electrode structures along with pore network pathways to intuitively explain tortuosity [25].

1.4.3 Porous Electrodes Modify the Intrinsic Transport Behavior

Kindly note that these properties and description present intrinsic behavior of each of these material phases. When these phases are simultaneously available in a porous battery electrode, each of these transport processes gets modified to account for the porous nature of the electrodes. The relation between the interfacial reaction rate and volumetric reaction rate (Eq. (4)) is one such translation. Similarly, in a porous electrode having a pore-network with porosity ε and tortuosity τ, the electrolyte phase transport relations (6) and (7) modify as:

$$J = -D\frac{\varepsilon}{\tau}\nabla C_e + \frac{t_+}{F}I \tag{8}$$

$$I = -\kappa\frac{\varepsilon}{\tau}\nabla\phi_e - \kappa_D\frac{\varepsilon}{\tau}\nabla\ln C_e \tag{9}$$

Here porosity describes the fraction of total electrode volume available for pore-phase transport. Note that in a porous-electrode, one can have open-pores (which are accessible for transport across electrode thickness) and close-pores (which do not partake in pore-scale interactions). Hence the porosity used in above expression refers to open-pore volume only. Tortuosity comments on the morphology of pore-network. Keeping the same porosity, one can construct multiple different connections and correspondingly each of them exhibits different transport resistance. Tortuosity accounts for this diversity in pore-network. Figure 6 shows different pore-phase transport paths obtained for electrodes with identical porosity.

1.5 Literature Review: Electrode Microstructures in LIBs

As described earlier, electrodes for LIBs are composite structures with multiple phases, with each of them adding different functionality and in turn making a working electrode. Consider a composite cathode of an LIB. It contains NMC as an active material, acetylene black (AB) as a conductive additive and polyvinylidenedifluoride (PVDF) as a suitable binder. For the rest of the discussion on LIB electrodes, this cathode (NMC, AB, PVDF) will be considered. Experimentally such electrodes are identified by weight percentages of the solid phases and porosity. Thus, say a 90: 5: 5 electrode contains 90% NMC by wt., 5% AB and 5% PVDF. Based on prescribed porosity, volume fractions of each of the four phases (NMC, AB, PVDF, and pore) can be computed. A typical battery electrode is prepared by the slurry drying process. Here a slurry of solid components in an appropriate solvent (often N-methylpyrolidine, NMP) is prepared and cast onto an

appropriate current collector (aluminum foil for cathodes). Then this sheet is dried in a controlled environment inside an oven. During drying the solvent evaporates and leaves behind the electrode microstructure. This process is schematically sketched in Figure 7. The slurry preparation steps (before drying) ensure that a homogeneous colloidal suspension is obtained. The drying stage is responsible for getting a specific arrangement of different phases, *i.e.*, electrode microstructure. The dried electrodes obtained in this fashion have high porosity (~50-55%) and correspondingly poorer energy density. Often an additional processing stage – calendaring is performed which essentially reduces the electrode porosity. Thus, the electrode composition is fixed during the slurry preparation stage, while porosity is finalized at the end of electrode fabrication step. An important descriptor of electrode microstructures is the active material particle size. It is determined by precursor (*i.e.*, active material powder used for slurry preparation). Sometimes, an additional step – ball milling is preformed to reduce the mean particle size before using it for slurry preparation. Slurry preparation and electrode drying do not affect particle size distribution. Calendaring step is recently found to introduce minimal modifications to the initial particle size distribution.

A study of the literature related to LIBs reveal that electrode-scale investigation can be roughly categorized into two types:

i. Electrode composition effects[26-48]

ii. Microstructural investigations[49-82]

Before discussing each of these in detail, refer to Figure 8 which sketches a typical cathode microstructure (not full electrode is shown; only a representative elementary volume, REV, is presented). The solid phases have different associated length-scales. Active material particle dimensions are of the order of 1 μm, conductive additives are often between 10-100 nm and the binder is a polymeric phase. Given this disparity in length-scales, one can represent conductive additives and binder as a pseudo phase (referred to as the secondary phase in the present discussions). In fact, it is even challenging to isolate this phase using detailed experimental imaging. Experimentally the relevant physical properties of this secondary phase (conductivity binder domain, CBD) have also been measured. Thus, going forward, unless stated otherwise, this effective description with active material as primary phase, CBD as secondary solid phase and pore network will be used for discussing electrode microstructure. Also, note that the dimension of a suitable REV is ~10 μm and electrode thicknesses are of the order of 100 μm.

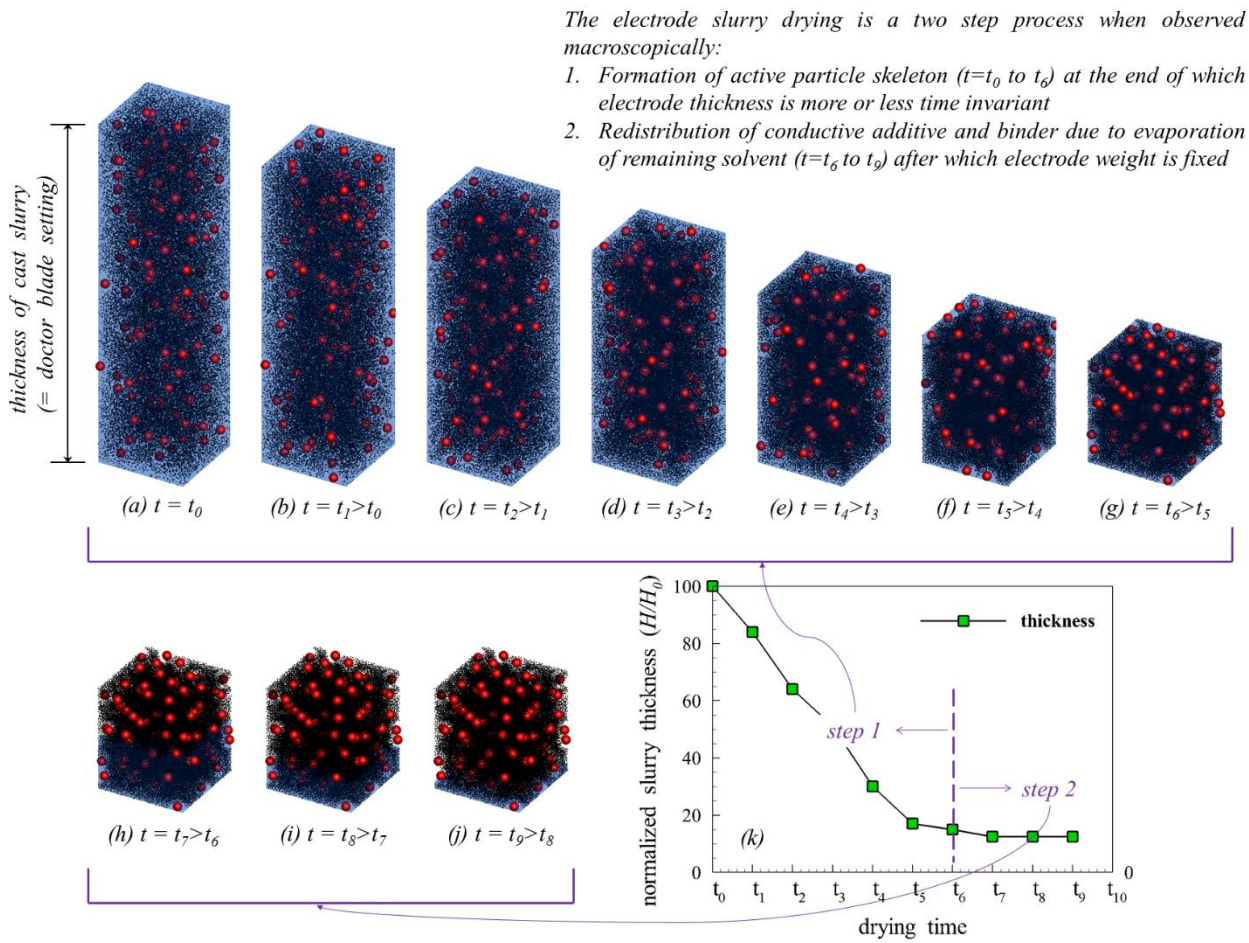

Figure 7: A schematic representation of electrode microstructure evolution during slurry drying stage [83].

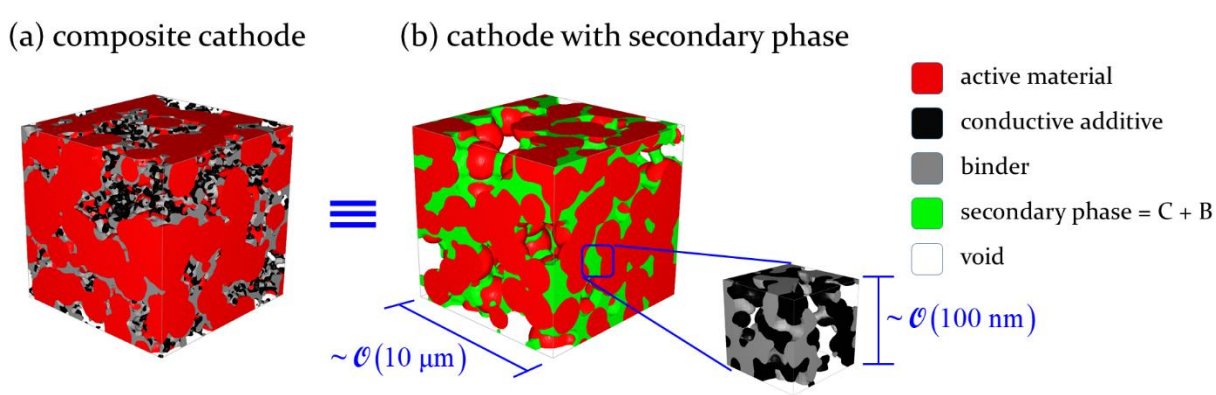

Figure 8: Conductive additives and binder can be expressed as a pseudo phase, given the large disparity in length scales of active material particles and these secondary solids.

1.5.1 Electrode Composition Effects

Such studies explore the effect of electrode composition and preparation stages such as calendaring and drying on resulting electrode performance. The electrochemical response of electrodes is characterized by (half) cell performance and/or electrochemical impedance spectroscopy (EIS) studies. Various questions of interest pertaining to electrode compositions are:

i. What should be the relative presence of conductive additives and binder?
ii. How active material loading affects cell performance?
iii. How electrode porosity correlates to the electrochemical response of the cell?
iv. How the electrode performance scale as a function of electrode thickness?
v. How calendaring affects cell dynamics? This is partly related to porosity effects.
vi. How drying temperature influences the electrochemical behavior of electrodes?

All these aspects, when combined together, provide guidelines for high energy density electrodes (higher than the present state-of-the-art electrodes).

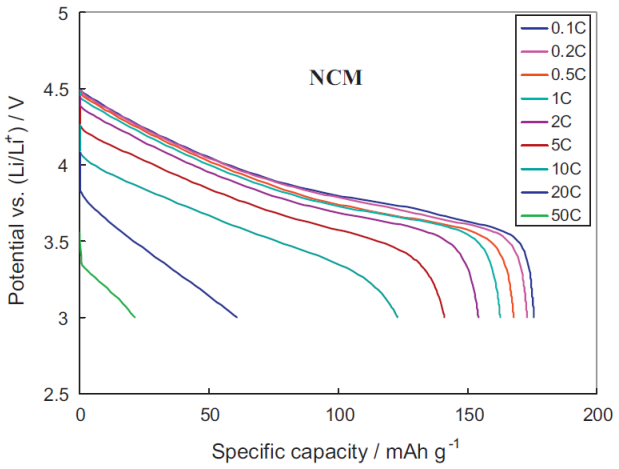

Figure 9: Electrode performance as a function of operating current [29].

Figure 9 presents the experimental electrode performance at various discharge rates. Here the electrodes are operated at a constant current between voltage window 4.2 and 3.0 V. The operating current is non-dimensionalized and expressed as C-rate. C-rate is inversely related to the theoretical time of discharge, *e.g.*, 5C operation means the cell theoretically discharges in 1/5 hours. Figure 7 reveals that as the operating current increases (proportional to C-rate), cell voltage and capacity monotonically decrease. Alternatively, upon decreasing the cell voltage, terminal

voltage profile approaches that of open circuit potential for the corresponding electrode material. The electrode used for this study is 24 μm thick with 85% active material (NMC), 7% conductive additive (AB) and 8% PVDF by wt.

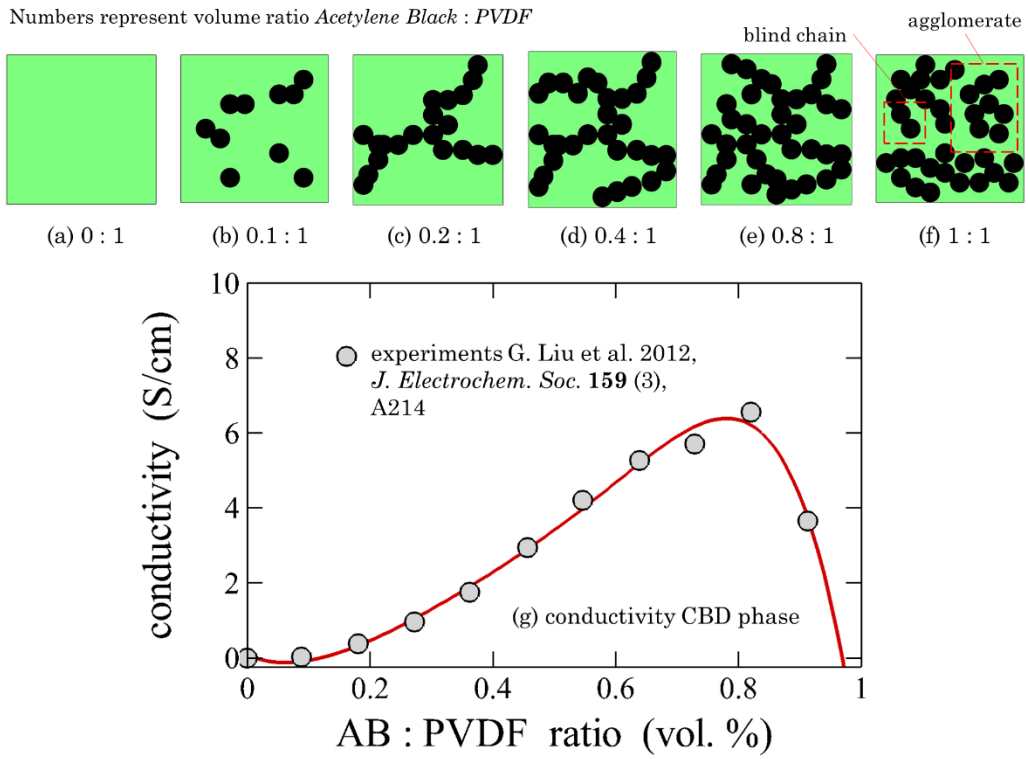

Figure 10: Electronic conductivity of acetylene black PVDF films for different AB : PVDF compositions[30, 33].

To explore the importance of conductive additive to binder ratio, thin films with a different conductive additive to binder amounts were fabricated (no active material). These films were further characterized to establish the dependence of CBD phase conductivity as a function of conductive additive to binder ratio. Figure 10 reveals this experimental dependence. A curious trend appears on this plot where electronic conductivity first increases with increase in conductive additive amount, but later on decreases drastically. The corresponding physical explanation is presented in Figure 10 subfigures. Initially, when no conductive additive is present, electronic conductivity is the same as intrinsic binder phase. Later on, with the addition of conductive additives, gradually electronic conduction percolation pathways establish. These are related to networks of conductive additives spanning across the thickness of the electrode. Electronic

conductivity of conductive additives is two-three orders of magnitude higher than that of the pure binder. Electronic conductivity monotonically increases with conductive additive weight percentage over a wide range of CBD compositions. This behavior correlates to the formation of more percolation pathways. Once a threshold CBD composition is reached, further addition of conductive additives does not form more through connections, rather conductive additives agglomerate or form blind chains. Both of these do not increase electronic conductivity and conductivity drops despite the presence of a higher amount of conductive additives. Such effects translate to composite electrodes (in the presence of active material and pore phase) in a qualitatively similar fashion, as is revealed by measurement of effective electronic conductivity of composite electrodes (Figure 11). Here effective conductivity is plotted as a function of active material loading (the remaining weight is CBD phase). With higher active material loading, amount of CBD phase decreases leading to a reduction in the conductive network for composite electrodes.

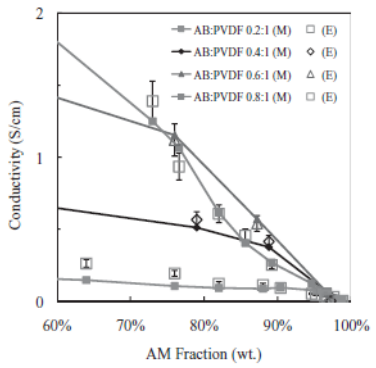

Figure 11: Effective electronic conductivities of composite electrodes as a function of composition[33].

Figure 12 explores the effect of CBD phase content on the electrochemical response of composite cathodes with different compositions. The area specific impedance (ASI) is measured for different recipes. In general, increasing AB : PVDF ratio from 0.2 : 1 to 0.8 : 1 reduces ASI values as electronic conduction becomes more efficient. There is another curious trend present here. For lower values of AB : PVDF ratio, increasing CBD phase content increases ASI, as in the presence of more CBD phase, electrochemically active area reduces which in turn increases the interfacial

resistance. For higher acetylene black compositions, this negative effect of reduced active area is compensated by a commensurate increase in electronic conductivity of these electrodes.

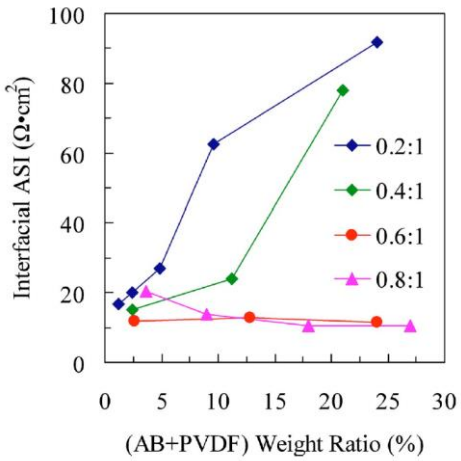

Figure 12: Area specific impedance for different electrode compositions: the role of conductive additive to binder ratio[27].

With increasing electrode thickness, various resistance contributions in general growth, thus further limiting cell performance (compared at identical C-rate) operation. Figure 13 shows how the discharge behavior of the same LIB electrode change as a function of electrode thickness when operated at the same rate – 5C. The curves are labeled using electrode thickness in μm. With increased electrode thickness, the onset voltage drops (shown as IR drop in the diagram). Moreover, the achievable cell capacity also significantly reduces. This is attributed to increased electrolyte transport resistance given the larger pore-network.

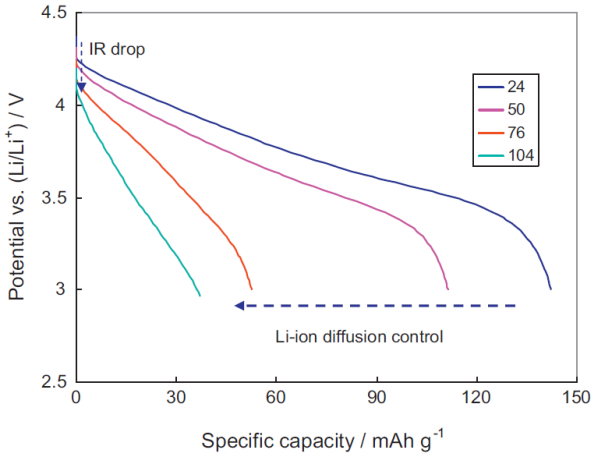

Figure 13: Electrode thickness strongly affects cell performance at identical operating rates[29].

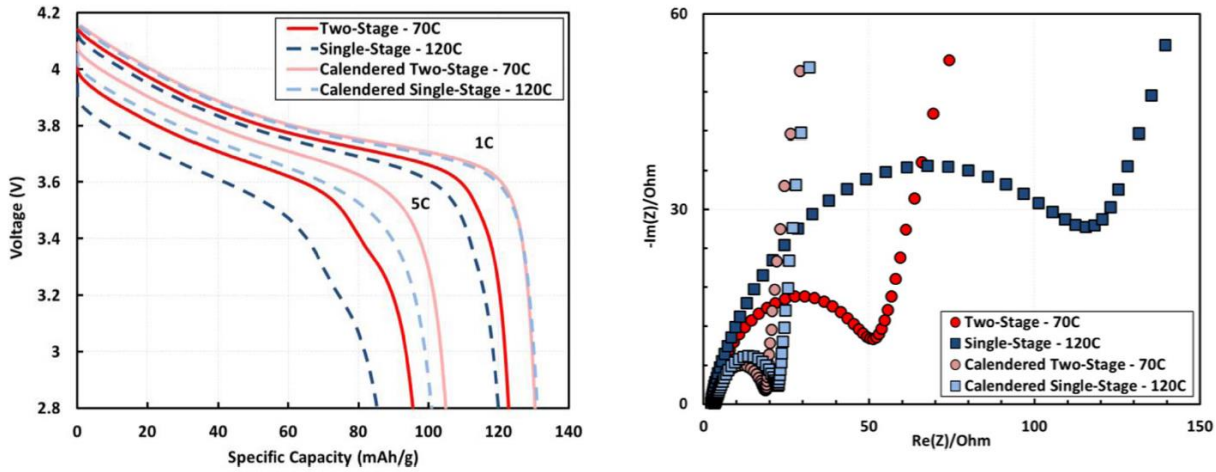

Figure 14: Changes in drying sequence changes electrode microstructure and in turn electrochemical behavior of these electrodes. Note that all these electrodes have identical composition, but different microstructure [83].

The drying step has a strong effect on resulting microstructure and in turn electrochemical response of the electrode. Despite its apparent impact, very little investigation has been carried out along this direction. Figure 14 presents performance as well as EIS data for four different electrodes with identical composition and different evaporation processing. Notice that even the C-rate dependence of electrode performance is qualitative different, for example, calendared electrodes dried at different temperatures demonstrate similar performance at lower rates (1C) but their response change markedly at higher rates (5C).

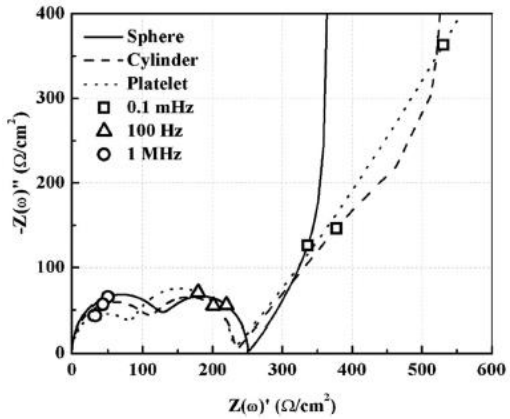

Figure 15: Impedance response of porous electrodes correlate well with active material particle morphology [46].

Particle morphology (shape and size) also affects electrochemical response as is apparent from EIS data[46, 48] for three electrodes with different particle morphologies (sphere, platelet, and cylinder) with otherwise identical specifications (Figure 15).

These different results strongly justify the role of electrode microstructure on the physicochemical response of resulting electrodes. Till date, no comprehensive approach exists that can explain all these observations. Since a fundamental understanding of microstructural effects is not available in a comprehensive fashion, no strategies or guidelines exist to improve or tune electrode response to the desirable window of operation (save for rather empirical procedures).

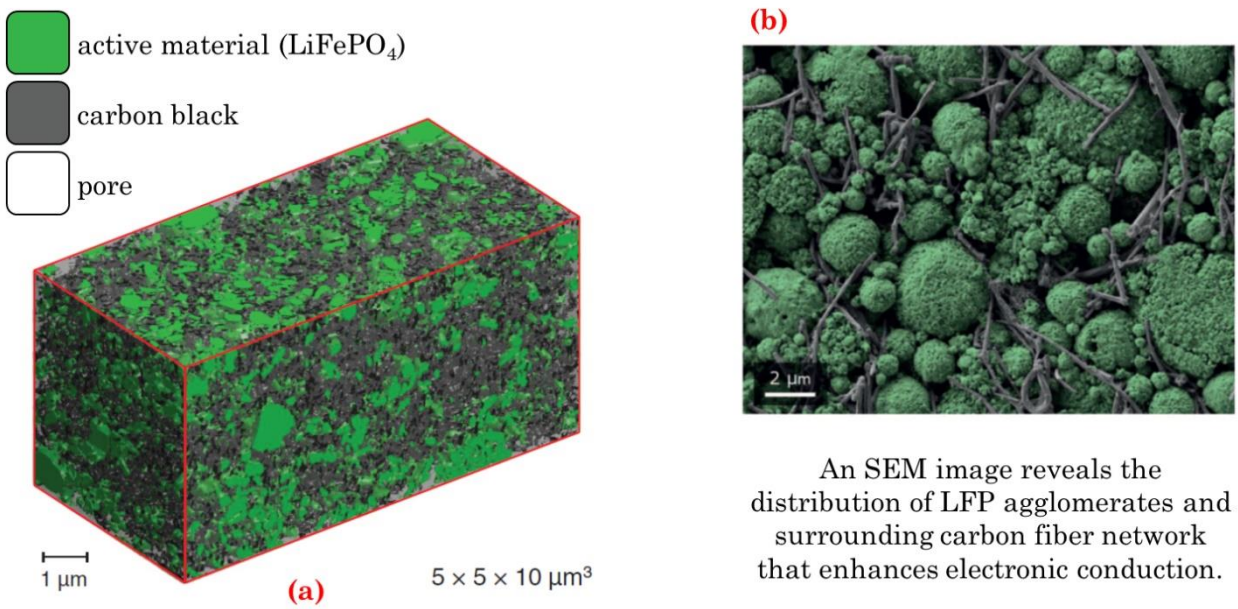

Figure 16: Representative FIB-SEM investigation of multiple solid phases in an LFP based cathode [84].

1.5.2 Microstructural Investigations

Given the need for a better understanding of microstructural scale geometrical features and pore-scale transport events, imaging studies have become popular over the past decade in the context of LIBs. There are two different set of approaches available for such a close probing. X-ray tomography (XRT)[63, 65-67, 69-74, 76, 77, 79-81, 85-91] and Focused-ion beam scanning electron microscopy (FIB-SEM)[51, 62, 75, 82, 84, 92-97]. X-rays have much better penetration depth compared to electrons (SEM) hence non-destructive volumetric imaging can be performed. On the other hand, FIB-SEM

requires one to successively remove surface layers and SEM images are taken consecutively. This results in a destructive testing procedure. Another fundamental difference between the two is related to the identification of different material phases. Using XRT one can only identify active material phase. The CBD phase results in poor contrast and one cannot isolate it from the pores, in turn, both of them are seen as a joint phase on XRT data. FIB-SEM, on the other hand, can distinguish all the different phases and provides a better local picture. FIB-SEM, unfortunately, has a much smaller observation window and often does not give large enough electrode volumes for in detail analysis at the electrode-scale.

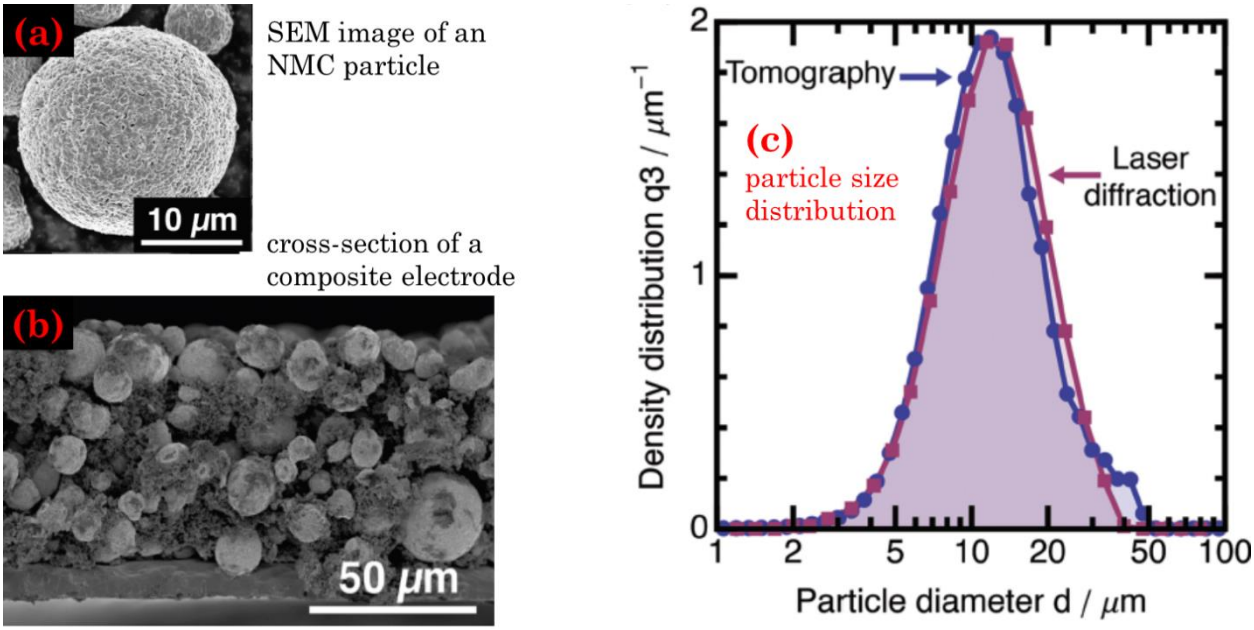

Figure 17: Imaging of NMC based electrode[80].

Figure 16 shows a reconstructed lithium iron phosphate ($LiFePO_4$, or LFP) composite cathode with carbon black as conductive additives[84]. Both the volumetric reconstruction as well as sample SEM image are shown. Thus, the reconstructed electrode sample is further analyzed to characterize relevant effective microstructural properties such as interfacial area, tortuosity, and effective conductivity. Note that the active material particles here appear to exhibit a range of particle dimensions. Another noteworthy detail here is that the binder phase is not resolved, thus apparent pore phase is actually pore + binder.

Representative XRT results for NMC composite cathode[80] are presented in Figure 17. An SEM image of the NMC particle is shown for comparison. The active material particle size distribution analyzed from reconstructed tomography data appears to closely follow the one from active material (NMC) powder used during electrode preparation. This study also images the electrodes for four different compositions and four calendaring conditions (thus total of 16 electrode sets). The analysis of all these sets reveals that the particle size distribution has changed negligibly upon calendaring thus suggesting that the calendaring process primarily affects electrode porosity.

When smaller volumes are probed using FIB-SEM, CBD phase can be identified with special treatment. This CBD phase often forms a secondary pore network. With appropriate contrasting agent (*e.g.*, ZnO), one can isolate these features. Figure 18 presents the result of such a detailed study for $LiCoO_2$ composite cathode. The secondary pores were made visible using ZnO as a contrast agent[75].

To circumvent these limitations of XRT and FIB-SEM, different routes have been proposed. One study[63] combines both the techniques: FIB-SEM is used to identify CBD phase morphology, while XRT allows one to image large enough electrode volume. In another study[65], the CBD phase is stochastically generated on top of XRT information. Though being useful in understanding the qualitative details of electrode microstructure, many important questions are still not addressed. The correlation among such pore-scale microstructural features and electrochemical behavior of such electrodes is still not clear, partly due to unavailability of complete microstructure information and partly due to high demand for computational requirements. Given such shortcomings the associated literature is quite scarce[50, 52, 56, 57, 59, 60, 98, 99]. Even the relationship between effective properties and microstructure is not clear[58, 61, 64, 100]. For example, traditionally Bruggeman relation is used to correlate electrode tortuosity with porosity. This relation is strictly valid for the granular structure of monodisperse spherical particles[101], while the electrode microstructure exhibits considerably departure from this state. In summary, the following issues need to be addressed in the context of microstructural imaging studies:

i. A suitable procedure to reconstruct large enough electrode samples which contain all the relevant phases is desired.
ii. The changes in electrode microstructure as a function of processing conditions such as composition, calendaring pressure, drying temperature are to be analyzed.

iii. Electrode microstructures have geometrical features at multiple length-scales. Each of them has to be appropriately correlated with physicochemical changes taking place during operation.

Careful analysis of these aspects will lead to fundamental insights into the interrelation among electrode microstructure and physicochemical changes in a battery electrode.

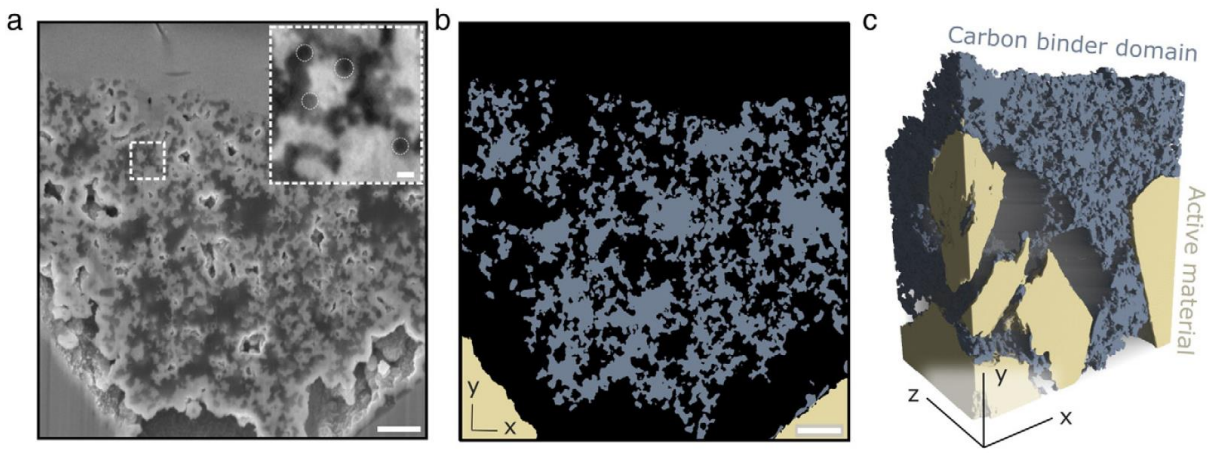

Figure 18: FIB-SEM can reveal different solid phases present in a composite electrode.[75]

1.6 Lithium-Sulfur Batteries (LISs)

The pursuit of high energy battery chemistry has initiated an interest in other lithium-based systems. Of these non-intercalation systems, lithium sulfur[102, 103 15, 104-108] is one of the most promising couple given an order of magnitude higher theoretical capacity (1675 mAh/g of sulfur compared to ~200 mAh/g of active material in typical LIBs). Figure 19 demonstrates a typical discharge performance of this chemistry. When the cathodes are fabricated, they have solid sulfur impregnated into them. This solid sulfur gradually dissolves in the electrolyte and successively gets reduced electrochemically to yield lower order polysulfides. The lower order polysulfides combine with incoming Li^+ ions from anode and precipitate as solid discharge products. Note that sulfur ring has covalent bonds and hence is soluble in the organic electrolyte in accordance with the like dissolved like theory[109]. Compounds of lower order sulfides with lithium ion have increasingly greater ionic bonding which makes them insoluble. Another lucrative feature of this chemistry is that the discharge voltage exhibits two voltage plateaus. This is desirable from applications standpoint as the cell is able to deliver an almost constant voltage over an appreciable

range of state of charge. Compared to LIB electrodes, LIS has a smaller voltage (roughly half). This is somewhat useful as the cell voltage will fall well within the electrolyte stability window[14, 110].

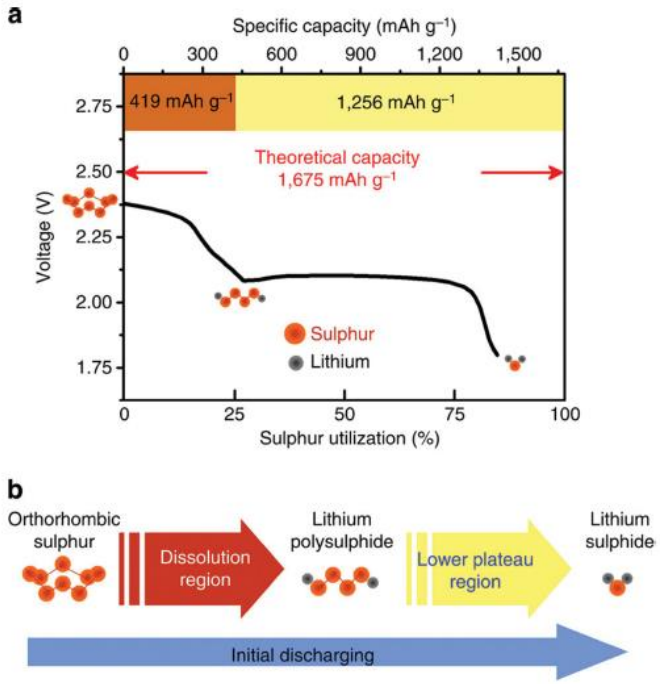

Figure 19: Typical discharge profile for LIS along with intermediate sulfur species [104].

LIS is considered to be a conversion type chemistry[111]. Here electrochemical reactions take place at the active interface and the electrolyte phase species undergoes successive transitions. Given a combination of fast phase change reactions (solid to dissolved sulfur and precipitation of lithium sulfides) and otherwise electrolyte phase species, cell reactions are considerably faster than conventional intercalation based LIB systems. These apparent advantages come at a cost of much complex system interplay. The essential details of LIS operation are not clear, for example, the identity of charge carriers in the solid phase, essentially across the precipitate film is poorly understood [112]. One troubling aspect of LIS is the formation of insulating precipitate products, *i.e.*, S_8 and Li_2S. Given their electronic resistivity, they passivate the part of the active interface upon their coverage. It has been found that this surface passivation can adopt different forms based on ionic concentrations and temperature [113]. The interfacial energy[114] and availability of nucleation sites joint determine the morphology of the precipitate film. Even a change in substrate considerably changes this dynamics[115].

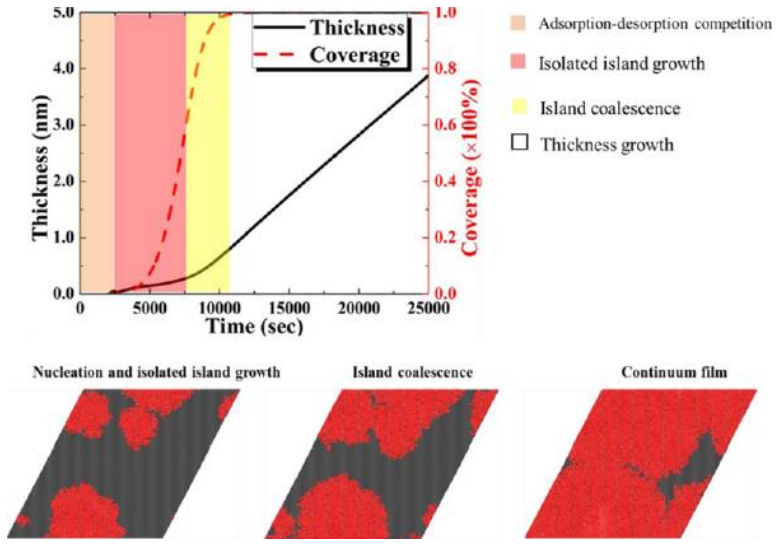

Figure 20: Precipitate growth at electrode-electrolyte interface in LIS cathodes is a strong function of interfacial energies as well as reactant concentrations and temperature [113].

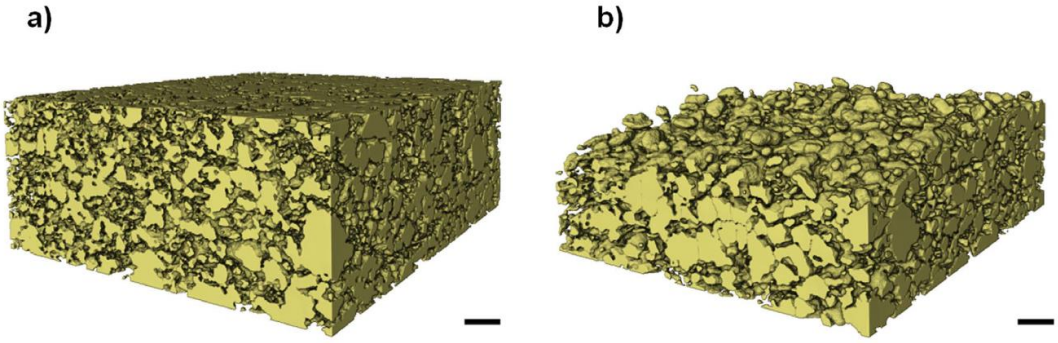

Figure 21: Solid sulfur distribution in (a) uncycled cathode and (b) after 10 cycles. Scale bar is 50 μm[116].

These precipitation and dissolution events continuously evolve the electrode microstructures. Even though such physical changes are always present during operation of LIS electrodes, they have not been explored in sufficient detail[116]. Except for one tomography study [116], this precipitation induced microstructure evolution has not been probed. Even this experiment does not comment on time evolution and only probes the microstructures the end of the operation. Thus, *in operando* details are not clear. Impedance spectroscopy could potentially provide insights into electrode microstructural evolution in terms of resistance to build up[117]. But save for a few investigations, such explorations have not been attempted [118-123]. The mathematical understanding of

microstructure evolution in the context of LIS is also very limited, as most of the mathematical results model microstructure growth in a somewhat unrealistic fashion [124-127].

Much of the earlier studies revolve around quantification, prevention and/or mitigation of the polysulfide shuttle effect[128-135]. More recent investigations identify the importance of other fundamental aspects such as fingerprinting of cell reaction pathway[136-142], complexities associated with electrolyte-phase transport[102, 143-145] and interfacial interactions of precipitation[112, 113, 115, 146, 147]. In fact, the reproducibility of many electrochemical results for Li-S cells has also been debated of late[148, 149]. Thus, the current state of understanding regarding lithium-sulfur battery and their physicochemical evolution is very limited.

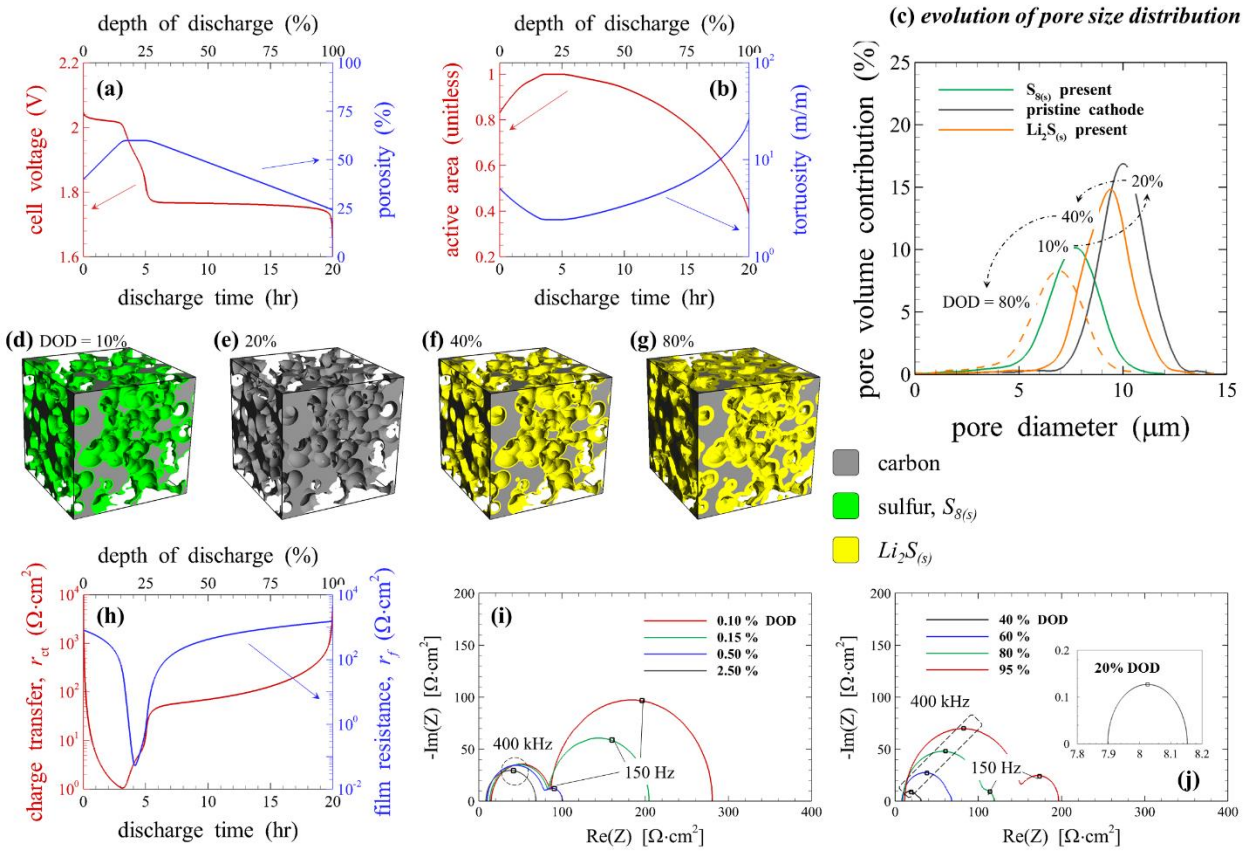

Figure 22: Evolution of electrode impedance as a function of microstructural evolution in LIS cathodes [117].

2. INTERCALATION ELECTRODES

Relevant Publications and/or Working Papers:

1. A. Mistry *et al.* (2016) *Analysis of Long Range Interaction in Lithium-ion Battery Electrodes* Journal of Electrochemical Energy Conversion and Storage 13(3) 031006 (doi: 10.1115/1.4035198)
2. A. Mistry, K. Smith and P. P. Mukherjee (2018) *Secondary-phase Stochastics in Lithium-ion Battery Electrodes* ACS Applied Materials & Interfaces 10(7) 6317 (doi: 10.1021/acsami.7b17771)
3. A. Mistry and P. P. Mukherjee (2019) *Probing Spatial Coupling of Resistive Modes in Porous Intercalation Electrodes through Impedance Spectroscopy* Physical Chemistry Chemical Physics 21(7) 3805 (doi: 10.1039/C8CP05109G)

Lithium-ion battery electrodes exhibit complex interplay among multiple electrochemically coupled transport processes, which rely on the underlying functionality and relative arrangement of different constituent phases. The electrochemically inactive solid phases (*e.g.*, conductive additive and binder, referred to as the secondary phase), while beneficial for improved electronic conductivity and mechanical integrity, may partially block the electrochemically active sites and introduce additional transport resistances in the pore (electrolyte) phase. In this work, the role of mesoscale interactions and inherent stochasticity in porous electrodes is elucidated in the context of short-range (interface) and long-range (transport) characteristics. The electrode microstructure significantly affects kinetically and transport-limiting scenarios and thereby the cell performance. The secondary phase morphology is also found to strongly influence microstructure-transport-kinetics interactions. Apropos, strategies have been proposed for performance improvement *via* electrode microstructural modifications.

2.1 Background

Lithium-ion batteries (LIBs) represent a complex non-linear system, for which, despite their widespread acceptance, quite a few fundamental questions[11-15, 17, 82, 110, 150-155] still need to be answered to enhance their performance (on volumetric and gravimetric basis), cycle life, and safety. The choice of electrode materials characterize the theoretical performance bounds, *i.e.*, the thermodynamic limit.[156, 157] On the other hand, a functioning battery does require other materials such as an electrolyte that ensure cell operation but do not store electrochemical energy.[14] Quite interestingly, depending on the three-dimensional arrangement of various phases constituting a

typical porous electrode microstructure (active material accounts for lithium inventory, conductive additive facilitates electron transport in the solid phase, binder provides mechanical connections among active material and conductive additive particles, and electrolyte enables ionic transport), it may be rate limiting.

Electrode preparation as well as specific composition decide the resulting microstructure and in turn cell performance. Various experimental studies carried out in the past decade allude to this intricate correlation among processing stage, performance, and life, but do not probe electrode microstructure.[27-30, 32-34, 36, 41, 45, 83, 158] Given the empirical nature of these measurements, questions such as which electrode composition gives better performance or improved rate capability cannot be accurately answered. With the advent of three-dimensional imaging techniques, *e.g.*, focused ion beam – scanning electron microscopy and X-ray tomography, many microstructural details of battery electrodes are available.[76, 77, 80, 81, 84, 86, 87, 92, 159, 160] Such studies suggest that the electrode microstructure is much more complex than that assumed in the otherwise accepted porous electrode theory-based performance model.[3, 40, 161] The microstructure information obtained through imaging techniques is not readily amenable to electrochemical insights since either only the active material (AM) particle structure is resolved (*e.g.*, X-ray tomography) or a large enough electrode sample cannot be probed (focused ion beam – scanning electron microscopy) or simply because the computational requirements for a simulation resolving vital length scales are enormous.

Since this connection among electrode processing conditions, resulting in microstructural features, and electrode operation is quite obscure at the present day, electrode preparation is more of an art rather than a science. For example, many experiments use excess conductive additives or keep porosities too high. The present work presents a comprehensive mathematical study where a composite electrode microstructure is analyzed over a wide range of recipes and drying conditions. A fairly overlooked aspect of LIB electrodes[49, 58, 59, 64, 162] is the implication of conductive additive + binder phase (secondary solids). (There are a few studies[25, 63, 65, 84, 163] accounting for them, but they neither incorporate secondary phase stochasticity arising from evaporation-driven electrode preparation nor correlate to the electrochemical response of composite electrodes.) The composite electrodes studied here account for different amounts of secondary solids as well as their spatial distribution. The generalized effective property (*e.g.*, tortuosity and active area) relations obtained from microstructural characterization are employed to identify the efficacy of short- and long-range interactions.

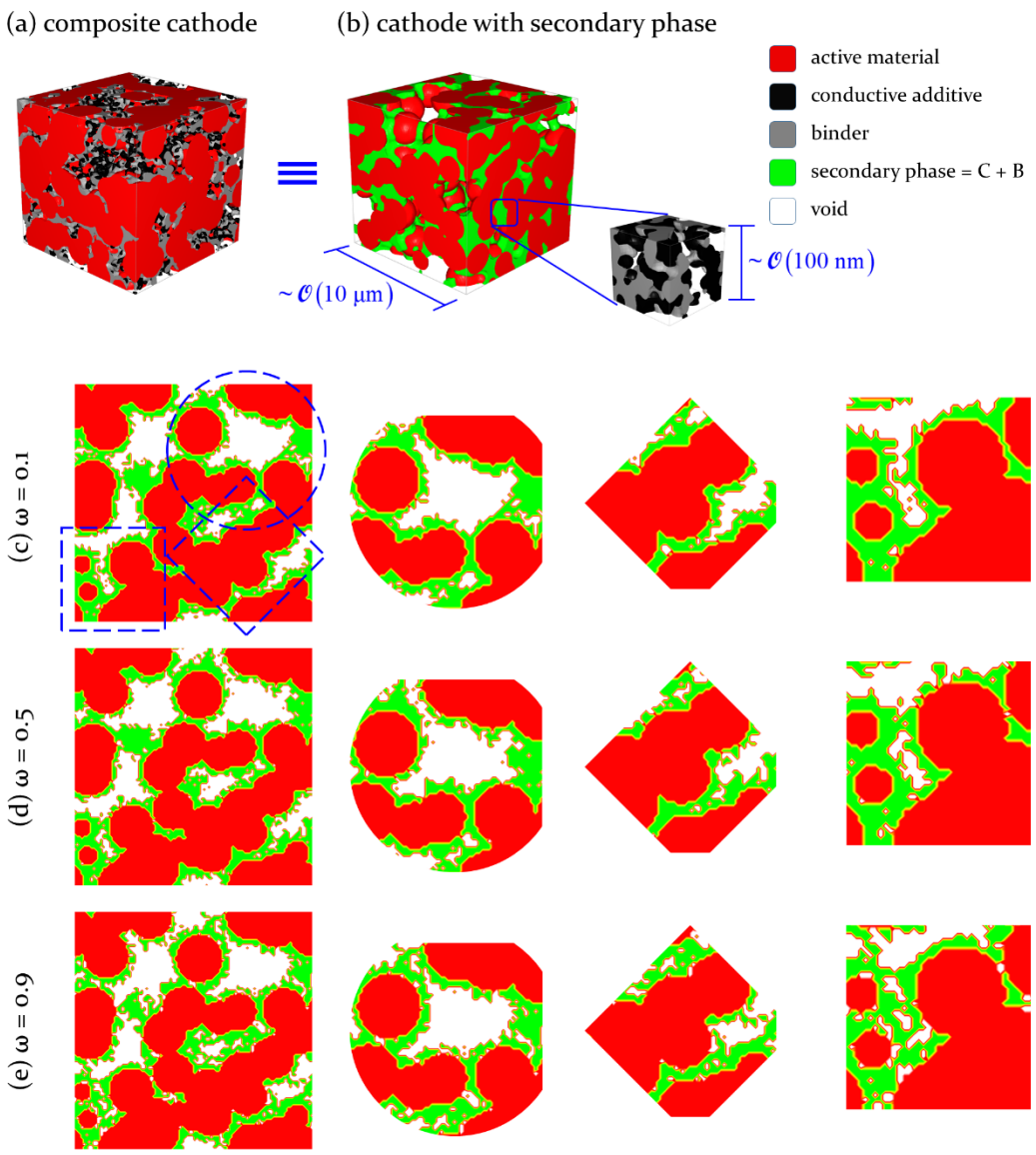

Figure 23. (a) A composite cathode for LIBs is made up of multiple phases: AM particles, conductive additives, binder, and voids for ionic transport. (b) Given the order of magnitude difference in length scales of conductive additives and AM, the distribution of conductive additives + binder (referred to as secondary phase or carbon binder domain) can be jointly expressed as a homogeneous phase. (c, d, e) The microstructure generation procedure outlined here grows the secondary phase with different morphologies varying between a film-type structure ($\omega = 0$) and a finger-like arrangement ($\omega = 1$). Also, going towards higher morphologies (*i.e.*, $\omega \rightarrow 1$) gives rise to a secondary pore network with a smaller pore size in thicker carbon binder domains.

These microstructural aspects are systematically translated to electrode scale to make performance predictions as well as provide new guidelines for electrode improvement. This modeling

philosophy (referred to here as pseudo direct numerical simulation, or pseudo-DNS) captures relevant, realistic electrode structure as well as marginalizing the computational cost. The calculations at different length scales are validated against limiting scenarios to ensure the veracity of predictions and subsequent suggestions.

2.2 Electrode Microstructure Complexations

Figure 23(a) shows a composite cathode structure with different solid phases. The AM particles are usually on the order of 1–10 μm, while conductive additives are comparatively much smaller (40–50 nm). This difference in length scale allows one to treat the conductive additive and binder as a joint phase.[25] This equivalent representation is depicted in Figure 23(b). Various experimental studies also identify the conductive binder domain (CBD) as a secondary phase,[27, 33, 63, 65] and relevant properties (especially electronic conductivity) have been measured and reported as a function of carbon-to-binder ratio. Here, the composite cathodes are generated in two stages. The first stage stochastically produces the AM skeleton, while the second stage adds the CBDs. The amounts of both AM and CBDs are calculated from a prescribed electrode composition (weight fractions of solids and porosity). Recently, an experimental study performed by the authors[83] found that for the same composition, the CBD phase distributes differently inside the electrode structure, and this secondary phase arrangement is a strong function of slurry drying conditions, especially evaporation rate (mesoscale simulations also revealed a similar dependence[164, 165]). These fabricated electrodes with the same composition and porosity exhibit distinct electrochemical response which in turn can only be explained based on different CBD phase arrangements. To emulate different CBD patterns, the secondary phase addition stage accepts an additional input, ω, referred to as morphology parameter, since it directly controls the spatial aspects of CBD growth on AM backbone. Qualitatively, the morphology parameter, ω, is a ratio of CBD's preference to deposit on pre-deposited CBD versus an uncovered AM surface. In other words, ω can be considered a ratio of the cohesive tendency of CBD to adhesive tendency forming CBD–AM contact and is thus related to interfacial energies[4] of CBD/CBD and CBD/AM interfaces. Smaller values of ω describe a CBD phase that has a strong affinity for AM and in turn cover more AM surface by forming a film-like secondary phase distribution. On the other extreme, a higher value of the morphology factor gives rise to a tentacle-like CBD phase arrangement as it has higher selectivity towards the pre-deposited CBD phase. For the present discussion, the morphology

factor is expressed as a normalized value falling in the range 0 to 1. Thence $\omega \rightarrow 0$ corresponds to layered deposits, while $\omega \rightarrow 1$ represents more three-dimensional fractal-like growth. These morphological variations are also presented in Figure 23(c) to (e). For these three structures, the AM backbone is identical. The same amount of CBD is added to these microstructures while only varying the morphology factor, ω. The first column presents the *x*-mid plane for a representative elementary volume (REV), and the successive columns magnify different locations on this slice to provide a better visual comparison across different morphologies. In addition to the morphological differences hypothesized based on the definition of ω, another interesting feature is also present. In closed corners, the higher morphologies have a secondary pore network of smaller pores taking shape in the CBD phase. Such an arrangement is expected to introduce additional pore transport resistance. (Note that these pores are filled with electrolyte in a cell, hence pore network resistance correlates to ionic transport resistance.) The algorithmic details to produce composite cathode structures are pictorially summarized in Figure 2, while associated subtleties like identification of appropriate REVs and spatial resolution for accurate porous media property calculations are discussed in the Supplementary Information (section S1). The present set of electrode microstructures and corresponding effective property relations are strictly valid for nickel manganese cobalt oxide (NMC) AM particles (proved to be spherical from tomography experiments[64, 80]), acetylene black (AB) as a conductive additive, and polyvinylidine difluoride (PVDF) as a binder, but the microstructure generation procedure is universally valid as well as the qualitative understanding of effective property and electrode performance trends. Note that the secondary phase arrangement results from the electrode preparation stage since the electrode microstructure is finalized at the end of drying. Thenceforth, electrolyte addition does not alter the secondary phase morphology. Sometimes it is observed that electrolyte is absorbed by the binder phase in excess quantities and leads to swelling of the CBD phase. This swelling physics is not considered here for the sake of simplicity.

Multiple composite cathode realizations are generated to map the different combinations of weight fractions, electrode porosity, and CBD morphology. Each of these structures is analyzed to quantify the interfacial area (pore–AM, AM–CBD, and pore–CBD), pore phase tortuosity, and the effective electronic conductivity (in all three coordinate directions). The resultant data set is studied to understand the trends in effective microstructural properties. Regression analysis expresses these effective properties as a function of electrode recipe (Table 1).

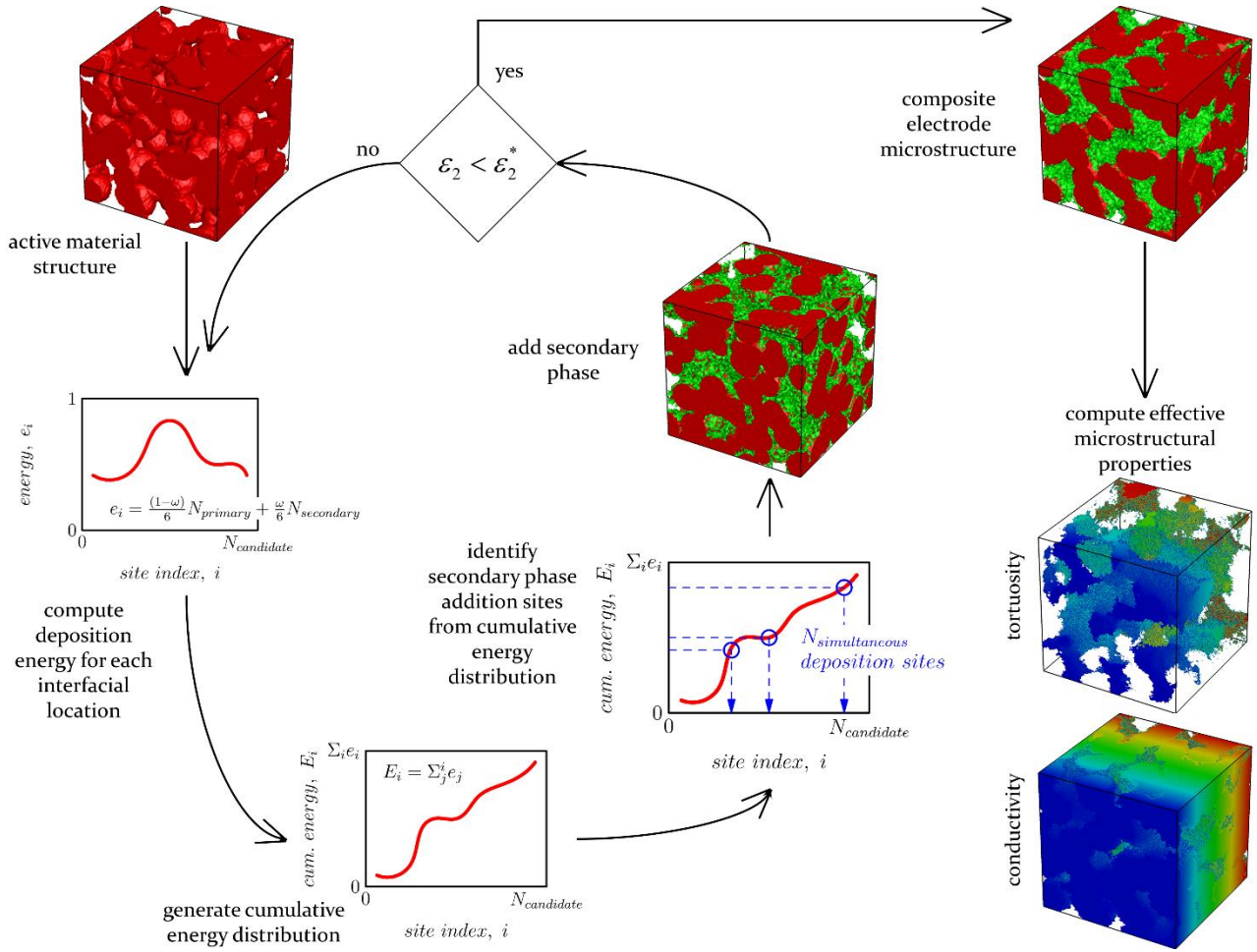

Figure 24. An overview of microstructure generation for composite LIB electrodes. The AM backbone is stochastically generated. The secondary phase addition starts with this AM structure. First, all the interfacial locations are identified, and an energy map generated to quantify the likelihood of secondary phase addition at that point. Subsequently, the cumulative energy landscape is generated to identify specific secondary-phase addition locations and a revised composite structure is obtained. If the prescribed amount of secondary phase is added, subsequent microstructural simulations are carried out; otherwise, further secondary-phase addition rounds are performed.

These functional forms (Table 1) reveal that the correlations are quite involved compared to traditionally assumed forms, *e.g.*, the Bruggeman relation for tortuosity. This is expected since the conventional relations for tortuosity and active area are strictly valid for a granular microstructure made up of non-overlapping monodisperse spheres,[101] while the composite cathodes for LIBs have appreciable amounts of the secondary solids. Moreover, for higher AM loading, the spherical particles overlap, and the microstructure departs further from the traditional assumption. (The details of effective property calculations are available in Computations for Effective Microstructural Properties, Comments on Bruggeman Relations and Extracting Correlations for Effective Microstructural Properties. Also, the limits of traditional relations are discussed therein.)

Table 1. Pore-scale simulations quantify effective microstructural properties as a function of electrode composition and secondary-phase morphology. Regression analysis helps quantify the functional form of these relationships.

Effective microstructural property	***Expression***	***Coefficient of determination,*** R^2
Pore–AM area[a]	$a_{01} = \left(-1.8079\left(1-\varepsilon-\varepsilon_2\right)^2 + 1.4103\left(1-\varepsilon-\varepsilon_2\right) + 0.9247\right) \cdot e^{-\varepsilon_2\left(28.2684+5.1843\varepsilon_2-21.9745\omega\right)}$	0.9981
AM–secondary phase area[a]	$a_{12} = \varepsilon_2\left(1-1.6119\varepsilon_2-0.0663\omega\right)\cdot \left(7.4654\left(1-\varepsilon-\varepsilon_2\right)^2 + 2.3173\left(1-\varepsilon-\varepsilon_2\right) + 4.2340\right)$	0.9341
Total AM surface area[a]	$a_{1(0+2)} = -3.5932\left(1-\varepsilon-\varepsilon_2\right)^2 + 4.3319\left(1-\varepsilon-\varepsilon_2\right) - 0.2483$	0.9580
Pore–secondary phase area[a]	$a_{20} = \varepsilon_2\left(1-1.8744\varepsilon_2+0.0521\omega\right) \left(-59.5423\left(1-\varepsilon\right)^2 + 74.1352\left(1-\varepsilon\right) - 10.3652\right)$	0.9435
Tortuosity	$\tau = \left(0.6768-5.1707\varepsilon_2+12.0492\varepsilon_2^2+0.5283\varepsilon_2\omega\right) \cdot \varepsilon^{-\left(1.2790+9.2521\varepsilon_2-22.9833\varepsilon_2^2-0.2939\varepsilon_2\omega\right)}$	0.7432
Conductivity[b]	$\sigma = \varepsilon_2\left(0.1839-0.4219\varepsilon+1.0475\varepsilon_2-0.0186\omega\right)$	0.9900
	[a] dimensionless area; divide by particle radius to obtain in m^2/m^3. [b] normalized conductivity; multiply by secondary-phase conductivity to obtain in S/m; secondary phase conductivity as a function of C/B ratio is expressed in Supplementary Information Figure 28(c).	

Different microstructural properties affect transport processes that govern the cell behavior, thus, in turn, dictating electrochemical operation. For instance, the electrochemically active area is responsible for providing reaction sites for intercalation to take place. Effective electronic conductivity quantifies the ease of electronic conduction, while pore phase tortuosity is an indicator of pore network resistance experienced by ionic conduction in the electrolyte phase. To express microstructural effects on these different transport modes, two dimensionless quantifiers are identified: reaction blockage quotient N_r, and pore network resistance quotient N_p (expressions (10) and (11)). As the amount of CBD increases in the electrode recipe, it covers more AM surface and effectively reduces the interfacial area available for intercalation reaction. This negatively affects the electrochemical reaction. Here, a is the active area of a given composite cathode, while a_0 is corresponding active area of the equivalent non-overlapping spherical particulate structure. Thence, $N_r \rightarrow 1$ quantifies increased reaction resistance. Similarly, the ratio of porosity (ε) to tortuosity (τ) expresses the effectiveness of ionic transport. Following the same concept as N_r, N_p describes the pore phase transport resistance. As N_p approaches 1, pore phase transport resistance becomes severe.

$$N_r = 1 - \left(a / a_0 \right) \tag{10}$$

$$N_p = 1 - \left(\varepsilon / \tau \right) \tag{11}$$

Note that the electrochemically active area is related to the AM–pore interface. For an electrochemical reaction to take place, one requires AM that could accept Li, contact with the electrolyte to have sufficient Li^+ as well as the presence of ample electrons. In addition, the spread in cell resistance data for same porosity and different AM loading electrodes[27] can only be explained if the pore–AM interface is treated as electrochemically active (Identifying the Electrochemically Active Area provides the necessary logical support). In other words, Li intercalation can only take place at the pore–AM interface as the pore–CBD interface blocks Li^+ flux. Thus, the electrochemically active interface is the pore–AM surface. Figure 25(a) and (b) sketch the dependence of N_r and N_p on porosity and CBD morphology for a fixed AM weight fraction (95% by weight). As expected, the electrode becomes favorable to electrochemical reactions at higher morphologies, *i.e.*, $\omega \rightarrow 1$ (Figure 25(a)). In addition, as the porosity increases from 20% to 40% (by volume) more interfacial area is available, and in turn, N_r decreases.

Figure 25. Description of electrode microstructural limitations: (a) The reaction blockage quotient Nr, quantifies the resistance to an electrochemical reaction based on electrochemically active area. (e) Correspondingly, electrode recipes can be classified into kinetically limited combinations. (b) The pore network resistance quotient, Np, identifies (f) transport-limited electrodes from porosity and tortuosity variations. (g) A joint picture of microstructural limitations based on electrode classification into kinetically limited and transport-limited recipes. (h) The subset of microstructurally efficient (lower resistance) recipes becomes smaller as AM loading is decreased (*i.e.*, secondary phase amount increases). Note that the results (a), (b), (e), (f) and (g) are for electrodes with 95% AM loading. (c) The effective electronic conductivity of most of the electrode composition is better than the corresponding effective ionic conductivity, thus leading to negligible electron conduction limitation, save for a few critical combinations; the values reported here are for $\omega = 1$, *i.e.*, lowest conductive morphology for the same amount of secondary phase, (d) The conductivity trends predicted from microstructural simulations match quite well with equivalent experimental measurements (G. Liu *et al.* 2012, J. Electrochem. Soc., 159 (3), A214).

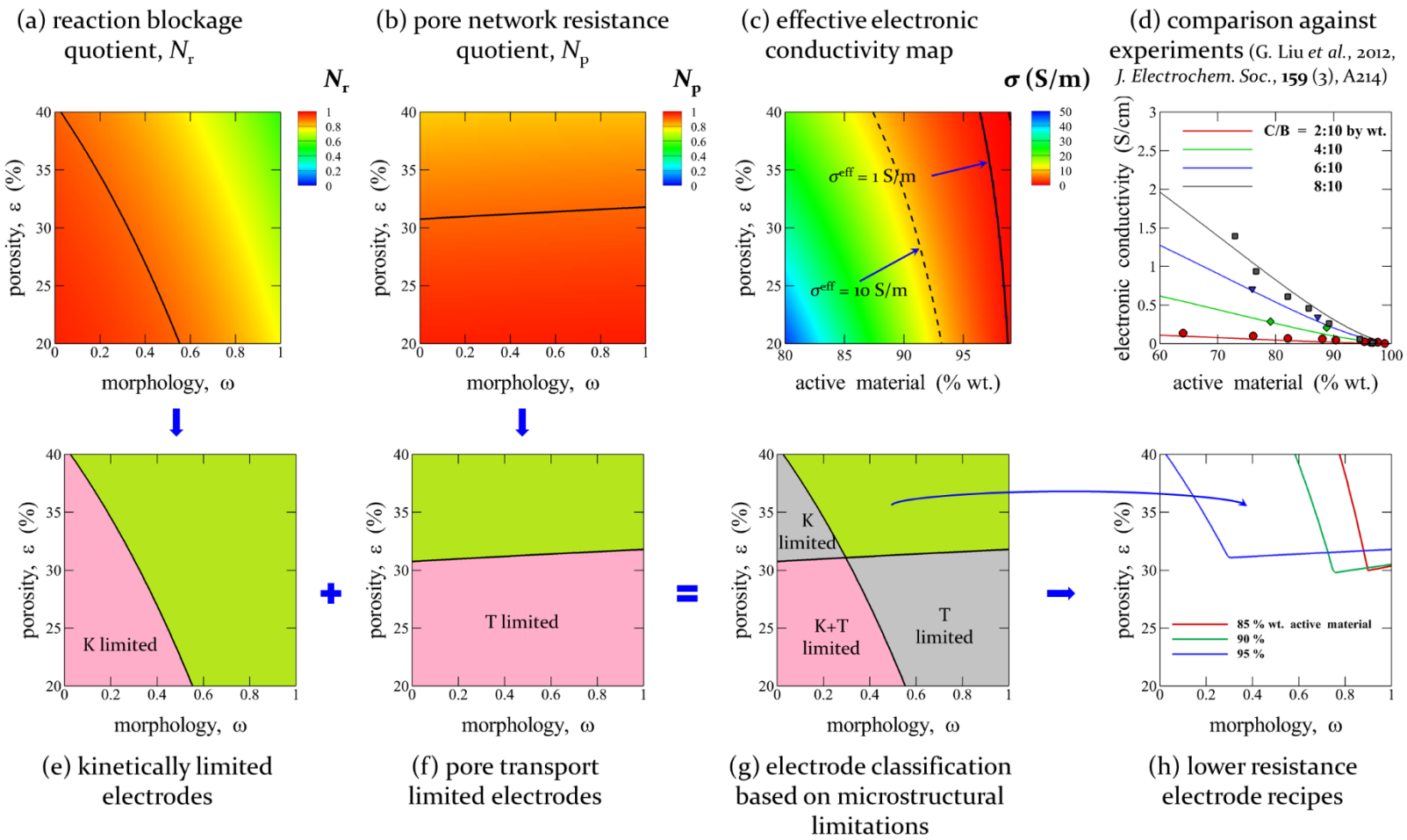

(e) kinetically limited electrodes

(f) pore transport limited electrodes

(g) electrode classification based on microstructural limitations

(h) lower resistance electrode recipes

Given this strong dependence on both electrode porosity and CBD morphology, the different electrodes presented in Figure 25(a) can be categorized into two regimes (Figure 25(e)) to identify the kinetically limiting recipes. Note that these trends are for 95% AM (by weight), and qualitatively similar maps can be plotted for other AM loadings. Examine Figure 25(b), which describes a similar dependence for pore network resistance N_p. As expected, higher electrode porosity leads to a smaller pore network resistance. An interesting trend is observed here. Higher morphologies ($\omega \rightarrow 1$) give rise to greater pore network resistance. Higher morphologies generate a tentacle-like CBD phase, which protrudes more in the pore phase and effectively creates more hindrance. Moreover, the secondary pore network (as identified in Figure 23(d) and (e)) is present in greater quantity. This pore network, given its smaller pore size, offers more resistance. Thus, these two effects lead to a higher tortuosity as CBD morphology is increased and presents higher pore network resistance, N_p. The pore network resistance map (Figure 25(b)), N_p, helps classify the electrodes into transport limiting and non-limiting recipes (Figure 25(f)). Qualitatively similar trends are experienced at different AM loading. Combining the kinetically and transport limited regions (Figure 25(e) and (f)), a comprehensive picture emerges for microstructural resistances of electrodes with 95% AM (Figure 25(g)). Note that both limitations do not necessarily occur simultaneously. For lower porosities and lower morphologies, the electrodes are both kinetically and transport limited. But there is a window of higher morphologies at lower porosities where the electrodes are not kinetically limited. And equivalently, a subset of smaller morphologies at higher porosities reveals that the electrodes are not transported limited. This is quite intriguing since it allows one to fine-tune electrode structures for the kinetically and transport limited operations separately. To express it differently, the functionality of the electrodes can be directly correlated to operational requirements. Figure 25(h) explores the effect of AM loading in terms of the resistance classifier diagram (Figure 25(g)). As AM loading decreases, the CBD amount for the same porosity increases, thus leading to a successively increasing reaction blockage. This expands the kinetically limited recipe towards higher morphologies ($\omega \rightarrow 1$). Another peculiar direction is apparent here. With decreasing AM loading, lower porosities also become accessible. To explain this, consider that the CBD phase is relatively amorphous in comparison to AM (since the CBD phase morphological features have a smaller length scale compared to AM particles). Thence, increasing the amount of CBD phase leads to a part of the AM volume being replaced by a relatively amorphous CBD phase, which in turn exhibits smaller tortuosity. Note that these maps

of different resistances comment on microstructural limitations over REV size, and this understanding is to be upscaled to electrode volume for a complete picture of physicochemical changes and resistance evolution during electrochemical operation (discussed later on). Such a description consistently accounts for microstructural multi-length scale features, different pore-scale transport processes, and experimentally observable electrochemical response.

The intrinsic ionic conductivity of the electrolyte is around 1 S/m (at a typical salt concentration).[24] Accounting for the porous cathode resistance, the corresponding effective ionic conductivity is on the order of 0.1 S/m ($\kappa^{eff} = \varepsilon \cdot \kappa / \tau$). A porous electrode gradually changes the identity of charge carriers from ions (*i.e.*, Li^+) to electrons and vice versa, with the total current at any cross-section along the thickness direction being constant and the same as the current flowing in the external circuit. Thus, a similar amount of current flows through both the electrolyte-filled pore network (related to ionic conductivity) and the composite solid phase (characterized by electronic conductivity). As long as the effective electronic conductivity of the solid phase is about an order of magnitude higher (*i.e.*, $\sigma^{eff} \geq 1$ S/m), the predominant voltage drop takes place in the electrolyte phase, and the solid phase offers comparatively negligible resistance to cell operation. Figure 25(c) sketches the variation of effective electronic conductivity as a function of electrode porosity and AM loading (% wt.). Two lines are identified to mark σ^{eff} = 1 S/m and 10 S/m, respectively. A CBD network made up of film-type deposits (ω = 0) represents better interconnections than a finger-like structure (ω = 1), thus giving rise to a higher conductivity for film-type deposits. Thence, to provide insights into the least-conductive secondary-phase network, Figure 25(c) demonstrates results for the ω = 1 morphology. The plot shows that except for a narrow band of AM loading and porosity combinations, most of the electrodes have reasonably larger electronic conductivities. Figure 25(d) compares conductivity predictions based on composite cathode modeling reported here against experimental data.[33] The experiments were performed with nickel cobalt aluminum oxide AM while keeping the same CBD phase constituents. The results reveal that the predictions account for all the measurements fairly well, thus justifying the truthfulness of composite electrode microstructure results.

2.3 Microstructure – Performance Interplay

The effective microstructure properties obtained here are appropriately integrated into a porous electrode theory-based electrochemical performance model. Special attention is paid to the

coupling between the porous electrode and the AM particle. Here, the volumetric current source term at the electrode scale is to be accurately translated to the boundary condition for AM particle dynamics, and the electrochemically active area definition becomes critical in conserving *Li* and Li^+ species fluxes. The mathematical details are presented in the Electrochemical Performance Model. Figure 26(a) presents a comparison of model predictions against experimental discharge measurements for 25-μm-thick NMC electrodes.[29] The electrode composition, porosity, particle size, *etc.*, are supplied with the experimental study.[29] Since the morphology is not reported experimentally, ω was tuned to obtain the best fit across a range of C-rates. The suitability of this pseudo-DNS model to make predictions is expressed through this comparison where a reasonable match is obtained over a wide range of C-rates. There appears a slight qualitative mismatch towards the end of discharge at higher rates, and it is the authors' opinion that this arises from concentration-dependent solid-state diffusivity. The present set of electrochemical predictions are with a constant solid-state diffusivity. (The contribution of this concentration overpotential is expected at higher rates, as is evident in Figure 26(c).) The electrochemical response of a Li-ion cell is the combination of four transport processes (the ionic transport in the electrolyte phase is closely tied to charge conservation):

1. *Li* conservation in AM particles
2. Intercalation reaction at the particle–electrolyte interface, representing the change in the identity of charge carriers
3. Charge conservation in the solid phase (electronic charge – e^-)
4. Charge conservation in the electrolyte phase (ionic charges – Li^+ and PF_6^-; electrolyte salt is $LiPF_6$).

Based on the rate of current flow (*i.e.*, C-rate), each of these processes offers different resistances that jointly manifest as cell internal resistance. To study the evolution of different types of resistances, a thin cathode (25 μm, 30% porosity, 90 wt% AM, ω = 0.5) is studied over a wider range of C-rates: C/5 to 50C. Figure 26(b) presents the corresponding rate capability simulations. The inset shows the dependence of discharge energy on C-rate. The ideal limit for cell energy in a given electrode volume is it being fully packed with AM and following open circuit potential. This theoretical limit is used to non-dimensionalize the discharge energy values in the present work. It can be seen from Figure 26(b) that at lower discharge rates, the cell voltage approaches that of the open circuit potential (for any electrode composition, cell voltage *vs.* capacity expressed as per

unit weight of AM approaches the open circuit potential as the C-rate is decreased; the maximum theoretical energy is achieved when the entire electrode volume is filled with AM and non-intercalating phases are absent, but such an electrode exhibits severe operational limitations), and as the C-rate increases, the cell overpotential increases monotonically, leading to successively lower average voltages as well as discharge capacities. Corresponding discharge energy trends are supplied in the inset image. Due to the composite nature of the porous cathode (*i.e.*, the presence of non-intercalating phases), the discharge energy saturates at less than 100% in the zero C-rate limit (C-rate → 0). Each of the different transport processes leading to electrochemical operation of these electrodes has an associated contribution to total overpotential (consider definitions (12) through (15)).

<u>*Concentration overpotential*</u>:

$$\eta_c = \frac{1}{L_{\text{cat}}} \int_{L_{\text{cat}}} \left\{ U\left(C_s^f\right) - U\left(\bar{C}_s\right) \right\} \mathrm{d}x \tag{12}$$

<u>*Kinetic overpotential*</u>:

$$\eta_k = \frac{1}{L_{\text{cat}}} \int_{L_{\text{cat}}} \eta_{\text{Butler-Volmer}} \, \mathrm{d}x \tag{13}$$

<u>*Ohmic drop in solid phase*</u>:

$$\eta_\sigma = \Delta\phi_s \big|_{0-L_{\text{cat}}} \tag{14}$$

<u>*Ohmic drop in electrolyte phase*</u>:

$$\eta_\tau = \Delta\phi_e \big|_{0-L_{\text{cat}}} \tag{15}$$

Each of these overpotentials is equivalently expressed in terms of internal resistance components, *i.e.*, R_k, R_c, R_τ, and R_σ. These resistances averaged over the cell operation at each of these C-rates are quantified and expressed in Figure 26(c). Since the electrode conductivity for this baseline is large enough (σ^{eff} = 12.142161 S/m >> 0.1 S/m), the solid-state conduction resistance is quite negligible (inset in Figure 4 (c)). The electrolyte phase ohmic resistance (related to tortuosity) manifests more strongly for thicker electrodes; hence, the kinetic resistance and diffusional resistance of the AM particles (R_c) largely dominate the internal resistance evolution over a range of C-rates for this cathode (Figure 26(c)). As the C-rate increases, the contribution of kinetic overpotential decreases due to the logarithmic dependence of Butler-Volmer kinetics. On the other hand, the particle concentration gradients become more severe at higher rates, thus leading to an increased contribution from particle resistance (*i.e.*, concentration overpotential).

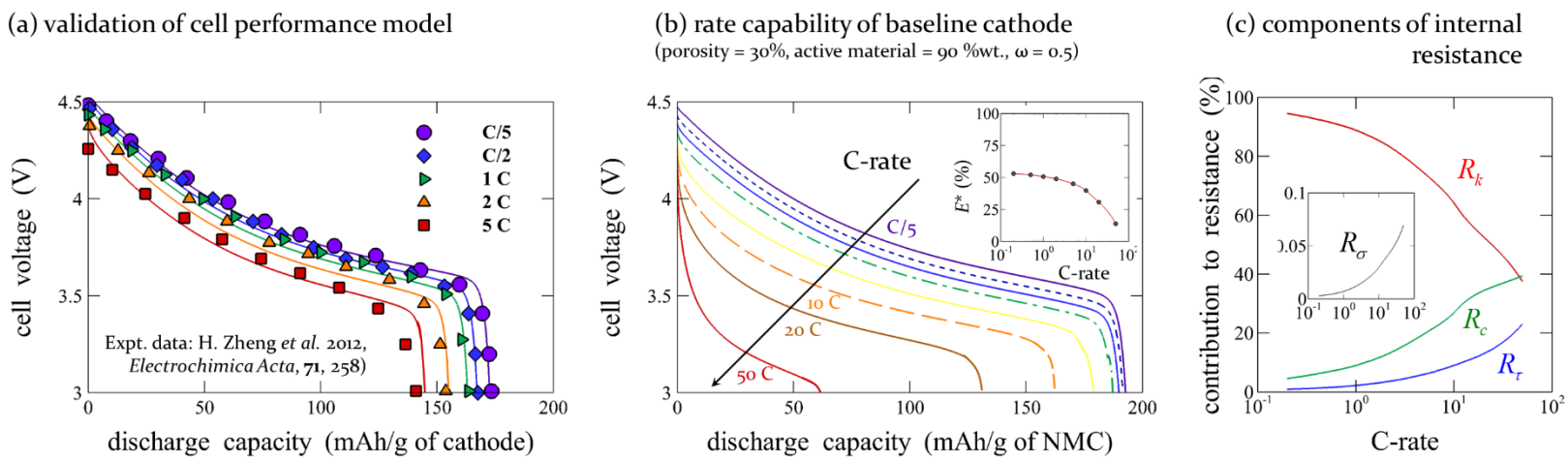

Figure 26. (a) Comparison of experimental results and predictions from pseudo DNS model shows that the simulations match quite accurately with measurements for 25-µm-thick electrode samples over a range of discharge rates. A slight mismatch in the qualitative nature towards the end of discharge is expected to be a result of concentration-dependent solid-state diffusivity (the constant value used for present simulations). (b) Rate capability of a baseline cathode (30% porosity, 90% wt. AM and ω = 0.5) is expressed over eight different C-rates varying over four orders of magnitude. The inset figure shows discharge energy as a function of C-rate (normalized using maximum volumetric energy if the cathode were filled with AM alone). (c) Evolution of different components to internal resistance over C-rate range simulated in (b). Inset figure shows that solid state conductivity limitation is quite negligible since σeff = 12.142161 S/m for this recipe and equivalently electron conduction is quite efficient compared to electrolyte phase transport.

In addition, the electrolyte phase transport resistance (which is often believed to be only responsible for thicker electrodes) also starts playing an important role towards higher C-rates. In conclusion, for a thin electrode, kinetic resistance dominates the internal resistance evolution and should be targeted for performance improvement. These resistance evolution trends are expected to be different for thicker electrodes. A comprehensive study discussing the thin and thick electrodes and suitable microstructural improvements will be reported in a future publication.

From resistance evolution (Figure 26(c)), it is suggested that reducing kinetic resistance should lead to improved electrode performance. The corresponding electrode is marked on a resistance classifier diagram (Figure 27(a)). Given the insights obtained from Figure 25, if one increases the AM loading (keeping the same porosity), reduced CBD uncovers more active area. Hence, AM loading is increased from 90% to 95%, and it expands the region of lower resistance electrode recipes on the resistance classifier diagram. Next, since the transport resistance is not dominant, porosity can be reduced to pack more AM (Figure 25(g) reveals that for this morphology, $\omega = 0.5$, the porosity reduction does not make the electrode kinetically limiting). Thus, porosity is reduced from 30% to 25%. Next, to reduce the kinetic resistance further, the secondary phase morphology is made more finger-like (from $\omega = 0.5$ to 1.0). These successive microstructural changes are demonstrated on the microstructure resistance map in Figure 27(a). A corresponding decrease in kinetic resistance plotted in Figure 27(b) shows that each of these steps decreases kinetic resistance consistently and improves performance (Figure 27(b) inset). Comparison of discharge performance (Figure 27(b) inset and Figure 27(c)) between the baseline and final microstructure reveals that the average cell voltage improves by about 0.1 V, and discharge energy increases by 12% on an absolute basis (~25% on a relative basis). Each of these intermediate recipes is described in Figure 27(d), along with dry electrode density, which reveals that the electrode density also increased consistently, signifying higher AM loading. The intriguing aspect of this electrode microstructural tuning is that without the understanding of the microstructural resistance map (Figure 25(g) and (h)), and components of internal resistance for the baseline recipe, one would not know which aspect to be improved upon. The steps like reducing porosity may seem counter-intuitive but with a thorough understanding of the electrode dynamics, one can make informed decisions. Figure 27(e) and (f) explore the correlation between cell performance and changes in secondary phase morphology.

Figure 27. Cathode performance can be improved by rational electrode microstructure tuning based on microstructural limitation maps (a). Baseline electrode microstructure is tuned in three stages: (○→Δ) the region of lower resistance is expanded by increasing AM loading (Δ→□) major contribution to internal resistance is due to kinetic limitation; hence, porosity is decreased while in the non-kinetically limiting microstructural zone (□→◊), the electrode is made kinetically more efficient by making secondary phase morphology more finger-like, thus providing higher active area. (b) The corresponding improvements in kinetic resistance are quantified over the range of C-rates. The inset shows equivalent enhancement in discharge energy. (c) This microstructural tuning also improves gravimetric cell performance. Average voltage improves by an order of 0.1 V. (d) Corresponding microstructural specifications are tabulated, along with dry electrode density. (e) and (f) quantitatively explain cell performance improvement by changing secondary phase morphology (extreme cases are shown). These electrodes have 30% porosity, 95%by weight AM, the carbon-to-binder ratio is kept 1:1 by weight. As secondary phase distribution changes from film-type ($\omega = 0.0$) to finger-like ($\omega = 1.0$), kinetic resistance decreases by about 20%, leading to improved cell performance and discharge characteristics.

(a) electrode modifications identified on microstructure limitations map

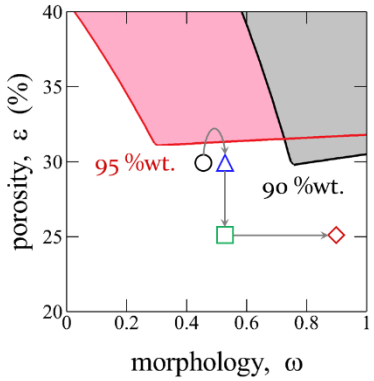

(b) reducing kinetic resistance = improved energy

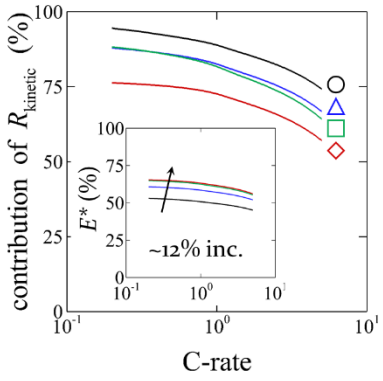

(c) performance improvement upon microstructural tuning

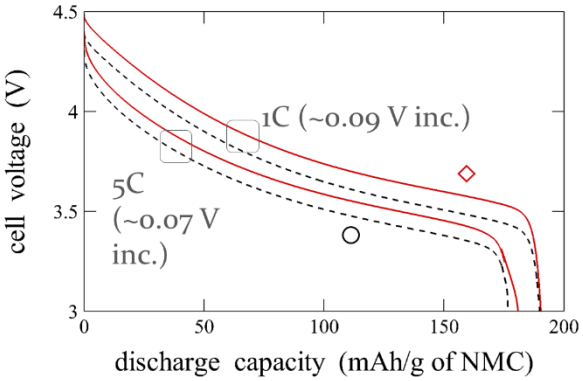

(d) electrode recipes

Electrode	Porosity (% vol.)	AM loading (% wt.)	ω	ρ^{eff} (g/cc)
○	30	90	0.5	2.88
△	30	95	0.5	3.09
□	25	95	0.5	3.31
◇	25	95	1.0	3.31

- (e) and (f) compare effect of morphology on electrode performance
- Effective density is dry electrode density
- All the electrodes have C/B = 1.0 by wt.

(e) kinetic resistance = f(morphology)

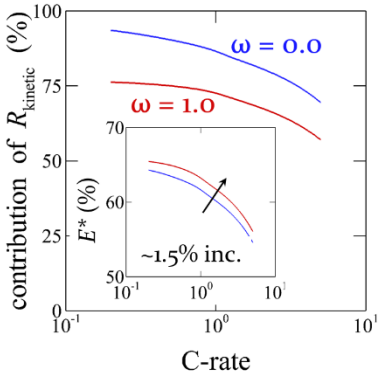

(f) effect of secondary phase morphology on performance

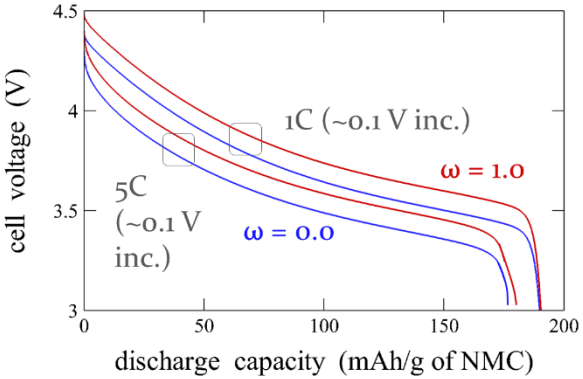

Without any change in porosity or AM loading, changing the CBD phase pattern from film-like to finger-type reduces kinetic resistance by about 20%, improves energy by 1.5% on an absolute basis (and ~2.5% on a relative basis), and boosts cell voltage by 0.1 V. Note that these improvements are proposed based on the mathematical understanding of microstructural limitations and should be experimentally verified for completeness. The confidence in the present discourse stems from different sets of comparisons (with experimental data) carried out to ensure the veracity of the microstructure and performance descriptions.

The present investigation probes the intricate relationship between the electrode microstructural arrangement and electrochemical performance for an LIB composite cathode. The non-intercalating solids (conductive additive and binder) exhibit nonlinear effects with respect to electrochemical performance. In small proportions, they ensure sufficient electron conduction and mechanical rigidity, but they also reduce the available reaction sites by reducing AM–electrolyte contact when used in excess. In addition, the pore phase transport resistance (which is often expressed in terms of tortuosity) decreases as the CBD phase content is increased. Quite interestingly, the specific arrangement (morphology) of the secondary phase is also found to critically influence various forms of microstructural resistances. Here, short-range (kinetic) and long-range (related to ionic and electronic conduction) resistances are quantified as a function of electrode recipes, and joint microstructural limitation maps have been reported.

This accurate microstructural information (in terms of effective properties) is suitably translated to electrode scale to study the resulting electrochemical response. Electrochemical operation of LIB cathodes is affected by four kinds of overpotentials: kinetic, concentration, and ohmic (in solid and electrolyte phases). They are expressed in terms of resistances to identify C-rate dependence and isolate the dominant limiting transport phenomenon. This understanding of microstructural limitations and evolution of internal resistance components with C-rate opens new avenues for improving cell performance *via* electrode microstructural modifications. As an example, a thin electrode (for which electrode thickness is of the same order as the REV dimension) is explored for microstructural modifications. From rate capability data on the baseline electrode, it is found that kinetic resistance is the most limiting. Correspondingly, electrode modifications are suggested to reduce kinetic resistance, and such changes bring about improvement in electrode performance (*i.e.*, voltage, capacity, energy, and power). Since the studied thin electrodes are kinetically limiting, finger-like CBD morphologies ($\omega \rightarrow 1$) are favorable. Appropriate controlled

experiments should be carried out to compare against these recommendations and identify unresolved physics if any.

2.4 Microstructure Generation for Composite Cathodes in LIBs

The composite cathodes have two distinct solid phases: AM and secondary phase (carbon binder domains). Correspondingly, the microstructure generation is carried out in two steps. The first step stochastically generates an AM backbone, which serves as a background phase for secondary phase addition. The secondary phase addition takes place at the solid–pore interface. An overview of the procedure is presented in Figure 24.

Note that the microstructure generation takes place in a controlled volume. In other words, these algorithms require one to prescribe volume fractions of different solid phases. On the other hand, experimental electrode recipes are prescribed in terms of electrode porosity and weight fractions of different solid phases. Using the bulk density of solid phases and electrode porosity, corresponding volume fractions are obtained, and they, in turn, serve as inputs to the microstructure generation routines. These relations expressing interconversion of solid-phase loading and related volume fractions are summarized hereafter.

$$\varepsilon_{AM} = \frac{\left(w_{AM} / \rho_{AM} \right)}{\left(\frac{w_{AM}}{\rho_{AM}} + \frac{w_C}{\rho_C} + \frac{w_B}{\rho_B} \right)} (1-\varepsilon) \tag{16}$$

$$\varepsilon_{C} = \frac{\left(w_{C} / \rho_{C} \right)}{\left(\frac{w_{AM}}{\rho_{AM}} + \frac{w_C}{\rho_C} + \frac{w_B}{\rho_B} \right)} (1-\varepsilon) \tag{17}$$

$$\varepsilon_{B} = \frac{\left(w_{B} / \rho_{B} \right)}{\left(\frac{w_{AM}}{\rho_{AM}} + \frac{w_C}{\rho_C} + \frac{w_B}{\rho_B} \right)} (1-\varepsilon) \tag{18}$$

Note that the secondary-phase addition algorithm also requires an additional input: ω, morphology factor. There are three length scales associated with the microstructures generated here:

- Active material particle size (radius R)
- Domain size (length L)

- Smallest length scale (resolution Δ)

Since NMC particles are spherical and there is no specific directional ordering, cubical electrode structures suitably express microstructure information. The domain length should be large enough to accommodate enough particles to capture their statistically averaged behavior.

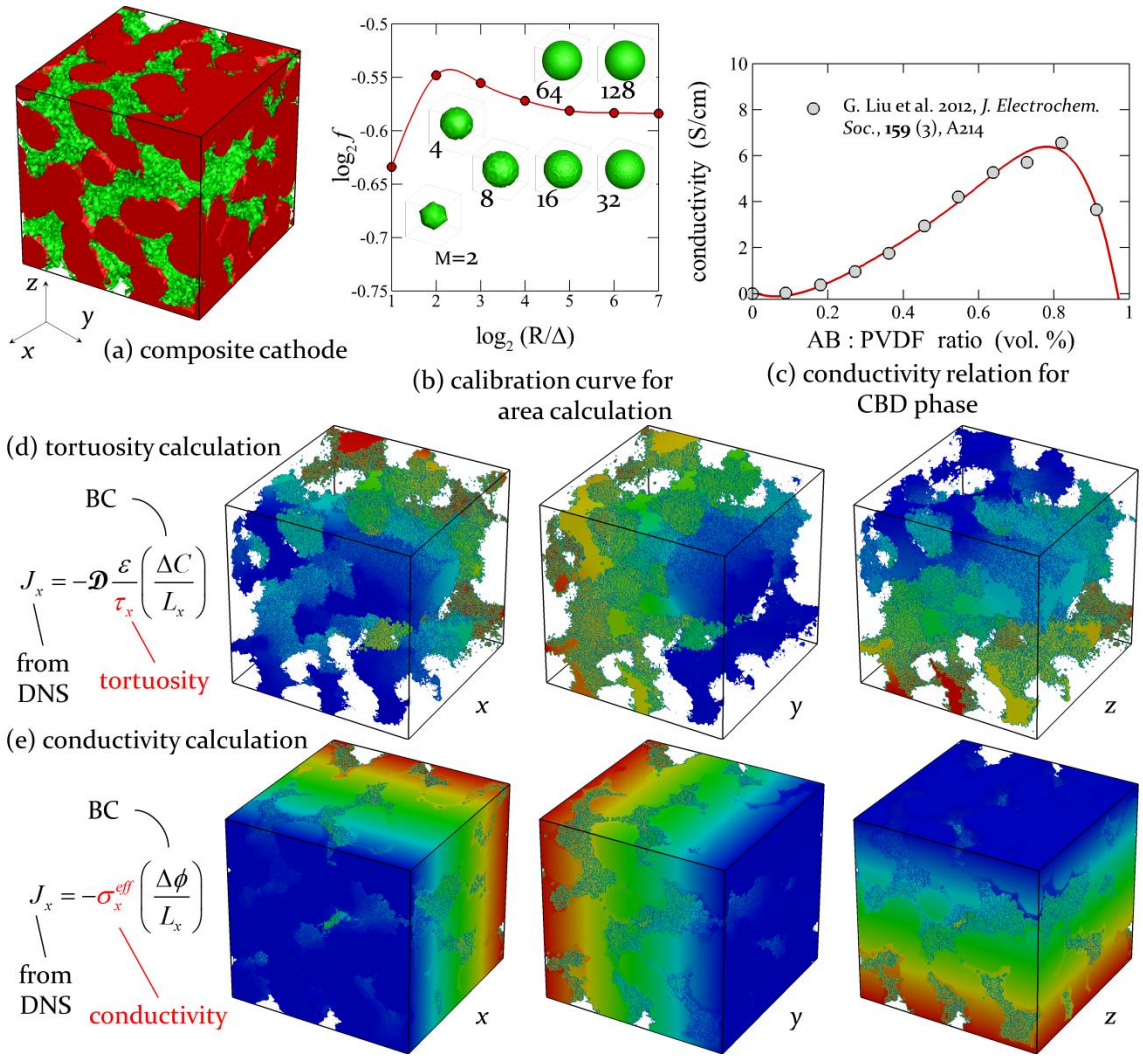

Figure 28. Effective property calculations: (a) composite electrode structure, (b) calibration curve for specific surface area calculations, (c) conductivity of secondary phase expresses as a function of C/B ratio (experimental data as well as fitted functional dependence), (d) tortuosity, and (e) effective conductivity calculations in three orthogonal directions.

Simultaneously, the resolution should be small enough to account for the smallest relevant detail, *e.g.*, the secondary-phase arrangement in the present situation. To reduce the number of simulations as well as to unify the results, the subsequent calculations are performed on

dimensionless grids (non-dimensionalized using the particle radius R). Thus, one has to ensure that the computation is insensitive to L/R and R/Δ ratios. In other words, L/R should be large enough to represent a statistically meaningful sample (representative elementary volume, REV), and R/Δ should be large enough to account for subscale details. Such independence tests are performed in terms of effective microstructural properties, and suitable ratios are found to be $L/R = 10$ and $R/\Delta = 10$.

2.5 Computations for Effective Microstructural Properties

Once the composite electrode structure is available as detailed in Microstructure Generation for Composite Cathodes in LIBs, it is analyzed to obtain equivalent effective microstructural properties. Effective microstructure properties, *e.g.*, tortuosity, abstract the 3D microstructural behavior in terms of fewer degrees of freedom.[9] Such an abstraction is only possible when the microstructure is large enough to account for the statistically meaningful number of details, *i.e.*, the REV size criterion is met. In the context of LIB electrodes, three properties are of interest:

- Electrochemically active area
- Tortuosity of the pore phase
- The effective electronic conductivity of the solid phase.

These three correlate to different transport processes taking place inside a Li-ion cell. In a composite electrode, multiple two-phase interfaces are formed: pore–AM, AM–CBD, and CB–pore. In addition, the total AM surface area is also a quantity of interest; thus, four different surface areas are to be characterized.

2.5.1 Specific surface area

The calculation for the specific surface area uses a slightly modified version of the Minkowski method. The essential idea is to compute the number of faces representing a particular interface of interest. For example, $I_{i=0,j=1}$ is the number of faces having a pore (i = 0) and an AM (j = 1) cell on either side. Next, since the surface area of a sphere is known analytically ($4\pi r^2$), the number of surface faces for a digitized sphere (Figure 28(b)) is computed. Let a sphere with radius $r = N\Delta$ have I_N number of faces. Since for discrete spheres with smaller radii are quite crude approximations, $f = N^2/I_N$ is computed for different approximations, and the converged value is

taken as a descriptor of spherical approximation (Figure 28(b) shows such a calibration curve). Later on, the interfacial area of any geometry is given by the following expression:

$$S = I_{ij} \cdot \frac{4\pi r^2}{I_N} = 4\pi I_{ij} f \Delta^2 \tag{19}$$

Equivalently, the specific surface area can be expressed as:

$$a = \frac{4\pi I_{ij}}{M_x M_y M_z \Delta} \cdot f \tag{20}$$

where M_x, M_y, and M_z are the number of cells representing the electrode geometry in each direction (here 100 each).

2.5.2 Pore phase tortuosity

The concentration balance equation (21) is solved in the pore phase to estimate pore phase tortuosity.

$$\nabla^2 C = 0 \tag{21}$$

For the tortuosity computation in the x-direction, the following boundary conditions are applied:

$x = 0$ face: $x = L_x$ face: (22)

$$C(x=0) = 0 \qquad C(x = L_x) = 1$$

Other four planes ($y = 0$, $z = 0$, $y = L_y$ and $z = L_z$): (23)

$$\partial C / \partial n = 0$$

Note that expression (21) is solved only in the pore phase. The discretization is performed in a finite volume fashion, and BiCGstab matrix solver[166] is employed to solve the linear equations expressing the elliptic equation (21). Once the solution is available, the species flux at $x = 0$ interfaces is computed (given the conservative nature of the governing equations, the flux leaving the $x = L_x$ face is identical) *via* integrating over pore faces:

$$J_x = -\int_{x=0 \text{ plane}} \left. \frac{\partial C}{\partial x} \right|_{x=0} \mathrm{dydz} \tag{24}$$

The corresponding tortuosity is computed from equality (25):

$$J_x = -\frac{\varepsilon}{\tau_x}\left(\frac{C(x=L_x) - C(x=0)}{L_x}\right) = -\frac{\varepsilon}{\tau_x}\left(\frac{1}{L_x}\right) \tag{25}$$

Note the transport coefficient, $\mathcal{D}_{pore}$ is set to one. To compute tortuosities in the y and z directions, the set of boundary conditions (22) - (23) and equality (25) are suitably rearranged. Figure 28(d)

pictorially shows the concentration solutions for the tortuosity calculations in each of the coordinate directions (the composite electrode structure is the same as Figure 28(a)).

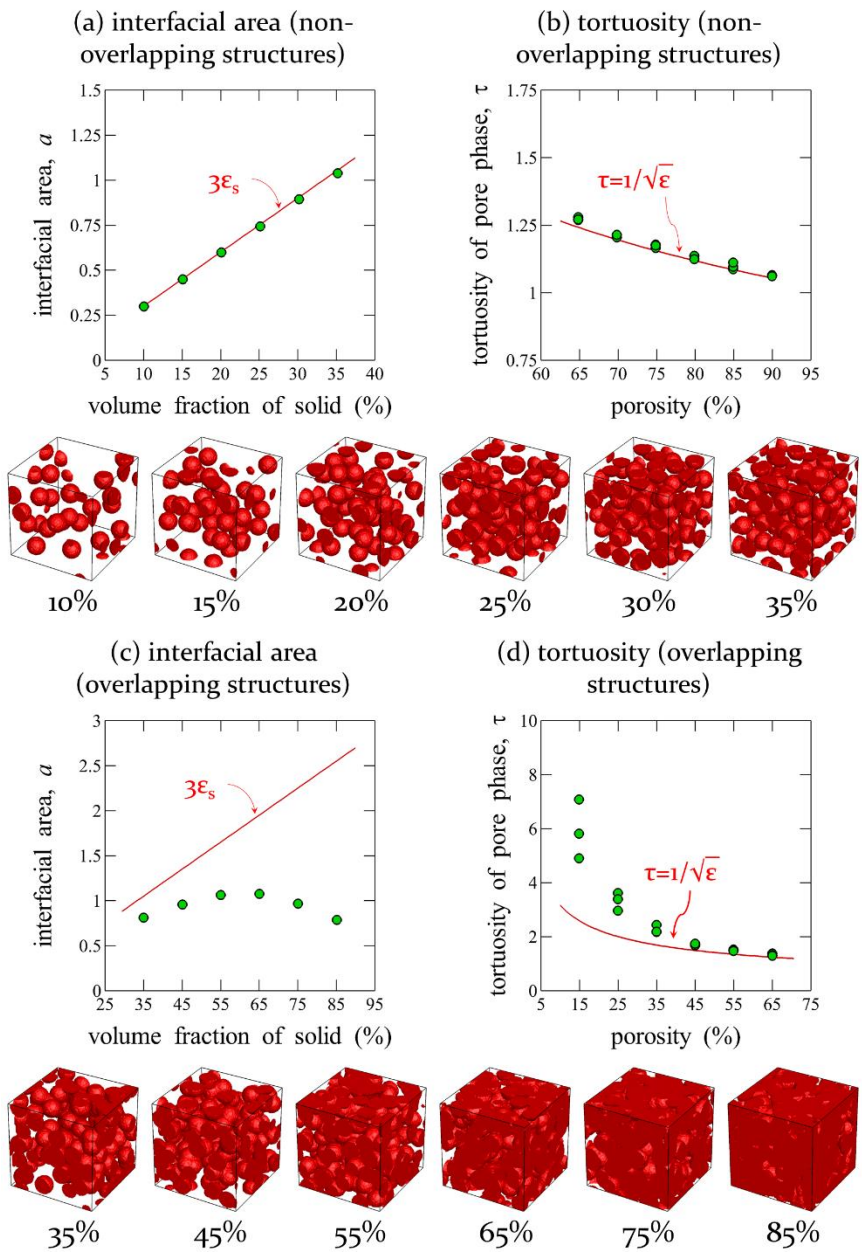

Figure 29. The conventional relations for the interfacial area and pore-phase tortuosity are strictly valid for microstructures with non-overlapping spherical particles. Such a situation arises when solid loading is smaller (<40%). For higher amounts of solid phases, the particles overlap, and the corresponding microstructural property relations depart from the conventional relations. Note that the dimensionless interfacial area is presented here. The corresponding microstructures are also shown alongside.

2.5.3 Solid-phase effective electronic conductivity

The calculation for solid-state electronic conductivity is similar to pore-phase tortuosity with minor changes. The governing equation is also an elliptic partial differential equation but with different transport coefficients in AM and CBD phase.

$$\nabla \cdot \left(\sigma \nabla \phi \right) = 0 \tag{26}$$

For simplicity and faster convergence, the conductivities are normalized using CBD phase conductivity corresponding to each of the secondary phase compositions (Figure 28(c)). The conductivity values at AM/CBD interface are estimated using the harmonic mean of the neighboring cells. The boundary conditions are applied in a similar fashion as tortuosity calculations. The electronic flux is computed at $x = 0$ interfaces as:

$$J_x = -\int_{x=0\ \text{plane}} \sigma \left. \frac{\partial \phi}{\partial x} \right|_{x=0} \mathrm{dydz} \tag{27}$$

Next, the effective electronic conductivity is back-calculated using the following identity (28):

$$J_x = -\sigma_x^{eff} \left. \frac{\partial \phi}{\partial x} \right|_{x=0} = -\sigma_x^{eff} \left(\frac{1}{L_x} \right) \tag{28}$$

The treatment for y and z direction conductivity calculations are straightforward. Figure 28(e) shows the solid-phase potential solutions for conductivity calculations in these three. Note that since the microstructures discussed here are isotropic, the effective properties do not exhibit any directional dependence.

Table 2. The porous granular structure composed of overlapping spherical particles exhibits quite different property relations compared to that of the one with non-overlapping particles.

Effective property	***Conventional relations***	***Based on pore-scale simulations***	
		Expression	***Coefficient of determination, R^2***
Specific surface area, a	$\left(a \cdot R\right) = 3\left(1-\varepsilon\right)$	$\left(a \cdot R\right) = -4.4079\left(1-\varepsilon\right)^2 + 5.2748\left(1-\varepsilon\right) - 0.5055$	0.9904
Pore phase tortuosity, τ	$\tau = \varepsilon^{-0.5}$	$\tau = 0.8025 \cdot \varepsilon^{-1.0244}$	0.9394

2.6 Comments on Bruggeman Relations

The traditional treatment of microstructure in LIB modeling[3, 167] assumes that all the particles are spherical and their surfaces are completely available for intercalation (no accounting for partial coverage due to secondary solids). This leads to the specific area relation (29), where ε_s is volume fraction of the solid (AM) phase:

$$a = \frac{3\varepsilon_s}{R} \tag{29}$$

Similarly, it is assumed that the pore-phase tortuosity is described by Bruggeman relation[101] (30):

$$\tau = 1/\sqrt{\varepsilon} \tag{30}$$

Both these relations are strictly valid for a porous structure made up of spherical non-overlapping particles according to the model assumptions. This is confirmed by pore-scale simulations shown in Figure 29(a) and (b). This occurs for lower solid fractions (<40% by volume). For high-power lithium batteries, the trend is to push for higher AM loadings. If AM loading is increased, the trends diverge from the conventional relations (29) and (30) as apparent in Figure 29(c) and (d). Regression analysis is performed on this dataset with higher solid fraction and the corresponding relations are tabulated in Table 2. The area expression has quadratic terms, while the Bruggeman exponent also increases from 0.5000 to 1.0244 to accommodate increased pore-phase tortuosity.

The close match between the traditional relations and pore-scale simulations in the lower solid fraction limit also establishes the validity of these microstructural characterization routines. Thus, microstructural results have been validated against traditional relations for AM structure as well as conductivity results for composite electrodes (Figure 25(d)).

2.7 Extracting Correlations for Effective Microstructural Properties

To comprehend the effects of electrode composition and secondary phase morphology on effective microstructural properties, different microstructures with a range of porosities, secondary phase loading, composition, and morphology are generated. Each of them is characterized using the routines described earlier to abstract the microstructural information in terms of effective properties. This resultant data set is analyzed to correlate different properties.

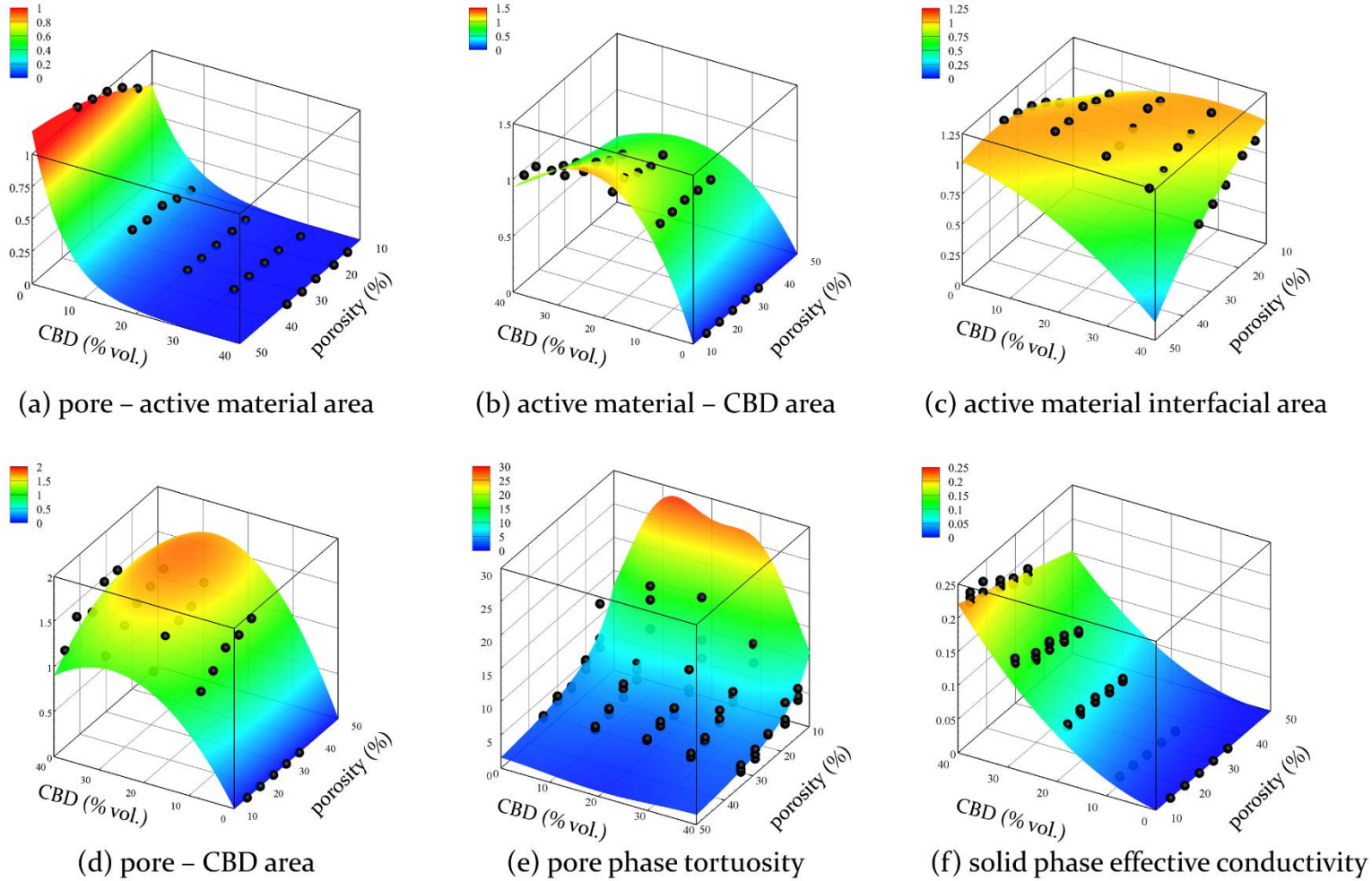

Figure 30. A comparison against electrode characterization (dots) and functional property relations (surfaces) obtained from regression analysis at a particular morphology ω = 0.5. The functional relations appear to capture the microstructural behavior quite well for different microstructural properties: (a) pore–AM area, (b) AM–CBD area, (c) total AM surface area, (d) pore–CBD area, (e) pore phase tortuosity, and (f) solid-phase electronic conductivity (normalized with respect to CBD phase conductivity).

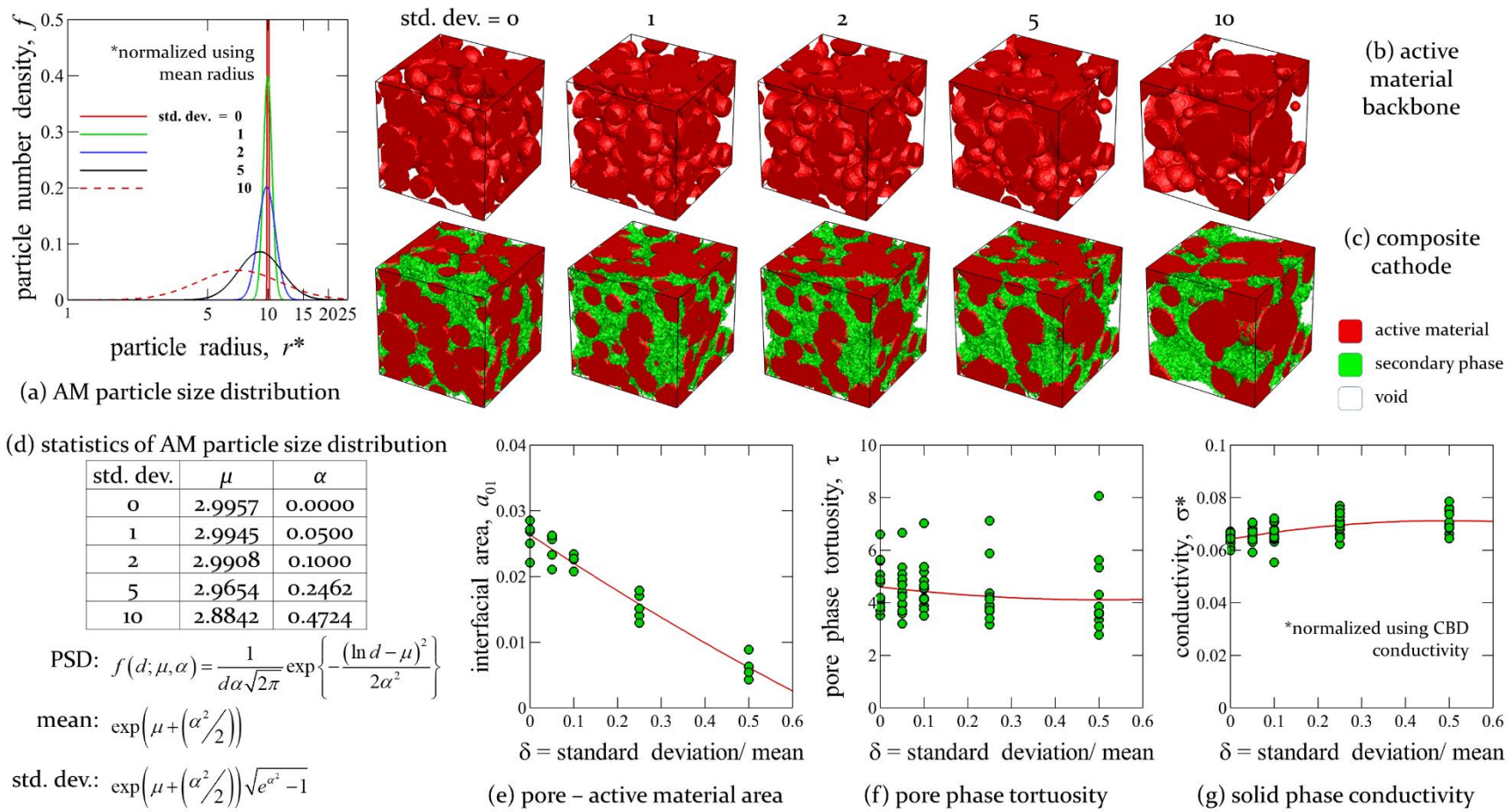

(d) statistics of AM particle size distribution

std. dev.	μ	α
0	2.9957	0.0000
1	2.9945	0.0500
2	2.9908	0.1000
5	2.9654	0.2462
10	2.8842	0.4724

PSD: $f(d;\mu,\alpha)=\frac{1}{d\alpha\sqrt{2\pi}}\exp\left\{-\frac{(\ln d-\mu)^2}{2\alpha^2}\right\}$

mean: $\exp\left(\mu+\left(\alpha^2/2\right)\right)$

std. dev.: $\exp\left(\mu+\left(\alpha^2/2\right)\right)\sqrt{e^{\alpha^2}-1}$

Figure 31. Effect of AM particle size distribution on microstructure and effective properties. (a) Five different particle size distributions, all with the same mean and different standard deviations are studied. Corresponding (b) AM backbone and (c) composite electrode structures. (d) Statistical information about these size distributions. (e) Pore–AM interfacial area as a function of standard deviation. (f) Pore phase tortuosity and (g) solid state conductivity are relatively insensitive to particle size distribution.

Once the qualitative variations are clear, multidimensional regression is performed to obtain quantitative functional relations (tabulated in Table 1). Figure 30 plots the effective property data along with surfaces representing the functional relations to help visually ascertain the goodness of fit (at a fixed secondary phase morphology, $\omega = 0.5$).

2.8 Effect of Particle Size Distribution on Effective Properties

Many imaging studies reveal that the AM particles show variation in particle dimensions, rather than representing a monodisperse population. The most common particle size distribution is log-normal.[80]

The microstructural relations developed so far assume all the particles to be the same size. To explore the importance of particle size distribution, multiple different structures with 25% porosity, 55% AM, and 20% secondary phase (all by volume) are generated with log-normal particle distribution (having different standard deviations, *i.e.*, spread) and the same mean size. The number density function, AM backbone, and composite structures are presented in Figure 31(a), (b), and (c), respectively. The relevant statistical descriptions are also presented (Figure 31(d)).

For each of these structures, all six microstructural properties described earlier are computed. To correlate the properties with particle size distribution, each of these properties is fitted to the function $\Gamma = a + b\delta + c\delta^2$, where δ is normalized deviation (= std. dev./ mean). Figure 31(e) shows that the active area shows reasonable dependence on distribution, but tortuosity and conductivity are relatively insensitive to particle size distribution.

Please note that these results are for the same mean particle size and suggest that mean particle size accounts for the first-order effect in effective properties. The size distribution has secondary effects, and the qualitative trends are quite similar across a range of particle size distributions (all being log-normal).

2.9 Electrochemical Performance Model

The electrochemical behavior of a LIB electrode is a combination of various transport processes taking place at pore and particle scales.[25, 167] The volume averaged set of governing equations can be expressed as follows:

<u>*Conservation of Li inside AM particles*</u>:

$$\frac{\partial C_s}{\partial t} = \frac{\mathcal{D}_s}{r^2}\frac{\partial}{\partial r}\left(r^2\frac{\partial C_s}{\partial r}\right) \tag{31}$$

<u>*Electron transport in the solid phase*</u>:

$$\sigma^{eff}\frac{\partial^2 \phi_s}{\partial x^2} = j \tag{32}$$

<u>*Conservation of Li^+ in electrolyte phase*</u>:

$$\varepsilon\frac{\partial C_e}{\partial t} = \frac{\partial}{\partial x}\left(\mathcal{D}_e\frac{\varepsilon}{\tau}\frac{\partial C_e}{\partial x}\right) + \left(\frac{1-t_+}{F}\right)j \tag{33}$$

<u>*Charge transport in electrolyte phase*</u>:

$$\frac{\partial}{\partial x}\left(\kappa\frac{\varepsilon}{\tau}\frac{\partial \phi_e}{\partial x}\right) + \frac{\partial}{\partial x}\left(\kappa_D\frac{\varepsilon}{\tau}\frac{\partial \ln C_e}{\partial x}\right) + j = 0 \tag{34}$$

Here, the x coordinate is along the thickness of the electrode. The volumetric current source term, j, represents the charge transfer between AM and the electrolyte phase. It is related to the active area per the following expression.

$$j = ak\sqrt{C_s C_e\left(C_s^{max} - C_s\right)}\left\{\mathrm{e}^{F\eta/2RT} - \mathrm{e}^{-F\eta/2RT}\right\} \tag{35}$$

The quantities highlighted in red in the above expressions (31) to (35) represent the microstructural effects.

The volumetric current source term is to be appropriately scaled to the particle level to ensure charge and species conservation between the solid and electrolyte phases. Let ε_s be volumetric AM loading. Let i be uniform Li intercalation flux experienced by the individual particle. Then, the rate of Li storage per particle is quantified as:

$$4\pi R^2 \cdot i$$

where R is the radius of an AM particle. Equivalently, the rate of Li storage in AM per unit electrode volume is given by

$$\left(\varepsilon_s \Big/ \frac{4}{3}\pi R^3\right)\cdot 4\pi R^2 \cdot i = \left(\frac{3\varepsilon_s}{R}\right)\cdot i = a_0 \cdot i \tag{36}$$

Here $\varepsilon_s/(4\pi R^3/3)$ is the number of AM particles per unit electrode volume. To ensure charge conservation, this must equate to the volumetric current source term, j. Comparing expressions (35) and (36):

$$i = \frac{a}{a_0}k\sqrt{C_s C_e\left(C_s^{max} - C_s\right)}\left\{e^{F\eta/2RT} - e^{-F\eta/2RT}\right\} \tag{37}$$

Recall that the factor a/a_0 is related to reaction blockage quotient, N_r.

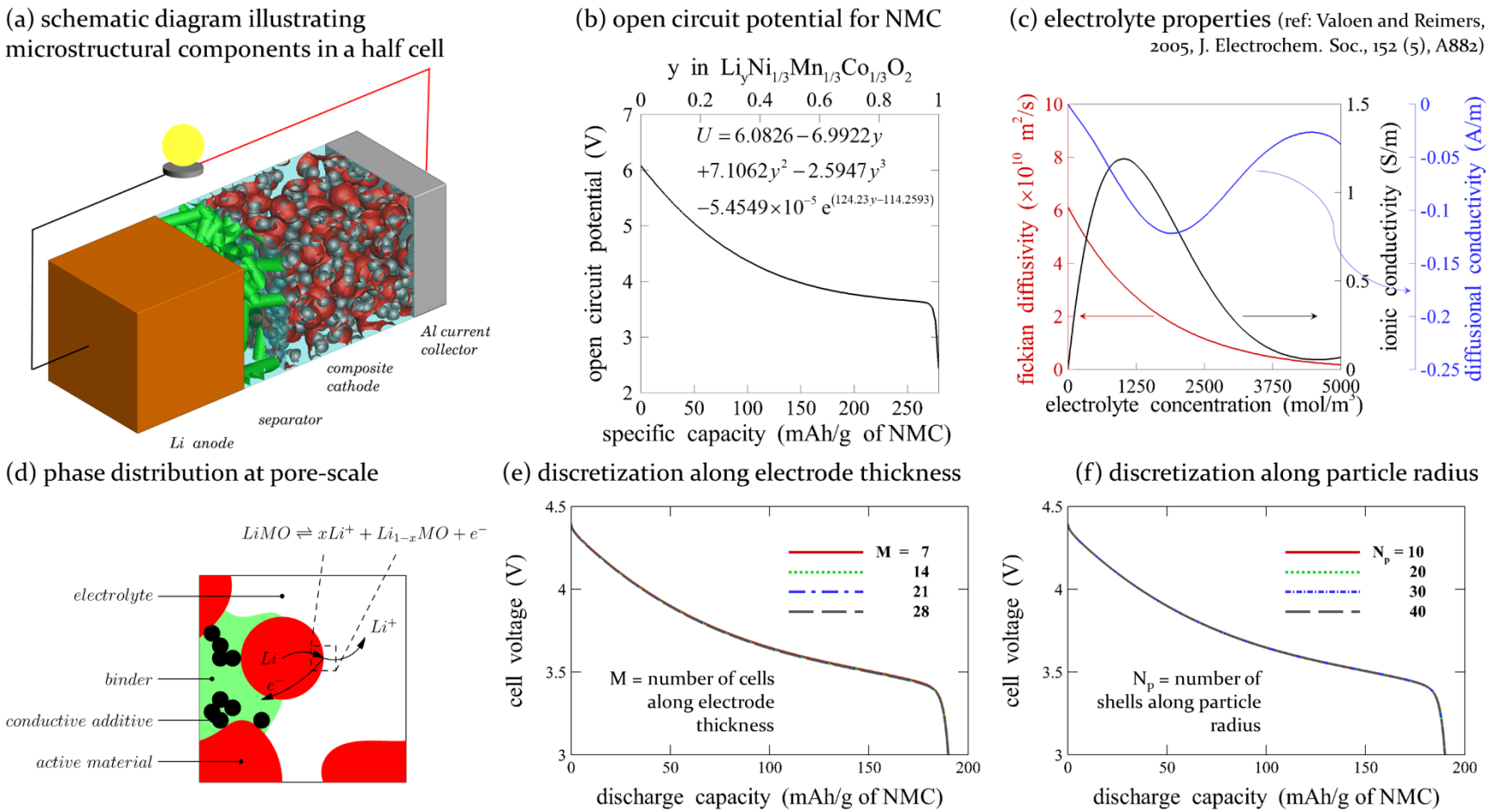

Figure 32. (a) A schematic diagram showing Li-ion half cell, along with suitable microstructural details.[25] (b) Corresponding pore-scale view of the electrode-electrolyte interface highlights the intercalation dynamics.[25] (c) Electrode and (d) electrolyte-phase properties used in the simulations. (e) and (f) report grid independence test proving sufficient resolution along both the electrode thickness and particle radius direction.

(a) area specific impedance measurements for same porosity and different AM/ (C+D) ratio
(ref: G. Liu, *et al.* 2008, *J. Electrochem. Soc.*, **155** (12), A887)

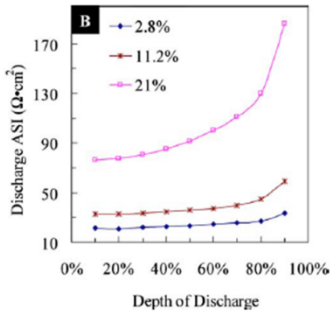

(b) internal resistance at 1C (active area = pore – AM interface)

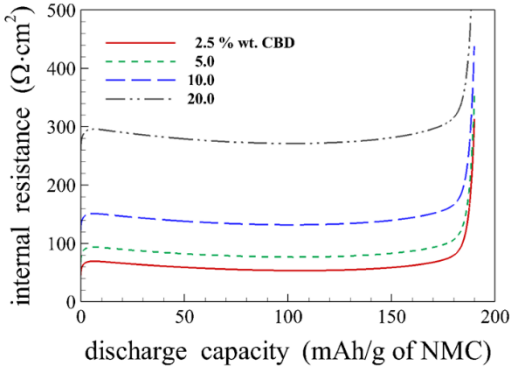

(c) internal resistance at 1C (active area = AM surface)

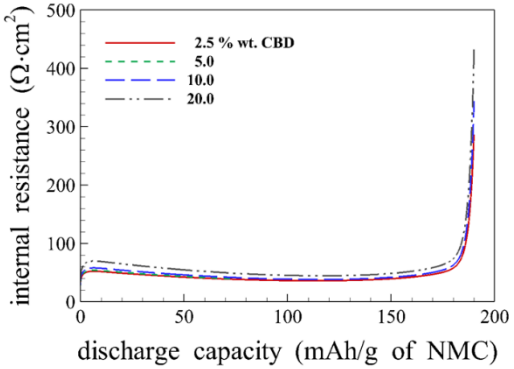

(d) electrode microstructure properties

CBD (% wt.)	*a* (pore-AM, m²/m³)	*a* (total, m²/m³)	tortuosity	conductivity (S/m)
2.50	110300	211430	2.6992	1.7117
5.00	58075	210820	2.5648	5.1626
10.0	17476	204710	2.0230	15.8704
20.0	2132	180740	1.9026	46.0223

(e) cell performance

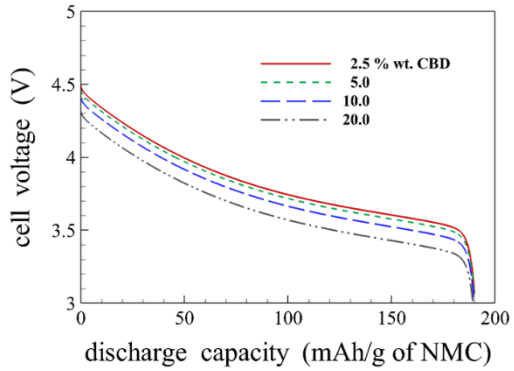

(f) cell performance

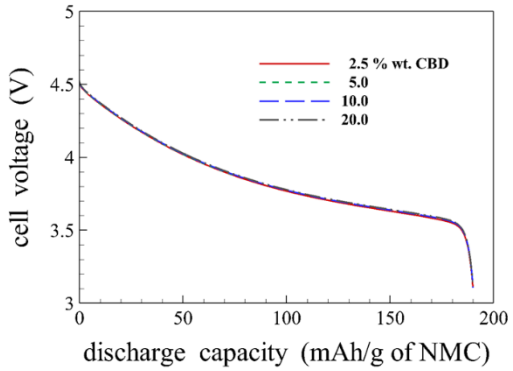

Figure 33. (a) Area-specific impedance measurements for electrodes with the same porosity and different secondary-phase loadings [Reprinted with permission from J. Electrochem. Soc., 155, A887 (2007). Copyright 2008, The Electrochemical Society]; internal resistance simulations assuming (b) pore–AM as electrochemically active surface and (c) total AM surface as active; (d) specific surface area values for these two sets are also tabulated; (e) and (f) present equivalent cell performance trends.

These set of equations are solved in a finite volume fashion, where both the electrode thickness and particle radius directions are separately discretized in the form of smaller volumes (M and N_p volumes, respectively). The numerical solution is to be proved to be independent of discretization. Such independence tests are demonstrated in Figure 32(e) and (f) for the baseline electrode (25 μm thick, 30% porosity, 90% AM by weight, and ω = 0.5). The electrode performance simulations are carried out for a half-cell arrangement with a *Li* counter anode. The geometry (Figure 32(a)) along with a pore-scale view of charge-conversion at the electrode-electrolyte interface (Figure 32(d)) is reproduced from the author's earlier publication.[25] Figure 32(c) and (d) present the relevant electrode and electrolyte phase properties.

The performance comparison in the main text also involves discharge energy. For a given electrode, the discharge energy is computed per the following expression:

$$E = \rho_{AM} \varepsilon_{AM} \int_0^Q V \, \mathrm{d}q \tag{38}$$

where V is the cell's terminal voltage and Q is the discharge capacity. ε_{AM} is volumetric AM loading, and the units of E are mAh/cc. Theoretically, the maximum energy is obtained when $\varepsilon_{AM} \rightarrow 1$, $V \rightarrow U$ and $Q \rightarrow Q_{max}$. Thus, the normalized discharge energy can be expressed as:

$$E^* = \varepsilon_{AM} \frac{\int_0^Q V \, \mathrm{d}q}{\int_0^{Q_{max}} U \, \mathrm{d}q} \tag{39}$$

The physical quantities that serve as inputs to the electrochemical predictions are summarized in Table 3.

2.10 Identifying the Electrochemically Active Area

As discussed, during microstructural characterization, a composite electrode forms multiple two-phase interfaces. Only the AM stores *Li*; thus, logically the AM–pore interface should participate in electrochemical reactions and should be identified as the electrochemically active interface. To make matters worse, specific surface area measurements such as the Bruanuer-Emmett-Teller adsorption rely on physisorption and count the binder–pore interface into the measurement. Thus, the identity of the electrochemically active area is debated in the literature. Given that the present

pseudo-DNS formulation quantifies each of these interfaces explicitly, this question is addressed with the help of analysis of previously reported experiments.[27]

Table 3. Summary of physical quantities and corresponding values and/or functional relations used for electrochemical predictions.

Quantity	***Description***
C_s	Intercalated Li concentration; ranges between 0 and 49,500 mol/m^3 for NMC; initial concentration set to have 4.5 V open circuit potential, *i.e.*, 14,850 mol/m^3
$\mathcal{D}_s$	Solid state diffusivity, 3×10^{-14} m^2/s
U	Open circuit potential, $U(y) = 6.0826 - 6.9922y + 7.1062y^2 - 2.5947y^3 - 5.4549\times10^{-5}\exp(124.23y - 114.2593)$ where $y = C_s / C_s^{max}$
t_+	Transference number, 0.38
$\mathcal{D}_e$	Electrolyte phase diffusivity[24]
κ	Ionic conductivity[24]
κ_D	Diffusional conductivity[24]
R_p	Particle radius, 5 μm
a	Active area, see Table 1
a_0	Theoretical active area, $a_0 = 3\varepsilon_s / R_p$; ε_s is AM volume fraction
τ	Pore phase tortuosity, see Table 1
σ	Solid phase conductivity, see Table 1
k	Intercalation rate constant, 2.3327×10^{-6} A/m^2/(mol/m^3)$^{3/2}$
R	Universal gas constant, 8.314 J/mol·K
T	Operating temperature, 298 K
F	Faraday's constant, 96,487 C/mol
V_{cut}^D	Discharge cutoff voltage, 3.0 V
L_{sep}	Separator thickness, 10 μm
L_{cat}	Cathode thickness, 25 μm

The essential idea is that if different electrodes with the same porosity and different AM:(C+B) loading are analyzed, the pore–AM interface changes quite substantially, and if the electrochemical measurements vary, the two are strongly correlated. Figure 33(a) reports the area-specific impedance (ASI) measurements were carried out using a hybrid pulse-power capability

protocol. Equivalent electrochemical simulations are performed with the internal resistance quantified throughout the discharge history (note that ASI and internal resistance are equivalent measures). Figure 33(b) reports internal resistance simulations assuming that pore–AM is the active area, while Figure 33(c) assumes the total AM surface (pore + CBD) as the electrochemically active interface (note that electrode porosity and thickness are kept the same as experiments to ensure comparison across results is valid). The results show that the spread in resistance data is observed only if the AM–pore interface is treated as active. The rationale can be made clear with the help of Figure 30. For different electrode recipes, the total AM surface is about 1 to 2 orders of magnitude higher than the corresponding pore–AM interface and stays fairly constant. On the other hand, the pore–AM area drops quite rapidly with the addition of the secondary phase. Thus, varying the CBD amount at constant porosity strongly affects the pore–AM area, and the corresponding kinetic resistance changes appreciably, while if the total AM surface area were employed in the calculations, such a spread would not be observed. Figure 33 (e) and (f) report equivalent performance simulations and reveal that a similar spread is also present on the performance curves. Interpreting these figures differently, they justify the requirements to study the effect of secondary solids on the electrochemical response of LIBs.

2.11 Probing Spatial Coupling of Resistive Modes

In porous intercalation electrodes, coupled charge and species transport interactions take place at the pore-scale, while often observations are made at the electrode-scale. The scale-up of these interactions from pore- to electrode-scale is poorly understood. Moreover, the spatial arrangement of the constituent material phases forming a porous electrode significantly affects the multi-modal electrochemical and transport interplay. In this study, the relation between the electrode specification, resultant porous microstructure, and electrode-scale resistances is delineated based on a virtual deconvolution of the impedance response. Relevant short- and long-range interactions are identified. Without altering the microstructural arrangement, if the electrode thickness is increased, the resistances do not scale linearly with thickness. This dependence is also probed to identify the fundamental origins of thick electrode limitations.

The transient electrochemical response of porous intercalation electrodes is a combination of various finite rate interactions taking place at the pore-scale, for example, ionic transport through the electrolyte-filled pore network. The geometrical arrangement of material phases

constituting a porous electrode modulates the severity of these interactions, and consequently the electrode-scale response. Thus, the porous intercalation electrodes represent a fascinating electrochemical system where the transient behavior strongly relies on the presence of non-intercalating phases, while the energy storage capacity correlates to the amount of intercalation material[11, 13, 14, 151, 153, 155, 168-171]. Physically the geometrical arrangement (more commonly known as the electrode microstructure) changes as electrode recipe is varied. Given the correlation among pore-scale physicochemical interactions and microstructural arrangement, an "appropriate" electrode recipe should culminate in desired electrochemical behavior. The importance of this connection from recipe to microstructure to performance has been recognized[29, 30, 33, 63, 65, 69, 72, 80, 83, 86, 91, 172, 173] however the exact correlation is not clearly understood[25, 174]. Fundamentally, such incertitude is rooted in two closely related questions:

- How do relevant microstructural properties vary with electrode recipe? In recent years, advanced imaging studies have provided quite a few detailed insights into active particles and their arrangement, however, sufficient visualization of electrolyte and carbon-binder network is challenging[89] and makes a correlation between recipe and microstructure difficult to ascertain.
- How do different pore-scale interactions convolve to electrode-scale, *i.e.*, observable, electrochemical response? Porous electrodes gradually convert ionic current (porosity and tortuosity are relevant descriptors) into electronic *via* electrochemical reaction (relates to the active area). Thus, at different locations in an electrode, the relevance of the associated resistive modes is dissimilar[174].

Authors have recently developed accurate microstructural reconstructions for composite porous electrodes containing all the essential material phases[174] (verified against relevant experiments). Such investigations[174, 175] delineate the electrode recipe variations in terms of effective microstructural properties. The present study establishes reciprocity among pore-scale interactions, their geometrical descriptors and electrochemical complexations as measured *via* impedance spectroscopy.

2.12 Electrochemical Impedance Response of a Porous Electrode

Impedance spectroscopy probes electrode-scale electrochemical response over a range of timescales, *i.e.*, excitation frequencies[176]. Each of the physicochemical interactions contributes to

the electrode's impedance signature. If the coupling of these resistive modes can be identified, the impedance signature could be deconvolved to explicitly understand the underlying interactions. Since the timescales for these pore-scale interactions vary, their coupling differs at dissimilar frequencies, and in principle provides a consistent interpretation of geometrical characteristics from the electrochemical response.

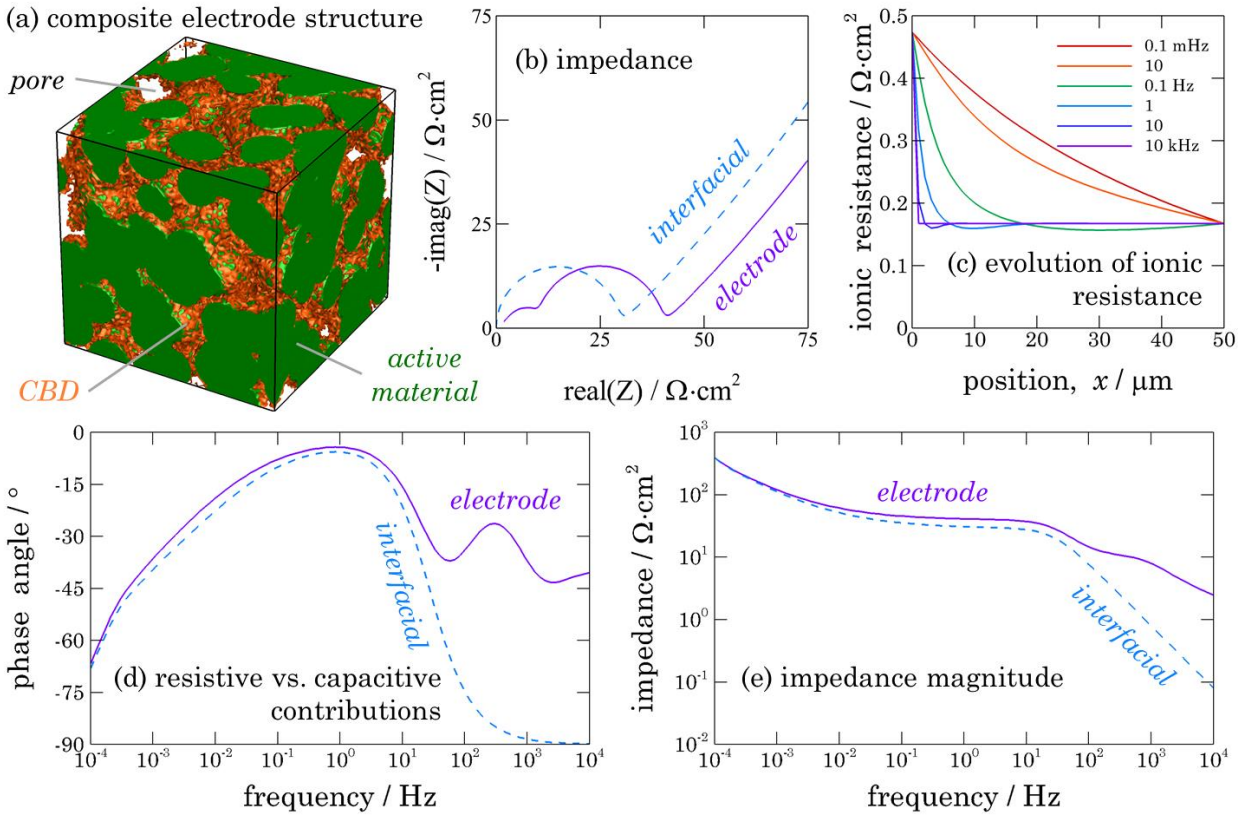

Figure 34. Electrochemical impedance response of a 50 μm thick porous composite electrode having 25% porosity and 95 : 2.5 : 2.5 %wt. composition with spherical active material particles. (a) An RVE of such electrode is shown along with all the constituents; (b) Corresponding electrode impedance response and contribution of the interfacial impedance at electrode scale; (c) Ionic resistance (Eq. (40)) trends at different excitation frequencies (x = 0 is electrode – separator interface, while $x = L$ is electrode – current collector boundary); (d) and (e) comparison between total electrode impedance and interfacial impedance at the electrode scale in terms of phase angle and magnitudes, respectively. The impedance of a porous intercalation electrode relies on (a) electrode microstructure, *i.e.*, the spatial arrangement of different material phases. Given that, the electrode scale impedance (b) is an outcome of spatial coupling of short-range (*i.e.*, interfacial (b)) and long-range (*e.g.*, ionic transport (c)) interactions. (d) Phase angle quantifies the relative contribution of resistive and capacitive effects. (e) Impedance decreases with the frequency of excitation.

State-of-the-art Li-ion battery composite electrodes house active material to store electrochemical energy, conductive-binder domains, CBD, ascribe (electronic) conduction pathways as well as structural rigidity and electrolyte-filled pore network ensures ionic conduction. Figure 34(a) presents a typical RVE of such a porous electrode composed of spherical active material particles (Nickel Cobalt Manganese oxide, NCM111). The active material backbone is stochastically generated in GeoDict[177, 178] and is consistent with particle distribution observed experimentally[80], while the CBD phase is added in the form of physics-based description developed recently[174] to reconstruct the composite electrode structures. Electrochemical energy is stored in the active material particles in the form of intercalated Li. Lithium intercalation is inherently composed of two distinct processes: (i) electrochemical reaction at the active material – electrolyte contact, *i.e.*, electrochemically active area; and (ii) Li diffusion inside the particle. This jointly amounts to the faradic component of interfacial impedance (106). In addition to this intercalation dynamics, ionic and electronic transport experiences resistance due to finite conductivities of the bulk phases (electrolyte and CBD) and their geometrical arrangements. The geometrical properties such as tortuosity are obtained from pore-scale calculations on RVEs. The RVE scale ionic impedance, z_e, and electronic impedance, z_s, are mathematically expressed in (40) and (41). It should be recognized that z_e and z_s are not point values but rather defined over RVE length-scale Δx, and thus measured in the units of $\Omega\cdot\text{cm}^2$. It is interesting to see that the RVE scale ionic resistance depends on the electrolyte concentration profile that changes along the electrode thickness, thus the electrode impedance represents a nontrivial combination of RVE scale effects.

$$z_e(x) = \frac{-d\tilde{\phi}_e/dx \cdot \Delta x}{\tilde{I}_e} = \frac{-d\tilde{\phi}_e/dx \cdot \Delta x}{-\kappa\frac{\varepsilon}{\tau}\cdot d\tilde{\phi}_e/dx - \frac{\kappa_D}{C_e}\frac{\varepsilon}{\tau}\cdot d\tilde{c}_e/dx} = \frac{\Delta x}{\kappa\frac{\varepsilon}{\tau} + \frac{\kappa_D}{C_e}\cdot\frac{\varepsilon}{\tau}\cdot\frac{d\tilde{c}_e/dx}{d\tilde{\phi}_e/dx}} \tag{40}$$

$$z_s(x) = \frac{-d\tilde{\phi}_s/dx \cdot \Delta x}{\tilde{I}_s} = \frac{-d\tilde{\phi}_s/dx \cdot \Delta x}{-\sigma^{\text{eff}}\, d\tilde{\phi}_s/dx} = \frac{\Delta x}{\sigma^{\text{eff}}} \tag{41}$$

Here κ is ionic conductivity of the electrolyte, ε is porosity, τ is tortuosity, κ_D is diffusional conductivity and σ^{eff} is effective electronic conductivity (effective since it accounts for both the spatial arrangement of carbon binder domains). C_e is electrolyte concentration, ϕ_e is electrolyte phase potential (related to ionic conduction), while ϕ_s is solid phase potential (responsible for electronic conduction). Refer to Mathematical Details of Electrode Impedance for mathematical

details. The transport properties of the electrolyte (conductivity, κ, diffusivity, D, diffusional conductivity, κ_D, and transference number, t_p) reflect the inter-ionic interactions taking place microscopically. The background solvent not only provides a medium for ions to move around and interact, but the solvent molecules also rearrange themselves around the ions and effectively act as a screening shield. The better the screening, the higher can be the salt concentration. The dielectric constant of the solvent quantifies the screening interactions[4, 179]. Thus, the electrolyte transport properties implicitly depend on the solvent's dielectric constant. Since such a solvent stabilizes the ionic charges, one expects a greater double layer capacitance.

Notice that these different physicochemical interactions have distinct length-scales. Each representative subdomain (*i.e.*, RVE) contains multiple active material particles. The ionic and electronic conduction (*i.e.*, transport) are long-range effects and become measurable at RVE length-scale. On the other hand, Li intercalation (reaction at the active surface and diffusion inside particles), as well as double layer charging, takes place at particle-scale (*i.e.*, a short-range interaction). This constitutes the interfacial impedance. The current is completely ionic at electrode – separator interface. Gradually, going from separator to current collector, the charge carriers convert to electrons from ions and at the electrode – current collector interface the outgoing current is completely electronic in nature. Electrochemical reactions thus take place inside the electrode, while concurrently changing the identity of the charge carriers. At any cross-section along the electrode thickness, both ionic and electronic currents are present. Mathematically, the interfacial impedance (107) accounts for the conversion of charge carriers as well as double layer charging/ discharging, while the ionic and electronic impedances, as defined by (40) and (41), relate to ionic and electronic conduction, respectively. If the long-range interactions were negligible, only the short-range effects dominate the electrochemical response. In this instance, the (ionic) current, $\tilde{I}_{app}$, flowing in from the electrode – separator interface spatially distributes as volumetric current, $\tilde{j}$. Effectively, the interfacial impedance, Z_i, at the RVE scale becomes electrode scale interfacial impedance, Z_i^L (where L is the electrode thickness):

$$Z_i^L = Z_i / L \tag{42}$$

Note that Z_i is RVE scale interfacial impedance, while Z_i^L is the measurable response at the electrode scale.

Figure 34(b) presents the impedance response (over the frequency range 0.1 mHz to 10 kHz) of a 50 μm thick composite electrode containing 95 : 2.5 : 2.5 by weight distribution of NCM, conductive additive, and binder, respectively. The recipes considered here are consistent with the state-of-the-art electrodes[180]. The mean NCM particle radius is 5 μm and the electrode porosity is 25 % (fraction of electrode volume occupied by electrolyte-filled pores). For comparison, the electrode scale interfacial impedance (42) is also shown alongside. It appears that the interfacial impedance quite closely accounts for the larger semi-circle as well as the sloping tail. This argument is further confirmed from the phase angle (Figure 34(d)) and impedance magnitude (Figure 34(e)) trends for the total electrode impedance and the interfacial impedance. Over a broad range of frequencies, the interfacial impedance dominates the response, and unless further higher frequencies are probed, the long-range effects are hidden due to relatively smaller contributions at these lower frequencies. At higher frequencies (greater than 0.1 kHz), the interfacial impedance is mostly capacitive in nature (Figure 34(d)). Since the capacitive and faradic impedances act in parallel (A63), this reduces the magnitude of interfacial impedance considerably (Figure 34(e)). The ionic (40) and electronic (41) resistances are present at all frequencies, and once the resistive contribution of the interfacial impedance drops, these effects appear prominently on impedance plot (Figure 34(b)). The second semi-circular feature on the total impedance (Figure 34(b)) is related to long-range effects, especially the ionic resistance (for this recipe 95 : 2.5 : 2.5, the electronic conductivity is fairly large; refer Figure 36 and corresponding discussion). The capacitive contribution from the electrode-electrolyte interface is still present at these frequencies and accounts for the non-zero phase angle in this higher frequency range (Figure 34(d); purely resistive effects lead to zero phase angle). Ideally, capacitive impedance is infinite at zero frequency (a dc current) and zero at an infinite frequency (a very high-frequency ac current). Since impedance measurements are carried out in a finite frequency range, capacitive effects are present at all frequencies (hence the non-zero imaginary part). Figure 34(e) reveals that the transport resistances are fairly greater than the interfacial impedance, which explains the smaller dimensions of the associated semi-circle (Figure 34(b); the reactive contribution comes from the interfacial impedance and since it is smaller the highest point on the higher frequency semi-circle is at a lower height than the highest point on the low-frequency semi-circle). The electronic resistance (41) does not exhibit a frequency dependence and is constant. On the other hand, the ionic resistance (40) changes with the excitation frequency (Figure 34(c)). Li^{+} ions are the charge carriers in the

electrolyte phase and their distribution (*i.e.*, perturbation in their equilibrium distribution) changes as per expressions (108) at different frequencies. This, in turn, affects the electrolyte phase potential distribution, dictated by expression (110). Both these effects jointly cause the frequency dependence of ionic impedance (40).

This spatial distribution of ionic impedance (Figure 34(c)) is thought-provoking. The ionic resistance is highest at the electrode – separator interface ($x = 0$) and gradually converges (not always monotonically) to a lower constant value at electrode – current collector interface ($x = L$) for all frequencies. This behavior is fundamentally related to interconversion of charge carriers. As the ionic current changes to the electronic, smaller current passes through the electrolyte phase, which in turn reduces the gradients in the Li^+ concentration profile and subsequently decreases the ionic resistance going towards the current collector. The solution of frequency-domain governing equations (108) – (110) over a range of frequencies provide quantitative values of complex impedance (Figure 34(b)). As a part of this solution, perturbation profiles in concentrations and potentials are computed. Based on these profiles, equations (40) and (41) describe the local variation of ionic and electronic impedances. Figure 34(c) plot the spatial variation of this ionic resistance at a few representative excitation frequencies. The electrode scale impedance sketched in the complex plane (Figure 34(b)) is further analyzed to plot dependence of phase angle (Figure 34(d)) and impedance magnitude (Figure 34(e)) against excitation frequencies. Resistivity, ρ, of a bulk medium (inverse of conductivity) is measured in $\Omega\cdot$cm. Total resistance, R, is related to resistivity, ρ, as per the expression $R = \rho\ell/A$, and is measured in Ω. After rearrangement, the area specific resistance $R^* = \rho\ell$ has the units of $\Omega\cdot\text{cm}^2$. Since the discussion in Figure 34(c) (and later in Figure 35(i) and (j)) is in terms of area specific impedance, $\Omega\cdot\text{cm}^2$ is a suitable unit. Δx is the RVE dimension (not just a numerical parameter). Effective properties like active area, tortuosity and conductivity are computed from the pore-scale characterization of RVE sized electrode volumes. Equations (40) and (41) quantify these RVE scale impedances and correspondingly Figure 34(c) shows their distribution along the electrode thickness.

The porous electrode structure here is representative of slurry evaporation-based electrode fabrication[83]. Such an approach leads to a quite stochastic distribution of solid phases, *e.g.*, the microstructure in Figure 34(a). Many different microstructural arrangements are possible, which in turn alters the relative features on the impedance plot[48] (Figure 34(b)) while retaining the general nature. Recently, ordered structures with ion channels are being investigated as electrode

architectures[181]. The straight ion channels reduce the through-plane tortuosity and effectively ameliorates the transport limitation.

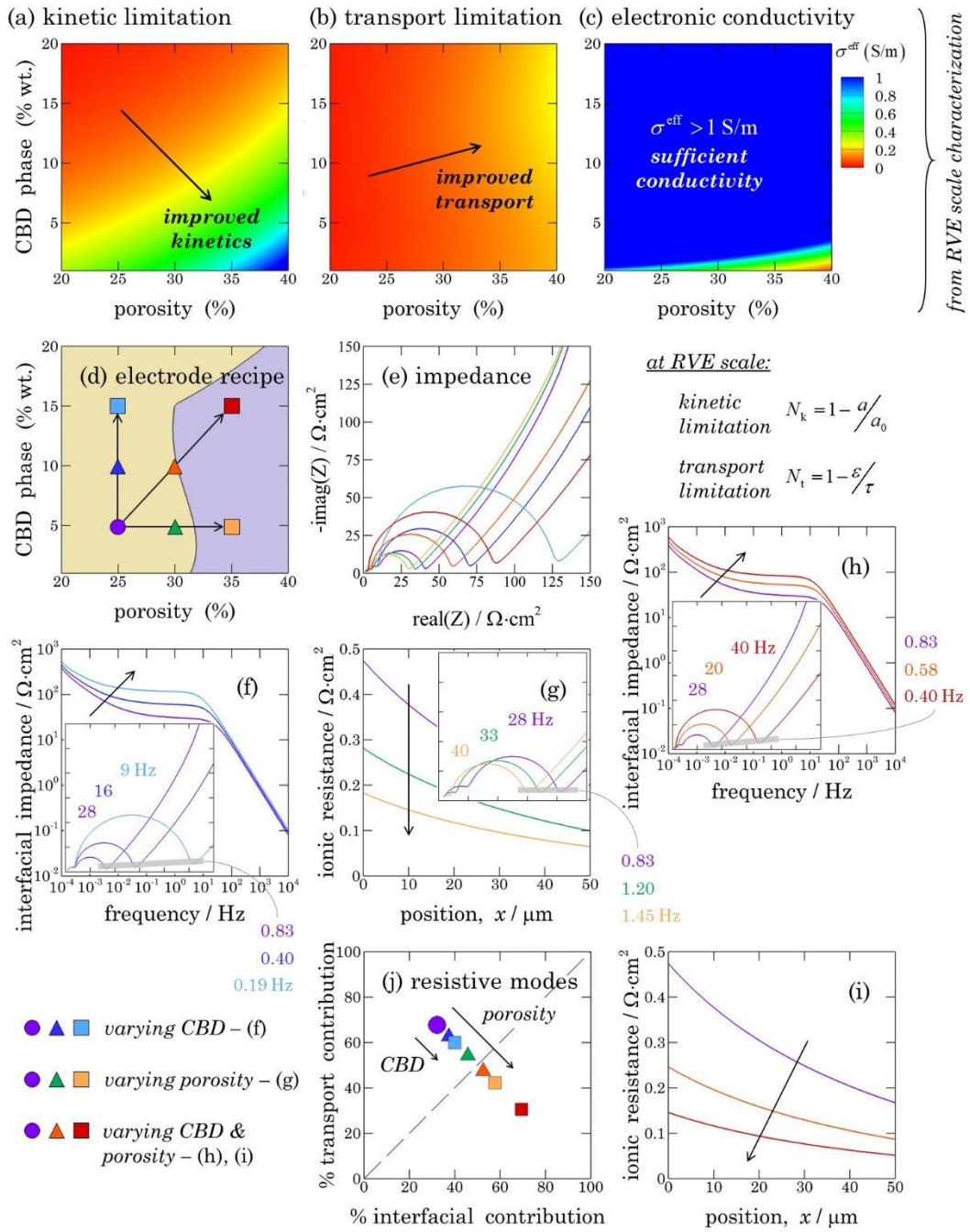

Figure 35. Role of electrode recipe on impedance is intricate as physicochemical interactions scale differently with microstructural specifications.

For such electrodes, the impedance profile is expected to contain a very small high-frequency semi-circle. The rest of the features largely result from particle (*i.e.*, interfacial) scale effects and probe the intercalation dynamics.

2.13 Electrode Microstructure Dictates the Impedance Components

Electrode composition correlates with effective properties such as active area and tortuosity, which in turn define different forms of microstructural resistances. Given the presence of CBD, not all the active material – electrolyte interface is available for intercalation. This reduction in active area (compared to the conventional limit of $a_0 = 3\varepsilon_s / R_p$) manifests as increased reaction overpotential, *i.e.*, a kinetic limitation. Figure 35(a) sketches the dependence of kinetic limitation on electrode recipe. The contours are colored as per $N_{\mathrm{k}} = 1 - a / a_0$ where a is the actual active area and a_0 is the theoretical limit. At higher CBD contents, the active material surface is covered to a greater extent reducing the electrochemically active area and causing higher kinetic hindrance. Similarly, if the porosity is increased, active material volumetric loading decreases (keeping the same active material to CBD weight ratio) which in turn reduces the available area (authors have recently proved that the active material – electrolyte interface is the major contribution to active surface, and CBD – electrolyte or active material – CBD interfaces have minor contributions to electrochemical activity[174]). Note that expression (106) has the ratio a/a_0 as a prefactor to the charge transfer resistance. Presence of CBD also affects the electrode tortuosity. For the same porosity, increasing the CBD content reduces the pore phase tortuosity since the geometrical features associated with CBD are of smaller length scale as compared to the active material particles and makes for a relatively smoothly varying pore network[174]. The pore-scale calculations[174] were instrumental in identifying these trends as the conventionally employed relations such as the Bruggeman relation do not capture these effects arising from the presence of secondary solids. Pore network transport limitation at the RVE scale is quantified using $N_{\mathrm{t}} = 1 - \varepsilon / \tau$ and sketched in Figure 35(b). Figure 35(b) reveals that the transport becomes effective at higher porosities (stronger dependence) and increased CBD content. The governing equations (108) and (110) have ε / τ as a prefactor to different ionic transport modes (diffusion and migration). Similarly, effective electronic conductivity trends are presented in Figure 35(c). It has been proved recently[25] that once the effective conductivity reaches 1 S/m, a major source of

long-range limitations is electrolyte phase transport. In light of this, Figure 35(c) highlights the electrode recipes having conductivities smaller than 1 S/m. For the same CBD content (% wt.), increasing the electrode porosity decreases effective conductivity as the volumetric amount of CBD decreases and in turn cannot form strong conduction pathways. For the practical porosities, as long as CBD is present in excess of 5 % wt. and carbon to binder ratio (C/B) is 1 : 1, the electronic conduction does not become rate limiting.

Following up on this discussion, seven different electrode recipes were identified to probe the importance of the electrode composition and associated microstructural differences. The baseline recipe is 5 % wt. CBD and 25 % porosity (same as Figure 34) and all the electrodes have identical thicknesses (50 μm). Figure 35(d) identifies these recipes on the composition diagram along with their color codes. Figure 35(e) compares the impedance response of these various different electrodes. By and large, their microstructural differences lead to different impedance profiles. Figure 35(f) compares the changes in impedance behavior with CBD contents (at fixed porosity). As CBD content is increased, kinetic limitation becomes more pronounced, which results in increased interfacial impedance (Figure 35(f)) and in turn, the lower frequency semi-circle grows (Figure 35(f) inset). Consider Figure 35(g) which explores the porosity variation. Increased porosity reduces the ionic resistance (Figure 35(g)) as tortuosity decreases. This reflects as the impedance profile moves closer to the origin (Figure 35(g) inset). When both the CBD content and porosity are increased, the effect on the impedance response is cumulative (Figure 35(h) and (i)). Increased CBD content explains the higher interfacial impedance (Figure 35(h)) given higher coverage of the active material surface. This also explains the impedance growth in the lower frequency semi-circle (Figure 35(h) inset). In addition to this, increased porosity reduces the ionic resistance (Figure 35(i)). This features as the electrode impedance profile moving closer to the origin (Figure 35(h) inset). Thus, electrode impedance is strongly associated with microstructural arrangements (*i.e.*, electrode recipe). In other words, a specific recipe leads to certain microstructural arrangements which translate into different contributions from short- and long-range limitations. Figure 35(j) sketches these recipes on transport *vs.* interfacial impedance contribution map (high-frequency impedance is dissected for this figure). It quantitatively summarizes the origins of electrode impedance (at the highest frequency – 10 kHz). Electrode scale interfacial resistance is estimated from (42), while the ionic and electronic contributions are related to their local variation as per the following expressions:

$$Z_e^L = \sum z_e \tag{43}$$

$$Z_s^L = \sum z_s \tag{44}$$

Here summation is carried out over all the sub-volumes constituting the electrode thickness. Note that all these quantities (including Z_i^L) have identical units of $\Omega \cdot cm^2$ and allows for a direct comparison. As CBD content is increased, the interfacial contributions grow and accordingly the data points move closer to the equal contribution line (at 45°). With porosity changes, the transport resistance diminishes and in turn symbols show the increased contribution from interfacial effects. When both CBD content and porosity are increased, kinetic limitation grows, and transport limitations diminish concurrently, leading to the highest shift (among the recipes studied) in corresponding behavior in Figure 35(j).

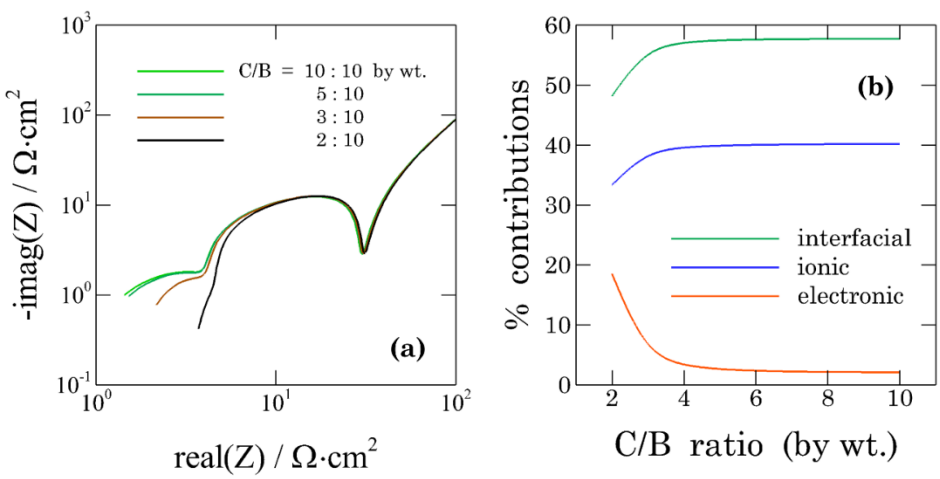

Figure 36. Effect of carbon – to – binder ratio (C/B) on electrode impedance at constant porosity (25%) and active material loading (95 %wt.). Electronic conductivity varies with C/B ratio and in turn impedance response (a) changes, especially at higher frequencies when long-range limitations are dominant. (b) Relative contributions of interfacial, ionic and electronic components are assessed at the highest frequency – 10 kHz. Marked changes are observed when the carbon to binder ratio drops below 5:10 wt. Since the logarithmic axis is used on the impedance plot to express this effect, spectra are visually different than the other figures.

It has been sown earlier that the CBD phase exhibits the highest conductivity near the C/B ratio of 1[30, 33]. Hence this C/B ratio is used for the most part. If the conductive additives are reduced, effective electronic conductivity drops and which in turn makes the solid-state conduction

limitations more prominent. As discussed earlier, these long-range limitations alter the high-frequency response. Figure 36(a) shows the change in impedance response with a reduction in the C/B ratio while keeping other phases invariant (*i.e.*, 95 % wt. active material and 25 % porosity). Figure 36(b) reports the relative contribution of different mechanisms to the total impedance at the highest frequency studied here, *i.e.*, 10 kHz. It appears that once the C/B ratio drops below 0.5, appreciable electronic conduction limitations arise. This is an interesting observation as a smaller C/B ratio (in the range 0.5 to 1.0) allows one to use more binder to improve structural rigidity as well as accommodate intercalation stresses without detrimentally altering the electronic conduction. In line with this discussion, Figure 35(c) would change considerably once the C/B ratio becomes smaller than 0.5. Note that Figure 36(a) uses logarithmic axes in order to sufficiently delineate the high-frequency signature of the C/B ratio.

2.14 Pore-scale Resistances translate Non-monotonically to Electrode-scale

Recent years have seen increased efforts towards enabling the thick electrode technology, however, the fundamental origins for underutilization remain unclear[29, 161, 182, 183]. Approaches like reduced particle size[182] or graded electrodes[183] are proposed with marginal improvement in performance. The composite electrodes exhibit complexations associated with the presence of multiple phases. Expressions (42), (43) and (44) suggest that the pore-scale interactions resulting in an electrochemical response of an electrode do not scale identically. To further probe this spatial coupling and associated speciation, impedance behavior of electrodes with different thicknesses is probed in Figure 37. These electrodes have identical microstructural arrangements (same as the baseline) and only their thicknesses are varied from 25 μm (thin) to 200 μm (thick) electrode. Figure 37(a) and (b) show their respective (area specific) impedances. Curious trends are observed here. Increasing electrode thickness from 25 μm to 100 μm (Figure 37(a)) shows a decrease in the overall impedance behavior, while at further higher thicknesses (100 to 200 μm; Figure 37(b)) the impedance grows, though this growth is much slower in comparison to the initial drop. Additionally, the higher frequency semi-circle that reflects the transport limitations grows steadily as the thickness is increased from 25 to 200 μm. At higher thicknesses (125 μm and above; Figure 37(b)), it merges with the lower frequency semi-circle and one cannot visually isolate the two.

As the electrode volumes increase with increasing thickness, a comparison based on area specific impedance does not seem appropriate. Impedance data is rescaled to obtain volume specific impedance $\left(Z^{*} = Z \cdot L\right)$, and the corresponding profiles are shown in Figure 37(c).

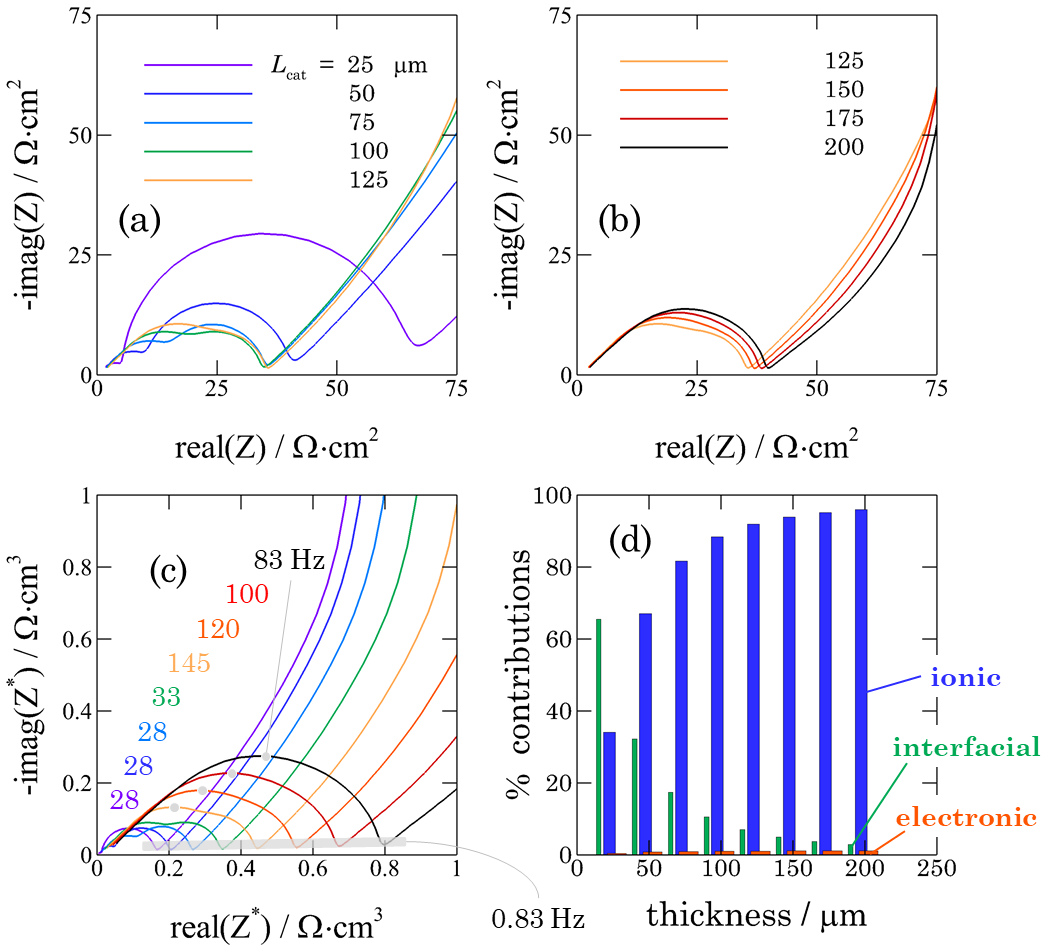

Figure 37. The RVE scale impedance contributions scale differently at electrode scale. (a) and (b) Area-specific impedance gives non-monotonic progression with electrode thicknesses highlighting this non-linear scaling of pore-scale physicochemical interactions. On the other hand, the trends become clearer when volume specific impedances (c) are plotted. The lowest thickness electrode shows two clear semi-circles, the lower frequency one corresponding to charge transfer kinetics and the higher frequency one related to transport effects. As electrode thickness is increased, the two semi-circles merge and for thicker electrodes, only one semi-circle is observed. (d) Relative contributions from interfacial, ionic and electronic impedances are characterized at the highest excitation frequency – 10 kHz and reveal that the long-range transport effects become prominent as electrode thickness is increased. All these electrodes have 95 % wt. active material (*i.e.*, 5 % wt. CBD) and 25 % porosity. As the CBD phase content is fairly sufficient to provide conduction pathways (Figure 35(c)), the impedance contribution of the electronic mode is minimal in (d).

Figure 37(c) reveals a clear monotonic trend. As intuitively expected, the impedance grows with electrode thickness. Also, the gradual reduction in lower frequency semi-circle (related to the short-range effects) and impedance build up in the high-frequency semi-circle (describes the long-range interactions) are clearly demarcated. Figure 37(d) compares the contributions of these various physicochemical interactions with electrode thickness (volume specific impedance values are employed) at a certain higher frequency (10 kHz here). Such a behavior sheds light on the spatial coupling of these interactions. As the incoming current distributes locally to form the intercalation and capacitive current, the overall effect of the interfacial impedance felt at the electrode scale diminishes with increased electrode thickness. On the other hand, the transport resistances act in series and in turn their magnitude grows with thickness. Expressions (42) and (44) mathematically highlight these behavioral differences among the interfacial (short-range) and transport (long-range) effects. Reconsider Figure 37(d). For thin electrodes, the kinetics is the limiting contribution and accordingly the strategies that increase the active area lead to better performance[174]. For thick electrodes, transport becomes the rate limiting factor and consequently, the same strategies as before would not result in considerable improvement. Appropriate microstructural modifications that lead to improved thick electrode behavior are required. To the best of authors' knowledge, there is only one careful experimental study (Ogihara *et al.*[184]) that compares impedance response as a function of electrode thickness and finds qualitatively similar trends as Figure 37(a). However, given their circuit-based interpretation, fundamental mechanisms leading to such a response could not be identified[184]. The physics-based impedance analysis presented here consistently connects pore-scale events to electrode-scale and provides new insights.

2.15 Impedance Response of Multivalent Chemistries

Lithium (Li^{+}) is a monovalent cation. With depleting lithium reserves, various other cations, for example, magnesium (Mg^{2+}), aluminum (Al^{3+}) are being considered. Two distinct effects become relevant as these multivalent cations are considered. First, for the same current, lesser atoms intercalate which reduces the diffusional impedance and in turn slope of the low-frequency tail increases. Second, the transference number increases in the electrolyte which amounts to reduced transport resistance. Figure 39 sketches these representative differences, assuming all the kinetic and transport properties to be identical. In reality, whenever a new cation is considered for electrochemistry, intercalation host, electrolyte, *etc.* are revised. Many of these intercalation hosts

undergo multiphase intercalation[185, 186] which requires a reformulation of interfacial resistance. However, even in the absence of these material nonlinearities, the impedance response varies nonmonotonically given the direct relation of cationic charge with diffusional flux and electrolyte transference.

State-of-the-art porous electrodes are a multiphase system with each phase aimed at improving a specific physicochemical interaction. Impedance spectroscopy is often used to characterize the electrochemical response of such electrodes, but the traditionally employed equivalent circuit-based interpretation offers rather qualitative insights.

This work develops a consistent description of the electrochemical impedance of composite porous electrodes. Such an account correlates various impedance features to relevant pore-scale events as well as effective microstructural properties. Frequency dependence of impedance can be interpreted in terms of timescales. Based on the time scale (*i.e.*, probing frequency), these interactions couple differently. It is found that even for a moderate size electrode (~ 50 μm) if large enough excitation frequencies are employed, the transport limitations appear as a second semi-circle on the impedance spectra (in addition to the lower frequency semi-circle associated with interfacial short-range effects).

The choice of electrode recipe uniquely identifies the spatial arrangement of the material phases constituting these electrodes and positively alters the impedance response. Specifically, when CBD weight fraction (active material and CBD are the solid phases) is increased, it reduces the available intercalation area and in turn, the lower frequency impedance grows. On the other hand, porosity variations lead to changes in transport resistance. Interestingly, the CBD weight fraction also changes the tortuosity (and in turn high-frequency impedance) at the same porosity, and porosity changes affect the lower frequency impedance. These secondary effects are a result of the composite electrode structure.

As the length-scales of these different interactions are different as well as their spatial coupling, changes in electrode thickness do not scale these interactions identically. With increased electrode thickness, the contribution of interfacial impedance decreases, and the transport effects become more pronounced which leads to appropriate changes in the respective semi-circles. For thick enough electrodes, both the semi-circles merge as the transport effects become activated at lower frequencies.

2.16 Concentrated Solution Theory Based Electrolyte Transport Description

Typical Li-ion battery electrolyte is prepared by dissolving a lithium salt, *e.g.*, $LiPF_6$ in an organic solvent(s). For the sake of generality, let this salt be $Li_{\nu_p}X_{\nu_n}$ with stoichiometric coefficients ν_p, ν_n and anion X^{z_n}. Appropriate salt dissolution equilibrium is:

$$Li_{\nu_p}X_{\nu_n} \rightleftharpoons \nu_p Li^{z_p} + \nu_n X^{z_n} \tag{45}$$

The electrolyte consists of three species:

$$\left.\begin{array}{c} p\text{, cation: } Li^{z_p} \\ n\text{, anion: } X^{z_n} \\ s\text{, solvent} \end{array}\right] \tag{46}$$

Charge neutrality is ensured in an electrolyte everywhere except inside the double layers:

$$\nu_p z_p + \nu_n z_n = 0 \tag{47}$$

When the electrolyte is prepared, one can only alter salt concentration, C. Ionic concentrations are subsequently defined through their association with stoichiometries:

$$C = \frac{C_p}{\nu_p} = \frac{C_n}{\nu_n} \tag{48}$$

And the statement of charge neutrality can be mathematically expressed as:

$$C_p z_p + C_n z_n = 0 \tag{49}$$

Let electrochemical potentials of the species (chemical potential for charge-less species) be noted by μ. Gibbs – Duhem relation correlates these thermodynamic quantities with concentrations as follows:

$$C_p \nabla\mu_p + C_n \nabla\mu_n + C_s \nabla\mu_s = 0 \tag{50}$$

The salt dissolution equilibrium (45) correlates salt's chemical potential with individual ionic electrochemical potentials *via* stoichiometries:

$$\mu = \nu_p \mu_p + \nu_n \mu_n \tag{51}$$

This gives an alternative expression of the Gibbs – Duhem relation:

$$C\nabla\mu + C_s \nabla\mu_s = 0 \tag{52}$$

Electrochemical potentials of each of the ionic species are related to their respective concentrations, individual activities, and local electric potential[22]. The gradient in salt's chemical potential exhibits the following dependence:

$$\begin{aligned} \nabla\mu &= \nu_p \nabla\mu_p + \nu_n \nabla\mu_n \\ &= \nu RT \nabla\left(\ln\left(fC\right)\right) \end{aligned}$$

$$\nabla\mu = \nu RT\left(1+\frac{d\ln f}{d\ln C}\right)\nabla\ln C = \nu RT\chi\nabla\ln C \tag{53}$$

with $\nu = \nu_p + \nu_n$ and $\chi = 1+\left(d\ln f / d\ln C\right)$. Note that f is salt activity coefficient and C is salt concentration. f is in fact made up of individual ionic activity coefficients, f_p, f_n. χ is otherwise known as the thermodynamic factor[22, 23].

As mentioned earlier, there are more than one solute species. For such a multicomponent system, transport is dictated by Onsager – Stefan – Maxwell (OSM) relation (essentially a constitutive relation connecting fluxes with concentration gradients):

$$-\frac{C_i C_T}{RT}\nabla\mu_i = \sum_{j,j\neq i}\left(\frac{C_j N_i - C_i N_j}{\mathcal{D}_{ij}}\right) \tag{54}$$

The binary diffusivity tensor $\mathcal{D}_{ij}$ is symmetric, *i.e.*, only three independent diffusivities, namely $\mathcal{D}_{ps}$: cationic diffusivity in the solvent, $\mathcal{D}_{ns}$: anionic diffusivity in the solvent and $\mathcal{D}_{pn}$: mutual diffusivity of cationic – ionic species. Thus, for the electrolyte system under consideration, one has to explicitly measure four properties: $\chi, \mathcal{D}_{ps}, \mathcal{D}_{ns}, \mathcal{D}_{pn}$. However, it is quite difficult to individually study ionic motion as the electrolyte solution is charge neutral for most practical length scales (except recent NMR measurements[187, 188]). The concentrated solution theory is a formalism which appropriately converts these immeasurable properties into measurable transport properties: salt diffusivity - D, transference number - t_p, ionic conductivity - κ and diffusional conductivity - κ_D. As this alternate set is measured, the respective transport relations are used in the mathematical description.

Even if one can write three OSM relations for each of the three species (*p*, *n* or *s*), only two of these are independent as the Gibbs – Duhem does not let all potentials be set independently. Given the interest in the ionic species, the solvent is treated as the reference phase to identify species flux. This is often stated as "carrying out calculations in the solvent frame"[22]. Solvent flux, $N_s = C_s u_s$ where u_s is solvent velocity. This is the bulk velocity and will contribute to the presence of solvent flow, *e.g.*, redox flow battery[189].

$$-\frac{C_p C_T}{RT}\nabla\mu_p = \frac{C_n N_p - C_p N_n}{\mathcal{D}_{pn}} + \frac{C_s N_p - C_p C_s u_s}{\mathcal{D}_{ps}} \tag{55}$$

$$-\frac{C_n C_T}{RT}\nabla\mu_n = \frac{C_p N_n - C_n N_p}{\mathcal{D}_{pn}} + \frac{C_s N_n - C_n C_s u_s}{\mathcal{D}_{ns}} \tag{56}$$

With rearrangement:

$$N_p\left(\frac{C_n}{\mathcal{D}_{pn}} + \frac{C_s}{\mathcal{D}_{ps}}\right) - N_n\left(\frac{C_p}{\mathcal{D}_{pn}}\right) = -\frac{C_p C_T}{RT}\nabla\mu_p + \frac{C_p C_s}{\mathcal{D}_{ps}}u_s \tag{57}$$

$$-N_p\left(\frac{C_n}{\mathcal{D}_{pn}}\right) - N_n\left(\frac{C_p}{\mathcal{D}_{pn}} + \frac{C_s}{\mathcal{D}_{ns}}\right) = -\frac{C_n C_T}{RT}\nabla\mu_n + \frac{C_n C_s}{\mathcal{D}_{ns}}u_s \tag{58}$$

Note that $C_T = C_p + C_n + C_s$ is total concentration. Further, a solvent contribution can be eliminated from the above two expressions as $\frac{C_n}{\mathcal{D}_{ns}}\times(57) - \frac{C_p}{\mathcal{D}_{ps}}\times(58)$:

$$N_p\left(\frac{C_n C_p}{\mathcal{D}_{ps}\mathcal{D}_{pn}} + \frac{C_n C_n}{\mathcal{D}_{ns}\mathcal{D}_{pn}} + \frac{C_n C_s}{\mathcal{D}_{ps}\mathcal{D}_{ns}}\right) - N_n\left(\frac{C_p C_p}{\mathcal{D}_{ps}\mathcal{D}_{pn}} + \frac{C_p C_n}{\mathcal{D}_{ns}\mathcal{D}_{pn}} + \frac{C_p C_s}{\mathcal{D}_{ps}\mathcal{D}_{ns}}\right)$$
$$= -\frac{\nu_n C_p C_T}{RT}\left(\frac{1}{\mathcal{D}_{ns}}\nabla\mu_p - \frac{1}{\mathcal{D}_{ps}}\nabla\mu_n\right)$$

$$\therefore N_n = \frac{\nu_n}{\nu_p}N_p + \frac{C_T}{RT}\cdot\frac{\left\{\left(\frac{C_p}{\mathcal{D}_{ps}} + \frac{C_n}{\mathcal{D}_{ns}}\right)\nabla\mu_p - \frac{C}{\mathcal{D}_{ps}}\nabla\mu\right\}}{\left(\frac{C_p}{\mathcal{D}_{ps}\mathcal{D}_{pn}} + \frac{C_n}{\mathcal{D}_{ns}\mathcal{D}_{pn}} + \frac{C_s}{\mathcal{D}_{ps}\mathcal{D}_{ns}}\right)} \tag{59}$$

where $\nabla\mu = \nu_p\nabla\mu_p + \nu_n\nabla\mu_n$ is used to eliminate gradient in anion electrochemical potential, μ_n. Substituting (59) in (57):

$$N_p = -\frac{C_p C_T}{RT\mathcal{D}_{pn}(\ )}\nabla\mu - \frac{C_p C_T}{RT\mathcal{D}_{ns}(\ )}\nabla\mu_p + C_p u_s \tag{60}$$

where $(\ ) \equiv \left(\frac{C_p}{\mathcal{D}_{ps}\mathcal{D}_{pn}} + \frac{C_n}{\mathcal{D}_{ns}\mathcal{D}_{pn}} + \frac{C_s}{\mathcal{D}_{ps}\mathcal{D}_{ns}}\right)$.

Ionic current is given by:

$$I = z_p F N_p + z_n F N_n \tag{61}$$

Substituting for N_p and N_n (equations (59) and (60)):

$$I = -\kappa\nabla\phi - \kappa_D\nabla\ln C \tag{62}$$

$$\kappa = -z_n F^2\cdot\frac{CC_T}{RT}\left(\frac{\nu_p}{\mathcal{D}_{ps}} + \frac{\nu_n}{\mathcal{D}_{ns}}\right)/(\ ) \tag{63}$$

$$\kappa_D = z_n \cdot \frac{CC_T}{RT} \cdot \frac{F}{\mathcal{D}_{ps}} \cdot \nu RT \chi / (\ ) \tag{64}$$

Replacing $\nabla \mu_p = F \nabla \phi$ in (60) with (62):

$$N_p = -\nu_p D \nabla C + t_p \frac{I}{z_p F} + \nu_p C u_s \tag{65}$$

$$D = \frac{\nu C_T \chi}{(\ )} \left\{ \frac{1}{\mathcal{D}_{pn}} + \frac{1}{\nu_p \mathcal{D}_{ns} + \nu_n \mathcal{D}_{ps}} \right\} \tag{66}$$

$$t_p = \frac{\nu_n / \mathcal{D}_{ns}}{\left(\nu_p / \mathcal{D}_{ps}\right) + \left(\nu_n / \mathcal{D}_{ns}\right)} \tag{67}$$

Equivalently, the anionic flux can be obtained by substituting N_p (65) in I (61):

$$N_n = \frac{I}{z_n F} - \frac{z_p}{z_n} N_p \tag{68}$$

$$\therefore N_n = \frac{I}{z_n F} - \frac{z_p}{z_n} \left(-\nu_p D \nabla C + t_p \frac{I}{z_p F} + \nu_p C u_s \right) = -\nu_n D \nabla C + \left(1 - t_p\right) \frac{I}{z_n F} + \nu_n C u_s \tag{69}$$

In summary, one requires the knowledge of four independent properties - D, t_p, κ and κ_D to thoroughly characterize a typical Li-ion battery electrolyte (*e.g.*[24]). Given the local charge neutrality, one often uses one of the fluxes and ionic current expression for the transport description. In LIBs, since Li^+ is the ion of choice, equations (62) and (65) are used as representative transport laws. Note that the salt diffusivity, D, has contributions from all the binary diffusivities as well as the thermodynamic factor. The elegance of this theory lies in the fact that one need not back-compute 'elemental' properties (*i.e.*, $\mathcal{D}_{ps}, \mathcal{D}_{ns}, \mathcal{D}_{pn}, \chi$) and measurement of composite properties D, t_p, κ, κ_D is sufficient. This is also mathematically efficient as one need not explicitly worry about anion transport.

As a side note, a dilute solution theory employs Nernst – Planck relations to express ionic fluxes (*i.e.*, the constitutive relation). Such a description does neither account for interspecies interaction (resulting from cross-diffusion, *e.g.*, $\mathcal{D}_{pn}$) nor intraspecies interaction (resulting from activity coefficient/ thermodynamic factor).

2.17 Electrochemical Response of a Double Layer

The assumption of local charge neutrality is in general not valid near a solid – electrolyte interface. Ionic species often get preferentially adsorbed at the interface and to counter this charged surface, the electrolyte in the close proximity adopts an opposite charge (often referred to as the screening charge). Such an ordering spans a couple of nanometers and the relevant length scale is commonly referred to as the Debye length[4, 22]. This confined structure incorporates the Helmholtz planes and the diffuse layer (which contains the screening charge) and is referred to as the (electrochemical) double layer. Notice that the charge separation takes place within this space and as a whole (*i.e.*, globally) the double layer is charge neutral (equivalent to saying that the capacitor is charge neutral with identical but opposite charges on either plates[190]). This is different than both the bulk phases (solid and electrolyte) which are both globally as well as locally charge neutral.

In porous electrodes, the electrode-electrolyte interface is present throughout the electrode volume. Hence, the double layer dynamics is to be appropriately scaled up to the representative elementary volume length scale. Following up the same notation as earlier, the adsorbed charge is:

$$q^{ad} = z_p F c_p^{ad} + z_n F c_n^{ad} = -q^{sc} \tag{70}$$

where the first equality follows from the Faraday's law[22], while the second one expresses the global charge neutrality of the double layer, *i.e.*, $q^{ad} + q^{sc} = 0$. Note that the lower-case concentration c's are area specific, *i.e.*, in mol/m^2, in contrast to the volumetric counterparts used in transport discussion (C's are expressed in mol/m^3). Effectively, $c = \int C \, \mathrm{d}x$ with integration being carried out over the adsorbed or screen layers. The screening charge, q^{sc}, is correlated to corresponding ionic concentrations as:

$$q^{sc} = z_p F c_p^{sc} + z_n F c_n^{sc} \tag{71}$$

Total salt concentration in the double layer is:

$$c = \frac{c_p^{ad} + c_p^{sc}}{\nu_p} = \frac{c_n^{ad} + c_n^{sc}}{\nu_n} \tag{72}$$

The statement of global double layer charge neutrality, in fact, follows from (47) and (72):

$$q^{ad} + q^{sc} = z_p F \left(c_p^{ad} + c_p^{sc} \right) + z_n F \left(c_n^{ad} + c_n^{sc} \right) = \left(\nu_p z_p + \nu_n z_n \right) F c = 0 \tag{73}$$

In general, both the ionic species can be present in 'adsorbed' as well as 'screening' states. Hence, the total salt concentration in a double layer, c, and double layer charge, q^{ad} (or equivalently q^{sc}) are not one-to-one related. Let $\tilde{c}$ be the charge corresponding to the degree of non-neutrality as:

$$\tilde{c} = \frac{c_p^{ad}}{\nu_p} - \frac{c_n^{ad}}{\nu_n} \tag{74}$$

If cations adsorb more than the anions, $\tilde{c}$, is positive, else it is negative. $\tilde{c} = 0$ signifies identical adsorption for both the ions. Substituting for c_p^{ad} in (70):

$$q^{ad} = z_p F c_p^{ad} + z_n F c_n^{ad} = z_p F \left(\nu_p \tilde{c} + \frac{\nu_p c_n^{ad}}{\nu_n} \right) + z_n F c_n^{ad} = \nu_p z_p F \tilde{c} \tag{75}$$

Equivalently, it can be shown that,

$$q^{sc} = \nu_n z_n F \tilde{c} \tag{76}$$

Thus, concentration $\tilde{c}$ directly correlates to the amount of charge separated (equivalently stored) in the double layer. Consequently, the total salt concentration in the double layer is:

$$c = \frac{c_p^{ad} + c_p^{sc}}{\nu_p} = \left(\frac{c_p^{ad}}{\nu_p} - \frac{c_n^{ad}}{\nu_n} \right) + \frac{c_p^{sc}}{\nu_p} + \frac{c_n^{ad}}{\nu_n} = \tilde{c} + \frac{c_p^{sc}}{\nu_p} + \frac{c_n^{ad}}{\nu_n}$$

Let neutral salt concentration in the 'adsorbed' and 'screened' states be c^{ad} and c^{sc}, respectively. Hence, the above expression can be simplified as:

$$c = \tilde{c} + c^{ad} + c^{sc} \tag{77}$$

Equation (77) divides the total salt concentration in the double layer into three forms: $\tilde{c}$ related to stored charge, and c^{ad}, c^{sc} which characterize the portions of adsorbed (and screened) ions that nullify each other. Based on charge measurements, $\tilde{c}$ can be back inferred, while the other two cannot be so easily detected. Here on it is often assumed that cation is present in the adsorbed state, while anion is the screening charge[191]. This makes $c^{ad} = c^{sc} = 0$, and double layer charge and salt concentration become uniquely related:

$$q^{ad} = \nu_p z_p F c \tag{78}$$

This assumption is important since the electrolyte species balance is expressed in terms of salt concentration. The adsorbed charge relates to the potential drop between the (bulk) electrode and (bulk) electrolyte as, with $\mathcal{C}_{dl}$ being area specific double layer capacitance – measured in F/m^2:

$$q = \mathcal{C}_{dl} \left(\phi_s - \phi_e \right) \tag{79}$$

Or, in terms of charging/ discharging:

$$\frac{dq}{dt} = \mathcal{C}_{dl} \frac{d\left(\phi_s - \phi_e \right)}{dt} \tag{80}$$

Here it is assumed that the double layer capacitance, $\mathcal{C}_{dl}$ is not a function of salt concentration or potentials. Combining, (78) and (80):

$$\frac{dq}{dt} = \mathcal{C}_{dl} \frac{d\left(\phi_s - \phi_e\right)}{dt} = \nu_p z_p F \frac{dc}{dt} \tag{81}$$

dc/dt can be interpreted as salt flux into the double layer, per unit electrode – electrolyte surface. For a porous electrode, the equivalent volumetric form is:

$$\frac{dQ}{dt} = a_0 \mathcal{C}_{dl} \frac{d\left(\phi_s - \phi_e\right)}{dt} = \nu_p z_p F a_0 \frac{dc}{dt} = \nu_p z_p F \frac{dC}{dt} \tag{82}$$

where Q is charge stored in double layer per unit electrode volume, a_0 is electrode – electrolyte interfacial area and C is a salt concentration in the double layer per unit electrode volume. A positive dQ/dt signifies charging of the electrochemical double layer and is equivalent to the charging current. When current dQ/dt is passed, cations (in the present context) get adsorbed at a rate $dC_p / dt = \nu_p dC / dt$, and correspondingly anions arrange in the diffuse layer to screen this charge.

2.17.1 Sign convention

There are two forms of current at the electrochemically active interface – faradic (related to electrochemical reactions; here intercalation) and capacitive (related to double layer charging). The faradic current is considered positive when cations are generated in the electrolyte (*i.e.*, the deintercalation process). Double layer charging in a given electrode volume implies, accumulation of additional ions at the active interface. To be consistent with the sign convention of the faradic current, capacitive current is considered positive when it stores more ions. Mathematically,

$$j_c = \frac{dQ}{dt} = a_0 \mathcal{C}_{dl} \frac{d\left(\phi_s - \phi_e\right)}{dt} \tag{83}$$

with Q being the double layer charge. Thus, the salt concentration can increase due to ionic flux (diffusive, migrative or advective), electrochemical reactions and double layer charging. The net salt concentration, C, in a given electrode volume implicitly accounts for the charge stored in the double layer as well and one does not require independent species balance equation.

$$\therefore \varepsilon \frac{\partial C_p}{\partial t} = -\nabla \cdot N_p + \left(r_f + r_c\right) \tag{84}$$

where r_f is generation term from the faradic current and r_c for the double layer charging. Equivalent charge balance is:

$$-\nabla \cdot I + \left(j_f + j_c \right) = 0 \tag{85}$$

Since, intercalation reaction is always expressed as the generation of one Li^+, $r_f = j_f/z_pF$. And, $r_c = j_c/z_pF$. With these substitutions, (84) simplifies to,

$$\varepsilon \frac{\nu_p \partial C}{\partial t} = \nu_p \nabla \cdot \left(D \frac{\varepsilon}{\tau} \nabla C \right) - \frac{1}{z_p F} \nabla \cdot \left(t_p I \right) + \frac{j_f}{z_p F} + \frac{j_c}{z_p F} \tag{86}$$

$$\therefore \varepsilon \frac{\nu_p \partial C}{\partial t} = \nu_p \nabla \cdot \left(D \frac{\varepsilon}{\tau} \nabla C \right) - \frac{t_p}{z_p F} \left(j_f + j_c \right) + \frac{j_f}{z_p F} + \frac{j_c}{z_p F} \tag{87}$$

$$\therefore \varepsilon \frac{\nu_p \partial C}{\partial t} = \nu_p \nabla \cdot \left(D \frac{\varepsilon}{\tau} \nabla C \right) + \frac{j_f}{z_p F} \left(1 - t_p \right) + \frac{j_c}{z_p F} \left(1 - t_p \right) \tag{88}$$

where transference number, t_p, is fairly constant over a wide range of concentrations and its spatial dependence can be neglected (going from (86) to (87)). For Li^+, $z_p = 1$, and for a typical salt such as $LiPF_6$, $\nu_p = 1$. This simplifies (88) as:

$$\varepsilon \frac{\partial C}{\partial t} = \nabla \cdot \left(D \frac{\varepsilon}{\tau} \nabla C \right) + \frac{\left(1 - t_p \right)}{F} j \tag{89}$$

and charge balance in solid and electrolyte phases as:

$$\nabla \cdot \left(\kappa \frac{\varepsilon}{\tau} \nabla \phi_e \right) + \nabla \cdot \left(\kappa_D \frac{\varepsilon}{\tau} \nabla \ln C \right) + j = 0 \tag{90}$$

$$\sigma^{\text{eff}} \nabla^2 \phi_s = j \tag{91}$$

where intercalation and double layer charging terms are grouped together as $j = j_f + j_c$. Note that for transport through porous electrodes, porosity and tortuosity terms appear as pre-factors. In most of the existing literature (except[191, 192]), the origins of the double layer impedance are not explained. The preceding discussion is incorporated so as to revisit the specific details of double layer description, specifically the associated assumptions.

2.18 Mathematical Details of Electrode Impedance

For the most part, literature analyzes the impedance data *via* circuit-based models[29, 68, 193-198], except a few works[191, 199-201]. At best this sort of interpretation identifies the order of various transport processes but offers little insights into microstructural details or spatial coupling of different resistive modes. For a typical electrode, lateral dimensions are quite larger than the thickness, hence the derivative operator, ∇, needs to be expressed in this direction. Accounting for the intercalation based *Li* storage in active material particles, the electrochemical response of

a porous intercalation electrode is mathematically described by the following set of governing equations. Subscripts '*s*' and '*e*' denote solid and electrolyte phase properties, respectively.

Li storage in active material particles:

$$\frac{\partial C_s}{\partial t} = \frac{1}{r^2}\frac{\partial}{\partial r}\left(D_s r^2 \frac{\partial C_s}{\partial r}\right) \tag{92}$$

Li^+ transport in the electrolyte phase:

$$\varepsilon \frac{\partial C_e}{\partial t} = \frac{\partial}{\partial x}\left(D_e \frac{\varepsilon}{\tau}\frac{\partial C_e}{\partial x}\right) + \left(\frac{1-t_p}{F}\right) j \tag{93}$$

(Electronic) Charge conservation in the solid phase:

$$\sigma^{\text{eff}} \frac{\partial^2 \phi_s}{\partial x^2} = j \tag{94}$$

(Ionic) Charge conservation in the electrolyte phase:

$$\frac{\partial}{\partial x}\left(\kappa \frac{\varepsilon}{\tau}\frac{\partial \phi_e}{\partial x}\right) + \frac{\partial}{\partial x}\left(\kappa_D \frac{\varepsilon}{\tau}\frac{\partial \ln C_e}{\partial x}\right) + j = 0 \tag{95}$$

As discussed earlier, the electrolyte transport description is in accordance with the concentrated solution theory[22, 23]. Transport of both anion and cation take place in such liquid electrolytes, and given the local charge neutrality, only cation transport (93) is explicitly followed in the present discussion. Porosity (ε), tortuosity (τ) and effective electronic conductivity (σ^{eff}) appearing in these expressions account for electrode microstructural effects. Additionally, electrochemically active area factors in this electrochemical response when charge conversion from electronic to ionic or vice versa (*i.e.*, electrochemical reaction flux) is considered. Volumetric current source term, j, quantifies the reactions taking place at the RVE scale, and has both faradic and capacitive contributions, *i.e.*, $j = j_f + j_c$. The faradic (or intercalation) term has the following functional dependence:

$$j_f = ak\sqrt{C_s^f C_e \left(C_s^{max} - C_s^f\right)}\left\{e^{\frac{F}{2RT}(\phi_s - \phi_e - U)} - e^{-\frac{F}{2RT}(\phi_s - \phi_e - U)}\right\} \tag{96}$$

As the active material – electrolyte interface is partly covered due to the presence of the CBD phase, this volumetric flux (only the faradic component) has to be appropriately redistributed over the particle surface to ensure flux continuity. Subsequently, the intercalation flux at the active material surface becomes:

$$-D_s \left.\frac{\partial C_s}{\partial r}\right|_{r=R_p} = \frac{j_f}{a_0 F} \tag{97}$$

where $a_0 = 3\varepsilon_s / R_p$ is the theoretical active area. The capacitive flux results from double layer charging/ discharging at the solid – electrolyte interface. Double layer as a whole is charge neutral[22] and accordingly, its participation can be quantified as a flux of either of the ions. Here electrolyte interactions are presented in the form of cation transport (93) and ionic charge balance (95).

The microstructural properties have been characterized based on pore-scale analysis of composite electrode. Based on these calculations, relevant properties such as tortuosity, conductivity, and electrochemically active area have been expressed as functions of electrode recipe. Interested readers are encouraged to read[25, 174]. These expressions detail the electrode response in the time domain. These governing equations are transformed to the frequency domain using the Laplace transform. The mathematical treatment is similar to that carried out earlier[201-203] with advances made to account for electrode microstructural properties coming from pore-scale calculations. First, the equations are linearized around an equilibrium state (impedance measurements are often carried out in the rest phase). This leads to the following forms of equations (92) to (96):

$$\frac{\partial c'_s}{\partial t} = \frac{D_s}{r^2}\frac{\partial}{\partial r}\left(r^2 \frac{\partial c'_s}{\partial r}\right) \tag{98}$$

$$\varepsilon \frac{\partial c'_e}{\partial t} = D_e \frac{\varepsilon}{\tau}\frac{\partial^2 c'_e}{\partial x^2} + \left(\frac{1-t_p}{F}\right) j' \tag{99}$$

$$\sigma^{\text{eff}} \frac{\partial^2 \phi'_s}{\partial x^2} = j' \tag{100}$$

$$\kappa \frac{\varepsilon}{\tau}\frac{\partial^2 \phi'_e}{\partial x^2} + \frac{\kappa_D}{C_e}\cdot\frac{\varepsilon}{\tau}\frac{\partial^2 c'_e}{\partial x^2} + j' = 0 \tag{101}$$

$$j'_f = a\left[k\sqrt{C_s^f C_e\left(C_s^{max} - C_s^f\right)}\right]\frac{F}{RT}\left(\phi'_s - \phi'_e - c'^f_s \frac{\partial U}{\partial C_s}\right) \tag{102}$$

where transport properties and rate constants are computed using equilibrium state concentrations and potentials. All the dashed quantities correspond to fluctuations around the respective rest phase properties. Note that expression (102) is the faradic current, *i.e.*, associated with electrochemical reactions. The terms inside the square brackets refer to exchange current density, that is dependent on the lithiation extent.

$$i_0\left(C_s\right) = k\sqrt{C_s C_e\left(C_s^{max} - C_s\right)} \tag{103}$$

An additional current contribution arises from charging/ discharging of the double layer capacitor associated with the electrified interface[4, 22, 191], and is expressed as follows (assuming that the capacitance is same for the active material – electrolyte and CBD – electrolyte interfaces):

$$j'_c = a_0 \mathcal{C}_{dl} \frac{d\left(\phi'_s - \phi'_e\right)}{dt} \tag{104}$$

Net volumetric current appearing at the RVE scale is $j' = j'_f + j'_c$. Taking the Laplace transform of expression (98) and using the rule for the transform of differentiation[204], the following ordinary differential equation results ($s = i\omega$):

$$\frac{1}{r^2}\frac{d}{dr}\left(r^2 \frac{d\tilde{c}_s}{dr}\right) - \left(\frac{s}{D_s}\right)\tilde{c}_s = 0$$

whose solution is (where $\lambda^2 = s / D_s$):

$$\tilde{c}_s = \frac{A}{r}\sinh\left(\lambda r\right)$$

Note that boundary condition at the particle center (that the concentration should be finite) has been used. The remaining integration constant – A, shall be identified using the interface condition (frequency domain counterpart of expression (97):

$$A = \frac{a i_0}{a_0 RT}\left(\tilde{\phi}_s - \tilde{\phi}_e\right) \Bigg/ \left\{\frac{1}{R_p}\sinh\left(\lambda R_p\right)\left(\frac{a i_0}{a_0 RT}\cdot\frac{\partial U}{\partial C_s} + \frac{D_s}{R_p}\right) - \frac{\lambda D_s}{R_p}\cosh\left(\lambda R_p\right)\right\} \tag{105}$$

Subsequently, the volumetric faradic current (Eq. (102)) is:

$$\tilde{j}_f = \frac{\tilde{\phi}_s - \tilde{\phi}_e}{\left\{\frac{a_0}{a}R_{ct} + \frac{1}{a_0}\cdot\frac{\partial U}{\partial C_s}\cdot\frac{R_p}{F D_s}\cdot\frac{\tanh\left(\lambda R_p\right)}{\tanh\left(\lambda R_p\right) - \left(\lambda R_p\right)}\right\}} = \frac{\tilde{\phi}_s - \tilde{\phi}_e}{Z_f} \tag{106}$$

with $R_{ct} = RT / a_0 i_0 F$. Both the capacitive and faradic currents flow in parallel, resulting in the following form of the interfacial impedance at the RVE scale:

$$\tilde{j} = \tilde{j}_f + \tilde{j}_c = \frac{\tilde{\phi}_s - \tilde{\phi}_e}{Z_f} + \frac{\tilde{\phi}_s - \tilde{\phi}_e}{Z_c} = \frac{\tilde{\phi}_s - \tilde{\phi}_e}{Z_i} \tag{107}$$

where $Z_c = 1 / a_0 i\omega \mathcal{C}_{dl}$ and $Z_i = Z_f Z_c / \left(Z_f + Z_c\right)$.

Note that this derivation assumes a monodisperse active material particle system since the motivation for the present study is to understand the coupling of RVE scale effects and their

upscaling to the electrode scale. The complexations arising in the intercalation dynamics due to particle size distribution are fairly straightforward[201].

Given the analytical expression (107) for the interfacial impedance, the set of equations describing the electrode scale impedance reduces to the following:

$$s\varepsilon\tilde{c}_e = D_e \frac{\varepsilon}{\tau}\frac{d^2\tilde{c}_e}{dx^2} + \left(\frac{1-t_p}{F}\right)\tilde{j} \tag{108}$$

$$\sigma^{\text{eff}} \frac{d^2\tilde{\phi}_s}{dx^2} = \tilde{j} \tag{109}$$

$$\kappa\frac{\varepsilon}{\tau}\frac{d^2\tilde{\phi}_e}{dx^2} + \frac{\kappa_D}{C_e}\cdot\frac{\varepsilon}{\tau}\frac{d^2\tilde{c}_e}{dx^2} + \tilde{j} = 0 \tag{110}$$

along with the set of boundary conditions:

electrode – separator boundary	*electrode – current collector boundary*	
$-D_e \frac{\varepsilon}{\tau}\frac{d\tilde{c}_e}{dx} = \frac{\left(1-t_p\right)}{F}\tilde{I}_{app}$	$\frac{d\tilde{c}_e}{dx} = 0$	(111)
$-\kappa\frac{\varepsilon}{\tau}\frac{d\tilde{\phi}_e}{dx} - \frac{\kappa_D}{C_e}\cdot\frac{\varepsilon}{\tau}\frac{d\tilde{c}_e}{dx} = \tilde{I}_{app}$	$\tilde{\phi}_e = 0$	(112)
$\frac{d\tilde{\phi}_s}{dx} = 0$	$-\sigma^{\text{eff}}\frac{d\tilde{\phi}_s}{dx} = \tilde{I}_{app}$	(113)

The specification of these boundary conditions is critical to quantification of the electrode impedance spectra. Experimentally electrode impedance is measured in a half-cell setting where the test electrode is set against Li metal anode and the two are separated by a porous separator[193]. At the anode-separator interface, applied current translates to ionic current. No electrochemical reactions take place inside the separator and in turn, the ionic fluxes remain invariant across the separator (this does allow a concentration profile to evolve such that the ionic fluxes are spatially invariant). At anode-separator interface, Li^+ ions are generated. This leads to the flux balance: $N = -D_e \frac{\varepsilon}{\tau}\frac{\partial C_e}{\partial x} + \frac{t_p}{F} I_{app} = \frac{I_{app}}{F} \Rightarrow -D_e \frac{\varepsilon}{\tau}\frac{\partial C_e}{\partial x} = \frac{\left(1-t_p\right)}{F} I_{app}$. Also, the ionic current at any location in the separator is equal to the total current being passed through the cell, *i.e.*, $I_{app} = -\kappa\frac{\varepsilon}{\tau}\frac{\partial \phi_e}{\partial x} - \kappa_D \frac{\varepsilon}{\tau}\frac{\partial \ln C_e}{\partial x}$. Since no electronic current can enter through the separator – cathode interface, the corresponding gradient in the solid phase potential is set to zero in expression (112). On the other hand, the current collector is impervious to ionic flux, *i.e.*, $\partial C_e / \partial x = 0$. To

make the set of governing equations well-posed, one has to fix one of the potentials. Electrolyte phase potential is fixed at the current collector boundary (112). At current collector, all the current becomes electronic in nature and equation (113) ensures this physics.

The set of ordinary differential equations (108) to (110) along with the boundary conditions (111) to (113) are numerically solved. Afterward, the electrode impedance is computed as the equation:

$$Z_{electrode} = \frac{\tilde{\phi}_s\left(x=L\right) - \tilde{\phi}_e\left(x=0\right)}{\tilde{I}_{app}} \tag{114}$$

Here $\tilde{I}_{app}$ is applied current density (A/m^2) in the frequency domain. Note that this is the impedance of the porous electrode only. Experimentally one uses a half-cell setup in order to measure the electrode impedance. A half-cell configuration involves a Li metal anode, suitable separator and the test porous electrode. The half-cell impedance involves contributions from the interfacial impedance of Li metal anode as well as ionic transport resistance of separator (a function of separator microstructure), in addition to the electrode impedance. One needs to carry out further post-processing steps on experimentally measured impedance spectrum (*i.e.*, a half-cell) in order to extract electrode only impedance.

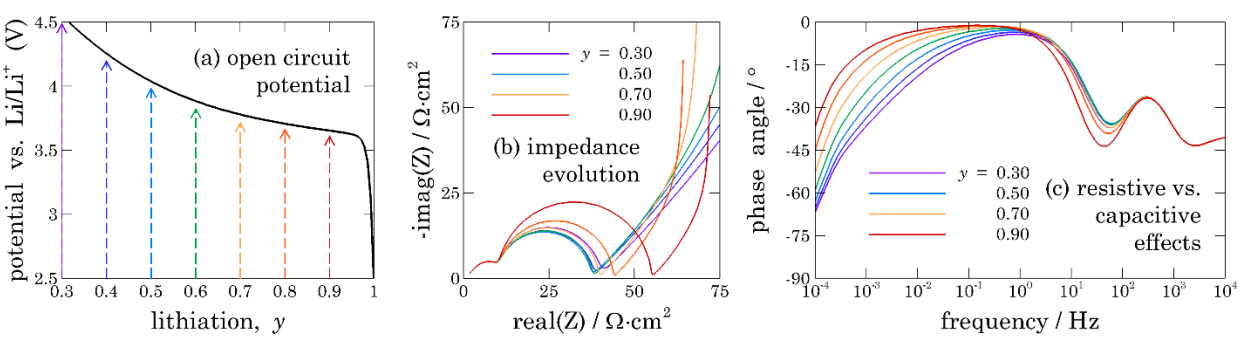

Figure 38. Lithiation dependence stems from changes in exchange current density and electrode potential with intercalation (a). This directly correlates to interfacial effects and accordingly, the lower frequency behavior (b) and (c) changes with lithiation.

Figure 38 reports the evolution of impedance with lithiation, for 50 μm thick porous intercalation electrodes with Nickel Cobalt Manganese oxide (NCM 333) active material, acetylene black conductive additives and poly (vinyldenedifluoride) binder in proportional 95 : 2.5 : 2.5 by weight and 25 % porosity. The active material particles have a mean particle radius of 5 μm. Relevant

material properties have been borrowed from literature and have also been listed in authors' earlier articles[25, 174]. The respective microstructural properties have been estimated based on the effective property relations reported recently[174]. With lithiation (Figure 38(a)), the interfacial impedance changes in response to changes in the exchange current density as well as the slope of the open circuit potential profile (105), while the microstructural properties stay unchanged. Corresponding impedance spectra are sketched in Figure 38(b) and report the variation of impedance over a range of excitation frequencies 0.1 mHz to 10 kHz. General nature of the impedance plot (Figure 38(b)) shows two smoothly joined circular portions and a low-frequency tail. Since the impedance in intercalation electrodes has contributions from various resistive mechanisms and double layer capacitance, corresponding phase angle quantitatively isolates the relative contribution of these effects (Figure 38(c)). The closer the phase angle to zero, the greater is the resistive contribution. Figure 38(c) reveals that changes in lithiation only affects the lower frequency impedances, while the higher frequency response stays invariant. In other words, higher frequency behavior is dominated by interactions not associated with intercalation. These higher frequencies, in fact, probe the transport characteristics. Interestingly, even at much higher frequencies, the phase angle is not zero, suggesting that the double layer charging does contribute in this range. This joint interplay between double layer effects and transport resistances (both ionic and electronic) give rise to the second high-frequency semi-circle as apparent in Figure 38(b). Note that this feature appears in the frequency range of 0.1 – 10 kHz.

2.19 Impedance for a Multivalent Intercalation Chemistry

If the ionic charge on the cation is higher than 1+, the previous set of equations have to be appropriately revised. Specifically, a higher valence cation exhibits a smaller molar flux, subsequently reducing the diffusional impedance (106):

$$Z_f = \frac{a_0}{a} R_{ct} + \frac{1}{z_p a_0} \cdot \frac{\partial U}{\partial C_s} \cdot \frac{R_p}{F D_s} \cdot \frac{\tanh\left(\lambda R_p\right)}{\tanh\left(\lambda R_p\right) - \left(\lambda R_p\right)} \tag{115}$$

This effectively increases the capacitive contribution and the low-frequency diffusional tail demonstrates a greater slope on the impedance profile as apparent in Figure 39. Another representative change occurs for the electrolyte transport (refer equation (67)), where a multivalent cation has a higher transference number:

$$t_p = \frac{\nu_n / \mathcal{D}_{ns}}{\left(\nu_p / \mathcal{D}_{ps}\right) + \left(\nu_n / \mathcal{D}_{ns}\right)} = \frac{z_p \mathcal{D}_{ps}}{z_p \mathcal{D}_{ps} - z_n \mathcal{D}_{ns}} \tag{116}$$

Note that the diffusivities in the above expression also change in response to changes in ionic radii as well as background solvent. This A higher transference number implies that the contribution of cationic flux to total current increases[22, 205], and effectively the electrolyte phase potential drop decreases. This attenuates the second – higher frequency semicircle (Figure 39). Figure 39 sketches these qualitative differences among the intercalation response with multivalent cations.

$$s\varepsilon\tilde{c}_e = D_e \frac{\varepsilon}{\tau} \frac{d^2\tilde{c}_e}{dx^2} + \left(\frac{1 - t_p}{\nu_p z_p F} \right) \tilde{j} \tag{117}$$

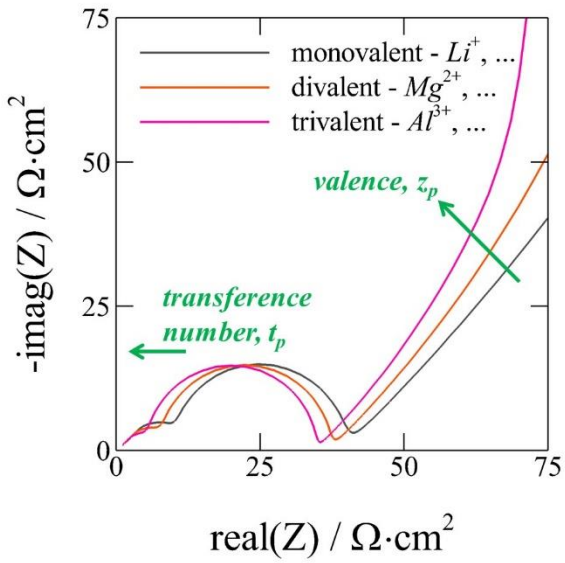

Figure 39. As cationic charge increases; diffusional impedance decreases which result in a higher slope low-frequency tail. Moreover, a multivalent cation has a greater transference number and in turn, electrolyte transport resistance decreases. Here material nonlinearities, *e.g.*, multiphase intercalation, have not been accounted for.

In addition to these non-monotonic trends, often intercalation for multivalent cations takes place in multiple stages. Such multistage intercalation[185, 186] brings in material nonlinearities and further alters the impedance response.

3. THERMO – ELECTROCHEMICAL COMPLEXATIONS

Relevant Publications and/or Working Papers:

1. A. Mistry, K. Smith and P. P. Mukherjee (2018) *Electrochemistry Coupled Mesoscale Complexations in Electrodes Lead to Thermo-Electrochemical Extremes* ACS Applied Materials & Interfaces 10(34) 28644 (doi: 10.1021/acsami.8b08993)
2. A. Mistry, H. Reddy-Palle and P. P. Mukherjee (2019) *In Operando Thermal Signature Probe for Lithium Ion Cells* Applied Physics Letters 114(2) 023901 (doi: 10.1063/1.5082794)
3. A. Mistry, A. Verma and P. P. Mukherjee (2019) *Controllable Electrode Stochasticity Self-heats Lithium-ion Batteries at Low Temperatures* working paper
4. A. Mistry *et al.* (2019) *Atypical Mechanistics of Electrodeposition in Intercalation Electrodes* working paper

Thermo-electrochemical extremes continue to remain a challenge for lithium-ion batteries. Contrary to the conventional approach, we propose herein that the electrochemistry coupled and microstructure mediated cross-talk between the positive and negative electrodes ultimately dictates the off-equilibrium coupled processes, such as heat generation and the propensity for lithium plating. The active particle morphological differences between the electrode couple foster thermo-electrochemical hysteresis, where the difference in heat generation rates changes the electrochemical response. The intrinsic asymmetry in electrode microstructural complexations leads to thermo-electrochemical consequences, such as cathode-dependent thermal excursion; and co-dependent lithium plating otherwise believed to be anode-dependent.

3.1 Background

Recent years have witnessed an escalated interest in the lithium-ion batteries (LIBs) for vehicle electrification and stationary storage[11, 13, 151, 153, 155, 168, 169, 206-208]. Physicochemical interactions in these batteries are electrochemical (*i.e.*, performance), thermal (*i.e.*, heat generation), chemical and mechanical (*i.e.*, degradation) in nature[12, 13, 16, 105, 150, 154, 157, 170, 209-220]. Each of these phenomena occurs at the pore-scale in porous electrodes, and in turn manifests as observables like voltage, capacity, and temperature. Most of the studies in the literature investigate only one or a few of these interactions leading to an incomplete understanding of the cell dynamics. Especially, the knowledge interrelation among these interactions remains largely elusive given such a myopic treatment. The battery electrodes are in the form of composite porous structures[63, 80, 91, 221] where

each phase assists one or multiple forms of transport processes. The charge transfer, as well as electrochemical reactions, give rise to heat generation[117, 222, 223], which in turn is to be carried away by a cooling system for temperature control. Since the associated transport processes are affected by electrode microstructure, a rational choice can potentially alter heat generation rates. Similarly, the chemical and electrochemical side reactions causing performance decay are also closely intertwined with the microstructural arrangement. Often studies characterizing novel phenomenon are carried out on individual electrodes, while in practice the LIBs operate in a full cell configuration. During operation, both the battery electrodes (anode and cathode) exchange charge and species signals, and correspondingly their behavior become closely interdependent. This tight coupling among the transport and kinetic interactions[25, 174] leads to a reciprocal relationship between electrochemical performance, temperature rise, and degradation.

The present investigation is aimed at elucidating the role of electrode microstructures on speciation and physical evolution inside LIBs. Specifically, the importance of anode and cathode microstructures and how it alters the physicochemical response is studied. For a coupled thermal-electrochemical performance, change in direction of current (charging *vs.* discharging) is found to foster different heat generation behavior. This thermal hysteresis is also summarized. During the charging operation, Li plating at the anode is an unwanted side reaction. How microstructural variation affects this plating potential is also probed. The following illustration provides an overview of these inseparable effects and helps to recognize the objectives of the present study.

3.2 Physicochemical Evolution inside a Li-ion Cells

Electrodes are electrochemical reaction zones that gradually translate ionic current into electronic, and vice versa. In LIBs, energy is stored in the form of intercalated Li, adding an additional intricacy to the electrode physics. The sequence of events is opposite at the two electrodes, for example, during charging, cathode deintercalates and converts electronic current (from the external circuit) into ionic (internal circuit), while anode follows this in reverse. Given the local and global charge neutralities, there is no time lag in response of the two electrodes. At any instant, the same amount of total current (ionic + electronic) flows through any cross-section of the cell along the thickness direction.

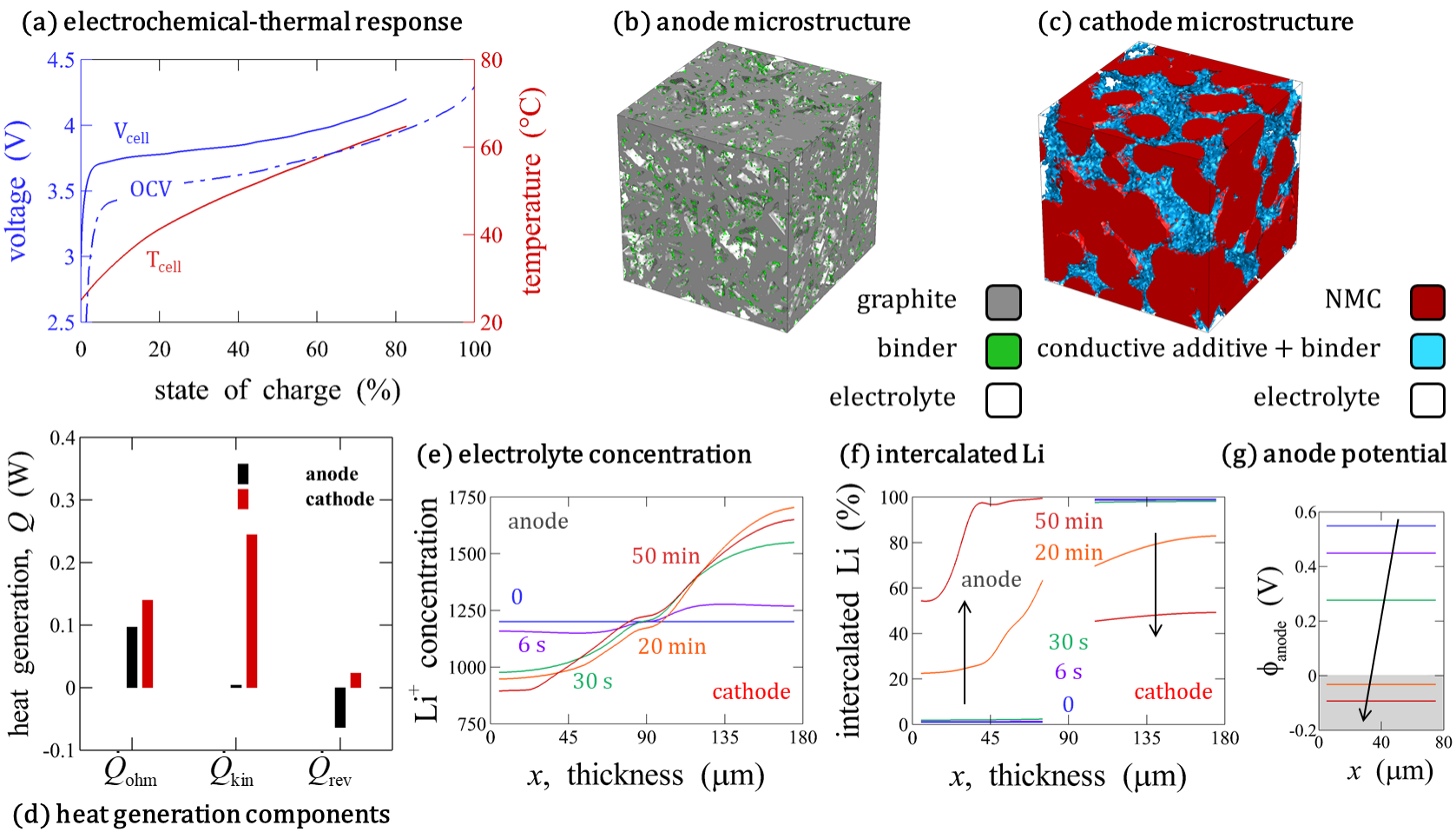

Figure 40. Physicochemical Interactions in a Li-ion Cell: Electrochemical-thermal response of a graphite-NMC full cell under adiabatic conditions and evolution of internal states. (a) voltage and temperature rise for a 1C charging operation between 2.8 – 4.2 V; (b) representative anode microstructure with 95 %wt. graphite and (c) cathode has 90 %wt. NMC; (d) deconvolution of total heat generation; progression of (e) electrolyte concentration and (f) intercalated Li in the active material; (g) anode voltage can drop below zero towards the end of charging and cause irreversible loss of Li inventory.

Since most of the cathode active materials have very poor electronic conductivity[19], conductive additives like acetylene black are added to facilitate electron transport. On the other hand, the most commonly used anode – graphite is quite a good conductor. Both the electrodes have a polymeric binder to ascribe mechanical rigidity to the porous structure. Of many different morphological forms of graphite, platelet particles are studied here (Figure 40(b)). Platelet graphite offers appealing advantages given its geometrical proportions. It has much higher interfacial area and shorter diffusion length (as thickness becomes the preferred intercalation direction) when compared against spherical counterparts. Higher interfacial area reduces the kinetic overpotential while shorter diffusion length reduces mechanical degradation[224, 225]. On the flip side, the resultant microstructure has platelets which make for a highly distorted pore network (compared to spherical particles) and equivalently results in a higher pore phase resistance (tortuosity). Refer to Microstructural Comparison – Platelet Graphite *vs.* Spherical NMC for more details. For the cathode, nickel manganese cobalt oxide is the present-day material of choice (here NMC111 is used for discussion, while the implications stay relevant for other NMC types as they have similar microstructural attributes and equivalently signatures for physicochemical interactions). The corresponding particles are spherical in shape (Figure 40(c)). Figure 40(a) presents the evolution of cell voltage and temperature under adiabatic conditions as it captures all the generated heat and identifies the upper bound on temperature rise (similar conditions are used for most of the results presented here; the mathematical description employed here has been presented and validated in an earlier work[117]). The open circuit voltage (OCV) is also shown alongside for comparison. The microstructural attributes of both these composite electrodes have been abstracted in terms of effective properties as a function of electrode recipe based on detailed pore-scale simulations[174]. Table 4 summarizes these trends for the anode, while the expressions for the cathode are presented earlier by the authors[174].

The temperature rise directly corresponds to heat generation rates, namely, ohmic heat (related to long-range interactions, *i.e.*, transport of charge and species over the electrode length), kinetic heat (related to short-range interactions, *i.e.*, electrochemical reactions at the electrode-electrolyte interface) and reversible/ entropic heat (as per the Second Law of Thermodynamics, not all the stored energy can be converted to electricity/ work and a part manifests as heat). Here ohmic and kinetic heat jointly constitute the Joule or irreversible heat. Mathematically, these distinct modes of heat generation can be expressed as follows:

<u>*Ohmic heat*</u>:

$$\dot{q}_{ohm}\left(\boldsymbol{x}\right)=\sigma\nabla\phi_s\cdot\nabla\phi_s+\kappa\frac{\varepsilon}{\tau}\nabla\phi_e\cdot\nabla\phi_e+\kappa_D\frac{\varepsilon}{\tau}\nabla\phi_e\cdot\nabla\ln C_e \tag{118}$$

<u>*Kinetic heat*</u>:

$$\dot{q}_{kin}\left(\boldsymbol{x}\right)=j\eta=j\left(\phi_s-\phi_e-U\right) \tag{119}$$

<u>*Reversible heat*</u>:

$$\dot{q}_{rev}\left(\boldsymbol{x}\right)=-jT\frac{\partial U}{\partial T} \tag{120}$$

Here j is the volumetric rate of electrochemical reaction (in A/m^3), and q's are local heat generation rates (in W/m^3). As the cell is operated, heat generation rates change, in both time and space, in response to the evolution of chemical, electrochemical and thermal states. Figure 40(d) reports time-averaged contribution for each of these source terms. Contributions from anode and cathode are expressed separately to highlight trends arising from microstructural differences. Given the high surface area (equivalently smaller overpotential), kinetic heat contribution at the anode is quite negligible compared to the cathode. Ohmic heat is the dominant heat generation mode at anode due to higher tortuosity resulting from a platelet active material particle microstructure. On the other hand, at the cathode, both kinetic and ohmic heats have comparable contributions. The cathode has the appreciably higher amount of non-intercalating secondary solids compared to the anode. They partially cover the electrochemically active interface, thus leading to a higher kinetic loss. Moreover, the spherical particles have a smaller interfacial area compared to the anode. Both these aspects jointly give rise to higher kinetic heat at the cathode. The tortuosity values for the cathode are smaller compared to a platelet graphite anode, while given the higher presence of secondary solids, cathode porosities are to be kept smaller than anode for the same electrode capacity. The ratio of porosity to tortuosity accounts for pore phase resistance[174] and equivalently cathode ohmic heat is of similar magnitude as an anode. Reversible heat trend reflects the nature of dU/dT profiles for individual electrode materials (U is open circuit potential pertaining to the electrode active material). Fundamentally, OCP relates to exergy change and entropic coefficient, dU/dT represents entropy change associated with the lithiation/ delithiation reaction at each electrode. Both of these combined account for enthalpy of insertion reactions and are material properties. For the present discussion, functional dependences of U and dU/dT have been borrowed from the experimental literature[226-229].

Table 4. The effective microstructural property relations for an electrode containing platelet-shaped active material particles (semi-major axis: *a*, semi-minor axis: *b* and thickness: *h*), porosity ε and secondary phase content ε_2 (by vol.) with morphology ω are obtained based on pore-scale characterization studies.

Effective microstructural property	***Expression***
Pore – AM area[a,b]	$a_{01} = \left(1.6552 + 8.9631\left(1-\varepsilon-\varepsilon_2\right) - 9.0132\left(1-\varepsilon-\varepsilon_2\right)^2\right) \cdot \exp\left(-\varepsilon_2\left(8.0502 + 1.8920\varepsilon_2 - 4.7374\omega\right)\right) \cdot \left(1.4039 - 2.3096H + 1.5308H^2\right)\left(1.9284 - 1.6294B + 0.7602B^2\right)$
AM – binder area[a]	$a_{12} = \left(1.6292 + 12.1075\left(1-\varepsilon-\varepsilon_2\right) - 5.3096\left(1-\varepsilon-\varepsilon_2\right)^2\right) \cdot \varepsilon_2\left(1 - 1.1578\varepsilon_2 - 0.2646\omega\right) \cdot \left(2.2969 - 2.6953H + 1.7510H^2\right)\left(2.4435 - 1.4222B + 0.6747B^2\right)$
Total AM surface area[a]	$a_{1(0+2)} = \left(-0.3816 + 9.9848\left(1-\varepsilon-\varepsilon_2\right) - 8.6440\left(1-\varepsilon-\varepsilon_2\right)^2\right) \cdot \left(1.6054 - 2.4667H + 1.6379H^2\right)\left(2.2784 - 1.7966B + 0.8503B^2\right)$
Pore – binder area[a]	$a_{20} = \left(0.8906 + 8.8621\left(1-\varepsilon-\varepsilon_2\right) - 8.6711\left(1-\varepsilon-\varepsilon_2\right)^2\right) \cdot \varepsilon_2\left(1 - 1.5796\varepsilon_2 + 0.0303\omega\right) \cdot \left(2.8220 - 0.8011H + 0.2611H^2\right)\left(2.8624 - 0.6761B + 0.2126B^2\right)$
Tortuosity	$\tau = \left(0.5808 + \varepsilon_2\left(2.4100 - 1.8620\varepsilon_2 + 0.5333\omega\right)\right) \cdot \left(0.6617 + 0.2643H + 3.4104H^2\right)\left(0.6441 - 0.8419B + 0.3891B^2\right) \cdot \varepsilon^{-\left(1.0522 - \varepsilon_2\left(1.2666 - 0.9306\varepsilon_2 - 0.5961\omega\right)\right)\left(1.5636 - 2.1463H + 1.1537H^2\right)\left(2.1711 + 1.2525B - 0.2530B^2\right)}$
Conductivity[c]	$\sigma = \left(0.9547 + \varepsilon_2\left(0.9852 - 1.4836\varepsilon_2 - 0.0697\omega\right)\right) \cdot \left(0.9472 + 0.3806H - 0.2624H^2\right)\left(0.9469 + 0.2492B - 0.1241B^2\right) \cdot \left(1-\varepsilon-\varepsilon_2\right)^{\left(1.6507 + \varepsilon_2\left(0.5783 - 2.8421\varepsilon_2 - 0.0575\omega\right)\right)\left(1.0176 + 0.8864H - 0.6257H^2\right)\left(1.0420 + 0.5237B - 0.3041B^2\right)}$
[a] divide by semi-major axis a to obtain value in physical units; the expressions represent dimensionless values	
[b] *H* and *B* are normalized thickness and semi-minor axis: $H = h/a$ and $B = b/a$	
[c] multiply by the bulk conductivity of graphite $\sigma_0 = 16{,}700$ S/m to obtain value in the physical units	

The evolution of internal states is presented subsequently. Figure 40(e) describes the spatiotemporal distribution of Li^+ ions. During charging, Li inventory shifts from the cathode to

the anode. This transport takes place *via* electrolyte and equivalently a gradient in Li^+ concentration profile manifests from cathode to anode direction. The slope of concentration profile changes locally as Li^+ participates in electrochemical reactions at electrodes. The electrolyte phase concentration profile exhibits non-monotonic evolution in time. Initially, the gradients build up as more and more Li deintercalates at the cathode, migrates to the anode as Li^+ and intercalates there. After a time (~20 min) the slope appears to decrease despite the cell operation proceeding in the same direction. This qualitative change is correlated to the temperature dependence of transport coefficients[24, 117, 230]. The electrolyte phase diffusivity (transport property responsible for C_e profile) improves with temperature. After this time instant, the cell temperature has risen sufficiently high in order to bring about a positive change in the concentration profile. The intercalation states are presented in the form of Li concentration at the active interface (Figure 40(f)). Since intercalation is a reversible reaction, one would expect similar concentration evolution for intercalated Li. The microstructural differences alter the local distribution of reaction rates, which in turn emerges as dissimilar concentration evolution at both the electrodes. Specifically, the deintercalation events at cathode appear more uniform compared to intercalation at the anode, which points to a higher transport resistance at the anode. This is confirmed by a more biased electrochemical reaction distribution (biased towards the anode-separator interface). Figure 40(g) shows the evolution of the anode potential during the above-described operation. Towards the end of the operation, it adopts subzero values and triggers Li plating. Li plating culminates in an irreversible loss of Li inventory.

Following up on this discussion of microstructure mediated physicochemical evolution, here different forms of microstructural influences are presented. The predictions discussed here are based on a pseudo-DNS (direct numerical simulation) electrochemical-thermal model developed earlier[117, 230]. This description accounts for realistic microstructural details based on explicit pore-scale interactions[174] and appropriately scales up from RVE (Representative Elementary Volume) to electrode lengths. Such detailed analysis accounts for the observed nonmonotonic trends in performance as a function of non-intercalating phases that have been recorded in half-cell testing[27, 30, 33, 173, 231] but remained elusive to explain up until recently[25, 174]. Additionally, the role of electrode preparation stage[83, 164] is also captured in the form of secondary phase morphology[174]. A recent work by authors studied the variability of cathode structure[25, 174],

while joint interactions among anode and cathode are yet quite poorly understood and are the focus of the present exploration.

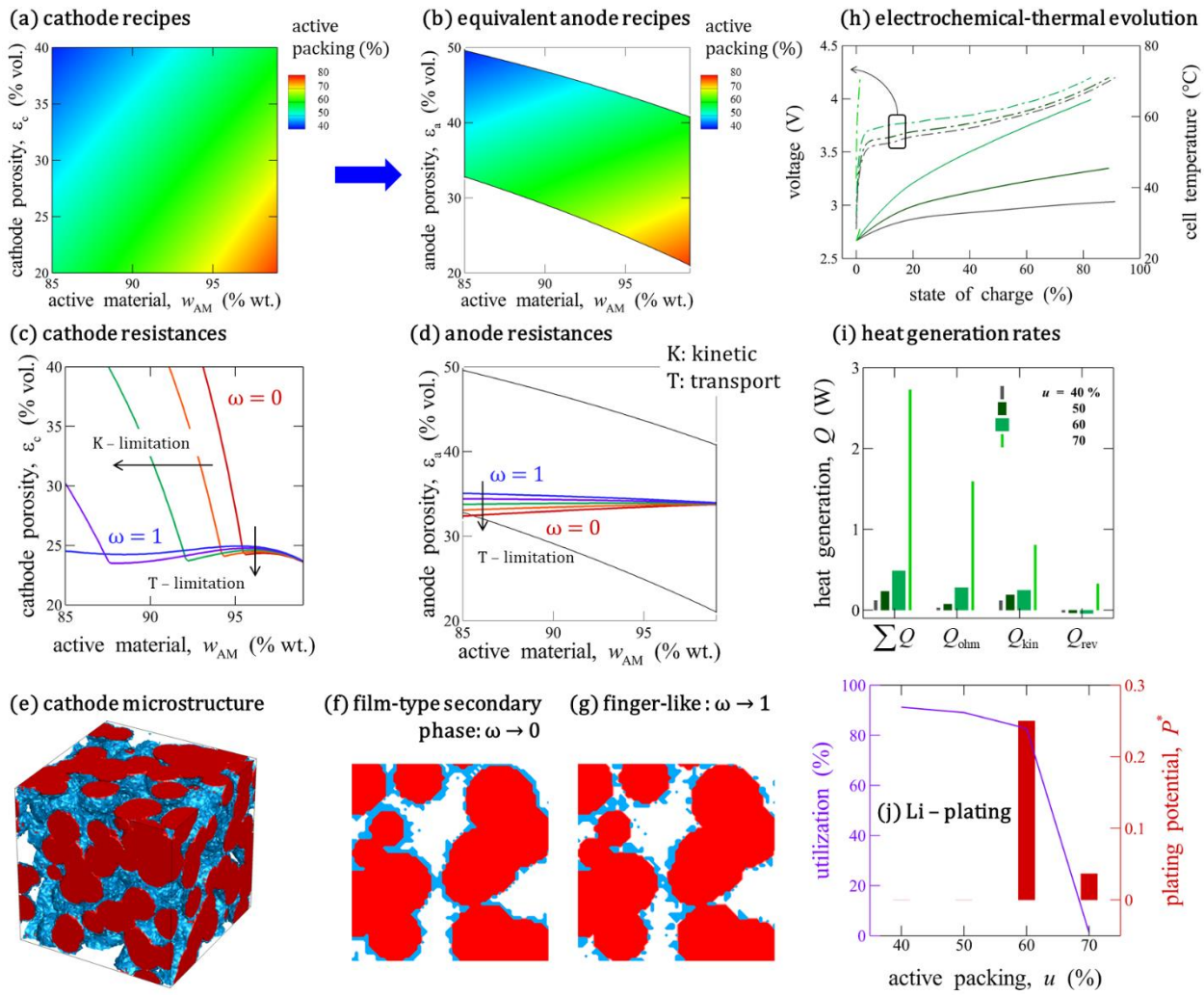

Figure 41. Interdependence of Electrode Recipes and Microstructural Limitations: Electrode selection for a Li-ion full cell requires one to balance Li storage capacities at (a) cathode and (b) anode. Since the active and secondary phase have different constituents for both the electrodes, one cannot freely choose anode specifications. Based on cathode recipe (a), only a subset of anode microstructures (b) leads to a balanced cell. Such thermodynamic considerations (a) and (b) do not account for microstructural limitations. Electrode microstructural characterization elucidates the severity of different resistive modes at (c) cathode and (d) anode. Given the different microstructural arrangements, cathode experiences both kinetic and transport (ionic and electronic) limitations, while anode behavior is largely dictated by long-range electrolyte transport effects. Moreover, the secondary phase morphology has a much stronger effect at the cathode. For the same arrangement of active particles (e), these morphological differences are shown in (f) and (g). Active packing, u = theoretical capacity/ maximum theoretical capacity is a direct measure of energy density. Differences in electrochemical-thermal response with energy density are shown in (h) – (j).

Past studies explored the effects, such as carbon – to – binder ratio,[25, 33, 174] particle size,[224, 225] and electrode thickness[29]. The focus here is to probe the intricate complexations stemming from composition – microstructure interplay, where carbon – to – binder ratio is fixed at 1:1 by weight (proved to provide good electrical conduction and mechanical stability); mean particle volumes are kept identical to demonstrate the shape dependent effects (5μm radius for NMC particle, and 2μm thickness for graphite platelet), and each electrode having a thickness of 80 μm.

3.3 Electrode Specifications are Interdependent

Conventionally, the LIBs are designed to be cathode limited[150, 232-235] to combat anode centric degradation behavior. Theoretically, the upper bound on lithium storage is realized when the entire electrode volume is filled with an active material (*i.e.*, no porosity), but such an electrode cannot operate because of kinetic and transport limitations[14] and a working electrode invariably requires other material phases. Figure 41(a) presents active packing for different electrode specifications, *i.e.*, cathode porosity and active material (NMC) weight percentages. Active packing, u = theoretical capacity/ maximum theoretical capacity. Secondary solids are assumed to be present in a 1 : 1 weight ratio (acetylene black : PVDF binder) as this ratio gives the highest electronic conductivity[27, 30, 174]. A unique aspect of composite cathodes is the presence of secondary solids and their interfacial arrangement. The spatial distribution of these phases can assume a range of morphologies[174]. Authors recently proposed a description for composite cathode microstructures which accounts for the secondary phase and its morphology. These morphological arrangements span in between a film-like (2D) and a finger-type (3D) deposition and are expressed using a dimensionless descriptor, ω, called the morphology factor. $\omega \rightarrow 0$ leads to the film-type secondary phase, while $\omega \rightarrow 1$ represents the other extreme. These morphological arrangements are schematically shown in Figure 41(f) – (g), and strongly dictate the kinetically and transport limited electrode recipes (Figure 41(c)). For the same amount of secondary phase, a 2D morphology covers more active area (compared to a 3D) and in turn leads to a higher kinetic limitation. On the other hand, a 3D structure has a greater interference with the pore (electrolyte) phase and results in a higher tortuosity, *i.e.*, a greater transport resistance. The kinetic and transport limitations do not necessarily occur simultaneously, as is evident by the joint cathode microstructural limitations map – Figure 41(c).

Since anode and cathode materials have different Li storage capacities, the anode recipes that match the capacities of corresponding cathode specifications are limited (Figure 41(b)). Note that the anode recipes sketched in Figure 41(b) ensure 1 : 1 anode – to – cathode loading, *i.e.*, identical Li storage capacities. As mentioned earlier, the platelet graphite anode has quite a large active area and subsequently, kinetic limitations are almost absent from the range of anode recipes presented in Figure 41(b). The microstructural resistance map for this range of anode recipes, Figure 41(d), show dominant transport limitations arising from higher tortuosity of anode microstructure. Given the smaller (volumetric) amount of binder at the anode, binder morphology does not quite strongly alter the zones (Figure 41(d)). Additionally, the platelet geometry has a higher interfacial area, leading to a relatively smaller amount of coverage when compared to a spherical particle for the same amount of secondary phase. Note that the density of cathode active material is about 2.5 times that of the anode, and in turn for the same weight percentage, secondary phase volumes at the cathode are about twice that of the binder at the anode. All these combined together result in a weaker morphology dependence at the anode.

Here Figure 41(a) and (b) illustrate the correlation among the specifications of the electrode couple, while Figure 41(c) and (d) demonstrate the expected resistive modes. An ongoing challenge is to fabricate energy dense electrodes that are also power dense[29, 161, 182, 236, 237]. As energy density is increased, either by increasing active material content (*i.e.*, active packing, u) or electrode thickness, the physicochemical complexations manifest as various phenomena are mutually coupled and alter the overall behavior rather nonlinearly. To demonstrate these complications, Figure 41(h) – (j) compare the cell response for 1C charging as active packing is increased from u = 40% to 70%. Active packing simply denotes the amount of electrode volume filled in by active material. Increasing active packing, cell voltage increases since the microstructural resistances intensify (Figure 41(h)). This resistance increase concurrently manifests as increased heat generation rates in the thermal space (Figure 41(i)). Interestingly, at higher packing (u = 70%), the resistances (and so heat generation) are so high that the cell voltage suddenly reaches the upper voltage cutoff, and capacity drastically reduces (Figure 41(h) and (j)). Temperature rise is proportional to both the heat generation rate as well as capacity and since the internal resistance is so high at higher active packing, the temperature rise is lower. In other words, temperature rise exhibits a quadratic trend with active packing. As mentioned earlier, anode potential is tracked during the operation in order to quantify the likelihood of Li plating. Figure

41(j) reports this propensity (mathematical definition is supplied later on). It shows that lower active packing has no plating while higher energy cells exhibit a plating problem. Notice that the plating trend is also not a monotonic one. In other words, as the energy density is increased, various phenomena interact more closely and demonstrate a rich dynamics. In a broader picture sense, this demands an all-encompassing investigation.

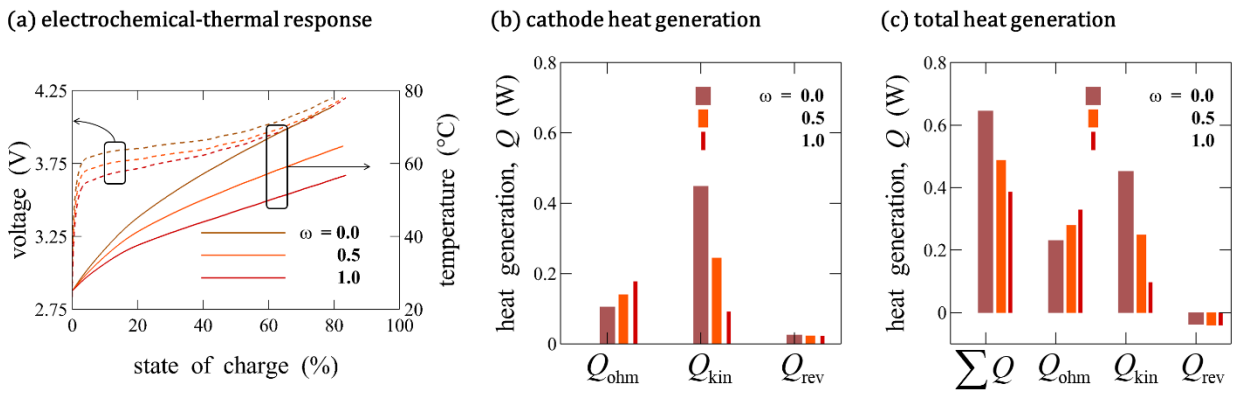

Figure 42. Secondary Phase Morphology at Cathode: Both the electrodes have identical compositions and only the morphology of secondary phase (conductive additive + binder) at the cathode is varied. (a) Voltage and temperature evolution during 1C charging in the voltage window 2.8 – 4.2 V (b) kinetic and ohmic heat generation at cathode vary with secondary phase morphology, and these trends translate to (c) total heat generation components.

3.4 Effect of Secondary Phase Morphology at Cathode

Figure 42 presents the cell behavior for three different cathode microstructures. The morphology of conductive binder domains (*i.e.*, the secondary phase at the cathode) is varied to realize different cathode microstructures while keeping the phase contents unchanged. Also, the anode structure is kept identical with anode – to – cathode loading ratio set to 1. Going from ω = 0 to 1, the active area at the cathode increases which decreases the kinetic overpotential and in turn the cell voltage decreases and capacity increase (Figure 42(a) voltage trends). Concurrently, the temperature rise is smaller, *i.e.*, the total heat generation also decreases. Figure 42(b) presents the deconvolution of cathode heat generation. The kinetic heat decreases monotonically with ω, while the ohmic heat shows an opposite trend. Higher morphology factor, ω, leads to a greater active area as the secondary solids make more 3D arrangements. It also gives rise to a higher tortuosity (*i.e.*, pore phase transport resistance) as 3D secondary phase distribution forms an additional pore network

with smaller pores[174]. Higher active area leads to smaller kinetic overpotential and in turn smaller kinetic heat generation as a function of secondary phase morphology. Higher tortuosity leads to greater ohmic heat with increasing morphology. The decrease in kinetic heat is greater than the increase in ohmic heat, resulting in an overall decrease in total heat generation. Both the electrodes are 80 μm thick for the set of calculations reported here. As electrode thickness is increased, the dominant resistance shifts from kinetic (thin electrodes) to transport (thick electrodes)[29]. Hence the qualitative nature of total heat generation as a function of morphology is intertwined with electrode thickness. For thicker electrodes, it is expected that the increase in ohmic heat is more dominant and subsequently higher morphologies ($\omega \rightarrow 1$) could prove detrimental. As anode structure is not altered, the total heat generation trends qualitatively follow the cathode heat generation behavior (Figure 42(c)).

3.5 Anode – to – Cathode Loading Ratio

Often it is argued to have higher anode storage capacity than cathode (*i.e.*, A/C > 1) in order to mitigate the anode – centric degradation response. The first argument relates to the OCP of graphite which reaches zero upon complete lithiation. Li plating takes place if the graphite potential drops below zero. Hence from thermodynamic reasoning, it is advisable to have a higher anode capacity that in turn ensures that graphite is never fully lithiated and equivalently plating is circumvented. The second reasoning for higher anode capacity relates to irreversible capacity loss[235]. Anode experiences two deleterious side reactions – plating and SEI formation. A higher capacity anode is expected to provide for the irreversible loss without appreciably affecting the (reversible) achievable cell capacity. A third but less common justification points that the current per unit mass of graphite reduces as anode loading is increased. Since the degradation reactions are slower at lower currents, a higher loading should reduce capacity decay. Though being true in principle, these rationalizations do not account for the involved transitions taking place at the pore-level and are often misleading. Figure 43 reports the influence of the anode – to – cathode ratio on cell dynamics. The cathode is kept unchanged, while anode porosity is varied to increase active material content (volumetric) at the anode (composition is fixed at 95 %wt. graphite and 5 %wt. binder). Since both the electrodes are 80 μm thick, the ratio of electrode storage capacities is related to microstructure descriptors *via* the following relation:

$$A/C = \frac{\varepsilon_{Gra}\Delta C_a L_{andode}}{\varepsilon_{NMC}\Delta C_c L_{cathode}} = \frac{\varepsilon_{Gra}\Delta C_a}{\varepsilon_{NMC}\Delta C_c} \tag{121}$$

where ε_{Gra} and ε_{NMC} are volume fractions of graphite and NMC at anode and cathode respectively. ΔC_a and ΔC_c correspond to the range of intercalated Li concentrations for the voltage window of operation (2.8 to 4.2 V cell voltage). Note that these concentration ranges are identified from OCP profiles of individual electrode materials. Thus, for the same cathode structure, A/C ratio is increased by increasing ε_{Gra}, *i.e.*, decreasing the anode porosity as the rest of the terms are material properties in Equation (121). Note that the A/C ratio alters the OCV as well.

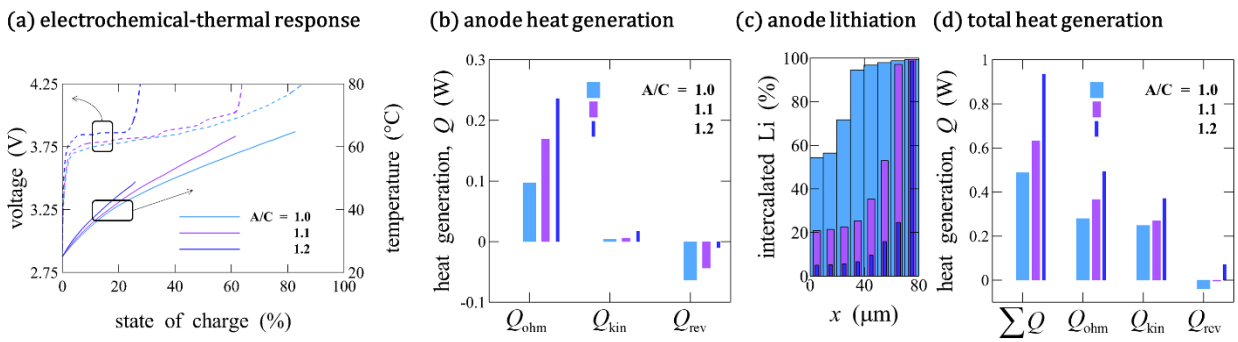

Figure 43. Anode – to – cathode Ratio: Anode Li storage capacity increases at higher A/C ratio, but this negatively affects the finite rate electrochemical performance as transport resistance also increases concurrently. (a) Cell voltage and temperature trends for 1C charging (b) components of heat generation at anode (c) intercalation state of the anode at the end of charge (d) total heat generation components averaged over the time of charging for each cell.

Figure 43(a) examines the effect of the A/C ratio on cell voltage and temperature response. The overpotential seems to increase going to a higher A/C ratio and equivalently the cell capacity decreases when charged at 1C. Though the maximum cell temperature shows a quadratic trend with A/C ratio, the rate of temperature rise (*i.e.*, heat generation) is monotonically related. The maximum temperature rise depends both on the heat generation rate as well as the capacity, and since the capacity markedly decreases going for higher A/C values, the maximum temperature rise shows such a non-monotonic variation. When the heat generation rates at the anode (Figure 43(b)) are dissected, it is revealed that the ohmic heat generation shows a considerable increase with A/C loading ratio. The kinetic heat also shows an associated increase. This behavior is quite thought-provoking and is noticeably different than the cathode morphology effects. When the anode

intercalation profiles (at the end of operation) are compared, the root cause is revealed (Figure 43(c)). With higher anode loading, the transport resistance becomes quite prevalent. Li^+ ions coming from the cathode side only partially penetrate the anode thickness. This penetration depth refers to the fraction of anode available for intercalation. Going for a higher A/C ratio, successively a smaller portion of the anode is amenable to intercalation and effectively, preferentially intercalation takes place near the anode – separator interface. As these locations are fully intercalated and Li^+ flux cannot supply reactants to sustain electrochemical reactions in the interior of the anode (given the increased transport resistance), the overpotential is driven to high enough values cause the cell shutdown. This increased transport resistance reflects on ohmic heat generation trends. Additionally, as the same amount of current is now concentrated over a smaller portion of the anode (at a higher A/C value), the corresponding kinetic overpotential increases, resulting in a higher kinetic heat generation. Note that the cathode is not varied and equivalently the charging current is identical for these different cells with varying A/C ratio. Thus, the difference in behavior stems from microstructural changes at the anode. Figure 43(d) presents the components of total heat generation which follow the trends at the anode (Figure 43(b)). In summary, with increased A/C ratio, the anode transport resistance increases considerably which in turn leads to localized intercalation as well as a capacity limitation. Since at higher anode loading, intercalation predominantly takes place near the anode – separator interface, it does not mitigate plating but rather just shifts the location of the highest Li electrodeposition. Note that such coupled interactions are a signature of cells with high energy electrode couples as explained in Figure 41(h) – (j), and are to be carefully looked into for the next generation battery technology. Such (largely) unexpected response suggests a revision in battery design where electrochemical specifications are not sufficient. Instead of accounting for thermal effects as an afterthought (as is being done for present-day applications), they would have to be considered from the very beginning.

3.6 Thermo-electrochemical Hysteresis

With the presence of different microstructural arrangements at anode and cathode, if the direction of current flow is reversed (*i.e.*, charging *vs.* discharging), one would expect different heat generation behavior. This thermal hysteresis is investigated in Figure 44. Representative voltage and temperature trends at 1C are presented in Figure 44(a) and (b), respectively. The start of

individual operations is marked with red circles. The cell is being charged is at 2.8 V OCV, while the one being discharged is at 4.2 V OCV, to begin with. The cell voltages at the onset do not coincide with these values given the initial overpotential (Figure 44(a)). The width of the gap between the two voltage profiles represents the cumulative contributions of various forms of resistance.

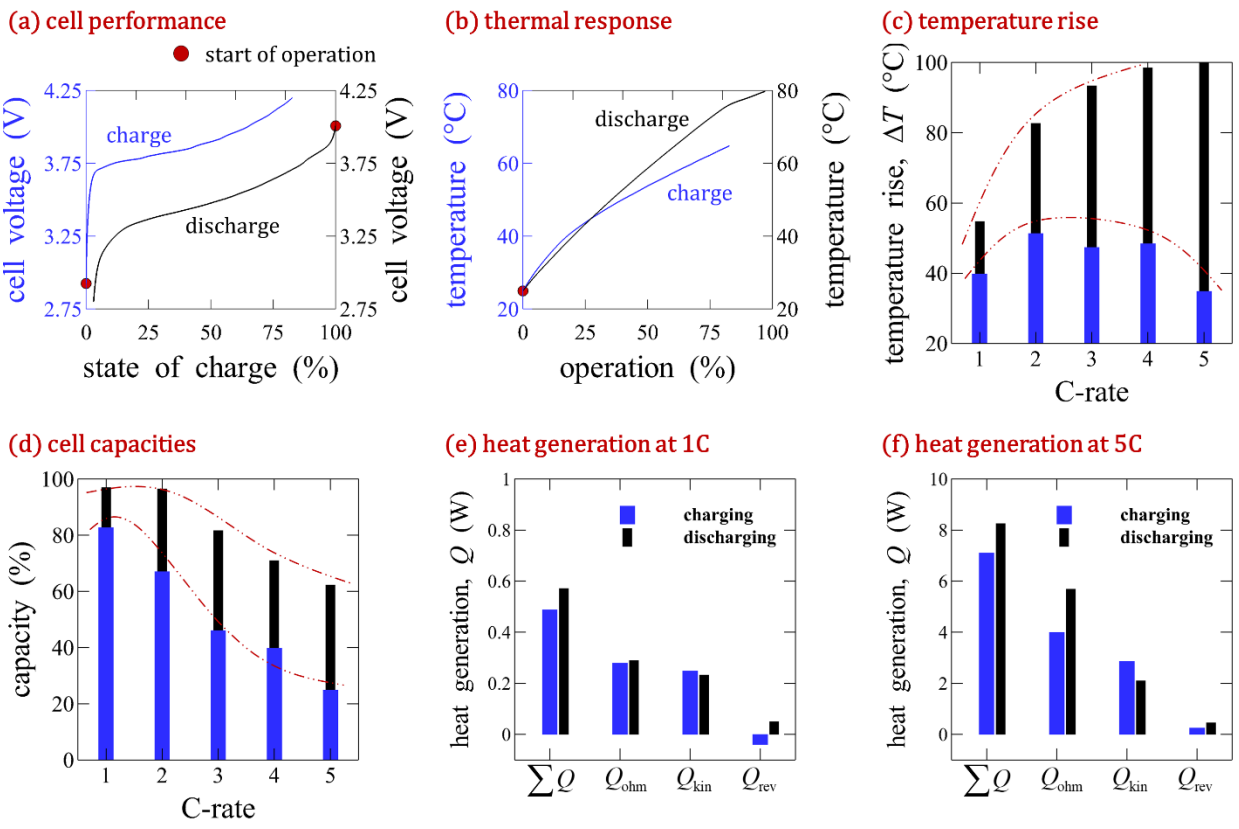

Figure 44. Charge-discharge Hysteresis: Given dissimilar microstructures at anode and cathode, the direction of current flow (*i.e.*, charging or discharging) brings about different thermal behavior. A comparison of (a) cell voltage and (b) temperature for charging and discharging operation at 1C. (c) Temperature rise and (d) cell capacity exhibit different trends with C-rate for charging and discharging operation. Deconvolution of total heat generation at (e) 1C and (f) 5C identify the cause of thermal hysteresis. These results describe the thermally triggered hysteresis for the same cell as Figure 1, *i.e.*, 95 %wt. graphite and 90 %wt. NMC with identical capacities.

The corresponding temperature evolutions are shown in Figure 44(b) and the trends demonstrate the differences in heat generation rates, *i.e.*, thermal hysteresis. Cell temperature rise and capacities over a range of operating rates are shown in Figure 44(c) and (d), successively. As mentioned

earlier, the temperature rise is correlated with both the rate of heat generation as well as capacity. The heat generation rates increase with increasing C-rates. The charging capacities fall faster and equivalently the temperature rise exhibits a quadratic trend with C-rate for the charging operation. On the other hand, the discharge capacities are fairly high giving rise to a monotonic trend over the range of C-rates studied (Figure 44(c)). Notice that the discharge temperature rise saturates as going from 1 to 5C, which in turn suggests that the quadratic behavior will be observed at higher rates for the discharge operation. This is an interesting situation where the thermal effects lead to different charge and discharge capacities (*i.e.*, electrochemical hysteresis), and given this cause-and-effect relationship from thermal to electrochemical effects, this phenomenon is termed as "thermo-electrochemical hysteresis". For the present results, it has been assumed that all the generated heat contributes to raising the cell temperature. Under adiabatic operation, this is a fairly accurate assumption and is in line with past investigations[117, 230].

To understand the mechanisms leading to such an intricate response, the components of total heat generation are quantified for two different operating rates: 1C and 5C (Figure 44(e) and (f)). Average heat generation is found to be higher for the discharge operation, explaining the corresponding higher temperature rise. At 1C, the difference in total heat generation stems from a change in signs of reversible heat contribution (Figure 44(e)). While at a higher rate of 5C, the disagreement is a result of kinetic and ohmic heat (Figure 44(f)). Comparing across Figure 44(e) and (f), one can surmise that the ohmic heat is more for the discharge operation, while the kinetic heat is higher during charging. Higher ohmic heat for the discharge signifies greater pore phase transport resistance (all the electrode recipes studied here have electronic conductivities of the order of 1 S/m, and higher, and equivalently electronic conduction limitations do not arise in the solid phase[25, 174]). The anode is the source of pore phase transport resistance. During charging, Li^+ ions transport from the cathode to anode, while during discharge the motion in the opposite direction takes place. This flux of Li^+ does not necessarily traverse the entire thickness of anode during charging since the incoming Li^+ prefer to participate in an electrochemical reaction when transport resistance is higher. The situation differs during discharge where electrochemical reactions generate Li^+ throughout the anode thickness. The generated ions have to travel a greater distance in the anode, which in turn leads to a higher effective transport resistance and ohmic heat generation as observed in Figure 44(e) and (f).

The kinetic heat exhibits a different trend. Note that the kinetic heat contributions are due to the cathode. During charging the intercalated Li fraction at the cathode goes from $x \approx 1$ to $x \approx 0.3828$ (for OCV = 4.2 V), while discharge operation observes the opposite shift, *i.e.*, from $x \approx 0.3828$ towards 1. The local current source term has the following functional form:

$$j = ak(T)C_s^{max}\sqrt{C_e x(1-x)}\left\{e^{F\eta/2RT} - e^{-F\eta/2RT}\right\} \tag{122}$$

The group $x(1 - x)$ takes the highest value at $x = ½$. Also, the rate constant k exhibits an Arrhenius dependence on temperature. Now during discharge, the intercalation content starts at $x \approx 0.3828$ reaches 0.50 and then increases to 1. In other words, the prefactor $x(1 - x)$ decreases towards the end of the discharging operation. This decrease is partly compensated by a temperature-induced increase in rate constant k. While during charging, at the onset $x \approx 1$, as well as the temperatures, are smaller, both of which gives rise to a high value of kinetic overpotential and subsequently a higher kinetic heat compared to discharge (Figure 44(e) and (f)).

3.7 Electrodics Cross-talk

As alluded to during the discussion on electrode recipe and microstructure (Figure 41), different electrode specifications can have a similar capacity (related to active material volume). Figure 45 studies the physicochemical response for a range of electrode recipes having identical theoretical capacity (*i.e.*, active packing). Henceforth, observed differences are predominantly correlated to microstructural complexations. First, consider Figure 45(a) where 1C charging capacity is plotted for a broad range of anode and cathode structures. A few representative structures are also shown in order to aid visual comparison. Porosity and secondary solid contents are varied to maintain identical electrode capacities. The plotted 1C charging capacity is reported in a normalized fashion.

As the kinetic and transport resistances for these structures vary, the cell performance is expected to change despite each having identical active material content. It is apparent that the capacities show a spread of about 30% (Figure 45(a)). Interestingly this capacity map, Figure 45(a), is more sensitive to changes in anode structure as stronger gradients exist along the anode axis. As binder content is increased at the anode, porosities are accordingly decreased to maintain constant active material (graphite) volume. This comes at the cost of a higher transport resistance. The higher transport resistance renders a part of the anode inactive during charging and equivalently leads to a smaller capacity.

Figure 45(b) analyses these electrode combinations in terms of their heat generation and eventual temperature rise. Intriguingly, the microstructural variations at the cathode seem to most strongly alter the thermal response. Going from a 99 %wt. NMC to a 90 %wt. (cathode active material), cathode porosity is decreased to maintain constant capacity. This leads to a higher tortuosity as well as a smaller active area since the secondary solids occupy a larger portion. Both these effects are deleterious as smaller porosity and higher tortuosity increase the ohmic heating, while a smaller active area raises kinetic heat contribution. Thus, cathode alterations bring about a stronger shift in thermal response. The temperature rise over this range of electrode combinations for a full cell varies from 20 ºC to 40 ºC. The anode structure also modifies this thermal response, but the correlation is not as potent. Given the differences in active material densities at anode and cathode, the structural variation at the anode is in comparison milder, thus fostering a weaker dependence.

During the charging, the anode potential can drop below zero towards the end of the operation, which effectively promotes plating at the anode. This propensity for Li plating is characterized here *via* the following dimensionless quantifier:

$$P^* = \frac{1}{\bar{U}_\mathrm{a}} \cdot \frac{1}{t_{operation}} \int_{\text{if } \phi_a < 0} -\phi_a \, \mathrm{d}t \tag{123}$$

ϕ_a is the anode potential and non-dimensionalization is performed using the average anode OCP, $\bar{U}_\mathrm{a}$. Zero value of P^* suggests no plating, with successively higher values characterizing greater plating tendencies. Figure 45(c) discusses the effect of electrode microstructural variations on plating potential, P^*. Offhand, one would expect anode microstructure to have an effect on plating tendency, but curiously both the electrodes have a marked role on the propensity for plating. Note that all the electrode combinations studied in Figure 45 have similar anode and cathode capacities. Electrodes with smaller amounts of secondary solids have very negligible plating, while the ones with higher amounts (about 10 %wt.) seem to promote the highest irreversible Li deposition (Figure 45(c)). With decreasing anode porosity, anode transport resistance becomes so high that not the entire electrode is accessible to the incoming Li^+ flux from the cathode. This results in localized intercalation and pushes the anode potential, ϕ_a , below zero. The cathode microstructural effect on plating is somewhat more involved. As the secondary phase content increases on the cathode, the electrolyte phase transport resistance increases which in turn leads to a starker electrolyte phase potential drop, $\Delta\phi_\mathrm{a}$. Now due to a higher surface area of platelet

particles, kinetic overpotential at the anode is almost negligible, *i.e.*, $\eta_a = \phi_a - \phi_e - U_a \approx 0$. Which results in $\phi_a \approx U_a + \phi_e$, where $U_a \geq 0$ but $\phi_e < 0$. With a high cathode pore resistance, electrolyte phase potential becomes so small at anode such that $\phi_e < 0$. Thus, cathode microstructural modifications can also trigger Li plating at the anode (Figure 45(c)).

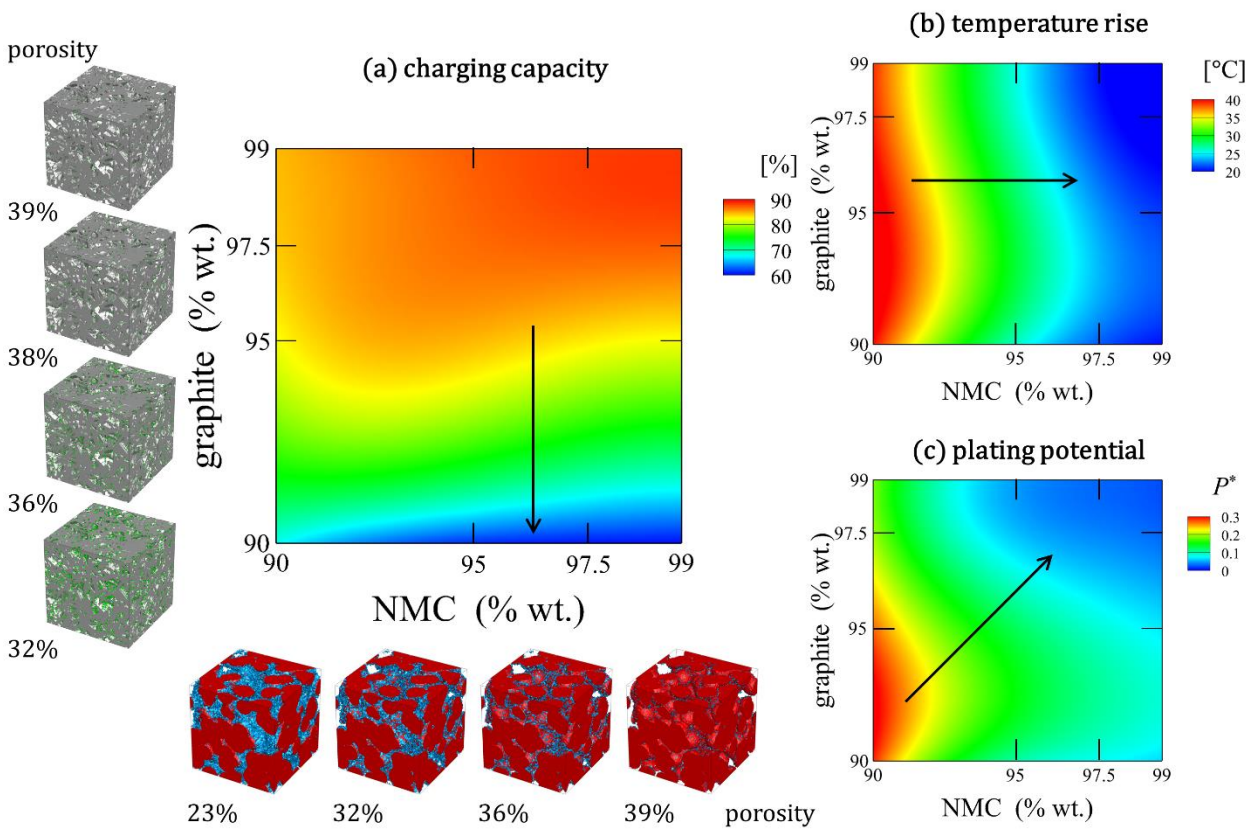

Figure 45. Electrode Recipes: Microstructural arrangement directly affects (a) electrochemical (b) thermal and (c) chemical interactions in a Li-ion cell. All the cells have the identical theoretical capacity and are charged at 1C. (a) Charging capacity (scaled using theoretical capacity) shows a stronger reliance on anode microstructure, while (b) the temperature rise appears to be correlated to cathode specifications. (c) Li plating behavior depends on both anode and cathode. Note that the anode and cathode are chosen such that each has the identical theoretical capacity (*i.e.*, A/C = 1.0). Representative electrode microstructures are also shown alongside.

Most of the studies on lithium plating in full cells focus on usual suspects like C-rate, temperature and charging voltage[238, 239]. However, these cannot explain curious observations, for example, a recent article[240] reports that "Lithium deposition on anodes of commercial cells is possible even at an ambient temperature of 25 ºC and charge C-rates as low as 0.5C." Given the engineering nature

of such records, one cannot pinpoint the origins of plating within the conventionally considered "safe" limits. Here in plating phenomenon has been found to depend on microstructural specifications as well and proffers a possible explanation for such odd observations. It is illuminating to see that the electrode microstructural modifications can potentially alter electrochemical performance, thermal response and chemical degradation (here Li plating). More intriguing is the unexpected correlation among these. For example, the electrochemical response is believed to be cathode limited but the anode is found to strongly affect the same (Figure 45(a)). Such interdependency underscores the coupled physicochemical evolution in both the electrodes.

3.8 Representative Heat Generation: Environmental Effects

High energy cells generate more heat and are accordingly more prone to safety risks. Thermal management systems are designed to control the cell temperature rise. These cooling strategies start with heat generation rates as an important design specification. As the cell internal resistance is strongly dependent on temperature (transport processes being thermally activated), the choice of thermal characterization technique can change the test outcome. For example, the cell internal resistance (and equivalently the heat generation) under an adiabatic condition is expected to be different than that during an isothermal operation, given the internal feedback loop among the transport processes and thermal behavior.

Figure 46 compares heat generation rates for 1C charging for two thermal extremes: adiabatic (no cooling) and isothermal (best cooling) conditions. An adiabatic characterization has no external intervention and correspondingly all the heat generated due to electrochemical operation goes towards raising the cell temperature (Figure 46(a)). On the other hand, in an isothermal operation, all the generated heat is carried away *via* a thermal management system and the cell temperature stays invariant (Figure 46(b)). A comparison among Figure 46(a) and (b) reveals that the isothermal operation gives rise to a higher amount of heat generation. The excess heat generation is presented in Figure 46(c) as a normalized value (refer to Equation (124)). It appears that an isothermal operation generates about 20 – 50% more heat. Such a distinction is quite relevant in practice for the cooling system design, as a better cooling system has a smaller temperature window and subsequently higher thermal load.

$$\delta Q = \frac{Q_{isothermal} - Q_{adiabatic}}{\left(Q_{isothermal} + Q_{adiabatic}\right)/2} \times 100\% \tag{124}$$

An adiabatic operation, where all the generated heat goes to raising the cell temperature, has an improved species and charge transport. This leads to the reduced amount of heat generation as the operation proceeds and manifests as the gradually decreasing temperature slope (refer to previous figures). Figure 46(c) also reveals that a suitable combination of anode and cathode microstructures can decrease this discrepancy between the two operations.

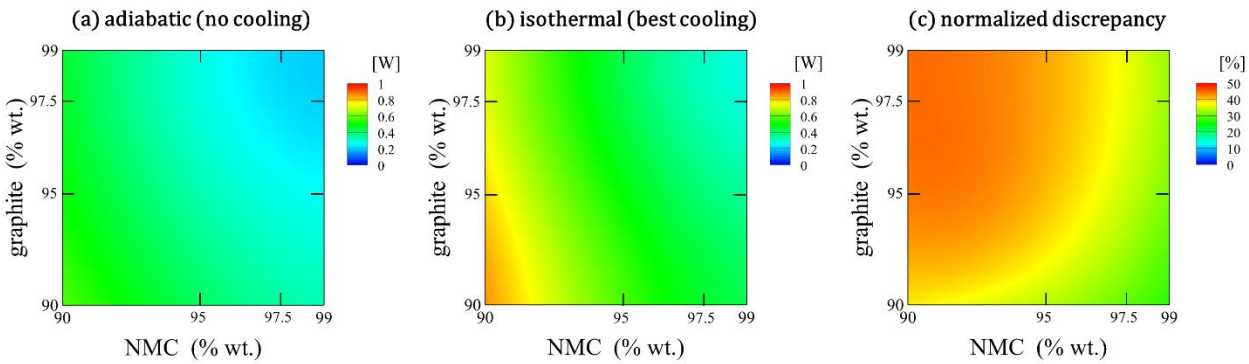

Figure 46. Role of Ambient Environment: The electrochemical and thermal responses in an LIB are closely intertwined. Hence, the choice of thermal conditioning affects heat generation as well as cell performance. Smaller average temperature leads to a higher amount of heat generation. In other words, (a) an adiabatic characterization underpredicts the heat generation rate compared to (b) an ideal thermal management system. This difference, $\delta Q = 100 \times 2\,(Q_{\text{isothermal}} - Q_{\text{adiabatic}})/(Q_{\text{isothermal}} + Q_{\text{adiabtic}})$ is a strong function of (c) electrode microstructure.

Transport processes are at the heart of every electrochemical system such as Lithium-ion batteries. The structural arrangement of multiple phases constituting a porous electrode modulate the short- and long-range interactions, which jointly manifest as the physicochemical evolution of the system during operation. Given the coupled dynamics, the observed electrochemical (performance), thermal (safety) and chemical (degradation) responses are intertwined and are fundamentally affected by electrode microstructure for a given choice of materials. The coupling of these interactions grows stronger for high energy cells and the nonlinearity in the responses manifest more clearly.

Here electrochemical-thermal behavior of graphite – NMC111 Li-ion cells are studied to delineate the effect of various electrode specifications. The morphological differences between the graphite and NMC active material particles add to the richness of the associated interplay. The

validity of these observations holds beyond the specific choice of electrode materials as long as physicochemical interactions are of a similar nature. Key findings are as follows:

- For a given set of cathode recipes, a balanced cell (*i.e.*, Li storage capacity of the anode is greater than or equal to that of the cathode) is obtained only for a subset of anode specifications.
- An NMC electrode (spherical active material particles) exhibits both kinetic and transport limitations. On the other hand, an anode containing platelet graphite particles predominantly shows transport (long-range) resistance. These differences directly correlate to the forms of heat generation at either of the electrodes.
- The interfacial arrangement of conductive binder domains at cathode dictates the relative importance of kinetic and ohmic heats, with 2D film-like distribution exhibiting higher kinetic heat. The ohmic heat contribution increases (and kinetic heat decreases) as going towards more 3D finger-type secondary phase.
- For high energy high power cells, increasing anode – to – cathode ratio leads to enhanced transport resistance at anode which in turn contributes to higher ohmic heat as well as more Li plating and reduced capacity.
- The microstructural differences between the anode and cathode foster thermo-electrochemical hysteresis where charging and discharging operation demonstrates distinct trends. The qualitative nature of this hysteresis is closely dependent on the rate of electrochemical reactions (*i.e.*, operating current).
- For identical theoretical energy and Li storage capacity, the electrode recipe strongly alters the observed response with performance being a strong function of anode structure, safety being more closely related to cathode specification and degradation being a joint outcome of both.
- It is quite interesting to see that the electrode specific phenomena (*e.g.*, Li plating at the anode) are also strongly related to the choice of the other electrode.
- As speciation is temperature dependent, resultant heat generation rates vary based on thermal constraints. For a given choice of electrode recipes, lowest heat generation is observed under adiabatic conditions while the highest is observed for isothermal operation.

The traditional practice is to study a specific form of cell response without realizing the strongly coupled non-linear relation among the three descriptors: performance, safety, and degradation.

However, the two porous electrodes in a full cell communicate *via* species and charge signals, and subsequently, a much detailed and comprehensive picture emerges (which remains unidentified in a half-cell testing). In nutshell, high energy high power cells operate at severely off-equilibrium states and in turn experience complex dynamics. Such nonlinearity is a bane to conventional wisdom and accordingly, the perception of such electrochemical systems needs an evolution.

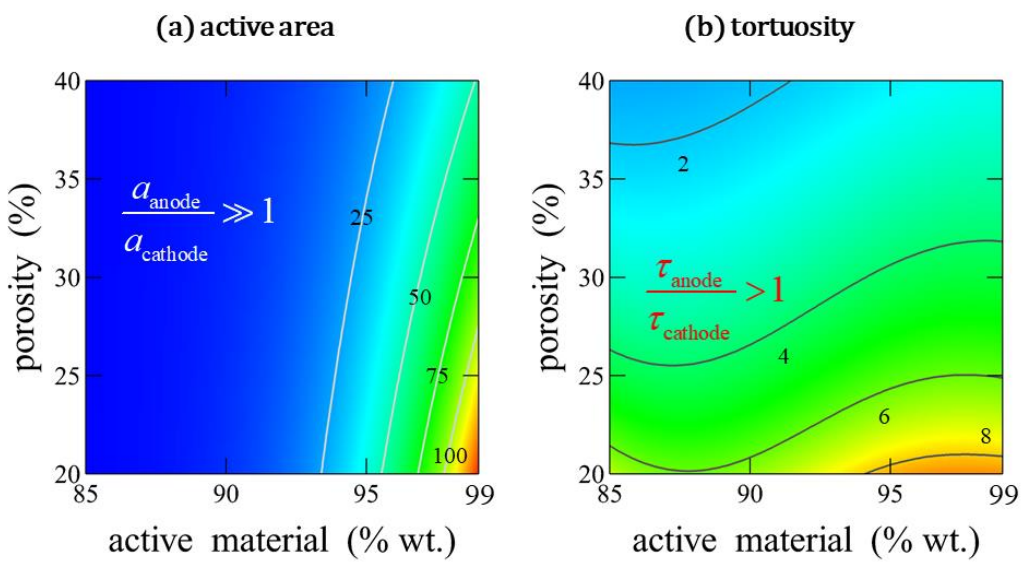

Figure 47. A comparison of anode and cathode microstructures in the form of (a) active area and (b) tortuosity ratio indicate that platelet graphite has the much higher active area, but also results in more server pore network resistances. Active particles in both these electrodes have identical volumes. Label denote the respective ratios.

3.9 Microstructural Comparison – Platelet Graphite *vs.* Spherical NMC

As outlined in the manuscript, active material particles have different shapes at the anode and cathode. This dissimilarity results in effective properties and in turn contribute to the difference in the physicochemical evolution of the two electrodes. The particle geometries have been recognized from imaging studies[72, 80, 160] and the associated microstructural difference have been hypothesized[64, 241]. Given the requirement for cumbersome tests for such investigations, a sufficiently detailed description of composite electrode structures and the corresponding effective property trends has not been hitherto resolved. A major shortcoming of such studies is the improper (often absent) treatment of secondary solids that exacerbates the complexations in microstructural responses. Previously authors' have reported comprehensive trends for spherical NMC

structures[174], while here similar relationships (Table 4) are derived for platelet-type graphite anode from pore-resolved calculations.

Figure 47 graphically compares the two types of electrodes in terms of their active area (*i.e.*, active material – pore interface) and pore phase tortuosity. The contours are appropriately labeled to assist visualization. Individual particle volumes are kept identical for a fair comparison. The sphere is the most compact shape for a given volume and hence platelet graphite has a much higher area (Figure 47(a)). This difference manifests as different scales of interfacial effects. On the other hand, the pore network resulting in a platelet structure is much distorted and equivalently the tortuosity is higher than spherical microstructure (Figure 47(b)). Tortuosity differences alter electrolyte transport behavior.

The difference in particle shapes also alter the intercalation dynamics (*e.g.*,[46]) since the intercalation direction changes accordingly, for example, a platelet particle experience the most dominant intercalation along the thickness coordinate. Subsequently, other associated phenomena such as mechanical degradation also changes[211, 225]. Zhang *et al.*[225] explicitly analyzed the effect of particle shape on intercalation induced stresses and concluded that particles with a smaller size and larger aspect ratio result in reduced stresses.

3.10 Thermal Signature Probe for Lithium-Ion Batteries

Thermal metastability is an inescapable trait of lithium-ion batteries. However, canonically only electrochemical signatures are studied as calorimetry imposes a controlled environment to isolate the self-heating signal. We propose an unconventional paradigm for characterizing the thermal signatures during operation. Using an inverse heat transfer formulation, we deconvolve the self-heating signature from other simultaneous heat transfer modes. Temporal variation of heat generation is subsequently estimated. This approach does not presuppose a particular electrochemical operation and is agnostic to materials used in the Li-ion cells. The generality and simplicity of this experimental approach rely on inverse thermal analysis and concurrent calibration of ambient natural convection response.

Lithium-ion (Li-ion) batteries have become the customary technology for high energy and high power applications, *i.e.*, electric vehicles and grid storage[16, 151, 169]. Thermal interactions are integral to such extreme functioning. Electrochemical complexations in porous battery electrodes are composed of charge transport and interfacial reactions at the microstructural scale[175, 223]. These

pore-scale events manifest as battery internal resistance, r_{in}, and leads to Joule heating. This self-heating is characterized as:

$$\dot{Q} = I^2 r_{\text{in}} + T\Delta\dot{S} \tag{125}$$

where the second term, $T\Delta\dot{S}$, specifies the entropic penalty to interconversion of chemical (intercalation of lithium) and electrical (voltage and current) energy modes. The self-heating behavior is intrinsic to electrochemical abuse scenario[242], *e.g.*, external short and overcharge, as well. The self-heating, if not modulated appropriately, leads to unattenuated temperature rise and triggers thermally activated autocatalytic side reactions[243] that burgeon to thermal runaway[244, 245]. Repeated operation prompts chemical degradation, altering the thermal response. Such temperature-dependent metastability of Li-ion cells makes an *in operando* characterization of heat generation vitally important[246, 247]. Temperature and heat generation rate jointly provide necessary insights into thermal metastability, thus defining the thermal signature for Li-ion Batteries.

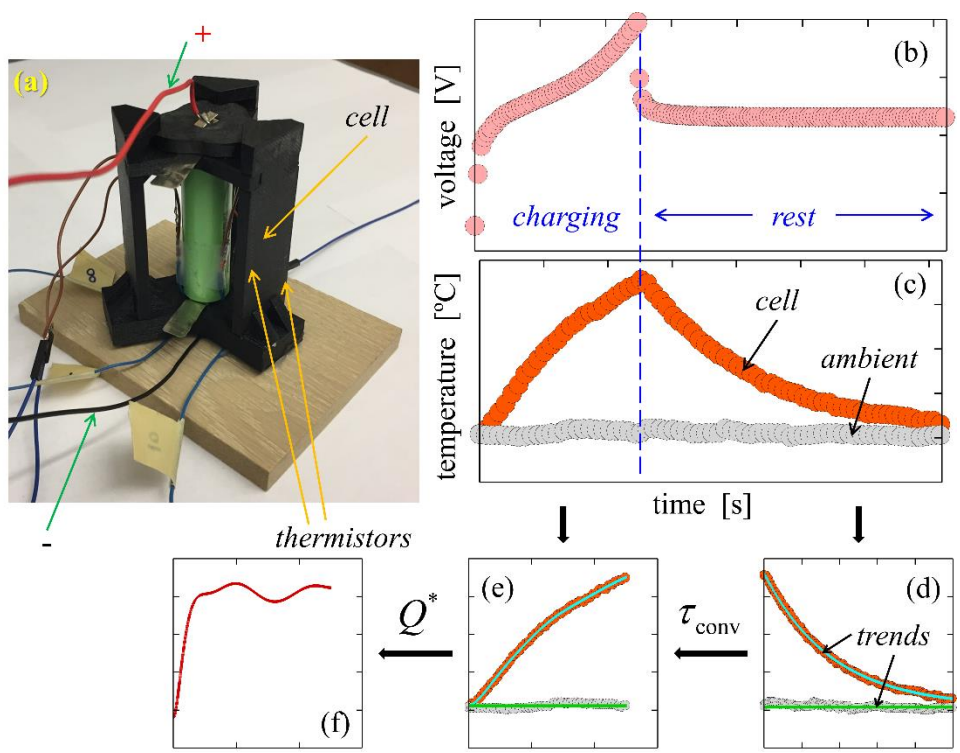

Figure 48. Outline of the methodology. (a) Experimental setup to measure heat generation in ambient; (b) Cell voltage and (c) temperature evolution during operation (here charging) and rest phases; (d) Rest data is interpreted to obtain convection timescale, τconv; (e) Subsequently, temperature evolution during operation is interpreted to extract (f) heat generation variations with time.

The thermal interactions have largely been overlooked since calorimeter[248-252] is the only tool at a researcher's disposal to evaluate heat generation for energetic systems. Calorimetry is prohibitive given the specific instrumentation needs, *e.g.*, thermal isolation for adiabatic testing (not to mention the cost constraints). It is neither suitable for field testing nor for continuous monitoring. These attributes are fundamentally tied into achieving thermally isolated and noise-free test environment. Here we propose an elegant approach to probe the cell's thermal signature using an Inverse problem formulation[253]. Essentially, the experimental difficulties are transformed into the more involved analysis of the measurand (*i.e.*, temperature).

The electrochemical operation of the Li-ion cell (in ambient) is accompanied by temperature rise that follows the energy balance:

$$mC\frac{dT}{dt} = \dot{Q} - hA\left(T - T_{\infty}\right) \tag{126}$$

There are two heat transfer mechanisms: conduction (internally) and convection (externally). Using Biot number argument[254], it can be shown that the ambient convection (*i.e.*, natural convection in air) is the limiting mechanisms. Hence, the internal thermal gradients can be neglected, and the general energy balance simplifies to Eq. (126). Re-expressing Eq. (126),

$$Q^{*} = {dT}/{dt} + {\left(T - T_{\infty}\right)}/{\tau_{\text{conv}}} \tag{127}$$

where the terms are re-scaled using heat capacity, *mC*. Despite its apparent simplicity, the above expression cannot be directly used to analyze temperature measurements. Temperature is recorded as discrete data (usually at equal time intervals). Such measurements invariably contain noise, and the difference formula is ineffective to estimate the time dereivative[253], making the problem ill-posed. The calorimeter analysis does not suffer from a similar predicament as in the absence of convection term, Eq. (126) can be recast as an integral problem. The heat generated in a finite time interval δt becomes $\delta Q = \int_{\delta t} \dot{Q}\mathrm{d}t = mC\delta T$ (without having to invoke derivatives).

Figure 48(a) presents the experimental setup with a cylindrical Li-ion cell operating in the ambient. Thermistors (calibrated to a 0.1ºC precision) measure surface temperatures as well as the ambient temperature. In the presence of considerable surface gradients, surface averaged temperature is to be used for analysis. The Li-ion cell (NCM cathode and graphite anode) is charged and discharged in an identical voltage range (2.8 – 4.2 V) using a potentiostat. Heat generation takes place during the electrochemical operations. An in-between rest period of two hours is used to ensure electrochemical and thermal equilibrium at the beginning of the next current

operation (*i.e.* heat generation sequence). Figure 48(b) and (c) show the evolution of cell voltage and temperature, respectively (only part of the rest phase data is shown here).

Since the measurements are carried out in the ambient whose convection characteristics can change in time, rest phase data is also analyzed to self-consistently calibrate the convection time constant, τ_{conv}. For a heated cell (both charge and discharge cause temperature rise), temperature decays gradually during the rest phase, governed by the expression:

$$dT/dt = -\left(T - T_\infty\right)/\tau_{\text{conv}} \tag{128}$$

whose analytical solution is:

$$\left(T - T_\infty\right) = \left(T_0 - T_\infty\right)\exp\left(-t/\tau_{\text{conve}}\right) \tag{129}$$

with cell temperature T_0 at $t = 0$ (time axis is reset to zero at the start of each test phase). Let the temperature data (discrete) be denoted by $\hat{T}$ and $\hat{T}_\infty$ for cell and ambient, respectively. The experiments are carried out inside the laboratory where the ambient temperature drift is much slower than the duration of each test. Further, it can be shown that $T_\infty = \text{mean}\left(\hat{T}_\infty\right)$, and the cell temperature data $\hat{T} = \hat{T}\left(t_j\right)$ is analyzed to seek the functional trend expressed in Eq. (129), and subsequently, identify the convention time constant. To quantify heat generation, the remaining difficulty is an accurate interpretation of the time derivative in Eq. (127).

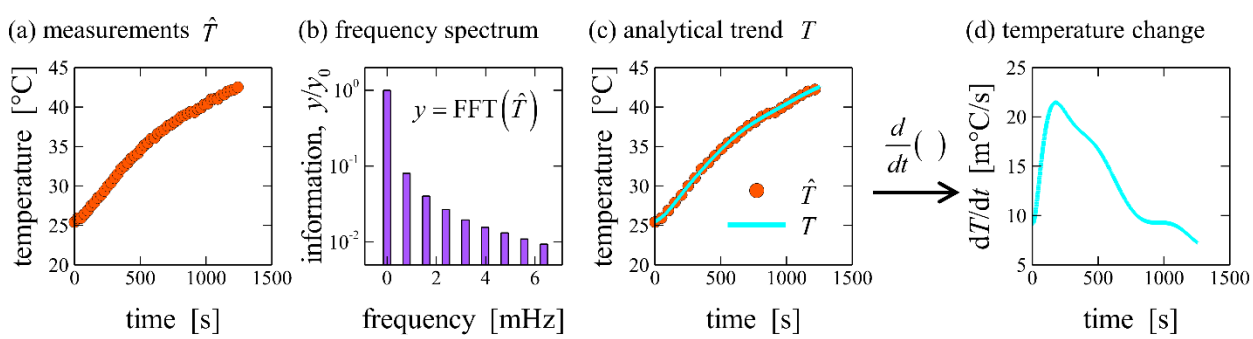

Figure 49. Interpreting the analytical nature of temperature evolution during electrochemical operation. (a) Measurements are in discrete time space and not directly amenable to differentiation; (b) Fast Fourier Transform helps identify the relevant frequencies; (c) Frequency spectrum is used to estimate coefficients of the analytical function; (d) Functional trends can be differentiated analytically as the noise is filtered out while transforming from discrete to continuous space.

The principles of Inverse heat transfer[253] suggest that in order to differentiate an experimental (discrete time) measurement, one should identify the underlying functional variation and subsequently employ analytical differentiation. Such an approach implicitly filters out noise (since noise is a high-frequency small amplitude signal and the interpreted analytical trends are insensitive to such components). Eq. (129) is a homogeneous solution of the differential Eq. (127). Given that the heat generation rate Q^* is time-dependent, a suitable analytical temperature trend can be assumed as[204]:

$$T = a_0 + a_1 t + \sum_{i=2}^{N} a_i \exp\left(-f_i t\right) \tag{130}$$

where coefficients a_i's and frequencies f_i's (*i.e.*, time constants $1/f_i$'s) capture the essence of temporal variation. Note that the number of frequency components, N, is to be determined from the spectral width of the discrete signal. Eq. (130) is agnostic to the details of battery operation. To determine the frequency information, Fast Fourier Transform (FFT) is carried out over the experimental time series $\hat{T}\left(t_j\right)$. This signal contains true frequencies spanning between 0 (stationary) and $f_s/2$ (Nyquist limit[255]), where $f_s = 1/\Delta t$ is the sampling frequency. On the FFT spectrum, higher order frequency information is corrupted by noise. Figure 49(a) shows the time series, $\hat{T}$, for a 2.25 Ah Li-ion cell charged at 4.5 A (2C current). The corresponding FFT spectrum is shown in Figure 49(b). The amplitudes are rescaled using the highest amplitude signal (*i.e.*, the stationary component). Any frequencies representing less than 1% of the information are discarded. The rescaling allows for automated data conditioning. The remaining frequencies are used to identify the coefficients in the expression Eq. (130). Figure 49(c) presents the derived temperature trend, T (the goodness of fit is better than 0.99) and visually justifies the accuracy of the procedure. Thus, a transformation from a discrete time signal $\hat{T}$ to a continuous time signal T filters out the noise and provides distilled temporal variations. The analytical trend (Eq. (130)) is further differentiated to quantify the rate of temperature change (here 'temperature rise'). Note that the temperature rise is higher at the beginning (Figure 49(c)) and gradually plateaus as a higher temperature leads to a greater convective loss. The differentiated signal (Figure 49(d)) captures such variations quite faithfully. Eq. (127) is subsequently employed to obtain the heat generation rate in the continuous time domain. Figure 50 demonstrates the resultant time dependence of the heat generation rate. As a comparison, the heat generation trend of the subsequent discharge is also shown alongside. The two trends are qualitatively different and suggest the existence of thermal

hysteresis. The direction of current flow is opposite for the two operations, and since the two electrodes are not identical in terms of material and microstructural aspects, an asymmetric thermal behavior originates[175]. Moreover, the sign of the entropic heat changes when the current switches the direction. Authors have recently predicted the existence of thermal hysteresis in Li-ion cells, and the present experiments confirm the peculiar response.

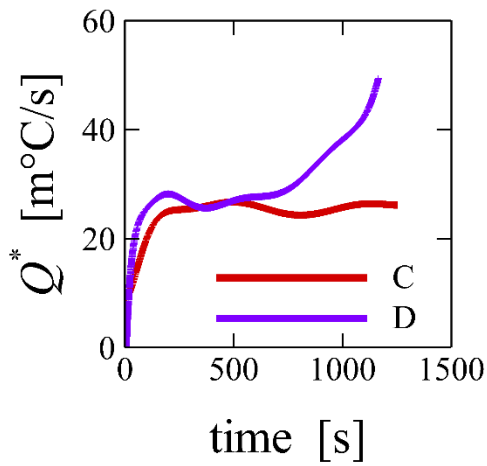

Figure 50. Evolution of heat generation rates (normalized) for 4.5 A operation of a 2.25 Ah cell. C = charging and D = discharging events.

Internal resistance as used in Eq. (125) is separately measured at multiple intermediate locations during operation and their average values are reported in Table 5. For higher currents, the Joule heating (*i.e.*, $I^2 r_{\text{in}}$ term) is the leading contributor to heat generation and is tabulated as well (Q_{r}). The cells used weigh 45 g and specific heat is assumed to be 823 J/kg·°C[230].With these, the average rate of heat generation is computed as per Eq. (131).

$$\bar{Q} = mC \cdot \frac{1}{t_{\text{operation}}} \int_0^{t_{\text{operation}}} Q^* \, \mathrm{d}t \tag{131}$$

Both $\bar{Q}$ and Q_{r} are of the same order (Table 5). Note that the departure $\left(\bar{Q} - Q_{\text{r}}\right)$ has opposite signs for charging and discharging operation. Since the difference between the two arises from entropic contributions and it changes sign, the estimations are logical. The reproducibility of the results is identified by carrying out ten charge-discharge operations. The corresponding statistics[256] are reported in Table 5 and reveal that the measurements are reproducible (coefficient of variation = std / avg).

Table 5. Heat generation rate estimates for 4.5 A operation of a 2.25 Ah cell. Statistics report the results of ten charge-discharge operations and prove the repeatability. Here $Q_r = I^2 \cdot r_{in}$ is heat generation rate estimate from internal resistance measurements, while $\bar{Q}$ is the mean heat generation rate over entire operation and subsequently avg. $\bar{Q}$ is average of $\bar{Q}$ for ten operations.

Measured Quantity	***Charging***	***Discharging***
$\bar{Q}$ (W)	0.9092	1.1049
r_{in} (mΩ)	48.1	50.4
Q_r (W)	0.9740	1.0206
avg. $\bar{Q}$ (W)	0.9091	1.0959
std. $\bar{Q}$ (mW)	7.82	28.3
coeff. var.	0.86%	2.58%

The proposed procedure is equally applicable to cells with different chemistries, shapes and electrochemical history (*e.g.*, fresh *vs*. aged cell). The analytical sophistication allows one to study thermal signatures for various electrochemical operations. Since the approach neither requires cell-level modifications (*e.g.*, drilling a hole to place internal thermocouple[257]) nor relies on the adiabatic environment, it is elegant *in operando* non-invasive technique with the potential to be a commonplace measurement for a laboratory setting, batch testing, and continuous monitoring. Such an approach in principle can be extended to monitor cells in a battery pack after appropriately accounting for (i) geometrical arrangement of the cells and (ii) limiting mode of heat transfer. The proposed thermal tracking procedure could allow decision making, *i.e.*, for a battery management system if reasonable estimates are available for frequencies and ambient convection from the preceding measurement set. The subjectivity of the experimentalist is also circumvented as no cell preparation is required. Essentially, the complexities of a controlled experiment are translated to the involved analysis of the measurements. We envision such '*thermal signature probe*' to provide detailed insights into the thermal metastability of Li-ion cells.

3.11 Self-heating at Low Temperatures

Cold-start is an ineluctable stipulation for electric vehicle operation under low-temperature extremes. It has typically been addressed through cell-level heating strategies. We advocate an electrode-level strategy leveraging pore-scale manifestation of thermal metastability that promotes

self-heating. Appropriate controllable stochastic characteristics of porous electrodes are delineated that contribute to the proposed solution at low temperatures. This approach is most conducive to high energy density Li-ion cells and devoid of extrinsic overheads.

Electromobility potential[258-262] of batteries is traditionally assessed in terms of energy (defines the range) and power densities (relates to acceleration and maximum speed). Given the subzero starting temperatures in various geographical locations (especially in North American[263] and European subcontinents) cold-start ability is an equally important specification. Electrochemical operation of Lithium-ion Batteries (LIBs) is a result of physicochemical interactions taking place at the electrode pore-scale[83, 174, 264]. The relevant kinetic and transport properties worsen at lower temperatures leading to severely restricted operation under freezing conditions[265]. Historically electrolyte modification for improved transport has been attempted[266, 267] with marginal success on the overall response, given the kinetic shutdown. If the battery is heated to a slightly warmer state (0 °C), the sluggish interactions are revitalized providing reasonable performance. External heating (*i.e.*, thermal management system) fails to be a reliable answer as it does not satisfactorily heat the interior locations[268], and the nonuniformity grows with heating rates. Internal heating, given its delocalized nature, is inherently a more efficient strategy (efficiency to be appraised in terms of energy spent as well as homogeneity of the thermal field). Following this rationale, Wang *et al.*[269] proposed a modified cell design where a nickel strip is packed with the conventional two-electrode configuration. Ni serves as an internal heating element and provides heating at the electrode-scale[270]. It has been shown to recuperate cells from starting temperatures as low as -40°C[263, 269]. However, this approach requires modified cell design and reduces energy density due to additional inactive material. The porous battery electrodes give rise to multimodal self-heating signatures in response to current flow (ohmic), charge conversion (kinetic) and entropic changes[271]. The particular geometrical arrangement constituting the porous electrode alters microstructural resistances and in turn the self-heating response[117, 175]. Such microstructure-assisted self-heating gives rise to heat generation at a pore-scale, in contrast to the Ni-strip (electrode-scale) or external heating (cell-level and/or pack-level), thus providing a greater degree of homogeneity. The present work analyzes the merits of this stochastic heating mechanism in the context of cold-start and tenders guidelines to enlist microstructural effects.

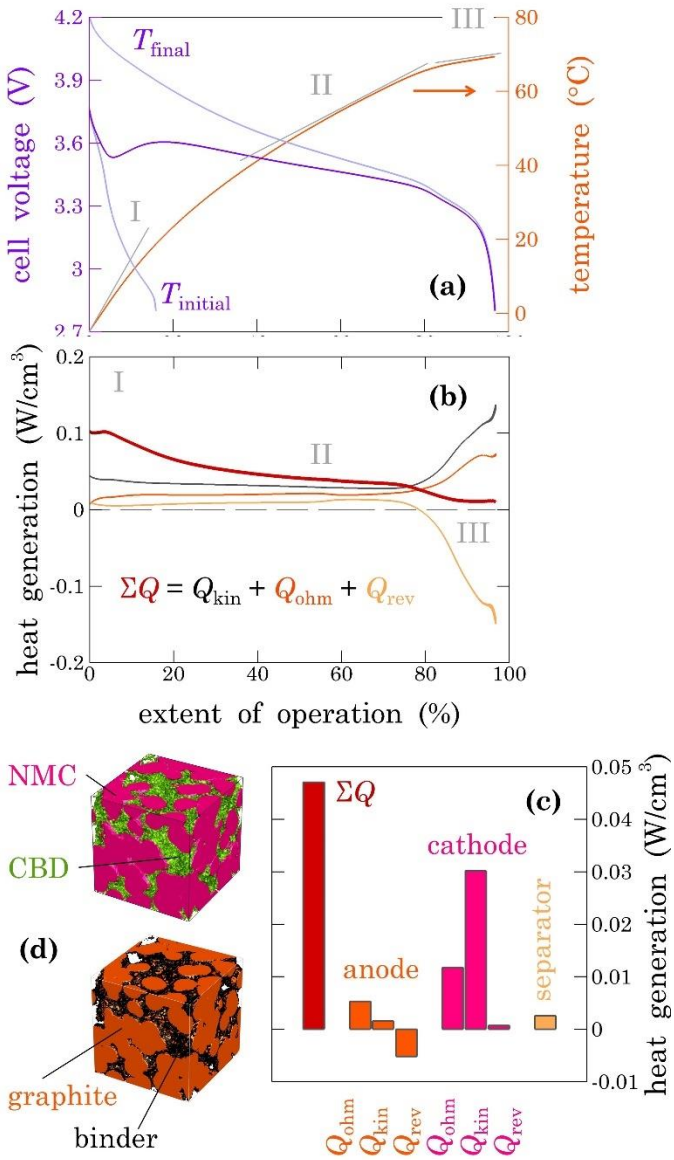

Figure 51. Self-heating property of energy-dense electrodes is used to examine graphite – NMC based Li-ion cell from a subzero temperature. (a) Voltage and temperature evolution when heat is contained in the cell. (b) Evolution of different heat generation modes. (c) A balance sheet to identify the origins of heat generation. (d) Representative electrode microstructures.

Consider cell voltage and temperature evolutions for a self-heating (purely due to pore-scale heat generation) graphite – NMC (nickel manganese cobalt oxide 333) couple as shown in Figure 51(a). The starting temperature is -5°C. Intuitively, the adiabatic operation is the most reliable indicator of self-heating as all the generated heat manifests as temperature rise (without thermal gradient errors). Isothermal operations at the initial and final temperatures are also sketched simultaneously

(Figure 51(a) lighter curves) and demonstrate the bounds on the adiabatic cold-start operation. At low temperatures transport properties and reaction rate constants (*i.e.*, exchange current densities) are very small causing considerable overpotentials. These transient interactions improve with temperature and decrease the overpotentials, which is marked by voltage recovery in Figure 51(a) at early times. Later the decrease in open circuit voltage overcomes the overpotential reduction causing the gradual decrease in voltage. The corresponding temperature evolution (Figure 51(a)) is marked by three distinct regimes, with successively smaller growth rate. For an adiabatic cell, thermal transients directly correlate to self-heating, $\mathrm{d}T/\mathrm{d}t \propto \dot{Q}$, which is apparent from heat generation evolution (Figure 51(b)). During regime I, both long- and short-range resistances are high due to lower temperatures, giving rise to higher heat generation and faster temperature rise. These interactions improve considerably near room temperature, marking the reduced heating in the second regime (II). Towards the end of the operation, kinetic resistances go up as anode is nearly delithiated and the cathode is almost lithiated. Simultaneously ionic concentration profile in the electrolyte phase is fully[175] developed showing lower overall conductivity (ionic conductivity is highest near typical salt concentrations 1-1.2M, and decreases at lower concentrations due to smaller charge carrier number density and at higher concentrations due to concentrated-solution effects[24, 188]). Entropic heating signature $\left(\partial U/\partial T\right)$ is a material property[271]. Graphite (anode here) has a stronger entropic response[260]. This gives rise to negative entropic heat, $Q_{\mathrm{rev}} = -jT\left(\partial U/\partial T\right)$ towards the end of discharge[175] (j is positive for the anode, T is high and $\partial U/\partial T$ becomes more positive when graphite is nearly delithiated[271]). The entropic heating counters these two, thus reducing the heat generation in the last regime (III). At every stage total heat is a result of kinetic, transport and entropic contributions of the two electrodes and separator (ohmic heating only). Figure 51(c) shows a heat generation balance sheet (in terms of average heat generations). The reversible heating is dominated by anode as discussed before. The trends in ohmic and kinetic heats strongly correlate to microstructural differences between the two electrodes (Figure 51(d)). Here cathode has 90% NMC by mass (1 : 1 binder and conductive additives for the remaining 10%), while anode has 95% graphite by mass (5% binder). The electrode porosities are such that to provide 60% active packing[175] (volume content of active material). This results in a smaller cathode porosity[175], and equivalently higher tortuosity and greater transport resistance and ohmic heat. For similar active particle dimensions, a higher

secondary phase content (10% at cathode *vs.* 5% at the anode), blocks greater active surface, thus increasing the effective ionic flux at the particle surface[174]. Moreover, the exchange current density for graphite is about an order of magnitude higher. Both these synergistically increase the kinetic overpotential at the cathode and equivalently a higher kinetic heat. The predictions presented here are based on rigorously verified coupled electrochemical-thermal description[117, 175, 230] and microstructural characterizations[174, 175, 272, 273]. Based on this discussion, an effectiveness measure, $\varepsilon_{\text{cold-start}}$ is proposed to assess the usefulness of self-heating as a cold-start strategy *via* comparing operation times:

$$\varepsilon_{\text{cold-start}} = 1 - \frac{t_{\text{isothermal@}T_{\text{start}}}}{t_{\text{adiabatic self-heating}}} \tag{132}$$

The best cold-start strategy is the one that can revive a nearly non-working cell (*i.e.*, $t_{\text{isothermal@}T\text{start}} \rightarrow 0$). In this limit, $\varepsilon_{\text{cold-start}} \rightarrow 1$ (*i.e.*, 100%).

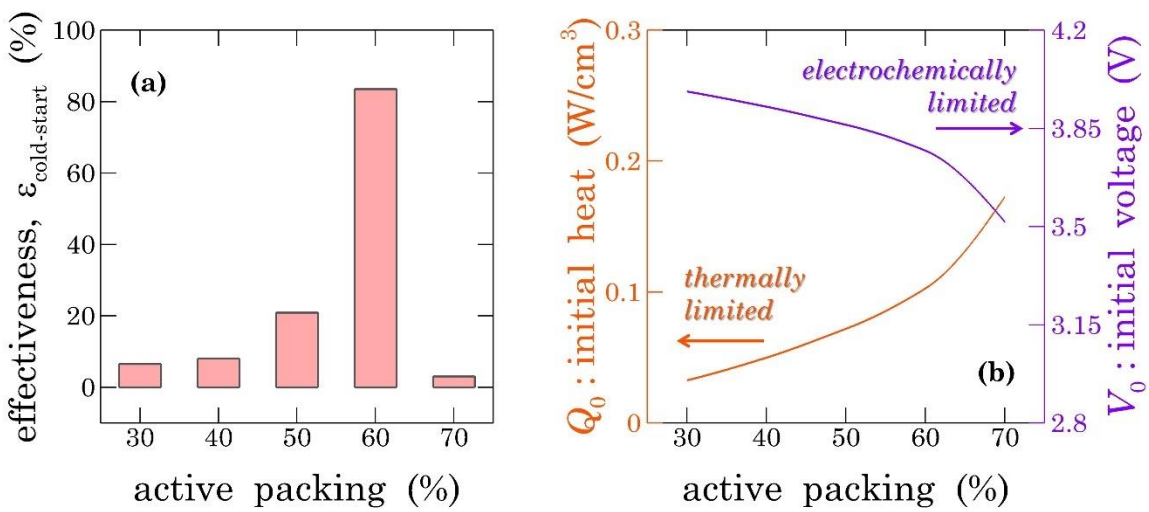

Figure 52. Suitability of self-heating for cold-start is intrinsically related to energy density, *i.e.*, active packing (a). Two competing mechanisms make low or very high energy density electrodes inappropriate for microstructure-assisted cold-start (b).

The proposed microstructure-assisted self-heating is a defining characteristic[274] of high active material loading, *i.e.*, energy density electrodes. Figure 53 explores the connection between electrode energy density (alternatively expressed as active packing) and its suitability for cold-start. Electrode thicknesses, recipes and C-rate (1C here) are kept invariant for a fair comparison. Figure 53(a) presents the cold-start effectiveness against active material packing. The plot reveals

that the effectiveness monotonically increases going from low to high packings, becomes optimal around 60% packing and then falls off rapidly. There are two competing mechanisms that lead up to such a nonlinear dependence of $\varepsilon_{\text{cold-start}}$ (Figure 52(a)). Heat generation rates positively correlate with energy density. Furthermore, a higher energy density electrode has greater resistances that increase the overpotentials and causes an electrochemical shutdown. Heat generation and cell voltage are related to internal resistance (r_{in}) *via* the following expressions:

$$Q \approx I^2 r_{\text{in}} = C^2 q^2 r_{\text{in}} \tag{133}$$

$$V = U - I r_{\text{in}} = U - (Cq) r_{\text{in}} \tag{134}$$

Here q is cell capacity and connect the C-rate and current as $q = I/C$ (q is proportional to active packing). As discussed in Figure 51(b) entropic heating is fairly minimal except towards the end of the operation. Hence, only the Joule heating contribution (ohmic + kinetic) is expressed in Eq. (133). As electrode energy density is increased, both q and r_{in} increase, which monotonically raises heat generation and decreases the cell (terminal) voltage. The rate of temperature rise is defined by heat generation, while the extent of operation is limited by terminal voltage, making temperature increment a mixed function:

$$T(t) - T_{\text{start}} \propto \int_0^t Q \mathrm{d}t \tag{135}$$

For low packing electrodes, heat generation is not high enough to rapidly increase cell temperature beyond 0°C, while at larger packings, cell voltage reduces rapidly and triggers a shutdown before temperature can build up through heat accumulation. Figure 52(b) presents heat generation and the voltage at the start of the operation and highlights the thermal and electrochemical shutdown modes.

The electrode preparation stage avails control over the stochastic nature of the composite porous networks. The (stochastic) geometrical attributes, for example, porosity, interfacial distribution of secondary solids, *etc.*, alter the electrochemical evolution and modulate thermal metastability[117, 175]. Figure 53 further analyzes the importance of such controllable stochasticity for cold-start. Note that the avenues discussed here are organic to the state-of-the-art electrode and cell manufacturing framework. Graphite particles are available in many different morphologies[273, 275]. Active particle morphology directly affects tortuosity and active area, which in turn dictate ohmic and kinetic heat generations[175]. Figure 53(a) compares different anode particle types in terms of their usefulness for cold-start.

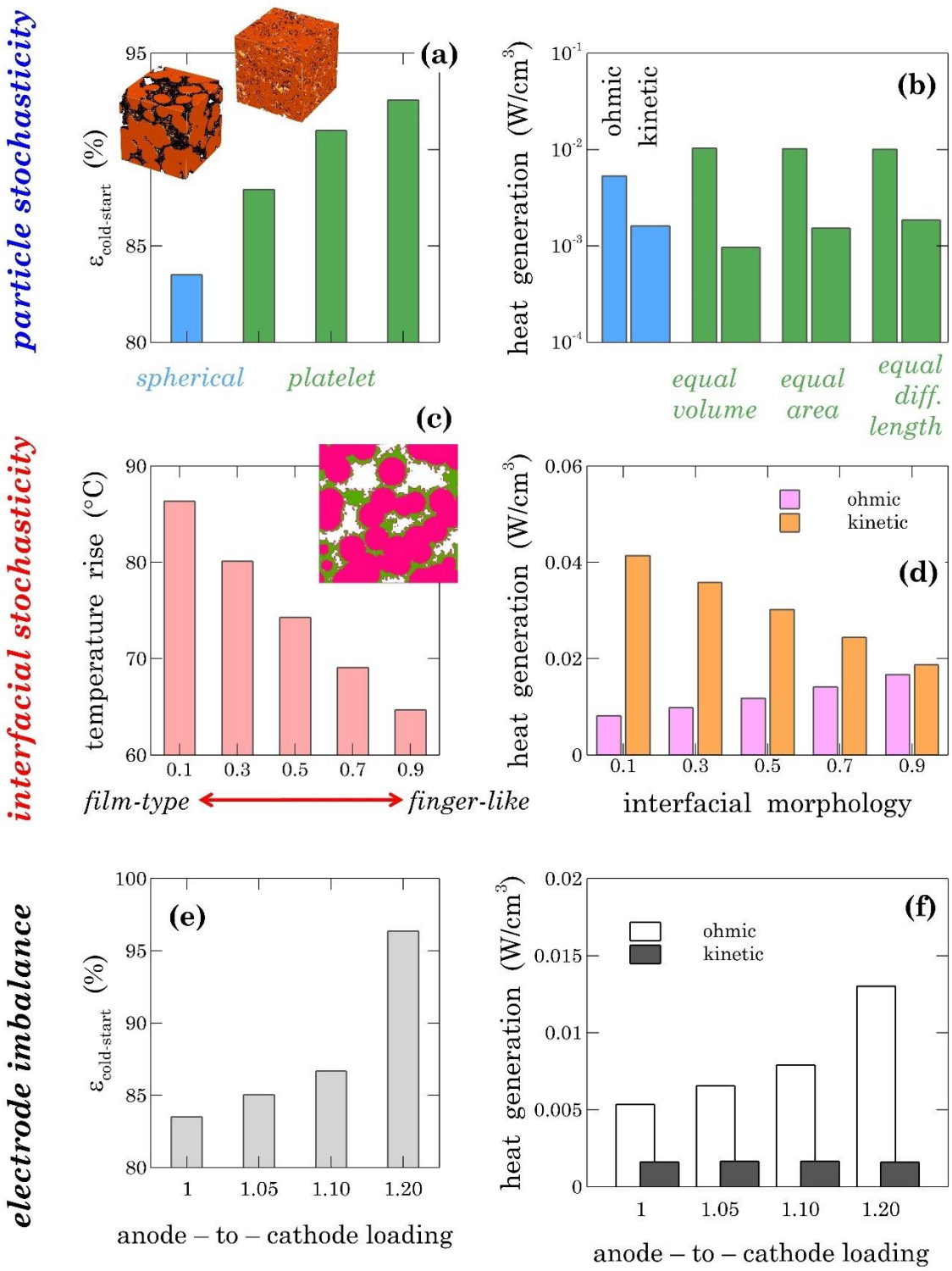

Figure 53. Effective microstructural-modification strategies (a), (c), (e) and their mechanistic origins for cold-start operation (b), (d), (f).

For equal particle volume (*i.e.*, active packing), platelet particles give rise to more tortuous pore-network[64, 273], and in turn anodes with platelet particles exhibit greater ohmic (transport) heat and consecutively better cold-start (Figure 52(b)). For equal volume particles, spherical particles have the smallest active area (*e.g.*, small water drops are spherical to minimize surface energy), hence kinetic heating is smaller compared to a spherical particle. For equal volume, the aspect ratio of the platelet particles makes the thickness as the preferred intercalation direction. For the identical surface area, larger platelets are required. This increases the diffusion distance which amounts to a larger solid-state concentration overpotential and reflects as a higher kinetic heat. If even larger platelets are chosen to match the diffusion length in spherical particles, its surface area reduces concurrently. Both these effects – increased intercalation length and decreased active are – escalate the kinetic heating (Figure 53(b)). Simultaneous changes in the transport heat are minimal as the platelet pore network is consistently more convoluted than that for a spherical particle. Notice that even for the same diffusion distances, kinetic heat is smaller in a platelet particle, which indirectly justifies a better intercalation response of the platelet particles[175]. Increased transport heat makes platelet particles more effective for cold-start (Figure 53(a)).

The secondary solids can form many different arrangements at the active particle – electrolyte interface[174, 272]. Such an interfacial morphology is defined during the electrode preparation stage[30, 83, 164], and affects both the short- and long-range resistance modes[174, 264] (and equivalently electrode operation[33, 83]). As the higher amount of secondary solids are present at cathode[175], interfacial stochasticity at cathode has a dominant implication for cold-start (Figure 53(c)). Recall that kinetic heat is the dominant contributor at the cathode (Figure 51(c)). As secondary phase morphology is varied from 3D finger-like to 2D film-type interfacial arrangement, it causes a greater ionic blockage for intercalation reaction and consequently a higher kinetic heat. Film-type secondary solids cause more conducive pore network (*i.e.*, smaller tortuosity for a given porosity), which reduces the ohmic heat contributions (Figure 53(d)). The increase in kinetic heat for more film-type (2D) secondary solids outweighs the ohmic heat decreases, and subsequently, it represents the preferred form of interfacial stochasticity (Figure 53(c)).

Lithium batteries are customarily prepared with a higher anode capacity to prolong cycle-life[235]. As predominant degradation mechanisms (*e.g.*, SEI formation, Li plating) are anode-centered[233, 276], its extra inventory is expected to make up for the lost lithium. The pore-scale complexations, however, are not so unilateral, especially for high energy porous electrodes[175],

where more anode capacity implicitly increases the resistance. As the microstructure-assisted cold-start benefits from higher electrode resistance (Eq. (133)), electrode imbalance is examined as a possible cold-start mechanism (Figure 53(e)). For a fixed cathode, anode capacity increase originates from greater active packing. The anode tortuosity (*i.e.*, transport resistance) increases collaterally. This gives rise to a higher ohmic heat generation at higher anode loadings (Figure 53(f)). Since kinetic heat is a secondary effect at the anode (Figure 51(c)), it does not show a marked variation (Figure 53(f)). Better heat generation at higher electrode imbalance leads to improved self-heating and as a consequence the cold-start effectiveness improves (Figure 53(e)).

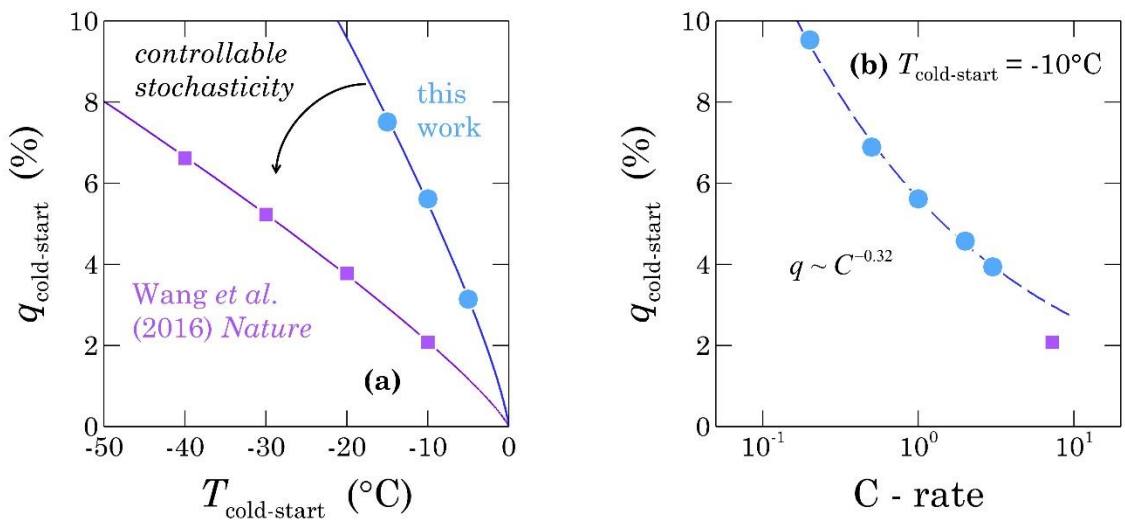

Figure 54. Capacity investment for cold-start with (a) cold-start temperature and (b) rate of operation. Data from Wang *et al.*[269] is shown alongside for comparison. Different stochastic variations discussed earlier proffer avenues for tuning the intrinsic cold-start signature.

The proposed approach is compared with the Ni-strip solution (Wang *et al.*[269]) in Figure 54. Figure 54(a) presents the fractional capacity consumed to alleviate cell temperature to 0°C. Both the approaches exhibit a power law dependence on initial temperature, $T_{\text{cold-start}}$:

$$q_{\text{cold-start}} \sim \left(-T_{\text{cold-start}}\right)^{\alpha} \tag{136}$$

Figure 54(a) discloses comparable merit for both the technologies for temperatures as low as -20°C, which covers the typical winter temperature range in United States[263]. Figure 54(a) compares the cold-start behavior of the baseline high energy density couple (Figure 51). The controllable stochastic mechanisms (Figure 52 and Figure 53) further refine the proposed solution. Additionally,

higher rates (similar to Wang *et al.*[269]) can be availed to make the microstructural-assisted self-heating a more lucrative strategy. Note that for a field operation, a high rate step is required only to recover the cell from subzero temperatures. After that, the normal cruising currents (of the order of C/10, *i.e.*, 8-10 hours of vehicle range) arrest the temperature rise. On the other hand, the adiabatic operation discussed here allows a direct measure of cold-start efficacy *via* a calorimeter testing.

In conclusion, high energy electrodes are thermally metastable due to their considerable self-heating property. This characteristic is inherently defined by electrode microstructure stochastics. Here we propose a microstructure-assisted cold-start strategy and highlight stochastic mechanisms to dictate the corresponding self-heating. Such a solution circumvents specialized cell fabrication and is more readily applicable for high energy density electrodes without sacrificing the cell level energy specifications as well as staying competitive to the other techniques.

3.12 Mechanistics of Electrodeposition

The conventional interpretation of lithium electrodeposition in porous intercalation hosts is based on near equilibrium arguments. However, high energy electrodes represent off-equilibrium complexations where ionic limitations give rise to an alternative electrodeposition landscape. Atypical conditions such as mild temperatures, moderate currents, and capacity imbalance cause this transport-driven lithium plating. Active particle morphology yields a compelling argument to alleviate electrodeposition by way of modulated microstructural resistive modes.

Lithium electrochemistry suffers from an unexpected plight where electrodeposition of film anodes is metastable[277-279], and comparatively non-trivial porous intercalation anodes exhibit a slower performance fading[234, 235, 280, 281]. The electrodeposition also coexists in intercalation electrochemistry; however, it functions as a degradation mode rather than an energy storage mechanism given its semi-reversibility[238]. The coupled interactions with other deleterious processes[233, 276, 282, 283] multiplicate the menace of deposited lithium. Based on near equilibrium arguments, it has been shown that unwanted lithium plating takes place[239, 284] at low temperatures, high rates and elevated voltages (*i.e.*, states of charge). Each of these mechanistically represents subzero anode potentials and has been accepted as indirect evidence of electrodeposition[232, 240, 284-286].

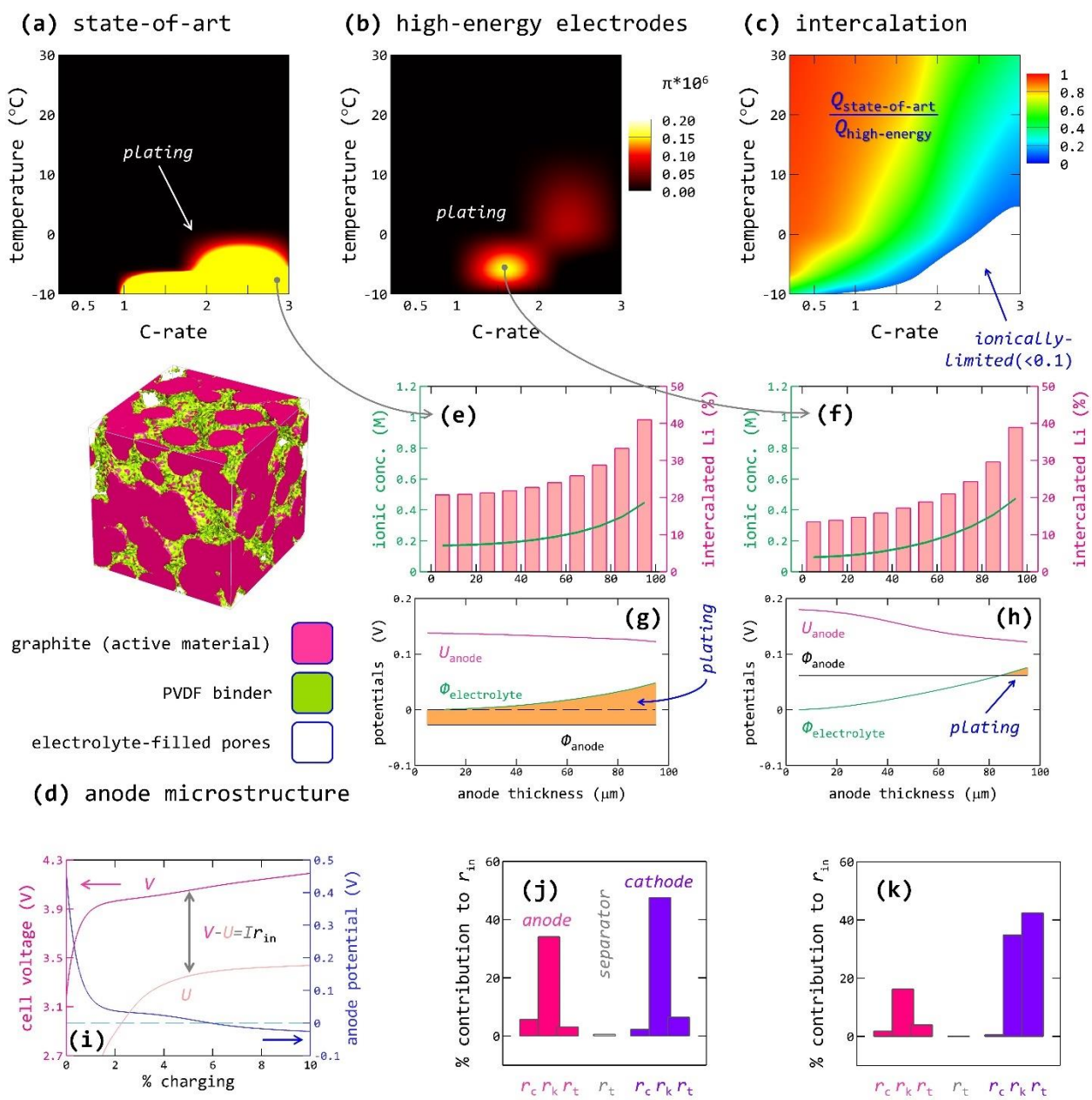

Figure 55. Electrodeposition in intercalation anodes exhibits two distinct regimes. The conventional interpretation holds for state-of-the-art electrodes (a), (e), (g), (i), (j), while high energy electrodes exhibit nonmonotonic dependence on temperature and charging current (b), (f), (h), (k). (c) Intercalation differences. (d) Representative anode microstructure reconstruction. (e), (f) Lithium fields, (g), (h) potentials and (j), (k) components of internal resistance at the end of charging.

Fundamentally, lithium electrodeposition requires local ionic concentration (reactants) and favorable potential gradient (overpotential)[22]. The overpotential $\eta_{\text{plating}} = \phi_{\text{anode}} - \phi_{\text{electrolyte}}$ is the

necessary imbalance to trigger the reaction $Li \underset{\text{deposition}}{\overset{\text{dissolution}}{\rightleftharpoons}} Li^{+} + e^{-}$. Transport limitation[175] in the electrode pore network can create an off-equilibrium situation that changes the electrolyte potential and in turn altering the driving force $\left(\eta_{\text{plating}}\right)$ for plating. The ionic transport effects become relevant as high energy and power electrodes are pursued[29, 172, 174, 273, 287, 288].

Figure 55 (a) and (b) compare the propensity for lithium plating in state-of-the-art cells and the ones with high energy electrodes (active materials: graphite and nickel manganese cobalt oxide, NMC333). Figure 55(a) shows that the conventional interpretation holds, while energy dense electrodes (Figure 55(b)) exhibit strongly nonmonotonic plating behavior. The plating quantification is based on local plating current, i_{plating} (Eq. (137)). Given the semi-reversibility of electrodeposition reaction in graphite, the charge transfer coefficient, α, is not symmetric.

$$i_{\text{plating}} = i^{0}_{\text{plating}} \left\{ e^{\frac{\alpha F \eta_{\text{plating}}}{RT}} - \frac{c_{\text{electrolyte}}}{c^{0}_{\text{electrolyte}}} e^{\frac{-(1-\alpha) F \eta_{\text{plating}}}{RT}} \right\} \tag{137}$$

There is an ambiguity in its estimation[283, 289] and literature often assume α [286] to be between 0 and 0.5, with $\alpha \to 0$ signifying more irreversibility. To isolate such incertitude, here lithium plating is assumed to be completely irreversible, which reflects the most severe outcome. Accounting for spatiotemporal variation of plating current, a generalized plating descriptor is defined to characterize the plating propensity:

$$\pi^{*} = \frac{1}{t^{\text{theoretical}}_{\text{operation}} L_{\text{anode}}} \int_{t=0}^{t_{\text{operation}}} \int_{x=0}^{L_{\text{anode}}} \left\{ 1 - \frac{c_{\text{electrolyte}}}{c^{0}_{\text{electrolyte}}} e^{\frac{-F \eta_{\text{plating}}}{RT}} \right\} \mathrm{d}x\,\mathrm{d}t \tag{138}$$

where theoretical operation time is related to the C-rate as $t^{\text{theoretical}}_{\text{operation}} = 3600 / \text{C-rate}\,[\text{sec}]$. Such a dimensionless descriptor allows one to consistently compare plating response of electrodes with varying structural attributes as well as operating conditions. Here (Figure 55) microstructural specifications[174, 175] correspond to the representative electrode capacities (~3.3 and 4.9 mAh/cm^2, respectively), while ensuring similar electrode dimensions. Figure 55(d) presents the microstructural reconstruction of a graphite electrode.

In anodes, the dominant electrochemical reaction is intercalation and dictates the field evolutions. In turn lithium plating, a side reaction is implicitly driven by intercalation. During lithiation, $\eta_{\text{intercalation}} = \phi_{\text{anode}} - \phi_{\text{electrolyte}} - U_{\text{anode}} < 0$, where the anode potential, ϕ_{anode}, is defined by local electronic current, electrolyte potential, $\phi_{\text{electrolyte}}$, relates to ionic flux, and open circuit

potential, U_{anode}, reflects the lithiation field. Given the high conductivity of graphite anodes[175, 273], the anode potential exhibits a negligible spatial dependence, *i.e.*, $\phi_{\text{anode}}(x,t) \approx \phi_{\text{anode}}(t)$. On the other hand, the electrolyte, $\phi_{\text{electrolyte}}$, and thermodynamic, U_{anode}, potentials display both spatial and temporal variations (Figure 55(g),(h)) in response to Li^+ and Li fields, respectively (Figure 55(e),(f)). The lithium fields exhibit stronger gradients for high energy (*i.e.*, low porosity) electrode, Figure 55(f) against (e). Figure 55(g) and (h) reveal the underlying difference between the potential evolution characteristics (shaded regions imply driving force for electrodeposition). For the start-of-the-art electrodes, subzero anode potential is present, while for energy dense cells, the stronger electrolyte potential gradients give rise to plating even when anode potential is above zero. As mentioned earlier, $\eta_{\text{intercalation}} + \phi_{\text{electrolyte}} + U_{\text{anode}} = \phi_{\text{anode}} \equiv \text{spatially invariant}$. If the kinetic overpotential, η_{anode}, is too severe ($\eta_{\text{intercalation}}$ is negative for intercalation), ϕ_{anode} drops below zero and causes plating. Alternatively, if the electrolyte transport is restricted, $\phi_{\text{electrolyte}}$ can adopt high values such that $\phi_{\text{electrolyte}} > \phi_{\text{anode}}$ and trigger plating. These two demarcate distinct modes of electrodeposition: kinetically- and transport-limited. The energy-dense electrodes have a higher active material content which represents the high active area and consecutively smaller kinetic overpotentials. The higher active material also implies a smaller porosity and equivalently starker electrolyte gradients. Thus, as energy density is increased, the long-range transport effects contribute more to lithium plating. To dissect the contributions from various resistive mechanisms, the internal resistance (Figure 55(i)) is deconvolved into the elemental contributions (Figure 55(j),(k)). The possible resistive modes[174, 264] are:

- Electronic resistance in the solid phase, r_s
- Ionic resistance in pore network, r_t
- Charge transfer resistance of reactions, r_k
- Concentration resistance due to diffusional gradients in the active material, r_c (nonuniform concentration field in active particles gives rise to gradients in thermodynamic potential)

Quantification of each of these modes is described earlier[174, 264]. Note that the separator only supplies the transport resistance. A comparison between Figure 55(j) and (k) shows that the contribution from kinetic and concentration resistances decrease for energy-dense electrodes and the transport resistance becomes more relevant. For two electrodes with similar materials, the

dependence on energy density arises due to microstructural differences. The electrode recipes are 95%wt. graphite (5% binder) and 90% NMC (5% conductive additives + 5% binder), respectively for anode and cathode[30, 175, 180]. The results presented here are based on thoroughly verified electrochemical[174, 175] and electrode-specific microstructural descriptions[174, 272, 273]. Charging is carried out from 2.8 V (delithiated graphite and lithiated NMC) to 4.2 V. The anode and cathode microstructural specifications are interdependent[175]. For identical electrode capacities (*i.e.*, anode – to – cathode loading, A/C = 1), smaller secondary phase content at anode results in higher anode porosity, and equivalently smaller tortuosity as compared to the corresponding cathode. Hence, the anode transport resistance is smaller (for each having spherical active particles) in Figure 55(j) and (k). In state-of-the-art cells, the operation is limited by short-range interactions – kinetics and lithiation gradients[29, 174]. Such interactions foster electrodeposition at the anode. On the other hand, in energy-dense electrodes, the long-range transport limitation becomes relevant, which reduces the driving force for electrodeposition, Figure 55(g) against (h). Figure 55(c) compares the two electrodes in terms of their intercalation response. Given the stronger transport effects in energy-dense electrodes, an ionically-limited regime is observed, especially for currents and temperatures that encourage plating in conventional practice. This accounts for the absence of lithium plating in high-energy cells (Figure 55(b)), and consequently more stable (sustained) intercalation.

The morphology (shape and size) of the active particles alters the geometrical arrangement of various constitutive phases in an electrode structure[175, 273]. Subsequently, diffusion distance (*i.e.*, characteristic length for intercalation), active surface topology and pore network change. Such configurational differences modulate the physicochemical interactions in the electrodes[175]. Figure 56(a) investigate the interplay between anode particle morphology and plating activity for the energy dense electrodes. The insets pictorially detail the microstructural differences between spherical and platelet active particle anodes. The corresponding potential fields (at the end of charging) are shown in Figure 56(b) to (e) to identify the mechanistic origins of electrodeposition signature summarized in Figure 56(a). Platelets form comparatively distorted pore network[175, 273], which reflects in greater electrolyte potential drops in Figure 56(b) to (e) (the electrode porosities are identical). For the same particle volume, the sphere has the smallest surface area (*e.g.*, small liquid drops tend to adopt spherical shapes to minimize surface energy). The active surface area in the platelet structure increases going from (c) to (e).

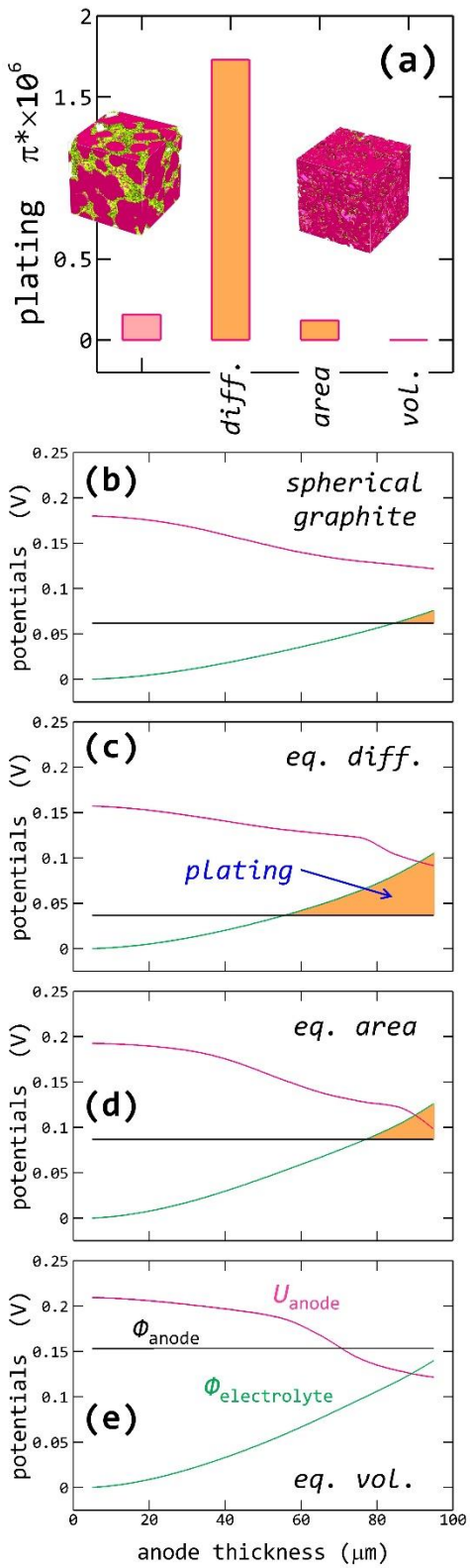

Figure 56. Particle morphology – lithium plating interplay (a). The behavioral differences arise from variations in potential evolution (b) to (e).

For the same diffusion length (5 μm), a platelet graphite electrode with equivalent diffusion length has an equivalent concentration gradient as the spherical structure (*i.e.*, similar concentration resistance, r_c), but higher kinetic and transport hinderances. Given this distribution of resistances, anode potential is smaller and electrolyte potential is higher, leading to a greater drive, $\phi_{\text{electrolyte}} - \phi_{\text{anode}}$, for plating (shaded area) as evident in Figure 56(c). For the equal area structure, particle dimensions are smaller, thus reducing the intercalation length (~3 μm), while the tortuosity differences are marginal. This amounts to a comparable kinetic resistance and a smaller concentration resistance, effectively reducing the plating tendency, Figure 56(c) *vs*. (d). The higher transport resistance as compared to the spherical structure decreases the charging time, $t_{\text{operation}}$, and in turn, the electrodeposition quantity is smaller (Figure 56(a); intercalation is less as well). For an equal volume platelet graphite particle, the diffusional length is smaller (*i.e.*, smaller r_c) and the active area is higher (*i.e.*, smaller r_k), which outweigh the higher transport resistance of a platelet structure, in turn suppressing plating as compared to a spherical microstructure (Figure 56(a),(e)). It is interesting to observe that small platelet particles can reduce lithium plating despite their higher tortuosity. Smaller particles are advocated to ameliorate mechanical degradation for graphite[211, 224]. Such a feature is duplicated here for a chemical degradation mode.

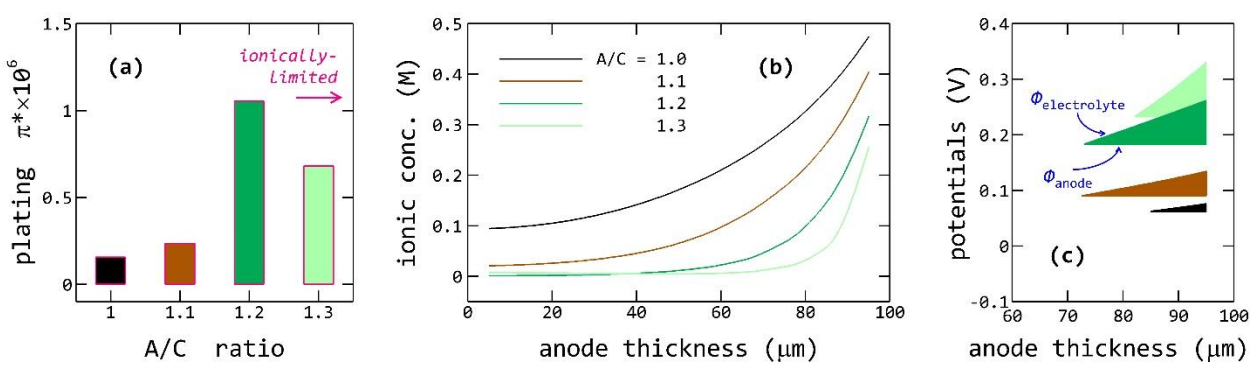

Figure 57. Electrode imbalance is detrimental for energy-dense electrodes where high A/C ratio foster lithium plating (a). (b) Ionic concentration and (c) plating driving force varies with imbalance.

The conventional rationale for safeguarding against anode-centric chemical degradation preachifies electrode imbalance[235, 238]. A higher anode capacity is expected to provide additional lithium inventory as well as shrink the lithiation window. The thermodynamic anode potential

approaches zero for a complete lithiation, hence a smaller lithiation window reduces the chances of subzero anode potentials (an argument based on near equilibrium considerations). However, energy dense electrodes promote off-equilibrium complexations and the electrode imbalance misdirects the plating tendency (Figure 57(a)). The imbalance implies lower porosities[175] and in turn higher pore network resistances, r_t. The particle dimensions are kept similar which provides a higher active area on account of more active material (*i.e.*, reduced r_k) and commensurate diffusional resistance, r_c. Higher transport resistance reigns the anode resistance (cathode is kept invariant), which reflects as a greater electrolyte potential drop and heavier predisposition exists for plating (Figure 57(c)). Lithium deposition (Eq. (138)) relates to reactants as well as driving force. A higher anode transport resistance decreases the ionic concentrations (Figure 57(b)). These two mechanisms counter each other, and the nonlinear plating trend ensues (Figure 57(a)). For a higher electrode imbalance (A/C = 1.3), locally ionic depletion takes place (Figure 57(b)) and decreases electroplating (Figure 57(a)). The concentration (Figure 57(b)) and potential (Figure 57(c)) fields correspond to the end of the operation. The deposited lithium exhibits a multitude of morphological features based on competing kinetic processes[290-292]. It is expected that the spatial variation of the plating overpotential, $\phi_{\text{anode}} - \phi_{\text{electrolyte}}$, gives rise to morphological differences within the same electrode.

In summary, transport effects engender an alternate regime of electrodeposition complexations in porous intercalation electrodes where lithium plating can take place above zero anode potential. High energy electrodes have enhanced transport resistance and exhibit a nonlinear dependence on temperature and charging current. As electrode imbalance further exacerbates the transport effects, higher anode – to – cathode loading proves to be penalizing. Morphological changes in active particle proffer an effective avenue to mitigate lithium plating.

4. ELECTRODE MICROSTRUCTURAL STOCHASTICITY

Relevant Publications and/or Working Papers:

1. A. Mistry, K. Smith and P. P. Mukherjee (2019) *Stochasticity at Scales Leads to Lithium Intercalation Cascade* working paper
2. A. Mistry and P. P. Mukherjee (2019) *Statistical Learning based Abstraction of Pore Network Resistance Descriptor in Porous Electrodes* working paper

Porous intercalation electrodes are synonymous to the promise of lithium-ion batteries toward electromobility. These electrodes exhibit stochastic geometrical features spanning different length-scales. The implication of stochasticity at the hierarchy of scales on the lithium intercalation dynamics is not yet established. Starting with 3D, X-Ray tomograms of intercalation electrode microstructures, we demonstrate, based on physics-based and statistical mesoscale analysis, that interfacial and pore-scale stochasticity leads to preferential and staged lithiation fronts. This study comprehensively suggests that the spatiotemporal underpinning of short-range (kinetic) and long-range (transport) stochastics results in intercalation cascade, which hitherto remains unexplored.

4.1 Background

Porous electrodes are an indispensable part of the Lithium-ion battery (LIB) technology[12, 13, 15-17, 259]. Fundamentally, electrodes are electrochemical reactors that facilitate interconversion of ionic and electronic charge carriers. Such an action is made up of reaction (kinetics of charge conversion) and transport interactions (the ability of ions and electrons to access the reaction locations). The microstructural arrangement of various constituents, in turn, define these complexations. Hence, the conventional interpretation of porous electrodes relies on volume averaged geometrical properties such as porosity, tortuosity[68, 198, 293,] and conductivity[27, 30, 33]. Electrode microstructure, however, exhibits spatial variations. Such stochasticity is inherent to the electrode preparation step[83, 294] where a combination of interfacial (evaporation, cohesion, and adhesion) and statistical (random thermal energy, $k_B T$) factors counter the bulk diffusive motion that would otherwise provide a homogeneous electrode. The implications of such spatial stochasticity have been quite poorly understood[295, 296], given the spatiotemporal limitations in simultaneously probing the electrochemical interactions over a wide range of scales – from pores to electrodes. This '*curse of dimensionality*' has affected both the experimental and computational investigations, alike[51, 60, 62,

[71, 74, 76, 81, 82, 91]. Here we examine the connection between microstructural stochasticity and intercalation dynamics for Li-ion battery electrodes. To circumvent the spatiotemporal limitations, we carried out a multiscale analysis that suitably translates information across scales.

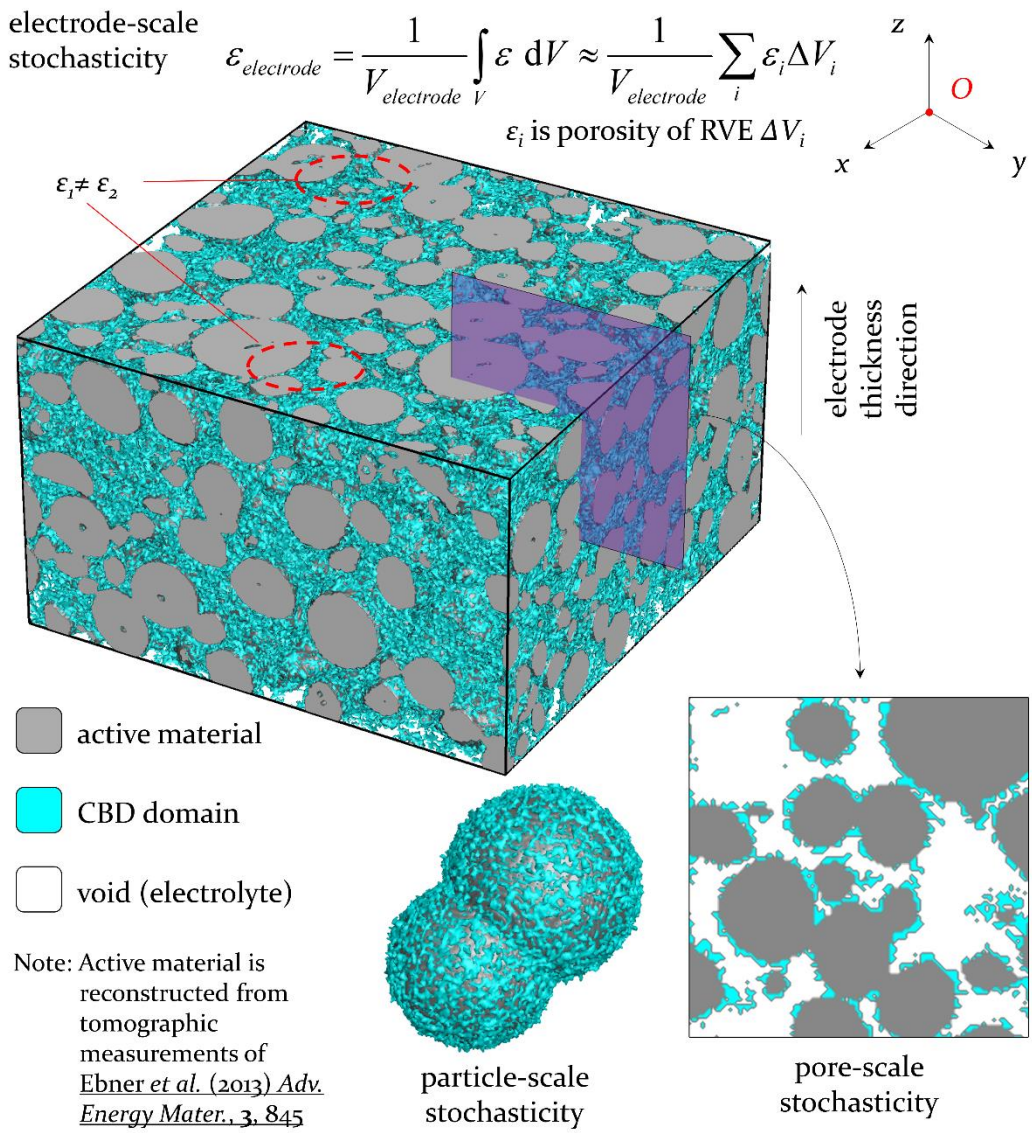

Figure 58. Stochastic Features in Porous Intercalation Electrodes. A composite Li-ion battery electrode microstructure is a multiphase multilength scale system, as different solids have disparate geometrical attributes. The electrode microstructure exhibits inhomogeneities at different length scales, depending on electrode processing conditions. Non-uniform distribution of CBD phase leads to distinct interfacial and transport resistances. Active material particles also exhibit spatial distribution, giving rise to electrode-scale variation (at a length-scale larger than the RVE).

Figure 58 demonstrates the different stochastic scales for a reconstructed electrode microstructure with necessary material phases. The active material is NCM333 (Nickel Cobalt Manganese oxide), and its geometrical arrangement is obtained through tomography[80]. X-ray tomography cannot differentiate between the pores and the secondary (nonintercalating) solids. The secondary phase (carbon binder domains, CBD) provides a percolating network for electron conduction as well as mechanical connections to hold active particles together. The CBD arrangement at the interface scale is reproduced *via* a physics-based description developed earlier[174]. Three representative stochastic scales emerge (Figure 58): the CBDs foster inhomogeneities at particle surface and simultaneously modify the pore network (resulting in pore-scale stochasticity), while the active particle agglomeration results in spatial variation at length scales much larger than pore or particle dimensions (essentially larger than representative volume element, RVE, dimensions).

4.2 Deconvolving Stochastic Contribution of Phases

The manifestation of stochasticity at different scales is inherently related to spatial arrangements of active material and CBD phases. For a given active material arrangement (Figure 59(a)), the CBD can form different networks[174] (Figure 59(c)-(g); ω (morphology factor) characterizes the CBD interfacial arrangement). In contrast, the active material arrangement varies over a larger length-scale as revealed by porosity gradients in an electrode (Figure 59(h), (l)). To explore the effects of these two arrangements, *i.e.*, AM distribution quantified in the form of porosity variations and CBD distribution specified in terms of morphology factor, Figure 59(i)-(k) compares relevant microstructural properties. These properties are estimated *via* pore-scale calculations[174] of RVE-sized sub-volumes. Here RVE size is the smallest domain-size for which effective properties can be defined[9, 10] (refer to Representative Volume Element (RVE) Identification). Essentially, each RVE contains a statistically significant amount of geometrical information so that volume-averaged properties define representative transport interactions. The smallest geometrical features are associated with CBD arrangement and reflect smaller lengths as compared to active particles. An RVE accommodates enough particulate and sub-particulate matter. On the other hand, an electrode is composed of multiple RVEs. Electrode dimensions, *i.e.*, thickness, and in-plane widths, are appropriate larger length-scales associated with a porous battery electrode.

Figure 59. Isolating Stochastic Contributions from CBD and AM. (a) RVE of a composite electrode; (b) x-mid plane reveals particle and secondary phase distribution; (c)-(g) various forms of CBD arrangement; (h) AM clustering expressed as porosity differences among RVE locations (l); Quantifying stochasticity in terms of effective properties (i), (j) and (k); (m) morphology dependence for effective properties; (n), (o) anisotropy in directional properties.

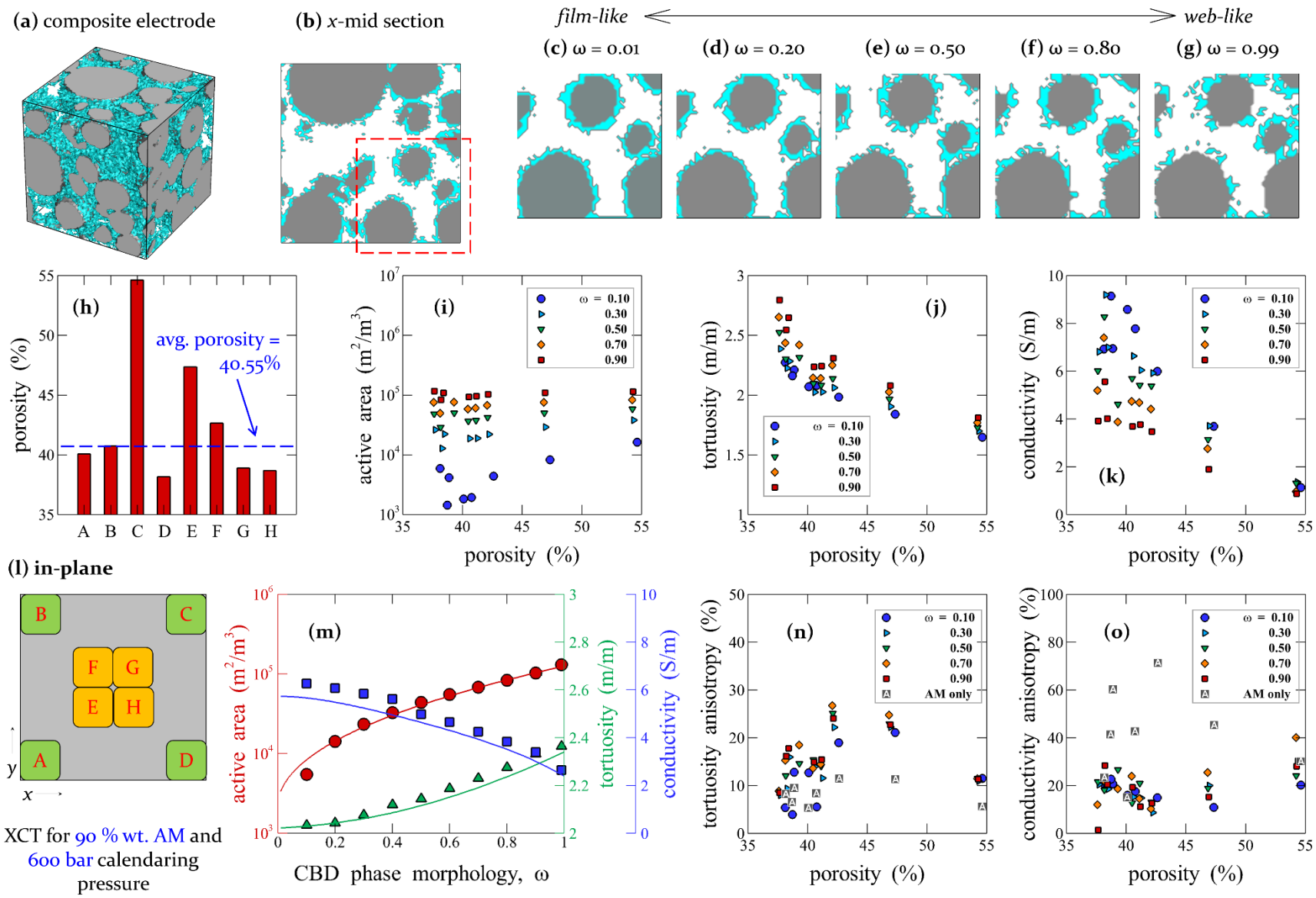
(a) composite electrode
(b) x-mid section
film-like
web-like
(c) ω = 0.01
(d) ω = 0.20
(e) ω = 0.50
(f) ω = 0.80
(g) ω = 0.99
(h)
avg. porosity = 40.55%
porosity (%)
A B C D E F G H
(i)
active area (m²/m³)
porosity (%)
(j)
tortuosity (m/m)
(k)
conductivity (S/m)
ω = 0.10
0.30
0.50
0.70
0.90
(l) in-plane
B C F G E H A D
y
x
XCT for 90 % wt. AM and 600 bar calendaring pressure
(m)
active area (m²/m³)
tortuosity (m/m)
conductivity (S/m)
CBD phase morphology, ω
(n)
tortuosity anisotropy (%)
(o)
conductivity anisotropy (%)
AM only

RVE sized volumes are selected from eight locations (Figure 59(l)) on a tomogram (90 %wt. 600 bar electrode[80]) and are found to exhibit considerable porosity departures from the electrode-averaged value (Figure 59(h)). The CBD content is identified from the electrode recipe[80]. Electrochemical (*i.e.*, intercalation) reaction predominantly takes place at pore – active material interface[174], hence, this surface represents the electrochemically active interface (Figure 59(i)). As the CBD morphology becomes more web-like, the active area increases as the cohesive tendency of CBD outweighs its adhesion to the active particle surface. The active area demonstrates a (counterintuitive) weak dependence on porosity. For a given electrode composition, CBD distribution throughout the electrode depends on the available active particle surface (since CBD arrangement is driven by interfacial energetics). The active particle surface area is smaller for both low porosity (when the particles are in very close proximity) and high porosity (when there is not enough active material left). For low porosities, the active particle surface area increases, which in turn increases the CBD content and effectively decreases the active area. Such quadratic trends are present across the range of CBD morphologies (Figure 59(i)). This reciprocity results in a weaker dependence of interfacial area on local porosity. The conduction predominantly takes place through the CBD network (active material conductivity is quite inferior[19]). As CBD content decreases for both the low and high porosities, conductivities (Figure 59(k)) also exhibit such quadratic behavior. More three-dimensional CBD arrangement ($\omega \rightarrow 1$) decreases the percolating bridges at the active particle surface, and effectively the conductivity decreases going towards a web-like CBD phase.

Tortuosity (Figure 59(j)) is a descriptor of pore-network resistance. The presence of CBD decreases the available pore-space, which increases the tortuosity. Active area (Figure 59(i)) and conductivity (Figure 59(k)) are strongly related to CBD arrangement, while it has a secondary monotonic effect on tortuosity (Figure 59(j)) as it always reduces the pore space available for ionic transport. There is a fair dependence on morphology as the three-dimensional CBD ($\omega \rightarrow 1$) creates more constriction as compared to the two-dimensional CBD ($\omega \rightarrow 0$). Based on these calculations, morphology dependence of microstructural properties (averaged over these eight locations) is shown in Figure 59(m), with corresponding analytical relations summarized in Table 7. It is interesting to note that even though all three descriptors exhibit a morphological dependence, the sensitivity is relatively weaker for tortuosity. Hence, it is inherently difficult to detect the CBD morphology *via* tortuosity measurements[297] alone.

The tortuosity and conductivity values reported in Figure 59(j) and (k) are averaged over three coordinate directions. There does exist quantifiable anisotropy (Figure 59(n)-(o)) in their values, and is estimated as per the expression:

$$\delta_{\psi} = \left(\frac{\psi_{max} - \psi_{min}}{\bar{\psi}} \right) \times 100\% \tag{139}$$

The anisotropy in composite structures is about 20% for both the forms of long-range interactions. Additionally, the anisotropy does not exhibit any clear trend with either local porosity or CBD morphology, thus quantitatively elucidating the stochastic nature. The presence of CBD alters the underlying anisotropy in the AM structure (plotted alongside). Curiously the tortuosity anisotropy appears to be amplified, while attenuated for conductivity. The primary mode of electronic conduction for composite electrodes is through the CBD phase (for AM backbone, conduction is through the AM particle network). Figure 59(o) reflects this change in conduction pathways. On the other hand, for pore phase transport, CBD anisotropy further supplements the pore phase anisotropy, and leads to an enhancement (for active material backbone obtained through tomography, pore phase is complementary to the active material phase; so equivalent amount of anisotropy exists in both the pore and active material phases in the raw XCT data).

4.3 Electrode-scale Stochasticity Profile

To gain insights into the electrode-scale stochasticity profile, Figure 60 examines the entire tomogram (CBD morphology is kept at $\omega = 0.50$). Effective property variations are mapped in all three dimensions (for the entire electrode sample), and the in-plane variations are shown here. Figure 60(e) describes the stochastic nature of active material distribution as available from XCT[80]. Such nonuniformity refers to clustering at the particle-scale. CBD is added to ensure the prescribed electrode composition (Figure 60(f)), while the porosity distribution results consecutively (Figure 60(a)). A higher active material content, attracts more CBD during the drying step[83, 174], and in turn, CBD map (Figure 60(f)) closely resembles the active material distribution (Figure 60(e)). This also reduces porosity further. Two locations (of low and high active material packing) are identified to discuss correlation among phase contents and effective properties (representative values are listed in Table 8).

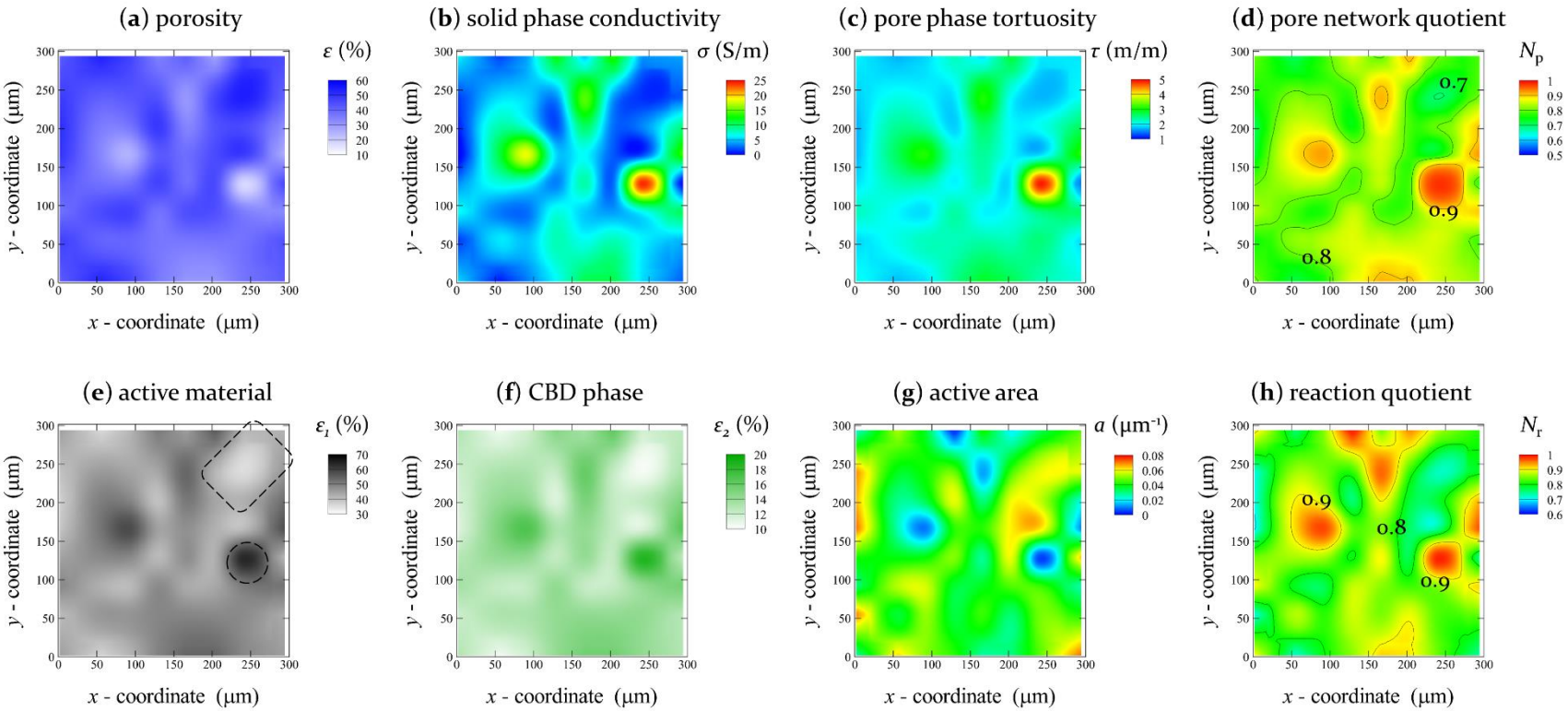

Figure 60. Profiles of Electrode-scale Stochasticity. The active material is obtained through XCT (e) and supplemented to account for CBD (f) to recover the true (a) pore phase. The microstructural complexations are quantified as transport (b), (c) and interfacial (g) properties. Dimensionless descriptors Np and Nr assist identification of transport limited (d) and kinetically limited (h) locations.

The long-range limitations (Figure 60(b)-(c)) appear to be closely related. Low porosity locations are a result of high AM and CBD, thus leading to a high tortuosity and a high conductivity. Complimentary variations result for high porosity locations. Such a correlated distribution of electronic and pore phase transport pathways results in distributed long-range limitations as the pockets of electronic and ionic resistances arise due to electrode-scale stochasticity. It is important to recognize this distributed nature. The electrode-average measurements[30, 198] would not be able to capture such localized limitations. These stochastic effects become more relevant as high AM electrodes are pursued (stochastic implications of electrode recipe are discussed in Supporting Information). As alluded earlier, active material clustering confines more CBD and effectively reduces the active area. The active area map (Figure 60(g)) confirms such a quadratic progression, where the high AM locations suffer from minimal reaction surface, *i.e.*, area blockage. Intermediate active contents have higher active area.

The spatial correlation for the short-range and long-range limitations is analyzed in Figure 60(d),(h). Quantitatively these limitations are described by the reaction blockage quotient, $N_r = 1 - (a/a_0)$ and the pore network quotient, $N_p = 1 - (\varepsilon/\tau)$ [174, 175, 264]. Figure 60(d),(h) reveals that the two types of limitations are not always spatially coincident. Mathematically speaking[9], phase fractions are bulk quantifiers, while the active area is an interfacial descriptor. One would expect a qualitative similarity among their profiles, but the order of variation need not be identical when comparing the two. Active area (Figure 60(g)) is not readily amenable to interpretations since a small active area could imply either low AM or high CBD (due to high AM). Of these, a high CBD small area location is more detrimental as it would cause a higher intercalation resistance even when enough active material is present for intercalation. Reaction quotient (Figure 60(h)) provides a better interpretation of limiting stochastic behavior. Such zones require higher overpotentials to sustain electrochemical reactions. On the other hand, high N_p locations (Figure 60(d)) hinder ionic transport and lead to electrolyte potential drops.

The stochasticity analysis presented here discusses the general nature of spatial variations. As macroscopic electrode descriptors are changed, *e.g.*, electrode composition and calendaring pressure, these profiles change and lead to different extents of inhomogeneity and anisotropy in electrodes.

4.4 Preferential Intercalation Dynamics

The microstructural analysis abstracts the relevant stochastic features of the porous electrodes in terms of effective properties. Such spatially varying, *i.e.*, three-dimensional, effective property maps are invoked to investigate the causality between microstructural stochasticity and intercalation dynamics (mathematical preliminaries are summarized in Supporting Information). Electrode-scale intercalation is examined at a constant rate of lithiation (Figure 61) to distinguish the implications of microstructural stochasticity from other time-varying factors (*e.g.*, constant voltage, non-isothermal[175] operations). Figure 61(d) presents the temporal progression of electrode-scale lithiation profile, starting from an initial homogenous state of lithiation. A comparison between Figure 60(d) (or (h)) and Figure 61(d) reveals that the lithiation profile gradually evolves in response to electrode-scale stochastic limitations. Traditionally, such preferential lithiation fronts[298-300] are observed in the context of multiphase intercalation material[185] (*e.g.*, Lithium Iron Phosphate) and/or particle-scale anisotropy for nano-sized active particles. Contrarily, here lithiation pockets are observed in an electrode material with single-phase intercalation response. The spatial correlation among the lithiation profile and microstructural stochasticity imply geometrical origins for such a nonlinear response. To further understand the lithiation dynamics, (intercalation) reaction distribution is examined in Figure 61(c). At the start of lithiation, low resistance spots ($N_r < 1$ and $N_p < 1$) are intercalated first as they are more conducive to both the reaction as well as reactant transport. The high resistance locations, $N_r \rightarrow 1$ and/or $N_p \rightarrow 1$ trail as it is easier to intercalate elsewhere. The reaction distribution (Figure 61(c)) at the beginning also maps to resistance diagrams (Figure 60(d),(h)) and justifies this argument. Gradually, when such locations are nearly intercalated, reaction current concentrates on the locations with greater microstructural resistances. This transition in reaction profile is also visible in Figure 61(c). Figure 61(b) presents the electrolyte potential difference, *i.e.*, $\Delta_z \phi_e = \phi_e(x,y)\big|_{z=0} - \phi_e(x,y)\big|_{z=L_z}$ profile over the electrode surface. Initially when intercalation takes place at low resistance locations, electrolyte potential is fairly uniform, and towards the end of lithiation, such gradients intensify in response to microstructural resistances.

It is interesting to note that such geometrical stochasticity does not manifest as a distinguishing signature (other than incomplete lithiation) when electrode potential evolution is examined (Figure 61(a)). Moreover, for small times, the inhomogeneity in the lithiation field has

not grown to be measurable. Thenceforth, the conventional single-point measurements[301] (rate capability, galvanostatic intermittent titration, cyclic voltammetry, *etc.*) have not identified this connection between stochasticity and intercalation dynamics. A recent *in situ* X-ray diffraction study has identified such lithiation profiles given the spatial probing of intercalation dynamics[302]. Since their spatial resolution is not small enough to capture microstructural stochasticity, the fundamental origins of such inhomogeneous intercalation have remained elusive.

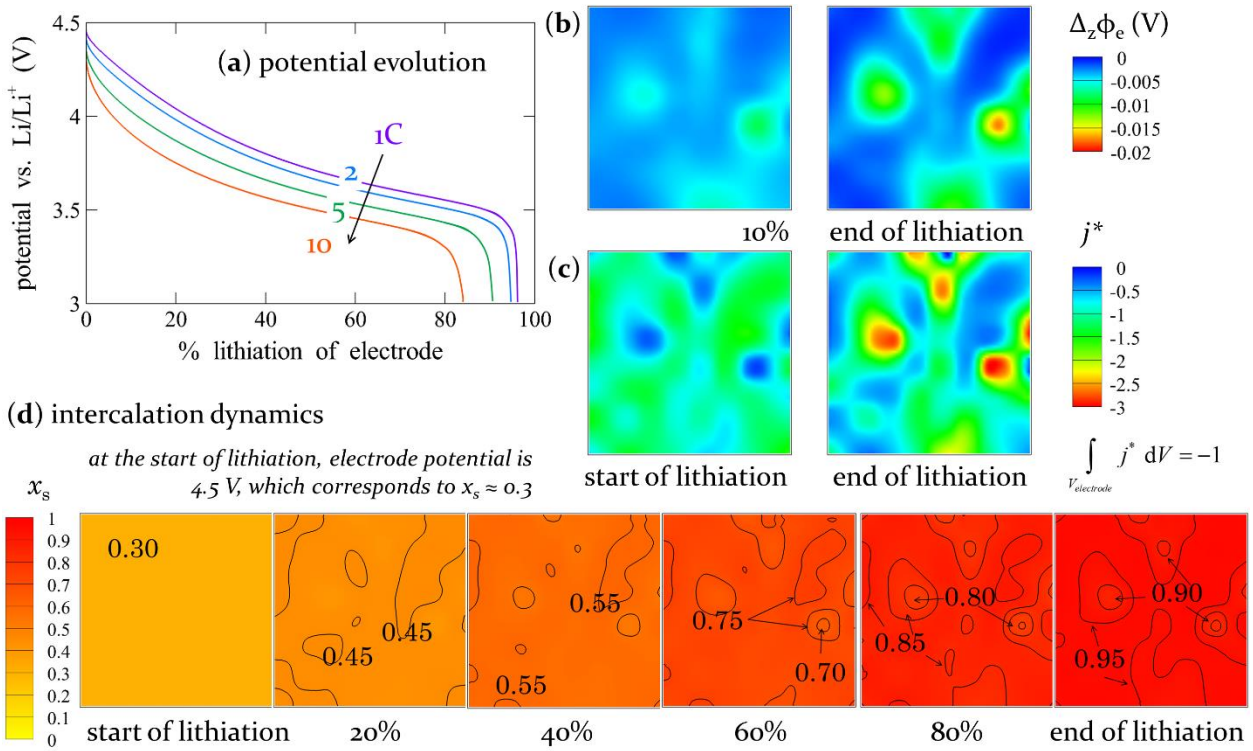

Figure 61. Preferential Intercalation Microstructural stochasticity reflects in spatially dependent fields. (b) electrolyte potential (c) reaction current and (d) lithiation, however, single-point descriptors such as electrode potential (a) do not exhibit stochastic explicit signatures.

4.5 Macroscopic Changes (Composition and Calendaring) alter Stochasticity Profiles

Electrode composition as well as calendaring lead to distinct microstructural arrangements. Figure 62 compares three electrodes with different compositions (AM loading 92, 94 and 96 %wt.) and identical calendaring (600 bar) pressure. CBD phase is added to be compatible with the prescribed recipes (at a fixed morphology $\omega = 0.50$). Figure 62(a) presents the mean porosity (bars) along with a spread in porosity (eight RVEs as discussed earlier). The electrode porosities increase

monotonically with increasing CBD content (*i.e.*, decreasing AM), despite the fact that these electrodes were prepared under identical environment[80]. This suggests a close interplay among the formation of active material structure and the presence of CBD phase. Essentially it appears that at a higher CBD content, a hollower active material structure is formed which in turn results in higher porosity composite electrodes for smaller active material loading. Such interaction has not been noticed in any previous study.

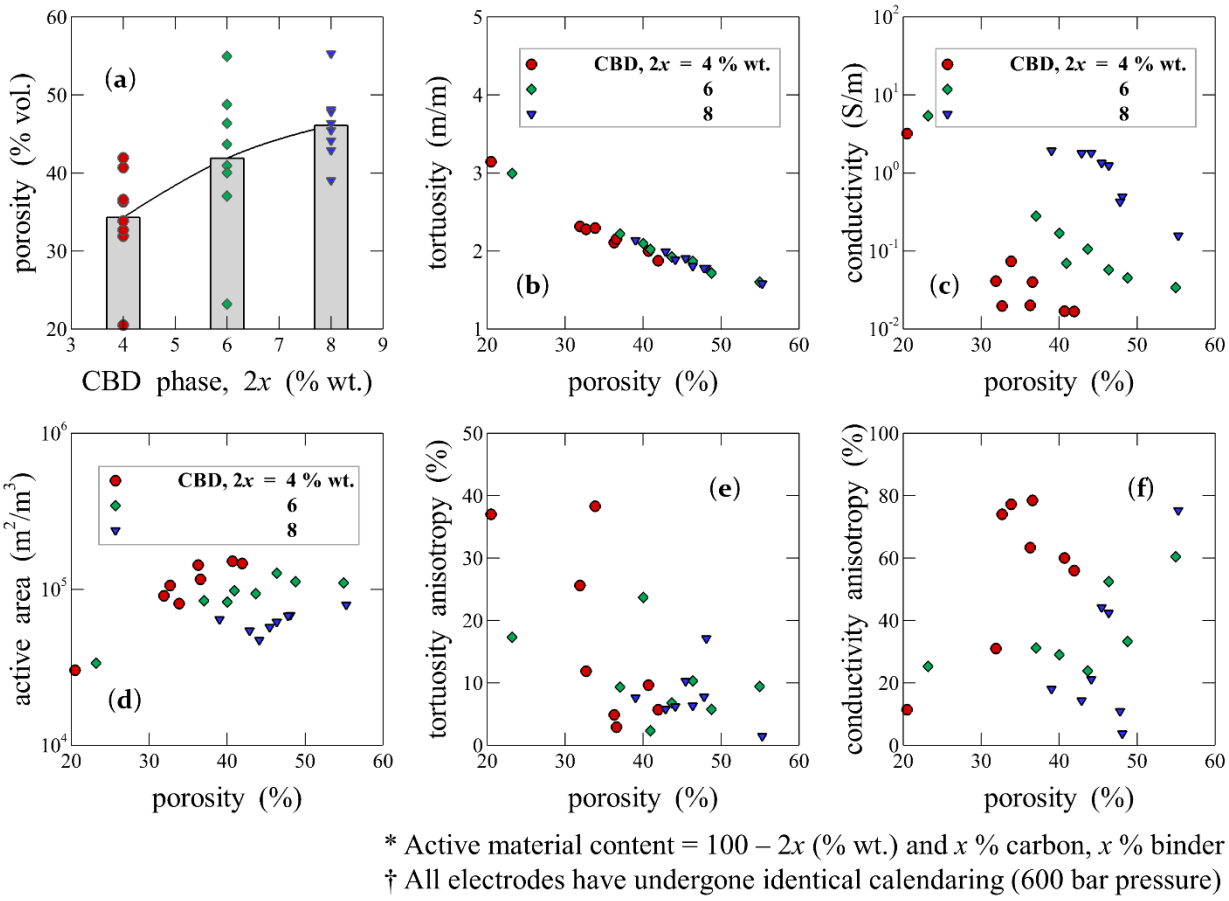

Figure 62. Electrode composition effects: three different electrode recipes with 4, 6 and 8 % wt. CBD phase (remaining AM) are studied in terms of their microstructural properties (a) porosity (b) pore phase tortuosity (c) solid phase conductivity (d) active area and anisotropy in tortuosity and conductivity (e) and (f), respectively.

Tortuosity values correlate monotonically to porosity (Figure 62(b)), with tortuosity clusters shifting towards higher values for higher active material (*i.e.*, lower CBD) electrodes. As electronic pathways increase with volume fraction (for same morphology, ω), smaller CBD amount gives smaller conductivities. For the lowest CBD content (4% by wt.), the effective electronic

conductivities fall between 0.01 to 0.1 S/m for the most part. This incurs appreciable solid state resistance to electron flow[25]. As proved earlier by authors, given a typical LIB electrolyte, solid state conduction limitations become negligible for effective electronic conductivities of 1 S/m or higher[25]. For higher CBD phase (8% by wt.), electronic conduction appears to be sufficiently large. Higher active material loading (*i.e.*, smaller CBD content) has a relatively smaller active interfacial blockage and correspondingly higher active area. Figure 62(d) confirms such expectations where smaller CBD amount (4%) has a higher interfacial area. Again, the active area appears to be weakly dependent on local porosity (same explanation as earlier).

$$\begin{array}{cccc} w_{CBD} & \varepsilon & \delta_\tau & \delta_\sigma \\ \uparrow & \uparrow & \uparrow & \uparrow \end{array}$$
$$\begin{bmatrix} 1 & 0.5813 & -0.3817 & -0.4408 \\ & 1 & -0.5944 & 0.0863 \\ & & 1 & -0.2198 \\ & & & 1 \end{bmatrix} \begin{array}{cc} \rightarrow & w_{CBD} \\ \rightarrow & \varepsilon \\ \rightarrow & \delta_\tau \\ \rightarrow & \delta_\sigma \end{array} \tag{140}$$

Anisotropy in tortuosity and conductivity is quantified and presented in Figure 62(e) and (f), respectively. As before (Figure 59(n) and (o)), the conductivity anisotropy is larger than the anisotropy in tortuosity. Also, visually one cannot isolate a clear trend with local porosity. A rather fascinating feature is that anisotropy increases monotonically with a reduction in CBD content. This would suggest that for smaller CBD loading (% wt.), secondary phase stochasticity becomes more prominent. A correlation matrix[303] (Equation (140)) is evaluated to quantify the interrelation among w_{CBD} % wt. CBD content (*i.e.*, active material loading), ε porosity, δ_τ tortuosity anisotropy, and δ_σ conductivity anisotropy. The higher values of off-diagonal elements signify stronger correlation among the corresponding row and column properties[303]. For example, element (1,2) is 0.5813 which reflects the fact that CBD content and porosity are closely related. Similarly, entries (1,3) and (1,4) allude that anisotropy is also composition dependent (a correlation matrix is always symmetric, hence lower diagonal values are not shown for brevity[303]). Reduction in local porosity fosters higher anisotropy in the pore phase which is apparent from entry (2,3) on correlation matrix (negative sign refers to the fact that tortuosity anisotropy increases with a decrease in porosity). On the other hand, conductivity anisotropy is primarily dependent on CBD content (entry (1,4)).

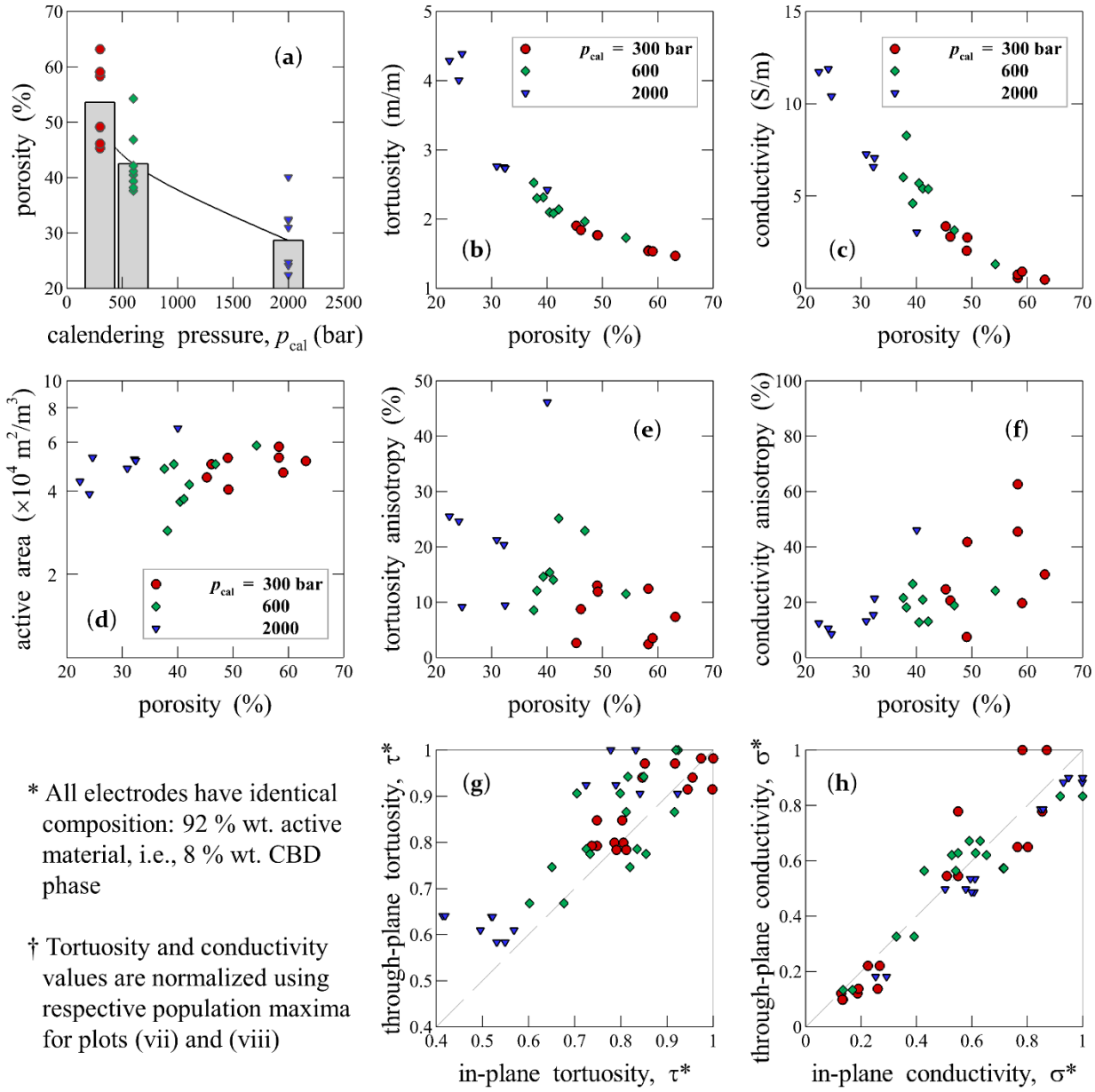

* All electrodes have identical composition: 92 % wt. active material, i.e., 8 % wt. CBD phase

† Tortuosity and conductivity values are normalized using respective population maxima for plots (vii) and (viii)

Figure 63. Effect of calendaring pressure at identical electrode compositions (92 % wt. AM): The resulting composite electrode structures are compared in terms of microstructural properties (a) to (d) and anisotropy in long-range interactions, tortuosity (e) and conductivity (f), respectively. Directional dependence of anisotropy is investigated in (g) and (h).

In the same spirit, Figure 63 explores the electrode microstructural variations resulting from the calendaring process. All the electrodes have identical active material loading (92 % wt.). As expected, electrode porosity monotonically decreases with the calendaring process (Figure 63(a)). That leads to increased pore phase tortuosity (Figure 63(b)) as well as higher solid-state

conductivity (Figure 63(c)). At the same composition, reduction in porosity leads to increased volumetric loading of solid phases. Thus, increased CBD volume has more pathways for electronic conduction and effectively higher conductivity (Figure 63(c)). Given the constant composition, one would expect relatively constant active area (as before). This is confirmed by Figure 63(d) where an active area exhibits a weak dependence on both local porosity as well as calendaring. In fact, calendaring is carried out to reduce the (mean) porosity of electrodes[42, 172]. And in turn, one would expect porosity-like dependence for mean properties.

The situation becomes more interesting when anisotropy is studied as a function of calendaring pressure (Figure 63(e) to (h)). Tortuosity anisotropy increases with calendaring while conductivity anisotropy decreases. It appears that the calendaring process distorts the pore network, giving rise to further anisotropy as electrodes are calendared. On the other hand, with calendaring, the CBD phase establishes more connections which effectively reduces the spread. An associated question is whether this anisotropy is directional or not. Often it is argued that calendaring introduces anisotropy in the electrode thickness (through-plane) direction. Figure 63(g) and (h) plot these long-range transport properties: their through-plane (z) values against in-plane (x, y) ones. Data for each electrode is normalized using the population maximum for better visualization on Figure 63(g) and (h). A 45° line (dashed) is also shown along with. The closer the values are to this 45° line, smaller is the anisotropy. Careful study of Figure 63(g) reveals that with increased calendaring pressure, through-plane tortuosity starts increasing. For lower calendaring pressure (300 bar), the values are quite symmetrically distributed around the 45° line, while for the highest pressure (2000 bar), most of the points fall in the upper triangle. This implies that instead of being compressed in a vertical fashion, the pore phase undergoes lateral rearrangement leading to a more tortuous path for the through-plane ionic transport. On the other hand, the opposite trend is observed for electronic conductivity (Figure 63(h)). Upon calendaring, in-plane conductivities become larger than through-plane values. From a structural standpoint, this suggests that upon compression CBD phase rearranges in the lateral direction leading to better contacts. To summarize, the calendaring process increases tortuosity and reduces conductivity for the through-plane direction (compared to in-plane). Both of these negatively affect ionic and electronic transport, respectively. It is interesting to see that the calendaring process start affecting second order descriptors rather strongly. From the microstructural standpoint, a calendared electrode is not simply an electrode with reduced porosity but also with modified structural arrangements.

Figure 63(e) to (h) reveal that anisotropy in transport properties have two distinct attributes: quantity (Figure 63(e), (f)) and quality (*i.e.*, directionality; Figure 63(g), (h)). In other words, spatial stochasticity in electrode microstructure is composed of inhomogeneity as well as anisotropy.

Porous electrodes are conventionally prepared in a top-down fashion which inherently discourages spatial control at smaller length scales, and results in microstructural stochasticity. The associated geometrical features span from the active interface to electrode lengths and define physicochemical complexations across these spatial scales. We find that the spatial arrangements of active material particles and carbon binder domains jointly define multiscale stochastic features for the porous electrode. Since the secondary phase assembles at the surface of active particles, its local content scales positively with active particle clustering, consequently constricting the pore network (such locations exhibit high electrolyte transport resistance). On the other hand, the lower secondary phase makes for an inferior percolation network, giving rise to spots with lower electronic conductivity. Effective reaction area diminishes with both dispersion as well as clustering of active particles and exacerbates the resistance to reaction kinetics. During intercalation, lithiation fronts preferentially propagate to locations with smaller resistances, and gradually the locations with higher resistances become accessible. The present investigation reveals that the electrochemical response of porous electrodes is quite different than the conventional interpretation based on electrode-averaged descriptors. It is imperative to recognize the stochastic nature of the porous electrodes to understand the localized limitations and electrochemical instabilities.

4.6 Representative Volume Element (RVE) Identification

RVE is the central concept in porous media approximation[9]. It is the required volume of the porous structure to treat it as an effective medium. Essentially this volume is large enough to contain statistically significant geometrical pore-scale features such that only their group behavior is observed at larger length scales. If appropriate RVE is not employed for effective property calculations (details outlined earlier[174]), estimated values are inaccurate. Since each of the properties (area, tortuosity, and conductivity) represent different pore-scale physics, their corresponding RVE sizes are expected to be different. Appropriate length scale for the interfacial area is CBD phase features, while length scale for pore phase transport is pore dimension (here of

the order of active material particle size). Thus, one expects a larger RVE for tortuosity predictions. This fact is apparent from Figure 64(a) and (b) where tortuosity saturates for higher voxel counts, while the active area is weakly changing for five different volume sizes considered as it already has sufficient volume. The mild variation in the active area (Figure 64(a)) and conductivity (Figure 64(c)) stems from stochasticity at length scales larger than RVE size[72, 304].

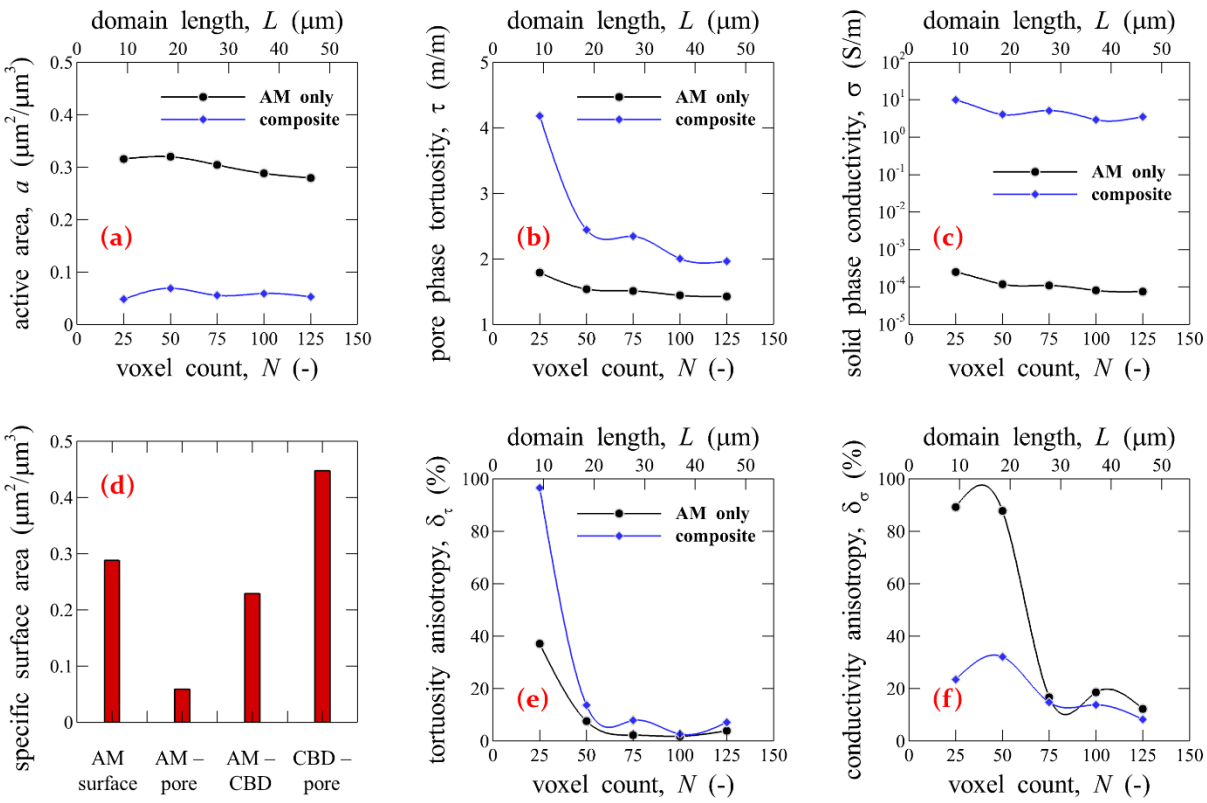

Figure 64. An appropriate RVE size leads to converged microstructural properties like (a) active area (b) pore phase tortuosity and (c) solid phase conductivity as well as bounded anisotropy in directional properties such as (e) tortuosity and (f) conductivity. For comparison, data from both AM structures as well as composite electrode microstructures are presented. As CBD has a length scale smaller than AM particles, an RVE size suitable for AM is appropriate for the composite electrode as a rule of thumb. Given the presence of three distinct phases, a composite electrode has three different two-phase interfaces (equivalently specific surface area), whose converged values are presented in (d).

For porous structures made up of an isotropic distribution of geometrical features, ideally one expects isotropy in directional properties like tortuosity or conductivity. If the chosen volume is not large enough, *i.e.*, smaller than RVE size, one would observe stronger anisotropy. Figure 64(e)

and (f) present the anisotropy in tortuosity and conductivity calculations, respectively. For the present set of composite structures, anisotropy subdues for 100 or larger voxel dimensions, and accordingly RVE size is fixed at 100 voxels (*i.e.*, 37 μm). One often confounding argument in the literature is that anisotropy should completely die out for the RVE size. This is somewhat misleading[9] as analysis of finite-sized volumes invariably has some anisotropy. One should rather look out for slowly varying (or stabilized) anisotropy to fix the RVE size. Comparison of Figure 64(b) and (e) (or equivalently (c) and (f)) reveals that anisotropy fluctuations are stabilized along with property values themselves when the RVE size is reached.

In the present discussion, both composite structures, as well as the original active material backbone, are analyzed (Figure 64). It is apparent that similar RVE sizes are appropriate for each of these effective properties. This makes sense since the CBD has a length scale smaller than active particles, hence an RVE based on the active material skeleton is large enough to contain a statistically significant amount of CBD features. These representative results are for volumes extracted from 90 %wt. AM and 600 bar calendaring pressure electrode sample and CBD morphology $\omega = 0.50$ (similar trends are observed for the other structures discussed herein). For visual comparison, different interfacial area for the RVE sized composite structure are also shown in Figure 64.

4.7 Electrochemical Description accounting for Multi-length scale Stochasticity

The spatial stochasticity manifests in many different forms, leading to observations of inhomogeneity and anisotropy. The geometrical features associated with distinct length-scales influence the electrochemical evolution of a porous (intercalation) electrode. Specifically,

- Interface-scale stochasticity – affects intercalation behavior given active area variations
- Pore-scale stochasticity – distorts the pore network and results in increased pore phase transport resistance
- Electrode-scale stochasticity – results from active material particle clustering and associated gradients in structural compositions

The length scale for the first two (interface and pore-scale heterogeneity) are smaller than the RVE size and subsequently, the effective properties inherently account for these. On the other hand, the electrode scale heterogeneity takes place at a length scale larger than the RVE size. To account for

this, the effective property variations over the electrode volume are to be incorporated into the discussion. With this background, an appropriate set of governing equations are as follows:

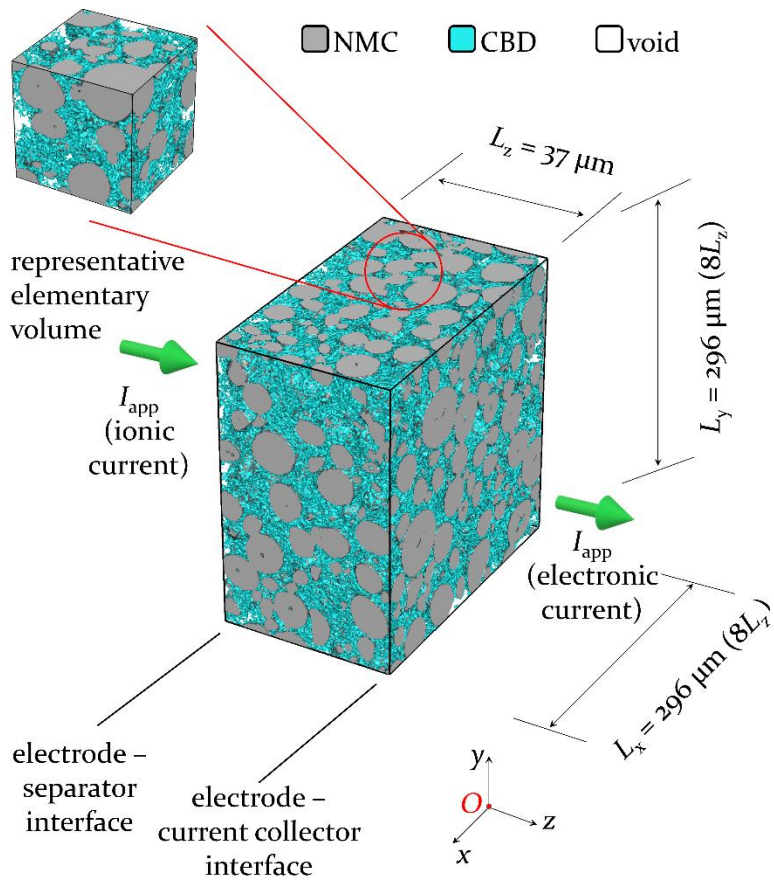

Figure 65. A schematic diagram illustrating the boundary conditions for the intercalation calculations.

<u>*Li intercalation in active material*</u>:

$$\frac{\partial C_s}{\partial t} = \frac{1}{r^2}\frac{\partial}{\partial r}\left(\mathcal{D}_s \frac{\partial C_s}{\partial r}\right) \tag{141}$$

<u>*Li^+ transport in electrolyte phase*</u>:

$$\varepsilon \frac{\partial C_e}{\partial t} = \frac{\partial}{\partial x}\left(\mathcal{D}_e \frac{\varepsilon}{\tau_x}\frac{\partial C_e}{\partial x}\right) + \frac{\partial}{\partial y}\left(\mathcal{D}_e \frac{\varepsilon}{\tau_y}\frac{\partial C_e}{\partial y}\right) + \frac{\partial}{\partial z}\left(\mathcal{D}_e \frac{\varepsilon}{\tau_z}\frac{\partial C_e}{\partial z}\right) + \left(\frac{1-t_+}{F}\right) j \tag{142}$$

<u>*Conservation of electronic charge*</u>:

$$\frac{\partial}{\partial x}\left(\sigma_x \frac{\partial \phi_s}{\partial x}\right) + \frac{\partial}{\partial y}\left(\sigma_y \frac{\partial \phi_s}{\partial y}\right) + \frac{\partial}{\partial z}\left(\sigma_z \frac{\partial \phi_s}{\partial z}\right) = j \tag{143}$$

<u>*Conservation of ionic charge*</u>:

$$\frac{\partial}{\partial x}\left(\kappa\frac{\varepsilon}{\tau_x}\frac{\partial\phi_e}{\partial x}\right)+\frac{\partial}{\partial y}\left(\kappa\frac{\varepsilon}{\tau_y}\frac{\partial\phi_e}{\partial y}\right)+\frac{\partial}{\partial z}\left(\kappa\frac{\varepsilon}{\tau_z}\frac{\partial\phi_e}{\partial z}\right)$$
$$+\frac{\partial}{\partial x}\left(\kappa_{\mathcal{D}}\frac{\varepsilon}{\tau_x}\frac{\partial\ln C_e}{\partial x}\right)+\frac{\partial}{\partial y}\left(\kappa_{\mathcal{D}}\frac{\varepsilon}{\tau_y}\frac{\partial\ln C_e}{\partial y}\right)+\frac{\partial}{\partial z}\left(\kappa_{\mathcal{D}}\frac{\varepsilon}{\tau_z}\frac{\partial\ln C_e}{\partial z}\right)+j=0 \tag{144}$$

<u>*Volumetric reaction current*</u>:

$$j=ak\sqrt{C_sC_e\left(C_s^{max}-C_s\right)}\left\{e^{\frac{F}{2RT}\left(\phi_s-\phi_e-U_s(C_s)\right)}-e^{-\frac{F}{2RT}\left(\phi_s-\phi_e-U_s(C_s)\right)}\right\} \tag{145}$$

<u>*Current flux at particle surface*</u>:

$$i={}^{j}\!/_{a_0} \tag{146}$$

Table 6. Set of boundary conditions employed for investigating microstructural effects on electrochemical behavior.

Physical Variable (Equation)	***particle center (r = 0)***	***particle surface (r = R)***	
C_s (141)	$\left.\frac{\partial C_s}{\partial r}\right\|_{r=0}=0$	$-\mathcal{D}_s\left.\frac{\partial C_s}{\partial r}\right\|_{r=R}={}^{i}\!/_{F}$	
	electrode – separator interface ($z = 0$)	electrode – current collector interface ($z = L_z$)	lateral faces ($x = 0$, $x = L_x$, $y = 0$, $y = L_y$)
C_e (142)	$-\mathcal{D}_e\frac{\varepsilon}{\tau_z}\frac{\partial C_e}{\partial z}=\left(\frac{1-t_+}{F}\right)\frac{I_{app}}{A_{cs}}$	$\frac{\partial C_e}{\partial z}=0$	$\frac{\partial C_e}{\partial n}=0$ [a)]
ϕ_s (143)	$\frac{\partial\phi_s}{\partial z}=0$	$-\sigma_z\frac{\partial\phi_s}{\partial z}=\frac{I_{app}}{A_{cs}}$	$\frac{\partial\phi_s}{\partial n}=0$ [a)]
ϕ_e (144)	$\phi_e=0$	$\frac{\partial\phi_e}{\partial z}=0$	$\frac{\partial\phi_e}{\partial n}=0$

[a)] n is outward normal direction

Table 7. Analytical relations describing porosity and morphology variations for effective properties.

Microstructural property	***Functional relation***
Active area, a	$a=\left(a_0+a_1\varepsilon+a_2\varepsilon^2\right)e^{\left(p_0+p_1\sqrt{\omega}+p_2\omega\right)}$
Pore phase tortuosity, τ	$\tau=\left(\tau_0+\tau_1\omega+\tau_2\omega^2\right)\varepsilon^{\left(q_0+q_1\omega+q_2\omega^2\right)}$
Effective electronic conductivity, σ	$\sigma=\left(\sigma_0+\sigma_1\omega+\sigma_2\omega^2\right)\varepsilon^{\left(r_0+r_1\omega+r_2\omega^2\right)}$

Associated boundary conditions are summarized in Figure 65 and Table 6. The finite volume based in-house solver is developed to solve these equations (choice of numerical parameters such as grid spacing has been carefully evaluated *via* appropriate independence tests). The electrode scale governing equations (Equation (142) to (144)) involve directional dependence of long-range interactions. At each (x, y, z) location Li interaction is evaluated (Equation (141)). Note that each of the microstructural features varies with spatial coordinates, *i.e.*, $a = a(x, y, z)$, $\tau_y = \tau_y(x, y, z)$, and so on. When volumetric reaction source term, j, is translated to the particle surface, i, one needs to be cautious in order to ensure flux conservation. The redistribution the flux over the entire particle surface takes care of this physics[25, 174].

Table 8. A summary of microstructural stochasticity present in the electrode microstructure.

Microstructural property	***(volume) Averaged***	***Maximum***	***Minimum***	***Units***
Active material	46.04	63.63	35.37	% vol.
CBD phase	13.41	18.60	10.39	% vol.
Porosity	40.55	54.24	17.77	% vol.
Active area	0.0421	0.0622	0.0047	$\mu m^2/\mu m^3$
Pore phase tortuosity	2.23	7.66	1.60	m/m
Solid phase conductivity	5.98	26.25	0.26	S/m

4.8 Statistical Learning based Abstraction of Inhomogeneity in Pore Networks

Transport effectiveness of porous electrodes is characterized by tortuosity. Despite its usefulness, it is one of the most debated concepts given the absence of a unique relation defining tortuosity for all structures. The conventional approach (electrode-specific correlations based on direct numerical simulations) falls short of abstracting essential pore network variations without leading to exhaustive computations. Here an alternate formalism is presented that first quantifies the pore networks in terms of pore size distribution and connectivity. Subsequently, statistical procedures are employed to extract meaningful geometrical features. Since the proposed approach seeks a relationship among pore network attributes and tortuosity, it proffers a self-consistent route to describe spatial inhomogeneity as well as anisotropy of pore networks.

Electrochemical devices facilitate interconversion of chemical and electrical energy. Such a transformation represents electrochemical reactions[22, 305], which by their very nature occur at the electrode-electrolyte interface (often referred to as the active surface). To ensure thorough contact between the electrode and the electrolyte phases, the electrodes are made porous. These porous electrodes function as electrochemical reactors. The porous nature of the electrodes not only affects the reaction kinetics (by providing more area for reactions) but also impedes the ionic transport to reaction sites. An accurate geometrical description of these porous electrodes is essential to interpreting microstructure-assisted modulation of various physicochemical interactions taking place at the pore-scale. However, the multiscale nature of the porous electrodes makes the detailed description of an involved construct. It is found that the physicochemical fields (*e.g.*, temperature, concentration) are fairly homogeneous at smaller length-scales. This allows one to define a representative volume element (RVE) that contains enough porous medium to abstract microstructural transport resistance, while fields vary at larger lengths. Such a scale separation approach is more commonly known as the porous media theory or the effective medium approximation[9, 306-308].

For battery electrodes, species transport in pore networks is dominated by diffusion and migration modes. Tortuosity and porosity are the relevant effective properties (at the RVE scale) that delineate geometrical effects of the electrode microstructure[1, 264, 309, 310]. Figure 46(a) illustrates a characteristic Li-ion battery electrode structure as visualized in X-ray tomography[80]. Corresponding RVE is also highlighted for a comparison of length scales. The conventional approach is to correlate tortuosity to bulk descriptors (*e.g.*, porosity[61, 64, 272, 311] and in general to phase fractions[174, 175, 273, 312] when more than two phases are present in a microstructure). Such correlations are developed based on direct numerical simulation (DNS) of a large number of microstructural realizations – typically of the order of 100 structures [174, 175, 312], thus being computationally intensive.

A pore network is characterized by pore shapes, size distribution, and interconnectivity. The aforementioned approach of identifying tortuosity as a function of porosity (or multiple phase fractions) does not account for size distribution or interconnectivity. As a result, it is difficult to recognize anisotropy in the microstructure. For example, Figure 46(b) shows tortuosity variation with local porosity (*i.e.*, for multiple RVEs) for the electrode sample of Figure 46(a). There is a considerable anisotropy in the pore network. Moreover, there are multiple RVEs with similar

porosities, but appreciably different tortuosity trends. Such features point to inadequacies of the conventional approach of tortuosity correlations.

Here we propose an alternate approach to abstract tortuous pore networks. Essential geometrical features of the pore network are first identified using two-point correlation functions[313-317]. Subsequently, these extracted features are associated to explicitly computed tortuosity values to build a formal relationship. As the pore network is described in terms of geometrically meaningful features, tortuosity function is identified with a minimal number of DNS calculations (at least an order of magnitude smaller number of RVEs).

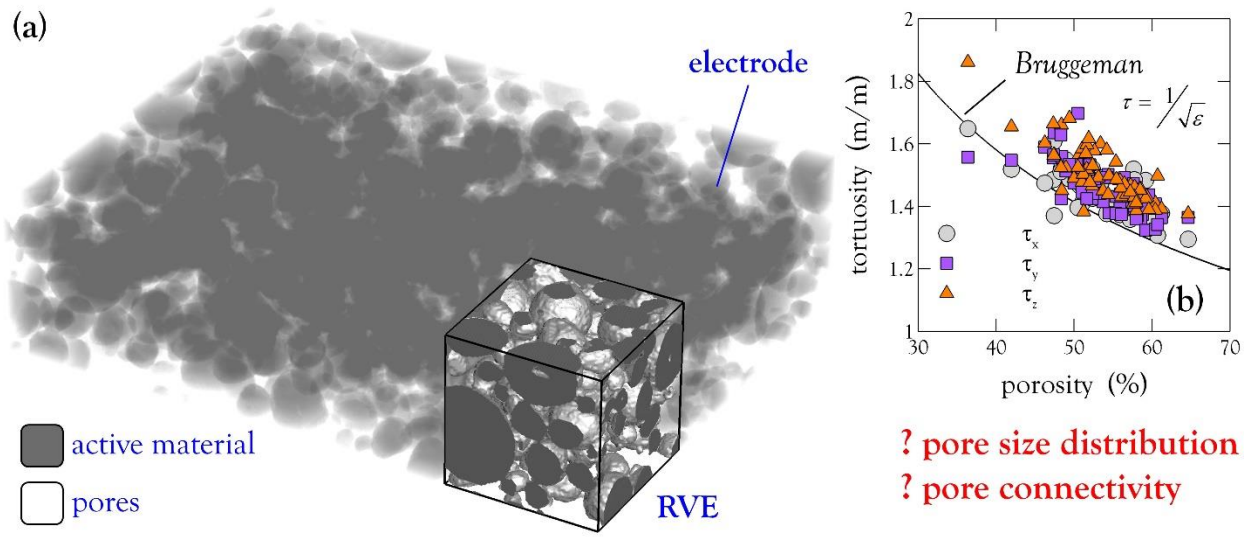

Figure 66. (a) Tomographic reconstruction of a Lithium-ion battery electrode. Active particles are visually identified. An RVE contains enough particulate matter to allow a porous medium approximation and is much smaller than the electrode dimensions. (b) Tortuosity and porosity variation over a large electrode sample. Electrode tomogram is obtained from an open source data archive[80].

4.9 Quantitative Description of Pore Network

Pore network is formed in electrodes during the electrode preparation stage[83]. The pore shapes largely depend on the morphology of the solid phase[64, 175, 273]. However, within the same electrode, pore size distribution and connectivity differ based on aggregation of the solid phase and other processing factors[91, 296]. The size distribution refers to both the range of pore dimensions as well as their spatial arrangement (statistically speaking this amounts to a histogram in four dimensions: size – r and three coordinates – x, y, z). The connectivity represents directional information

assigning relative positions to connected pores. The simplest descriptor that accounts for both the distribution and connectivity of pores is a two-point correlation function, $\psi_{\vec{r}}^{h,g}$ (Eq. (147)). It builds upon local phase information, as encoded by the one-point correlation function, $\phi\left(\vec{x}\,|\,h\right)$ (Eq. (148)).

$$\psi_{\vec{r}}^{h,g} = \frac{1}{\mathrm{vol}\left(\Omega\right)} \int_{\Omega} \phi\left(\vec{x}\,|\,h\right) \phi\left(\vec{x}+\vec{r}\,|\,g\right)\, \mathrm{d}\vec{x} \tag{147}$$

$$\phi\left(\vec{x}\,|\,h\right) = \begin{cases} 1 & \text{if } \vec{x} \in \text{phase } h \\ 0 & \text{otherwise} \end{cases} \tag{148}$$

Commonly three-dimensional electrode microstructures are investigated using x-rays or electron beams to provide sufficient submicron resolution as well as phase contrast[89, 159, 318]. After segmentation, such a dataset contains phase information over voxels (small 3D volumes). This can be easily converted to the one-point correlation function, $\phi\left(\vec{x}\,|\,h\right)$. The two-point correlation function[316, 317] as defined in Eq. (147) refers to the probability of finding two locations (*i.e.*, voxels) with phases 'h' and 'g' separated by a vector $\vec{r}$. Hence the function $\psi_{\vec{r}}^{\text{pore,pore}}$ is the quantitative representation of the pore network in a given RVE volume Ω. The function $\psi_{\vec{r}}^{\text{pore,pore}}$ is a scalar function (between 0 and 1) implicitly containing directional information in the form of vector $\vec{r}$. Figure 67(a) shows an RVE from the same electrode as Figure 46(a). If the RVE contains $N_x \times N_y \times N_z$ voxels, corresponding two-point correlation function (Figure 67(b)) has $N_x \times N_y \times N_z$ directions, including the null vector. (Definition presented in Eq. (147) is quite cumbersome for large structures; alternatively, Fast Fourier Transform is used to reduce the computations[316]).

The function $\psi_{\vec{r}}^{\text{pore,pore}}$ simplifies to porosity when $\vec{r} = \vec{0}$, gradually decreases as the separation vector increases (Figure 67(b)). For larger distances, the perturbations in the correlation function become comparable to the mean trends. The two-point correlation function is analogous to the radial distribution function often used in statistical mechanics[319-321]. However, unlike the radial distribution function which describes the structure of matter in terms of separation between two points, the two-point correction function also provides the directional information. The radial distribution function for the pore network is shown in Figure 67(c) for a comparison. The mathematical relation between the two can be described as:

$$\theta_{r=|\vec{r}|}^{\text{pore,pore}} = \text{average}\left(\psi_{\vec{r}}^{\text{pore,pore}}\right) \tag{149}$$

where the average is taken over all the data points for the same separation, r. To demonstrate the perturbations at larger separation vectors, averaging is not carried out in Figure 67(c).

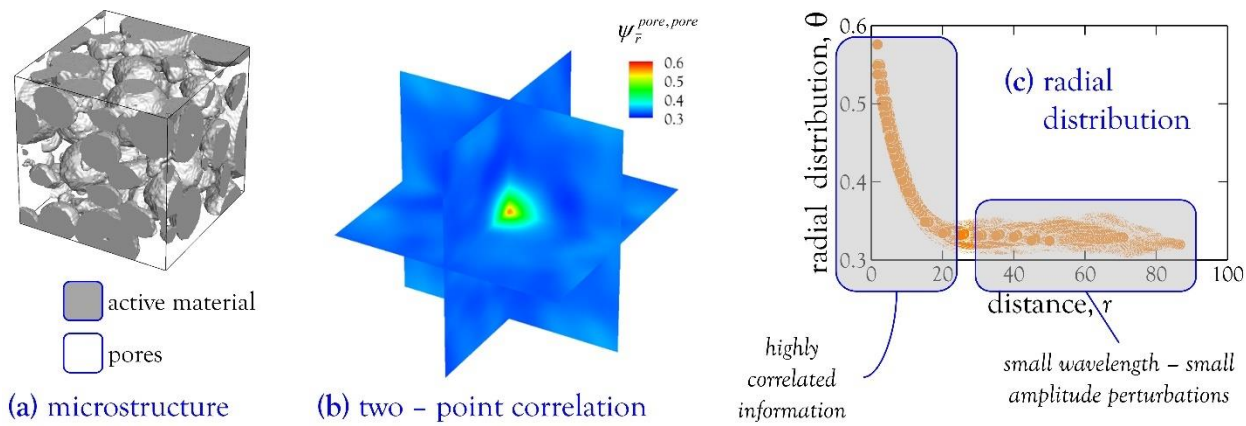

Figure 67. Different forms of microstructural representations: (a) visual reconstruction and quantitative description of pore networks in terms of (b) two-point correlation and (c) radial distribution functions. Distance is in terms of voxel units.

4.10 Extracting Network Features

The function $\psi_{\vec{r}}^{\text{pore,pore}}$ converts the microstructural information into quantitative details of the pore network, without reducing the degrees of freedom $\left(N_x \times N_y \times N_z\right)$. Figure 67(b) and (c) describe the general distribution of information in directional and adirectional fashions, respectively. Most of the information is retained at shorter separations and appears to be highly correlated. In other words, the dimension of the two-point correlation function can be substantially reduced. The function $\psi_{\vec{r}}^{\text{pore,pore}}$ can be alternatively written as:

$$\psi_{\vec{r}}^{\text{pore,pore}} = a_0 + a_1\vec{r}_1 + a_2\vec{r}_2 + \cdots = a_0 + \sum_{i=1}^{N-1} a_i\vec{r}_i \tag{150}$$

where the vectors only identify the direction associated with each of the coefficients. The coefficients a_i's, form entries in the 3D matrix as discussed earlier. Note that a_0 is porosity of the RVE being studied. Each of the higher order coefficients describes the degree of information along the respective separation vector, $\vec{r}$, thus concurrently providing both quantitative (a_i's) as well as qualitative ($\vec{r}_i$'s) information about the pore network.

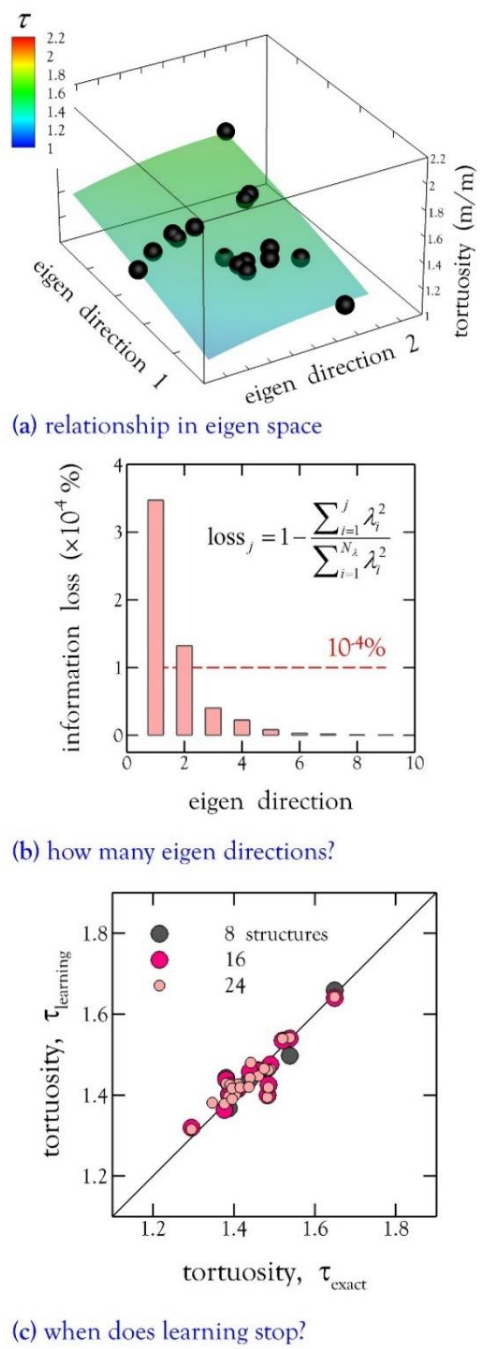

Figure 68. Identifying the tortuosity function. (a) Function surface in the eigen space, (b) eigen directions and (c) structures required to accurately define the relationship.

If M sufficiently different RVEs (of the same electrode) are studied, one can decompose the pore network data $\psi_{\vec{r}}^{\text{pore,pore}}|_1, \psi_{\vec{r}}^{\text{pore,pore}}|_2, \cdots, \psi_{\vec{r}}^{\text{pore,pore}}|_M$ into electrode specific and RVE specific information:

<u>*Electrode specific features*</u>:

$$\bar{\psi}_{\vec{r}}^{\text{pore,pore}} = \bar{a}_0 + \sum_{i=1}^{N-1} \bar{a}_i \vec{r}_i \tag{151}$$

<u>*RVE specific features*</u>:

$$\delta\psi_{\vec{r}}^{pore,pore}\,|_i = \psi_{\vec{r}}^{\text{pore,pore}}\,|_i - \bar{\psi}_{\vec{r}}^{\text{pore,pore}} \tag{152}$$

The electrode specific features contain the attributes of the pore shapes and general connectivity pattern, while the RVE specific features account for variations across different RVEs of the same electrode. The RVE specific information, $\delta\psi_{\vec{r}}^{pore,pore}\,|_i$, can be concisely presented in terms of a few independent directions (eigen directions) given the strong correlation among information associated with multiple separation vectors, $\vec{r}$. Mathematically, this is equivalent to an eigen decomposition:

$$\delta\psi_{\vec{r}}^{\text{pore,pore}}\,|_i = \delta a_0 + \sum_{i=1}^{N-1} \delta a_i \vec{r}_i \approx \sum_{j=1}^{N_\lambda} b_j \hat{e}_j \tag{153}$$

with $\hat{e}_j$ as the eigen directions and b_j as corresponding projections. This is also known as Singular Value Decomposition (SVD) or Principle Component Analysis (PCA). The eigen directions (*i.e.*, principal component) with larger eigen values (magnitude) contain more important information. Relevant eigen directions are identified using an information loss function (on a set ordered in terms of decreasing eigen values):

$$\text{loss}_j = 1 - \frac{\sum_{i=1}^{j} \lambda_i^2}{\sum_{i=1}^{N_\lambda} \lambda_i^2} \tag{154}$$

The function loss$_j$ refers to the amount of information lost when eigen directions beyond '*j*' are discarded. Moreover, the number of structures, *M*, used to dissect the pore network information, $\psi_{\vec{r}}^{\text{pore,pore}}$, into electrode and RVE specific features is not known beforehand. Incrementally more structures are selected to learn the network features and predict tortuosities (for these structures exact tortuosity values are obtained through DNS). Figure 68(c) graphically presents the search for the number of structures used to extricate electrode specific information (Eq. (151)) and eigen directions. As initial structures are increased from 8 to 16, more variation is captured, however, beyond that, the improvement is only marginal. The appropriate number of eigen directions are justified in Figure 68(b) where the first two eigen values account for most of the data spread (minimal loss: $<10^{-4}$%). Figure 68(a) shows the functional relationship (surface) obtained through

correlating pore network features (distilled to a few eigen directions) against DNS predictions for *x*-direction tortuosity. Data points refer to corresponding DNS values.

4.11 Tortuosity Predictions

Once the formal relationship between the network features and tortuosities is available (Figure 68(a)), for any new RVE from a similar set, tortuosities are predicted as per the following steps:

1. Compute the two-point correlation function, $\psi_{\vec{r}}^{\text{pore,pore}}$;
2. Obtain RVE specific information (Eq. (152));
3. Project $\delta\psi_{\vec{r}}^{\text{pore,pore}}$ on eigen directions;
4. Estimate tortuosity *via* relationship Figure 68.

Figure 69(a) compares such predictions (τ_{learning}) against explicit (τ_{eaxct}) calculations for the *x*-direction tortuosities. The predictive accuracy is quantified using the following descriptor:

$$\epsilon = \sqrt{\frac{1}{N}\sum_{i=1}^{N}\left(\tau_{\text{learning}_i} - \tau_{\text{exact}_i}\right)^2} \tag{155}$$

The functional relationship (Figure 68(a)) is developed using 16 RVEs, while Figure 69(a) presents predictions for 64 non-identical RVEs. The obtained predictive accuracy is 2.0995×10^{-3} (Table 9), which amounts to less than 0.1% error (for the current discussion, tortuosity values range between 1 and 2). All the data is close to the 45° line, *i.e.*, general nature is consistently identified.

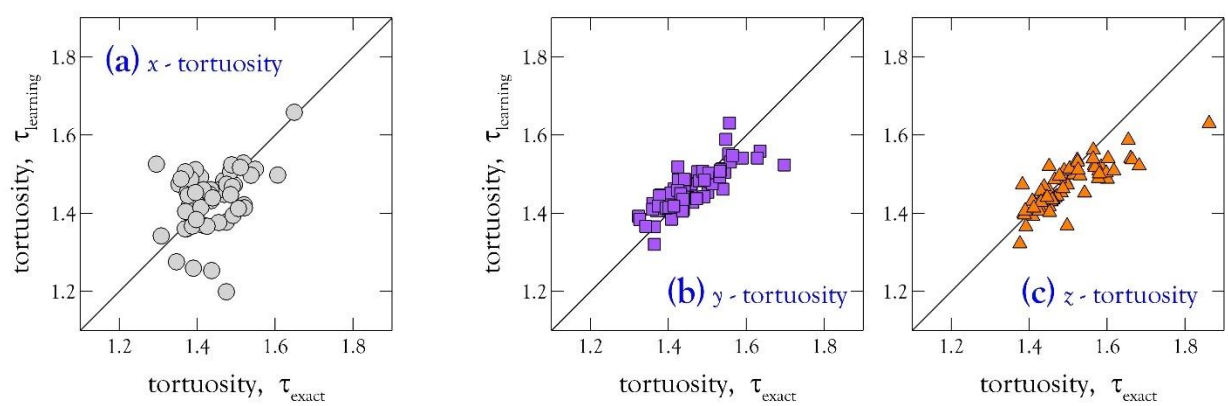

Figure 69. Tortuosity predictions are comparable to exact estimates (a) along the direction used for training as well as (b), (c) other directions, thus implicitly accounting for the anisotropy of the pore network.

The predictions are positively correlated to the exact values. On such a plot, an outlier point would exhibit a negative correlation (small τ_{learning} for a high τ_{eaxct}, or vice versa).

Calculation of the two-point correlation function does not involve any directional bias. It provides an unbiased description of the directional information of the pore network. During the training stage, pore network features are correlated to *x*-directional tortuosities. Hence, the tortuosity in other directions could, in principle, be predicted if directions are appropriately interchanged (without having to recompute the two-point correlation function):

$$y \qquad \vec{r} = (y, z, x) \tag{156}$$

$$z \qquad \vec{r} = (z, x, y) \tag{157}$$

Table 9. The accuracy of tortuosity predictions.

Direction	***Accuracy,*** ϵ
x	2.0995×10^{-3}
y	5.1569×10^{-4}
z	2.3416×10^{-4}

Figure 69(b) and (c) proffer corresponding comparisons. These predictions exhibit the desired positive correlation with the exact values as well as a similar level of accuracy as before (<0.1% error).

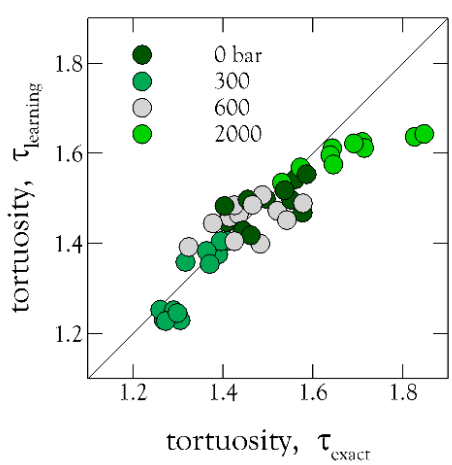

Figure 70. Identifying pore network changes with compression (*i.e.*, calendaring pressure).

In the present approach, the pore network is defined in terms of geometrical features, rather than just the porosity (conventional practice), and for predictions in different coordinate directions, appropriate connectivity information is picked along the respective direction.

Porous electrodes are often compressed to increase their energy density[42, 172]. The solid phase is often brittle and is likely to fracture. However, it can be argued intuitively that before the stresses are too high (initiation of particle fracture), the particles are more likely to rearrange. Such a particle relocation should not change the nature of the pore network and only alter the size distribution and connectivity. The tortuosity description developed here is based on an electrode calendared to a 600 bar pressure. Other electrode tomograms (from the same repository[80]) with different calendaring conditions are analyzed at identical electrode compositions.

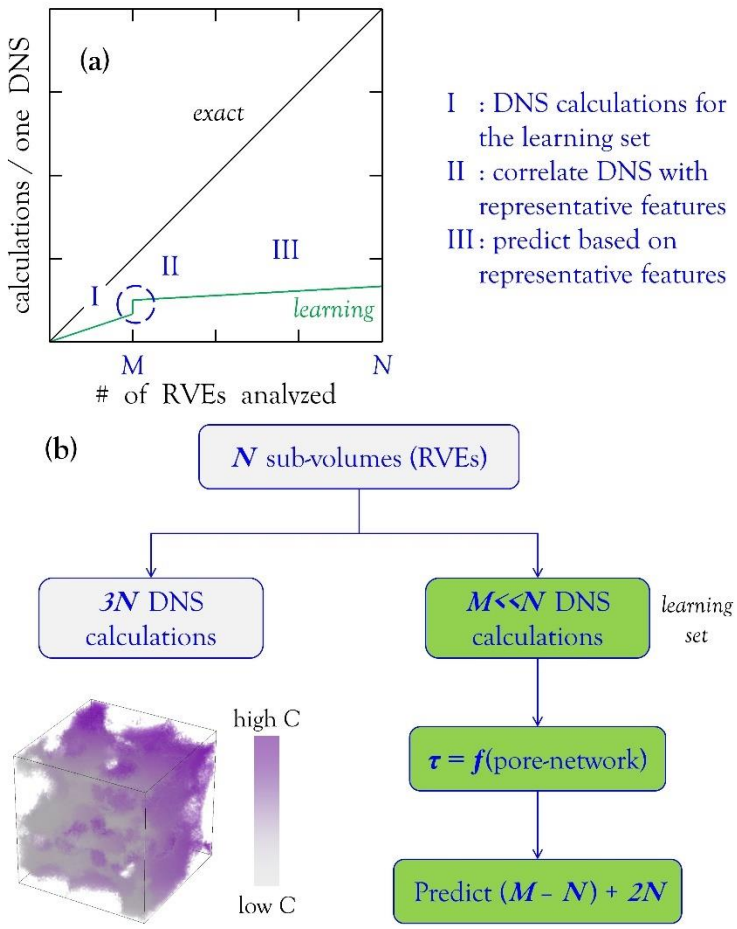

Figure 71. Comparing conventional and proposed approach to tortuosity estimation in terms of (a) computational cost and (b) workflow.

Figure 70 reveals that the same functional relation (Figure 68(a)) consistently predicts trends at lower pressures, while at a higher pressure of 2000 bar, the predictions monotonically diverge. Such a trend proves the hypothesized regimes for microstructural changes upon calendaring:

1. For lower calendaring pressures, electrode compaction is due to particle relocation (no qualitative change in the pore network).
2. Above a threshold calendaring pressure, particle fracturing takes place which considerably alters the pore shapes and in turn pore network undergoes qualitative changes.

Accurate characterization of tortuous pore networks is essential to understanding the limits of high energy and high power electrodes. The conventional approach to pore network characterization carries out diffusion calculations (DNS) over a representative sub-volume (Figure 71). Such an approach becomes cumbersome when the appreciable microstructural variation is present and demands explicit calculations for each possible sub-volume.

Here an alternate approach is proposed to identify the pore network attributes and correlate them with tortuosity. The pore network features are extracted in terms of two-point correlation function which requires much fewer calculations as compared to solving partial differential equations at the pore-scale. In addition to computational efficiency (Figure 71(a)), the direct correlation among the network attributes and tortuosity implicitly account for directionality (*i.e.*, anisotropy). Such an approach also has investigative merit to help discern qualitative differences among pore networks.

The present concept differs from '*machine learning*' applications[322-324] where learning is based on a large dataset. Here physics-based reasoning is used to extract meaningful geometrical characteristics of the pore network and subsequently learn their relation to tortuosity, based on a smaller raw data. Given this underlying difference, we refer to the present formalism as '*statistical learning*'.

5. CONVERSION ELECTRODE: LITHIUM-OXYGEN

Relevant Publications and/or Working Papers:

1. A. Mistry *et al.* (2019) *Non-equilibrium Thermodynamics in Electrochemical Complexations in Li-oxygen Porous Electrodes* Journal of Materials Chemistry A (accepted)

The lithium-oxygen conversion chemistry relies on solid – electrolyte interface centered energy storage, rather than bulk considerations in intercalation chemistry. The electrochemical complexations in porous air electrodes are, however, a manifestation of coupled interface-transport-kinetic interactions. The non-equilibrium thermodynamics behind such multi-modal coupling, hitherto unappreciated, forms the central argument of this work. We comprehensively demonstrate the role of reciprocity between electrode architecture and off-equilibrium interactions in Li-O_2 electrochemistry based energy storage.

5.1 Background

Among futuristic battery chemistries, only Lithium-oxygen promises energy densities comparable to the gasoline engine[325-328], partly since one of the reactants, *i.e.*, oxygen, is not stored in the cell and continuously *inhaled* from the atmosphere. Moreover, in contrast to the conventional Li-ion system, it is devoid of sluggish intercalation[29, 174, 329] reaction that limits the rate capability, and higher voltages that destabilize the electrolyte[14]. Despite the superficial elegance, experimental performance is found to be quite inferior as compared to the thermodynamic limit (Table 12), even when operated at very low rates[330-332]. Theoretically, the discharge should continue till all the pores are filled with the discharge product – lithium peroxide, Li_2O_2. However, the insulating nature[333-335] of Li_2O_2 prohibits a sustained discharge once its deposition reaches the critical tunneling length for charge carriers. To circumvent the short-range limitation, most of the scientific investigations have focused on solvent modifications to promote solution-phase reactions[336-342] or tuning interfacial properties[343-345]. These kinetically-limited studies[346-354] fall short of outlining the coupled non-equilibrium interactions resulting due to the porous nature of battery electrodes and associated multimodal transport effects. Given the lack of understanding of porous electrode response in such an evolving system, performance comparisons are often ambiguously reported and the potential for electrode microstructural engineering remains unrecognized.

5.2 Electrochemical Response of a Porous Li-oxygen Electrode

The formation of Li_2O_2 is effectively an electrodeposition reaction with the driving force being the difference in (electro)chemical potentials (Eq. (158)):

$$\Delta\mu = \frac{1}{2}\mu_{Li_2O_{2(s)}} - \left(\mu_{Li^+} + \frac{1}{2}\mu_{O_{2(l)}} + \mu_{e^-}\right) \tag{158}$$

However, unlike more commonly known metallic electrodeposition[278, 355-358], the newly formed solid phase is insulating in nature. Consequently, the surface activities for solid and solution phase species vary in time (refer to Reaction Kinetics with an Insulating Insoluble Reactant). The particular morphology of the precipitate phase is an outcome of competing kinetic events, *e.g.*, surface diffusion, at the interface scale (~1-10 nm) and also accounts for surface energies of various interacting phases. In a coarse-grained sense (~50-100 nm), such morphological differences manifest in between a 2D – planar electrodeposition and a fractal-like 3D interface growth[174, 312]. At the pore-scale (~1-10 μm), this relates to critical precipitation that marks the complete coverage of the electrode-electrolyte interface (Figure 72(a)-(b)). Thus, the interface-scale morphology can be inferred based on the critical precipitation that leads to a kinetic shutdown. Here the critical precipitation is estimated from capacity (experimental) and surface coverage based on carbon – electrolyte area evolution as abstracted from pore-scale calculations on representative porous structures (Abstracting Porous Electrode Evolution upon Precipitation). For deposition occurring in the same pristine structure (here 80% pristine porosity), different critical precipitations directly correlate to a dimensionless characteristic, ω, referred hereafter as the deposition morphology. From surface coverage relation (Eq. (159)), it can be shown that the critical precipitation (when $a/a^0 \rightarrow 0$), $\varepsilon_p^* = 0.452\omega^{2.751}$ where various coefficients characterize the interface evolution (at the pore-scale). The deposition morphology, ω, fundamentally relates to the interfacial current, $I_d = j/a^0$ where j is local (volumetric) reaction current in A/m^3, and a^0 is the BET (Brunauer-Emmett-Teller) area of the pristine structure (Figure 72(c)).

$$\text{surface coverage, } a/a^0 = 1 - \left(\frac{\varepsilon_p}{0.452\omega^{2.751}}\right)^{1.1} \tag{159}$$

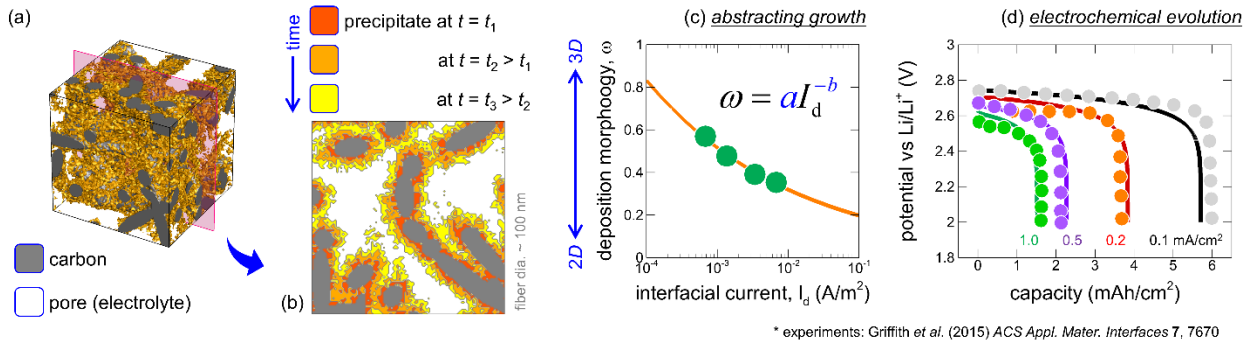

Figure 72. (a) Porous electrode evolution due to (b) precipitate growth. (c) Deposition morphology is directly related to interfacial current, with higher currents promoting more layered – 2D growth. (d) The electrochemical dynamics at low currents directly correlate to deposition morphology.

It is important to recognize the multiscale nature of the Li_2O_2 formation. At nanoscale lengths, discrete geometries (*e.g.*, toroid, disk, *etc.*) are visible, and equivalently the elemental reaction steps (*e.g.*, superoxide formation, disproportionation, *etc.*) have to be accounted for. On the other hand, at the pore-scale (or equivalently substrate, here fiber, dimensions), it is to be represented in terms of coarse-grained morphology, ω, resultant effective property variations and (locally uniform) interfacial current, I_d. Figure 72(c) summarizes the gradual transition in deposition morphology with the interfacial current. Such a derived behavior faithfully captures the nanoscale geometrical variations in the corresponding experiments[330] where the aspect ratio of Li_2O_2 particles monotonically show increasing particle specific surface area (*i.e.*, surface – to – volume per particle), thus describing a more 2D growth at higher currents.

The electrochemical description, accounting for the evolving nature of the porous electrode, accurately predicts the experimental trends (Figure 72(d)), thus confirming the veracity of the relevant physicochemical mechanisms at the electrode microstructural scale. The characterization of deposition morphology in terms of interfacial current carefully deconvolves the interfacial growth features from the other simultaneous chemical and physical evolutions, *i.e.*, the non-equilibrium interactions. The interfacial growth characteristic $\left(\omega = aI_d^{-b}\right)$ abstracts the dynamics at the substrate – electrolyte interface and is equally applicable to different electrode microstructural arrangements with same substrate and electrolyte combination (here carbon as substrate and 1M LiTFSI in DME electrolyte). Given the porous electrode structure, the

electrochemical complexations are an intricate convolution of material and microstructural effects. Keeping the same materials, the electrode-scale response can still be modulated through an appropriate selection of microstructural arrangement. The choice of physical attributes (pristine porosity, substrate geometry, *etc.*) and chemical composition (*e.g.*, salt and solvents in the electrolyte) represent two principal directions for affecting the electrode response. The description of physicochemical interactions presented here is extensible to other materials after carefully deconvolving the electrode response from controlled experiments. It should be noted that in the presence of a catalyst, the interfacial characteristics, namely both the growth morphology and kinetics, get affected.

The concentrated electrolyte provides a medium for oxygen transport during operation, the presence of which complicates the transport characteristic beyond the conventional Li-ion electrolyte (with only primary salt dissolved in a solvent). Essentially, the inter-species interactions of oxygen and ions necessitate a transport description based on Onsager-Stefan-Maxwell relations[22, 359-361]. Accounting for the limited solubility of oxygen in nonaqueous electrolytes (millimolar[345, 362]), it can be shown that the cation and oxygen fluxes are related to the salt and oxygen concentration gradients as (refer to Concentrated Solution Theory for a Liquid Electrolyte containing Dissolved Oxygen):

$$N_p = -\upsilon_p \mathcal{D}_{pp} \frac{\varepsilon}{\tau} \nabla c - \mathcal{D}_{po} \frac{\varepsilon}{\tau} \nabla c_o + \mathcal{I}_p \, I \big/ F z_p + \upsilon_p c u_s \tag{160}$$

$$N_o = -\mathcal{D}_{oo} \frac{\varepsilon}{\tau} \nabla c_o + c_o u_s \tag{161}$$

where u_s is the bulk electrolyte velocity (nearly absent for Li-oxygen electrodes). The oxygen diffusivity in the electrolyte, $\mathcal{D}_{oo}$, is smaller than its measurement[362] in the pure solvent, D_{so}, given the presence of additional species. Such hindrance is considerable since the typical salt is present in molar concentrations.

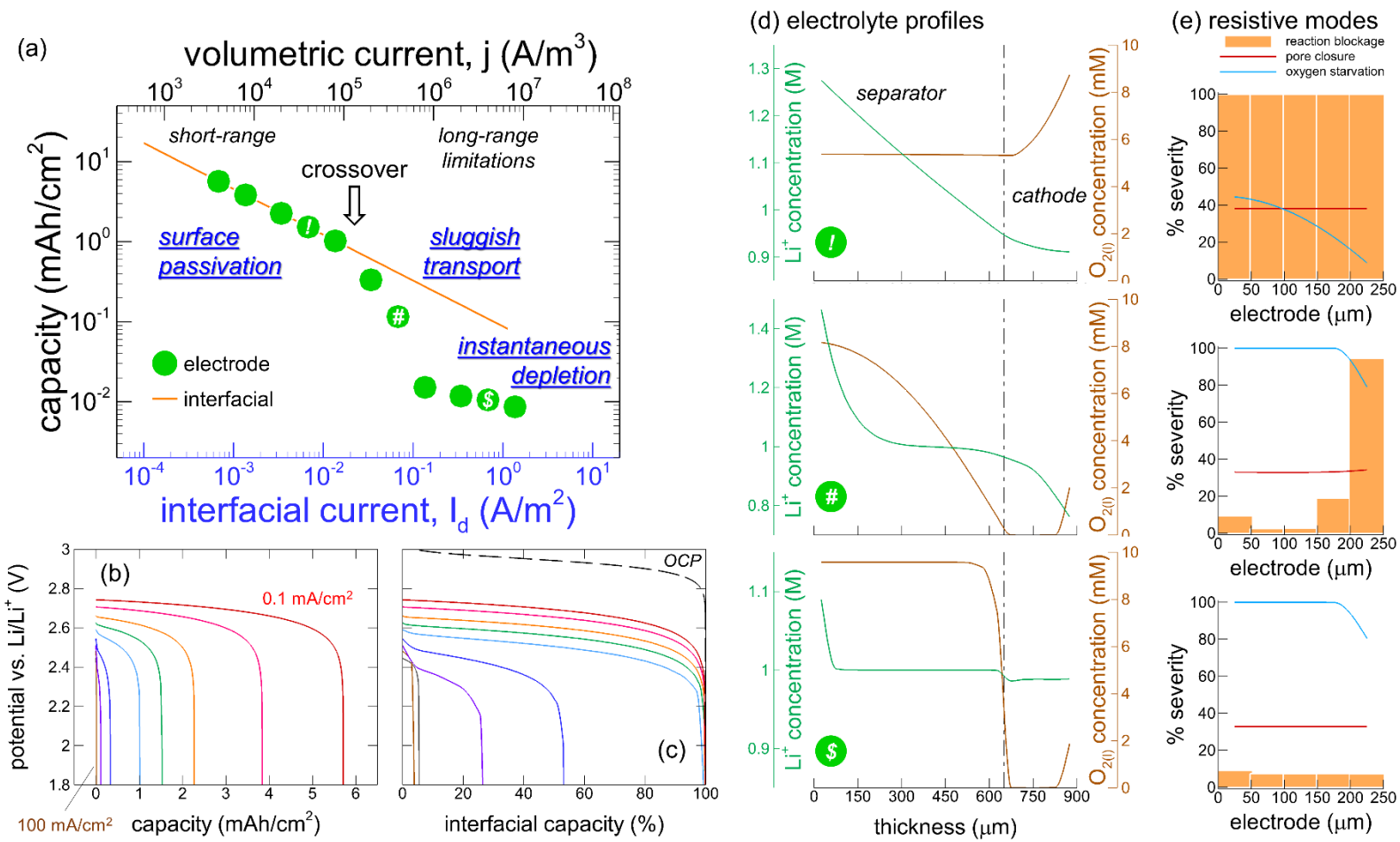

Figure 73. Electrochemical complexations result from coupled interactions among the interfacial dynamics, porous electrode evolution and electrolyte transport. (a) Regimes of porous electrode electrochemical response; corresponding potential evolutions represented in terms of (b) bulk and (c) interfacial capacities. (d) Evolution of electrolyte phase profiles and (e) different resistive modes for three representative operations. The vertical dashed line in (d) identifies the separator-electrode interface.

Furthermore, the oxygen enters the porous electrode through an electrolyte – air interface. The dissolution of oxygen from the air into the electrolyte is a finite rate process, and follows the kinetics:

$$-\mathcal{D}_{oo}\nabla c_o \cdot \hat{n} = k_{\text{dissolution}}\left(c_o - c_o^{\text{solubility}}\right) \tag{162}$$

The oxygen solubility relates to the atmospheric pressure and Henry's constant[179] as $c_o^{\text{solubility}} = k_H\, p_{\text{atm}}$. Typical solubility measurements (or calculations) report equilibrium oxygen concentration in the electrolyte solvent[362]. It has recently been reported that the oxygen solubility decreases with the salt concentration[363]. Reduced solubility shifts the onset of transport limitations to smaller currents. In light of limited solubility data, the present analysis uses its value for pure DME (9.57 mM)[345].

Figure 73 presents electrochemical regimes for the same 80% pristine porosity fibrous microstructure (Figure 72) over an extended range of operating currents. Figure 73(a) describes the capacity dependence on interfacial current. For comparison, the interfacial current based capacity (solid line) is sketched as well. At low currents, the electrode capacity matches quite closely with the maximum interfacial capacity, while at higher currents the electrode capacity is markedly different signifying presence of additional resistive modes (characterized by non-equilibrium complexations). To identify the origins of capacity discrepancy, the electrolyte profiles are sketched at the end of the operation for three representative currents in Figure 73(d). At high currents, Figure 73(d#,$), the oxygen concentrations in the electrode reach zero, while at a low current, Figure 73(d!), still appreciable amount of oxygen exists at the final stage. Also, note that it is easier for oxygen to diffuse from separator to electrode in comparison to its dissolution from ambient, thus comparatively smaller oxygen concentration gradients exist along the separator thickness in Figure 73(d!). There exist two distinct modes of oxygen starvation in Figure 73(d). At moderate currents, both the transport from separator and dissolution through ambient are sluggish enough to supply oxygen at smaller rates than its consumption in the peroxide formation. Concurrently, the Li^+ profile also exhibits a gradient going from anode to cathode (at the anode – separator interface, cation completely contributes to ionic current). Notice the inflection point (nearly zero slope) close to the separator – cathode interface in the cation concentration (Figure 73(d#), which indicates that the cross-diffusion, *i.e.*, $\mathcal{D}_{po}$ term, drives the cation flux locally. At very high currents, the electrode reactions are fast enough to locally deplete the dissolved oxygen,

before oxygen can travel to the reaction zone from either side (nearly uniform oxygen in the separator implies little oxygen infusion from the separator – cathode interface). The electrochemical resistance for such an evolving porous electrode is composed of (i) reaction blockage, *i.e.*, local reduction in carbon – electrolyte contact area, (ii) pore closure, *i.e.*, local precipitation erodes the electrolyte pore-network, and (iii) oxygen starvation, *i.e.*, locally oxygen concentration being smaller than the solubility. The severity of each of these resistive modes is assessed in terms of dimensionless descriptors, $N_r = 1 - (a/a^0)$, $N_p = 1 - (\varepsilon/\tau)$ and $N_o = 1 - (c_o/c_o^{solubility})$, respectively. Figure 73(e) sketches these components for the end of the operation for the three representative currents discussed in Figure 73(d). It is apparent that the reaction blockage is the leading order effect at low currents, while at higher currents oxygen starvation becomes dominant. Also notice that the reaction distribution becomes more nonuniform at higher currents, as revealed by the nonmonotonic reaction blockage. The pore closure is not dominant at present since the pristine porosity is high enough to cause minimal change in the pore network.

A unique characteristic of Li-oxygen system is that the electrochemical energy is stored at the substrate – electrolyte interface (unlike intercalation-based Li-ion where energy storage is in the bulk). Hence, it is more representative to describe the operational regimes in terms of interfacial capacity (defined by complete interface coverage with Li_2O_2), rather than the bulk capacity (relates to complete pore filling with Li_2O_2). As discussed in Reaction Kinetics with an Insulating Insoluble Reactant, the open circuit potential relates to the interfacial activities, $U = U^0 + RT\log\left(\theta_e^{3/2}/\theta_s^{1/2}\right)/F$, where θ_e and θ_s represent activities of the substrate – electrolyte and precipitate – electrolyte interfaces, respectively. At the onset of Li_2O_2 formation, $\theta_e \approx 1$ and $\theta_s \approx 0$, as Li_2O_2 forms, electrolyte activity decreases, and precipitate activity increases. Such a rescaling in terms of interfacial capacity (which is equivalent to θ_s during peroxide formation, and θ_e during dissolution), collapses the potential profiles in Figure 73(b) (based on bulk capacity) into two distinct regimes as shown in Figure 73(c). For operations limited by short-range effects, complete interfacial utilization is present with average voltages gradually decreasing at higher currents (*i.e.*, more 2D precipitates). On the other hand, the long-range effects lead to inferior interfacial utilization. The crossover point coincides with the one shown in Figure 73(a). Given the interfacial storage of energy, the thermodynamic limits have to be reevaluated in terms of interfacial capacities and clarifies the dilemma of the capacity mismatch for near equilibrium conditions.

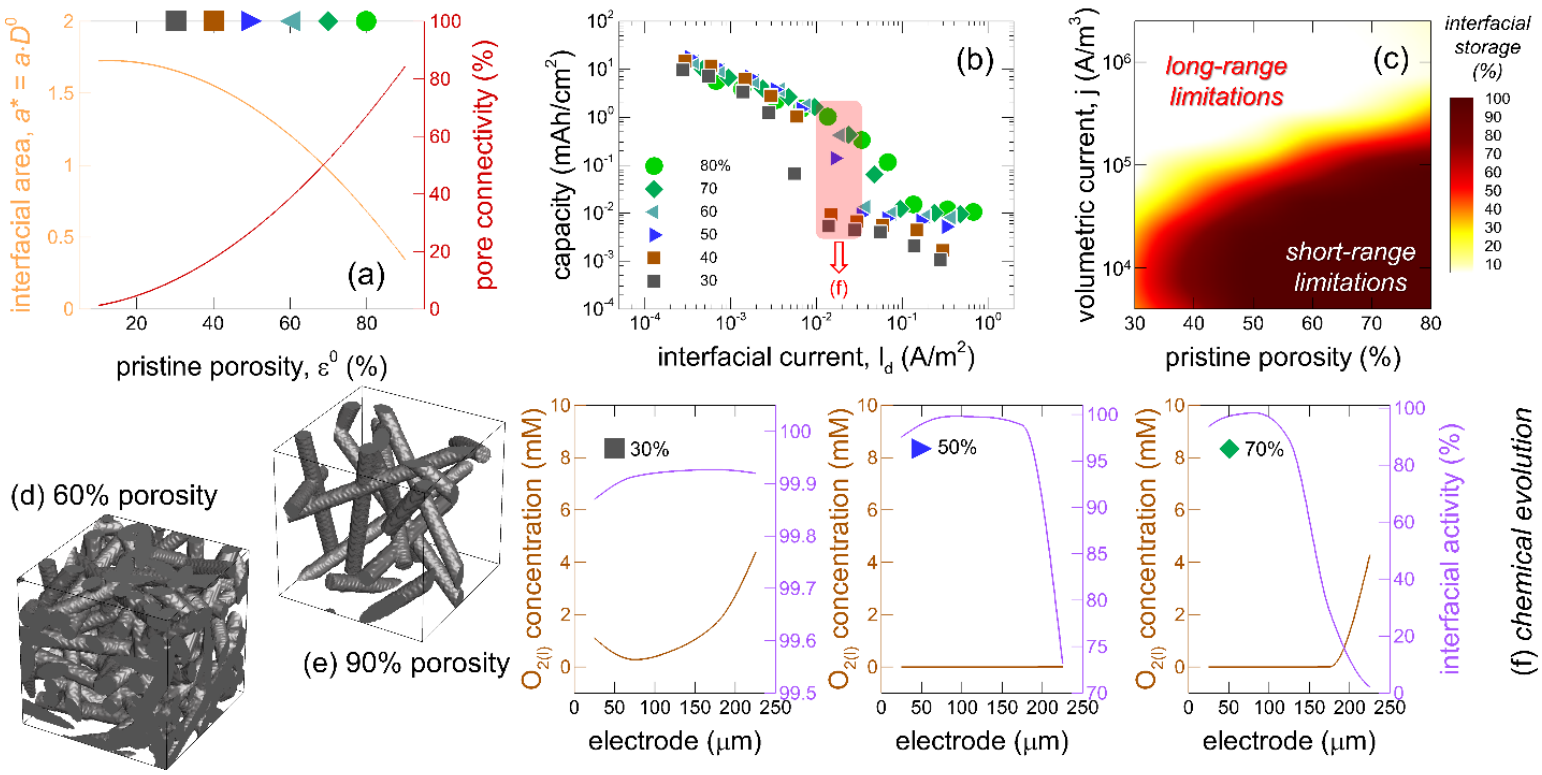

Figure 74. Pristine porosity simultaneously alters the interfacial area and pore network connectivity (a), thus shifting the electrochemical complexations modes (b), (c). Representative electrode structures at (d) 60% and (e) 90% pristine porosity. (f) Chemical evolutions are compared for a moderate current operation where transport effects are relevant.

5.3 Effect of Pristine Electrode Geometry

The interfacial nature of energy storage would deceptively assure higher energy storage for a greater surface area. The coupled interactions among the short- and long-range effects culminate into non-trivial implications. Figure 74(a) presents the specific surface area and pore network connectivity (ε/τ) variations with the pristine porosity for the fibrous electrode microstructure. The substrate – electrolyte area increases as pristine porosity is decreased since it provides for a higher fiber density and in turn a greater electrolyte contact, and equivalently a higher interfacial capacity (for identical precipitate morphology). However, simultaneously the reduced pore connectivity ensues, which marks the earlier onset of transport effects (Figure 74(b)). Even if the 30% pristine porosity structure has the highest interfacial area, the corresponding electrode capacity is not maximum even for the lowest current operation in Figure 74(b). Thus, the pore closure could trigger the transport effects at much lower currents (as observed recently[364]). To delineate the role of electrolyte pore network (*i.e.*, pristine porosity), electrode-scale chemical profiles are outlined in Figure 74(f) near the end of discharge for three distinct electrodes being operated at identical currents (equal to the crossover current for the largest porosity electrode). Nearly depleted oxygen concentration hints the transport limited behavior. More importantly, the interfacial activities, *i.e.*, θ_e, are vastly different. For the lowest (30%) porosity electrode, interfacial activity is nearly 100%, thus signifying negligible (interfacial) energy storage close to termination. The interfacial activity monotonically decreases as going to higher porosity electrodes, thus signifying successively greater storage in 50% and 70% pristine porosity electrodes at this current (Figure 74(f)). As mentioned earlier, the interfacial current directly correlates to the precipitate morphology (and equivalently the maximum energy storage at that current). The late occurrence of the crossover point is desirable as it implies a better interface utilization at higher currents. The volumetric current, $j = a^0 \cdot I_d$, compares the rate response across electrodes with different pristine surface area. The dependence of interfacial storage on volumetric current and pristine porosity is depicted in Figure 74(c). It is revealed that despite the lower surface area, the high porosity electrodes facilitate a superior interface utilization at higher currents due to the delayed transport limitations. At lower currents, moderate pristine porosity (~50%) electrode entails a better response as the porosity is low enough to avail the increased surface area for energy storage without causing the deleterious transport limitations.

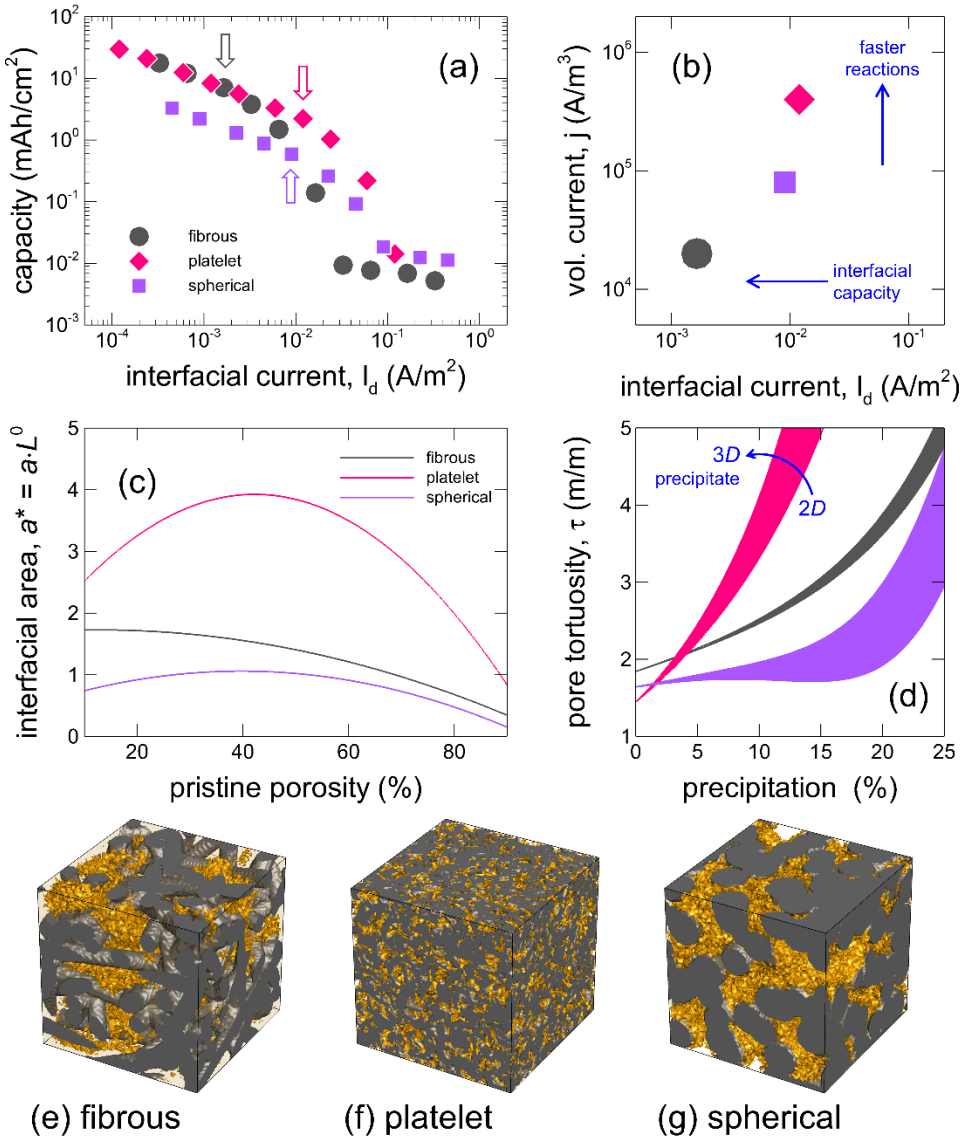

Figure 75. Different carbon forms affect electrochemical response (a), (b) as they exhibit dissimilar microstructural evolutions (c), (d). Representative electrode microstructures are shown with similar pristine porosities and Li_2O_2 formation (e), (f) and (g).

5.4 Effect of Electrode Particle Geometry

Porous carbon structures can be fabricated in many different geometrical shapes, *e.g.*, platelet, spherical, each of which proffers characteristic microstructural disposition[174, 175, 312] (Figure 75(c), (d)). Figure 75(a) compares the electrochemical response of three dissimilar geometries with identical pristine porosity (50%) and representative dimension, L^0 (fiber diameter, platelet longer axis and sphere radius). Figure 75(a) reveals peculiar trends where platelet demonstrates superior

capacity at low currents, while spherical structure outperforms at high currents. Such reciprocal behavior is intrinsically related to the microstructural arrangement. Platelet has the highest surface area for a given pristine porosity, *i.e.*, the highest interfacial capacity, which dictates the low current response. However, the platelet tortuosity increases the most rapidly as compared to the other two structures, thus severely limiting its operation during transport dominated regime. Figure 75(d) compares the tortuosity evolutions for a range of precipitate morphologies for the three electrode types. Each structure is associated with its unique crossover point. Figure 75(b) plots the interfacial and volumetric currents at the crossover points. A smaller interfacial current at the crossover point reflects a better interfacial capacity, while a high volumetric current represents faster reactions. An optimal structure would be the one with low I_d and high j at the crossover point, which would, in turn, require a high surface area at low tortuosity. However, the geometrical arrangement in random porous electrodes does not simultaneously furnish both these attributes, and a high surface area often comes at the cost of increased tortuosity.

Despite the prominence of short-range interactions leading to interfacial energy storage in Li-oxygen porous electrodes, non-equilibrium effects, *i.e.*, inter-species transport interactions and microstructure-modulated coupling of resistive modes foster noncanonical electrochemical functionality which is characterized by incomplete interfacial utilization. The synergy among the geometry and species evolutions certifies the potential of stochastic tailoring.

5.5 Concentrated Solution Theory for a Liquid Electrolyte containing Dissolved Oxygen

An electrolyte is prepared by mixing salts (containing the ions of interest, *e.g.*, Li^+ for lithium batteries) in solvents. At lower concentrations, each of the solute molecules behaves independently of each other. Such a state is knowns as the '*dilute solution limit*' in literature. As the solute concentration increases, the solvation shells of neighboring species overlap and causes an increased hindrance to mobility (in addition to the solvent viscosity effect). In such a concentrated state, electrolyte transport is described by the '*concentrated solution theory*'[22, 23, 188, 361].

The electrolyte transport description for Li-oxygen electrochemistry is more involved due to the presence of an extra solute species – dissolved oxygen, $O_{2(l)}$:

$$\text{electrolyte} \equiv \text{solvent}(s) + Li_{\upsilon_p} X_{\upsilon_m}(\text{salt}) + O_{2(l)} \tag{163}$$

A common salt for Li-oxygen system is *LiTFSI* (Lithium bis(trifluoromethanesulfonyl)imide) that decomposes into Li^+ cation and $TFSI^-$ anion upon dissolution in appropriate organic solvents (*e.g.*, DME, DMSO, *etc.*). The corresponding salt dissolution (assuming complete dissociation) is:

$$Li_{\upsilon_p} X_{\upsilon_m} \longrightarrow \upsilon_p Li^{z_p} + \upsilon_m X^{z_m} \tag{164}$$

where υ's are stoichiometric coefficients and z's are ionic valences ($z_p = +1$ for Li^+). The electrolyte solutions are locally charge neutral, *i.e.*,

$$\upsilon_p z_p + \upsilon_m z_m = 0 \tag{165}$$

If the dissolved salt concentration is c, equivalent ionic concentrations (after dissociation) are:

$$c = \frac{c_p}{\upsilon_p} = \frac{c_m}{\upsilon_m} \tag{166}$$

and the charge neutrality statement (Eq. (165)) can be alternatively written as:

$$c_p z_p + c_m z_m = 0 \tag{167}$$

The chemical potential of the salt can be equivalently expressed as a combination of individual ionic electrochemical potentials:

$$\mu = \upsilon_p \mu_p + \upsilon_m \mu_m$$
$$\therefore \mu = \mu^0 + \upsilon RT \log\left(fc \right) \tag{168}$$

where the salt stoichiometric coefficient is:

$$\upsilon = \upsilon_p + \upsilon_m \tag{169}$$

and f is a thermodynamic factor for the salt. The thermodynamic factor accounts for the activity of salt. In the dilute limit, all the dissociated ions partake in transport and $f \to 1$, while as the salt concentration increases, the thermodynamic factor value decreases. It can be shown that the salt thermodynamic factor relates to the individual ionic thermodynamic factors *via* the expression:

$$f^{\upsilon} = f_p^{\upsilon_p} f_m^{\upsilon_m} \tag{170}$$

As the oxygen is sparingly soluble in the organic electrolytes (mM concentrations in contrast to M salt concentrations), its thermodynamic activity can be assumed to be unity $\left(f_o \to 1 \right)$ and the corresponding chemical potential can be expressed as:

$$\mu_o = \mu_o^0 + RT \log c_o \tag{171}$$

In shorthand notation $o \equiv O_{2(l)}$. The chemical potential gradients for all the components forming an electrolyte are interrelated *via* the Gibbs-Duhem relation:

$$c_s \nabla \mu_s + c_p \nabla \mu_p + c_m \nabla \mu_m + c_o \nabla \mu_o = 0$$

$$\therefore c_s \nabla \mu_s + c \nabla \mu + c_o \nabla \mu_o = 0 \tag{172}$$

Species transport in such a multi-component environment follows the Stefan – Maxwell relation, where D_{ij}'s represent binary diffusivities and N_i's are species i fluxes:

$$-\frac{c_i c_\Sigma}{RT} \nabla \mu_i = \sum_{\substack{j \\ j \neq i}} \left(\frac{c_j N_i - c_i N_j}{D_{ij}} \right) \tag{173}$$

The total local concentration is $c_\Sigma = c_s + c_p + c_m + c_o$. For an electrolyte composed of four (solvent, anion, cation and neutral) species, there are ${}^4P_2 = 12$ binary diffusivities[204], out of which only 6 are independent given the symmetric nature of binary diffusivity tensor ($D_{ij} = D_{ji}$). Also, given the Gibbs-Duhem relation, only three species fluxes are independent. The following mathematical formulation is in terms of solute fluxes, *i.e.*, the fluxes are expressed with respect to the solvent. The motion of solvent molecules represents the bulk flow of the electrolyte solution, with a velocity u_s with respect to a stationary frame of reference.

Cation (Li^+) flux:

$$-\frac{c_p c_\Sigma}{RT} \nabla \mu_p = \left(\frac{c_m N_p - c_p N_m}{D_{pm}} \right) + \left(\frac{c_o N_p - c_p N_o}{D_{po}} \right) + \left(\frac{c_s N_p - c_p N_s}{D_{ps}} \right) \tag{174}$$

Anion (X^{zm}) flux:

$$-\frac{c_m c_\Sigma}{RT} \nabla \mu_m = \left(\frac{c_p N_m - c_m N_p}{D_{pm}} \right) + \left(\frac{c_o N_m - c_m N_o}{D_{mo}} \right) + \left(\frac{c_s N_m - c_m N_s}{D_{ms}} \right) \tag{175}$$

Dissolved oxygen (O_2) flux

$$-\frac{c_o c_\Sigma}{RT} \nabla \mu_o = \left(\frac{c_p N_o - c_o N_p}{D_{po}} \right) + \left(\frac{c_m N_o - c_o N_m}{D_{mo}} \right) + \left(\frac{c_s N_o - c_o N_s}{D_{so}} \right) \tag{176}$$

where D_{pm}, D_{po}, D_{mo}, D_{ps}, $D_{ms,}$ and D_{so} are the six independent binary diffusivities, and $N_s = c_s u_s$. Equations (174) to (176) implicitly express species fluxes N_p, N_m and N_o in terms of (electro-) chemical potential gradients. The potential gradients, in turn, relate to concentration gradients *via* expressions (168) and (171) In addition to the binary diffusivities, the thermodynamic factor is a physical property affecting the transport interactions. Thus, in the electrolyte (Eq. (163)) transport in Li-oxygen system is characterized by seven transport properties (in contrast to four for a typical Li-ion electrolyte[22]). However, these seven fundamental properties are difficult to measure in a typical electrochemical experiment and are to be rearranged to obtain more meaningful properties. It should be noted that recent NMR experiments[188] have tracked individual ions and can provide more direct estimates for binary diffusivities. Rearranging the expressions (174) to (176):

$$\left.\begin{aligned}
&N_p\left(\frac{c_m}{D_{pm}}+\frac{c_o}{D_{po}}+\frac{c_s}{D_{ps}}\right)-N_m\left(\frac{c_p}{D_{pm}}\right)-N_o\left(\frac{c_p}{D_{po}}\right)=-\frac{c_p c_\Sigma}{RT}\nabla\mu_p+\frac{c_p c_s}{D_{ps}}u_s\\
&-N_p\left(\frac{c_m}{D_{pm}}\right)+N_m\left(\frac{c_p}{D_{pm}}+\frac{c_o}{D_{mo}}+\frac{c_s}{D_{ms}}\right)-N_o\left(\frac{c_m}{D_{mo}}\right)=-\frac{c_m c_\Sigma}{RT}\nabla\mu_m+\frac{c_m c_s}{D_{ms}}u_s\\
&-N_p\left(\frac{c_o}{D_{po}}\right)-N_m\left(\frac{c_o}{D_{mo}}\right)+N_o\left(\frac{c_p}{D_{po}}+\frac{c_m}{D_{mo}}+\frac{c_s}{D_{so}}\right)=-\frac{c_o c_\Sigma}{RT}\nabla\mu_o+\frac{c_o c_s}{D_{so}}u_s
\end{aligned}\right] \tag{177}$$

The ionic current is a combination of anionic and cationic fluxes, $I = F\sum_i z_i N_i$:

$$\therefore I/F = z_p N_p + z_m N_m \tag{178}$$

Substituting for N_m in terms of I and N_p from (178) in (177):

$$\left.\begin{aligned}
&N_p\left(\frac{c_o}{D_{po}}+\frac{c_s}{D_{ps}}\right)-I/Fz_m\left(\frac{c_p}{D_{pm}}\right)-N_o\left(\frac{c_p}{D_{po}}\right)=-\frac{c_p c_\Sigma}{RT}\nabla\mu_p+\frac{c_p c_s}{D_{ps}}u_s\\
&-\frac{N_p z_p}{z_m}\left(\frac{c_o}{D_{mo}}+\frac{c_s}{D_{ms}}\right)-N_o\left(\frac{c_m}{D_{mo}}\right)+I/Fz_m\left(\frac{c_p}{D_{pm}}+\frac{c_o}{D_{mo}}+\frac{c_s}{D_{ms}}\right)=-\frac{c_m c_\Sigma}{RT}\nabla\mu_m+\frac{c_m c_s}{D_{ms}}u_s\\
&N_p c_o\left(\frac{z_p D_{po}-z_m D_{mo}}{z_m D_{po} D_{mo}}\right)+N_o\left(\frac{c_p}{D_{po}}+\frac{c_m}{D_{mo}}+\frac{c_s}{D_{so}}\right)-I/Fz_m\left(\frac{c_o}{D_{mo}}\right)=-\frac{c_o c_\Sigma}{RT}\nabla\mu_o+\frac{c_o c_s}{D_{so}}u_s
\end{aligned}\right| \tag{179}$$

Note that the (electro-) chemical potential gradients cause the fluxes, and to further use them in species balance, the fluxes are to be expressed in terms of the driving forces (*i.e.*, the gradients). However, the mathematical nature of the Stefan – Maxwell relations provides a linear combination of species fluxes against each of the driving forces (Eq. (179)). To obtain explicit species flux expressions, equations presented in (179) need to be reshuffled. Mathematically, it is equivalent to a matrix inversion to express three species fluxes as a combination of three gradients[361]. The first two expressions can be linearly added to eliminate solvent flow (local charge neutrality Eq. (167) is used to simplification):

$$\begin{aligned}
I/F\left(c_m\frac{D_{ps}}{D_{pm}}+c_p\frac{D_{ms}}{D_{pm}}+c_o\frac{D_{ms}}{D_{mo}}+c_s\right)&=-z_p\frac{c_p c_\Sigma}{RT}\left(D_{ps}\nabla\mu_p-D_{ms}\nabla\mu_m\right)\\
&-N_p z_p c_o\left(\frac{D_{ps}}{D_{po}}-\frac{D_{ms}}{D_{mo}}\right)+N_o z_p c_p\left(\frac{D_{ps}}{D_{po}}-\frac{D_{ms}}{D_{mo}}\right)
\end{aligned} \tag{180}$$

Similarly, using the first two expressions in (179) to eliminate the oxygen flux:

$$N_p z_p c_s \left(\frac{D_{po}}{D_{ps}} - \frac{D_{mo}}{D_{ms}} \right) = -z_p \frac{c_p c_\Sigma}{RT} \left(D_{po} \nabla \mu_p - D_{mo} \nabla \mu_m \right) + z_p c_p \left(\frac{D_{po}}{D_{ps}} - \frac{D_{mo}}{D_{ms}} \right) c_s u_s$$
$$- I/F \left(c_m \frac{D_{po}}{D_{pm}} + c_p \frac{D_{mo}}{D_{pm}} + c_o + c_s \frac{D_{mo}}{D_{ms}} \right) \tag{181}$$

To aid the simplification, recurring groups of properties are defined as shown in Table 10. Using these mixed variables, the last expression in (179) can be rewritten as:

$$N_o \left(\frac{\upsilon c}{D_o} + \frac{c_s}{D_{so}} \right) = -\frac{c_o c_\Sigma}{RT} \nabla \mu_o + \frac{c_o c_s}{D_{so}} u_s + N_p \left(\frac{\upsilon c_o}{\upsilon_p D_o} \right) + I/F z_m \left(\frac{c_o}{D_{mo}} \right) \tag{182}$$

Alternatively, summing the three linear equations in (179):

$$N_o \left(\frac{c_s}{D_{so}} \right) = -\frac{c_o c_\Sigma}{RT} \nabla \mu_o + \left(\frac{\upsilon c}{D_s} + \frac{c_o}{D_{so}} \right) c_s u_s - N_p \left(\frac{\upsilon c_s}{\upsilon_p D_s} \right) - I/F z_m \left(\frac{c_s}{D_{ms}} \right) - \frac{c c_\Sigma}{RT} \nabla \mu \tag{183}$$

Eliminating cation flux, Np, from Eq. (182) and (183) *via* linear operation:

$$N_o \left(\frac{\upsilon c}{D_o} + \frac{c_s}{D_{so}} \left(1 + \frac{c_o}{c_s} \cdot \frac{D_s}{D_o} \right) \right) = -\frac{c_o c_\Sigma}{RT} \left(1 + \frac{c_o}{c_s} \cdot \frac{D_s}{D_o} \right) \nabla \mu_o$$
$$+ \left(\frac{c_o}{D_{so}} \left(1 + \frac{c_o}{c_s} \cdot \frac{D_s}{D_o} \right) + \frac{\upsilon c c_o}{c_s D_o} \right) c_s u_s + I/F z_m \left(\frac{c_o}{D_{mo}} - \frac{c_o D_s}{D_{ms} D_o} \right) - \frac{c c_\Sigma}{RT} \cdot \frac{c_o D_s}{c_s D_o} \nabla \mu$$

Table 10. Mixed variables appearing in electrolyte transport description.

Mixed variable	***Expression***	***Associated relations***
t_p^s, cationic elemental transference number in solvent frame	$t_p^s = \frac{z_p D_{ps}}{z_p D_{ps} - z_m D_{ms}} = \frac{\upsilon_m D_{ps}}{\upsilon_m D_{ps} + \upsilon_p D_{ms}}$	$t_p^s + t_m^s = 1$ $D_{ps} = \frac{\upsilon_p D_s}{\upsilon t_m^s}$ $D_{ms} = \frac{\upsilon_m D_s}{\upsilon t_p^s}$
D_s, salt diffusivity in solvent frame	$D_s = \frac{\left(z_p - z_m \right) D_{ps} D_{ms}}{z_p D_{ps} - z_m D_{ms}} = \frac{\upsilon D_{ps} D_{ms}}{\upsilon_m D_{ps} + \upsilon_p D_{ms}}$	
t_p^o, cationic elemental transference number in oxygen frame	$t_p^o = \frac{z_p D_{po}}{z_p D_{po} - z_m D_{mo}} = \frac{\upsilon_m D_{po}}{\upsilon_m D_{po} + \upsilon_p D_{mo}}$	$t_p^o + t_m^o = 1$ $D_{po} = \frac{\upsilon_p D_o}{\upsilon t_m^o}$ $D_{mo} = \frac{\upsilon_m D_o}{\upsilon t_p^o}$
D_o, salt diffusivity in oxygen frame	$D_o = \frac{\left(z_p - z_m \right) D_{po} D_{mo}}{z_p D_{po} - z_m D_{mo}} = \frac{\upsilon D_{po} D_{mo}}{\upsilon_m D_{po} + \upsilon_p D_{mo}}$	

Table 10 continued.

	$\frac{c_s}{D_{ps}} - \frac{z_p}{z_m}\frac{c_s}{D_{ms}} = c_s\left(\frac{1}{\upsilon_p D_s / \upsilon t_m^s} + \frac{\upsilon_m}{\upsilon_p}\cdot\frac{1}{\upsilon_m D_s / \upsilon t_p^s}\right) = \frac{\upsilon c_s}{\upsilon_p D_s}$
	$\frac{z_p D_{po} - z_m D_{mo}}{z_m D_{po} D_{mo}} = \frac{\left(z_p - z_m\right)}{z_m}\left\{\frac{z_p D_{po} - z_m D_{mo}}{\left(z_p - z_m\right) D_{po} D_{mo}}\right\} = -\frac{\upsilon}{\upsilon_p D_o}$
	$\frac{c_p}{D_{ps}} + \frac{c_m}{D_{ms}} = \frac{\upsilon_p c}{\left(\frac{\upsilon_p D_s}{\upsilon t_m^s}\right)} + \frac{\upsilon_m c}{\left(\frac{\upsilon_m D_s}{\upsilon t_p^s}\right)} = \frac{\upsilon c}{D_s}$
	$\frac{c_p}{D_{po}} + \frac{c_m}{D_{mo}} = \frac{\upsilon_p c}{\left(\frac{\upsilon_p D_o}{\upsilon t_m^o}\right)} + \frac{\upsilon_m c}{\left(\frac{\upsilon_m D_o}{\upsilon t_p^o}\right)} = \frac{\upsilon c}{D_o}$
γ , diffusability (relative ability of salt to diffuse in solvent as compared to oxygen)	$\gamma = 1 + \frac{c_o}{c_s}\cdot\frac{D_s}{D_o}$
	$c_m \frac{D_{ps}}{D_{pm}} + c_p \frac{D_{ms}}{D_{pm}} = \frac{c}{D_{pm}}\left(\upsilon_m \cdot \frac{\upsilon_p D_s}{\upsilon t_m^s} + \upsilon_p \cdot \frac{\upsilon_m D_s}{\upsilon t_p^s}\right) = \frac{\upsilon_p \upsilon_m}{\upsilon}\cdot\frac{D_s}{D_{pm}}\cdot\frac{c}{t_p^s t_m^s}$
	$c_m \frac{D_{po}}{D_{pm}} + c_p \frac{D_{mo}}{D_{pm}} = \frac{c}{D_{pm}}\left(\upsilon_m \cdot \frac{\upsilon_p D_o}{\upsilon t_m^o} + \upsilon_p \cdot \frac{\upsilon_m D_o}{\upsilon t_p^o}\right) = \frac{\upsilon_p \upsilon_m}{\upsilon}\cdot\frac{D_o}{D_{pm}}\cdot\frac{c}{t_p^o t_m^o}$
	$D_{ps}\nabla\mu_p - D_{ms}\nabla\mu_m = \frac{D_s}{\upsilon}\left(\frac{\upsilon_p \nabla\mu_p}{t_m^s} - \frac{\upsilon_m \nabla\mu_m}{t_p^s}\right) = \frac{D_s}{\upsilon t_p^s}\left(\frac{\upsilon_p \nabla\mu_p}{t_m^s} - \nabla\mu\right)$
	$D_{po}\nabla\mu_p - D_{mo}\nabla\mu_m = \frac{D_o}{\upsilon}\left(\frac{\upsilon_p \nabla\mu_p}{t_m^o} - \frac{\upsilon_m \nabla\mu_m}{t_p^o}\right) = \frac{D_o}{\upsilon t_p^o}\left(\frac{\upsilon_p \nabla\mu_p}{t_m^o} - \nabla\mu\right)$
	$\frac{D_{ps}}{D_{po}} - \frac{D_{ms}}{D_{mo}} = \frac{D_s}{D_o}\left(\frac{t_m^o}{t_m^s} - \frac{t_p^o}{t_p^s}\right)$
	$\frac{D_{po}}{D_{ps}} - \frac{D_{mo}}{D_{ms}} = \frac{D_o}{D_s}\left(\frac{t_m^s}{t_m^o} - \frac{t_p^s}{t_p^o}\right)$

Or,

$$N_o\left(\frac{\upsilon c}{D_o}+\frac{c_s\gamma}{D_{so}}\right)=-\frac{c_oc_\Sigma}{RT}\gamma\nabla\mu_o-\frac{cc_\Sigma}{RT}(\gamma-1)\nabla\mu$$
$$+\frac{I}{F}\cdot\frac{\upsilon c_o}{\upsilon_m z_m D_o}\left(t_p^o-t_p^s\right)+\left(\frac{\upsilon c}{D_o}+\frac{c_s\gamma}{D_{so}}\right)c_o u_s \tag{184}$$

Similarly, simplified equivalents of (180) and (181) are:

$$I/F\left(\frac{\upsilon_p\upsilon_m}{\upsilon}\cdot\frac{D_s}{D_{pm}}\cdot\frac{c}{t_p^s t_m^s}+c_o\frac{D_s}{D_o}\cdot\frac{t_p^o}{t_p^s}+c_s\right)=-z_p\frac{c_pc_\Sigma}{RT}\cdot\frac{D_s}{\upsilon t_p^s}\left(\frac{\upsilon_p\nabla\mu_p}{t_m^s}-\nabla\mu\right)$$
$$-z_p\frac{D_s}{D_o}\left(\frac{t_m^o}{t_m^s}-\frac{t_p^o}{t_p^s}\right)\left(c_oN_p-c_pN_o\right) \tag{185}$$

$$N_pz_pc_s\frac{D_o}{D_s}\left(\frac{t_m^s}{t_m^o}-\frac{t_p^s}{t_p^o}\right)=-z_p\frac{c_pc_\Sigma}{RT}\cdot\frac{D_o}{\upsilon t_p^o}\left(\frac{\upsilon_p\nabla\mu_p}{t_m^o}-\nabla\mu\right)+z_pc_s\frac{D_o}{D_s}\left(\frac{t_m^s}{t_m^o}-\frac{t_p^s}{t_p^o}\right)c_pu_s$$
$$-I/F\left(\frac{\upsilon_p\upsilon_m}{\upsilon}\cdot\frac{D_o}{D_{pm}}\cdot\frac{c}{t_p^o t_m^o}+c_o+c_s\frac{D_o}{D_s}\cdot\frac{t_p^s}{t_p^o}\right) \tag{186}$$

Equations (184) through (186) are a restatement of (179). Substituting N_p and N_o expressions from (186) and (184) into ionic current relation (185), it can be shown that the total ionic current is a combination of migration and diffusive contributions:

$$I=-\kappa\nabla\phi_e-\tilde{\kappa}\nabla\ln c-\tilde{\kappa}_o\nabla\ln c_o \tag{187}$$

with the ionic conductivity, κ, and the two diffusional conductivities, $\tilde{\kappa}$ and κ_o, defined as:

$$\kappa=\frac{1}{\text{denom}}\left\{\frac{F^2\upsilon_p^2z_p^2}{\upsilon}\cdot\frac{cc_\Sigma}{RT}\cdot\frac{D_s}{t_p^s\left(1-t_p^s\right)}\gamma\right\} \tag{188}$$

$$\frac{\tilde{\kappa}}{\kappa}=-\frac{\upsilon^2RT}{F\upsilon_pz_p}\cdot\frac{t_p^s\left(1-t_p^s\right)}{\gamma}\left(1+\frac{d\ln f}{d\ln c}\right)\left\{\frac{1}{\upsilon t_p^s}\left(1+\frac{c_oD_s}{c_sD_o}\cdot\frac{t_m^o}{t_m^s}\right)+\frac{\left(t_p^o-t_p^s\right)c(\gamma-1)}{t_p^s\left(1-t_p^s\right)D_o\left(\frac{\upsilon c}{D_o}+\frac{c_s\gamma}{D_{so}}\right)}\right\} \tag{189}$$

$$\frac{\tilde{\kappa}_o}{\kappa}=-\frac{\frac{\upsilon RT}{F\upsilon_pz_p}\cdot\frac{c_o}{D_o}\left(t_p^o-t_p^s\right)}{\left(\frac{\upsilon c}{D_o}+\frac{c_s\gamma}{D_{so}}\right)} \tag{190}$$

$$\text{denom} = \frac{\upsilon_p \upsilon_m}{\upsilon} \cdot \frac{D_s}{D_{pm}} \cdot \frac{c\gamma}{t_p^s\left(1-t_p^s\right)} + c_s\left\{1+\frac{c_o D_s}{c_s D_o}\cdot\frac{t_m^o}{t_m^s}\right\}$$
$$+\frac{c_o D_s}{D_o}\left\{\frac{t_p^o}{t_p^s}+\frac{c_o D_s}{c_s D_o}\cdot\frac{t_p^o t_m^o}{t_p^s t_m^s}+\frac{\upsilon z_p c_p\left(t_p^o-t_p^s\right)^2}{\upsilon_m z_m D_o t_p^s t_m^s\left(\frac{\upsilon c}{D_o}+\frac{c_s\gamma}{D_{so}}\right)}\right\} \tag{191}$$

Similarly, the molar fluxes of oxygen (Eq. (184)) and the cation (Eq. (186)) reduces to the expressions (the ionic current expression is rearranged to substitute for $\nabla\phi_e$ in the cation flux):

$$N_o = -\mathcal{D}_{oo}\nabla c_o - \mathcal{D}_{op}\nabla c + \mathcal{T}_o \, {}^{I}\!/_{F} + c_o u_s \tag{192}$$

$$N_p = -\upsilon_p \mathcal{D}_{pp}\nabla c - \mathcal{D}_{po}\nabla c_o + \mathcal{T}_p \, {}^{I}\!/_{F z_p} + \upsilon_p c u_s \tag{193}$$

with the composite transport properties – diffusivities, $\mathcal{D}$, and transference numbers, $\mathcal{T}$, defined as follows:

$$\mathcal{D}_{oo} = \frac{\gamma c_\Sigma}{\left(\frac{\upsilon c}{D_o}+\frac{c_s\gamma}{D_{so}}\right)} \tag{194}$$

$$\mathcal{D}_{op} = \frac{\upsilon\left(\gamma-1\right)c_\Sigma}{\left(\frac{\upsilon c}{D_o}+\frac{c_s\gamma}{D_{so}}\right)}\left(1+\frac{d\ln f}{d\ln c}\right) \tag{195}$$

$$\mathcal{T}_o = \frac{\frac{\upsilon}{\upsilon_m z_m}\cdot\frac{c_o}{D_o}\left(t_p^o-t_p^s\right)}{\left(\frac{\upsilon c}{D_o}+\frac{c_s\gamma}{D_{so}}\right)} \tag{196}$$

$$\mathcal{D}_{pp} = \frac{c_\Sigma}{c_s}D_s\left(1+\frac{d\ln f}{d\ln c}\right)\left(\frac{\upsilon c}{D_o}+\frac{c_s}{D_{so}}\right)\Big/\left(\frac{\upsilon c}{D_o}+\frac{c_s\gamma}{D_{so}}\right) \tag{197}$$

$$\mathcal{D}_{po} = \upsilon_p\frac{c c_\Sigma}{c_s}\cdot\frac{D_s}{D_o}\Big/\left(\frac{\upsilon c}{D_o}+\frac{c_s\gamma}{D_{so}}\right) \tag{198}$$

$$\mathcal{T}_p = t_p^s - \left\{\left(\gamma-1\right)\left(t_p^s-t_p^o\right)\frac{c_s}{D_{so}}\Big/\left(\frac{\upsilon c}{D_o}+\frac{c_s\gamma}{D_{so}}\right)\right\} \tag{199}$$

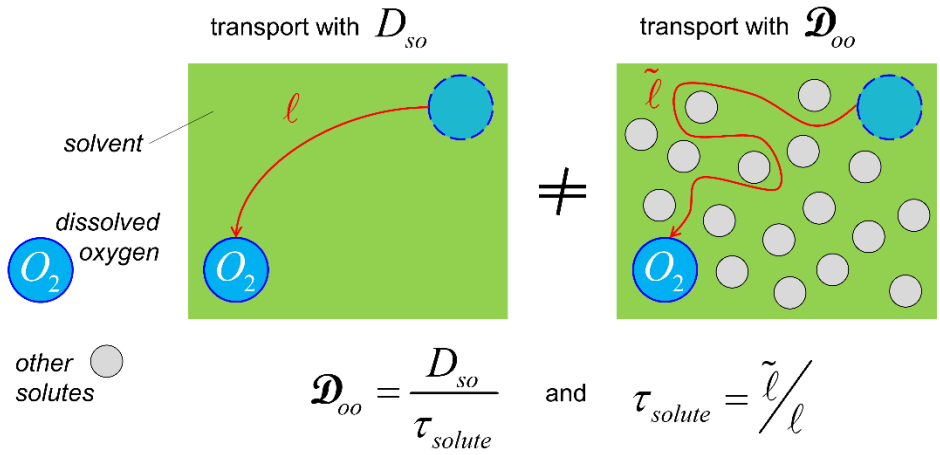

Figure 76. Diffusion characteristics of oxygen change in the presence of additional solutes (here ions).

5.5.1 Partial solubility approximation:

Out of nine composite properties (ionic conductivity, two diffusional conductivities, four diffusivities, and two transference numbers), only seven are independent. In other words, for a complete characterization of a Li-air electrolyte, seven separate tests are required (in contrast to four for a Li-ion electrolyte[24]), which proves to be an overwhelming argument against a more accurate transport description.

Oxygen is a sparingly soluble species in organic electrolytes, limiting its dissolved concentration to mM[345, 362]. This fact can be leveraged to simplify the transport description in the limit of one solute with minimal solubility. In the limit of $c_o \to 0$ (*i.e.*, $\gamma \to 1$), the expressions for the (composite) transport properties become:

$$\frac{1}{\kappa} \approx \frac{RT}{F^2 z_p^2 \upsilon_p^2 c_\Sigma}\left\{\frac{\upsilon_p \upsilon_m}{D_{pm}} + \frac{\upsilon c_s t_p^s \left(1-t_p^s\right)}{c D_s}\right\} \tag{200}$$

$$\frac{\tilde{\kappa}}{\kappa} = -\frac{\upsilon RT}{F}\cdot\frac{\left(1-t_p^s\right)}{\upsilon_p z_p}\left(1+\frac{d\ln f}{d\ln c}\right) \tag{201}$$

$$\frac{\tilde{\kappa}_o}{\kappa} \approx 0 \tag{202}$$

$$\mathfrak{D}_{oo} \approx \frac{D_{so}}{\left(1+\frac{\upsilon c D_{so}}{\gamma c_s D_o}\right)} = \frac{D_{so}}{\left(1+\frac{\upsilon c D_{so}}{c_s D_o}\right)} \tag{203}$$

$$\mathfrak{D}_{op} \approx 0 \tag{204}$$

$$\mathcal{I}_o \approx 0 \tag{205}$$

$$\mathcal{D}_{pp} \approx \frac{c_\Sigma}{c_s} D_s \left(1 + \frac{d \ln f}{d \ln c}\right) \tag{206}$$

$$\mathcal{D}_{po} \approx \frac{\upsilon_p}{\upsilon} \frac{c_\Sigma}{c_s} D_s \Big/ \left(1 + \frac{\gamma c_s D_o}{\upsilon c D_{so}}\right) = \frac{\upsilon_p}{\upsilon} \frac{c_\Sigma}{c_s} D_s \Big/ \left(1 + \frac{c_s D_o}{\upsilon c D_{so}}\right) \tag{207}$$

$$\mathcal{I}_p = t_p^s \tag{208}$$

where the expressions for $\kappa, \tilde{\kappa}, \mathcal{D}_{pp}$ and $\mathcal{I}_p$ reduce to those for a typical electrolyte[22]. The relations for $\mathcal{D}_{oo}$ and $\mathcal{D}_{po}$ deserve a detailed discussion. In the limit $c_o \to 0$, total concentration $c_\Sigma = c_s + c_p + c_m + c_o$ simplifies to $c_\Sigma \to c_s + \upsilon c$. For typical electrolytes, solvent concentration is an order of magnitude higher, *e.g.*, for a 1M *LiTFSI* in DME, $\upsilon = 2$, $c = 1\text{M}$ and $c_s \approx 9.6\text{M}$ (solvent properties[345] $\rho = 0.86370$ g/cc and $M = 90$ g/mol). Hence, $1 + \upsilon c / c_s \approx 1$. However, $\upsilon c D_{so} / \gamma c_s D_o$ does not vanish in the limit of limited oxygen solubility. When oxygen solubility is measured (or computed) in the pure solvent[23], it provides an estimate for the elemental diffusivity D_{so}, while in the presence of other solutes (here dissociated ions), the effective diffusivity is less (the denominator in (203) is always greater than one). The elemental diffusivity D_{so} is often an order of magnitude higher than salt diffusivity (in electrolyte frame) D_s. Assuming equivalent solvation structure, it can be argued that the salt diffusivity D_o in oxygen frame exhibits a similar qualitative and quantitative dependence, and in turn, the magnitude of $\upsilon c D_{so} / \gamma c_s D_o$ is not necessarily negligible in comparison to unity (Eq. (203) and (207)). The difference in solvation structure for oxygen diffusion with and without the lithium salt in the electrolyte is presented in Figure 76. The impediment caused due to the presence of the additional solute entities is phenomenologically equivalent to reduced diffusion in porous electrodes. In the same spirit, the stochastic structure of additional solutes can be characterized in terms of a '*solute tortuosity*' as Eq. (209).

$$\tau_{solute} = 1 + \frac{\upsilon c D_{so}}{c_s D_o} \tag{209}$$

In the limit of no salt concentration, $\tau_{solute} \to 1$ $\left(\tau_{solute} \geq 1\right)$.

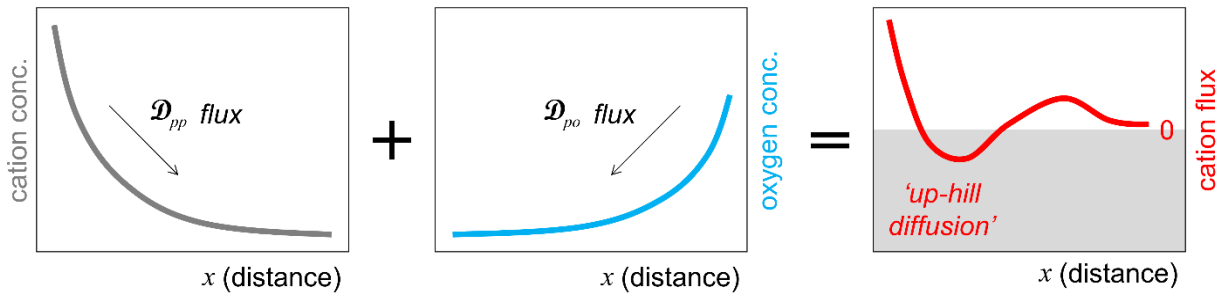

Figure 77. Multi-species complexations in transport interactions.

Given the interaction among the ions and (dissolved) oxygen molecules, the cross-diffusivity in cation transport (Eq. (207)) is affected by local solute structure (Figure 76). The cross-diffusion coefficient $\mathcal{D}_{po}$ can be expressed in terms of solute tortuosity, τ_{solute} as:

$$\mathcal{D}_{po} = \frac{\upsilon_p}{\upsilon}\frac{c_\Sigma}{c_s}D_s\left(\frac{\tau_{solute}-1}{\tau_{solute}}\right) = \frac{\upsilon_p}{\upsilon}\frac{c_\Sigma}{c_s}D_s\left(1-\frac{1}{\tau_{solute}}\right) \tag{210}$$

The cross-diffusivity $\mathcal{D}_{po}$ vanishes as salt concentration reduces since as solute number density decreases the inter-solute distances become larger than the interaction lengths for short-range potentials. Typical salt concentrations are high enough to lead to such cross-interactions. Such concentration dependence in solute tortuosity impedes oxygen transport, *i.e.*, locally causing larger gradients in oxygen concentration which coincides with high cross diffusion for cation flux. The concentration profiles for cation (here Li^+) and dissolved oxygen are negatively correlated in the porous electrode for Li-oxygen electrochemistry (Figure 77), which in the extreme conditions cause cation flux against its concentration gradient (similar to '*up-hill diffusion*' in alloys[365]).

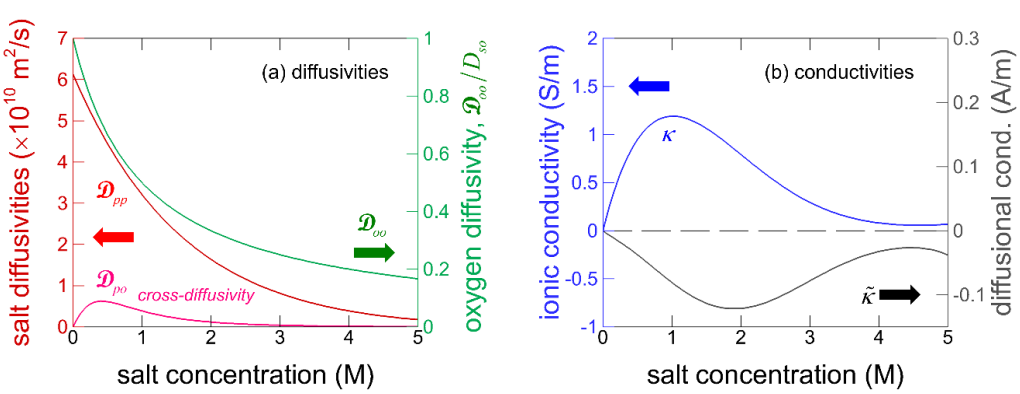

Figure 78. Transport properties for a Li-oxygen electrolyte.

The '*concentrated solution theory*' and its subsequent simplification discussed here (referred to as '*partial solubility approximation*') are disparate from the '*dilute solution theory*' where mutual interactions are not accounted for. The usefulness of such simplification lies in reducing the number of experimental tests required for a thorough characterization from seven to five. The cross diffusivity $\mathcal{D}_{po}$ can be estimated from a combination of $\mathcal{D}_{oo}, \mathcal{D}_{pp}$ and $\tilde{\kappa}/\kappa$. Based on the electrolyte transport properties of a Li-ion electrolyte and accounting for electrolyte description developed here, the complete set of transport properties can be obtained for an equivalent Li-oxygen electrolyte (Figure 78).

5.6 Reaction Kinetics with an Insulating Insoluble Reactant

The primary reaction responsible for (electrochemical) energy storage in Li-oxygen cathode (with organic electrolyte) is lithium peroxide, Li_2O_2, formation. It is fundamentally an electrodeposition reaction that deposits solid lithium peroxide. However, it differs from traditionally known electrodeposition sequences, *e.g.*, lithium plating[355], in that the depositing phase – Li_2O_2 – is electronically insulating. Electronic conductivity of the solid in contact with the electrolyte is essential to providing electrons to sustain the reduction reaction. Since Li_2O_2 is electronically insulating, reduction sites change in time (once the local Li_2O_2 thickness is greater than the '*tunneling length*', the nucleation site becomes unavailable for further reduction). Every phase-change reaction exhibits stochastic spatial variations at microscopic length-scales given the distribution of nucleation sites[356, 366]. Figure 80(a) highlights such a distributed nature of the reaction (211). An appropriate kinetic description of such a reaction scheme is absent from the literature.

$$\frac{1}{2}Li_2O_{2(s)} \underset{\text{reduction}}{\overset{\text{oxidation}}{\rightleftharpoons}} Li^+ + \frac{1}{2}O_{2(l)} + e^- \tag{211}$$

For the reaction (211), an equilibrium condition is related to (electro-) chemical potentials of participating species[22]:

$$\frac{1}{2}\mu_{Li_2O_{2(s)}} = \mu_{Li^+} + \frac{1}{2}\mu_{O_{2(l)}} + \mu_{e^-} \tag{212}$$

Correspondingly, the driving force for the reaction, *i.e.*, overpotential is defined as (per unit electron transfer):

$$\eta = \frac{1}{F}\left\{\frac{1}{2}\mu_{Li_2O_{2(s)}} - \left(\mu_{Li^+} + \frac{1}{2}\mu_{O_{2(l)}} + \mu_{e^-}\right)\right\} \tag{213}$$

Even if electrolyte contact exists along the entire electrode-electrolyte interface, only a part is available for electrolyte phase species to react. Let this surface reactivity be denoted as θ_e. The expressions for (electro-) chemical potentials of the electrolyte phase species subsequently become:

$$\mu_{Li^+} = \mu^0_{Li^+} + F\phi_e + RT\log\left(\theta_e c_p / c_p^{\text{ref}}\right) \tag{214}$$

$$\mu_{O_2(l)} = \mu^0_{O_{2(l)}} + RT\log\left(\theta_e c_o / c_o^{\text{ref}}\right) \tag{215}$$

Note that θ_e is surface activity, and in the bulk of the electrolyte, the expressions (168) and (169) are still applicable. Similarly, let the surface activity of Li_2O_2 be θ_s, and equivalently the chemical potential responsible for the equilibrium (213) is:

$$\mu_{Li_2O_{2(s)}} = \mu^0_{Li_2O_{2(s)}} + RT\log\left(\theta_s\right) \tag{216}$$

where $\mu^0_{Li_2O_{2(s)}}$ is chemical potential in the limit of complete surface coverage (*i.e.*, $\theta_s \to 1$). Substituting Eq. (214) to (216) in (213):

$$\eta = \frac{1}{F}\left\{\begin{array}{l}\frac{1}{2}\left(\mu^0_{Li_2O_{2(s)}} + RT\log\theta_s\right) \\ -\left(\mu^0_{Li^+} + F\phi_e + RT\log\left(\theta_e c_p\right)\right) - \frac{1}{2}\left(\mu^0_{O_{2(l)}} + RT\log\left(\theta_e c_o\right)\right) - \left(-F\phi_s\right)\end{array}\right\} = \phi_s - \phi_e - U \tag{217}$$

with the open circuit potential (OCP) expressions:

$$U = U^0 + \frac{RT}{F}\log\left(\left(\frac{\theta_e c_p}{c_p^{\text{ref}}}\right)\left(\frac{\theta_e c_o}{c_o^{\text{ref}}}\right)^{1/2} \Big/ \sqrt{\theta_s}\right) \tag{218}$$

$$U^0 = \left(\mu^0_{Li^+} + \frac{1}{2}\mu^0_{O_{2(l)}} - \frac{1}{2}\mu^0_{Li_2O_{2(s)}}\right) \tag{219}$$

U^0 is OCP at reference concentrations and temperature. Equation (218) is the extended Nernst equation for unequal surface activities (Figure 79).

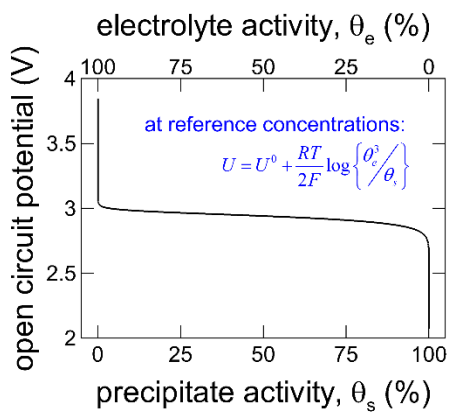

Figure 79. At reference concentrations, the open circuit potential varies with the activity of the precipitate phase, and equivalently the activity of the electrolyte phase.

The energy landscape corresponding to reaction (211) is shown in Figure 80(b), where Δg^f and Δg^b are driving forces for the forward and backward reaction halves (*i.e.*, oxidation and reduction, respectively). Since the potential energy of Li_2O_2 (*i.e.*, chemical potential) is smaller than the electrolyte phase species, the formation of Li_2O_2 is thermodynamically spontaneous and in turn, represent the energy producing (discharge) half. Based on the law of mass action[179], corresponding molar rates can be expressed as:

$$r^f = k^f \sqrt{\theta_s} = \left[k^{f0} \exp\left(-\Delta g^f / RT\right)\right]\sqrt{\theta_s} \tag{220}$$

$$r^b = k^b \left(\theta_e c_p\right)\sqrt{\theta_e c_o} = \left[k^{b0} \exp\left(-\Delta g^b / RT\right)\right]\left(\theta_e c_p\right)\sqrt{\theta_e c_o} \tag{221}$$

where the rate constants are related to activation energies *via* Arrhenius expressions[179]. The (balanced) reaction (211) is written in as a single electron reaction, and equivalently the reaction current (units of A/m^2) is:

$$\frac{i}{F} = r^f - r^b = \left[k^{f0} \exp\left(-\Delta g^f / RT\right)\right]\sqrt{\theta_s} - \left[k^{b0} \exp\left(-\Delta g^b / RT\right)\right]\left(\theta_e c_p\right)\sqrt{\theta_e c_o} \tag{222}$$

At equilibrium the energy barriers for the reaction halves are identical and the reactant concentrations approach their reference values, *i.e.*, the following equalities hold:

$$\Delta g_{eq}^f = \Delta g_{eq}^b \tag{223}$$

$$k^{f0} = k^{b0} c_p^{\text{ref}} \sqrt{c_o^{\text{ref}}} = k^0 \tag{224}$$

$$U = U^0 \tag{225}$$

Substituting relations (223) and (224) in current density (222):

$$i = Fk^0 \exp\left(-\Delta g_{eq}^f / RT\right)\left\{\sqrt{\theta_s}\exp\left(-\frac{\left(\Delta g^f - \Delta g_{eq}^f\right)}{RT}\right) - \left(\frac{\theta_e c_p}{c_p^{\text{ref}}}\right)\sqrt{\frac{\theta_e c_o}{c_o^{\text{ref}}}}\exp\left(-\frac{\left(\Delta g^b - \Delta g_{eq}^b\right)}{RT}\right)\right\} \tag{226}$$

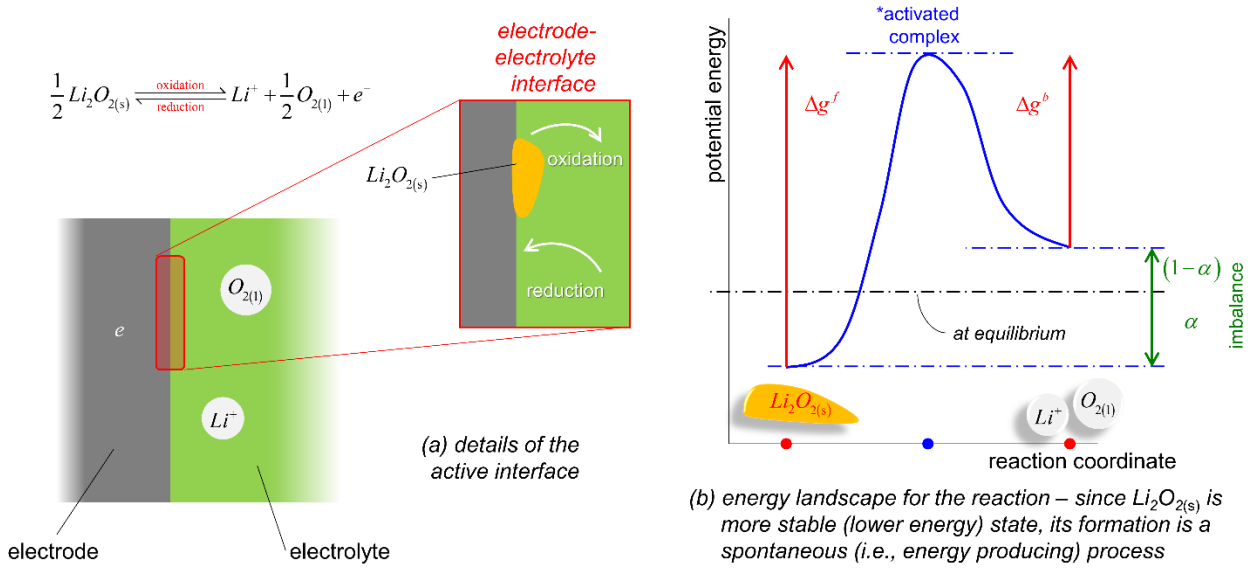

Figure 80. Electronic conductivity of the precipitate phase plays a crucial role in the corresponding reaction scheme.

To drive the reaction in either direction, the potential difference is varied (*e.g.*, cyclic voltammetry systematically changes solid phase potential, ϕ_s, to characterize electrochemical reactions[22]). The applied potential difference affects both the activation energies. Let the partition of this influence be α and (1-α), respectively to anodic (forward) and cathodic (backward) halves (Figure 80(b)). Thence, the free energy differences appearing in Eq. (226) can be expressed as:

$$\Delta g^f - \Delta g_{eq}^f = -\alpha F\left(\phi_s - \phi_e - U^0\right) \tag{227}$$

$$\Delta g^b - \Delta g_{eq}^b = (1-\alpha) F\left(\phi_s - \phi_e - U^0\right) \tag{228}$$

and the reaction current density expression (226) becomes:

$$i = Fk^0 \exp\left(-\Delta g_{eq}^f / RT\right)\left\{\sqrt{\theta_s}\,\mathrm{e}^{\frac{\alpha F\left(\phi_s - \phi_e - U^0\right)}{RT}} - \left(\frac{\theta_e c_p}{c_p^{\text{ref}}}\right)\sqrt{\frac{\theta_e c_o}{c_o^{\text{ref}}}}\,\mathrm{e}^{\frac{-(1-\alpha)F\left(\phi_s - \phi_e - U^0\right)}{RT}}\right\} \tag{229}$$

Standard OCP appearing in (231) can be replaced in terms of its concentration dependent counterpart using Eq. (218), to yield an alternate form of reaction kinetics (231):

$$i = Fk^0 \exp\left(-\Delta g_{eq}^f / RT\right)\left[\left(\frac{\theta_e c_p}{c_p^{\text{ref}}}\right)\sqrt{\frac{\theta_e c_o}{c_o^{\text{ref}}}}\right]^{\alpha}\left[\sqrt{\theta_s}\right]^{(1-\alpha)}\left\{\mathrm{e}^{\frac{\alpha F\left(\phi_s - \phi_e - U\right)}{RT}} - \mathrm{e}^{\frac{-(1-\alpha)F\left(\phi_s - \phi_e - U\right)}{RT}}\right\} \tag{230}$$

Or, expressed more concisely,

$$i = i^0 \left\{ \mathrm{e}^{\frac{\alpha F \eta}{RT}} - \mathrm{e}^{\frac{-(1-\alpha) F \eta}{RT}} \right\} \tag{231}$$

where the overpotential, $\eta = \phi_s - \phi_e - U$, varies with local concentration (Figure 79) and the exchange current density, i^0, has the form:

$$i^0 = F k^0 \exp\left(-\Delta g_{eq}^{f} / RT\right) \left[\left(\frac{\theta_e c_p}{c_p^{\mathrm{ref}}} \right) \sqrt{\frac{\theta_e c_o}{c_o^{\mathrm{ref}}}} \right]^{\alpha} \left[\sqrt{\theta_s} \right]^{(1-\alpha)} \tag{232}$$

The expressions (229) and (230) are alternate forms of the Butler – Volmer kinetics with insulating precipitates. These expressions are directly valid for planar electrodes. The two different expressions offer analytical advantages based on the desired application. For example, interpretation of cyclic voltammetry[341] is more straight forward with standard OCP form (Eq. (229)), while impedance spectroscopy[349] data is more amenable to a state of charge dependent OCP (Eq. (230)). For a porous electrode, appropriate volumetric current density (A/m^3) has the expression:

$$j = a_0 i \tag{233}$$

where a^0 is the total solid – electrolyte interfacial area (*i.e.*, BET area). Total area, a^0, is not necessarily equal to the active area for each of the reactions. The incorporation of surface activities provides a consistent representation for the reaction at intermediate length-scales equivalent to pore dimensions. At smaller length-scales, one has to explicitly account for each of the reaction halves and their interfacial distribution[113, 115, 344, 367, 368].

5.7 Abstracting Porous Electrode Evolution upon Precipitation

The porous electrodes for Li-oxygen are unique in that they exhibit considerable geometrical evolution during each operation, thus making a reliable quantification of the microstructure growth essential to comprehending the associated electrochemical complexations. Here electrode structures composed of fibers are studied. Authors have previously reported the evolutionary response of other geometrical arrangements[174, 175, 312]. As shown in Figure 81, the pristine structure is specified in terms of fiber dimension (here diameter, D^0) and pristine porosity, ε^0. Each of the pristine structures is evolved by growing (mesoscopic) precipitates with varying morphology, ω, and amounts, ε_p (m^3 of precipitate/ m^3 of electrode microstructure). Figure 81 shows a

representative evolved structure. Such representative structures are large enough to contain sufficient material distribution to behave as a porous medium, *i.e.*, are of RVE (representative volume element) dimensions[9]. The pristine structures are generated in GeoDict[177, 178], while coarse-grained precipitate growth is described through an interfacial energy based approach[174, 312].

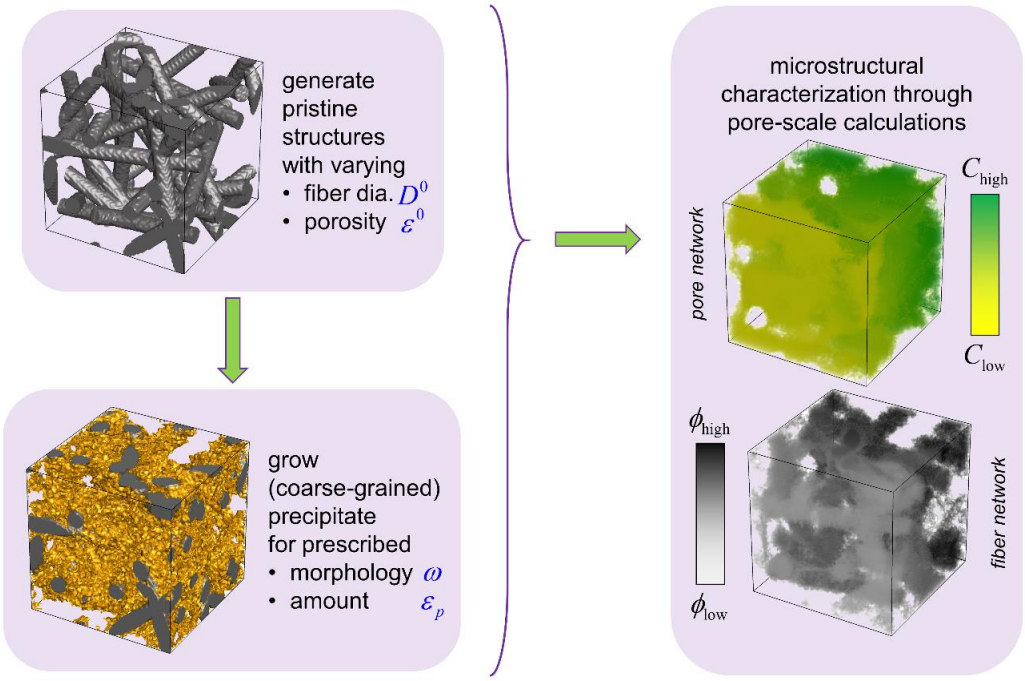

Figure 81. An outline of electrode microstructure generation and subsequent characterization.

Each of these microstructural representations are subsequently characterized to estimate effective properties (Table 11) relevant to species transport through the pore network (namely tortuosity), electron conduction through the fiber network (*i.e.*, electronic conductivity), and kinetics at the solid – pore interface (interfacial area directly correlates to surface activities that affect electrochemical reactions). Various two-phase interfaces are measured as per the modified Minkowski measure[174, 312], while tortuosity and effective electronic conductivities are estimated through pore-scale solutions of species balance and potential balance[174, 312], respectively. Figure 81 also demonstrates representative solutions to these equations. Once the sufficient number of representative structures are characterized, the resultant dataset is analyzed to extract functional relations that quantitatively describe the microstructural evolution upon precipitation. Table 11 presents such correlations for the pristine fibrous structure.

Table 11. Microstructural evolution is quantified in terms of effective property variation upon precipitation.

Property	***Expression***
Carbon – electrolyte interfacial area	$a_{01} = \frac{1}{D^0}\left(-0.038 + 4.043\left(1-\varepsilon^0\right) - 2.316\left(1-\varepsilon^0\right)^2\right)\left\{1-\left(\frac{\varepsilon_p}{0.452\omega^{2.751}}\right)^{1.1}\right\}$
Carbon – precipitate interfacial area	$a_{12} = \frac{\varepsilon_p}{D^0}\left(0.066 + 12.909\left(1-\varepsilon^0\right) - 10.002\left(1-\varepsilon^0\right)^2\right)\left(2.485 - 4.235\varepsilon_p - 0.171\omega\right)$
Precipitate – electrolyte contact area	$a_{20} = \frac{\varepsilon_p}{D^0}\left(1.279 + 3.776\left(1-\left(\varepsilon^0-\varepsilon_p\right)\right) - 0.780\left(1-\left(\varepsilon^0-\varepsilon_p\right)\right)^2\right)\left(5.079 - 10.498\varepsilon_p + 0.288\omega\right)$
Pristine carbon surface area	$a_{1(0+2)} = \frac{\varepsilon_p}{D^0}\left(-0.005 + 4.031\left(1-\varepsilon^0\right) - 2.632\left(1-\varepsilon^0\right)^2\right)$
Pore network tortuosity	$\tau = \left(0.967 + \varepsilon_p\left(1.209 - 5.730\varepsilon - 0.266\omega\right)\right)\left(\varepsilon^0 - \varepsilon_p\right)^{-\left(0.932-\varepsilon_p\left(0.376-5.525\varepsilon-0.607\omega\right)\right)}$
Fiber network conductivity	$\sigma/\sigma^0 = 0.680\left(1-\varepsilon^0\right)^{1.532}$

5.8 Electrochemical Description of a Porous Evolving Electrode

The electrochemical response of a Li-oxygen porous electrode is a joint outcome of coupled interactions as summarized in Figure 82. Previous studies in the literature do not recognize such mesoscopic coupling and make unjustified assumptions, *e.g.*, resistive but not insulating Li_2O_2[369-371], simpleton microstructural representation[368, 372-375], no inter-species interactions during transport[376-378] and ad-hoc description of interfacial kinetics and subsequent growth[379, 380]. To ameliorate such difficulties, here the mesoscopic interactions are coherently treated through non-equilibrium thermodynamics and pore-scale microstructural analysis. Mathematically, the following expressions govern the electrochemical evolution:

Cation (Li^+) transport in electrolyte:

$$\frac{\partial\left(\varepsilon c\right)}{\partial t} = \nabla\cdot\left(\mathcal{D}_{pp}\frac{\varepsilon}{\tau}\nabla c\right) + \nabla\cdot\left(\mathcal{D}_{po}\frac{\varepsilon}{\tau}\nabla c_o\right) + \left(1-\mathcal{T}_p\right)j/F \tag{234}$$

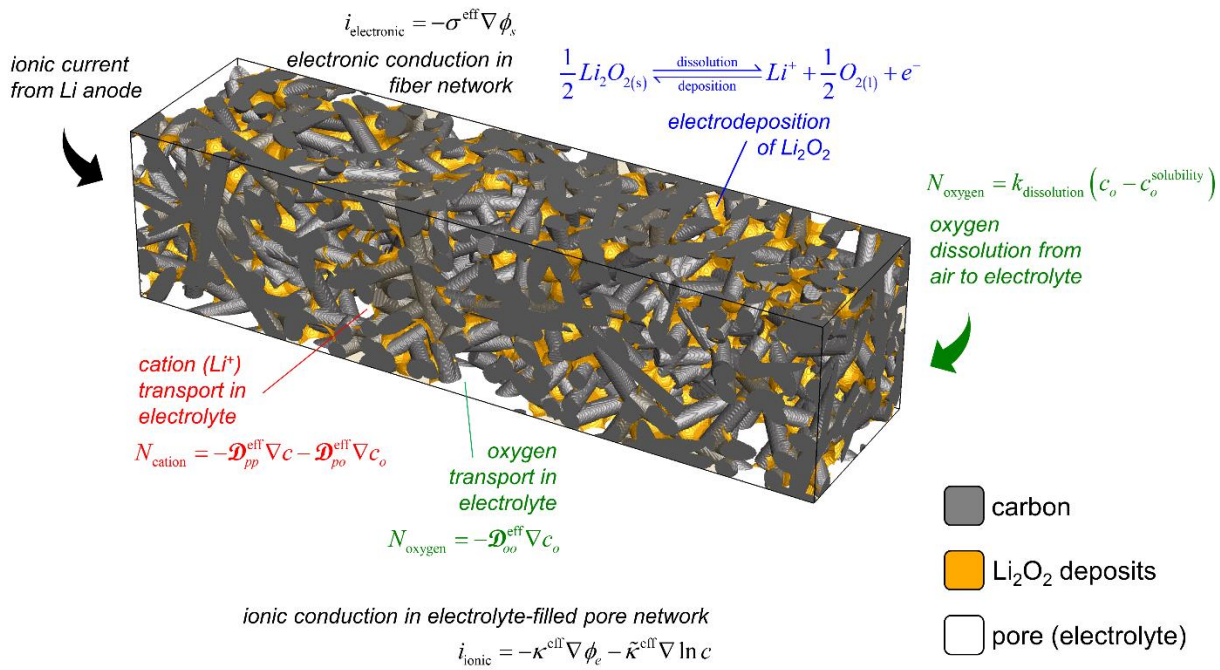

Figure 82. A graphical representation of various physicochemical interactions taking place in a porous electrode for Li-oxygen electrochemistry.

<u>*Oxygen (O_2) transport in electrolyte*</u>:

$$\frac{\partial \left(\varepsilon c_o \right)}{\partial t} = \nabla \cdot \left(\mathcal{D}_{oo} \frac{\varepsilon}{\tau} \nabla c_o \right) + j / 2F \tag{235}$$

<u>*Ionic current in the electrolyte*</u>:

$$\nabla \cdot \left(\kappa \frac{\varepsilon}{\tau} \nabla \phi_e \right) + \nabla \cdot \left(\tilde{\kappa} \frac{\varepsilon}{\tau} \nabla \ln c \right) + j = 0 \tag{236}$$

<u>*Electronic current in the substrate network*</u>:

$$\sigma^{\text{eff}} \nabla^2 \phi_s = j \tag{237}$$

<u>*Lithium peroxide formation*</u>:

$$\frac{\partial \varepsilon_p}{\partial t} = -\frac{V_p j}{2F} \tag{238}$$

<u>*Porosity evolution*</u>:

$$\frac{\partial \left(\varepsilon + \varepsilon_p \right) = 0}{\partial t} \tag{239}$$

where the reaction kinetics follows the expression (229), and microstructural evolution follows the relations presented in Table 11. Note that the surface activities appearing in the kinetic description are intrinsically defined by respective interfacial area evolutions. Appropriate boundary and interface conditions are as follows (in the same sequence as equations (234) to (237)):

anode – separator boundary	separator – cathode interface	cathode – current collector boundary	
$-\mathcal{D}_{pp}\dfrac{\varepsilon}{\tau}\dfrac{\partial c}{\partial x}=\left(1-\mathcal{T}_p\right)\dfrac{I_{\text{app}}}{F}$	*flux continuity*	$-\mathcal{D}_{pp}\dfrac{\varepsilon}{\tau}\dfrac{\partial c}{\partial x}=0$	(240)
$-\mathcal{D}_{oo}\dfrac{\varepsilon}{\tau}\dfrac{\partial c_o}{\partial x}=0$	*flux continuity*	$-\mathcal{D}_{oo}\dfrac{\partial c_o}{\partial x}=k_{\text{dissolution}}\left(c_o-c_o^{\text{solubility}}\right)$	(241)
$-\kappa\dfrac{\varepsilon}{\tau}\dfrac{\partial \phi_e}{\partial x}-\tilde{\kappa}\dfrac{\varepsilon}{\tau}\dfrac{\partial \ln c}{\partial x}=I_{\text{app}}$	*flux continuity*	$\phi_e=0$	(242)
–	$-\sigma^{\text{eff}}\dfrac{\partial \phi_s}{\partial x}=0$	$-\sigma^{\text{eff}}\dfrac{\partial \phi_s}{\partial x}=I_{\text{app}}$	(243)

At the anode – separator interface, the oxygen flux vanishes, *i.e.*, $N_o=-\mathcal{D}_{oo}\dfrac{\varepsilon}{\tau}\dfrac{\partial c_o}{\partial x}=0\Rightarrow\dfrac{\partial c_o}{\partial x}=0$.

Substituting this in the cation flux relation,

$N_p=-\mathcal{D}_{pp}\dfrac{\varepsilon}{\tau}\dfrac{\partial c}{\partial x}-\mathcal{D}_{po}\dfrac{\varepsilon}{\tau}\dfrac{\partial c_o}{\partial x}+\mathcal{T}_p\,{}^{I_{\text{app}}}\!/_{F}={}^{I_{\text{app}}}\!/_{F}\Rightarrow-\mathcal{D}_{pp}\dfrac{\varepsilon}{\tau}\dfrac{\partial c}{\partial x}=\left(1-\mathcal{T}_p\right){}^{I_{\text{app}}}\!/_{F}$, since the ionic current at the anode – separator interface is purely due to cation generation. The solution algorithm for the evolving porous electrode (with time-varying microstructural properties) has been reported in the authors' earlier work[312].

Table 12. Analyzing the experimental response of Li-oxygen porous electrodes[330] in near equilibrium conditions. Electrodes have a pristine porosity of 80%, thus a theoretical capacity of 500 mAh/cm^2.

I_{app} (mA/cm^2)	C-rate	Capacity (mAh/cm^2)	% storage
0.1	C/500	5.99366492	12.0
0.2	C/250	3.68507151	7.5
0.5	C/100	2.13193721	4.3
1	C/50	1.61830077	3.2

6. CONVERSION ELECTRODE: LITHIUM-SULFUR

Relevant Publications and/or Working Papers:

1. A. Mistry and P. P. Mukherjee (2017) *Precipitation-Microstructure Interactions in the Li-Sulfur Battery Electrode* Journal of Physical Chemistry C 121(47) 26256 (doi: 10.1021/acs.jpcc.7b09997)
2. A. Mistry and P. P. Mukherjee (2018) *Electrolyte Transport Evolution Dynamics in Lithium-Sulfur Batteries* Journal of Physical Chemistry C 122(32) 18329 (doi: 10.1021/acs.jpcc.8b05442)
3. A. Mistry and P. P. Mukherjee (2018) *"Shuttle" in Polysulfide Shuttle: Friend or Foe?* Journal of Physical Chemistry C 122(42) 23845 (doi: 10.1021/acs.jpcc.8b06077)
4. (joint first author) C.-F. Chen, A. Mistry and P. P. Mukherjee (2017) *Probing Impedance and Microstructure Evolution in Lithium-Sulfur Battery Electrodes* Journal of Physical Chemistry C 121(39) 21206 (doi: 10.1021/acs.jpcc.7b07245)

Formation and precipitation of insulating discharge products, such as Li_2S, in the lithium-sulfur (Li-S) battery cathode, leads to deleterious performance decay. Physicochemical interactions underlying the cathode microstructure evolution due to precipitation are hitherto poorly understood. In this work, a mesoscale understanding of the microstructure – precipitate interplay owing to surface passivation and pore blockage is presented. Mesoporous, carbon-based cathode microstructures are examined for disparate precipitate morphology and growth. The pore-scale manifestation of the microstructural and transport limitations on the electrochemical performance is elucidated. Surface passivation and pore blockage effects are examined for complexations due to sulfur loading, electrolyte volume, pore size, and precipitate morphology. This study provides critical insights into the underlying mesoscale physics and microstructural stochasticity on the Li-S battery performance.

6.1 Background

In addition to an order of magnitude higher theoretical capacity, lower material cost and earthly abundance, lithium-sulfur (Li-S) cells promise other advantages such as electrolyte-phase reaction pathway (thus bypassing sluggish solid-state intercalation as opposed to traditional Lithium-ion batteries)[102-104, 106-108, 325]. Much of the earlier studies revolve around quantification, prevention and/or mitigation of the polysulfide shuttle effect[128-135]. More recent investigations identify the importance of other fundamental aspects such as fingerprinting of cell reaction pathway[136-142],

complexities associated with electrolyte-phase transport[102, 143-145] and interfacial interactions of precipitation[112, 113, 115, 146, 147]. In fact, the reproducibility of many electrochemical results for Li-S cells has also been debated of late[148, 149].

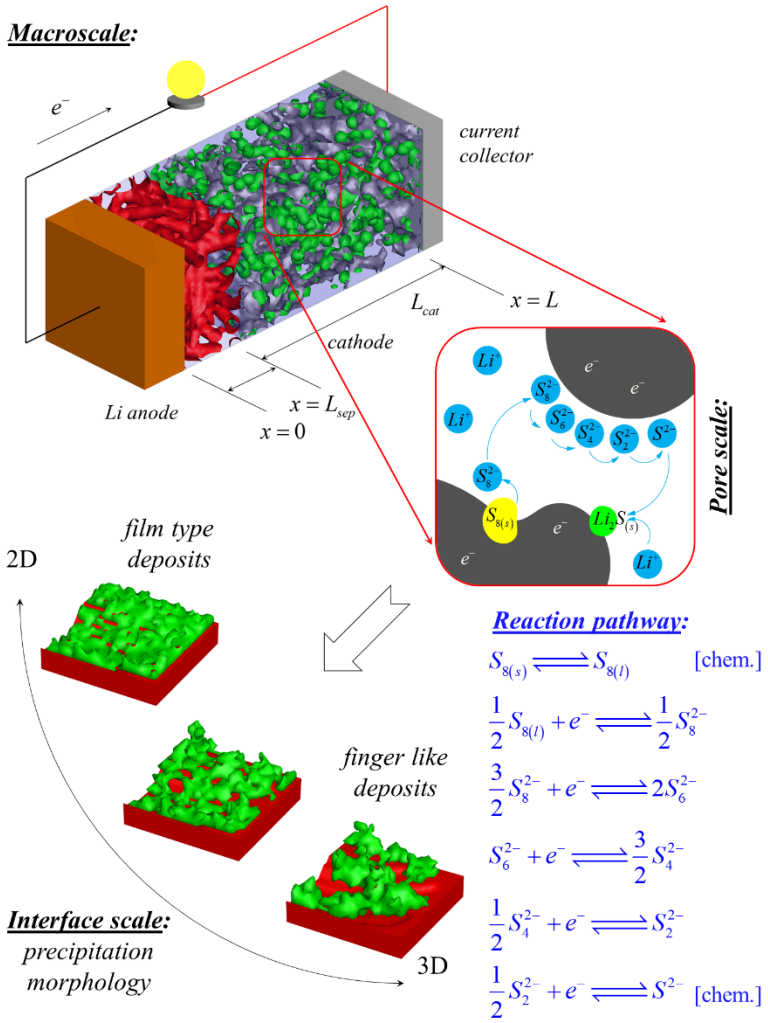

Figure 83. A schematic diagram illustrating the physical processes taking place at various time and length scales in a Lithium-sulfur cell: (macroscale) describes cell level information such as voltage and capacity, (pore scale) explores the reactions taking place at electrode-electrolyte interface as well as charge and species transport, while (interface scale) quantifies the growth and morphology of precipitation products. Due to the strong mutual coupling of these three scales, an explanation of the observed system behavior requires a simultaneous description of multiple scales, thus qualifying Lithium-sulfur batteries as a true multiscale energy storage system.

Consider Figure 83 that presents a qualitative sketch of Li-S unit cell (macroscale) and associated features at smaller length scales. Various electrochemical and chemical reactions occurring in the cathode coexist at pore level. The reaction pathway (borrowed from [127]) is also shown alongside. Following the reactions that account for phase change (here sulfur dissolution and $Li_2S_{(s)}$ precipitation), cathode structure grows as the cell is operated. The resulting growth pattern is found to be a strong function of different interfacial phenomena[113, 147] such as nucleation site density, the affinity of the precipitate for the substrate, deposition rate, surface diffusion, and temperature. This arrangement of the deposit phase manifests between two limiting behaviors of film type and finger (fractal) like structures[356]. The interface scale pictures on Figure 83 schematically illustrate the precipitate morphology. Depending on precipitation morphology, the dynamic solid phases (*i.e.*, solid sulfur, $S_{8(s)}$, and lithium sulfide, $Li_2S_{(s)}$) arrange differently at carbon – electrolyte interface leading to disparate electrochemically active area (locations where electrochemical reactions take place) coverage, for the same amount of precipitation. Equivalently, the pore network evolution is also expected to be qualitatively different leading to distinct pore constriction events, which is in turn expected to affect species transport in the electrolyte phase. Such physicochemical changes, in turn, lead to different impedance contributions[381].

The relevance of such an inspection is better perceived when the time scale of microstructure evolution is factored in. The evolution rate is positively correlated to the rate of electrochemical operation. There are only a few experiments that probe this progression of cathode[116], despite the fact that it is always present. Most of the modeling studies use Bruggeman relations to account for cathode evolution[127, 382]. The Bruggeman relation is strictly valid only for porous structures made up of monodispersed non-overlapping spherical particles[101], which is quite different from the carbon structures used in Li-S. The present analysis attempts to address the following set of questions (1) how a mesoporous carbon cathode would progress through successive stages of precipitation/ dissolution instances (2) abstracting the cathode growth upon precipitation in terms of effective properties (3) discerning electrode scale limitations related to microstructure evolution (4) quantitative and qualitative understanding of effect of cathode specifications such as sulfur loading, precipitation morphology, pristine porosity and pore size on cell performance at different discharge rates.

6.2 Understanding Cathode Microstructure Growth

Cathode growth is examined by growing precipitate phase in mesoporous carbon structures with different specifications (refer to Microstructure Generation for specific details). Figure 84(a) shows a representative cathode structure with 40% carbon (*i.e.*, 60% pristine porosity) and 10% precipitation. Note that these numbers are expressed as volumes per electrode volume. Pristine porosity refers to the porosity of the cathode without any precipitation and is different than porosity at the start of the first discharge (end of cathode fabrication) as at that stage the cathode is impregnated with solid sulfur. A 2D cross-section at the mid-x location is shown in Figure 84(b). Note that overlapping pores create a pore structure with a range of pore dimensions. The precipitate phase grows from the carbon – pore interface into the pore phase. On Figure 84(b) some chunks of the precipitate phase appear to be not contacting the carbon surface, but they are connected to deposit patterns in the lateral direction (perpendicular to the sectioning plane). It is ensured that the pristine structures have connected pores, so it contributes to pore phase ionic transport (*i.e.*, there are no closed pores). The deposition patterns are altered by varying the morphology factor, ω, which controls the locations for further precipitation (for $\omega \rightarrow 0$, precipitated phase deposits at carbon – pore interface, while $\omega \rightarrow 1$ favors pre-deposited precipitate phase – pore boundary for further precipitation). Physically this deposition preference is related to the interfacial energies of precipitate – carbon and precipitate – precipitate surfaces. Higher values of ω imply that the precipitate phase is more likely to self-deposit rather than depositing on unoccupied carbon surfaces (*i.e.*, cohesion is stronger than adhesion[4]). On the other hand, lower ω values represent the opposite condition where adhesion is dominant over cohesion. Intermediate ω's correspond to varying degrees of adhesive – to – cohesive contributions. The relative strengths of adhesive and cohesive effects lead to different deposition patterns. Figure 84(c) depicts such variations at a pore-scale for different sub-zones on the 2D slice (Figure 84(b)). The sub-figures reveal that going towards $\omega \rightarrow 0$, deposition pattern is more film-like and the prevalent growth direction being in parallel to the carbon – pore interface, thus leading to a more two-dimensional growth. On the other hand, approaching the limit of $\omega \rightarrow 1$, growth appears more finger (fractal) type and has more interference with the pore phase. It is important to identify the presence of additional length scales at the pore level. The pristine mesoporous carbon structure is identified with the mean pore size (say, radius). With the precipitate addition, average precipitation thickness becomes another relevant measure which correlates to precipitation amount.

Figure 84. Electrode microstructure (a-c) and resistances (d-i). (a) Mesoporous carbon structure with 40% carbon and 10% precipitation by volume. (b) the *x*-mid plane for this REV. (c) Changes in local precipitate arrangement (*i.e.*, morphology) for different adhesion tendencies between precipitate and carbon substrate. (d) Electrochemically active area evolution with precipitation for different precipitation morphologies help identify surface passivation related resistance (f). (e) Tortuosity increase and porosity reduction upon precipitation define pore phase transport resistance and in turn pore blockage (g). Surface passivation and pore blockage resistances jointly identify cathode starvation zones (h), the quantitative nature of which changes with pristine porosity modifications (i).

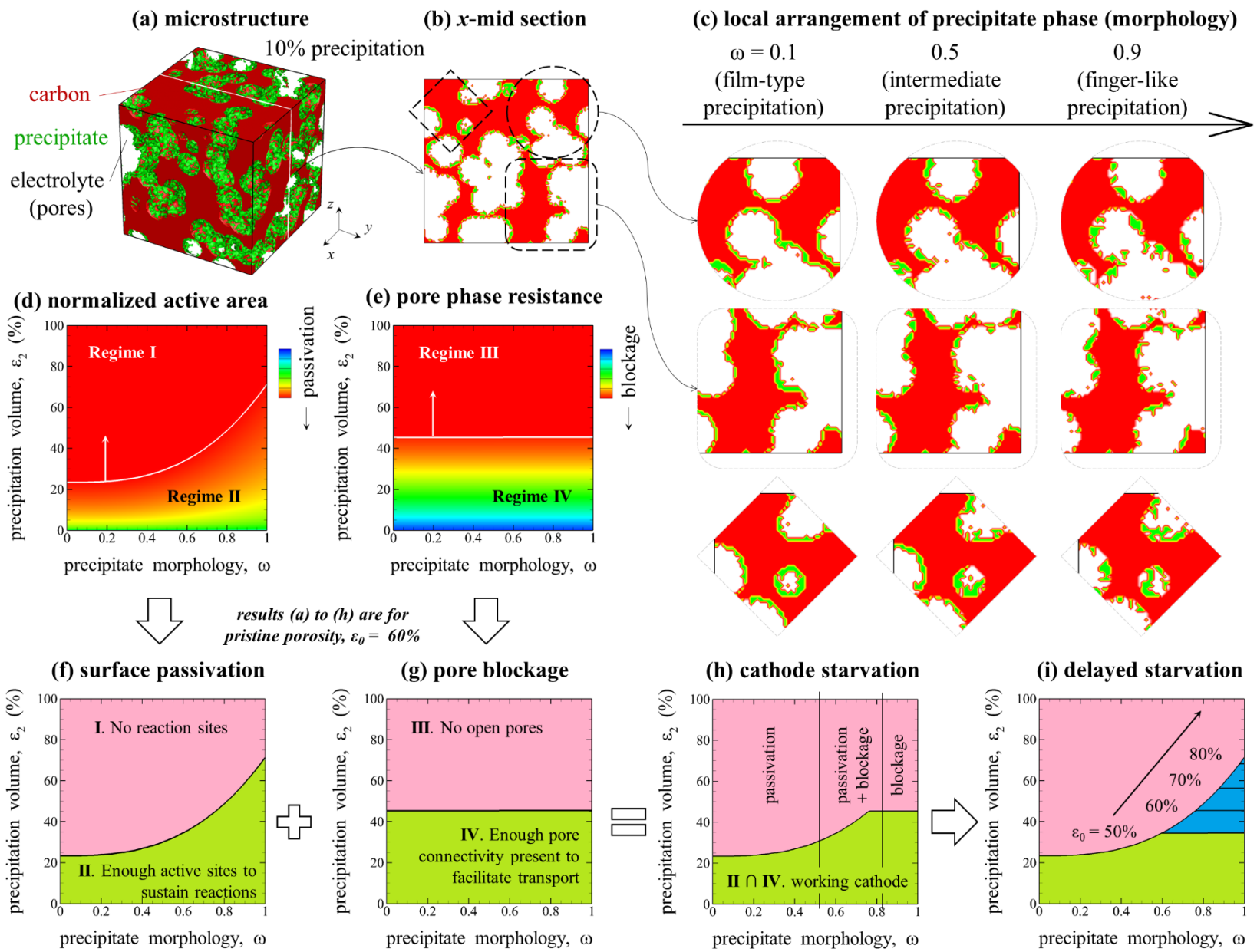
(a) microstructure
10% precipitation
carbon
precipitate
electrolyte (pores)
(b) x-mid section
(c) local arrangement of precipitate phase (morphology)
ω = 0.1 (film-type precipitation)
0.5 (intermediate precipitation)
0.9 (finger-like precipitation)
(d) normalized active area
Regime I
Regime II
← passivation
(e) pore phase resistance
Regime III
Regime IV
← blockage
precipitation volume, ε2 (%)
precipitate morphology, ω
results (a) to (h) are for pristine porosity, ε0 = 60%
(f) surface passivation
I. No reaction sites
II. Enough active sites to sustain reactions
(g) pore blockage
III. No open pores
IV. Enough pore connectivity present to facilitate transport
(h) cathode starvation
passivation
passivation + blockage
blockage
II ∩ IV. working cathode
(i) delayed starvation
ε0 = 50%
60%
70%
80%

Additionally, observe that as the deposition pattern becomes more fractal-like, the distance between neighboring branches also become relevant. At higher precipitation amount and 3D morphology, this also leads to the establishment of a secondary pore network due to non-film like precipitate growth (*e.g.*, Figure 84(c) diamond subzone, upper right corner).

The quality of microstructure generation has been justified earlier[383] *via* a comparison of stochastically generated mesoporous carbon cathodes against scanning electron microscopy (SEM) images (for both pristine carbon structure as well as in the presence of the precipitate phase). Note that the cathode at the start of cell discharge (*i.e.*, the fabricated electrode) is specified by pristine porosity, sulfur loading, mean pore size and precipitation morphology. Based on these specifications each cathode undergoes a distinct sequence of changes upon electrochemical operation. As the electrode experiences precipitation/dissolution changes, microstructural properties such as pore size distribution, interfacial area, pore phase tortuosity *etc.* evolve and are quantified using pore-scale simulations. An interesting aspect of this mesoporous carbon electrode in Li-S is the presence of insulating solid phases (solid sulfur and Li_2S), which alter both interfacial as well as pore phase characteristics. Many different such microstructural realizations are generated with a broad range of microstructural specifications, namely, carbon content (equivalently pristine porosity), precipitation, morphology and pore radius. Each of them is subsequently characterized in terms of effective microstructural properties[9], *i.e.*, specific surface area related to different phase boundaries, pore phase tortuosity and effective electronic conductivity of the solid skeleton (refer to Effective Property Calculations for algorithmic discussion). The results are statistically analyzed[303] and functional relations of these properties are extracted in terms of the above mentioned microstructural specifications (Table 13). Given the presence of three distinct phases (carbon, precipitate, and pore), there are three different two-phase boundaries: carbon-pore, carbon-precipitate, and precipitate-pore interfaces. The distinction between these interfaces is quite important in the context of Li-S cathodes as the precipitate phase is electronically insulating. The electrochemical reactions require the presence of electrons at the solid-electrolyte interface, hence the portion of the pristine carbon-pore interface that gets covered due to precipitate phase cannot sustain electrochemical reactions. With this fact in mind, the carbon-pore area is the essential descriptor of electrochemical activity of the electrode-electrolyte interface and is referred to as electrochemically active area hereafter. Over the dimension of a

representative elementary volume, local pore scale heterogeneities lead to isotropic transport properties (tortuosity and conductivity) if no explicit ordering exists in the microstructure.

Table 13. List of relations expressing effective microstructural properties as a function of precipitation amount, electrolyte porosity, and morphology factor. The corresponding R^2 values, tabulated alongside, justify the usefulness of these expressions.

Property	***Mathematical Relation***	***Coefficient of Determination, R^2***
Active area (carbon – electrolyte interface) [a]	$a_{01} = \left(0.194794 + 4.636493\left(1-\varepsilon_0\right) - 6.299025\left(1-\varepsilon_0\right)^2\right)\cdot \left(1-\left(\frac{\varepsilon_2}{0.247642 + 0.508887\omega^{2.862174}}\right)^{0.171546}\right) \Big/ R_p$	0.985191
Carbon – precipitate area [a]	$a_{12} = \left(0.878506 + 13.103100\left(1-\varepsilon_0\right) - 17.646530\left(1-\varepsilon_0\right)^2\right)\cdot \varepsilon_2\left(2.542701 - 4.502937\varepsilon_2 - 0.135818\omega\right) \Big/ R_p$	0.930318
Precipitate – electrolyte area [a]	$a_{20} = \left(2.484408 + 2.941363\left(1-\varepsilon_0\right) - 3.851792\left(1-\varepsilon_0\right)^2\right)\cdot \varepsilon_2\left(4.412241 - 7.543830\varepsilon_2 + 0.295009\omega\right) \Big/ R_p$	0.965530
Tortuosity	$\tau = \left(0.841432 - \varepsilon_2\left(0.582207 + 0.829378\varepsilon_2 - 0.121772\omega\right)\right)\cdot \varepsilon^{-\left(2.149351 - \varepsilon_2\left(1.936327 - 2.920928\varepsilon_2 + 0.173031\omega\right)\right)}$	0.968584
Conductivity [b]	$\sigma = 1.480809\sigma_0\left(1-\varepsilon_0\right)^{2.130685}$	0.983681
[a] R_p is pore radius [b] σ_0 is electronic conductivity of bulk carbon (16 700 S/m)		

Thence, the pore phase tortuosity and effective electronic conductivity of the solid skeleton in all three coordinate directions exhibit very small dispersion. Note that the expression for the tortuosity variation upon cathode evolution is a power law relation in terms of instantaneous porosity, where the coefficient and exponent are functions of precipitation and its morphology and account for qualitatively different pore space interference resulting from distinct growth patterns. Due to the insulating nature of the precipitating solids, they do not contribute to the effective electronic

conductivity and it (conductivity) stays unchanged upon precipitation. Given the porous nature of electrodes, there are two distinct modes of electron conduction. The electronic conductivity, as understood in the traditional sense, refers to the long-range electron conduction. As cathode has a carbon backbone and carbon is a highly conductive material, even for a structure with only 10% carbon (90% pristine porosity), the long-range electron conduction is quite efficient (revealed by effective conductivity trends, Figure 90). While this long-range conductivity accounts for the presence of percolation pathways across the cathode thickness, electrons should reach efficiently to the electrode-electrolyte interface to facilitate electrochemical redox reactions. This is acknowledged as the short-range electron conduction and is related to the availability of electrochemically active area. During discharging (or charging) this short-range conduction evolves in response to coverage (or exposure) of the pristine carbon surface upon precipitation and/or dissolution.

Figure 84(d) details the evolution of electrochemically active area (normalized with respect to the active area at no precipitation, *i.e.*, pristine structure active area) as precipitation takes place for different precipitation morphologies and 60% pristine porosity. Here morphology axis is identified by ω (morphology factor) values. A 2D film-type precipitation is expected to cover the surface at a smaller precipitation amount compared to 3D finger-like deposits. This feature is apparent from normalized active area contour Figure 84(d). As (normalized) active area approaches zero, the very little carbon-pore surface is available to sustain electrochemical reactions and leads to a sudden increase in kinetic overpotential and subsequent cathode starvation. This phenomenon is commonly known as surface passivation and the two distinct regimes of cathode evolution with (Regime I) and without (Regime II) passivation are specified on a resulting zone map (Figure 84(f)).

The pore phase resistance to species transport is related to the ratio of instantaneous porosity to instantaneous tortuosity, (ε/τ). Note that the pore phase transport resistance evolves in time upon cathode growth. The normalized ratio, *i.e.*, $1 - {}^{(\varepsilon/\tau)}/_{(\varepsilon 0/\tau 0)}$, is equivalently plotted in Figure 84(e) with precipitation and different morphologies, for a cathode with 60% pristine porosity. Note that as (ε/τ) decreases, the cathode constriction worsens and leads to higher transport resistance. As it approaches zero, the pore network locally clogs and stops reactant transport. The critical precipitation for a given morphology that leads to considerable transport resistance is sketched simultaneously in Figure 84(e). The critical precipitation value does not vary strongly with

morphology suggesting a poorer dependence of tortuosity on morphology. The corresponding zone map (Figure 84(g)) outlines the presence of two other regimes (III and IV) for cathode growth.

During cathode evolution, both these resistance buildup mechanisms are simultaneously active and their relative severity determines the cause for cathode starvation at a given state of precipitation and morphology. Consider Figure 84(h) that combines the two zone maps for passivation and pore blockage induced starvation to express overall picture of cathode limitations (II ∩ IV) due to microstructure evolution. On this comprehensive zone map, three distinct evolution patterns can be identified: lower order morphologies lead to surface passivation and higher order morphologies favor pore blockage, while for intermediate ω's, both passivation and blockage jointly decide the fate of cathode. Figure 84(i) demonstrates a similar starvation zone map with variation in pristine cathode porosity. With the increase in cathode pristine porosity, the cathode can accommodate more precipitation before it becomes transport limiting. This delays the critical precipitation amount for pore blockage and subsequently shifts the intersection of passivation and blockage zones (II ∩ IV) towards higher morphologies. Equivalently, this also stretches the extent of joint passivation + blockage starvation. The porosity dependent zone is colored separately (blue) to convey its significance.

6.3 Correlating Microstructure Evolution with Electrochemical Performance

The precipitation growth and microstructure evolution description are unified with a porous electrode theory[22] based formalism to simulate the electrochemical response of Li-S cathodes subject to different operating currents and explore the influence of cathode specifications (details, along with assumptions, are available in Electrochemical Performance Model). Kindly note that the aim of the present investigation is to discern microstructural effects on cell performance. Thence, other limitations are assumed to be absent (*e.g.*, side reactions) and the results report the electrochemical response of a cell having lithium metal anode, porous separator and mesoporous carbon cathode with prescribed specifications. First, consider 1C discharge of two different cathodes with the same pristine porosity (75%) but different sulfur loading and morphologies (Figure 85). From the discussion on cathode limitation (Figure 84(i)), it is expected that for ω = 0.1, the cathode experiences surface passivation, while for ω = 0.9 both passivation and blockage have comparable effects. Two dimensionless descriptors (Eq. (244) and (245)) – passivation quotient ($N_{passivation}$) and blockage quotient ($N_{blockage}$) – are also computed during the course of

calculations to quantitatively identify the cause for termination of cell operation. Figure 85(a) presents the results of cell performance. It is revealed that the cathode with 40% sulfur exhibits a higher capacity despite higher loading. This peculiar trend results from very different precipitation morphology (corresponding local precipitation arrangements are also shown), since a low ω value (here ω = 0.1) leads to faster passivation of the cathode and accordingly limits discharge capacity, while finger-like deposition pattern (ω = 0.9) allows for more precipitation before cathode microstructure resistance increases significantly. The microstructure evolution descriptors, $N_{passivation}$, and $N_{blockage}$ lie in the range [0, 1] with 0 being no and 1 representing extreme starvation:

$$N_{passivation} = 1 - a/a_0 \tag{244}$$

$$N_{blockage} = 1 - (\varepsilon/\tau)/(\varepsilon_0/\tau_0) \tag{245}$$

For the two different cathodes, Figure 85(b) and (c) plot the evolution of these quotients along the cathode thickness as discharge progresses. These quotients express the severity of respective resistive modes and are colored accordingly, where red being extreme starvation. Figure 85(b) reveals that for 20% initial sulfur loading and ω = 0.1, the cathode experiences considerable surface passivation towards the end of discharge. Throughout the cell operation, the cathode has reasonable pore connectivity and volume as revealed from the contour map of the blockage quotient. On the other hand, Figure 85(c) shows that both surface passivation and pore blockage are dominant towards the end of discharge, and leads to cell shutdown. Note that the current density at a prescribed C-rate is directly related to volumetric sulfur loading *via* the following expression:

$$J_{app} = \text{C-rate}\left(\frac{16F\varepsilon_{S_{8(s)}}L_{cat}}{3600\cdot\tilde{V}_{S_{8(s)}}}\right) \propto \varepsilon_{S_{8(s)}} \tag{246}$$

At the start of cell discharge, sulfur is impregnated into carbon structure. A small fraction of that has dissolved in the electrolyte during cell assembly stage and the electrolyte is saturated with dissolved sulfur (*i.e.*, the concentration of dissolved sulfur in the solution phases is equal to the solubility limit of solid sulfur – precipitation/ dissolution equilibrium). As cell discharge starts, dissolved sulfur electrochemically reduces to successively lower order polysulfide ions. Different electrochemical reduction stages (as shown in Figure 83) activate at successively lower voltages (open circuit potentials for respective reactions). Lithium sulfide (Li_2S) starts precipitating as soon as the ionic product $[Li^+]^2[S^{2-}]$ becomes greater than the solubility of the Li_2S salt in electrolyte[109].

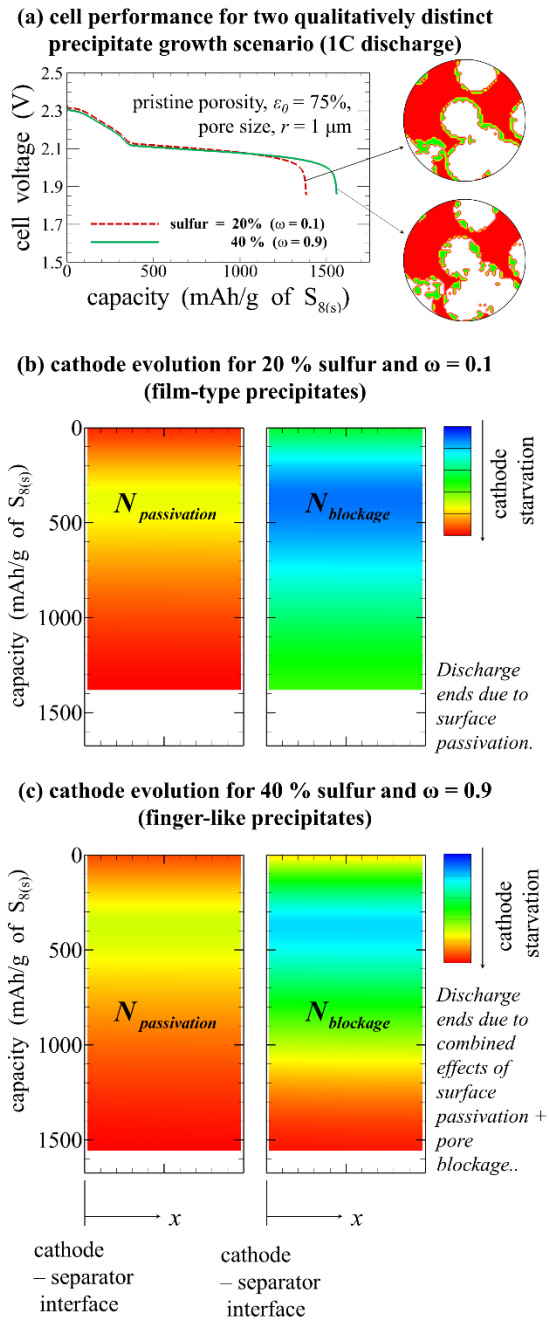

Figure 85. Cell performance (a) and internal resistance build-up (b-c) depend strongly on sulfur loading and precipitation morphology. (b) For film-type precipitation, dominant resistance comes from the electrode-electrolyte interface (*i.e.*, surface passivation). (c) For finger-like deposits, both electrode-electrolyte interfaces, as well as pore network, cause considerable resistance buildup. Cell performance (a) shows that the Li-S cell can be made to operate better at a higher sulfur loading by tweaking the precipitate morphology.

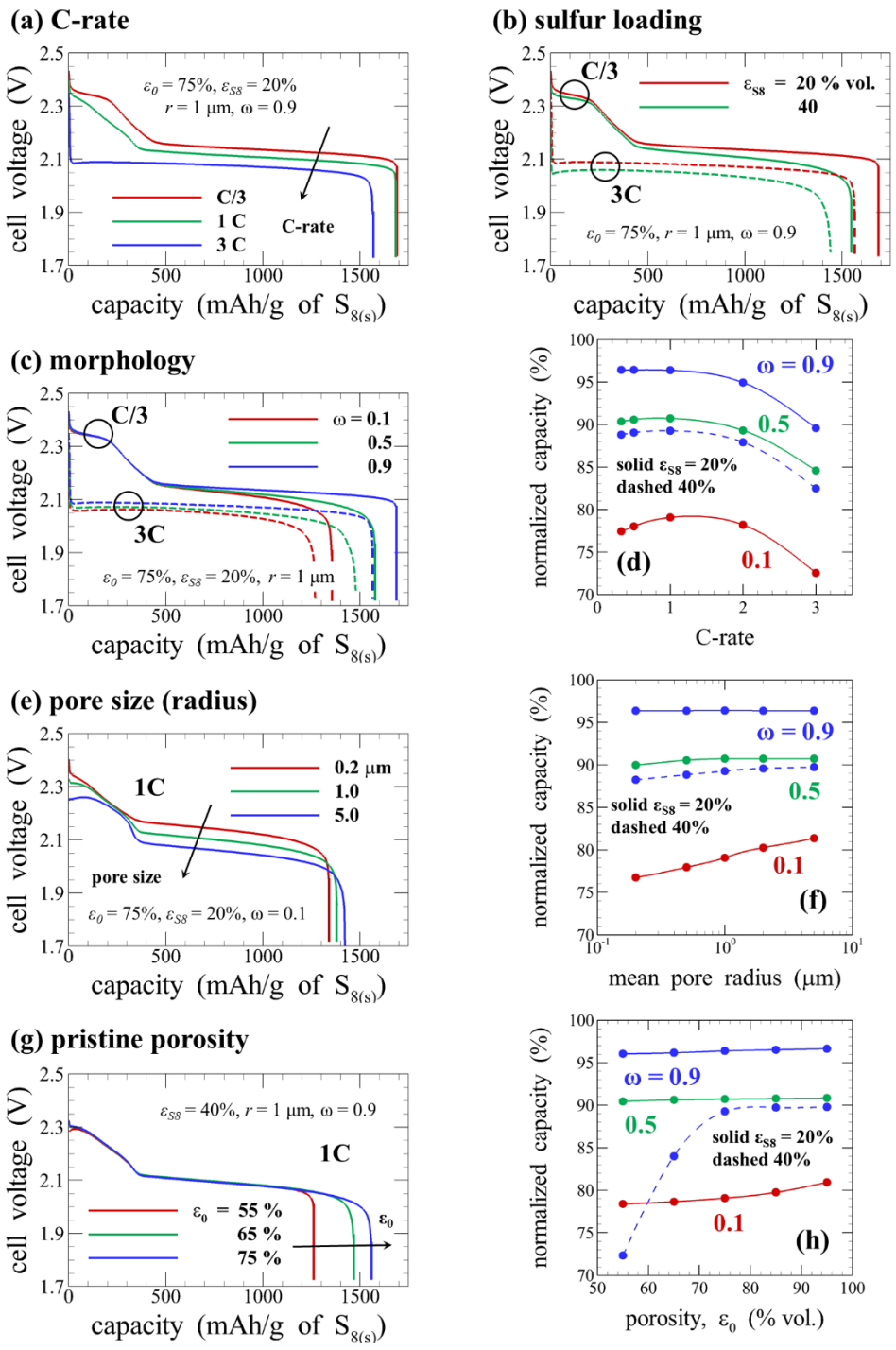

Figure 86. Effect of operating condition (a – discharge rate) and cathode microstructural descriptors (b – sulfur loading, c – precipitate morphology, e – pore size and g – pristine porosity) on discharge performance of Li-S cells. Normalized capacity plots summarize the dependence on (d) C-rate (f) mean pore size and (h) pristine porosity for different sulfur loading and precipitate morphologies.

The cathode evolution throughout the discharge phase, as well as typical distribution of electrochemical reactions across the breadth of the cathode, are shown in Figure 93. Qualitatively, a typical discharge of Li-S has the following three zones:

i. Upper plateau: sulfur dissolution and reduction of high order (longer chain) polysulfides (OCPs for $S_{8(l)}$ to S_8^{2-} and S_8^{2-} to S_6^{2-} are close)
ii. Lower plateau: electrochemical reduction to short chain (low order) sulfides and $Li_2S_{(s)}$ precipitation (OCPs for S_4^{2-} to S_2^{2-} and S_2^{2-} to S^{2-} are close)
iii. Sloping voltage profile joining upper and lower plateau: electrochemical reduction of medium chain polysulfides

Here the word "plateau" does not refer to a completely horizontal voltage profile (zero slopes) but to stages with dV/dQ values considerably smaller than the intermediate portion that joins the two.

Since the net electrochemical reaction rate is externally controlled in terms of applied current density, as C-rate is increased, more and more reduction takes place per unit time. On the other hand, the rates of chemical reactions (sulfur dissolution and $Li_2S_{(s)}$ precipitation) are correlated to reactant concentrations and intrinsic rate constants. This dichotomy leads to interesting cell behavior (Figure 86(a)). For slow discharges, sulfur dissolution and subsequent electrochemical reduction are in synchronization such that the dissolved sulfur amount remains fairly constant till solid sulfur is almost completely consumed. This represents a quasi-equilibrium stage for dissolved sulfur ($S_{8(l)}$) and manifests as the upper voltage plateau on the cell voltage plot. With increasing rates of discharge, the plateau length shortens and eventually disappears, which in turn corresponds to the gradual overlap between more and more number of reactions. In the extreme events, such as 3C (Figure 86(a)), the current demand is very high leading to appreciable overpotential and the cell voltage drops below the open circuit potential for all the electrochemical reactions. This leads to co-existence of all the reactions for the most part of discharge response. The higher is the C-rate, the earlier is the onset of Li_2S precipitation and faster the cathode starvation, and smaller the discharge capacity. This explains the capacity *vs.* C-rate trends in Figure 86(d) where capacity reduces with C-rate for different sulfur loading and most of the precipitate morphologies (except $\omega = 0.1$).

As sulfur loading is increased (Figure 86(b)) for the same pristine cathode, discharge current density increases (Eq. (246)) and cathode resistance buildup is faster as more precipitation takes place for a given time. This amounts to reduced specific cell capacity at a higher sulfur

loading. Moreover, larger plateau slopes correspond to higher resistance buildup. Variations in precipitate morphology (Figure 86(c)) affects the electrochemically active area. Higher ω means a more available active area and in turn higher average cell voltage and larger cell capacity. This strong correlation with ω demonstrates that surface passivation is a dominant resistance buildup mechanism in lithium-sulfur battery operation. For higher sulfur loading (*e.g.*, 40% by vol.) lower morphologies (ω = 0.1 and 0.5, for example) experience very strong surface passivation and correspondingly the cells do not produce appreciable capacity. Hence these data points are not shown in Figure 86(d).

It is a usual belief that as C-rate is lowered, the cell should deliver the theoretical capacity (*i.e.*, in the limit of thermodynamic operation)[22]. Figure 86(d) reveals that in the limit of vanishing C-rate (except ω = 0.1 line), the capacity does stabilize but that limiting value is a strong function of initial sulfur loading and precipitation morphology. This explains (at least in part) why most of the experimental studies could never recover theoretical capacity, even for the first discharge[134, 148, 149, 383-385] and even at very slow rates, *e.g.*, C/50[386]. Now consider the ω = 0.1 line (20% volumetric sulfur loading) where lower rate operation demonstrates a thought-provoking tendency. As C-rate is increased, capacity improves going from low to moderate C-rates. For these film type precipitate morphologies (ω = 0.1), the available interfacial area is much smaller compared to others (ω = 0.5 and 0.9) and leads to higher overpotential (and smaller voltage) for the same C-rate. Going from low to medium C-rate, cell voltage crosses the lower plateau OCPs earlier. Thence the low-order polysulfide reduction reactions trigger earlier and have increasingly greater overlap with medium order polysulfide reduction. As the net reaction current is the same but now divided between medium and low order polysulfide electrochemical reactions, each of them progresses slower than their successive scheme. Physically, this reduces the rate of $Li_2S_{(s)}$ precipitation and prolongs the discharge, effectively increasing discharge capacity. From moderate to higher rates, both $S_{8(s)}$ and $Li_2S_{(s)}$ coexist and lead to earlier cathode shutdown at increasingly higher rates. To summarize these two events: overlap between medium and low order polysulfide electrochemical reactions reduces the rate of Li_2S production and increases cell capacity (lower – to – medium C-rates), while at higher rates both $S_{8(s)}$ and $Li_2S_{(s)}$ coexist at cathode leading to higher electrode resistance and reduced capacity. The first sequence of events (co-reduction of medium and lower order polysulfides) rely on the smaller electrochemically active area, while the second

set (co-existence of $S_{8(s)}$ and $Li_2S_{(s)}$) depends on the onset of Li_2S precipitation before the entire $S_{8(s)}$ inventory has dissolved in the electrolyte.

The electrochemically active area is strongly influenced by two factors: precipitate morphology and mean pore size. The area also reduces as pore size increases and leads to co-reduction of medium and lower order polysulfides and subsequently higher cell capacity with increasing pore size (Figure 86(e)). As ω is increased, the available area increases and this pore size dependence becomes weaker as displayed in Figure 86(f) where going from ω = 0.1 to 0.9, this dependence on mean pore size diminishes. As pore dimensions are reduced, the number of pores per unit volume (number density) increases. Thence, for the same amount of precipitation, pore volume reduction remains the same and does not considerably change the tortuosity of the pore network or pore phase transport resistance.

The transport resistance of the pore network becomes more and more limiting as precipitates become more finger-like in nature (*i.e.*, $\omega \rightarrow 1$). For such a cathode, increasing pristine porosity improves cell capacity by reducing net electrode resistance (Figure 84(i)). Figure 86(g) examines the effect of pristine porosity on cell operation for different pristine cathode structures, 40% volumetric sulfur loading (high) and finger-like precipitation (ω = 0.9). These voltage lines demonstrate the importance of cathode pristine porosity. As for more film type morphologies (ω = 0.1 and 0.5) and lower sulfur loading (*e.g.*, 20%), the primary resistance build-up mechanism is surface passivation, capacity improvement is not so strong.

With these individual tests (Figure 86), sulfur loading, pristine porosity, and precipitate morphology are identified as the three most important microstructural descriptors for Li-S cathodes. The dependence of cell capacity on these three is summarized in Figure 87 based on a large number of simulations. Sulfur loading is expressed as sulfur – to – electrolyte ratio (S/E), given its more practical usefulness. For a given pristine porosity, controlling the precipitation morphology remarkably affects cell performance. More importantly, if morphology is varied from a film-type to finger-like, S/E ratio can be increased up to four times keeping the same electrode porosity. This is helpful as practical Li-S batteries are to have as high sulfur content as possible. Secondly, as pristine porosity (ε_0) is increased, S/E ratio should be decreased to maintain similar capacities, as S/E ratio is inversely related to pristine porosity (consider Eq. (247)). The results in Figure 87 are all for 1C discharge.

$$S/E = \rho_{S_8} \frac{\varepsilon_{S_{8(s)}}}{\left(\varepsilon_0 - \varepsilon_{S_{8(s)}}\right)} \tag{247}$$

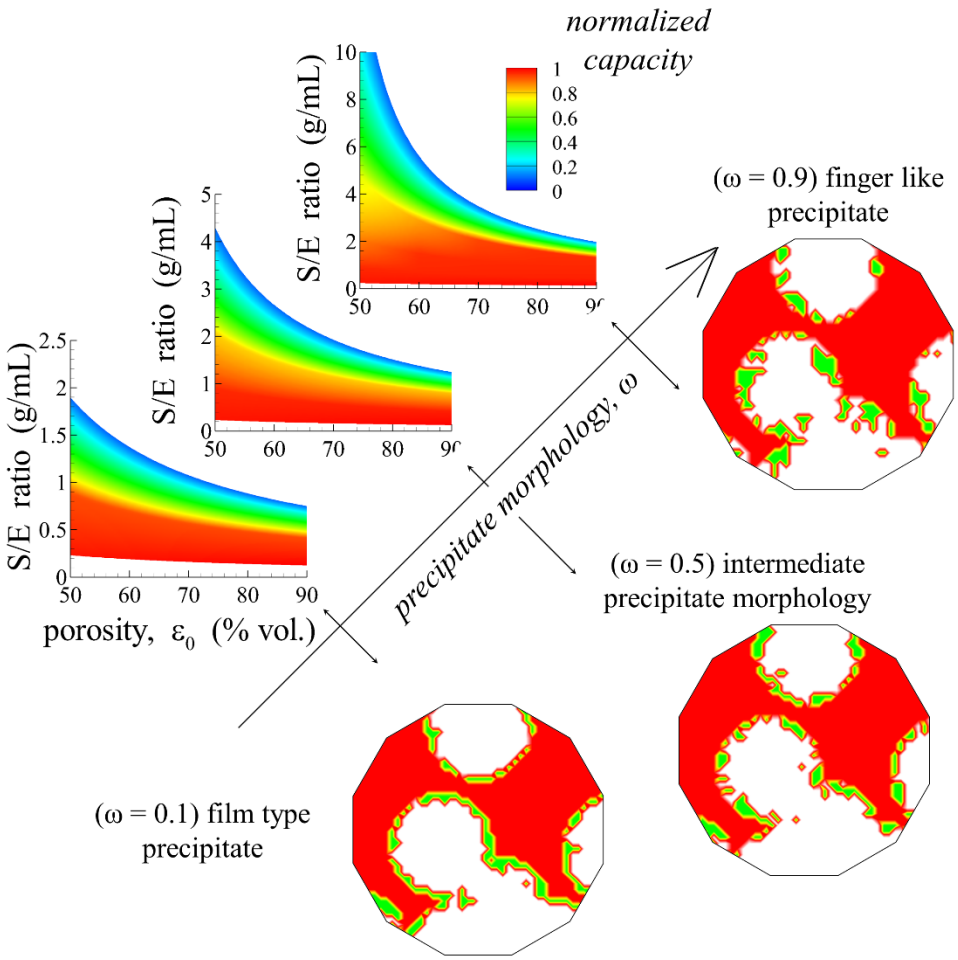

Figure 87. Performance of Li-S cells strongly relies on three cathode microstructural descriptors (i) S/E ratio (ii) pristine porosity and (iii) precipitate morphology. The contour plots describe normalized cell capacities for 1C operation.

In conclusion, the electrochemical performance of Li-S cells is a strong function of the cathode microstructure. Dominant microstructural limitations are (i) surface passivation and (ii) pore blockage. These cathode microstructural limitations in part account for less than theoretical first discharge capacity observed experimentally. The microstructure growth pattern varies based on precipitation morphology, leads to different resistance build-ups due to either of these mechanisms and in turn, produces distinct cell performance trends. For example, changing electrode porosity is most helpful when precipitation takes place in a finger-like fashion. If the precipitation is film-

type (large thin islands), altering the precipitate morphology towards finger-like geometry is quite more beneficial compared to electrode porosity or pore size modifications. S/E ratio, cathode porosity, and precipitate morphology are three microstructural descriptors having the strongest influence on cell performance.

6.4 Microstructure Generation

A mesoporous carbon structure is specified in terms of pore dimension and porosity. The precipitation takes place at either carbon/ pore interface or pre-deposited precipitation/ pore interface. The relative tendency to deposit on either of these interfaces determines the resulting precipitate structure.

Before going into the details of the microstructure generation, it is important to identify three distinct length scales associated with this type of microstructure:

i. Pore dimension, R_p
ii. Representative elementary volume, $\mathcal{L}$
iii. Spatial resolution, Δx

The representative elementary volume (REV) size ensures that the structure can be represented in terms of effective properties (data abstraction), while spatial resolution dictates the level of details present in the structure.

The precipitate addition routine starts with a (pristine) mesoporous carbon structure having prescribed pore radius, R_p, and pristine porosity, ε_0 (refer to Figure 88 for schematic details). Next all the interfacial locations (carbon/ pore and precipitation/ pore) are identified. At each of these locations, deposition energy is computed as per the following formula:

$$e_i = \frac{(1-\omega)}{6} N_{carbon} + \frac{\omega}{6} N_{precipitate} \tag{248}$$

Here N_{carbon} is the number of carbon neighbors to the interfacial site, $N_{precipitate}$ the number of precipitate neighbors to the interfacial site, ω controls precipitation structure (referred to as morphology factor elsewhere). As in three-dimensions, each grid cell has 6 neighbors, expression (248) has 6 in the denominator to ensure that deposition energy e_i always stays between 0 and 1. Multiple realizations are generated and characterized corresponding to a different porosity of pristine (mesoporous) structure, precipitation amount, and morphology.

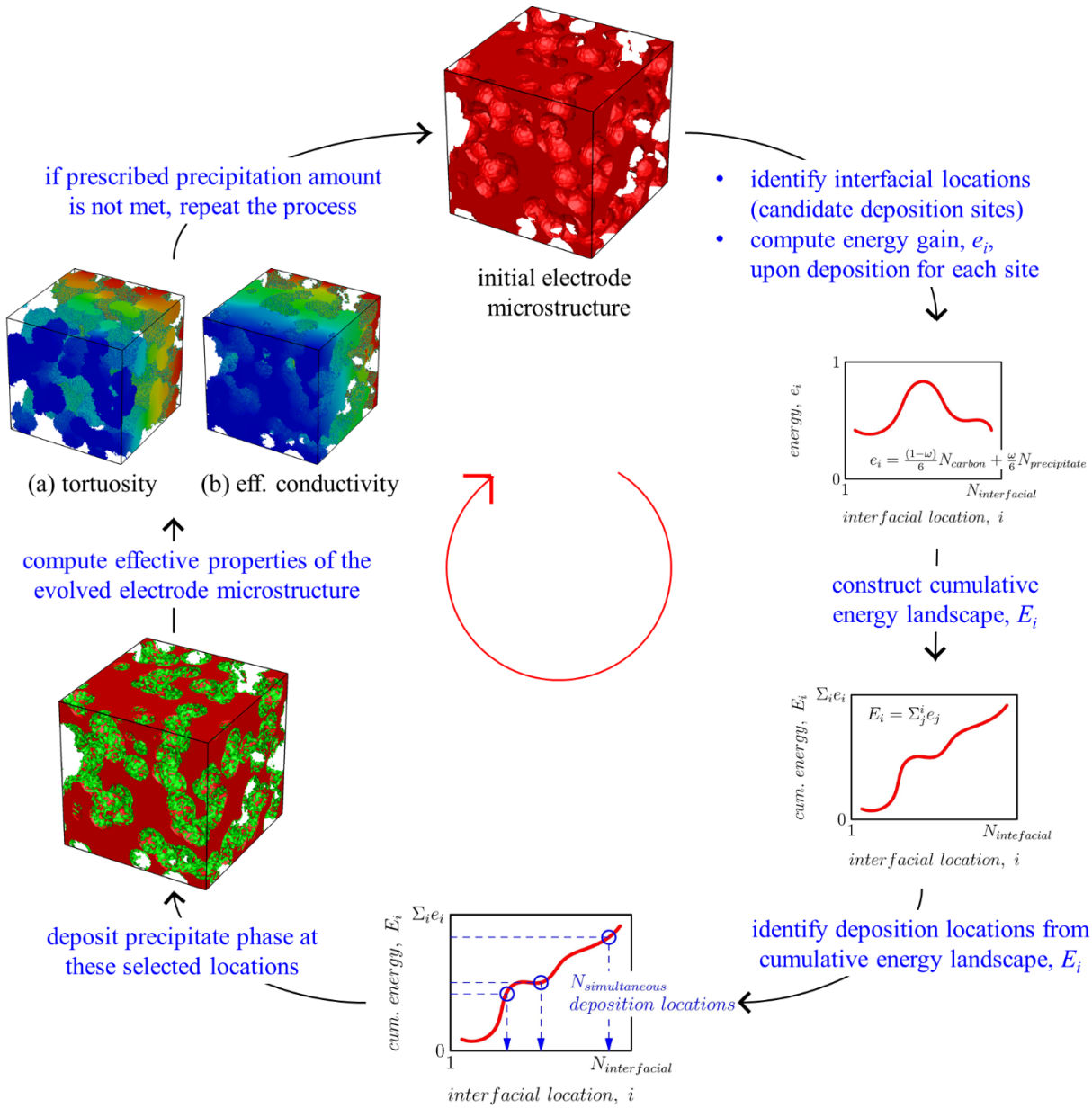

Figure 88. The growth of cathode microstructure due to precipitation is studied *via* generation of representative electrode volumes, sequential precipitation addition and subsequent characterization of resultant grown structures. The morphology of precipitate addition is factored in by using energy based deposition involving surface affinity (in a coarse-grained fashion).

Once the deposition energy is computed for each of the interfacial locations ($N_{intefacial}$ in total), a cumulative energy map is generated to consistently identify deposition locations ($N_{simultaneous}$). The resulting structure is characterized in terms of multiple different microstructural properties:

i. Carbon/ pore interfacial area

ii. Carbon/ precipitate interfacial area
iii. Precipitate/ pore interfacial area
iv. Tortuosity in three coordinate directions
v. Effective electronic conductivity in three coordinate directions

The cycle repeats until a prescribed amount of precipitation takes place in the pore network and at each cycle, all the effective properties are computed and stored. The realism of such structures has been justified earlier[383].

It is important to mention that the independence tests are performed before hand to ensure that the structures have sufficient spatial resolution to capture the relevant structural details and the simulation domain is large enough to qualify for porous electrode approximation. Moreover, multiple structures are generated for the same specifications to ensure that the predictions are statistically meaningful, given the stochastic component in the microstructure generation. To reiterate, different microstructural specifications are (i) pristine porosity (ii) precipitation volume fraction (iii) morphology factor, ω, and (iv) pore radius.

6.5 Effective Property Calculations

Tortuosity represents the resistance offered by the pore phase to solute transport in fluid stored in the pore network. Tortuosity is a direction dependent property and is computed for all the three coordinate directions in the present set of simulations. As the microstructure is isotropic, the tortuosity values do not exhibit considerable directional dependence and would only marginally vary in response to stochasticity associated with the structure generation.

To compute tortuosity[9] in, say *x*-direction, concentrations are fixed at the two ends, one at low and another at a high value to ensure net solute transport in the same direction. Neumann boundary conditions are maintained at other four faces (in parallel to the direction of interest) to ensure that solute flux entering from one face completely leaves through the opposite face and does not leak out through sides. To put it mathematically, for tortuosity simulation in the *x*-direction, the following boundary conditions are employed (here *n* is local surface normal):

$$C = 1 \text{ at } x = x_{left} \tag{249}$$

$$C = 0 \text{ at } x = x_{right} \tag{250}$$

$$\partial C / \partial n = 0 \text{ at other four planes} \tag{251}$$

$$\partial C / \partial n = 0 \text{ at pore – solid interface} \tag{252}$$

The steady state concentration balance is solved in the pore phase:

$$\nabla \cdot \left(\mathcal{D} \nabla C \right) = 0 \tag{253}$$

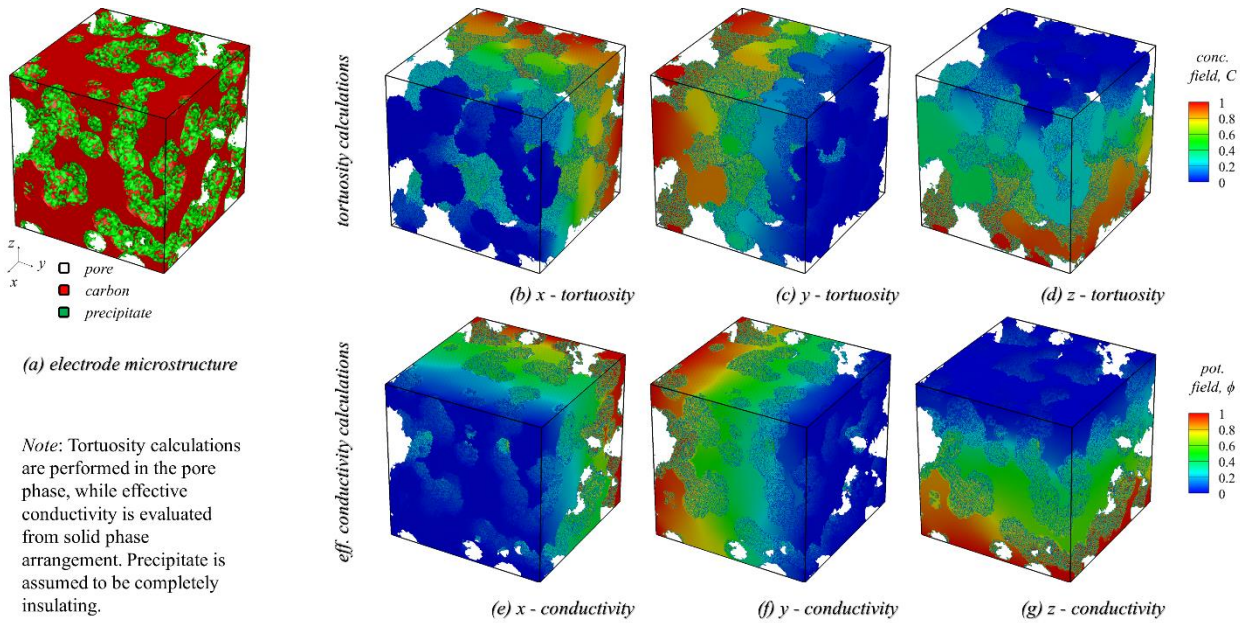

Figure 89. Computations for effective microstructural properties are performed at pore scale (Direct Numerical Simulation) with both local resolutions as well as computational domain size to be sufficient enough to produce statistically meaningful results, thus ensuring the validity of porous electrode approximation. (a) Representative microstructure with 60% pristine porosity, 10% precipitate growth at ω = 0.5. (b-d) represent concentration profiles (solution) in the pore phase used to evaluate tortuosity in each of the coordinate directions. Similarly, (e-g) present potential field (solution) in the solid phase used to evaluate effective electronic conductivity in respective coordinate directions.

The governing equation (253) along with the set of boundary conditions (249) to (251) and interface conditions (252) is solved in a Finite Volume framework. Here $\mathcal{D}$ is the bulk diffusivity in the solution phase. Once the solution field, *i.e.*, concentration C, is available, the following expression is utilized to back compute the tortuosity in the *x*-direction, where except tortuosity every other term is available from a solution of governing equation (253).

$$-\mathcal{D} \frac{\varepsilon}{\tau_x} \left(\frac{C\left(x_{right}\right) - C\left(x_{left}\right)}{x_{right} - x_{left}} \right) = - \int_{x = x_{left} \text{ plane}} \mathcal{D} \frac{\partial C}{\partial x} \, \mathrm{dydz} = - \int_{x = x_{right} \text{ plane}} \mathcal{D} \frac{\partial C}{\partial x} \, \mathrm{dydz} \tag{254}$$

Similar simulations are performed by appropriately setting the boundary conditions to compute τ_y and τ_z.

The calculations for effective conductivity are performed in a similar fashion. Instead of concentration balance, the governing equation dictates the conservation of charge. The conductivity of the precipitate phase and pore phase is set to zero. The boundary and interface conditions for effective conductivity simulation in the *x*-direction are as follows:

$$\phi = 1 \text{ at } x = x_{left} \tag{255}$$

$$\phi = 0 \text{ at } x = x_{right} \tag{256}$$

$$\partial\phi / \partial n = 0 \text{ at other four planes} \tag{257}$$

$$\partial\phi / \partial n = 0 \text{ at carbon – pore and carbon - precipitate interfaces} \tag{258}$$

And appropriate governing equation:

$$\nabla \cdot \left(\sigma \nabla \phi \right) = 0 \tag{259}$$

Here σ is a bulk conductivity of different solid phases. Once the potential field solution subject to boundary and interface conditions (255) – (258) is available, the effective electronic conductivity in the *x*-direction is computed *via* the following equivalence relation:

$$-\sigma_x^{eff} \left(\frac{\phi\left(x_{right}\right) - \phi\left(x_{left}\right)}{x_{right} - x_{left}} \right) = -\int_{x_{left}} \sigma \frac{\partial \phi}{\partial x} \, \mathrm{d}y\mathrm{d}z = -\int_{x_{right}} \sigma \frac{\partial \phi}{\partial x} \, \mathrm{d}y\mathrm{d}z \tag{260}$$

Similarly, potential field solutions are computed by appropriately setting boundary conditions in *y* and *z* coordinate direction. As the conductivity of the precipitate phase is zero (insulating phase), the effective conductivity will not be influenced by precipitation (both amount as well as morphology). Moreover, keep in mind that this refers only to the long-range conductivity, *i.e.*, availability of the electrons in the electrode. Thus, the effective conductivity will only vary with the amount of carbon (and equivalently with pristine porosity). The conductivity variation is plotted in Figure 90, for a typical Li-S mesoporous carbon cathode. Minimum conductivity on Figure 90 is ~ 2 S/cm, much higher than ionic conductivity in the electrolyte phase. Thus, the cathode structures will not have any transport limitations arising from long-range electron conduction. The effective property estimations are statistically analyzed and functional relations are constructed based on the porous electrode microstructural attributes, as summarized in Table 13.

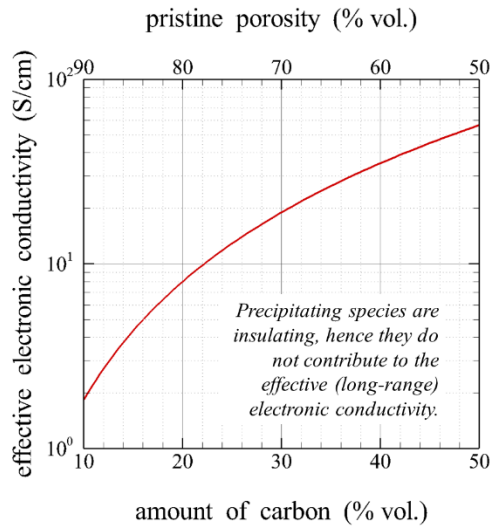

Figure 90. Effective electronic conductivity of a mesoporous carbon structure decreases as carbon content reduces. For a typical Li-S cathode, pristine porosity is between 50 and 90%, which corresponds to the range 10 – 50% carbon by volume.

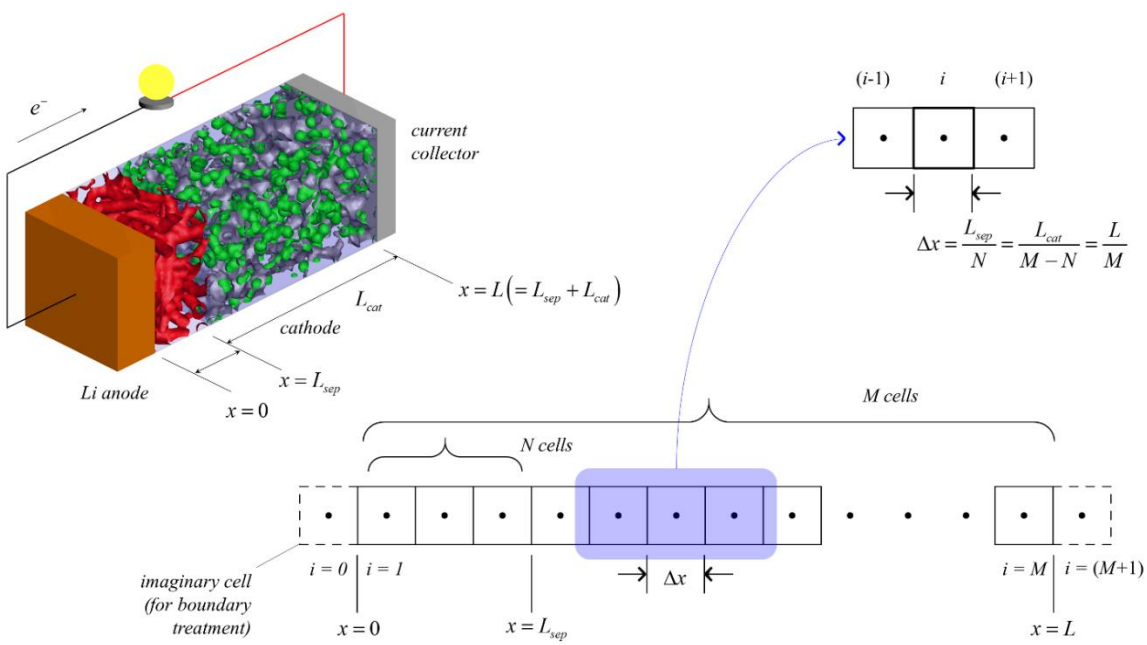

Figure 91. A schematic illustration of the computational domain is shown along with the battery diagram to explain the identification of different cell components on the discrete space. The domain is discretized into consecutive cells of width Δx to suit solution in a Finite Volume fashion. An ith cell is separately identified along with its neighbors – east neighbor (i+1) and west neighbor (i-1), to facilitate the development of algebraic equations amenable to numerical solution.

6.6 Electrochemical Performance Model

The electrochemical performance of the Li-S cathode is modeled using porous electrode theory[1, 22], where the microstructure growth is accounted for in terms of the evolution of effective properties as obtained from microstructure growth studies described in sections Microstructure Generation and Effective Property Calculations. Multiple transport processes take place in a Li-S cathode: species transport in the electrolyte phase, ionic charge conservation, species balance in solid phase and electronic charge conservation. The governing equations for these phenomena are as follows:

<u>*Species balance in electrolyte phase*</u>:

$$\frac{\partial}{\partial t}\left(\varepsilon C_j\right)=\frac{\partial}{\partial x}\left(\mathcal{D}_j\frac{\varepsilon}{\tau}\frac{\partial C_j}{\partial x}\right)+\frac{\partial}{\partial x}\left(z_jF\frac{\mathcal{D}_j}{\mathcal{R}T}C_j\frac{\varepsilon}{\tau}\frac{\partial\phi_e}{\partial x}\right)+R_j \tag{261}$$

where 'j' is species index and corresponds to $S_{8(l)}, S_8^{2-}, S_6^{2-}, S_4^{2-}, S_2^{2-}, S^{2-}$ and A^- (A^- is anion from primary salt)

<u>*Conservation of ionic charge*</u>:

$$\frac{\partial}{\partial x}\left(\left\{\sum_j z_j^2F^2\frac{\mathcal{D}_j}{\mathcal{R}T}C_j\frac{\varepsilon}{\tau}\right\}\frac{\partial\phi_e}{\partial x}\right)+\sum_j\left\{\frac{\partial}{\partial x}\left(z_jF\mathcal{D}_j\frac{\varepsilon}{\tau}\frac{\partial C_j}{\partial x}\right)\right\}+\sum_k aI_k=0 \tag{262}$$

where 'k' represents individual electrochemical reactions

<u>*Species balance in solid phase*</u>:

$$\frac{\partial\varepsilon_m}{\partial t}=Q_m \tag{263}$$

where 'm' is an index for solid phase species $S_{8(s)}$ and $Li_2S_{(s)}$

<u>*Conservation of electronic charge*</u>:

$$\sigma^{eff}\frac{\partial^2\phi_c}{\partial x^2}=\sum_k aI_k \tag{264}$$

The definition of various symbols is presented in the Nomenclature. Note that the term ε/τ in electrolyte phase transport signifies pore phase transport resistance, while σ^{eff} is related to the resistance offered to electron transport by the solid phase of the cathode (inverse of σ^{eff} is effective resistivity). The active area, a, appearing in source terms is electrochemically active area and it reduces as more precipitates form during discharge (or charge). Also note that the first curly bracketed term in equation (262) is the effective ionic conductivity, while the second summation accounts for diffusional conductivity due to different ions present in the solution phase (electrolyte). In other words, the first term accounts for a migrational component of the ionic current, while the second term describes the diffusional part.

The reaction pathway is assumed to consist of the following set of electrochemical and chemical reactions[127], with the forward direction being the same as observed during a discharge operation.

Electrochemical reactions:

$$\frac{1}{2}S_{8(l)} + e^- \underset{\text{charge}}{\overset{\text{discharge}}{\rightleftharpoons}} \frac{1}{2}S_8^{2-} \tag{265}$$

$$\frac{3}{2}S_8^{2-} + e^- \underset{\text{charge}}{\overset{\text{discharge}}{\rightleftharpoons}} 2S_6^{2-} \tag{266}$$

$$S_6^{2-} + e^- \underset{\text{charge}}{\overset{\text{discharge}}{\rightleftharpoons}} \frac{3}{2}S_4^{2-} \tag{267}$$

$$\frac{1}{2}S_4^{2-} + e^- \underset{\text{charge}}{\overset{\text{discharge}}{\rightleftharpoons}} S_2^{2-} \tag{268}$$

$$\frac{1}{2}S_2^{2-} + e^- \underset{\text{charge}}{\overset{\text{discharge}}{\rightleftharpoons}} S^{2-} \tag{269}$$

Chemical reactions:

$$S_{8(s)} \underset{\text{precipitation}}{\overset{\text{dissolution}}{\rightleftharpoons}} S_{8(l)} \tag{270}$$

$$2Li^+ + S^{2-} \underset{\text{dissolution}}{\overset{\text{precipitation}}{\rightleftharpoons}} Li_2S_{(s)} \tag{271}$$

For an electrochemical simulation, the above set of governing equations (261) to (264) have to be (numerically) solved using an appropriate set of boundary and initial conditions. During a constant current discharge, discharge current density is computed based on C-rate, sulfur loading and cathode thickness as per the expression:

$$J_{app} = \text{C-rate}\left(\frac{16F\varepsilon_{S_{8(s)}}L_{cat}}{3600\cdot\tilde{V}_{S_{8(s)}}}\right) \tag{272}$$

At all times during an electrochemical operation, the total electrochemical reaction in cathode must always be equal to applied current density (since local charge neutrality is always ensured). Mathematically, this physics is expressed as:

$$J_{app} = -\int_{L_{cat}}\left(\sum_k aI_k\right)\mathrm{d}x \tag{273}$$

Here negative sign signifies that during discharge cathode undergoes electrochemical reduction. The equality does not change for the charging operation, rather signs of applied current density and electrochemical reactions switch, while still maintaining the same identity. Expression (273) poses an interesting point: during the rest period, the applied current is zero but that does not necessarily mean that all the individual reaction rates are zero. Initially, there is expected to be a time interval that corresponds to non-zero electrochemical reaction rates such that the net as per

expression (273) is zero. At larger times, all the rates equilibrate and the cathode approaches electrochemical equilibrium.

Table 14. Boundary conditions used for the electrochemical simulation of Li-S cell discharge.

Equation	***Anode – separator boundary (x=0)***	***Separator – cathode boundary (x=L_{sep})***	***Cathode – current collector boundary (x=L_{sep}+L_{cat})***
Li^+ species balance	$-\mathcal{D}_j \frac{\varepsilon}{\tau}\frac{\partial C_j}{\partial x} = J_{app}/F$	flux continuity	$\frac{\partial C_j}{\partial x} = 0$
Other species balance	$\frac{\partial C_j}{\partial x} = 0$	flux continuity	$\frac{\partial C_j}{\partial x} = 0$
Electrolyte phase potential	$\frac{\partial \phi_e}{\partial x} = 0$	flux continuity	$\frac{\partial \phi_e}{\partial x} = 0 \ (\text{or } \phi_e = 0)$*
Solid phase potential	not applicable	$\frac{\partial \phi_c}{\partial x} = 0$	$-\sigma^{eff}\frac{\partial \phi_c}{\partial x} = J_{app}$

** to ensure a solution, explained in the text*

The set of boundary conditions are specified in Table 14. As separator is electronically insulating, the solid phase potential equation (264) is not solved in separator domain. Physically, at any time instant, J_{app} amount of flux enters at anode – separator interface as an ionic flux of Li^+, manifests as the ionic current through the separator and gradually converts to an electronic current in the cathode. At cathode – current collector interface, the outgoing current is completely electronic in nature. At any cross-section in the cathode, the summation of ionic and electronic currents is the same as applied current density, J_{app}. This ensures the overall charge conservation as well as global and local charge neutrality.

The mathematical nature of these governing equations is quite interesting. The species balance equations are parabolic partial differential equations, while the charge conservation statements are elliptic partial differential equations with non-linear source terms (non-linear Poisson equation). From a physical point of view, all the boundary conditions are Neumann type, but this constitutes an ill-posed problem given the elliptical equations[204, 387]. The existence of a solution to this set of governing equations requires that at least one of the boundary conditions is of Dirichlet (or mixed) type. To ensure this, electrolyte potential is set to zero at cathode – current collector boundary condition while solving the set of governing equations. This still ensures

physical consistency as the electrolyte and cathode potential equations are related *via* the same source term. This source term ensures that equal amount of charge is subtracted from the electrolyte phase and added to the solid phase (and vice versa). Additionally, total ionic current entering at anode – current collector boundary:

$$J_{ionic} = -\left\{ \sum_j z_j^2 F^2 \frac{\mathcal{D}_j}{\mathcal{R}T} C_j \frac{\varepsilon}{\tau} \right\} \frac{\partial \phi_e}{\partial x} - \sum_j z_j F \mathcal{D}_j \frac{\varepsilon}{\tau} \frac{\partial C_j}{\partial x} = J_{app} \tag{274}$$

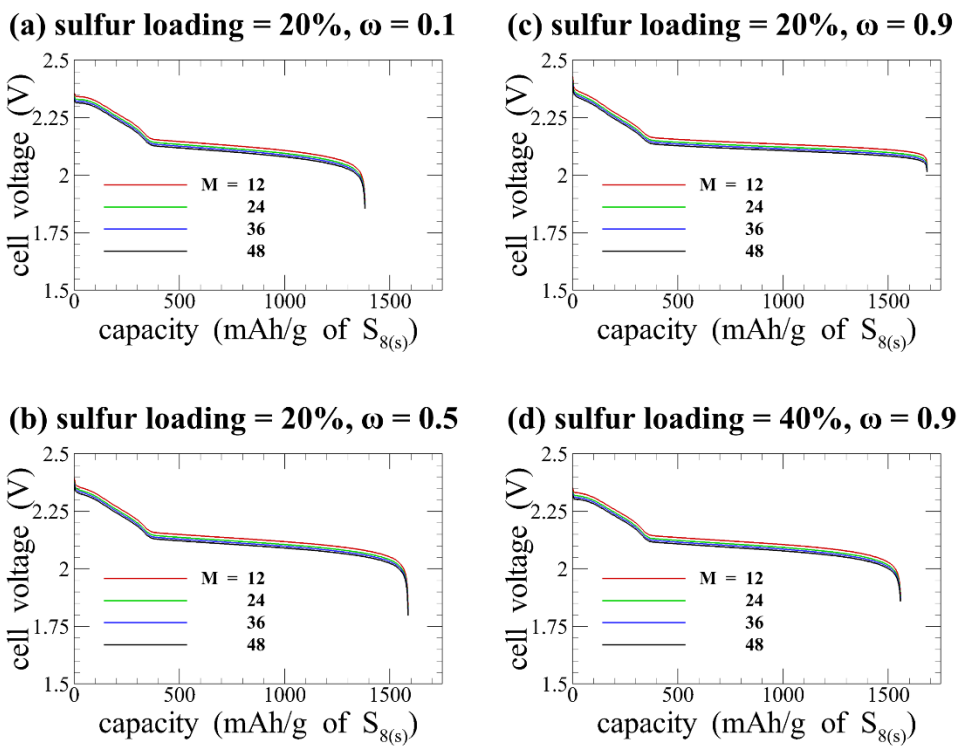

Figure 92. Results of grid independence test performed at different sulfur loading and precipitate morphology (pristine porosity = 75%, 1 μm pore radius, 50 μm thick cathode operated at 1C) prove that M = 36 is a suitable choice of discretization without sacrificing accuracy or substantially increasing computational time.

The numerical solution of this set of governing equations is sought in a Finite volume fashion as it intuitively ensures conservation[388]. The meshing details are presented in Figure 91. There are a couple of subtle points that make the solution of these governing equations challenging.

i. The porosity of the cathode evolves locally and it should be appropriately integrated in time. The time derivative term in species balance $\partial(\varepsilon C_j)/\partial t$ should be directly discretized

without employing chain rule. If chain rule is applied, it gives misleading answers and affects sulfur conservation.

ii. Most of the sulfur species concentrations go to zero at some point during discharge. If an explicit time discretization is employed, the variable time step would have to be used to ensure that the concentrations never become negative. A better approach is to use implicit time discretization. This alleviates the need for variable time step and improves solution time considerably at the cost of a more complex algorithm[389].

It has been found while dealing with numerical complexities, that for an accurate solver total sulfur must be conserved. Physically, sulfur does not leave the cell, but only changes its form. Thence if sulfur in various forms is stoichiometrically summed up, it should give the same amount. The following expression quantifies the total sulfur presence:

$$S = \int_L \left\{ \frac{\varepsilon_{S_{8(s)}}}{\tilde{V}_{S_{8(s)}}} + \varepsilon C_{S_{8(l)}} + \varepsilon C_{S_8^{2-}} + \frac{3}{4}\varepsilon C_{S_6^{2-}} + \frac{1}{2}\varepsilon C_{S_4^{2-}} + \frac{1}{4}\varepsilon C_{S_2^{2-}} + \frac{1}{8}\varepsilon C_{S^{2-}} + \frac{1}{8}\frac{\varepsilon_{Li_2S_{(s)}}}{\tilde{V}_{Li_2S_{(s)}}} \right\} \mathrm{d}x \qquad (275)$$

A physically reasonable simulation gives the constant value of S at every time step. Note that if care has not been taken while integrating through variable porosity or when polysulfide species approach zero concentration, total sulfur amount S changes substantially, giving a false impression of capacity decay. The in-house numerical solver developed by the authors ensures both physically as well as the mathematically consistent solution of the set of governing equations. Simulation results presented in the manuscript are for a fine enough grid. The grid selection is based on grid independence test results presented in Figure 92. The kinetic and transport parameters are adopted from Kumaresan *et al.*[127].

Figure 93 illustrates different chemical and physical changes taking place inside a lithium-sulfur cell during a typical first discharge. The cell performance (voltage *vs.* capacity Figure 93(a)) exhibits an upper and a lower plateau which corresponds to the presence of phase change reactions (sulfur dissolution and $Li_2S_{(s)}$ precipitation, respectively). In response to these physical changes in the form of sulfur, the cathode microstructure grows over time (Figure 93(b)). Such a microstructural growth, in turn, leads to building up of different kinds of cell resistances (Figure 93(c)).

As time-varying solid species ($S_{8(s)}$ and $Li_2S_{(s)}$) are electronically insulating, they lead to changes in coverage of the electrochemically active area and manifests as additional resistance at the electrode-electrolyte interface. Alternatively, these solid products could also lead to local

clogging of pore network (responsible for electrolyte phase transport) and bring in transport resistance. Such physical changes are accompanied by changes in the chemical nature of the sulfur. Sulfur molecule (S_8) successively reduces into smaller and smaller sized polysulfide chains *via* electrochemical reactions. The relative intensities of these reactions (Figure 93(d)) depend on species concentrations, available electrochemically active area, and current flow. As is revealed by the spatiotemporal distribution of different cell reactions, the early part (upper plateau) is dominated by sulfur and higher chain polysulfide reduction. The medium chain polysulfides actively participate where cell voltage gradually reduces to lower plateau, while the lower plateau is dominant by electrochemical reactions of low order sulfides.

6.6.1 Discussion on model assumptions

The description of electrochemical behavior presented here relies on the following assumptions, all of which help isolate the microstructural limitations:

i. Electrolyte phase species transport can be described by Nernst-Planck relation[22]. In other words, the dilute solution theory is assumed for electrolyte transport. The dilute solution theory overpredicts the ionic conductivity (in contradiction to the concentrated solution theory based description[22]).

ii. No side reactions such as chemical redox are assumed. Thence, the simulated cell voltage and capacity are a result of cathode microstructure limitations and the trends are not contaminated due to additional processes such as disproportionation of precipitation of lithium polysulfide salts, *etc.*

iii. The cell is composed of Li metal anode, typical separator, and mesoporous carbon cathode. Special components or treatment that are directed at polysulfide trapping are not considered here as they are often not commercially viable and/or lead to marginal gains[390]. Also, note that the presence of additional components reduces the overall energy and power densities. Mesoporous carbon backbone is chosen due to its commercial viability.

To summarize it all, the simulations are set up such that the results ensure physical consistency (related to the accuracy of sulfur conservation) and the observed performance trends are purely due to cathode microstructural effects (material effects such as concentrated solution theory or the presence of additional materials and interfacial coatings are excluded). Such an investigation leads to meaningful insights into the importance of microstructural effects.

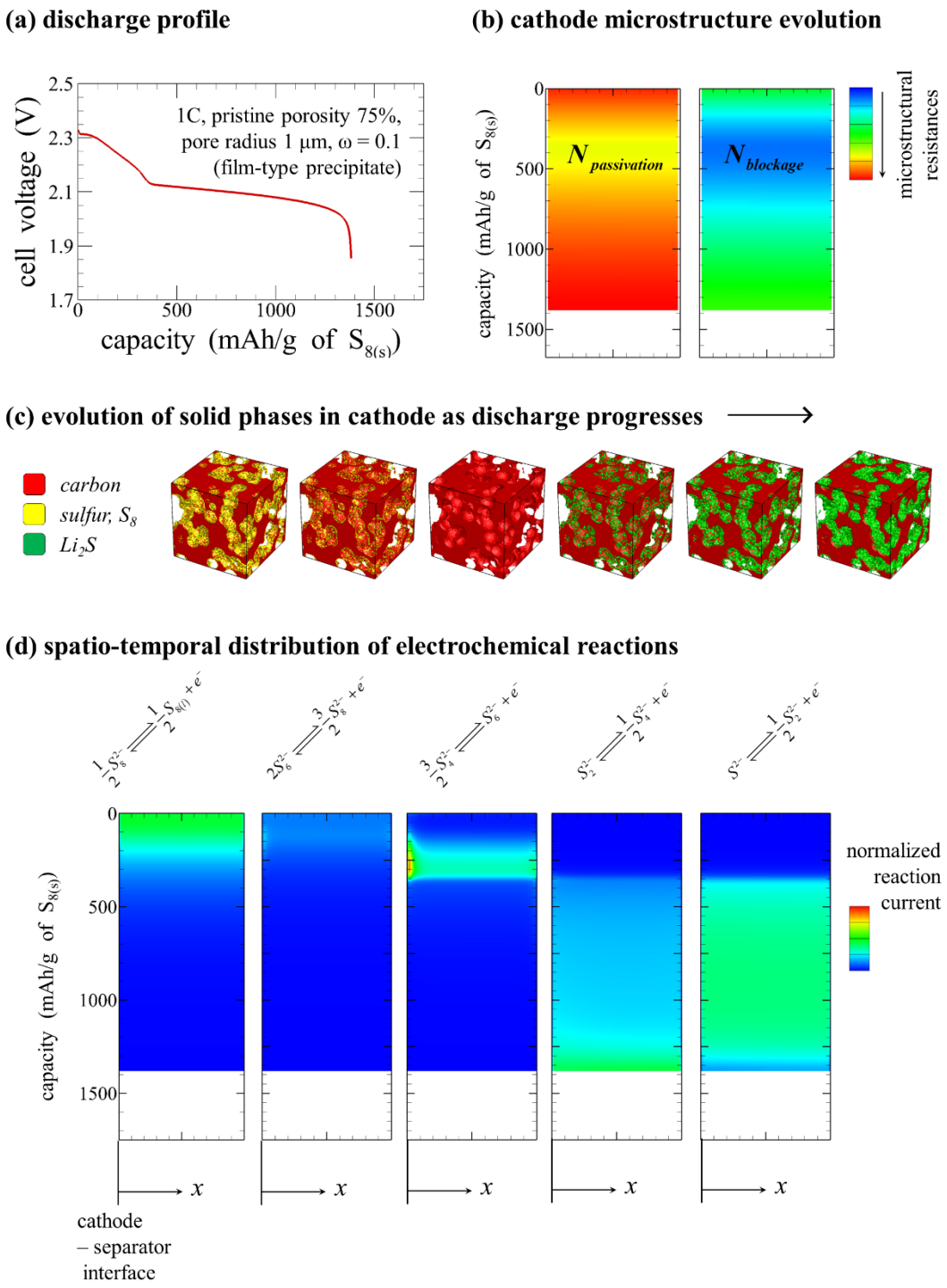

Figure 93. A representative discharge of a Li-sulfur cell observed from different perspectives: (a) voltage *vs.* capacity trend (b) evolution of microstructure resistances (c) growth of cathode structure at various depths of discharge (d) electrochemical reaction stages of the cathode for different discharge extents. The cathode specifications are 75% pristine porosity, 20% volumetric sulfur loading, 1 μm mean pore radius and film type precipitates. The cell is operated at the 1C rate.

6.7 On Specification of Sulfur Loading

The sulfur loading can be prescribed in many different ways. Many experimental studies express it as weight percent of dry cathode[148] (*i.e.*, before electrolyte filling) or as a sulfur-to-electrolyte ratio[146] in g/mL (or equivalently an electrolyte-to-sulfur ration in mL/g). On the other hand, from a modeling standpoint, volumetric loading seems a natural descriptor since it directly correlates to operating currents (expression (272)). Each of these descriptors is interrelated. For the set of electrodes presented in this study, each of them can be mathematically defined as follows (density of sulfur and carbon are comparable ~ 2 g/mL, hence simplification in expression (276)):

% wt.

$$w^*_{S_{8(s)}} = \frac{\text{mass of solid sulfur}}{\text{total dry electrode mass}} = \frac{\rho_{S_{8(s)}}\varepsilon_{S_{8(s)}}}{\rho_{S_{8(s)}}\varepsilon_{S_{8(s)}} + \rho_C\varepsilon_C} \approx \frac{\varepsilon_{S_{8(s)}}}{\varepsilon_{S_{8(s)}} + \varepsilon_C} \tag{276}$$

% vol.

$$\varepsilon_{S_{8(s)}} = \frac{\text{volume of solid sulfur}}{\text{total electrode volume (sulfur + carbon + voids)}} \tag{277}$$

S/E ratio (g/mL)

$$\mathrm{S}/\mathrm{E} = \rho_{S_{8(s)}} \frac{\varepsilon_{S_{8(s)}}}{\left(\varepsilon_0 - \varepsilon_{S_{8(s)}}\right)} \tag{278}$$

Terms appearing in these relations are defined hereafter:

- Pristine porosity, ε_0: is porosity of the carbon electrode without sulfur loading
- Carbon content, ε_C: is volume fraction of carbon in the electrode. Note that $\varepsilon_C + \varepsilon_0 = 1.0$
- Initial porosity, $\varepsilon(t=0)$: is porosity of the electrode at the onset of discharge, *i.e.*, $\varepsilon(t=0) = \varepsilon_0 - \varepsilon_{S_{8(s)}}$

Table 15. Comparison of three descriptors for sulfur loading for results reported in Figure 86(g).

Pristine porosity, ε_0 (% vol.)	Carbon content, ε_C (% vol.)	Volumetric sulfur loading, $\varepsilon_{S_{8(s)}}$ (% vol.)	Weight specific sulfur loading, $w^*_{S_{8(s)}}$ (% wt.)	S/E ratio (g/mL)
55	45	40	47.06	5.52
65	35	40	53.33	3.31
75	25	40	61.54	2.37

The discussion in the manuscript employs volumetric sulfur loading and pristine porosity as descriptors. For example, Figure 85 discusses the response of an electrode with 75% pristine porosity (*i.e.*, 25% carbon volume) and two sulfur loadings 20% and 40%. These translate to 44.44%

and 61.54% sulfur loading by wt. and S/E ratios of 0.75 and 2.37 g/mL, respectively, and are comparable to commonly reported experimental sulfur cathode recipes. Consider Figure 86(g) which discusses the effect of pristine porosity on cathode performance for a fixed volumetric loading of 40% sulfur. The three descriptors are tabulated in Table 15.

6.8 Electrolyte Transport Evolution Dynamics

The liquid electrolyte is a critical component in the Li-sulfur battery, which dissolves long-chain intermediate polysulfides, forms electrochemically active interface, and allows species and charge transport. The electrolyte transport dynamics is, however, intricately affected by the underlying evolution of chemical speciation. In this work, a comprehensive description is presented to identify the role of speciation, intra- and inter-species interactions on electrolyte transport dynamics. Evolutionary presence of different polysulfide species alters the transport characteristics which in turn affects electrochemical complexations. Microstructural changes and electrolyte evolution are concurrently present, and their mutual coupling is discussed. The role of sulfur to electrolyte ratio, that dictates speciation in the electrolyte phase and ionic transport limitations are elucidated.

The theoretical promise of Li-sulfur (LiS) chemistry for energy storage applications is irrefutable[107, 133, 325, 327, 391] but the practical performance is rather surprisingly poor. Polysulfide shuttle was earlier believed to be the limiting phenomenon[130, 392] but fundamental research has outlined many other scientific challenges such as nucleation, growth and conduction dynamics of precipitate phase[112, 113, 115, 146, 147, 393-395], speciation[138, 386, 396-399], the microstructural evolution of electrode[116, 312, 381, 400] and physicochemical interactions with Li metal anode[401-403]. Since the observed response is an intricate combination of these complexations, many unexpected trends are realized[148, 404] and a comprehensive understanding is still elusive. As a matter of fact, even the response over the first discharge has not been conclusively correlated with inherent physicochemical interactions. The electrolyte in LiS is quite unique as the identity of charge carriers is constantly changing in response to redox reactions. This represents an evolving electrolyte where constituents exhibit speciation. Consequently, the transport characteristics of LiS electrolyte change during operation and they need to be understood beyond interfacial stability[14, 385] and polysulfide solubility[103, 405].

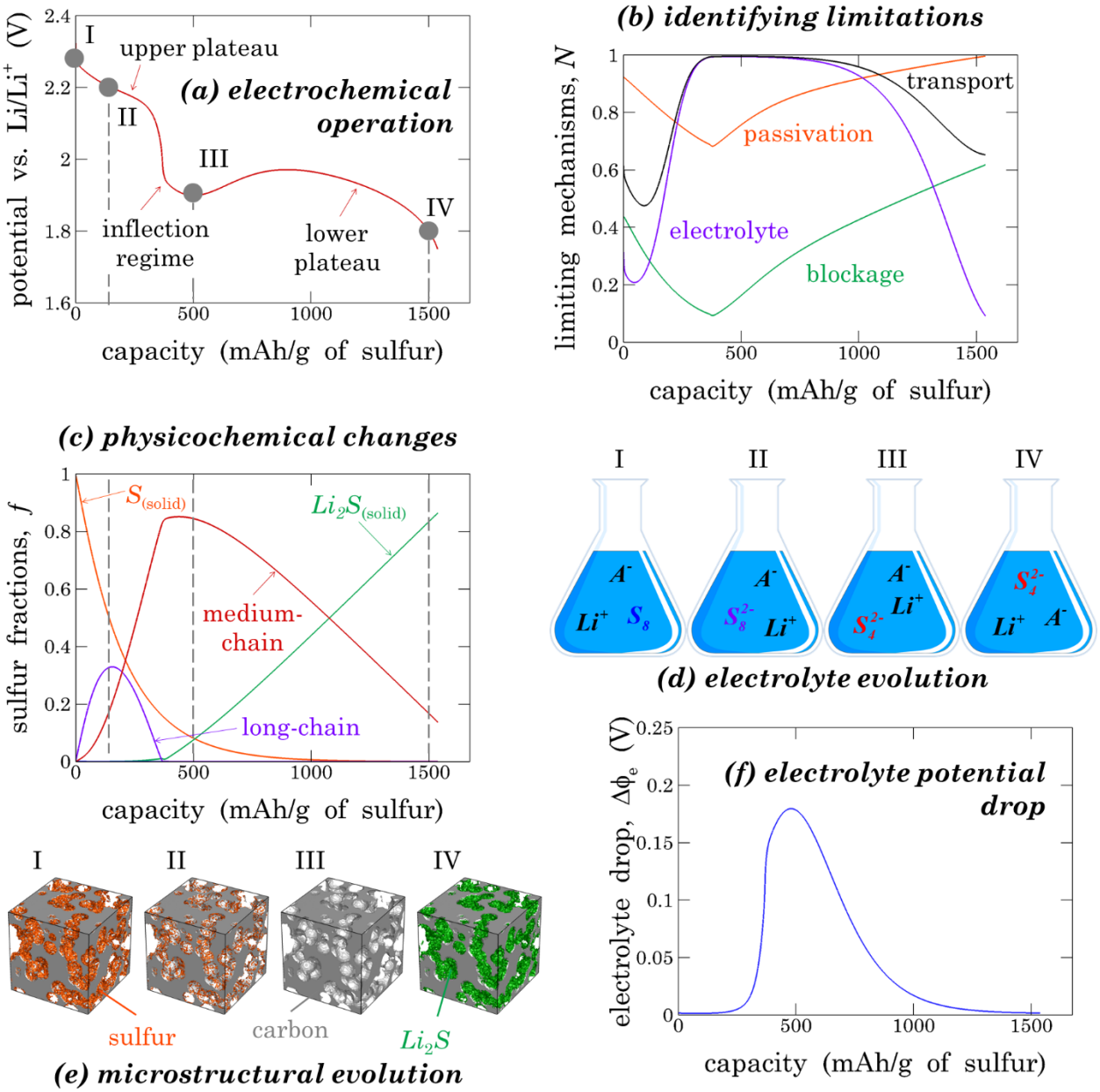

Figure 94. Fingerprinting speciation and electrochemical dynamics for electrochemical reduction (*i.e.*, discharge) of a carbon-sulfur composite electrode with 20 % vol. sulfur and 80 % pristine porosity operated at 1C. (a) Evolution of cell potential; (b) Mechanisms causing internal resistance build-up; (c) Morphosis of sulfur; (d) Chemical changes in the electrolyte; (e) Geometrical changes in electrode structure; and (f) Electrolyte phase potential drop, $\Delta\phi = \phi_{\text{anode-current·collector}} - \phi_{\text{cathode-current·collector}}$. The mesoporous carbon backbone is stochastically generated[177, 178] based on imaging experiments, while the precipitate phase is formed *via* a physics-based interfacial deposition description[312].

To explore the effect of speciation and associated electrolyte evolution, consider electrochemical reduction of sulfur from its initial state of impregnated solid in a porous carbon backbone to the final state of precipitated lithium sulfide, Li_2S (Figure 94(a)). During this operation, physical and chemical changes take place concurrently. If the electrode microstructural changes are tracked during this operation, pore space initially expands as solid sulfur dissolves, and later on, pore network shrinks as Li_2S starts precipitating (Figure 94(c) and (e)). Along with this physical progression, electrolyte phase composition evolves from primary salt (*i.e.*, the salt in the original electrolyte, *e.g.*, *LiTFSI*) and dissolved sulfur to primary salt and long-chain polysulfides such as S_8^{2-}, primary salt and medium-chain polysulfides (*e.g.*, S_4^{2-}) and eventually primary salt towards the end (if complete reduction of S_8 to Li_2S takes place). Based on the operating conditions and initial electrode composition (*i.e.*, sulfur loading and porosity) relative amounts of these sulfur species and their life-spans change (Figure 94(c) and (d)).

The presence of multiple different species in the electrolyte phase affects the individual species transport and overall ionic conduction as a result of two well-defined modes[4, 8, 22, 406, 407]:

- *Intra-species Interaction*: As the concentration of an ionic species increases, boundary layers of neighboring ions (*i.e.*, solvation shells) overlap and cause hindrance to their motion. This amounts to a reduction in mobility compared to the random Brownian motion which is often referred to as the dilute limit[408]. Also, note that the charged ions experience additional resistance given the mutual coulombic repulsion at higher concentrations (background solvent behaves as a dielectric for such interactions).
- *Inter-species Interaction*: In the presence of dissimilar species, mutual interactions cause additional forces and in turn further attenuate the agility for each of the constituents.

Concentrated solution theory helps abstract these myriad set of interactions at the continuum scale (*i.e.*, traditional measurement scale). For each of the dissolved species, such as Li^+, $S_{8(l)}$ or polysulfides in the present context, species flux is related to species gradients and ionic current (in response to electrolyte phase potential gradient) per the following expression:

$$N_i = -D_{ii}\nabla C_i - \sum_{j\neq i} D_{ij}\nabla C_j + t_i \frac{I}{z_i F} + C_i V_o \qquad (279)$$

where N_i is species molar flux. The first term on the right is the self-gradient flux. The concentration dependence of diffusivity accounts for the first mode described earlier. The second set of terms (inside the summation) are cross-diffusivities which quantify the mutual interactions

among dissimilar species. The third term identifies the migrational contribution, in other words, the fraction of total ionic current carried by the species i (transference number, t_i assigns this fraction). The last term is the bulk flow of species with solvent motion (advection). A complementary relation for ionic current is as follows:

$$I = -\kappa \nabla \phi_e - \sum_j \kappa_j \nabla \ln C_j \tag{280}$$

Here the first term is the migrational contribution to ionic current (in response to electrolyte phase potential gradient $\nabla \phi_e$). The second set of terms identify the ionic current carried by the diffusional fluxes. Note that the electrolyte solvent is treated as a background phase and hence represents a bulk flow. This bulk flow does not contribute to ionic current given the local charge neutrality of the electrolyte solution. (Relevant mathematical details are provided in Concentrated Solution Theory for LiS Electrolyte Transport. This discussion is based on a non-equilibrium thermodynamics approach[8, 22] that employ the Onsager – Stefan – Maxwell relations to account for all the coupled transport effects, in contrast to the Nernst – Planck equation based Dilute solution theory, *e.g.*[127, 312].) Take ionic conductivity for instance. At low concentrations, as the salt content increases, conductivity increases since more charge carriers are available. But beyond a certain critical concentration further increase in salt (assuming that it is still soluble) reduces the ionic conductivity in response to the deleterious concentrated solution effects. The dissolved sulfur concentration is fairly low due to it being sparingly soluble. The higher-chain polysulfides (*e.g.*, S_8^{2-}) are quite soluble and in turn, their concentration is higher than the dissolved sulfur. As the reduction of each long-chain polysulfide leads to multiple medium-chain polysulfide ions (*e.g.*, S_4^{2-}), respective ionic concentration is much higher. Additionally, since the small-chain polysulfides (*e.g.*, S^{2-}) are insoluble and precipitate out, their concentration in the electrolyte phase is marginal. These medium-chain polysulfides attain the highest concentration among the sulfur species in the electrolyte phase (Figure 94(c)). Also, note that the incoming Li^+ ions accumulate until they start precipitating and the primary salt also contains Li^+. Thus, Li^+ and medium-chain polysulfide[143] are two dominant ionic species and equivalently the ionic conductivity demonstrates quadratic dependence on both (this is same as saying that the ionic conductivity exhibits a non-monotonic dependence on two salts: primary salt, say, *LiTFSI*, and a secondary salt, Li_2S_4, both of which are completely soluble).

Reconsider Figure 94(a) which presents the 1C discharge of a cathode with a high enough sulfur loading (20 %vol. sulfur and 80 % pristine porosity). It exhibits the two plateaus: the first one related to a quasi-steady balance among sulfur dissolution and subsequent electrochemical reduction to long-chain polysulfides, while the second one (lower) describes Li_2S formation. These two are joined by an inflection zone in cell potential which recovers subsequently and joins the lower plateau. When these transitions (Figure 94(a)) are compared with associated physicochemical changes (Figure 94(c)) in the cell, it is revealed that the inflection coincides with intensified medium-chain polysulfide concentration. This suggests that the feature is likely associated with reduced ionic conductivity.

With the consideration of electrolyte transport evolution and electrode microstructural growth, there are three likely mechanisms to account for increased internal resistance and reduced potential:

i. *Surface Passivation*: both solid sulfur and Li_2S are electronically insulating and their presence causes a reduction in the electrochemically active area; if these (solid) species are present in excess quantities, they can cover the active interface and lead to increased kinetic resistance. The severity of this resistive mode is quantified as $N_{\text{passivation}} = 1 - a / a_0$ where a is a current active area, while a_0 is a maximum active area as defined by the pristine structure.

ii. *Pore Blockage*: due to temporal changes in the pore network (in response to precipitation/ dissolution dynamics), transport through the pore network could be severely hampered. The contribution of this mode is correlated to transport effectiveness, *i.e.*, $N_{\text{blockage}} = 1 - (\varepsilon / \tau) / (\varepsilon_0 / \tau_0)$ where again the 0's denote properties of the pristine carbon structure (without sulfur or Li_2S phase); ε and τ are local porosity and tortuosity, respectively.

iii. *Electrolyte Conduction*: is related to concentrated solution effect; when ionic conductivity drops to very small values, ionic current cannot be sustained without an additional electrolyte phase potential drop. Thus, $N_{\text{electrolyte}} = 1 - \kappa / \kappa_{\max}$ is a suitable indicator of electrolyte phase transport evolution.

Here blockage refers to the transport resistance due to pore-network evolution, while ionic conduction is correlated to intrinsic transport behavior. Both of them jointly identify the transport

resistance that is quantified as $N_{\text{transport}} = 1 - \left(\kappa\varepsilon / \tau\right) / \left(\kappa_{\max}\varepsilon_0 / \tau_0\right)$. Each of these quantifiers varies in both space and time and whichever indicator approaches one has the dominant contribution to the internal resistance. The passivation and blockage effects were identified by the authors' in a recent work[312] and are reconsidered here as they are closely coupled with the electrolyte transport evolution. Figure 94(b) plots the evolution of each of these indicators throughout the discharge history. The maximum value for each of these *N*'s is plotted here, *i.e.*, the highest resistance at each time instant. For the electrode considered in Figure 94, microstructural resistances (passivation and blockage) are each high at the start and towards the end. Complimentary to this, the electrolyte phase limitations appear at an intermediate discharge stage which coincides with the inflection on the potential plot (Figure 94(a)), as well as medium-chain polysulfide, being the dominant sulfur species (Figure 94(c)). To further corroborate this, the potential drop in the electrolyte phase, $\Delta\phi_e$, is computed and sketched in Figure 94(f) along discharge axis (the electrolyte phase potential difference between the anode – separator and cathode – current collector interfaces). This drop also shows a spike quite well coincident with the presence of medium-chain polysulfides and reaffirms the hypothesized role of electrolyte transport evolution. Note that the electrode porosity is highest in this regime of operation as most of the sulfur has dissolved and Li_2S precipitation is still not appreciable. In the thermodynamic limit, the pristine electrode structure is realized around the instant the medium-chain polysulfides reach their maximum concentration. The physicochemical origins of this inflection in the potential profile (Figure 94(a)) have recently been attributed to the nucleation barrier for Li_2S electrodeposition from slow rate measurements[146, 147]. The electrolyte transport is an additional effect that can lead to further resistance build-up and potential drop at moderate and higher rates (detailed discussion to follow).

6.9 Speciation is connected to Bulk Specifications

The electrochemical dynamics is studied here based on a porous electrode mathematical description that accounts for detailed pore-scale microstructural changes[312] and concentrated solution effects (refer to Supporting Information section S2 for explicit details). Figure 95 investigates the effect of electrode specifications, namely sulfur loading and porosity on the electrochemical response (1C discharge). Assuming the successive reduction of sulfur (*i.e.*,

thermodynamic limit), one can summarize the maximum concentrations for medium-chain polysulfide (here S_4^{2-}) and Li^+ per the following relations:

$$\max\left(C_{S_4^{2-}}\right) \approx \frac{2\varepsilon_S^0}{\varepsilon_0 \tilde{V}_S} \tag{281}$$

$$\max\left(C_{Li^+}\right) \approx \frac{4\varepsilon_S^0}{\varepsilon_0 \tilde{V}_S} + \left(\frac{\varepsilon_0 - \varepsilon_S^0}{\varepsilon_0}\right) C_{Li^+}^0 \tag{282}$$

Here ε_S^0 is volumetric sulfur loading, ε_0 is pristine porosity (before sulfur impregnation), $\tilde{V}_S$ is the partial molar volume of solid sulfur and $C_{Li^+}^0$ is an initial Li^+ concentration in the electrolyte (1M for the present results). Equation (281) reveals that as volumetric sulfur loading (*i.e.*, ε_S^0) is increased, the maximum polysulfide concentration also monotonically increases. This results in reduced ionic conductivity when medium-chain polysulfides are predominantly present. Going from a low sulfur loading (5 % vol.) to a higher one (25 % vol.), one observes these electrolyte phase conduction limitations distinctly. Figure 95(a) compares the cell potential trends for varying sulfur loading (at a constant pristine porosity of 80 % and equivalent operation at 1C). At low enough sulfur loading (5 and 10 % vol.), the potential drops monotonically with time. At an intermediate loading of 15 % vol. an imperceptible inflection develops which expands as the loading is increased to 20 % vol. With further increase in sulfur content, the ionic conductivity deteriorates so suddenly that the electrolyte phase potential drop alone is sufficient to drop the cell potential below discharge cutoff (set at 1.75 V). The evolution of $N_{\text{electrolyte}}$ is sketched concurrently in Figure 95(b) to correlate the occurrence of severe electrolyte transport limitations. This is of practical concern as the maximum sulfur loading which allows a reasonable capacity is in part dependent on electrolyte transport characteristics. Also note that as sulfur loading is increased, the zone of electrolyte conduction limitation expands monotonically as relevant in Figure 95(b). Electrode porosity appears in the denominator in Equation (281) and in turn, a qualitatively similar trend is expected as porosity is reduced. Figure 95(c) confirms this intuition where lower porosities terminate the cell operation after the reduction of long-chain polysulfides (*i.e.*, the upper plateau). Electrolyte drop profiles (Figure 95(d)) correlate this ‘sudden death’ behavior to ionic conduction limitation. Note that the sulfur loading is kept constant (at 20 % vol.) for the discussion in Figure 95(c) and (d). In summary, a higher sulfur content and/or a lower

porosity leads to intensified electrolyte transport evolution and associated deleterious effects on electrochemical response. Interestingly, a high energy LiS system requires either high volumetric sulfur content or lower porosity, thus making the study of electrolyte phase transport of considerable interest. Notice the capacity increases going from 90% to 80% porosity in Figure 95(c) since the later has a greater pristine active surface and comparatively experiences a slightly delayed passivation. The capacity trends for low sulfur loading (Figure 95(a)) and high porosity (Figure 95(c)) are associated with microstructural effects discussed previously[312].

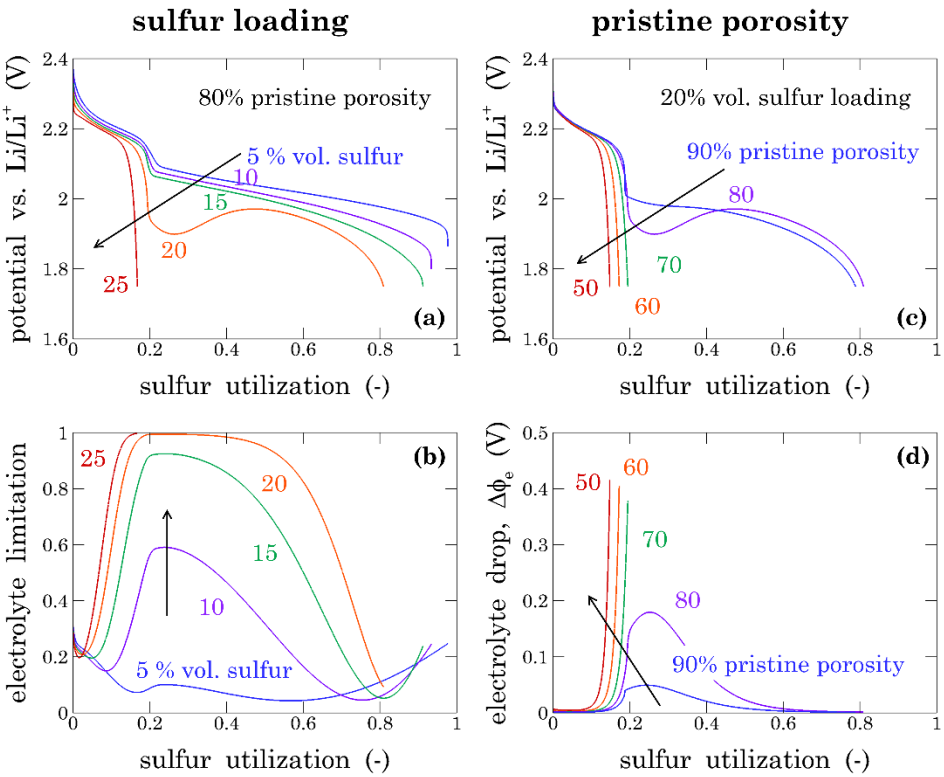

Figure 95. Electrode composition and microstructure dictate electrolyte transport evolution. Higher sulfur loading (a) leads to increased polysulfide concentration which in extreme events causes ionic conduction limitation (b). Reduction in pristine porosity increases electrolyte concentration of sulfur species and in turn, the concentrated solution effects increase electrolyte potential drop (d) causing sudden death (c). Electrochemical reduction of sulfur at 1C is studied here.

To further elucidate this intricate relation among electrode specifications, electrolyte dynamics, and rate capability, electrodes are categorized based on $N_{\text{electrolyte}}$ values at maximum

(thermodynamic) concentration of medium-chain polysulfide. Sulfur – to – electrolyte ratio rephrases the sulfur loading in a conducive manner:

$$\mathrm{S}/\mathrm{E} = \frac{\rho_S \varepsilon_S^0}{\varepsilon_0 - \varepsilon_S^0} \tag{283}$$

Figure 96(a) classifies these electrodes into two groups: (i) green – low S/E ratio electrodes which have sufficient ionic conduction $N_{\text{electrolyte}} < 1$ and (ii) grey – medium to high S/E ratio electrodes which have poor ionic conduction $N_{\text{electrolyte}} \approx 1$ in the thermodynamic limit. Note that the thermodynamic limit assumes a successive reduction of sulfur species. At any finite rate, reduction events overlap and the higher is the rate, higher is the degree of overlap among sulfur species and in turn lower is the medium-chain polysulfide concentration and higher is the ionic conductivity, *i.e.*, the ionic conductivity improves with C-rate due to the coupled speciation – electrochemistry dynamics. Keep in mind that the ionic conductivity characterizes the electrolyte phase transport and associated transport resistance becomes more important at higher rates. These two phenomena represent opposite trends: reduction in electrolyte transport resistance as C-rate is increased (overlapping speciation events) and an increase in electrolyte potential drop (positive scaling with C-rate). This explains why capacity somewhat improves going from C/10 to C/5 with this slight improvement in ionic transport (Figure 96(b)). On the other hand, for larger rates (going to C/2 and 1C), improved ionic conductivity cannot compensate for increased C-rate and equivalently the electrolyte phase drop monotonically increases. For lower rates (here C/10 and C/5), cell shutdown is due to surface passivation while at medium and higher rates (C/2 and 1C), cell capacity is limited by electrolyte transport. Thus, the nature of internal resistance changes from passivation to ionic interplay (Figure 96(c)). For low, enough S/E ratio (green electrodes), ionic conductivity is sufficient over the range of operating currents and hence the internal resistance evolution is predominantly dictated by microstructural effects[312] (Figure 96(d)). The difference in this structural evolution can be recognized from temporal changes in solid sulfur and Li_2S as revealed in Figure 96(e). Figure 96(f) compare these capacity trends for these two electrode types and reveal that at the high sulfur content (S/E ratio) the electrochemical functionality changes its qualitative nature with the rates.

Despite the electrolyte being so essential, its physicochemical implications have not been probed in the past save for cursory studies related to polysulfide solubility. Such investigations do not elucidate the ionic transport complexations which are the primary role of an electrolyte. The

present study represents a collective effort to both characterize charge and species transport in such complicated systems as well as its relevance in terms of electrochemical dynamics. In nutshell, the electrolyte in the LiS is a complex multi-component system which evolves in response to the speciation of different sulfur species. Based on the principles of non-equilibrium thermodynamics, a concentrated solution theory has been developed to abstract the progression of electrolyte transport characteristics, especially accounting for the self and interspecies interactions. Conduction of ionic current is the most sensitive to Li^+ and medium-chain polysulfide concentrations. The electrode microstructural specifications (sulfur loading and porosity) identify the limits on ionic concentrations. Reaction rates, species life-spans, electrolyte transport and microstructural evolution are strongly coupled and result in electrochemical complexations. The electrolyte phase limitations become more apparent as cathodes with higher S/E ratio are attempted.

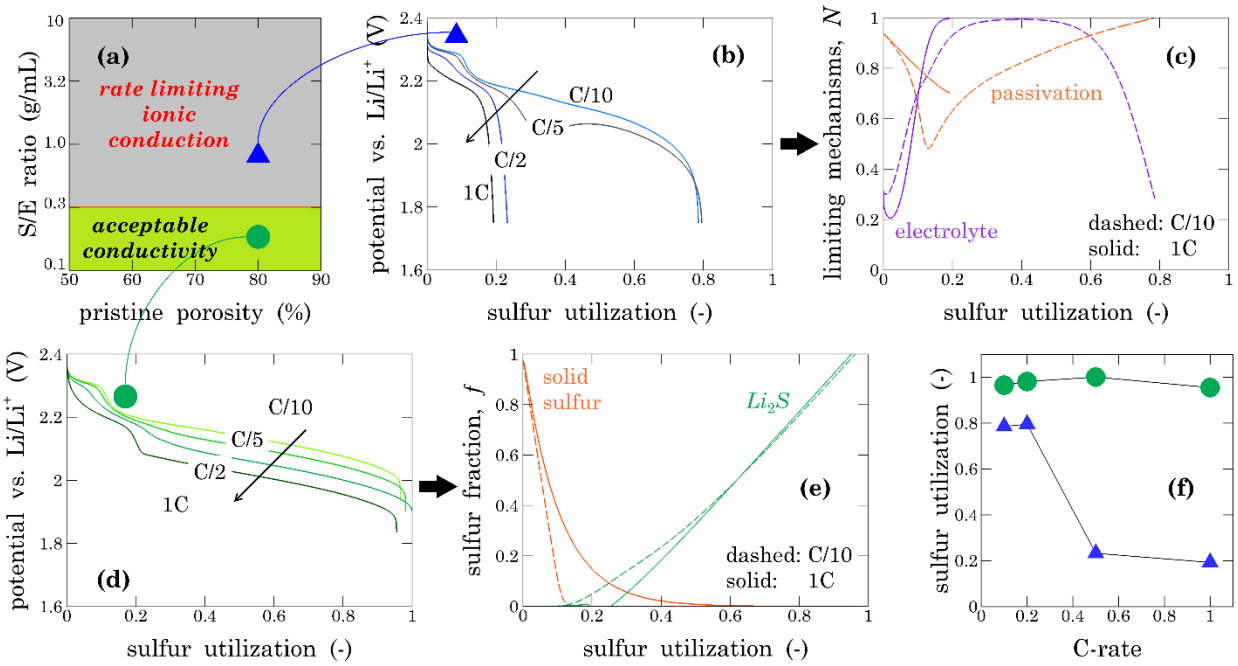

Figure 96. Regimes of electrolyte transport evolution. (a) An electrolyte with very high ionic concentration can become rate limiting, which manifests as (b) a sudden drop in performance as well as (f) sulfur utilization at higher rates (c) since ionic transport plays a more dominant role. In comparison, for reasonable conductivity electrolytes, performance (d, f) is dictated by microstructural interactions (e).

The discussion outlined hitherto explains the generalized characteristics of electrolyte transport in LiS. The change of background solvent affects the transport dynamics. Microscopically, it alters

the solvation shells of respective species (charged or neutral), which in turn readjusts the intra- and inter-species interactions (the dielectric constant is an apparent indicator of quantitative effects of solvation shell). At a continuum scale, this translates into different transport properties like diffusivities, ionic conductivities, *etc.* A proper characterization of each LiS electrolyte requires one to appropriately quantify the trends in diffusivities, ionic conductivity, diffusional conductivities, and transference numbers.

6.10 Concentrated Solution Theory for LiS Electrolyte Transport

The electrolytes used in the LiS are quite unique in that the identity of charge carriers, as well as their respective concentrations, continuously evolve during operation. In contrast, typical Li-ion electrolytes always contain the same set of charge carriers[14, 24, 110]. Typical discharge (lithiation) of LiS begins with the dissolution of solid sulfur and subsequent reduction to long-chain (say, S_8^{2-}), medium-chain (say, S_4^{2-}) and short-chain (say, S^{2-}) polysulfides[138, 312, 386, 409]. Given the very low solubility of lithium salt with short-chain polysulfide (*i.e.*, Li_2S) it immediately precipitates as solid. Thus, the simplest description of LiS electrolyte has the following species:

i. Lithium-ion, Li^+
ii. Anion in the primary salt, A^{z_a} (*e.g.*, $TFSI^-$)
iii. Long-chain polysulfide, X^{z_x} (*i.e.*, S_8^{2-})
iv. Medium-chain polysulfide, Y^{z_y} (*i.e.*, S_4^{2-})
v. Dissolved sulfur, S (*i.e.*, $S_{8(l)}$)
vi. Background solvent, O (*e.g.*, dioxolane (DOL) – dimethoxyethane (DME))

These multiple species (ions and neutral molecules) interact with each other and influence the ionic conduction. A traditional dilute solution theory based description does not account for these mutual interactions and in turn, provides a limited view. On the other hand, concentrated solution theory provides a comprehensive understanding that consistently captures all the different salt concentrations. The associated mathematical details are an extension of the theory for an electrolyte with a single salt by Newman and co-workers[22, 410, 411].

Since there are three anions and one cation, one can write dissociation equilibria for each of them. Here z's identify the charge per ion, while ν's represent stoichiometry.

<u>*Primary salt (from unused electrolyte)*</u>:

$$Li_{\nu_{p1}}A_{\nu_a} \rightleftharpoons \nu_{p1}Li^{z_p} + \nu_a A^{z_a} \tag{284}$$

<u>*Longer-chain polysulfide*</u>:

$$Li_{\nu_{p2}}X_{\nu_x} \rightleftharpoons \nu_{p2}Li^{z_p} + \nu_x X^{z_x} \tag{285}$$

<u>*Medium-chain polysulfide salt*</u>:

$$Li_{\nu_{p3}}Y_{\nu_y} \rightleftharpoons \nu_{p3}Li^{z_p} + \nu_y Y^{z_y} \tag{286}$$

Subsequently, it can be shown that the salt concentrations are related to individual ionic concentrations *via* stoichiometries:

Lithium-ion: $$C_p = \nu_{p1}C_1 + \nu_{p2}C_2 + \nu_{p3}C_3 \tag{287}$$

Primary salt anion: $$C_a = \nu_a C_1 \tag{288}$$

Long-chain polysulfide: $$C_x = \nu_x C_2 \tag{289}$$

Medium-chain polysulfide: $$C_y = \nu_y C_3 \tag{290}$$

Similarly, local charge-neutralities result in the following set of identities:

$$\nu_{p1}z_p + \nu_a z_a = 0 \tag{291}$$

$$\nu_{p2}z_p + \nu_x z_x = 0 \tag{292}$$

$$\nu_{p3}z_p + \nu_y z_y = 0 \tag{293}$$

The Gibbs – Duhem relation for this electrolyte (with six distinct species) can be written as:

$$C_p\nabla\mu_p + C_a\nabla\mu_a + C_x\nabla\mu_x + C_y\nabla\mu_y + C_s\nabla\mu_s + C_o\nabla\mu_o = 0 \tag{294}$$

where μ 's are chemical potentials of individual species. For the ions, they are correlated with the chemical potential change of each of the salts:

$$\nabla\mu_1 = \nu_1 RT\left(1 + \frac{d\ln f_1}{d\ln C_1}\right)\nabla\ln C_1 \tag{295}$$

$$\nabla\mu_2 = \nu_2 RT\left(1 + \frac{d\ln f_2}{d\ln C_2}\right)\nabla\ln C_2 \tag{296}$$

$$\nabla\mu_3 = \nu_3 RT\left(1 + \frac{d\ln f_3}{d\ln C_3}\right)\nabla\ln C_3 \tag{297}$$

For each salt, total stoichiometries, ν_i 's are correlated to a salt chemical formula, for example, $\nu_1 = \nu_{p1} + \nu_a$. Also, the bracketed terms in (295) to (297) are thermodynamic factors which identify the concentration dependence of activity coefficients, f_i 's.

The transport of each of the species is described by Onsager – Stefan – Maxwell (OSM) relation (in contrast to the Nernst – Planck in case of dilute solution theory), *i.e.*,

$$-\frac{C_i C_T}{RT}\nabla\mu_i = \sum_{j\neq i}\left(\frac{C_j N_i - C_i N_j}{\mathcal{D}_{ij}}\right)$$

For the present electrolyte system, this gives six OSM equations, out of which only five are independent (since Gibbs – Duhem is an identity). For the sake of simplicity, the solvent is treated as a background phase[22] with a bulk velocity, say, V_o . The five resultant OSM relations are as follows:

<u>*Cation flux*</u>:

$$\begin{aligned}-\frac{C_p C_T}{RT}\nabla\mu_p = &\left(\frac{C_a N_p - C_p N_a}{\mathcal{D}_{pa}}\right)+\left(\frac{C_x N_p - C_p N_x}{\mathcal{D}_{px}}\right)+\left(\frac{C_y N_p - C_p N_y}{\mathcal{D}_{py}}\right)\\ &+\left(\frac{C_s N_p - C_p N_s}{\mathcal{D}_{ps}}\right)+\left(\frac{C_o N_p - C_p N_o}{\mathcal{D}_{po}}\right)\end{aligned} \tag{298}$$

<u>*Primary salt anion flux*</u>:

$$\begin{aligned}-\frac{C_a C_T}{RT}\nabla\mu_a = &\left(\frac{C_p N_a - C_a N_p}{\mathcal{D}_{pa}}\right)+\left(\frac{C_x N_a - C_a N_x}{\mathcal{D}_{ax}}\right)+\left(\frac{C_y N_a - C_a N_y}{\mathcal{D}_{ay}}\right)\\ &+\left(\frac{C_s N_a - C_a N_s}{\mathcal{D}_{as}}\right)+\left(\frac{C_o N_a - C_a N_o}{\mathcal{D}_{ao}}\right)\end{aligned} \tag{299}$$

<u>*Long-chain polysulfide flux*</u>:

$$\begin{aligned}-\frac{C_x C_T}{RT}\nabla\mu_x = &\left(\frac{C_a N_x - C_x N_a}{\mathcal{D}_{ax}}\right)+\left(\frac{C_p N_x - C_x N_p}{\mathcal{D}_{px}}\right)+\left(\frac{C_y N_x - C_x N_y}{\mathcal{D}_{xy}}\right)\\ &+\left(\frac{C_s N_x - C_x N_s}{\mathcal{D}_{xs}}\right)+\left(\frac{C_o N_x - C_x N_o}{\mathcal{D}_{xo}}\right)\end{aligned} \tag{300}$$

<u>*Medium-chain polysulfide flux*</u>:

$$-\frac{C_y C_T}{RT}\nabla\mu_y = \left(\frac{C_a N_y - C_y N_a}{\mathcal{D}_{ay}}\right) + \left(\frac{C_x N_y - C_y N_x}{\mathcal{D}_{xy}}\right) + \left(\frac{C_p N_y - C_y N_p}{\mathcal{D}_{py}}\right) + \left(\frac{C_s N_y - C_y N_s}{\mathcal{D}_{ys}}\right) + \left(\frac{C_o N_y - C_y N_o}{\mathcal{D}_{yo}}\right) \tag{301}$$

Dissolved sulfur flux:

$$-\frac{C_s C_T}{RT}\nabla\mu_s = \left(\frac{C_a N_s - C_s N_a}{\mathcal{D}_{as}}\right) + \left(\frac{C_x N_s - C_s N_x}{\mathcal{D}_{xs}}\right) + \left(\frac{C_y N_s - C_s N_y}{\mathcal{D}_{ys}}\right) + \left(\frac{C_p N_s - C_s N_p}{\mathcal{D}_{ps}}\right) + \left(\frac{C_o N_s - C_s N_o}{\mathcal{D}_{so}}\right) \tag{302}$$

where $C_T = C_p + C_a + C_x + C_y + C_s + C_o$ is total (local) concentration and $N_o = C_o V_o$ is solvent flux (bulk electrolyte flow). Note that the binary diffusivities, $\mathcal{D}_{ij}$'s, are interrelated and not all are independent. Only 15 of these are independent and are identified so in the above OSM expressions (298) to (302). Rearranging these equations, one arrives at the following set of linear algebraic relations for individual species flux, N 's:

$$
\begin{bmatrix}
\left(\frac{C_a}{\mathcal{D}_{pa}}+\frac{C_x}{\mathcal{D}_{px}}+\frac{C_y}{\mathcal{D}_{py}}+\frac{C_s}{\mathcal{D}_{ps}}+\frac{C_o}{\mathcal{D}_{po}}\right) & -\frac{C_p}{\mathcal{D}_{pa}} & -\frac{C_p}{\mathcal{D}_{px}} & -\frac{C_p}{\mathcal{D}_{py}} & -\frac{C_p}{\mathcal{D}_{ps}} \\
-\frac{C_a}{\mathcal{D}_{pa}} & \left(\frac{C_p}{\mathcal{D}_{pa}}+\frac{C_x}{\mathcal{D}_{ax}}+\frac{C_y}{\mathcal{D}_{ay}}+\frac{C_s}{\mathcal{D}_{as}}+\frac{C_o}{\mathcal{D}_{ao}}\right) & -\frac{C_a}{\mathcal{D}_{ax}} & -\frac{C_a}{\mathcal{D}_{ay}} & -\frac{C_a}{\mathcal{D}_{as}} \\
-\frac{C_x}{\mathcal{D}_{px}} & -\frac{C_x}{\mathcal{D}_{ax}} & \left(\frac{C_p}{\mathcal{D}_{px}}+\frac{C_a}{\mathcal{D}_{ax}}+\frac{C_y}{\mathcal{D}_{xy}}+\frac{C_s}{\mathcal{D}_{xs}}+\frac{C_o}{\mathcal{D}_{xo}}\right) & -\frac{C_x}{\mathcal{D}_{xy}} & -\frac{C_x}{\mathcal{D}_{xs}} \\
-\frac{C_y}{\mathcal{D}_{py}} & -\frac{C_y}{\mathcal{D}_{ay}} & -\frac{C_y}{\mathcal{D}_{xy}} & \left(\frac{C_p}{\mathcal{D}_{py}}+\frac{C_a}{\mathcal{D}_{ay}}+\frac{C_x}{\mathcal{D}_{xy}}+\frac{C_s}{\mathcal{D}_{ys}}+\frac{C_o}{\mathcal{D}_{yo}}\right) & -\frac{C_y}{\mathcal{D}_{ys}} \\
-\frac{C_s}{\mathcal{D}_{ps}} & -\frac{C_s}{\mathcal{D}_{as}} & -\frac{C_s}{\mathcal{D}_{xs}} & -\frac{C_s}{\mathcal{D}_{ys}} & \left(\frac{C_p}{\mathcal{D}_{ps}}+\frac{C_a}{\mathcal{D}_{as}}+\frac{C_x}{\mathcal{D}_{xs}}+\frac{C_y}{\mathcal{D}_{ys}}+\frac{C_o}{\mathcal{D}_{so}}\right)
\end{bmatrix}
\begin{Bmatrix} N_p \\ N_a \\ N_x \\ N_y \\ N_s \end{Bmatrix}
=
\begin{Bmatrix} C_p/\mathcal{D}_{po} \\ C_o/\mathcal{D}_{ao} \\ C_x/\mathcal{D}_{xo} \\ C_y/\mathcal{D}_{yo} \\ C_s/\mathcal{D}_{so} \end{Bmatrix} C_o V_o - \frac{C_T}{RT}
\begin{Bmatrix} C_p\nabla\mu_p \\ C_a\nabla\mu_a \\ C_x\nabla\mu_x \\ C_y\nabla\mu_y \\ C_s\nabla\mu_s \end{Bmatrix}
$$

This system of equations is to be inverted to express the individual species fluxes in terms of electrochemical potential gradients, $\nabla\mu$'s, and solvent velocity, V_o. This system of equations become more tractable if the fluxes are expressed as species velocities, *i.e.*, $N = CV$:

$$
\begin{bmatrix}
\alpha_{pp} & -\alpha_{pa} & -\alpha_{px} & -\alpha_{py} & -\alpha_{ps} \\
-\alpha_{pa} & \alpha_{aa} & -\alpha_{ax} & -\alpha_{ay} & -\alpha_{as} \\
-\alpha_{px} & -\alpha_{ax} & \alpha_{xx} & -\alpha_{xy} & -\alpha_{xs} \\
-\alpha_{py} & -\alpha_{ay} & -\alpha_{xy} & \alpha_{yy} & -\alpha_{ys} \\
-\alpha_{ps} & -\alpha_{as} & -\alpha_{xs} & -\alpha_{ys} & \alpha_{ss}
\end{bmatrix}
\begin{Bmatrix} V_p \\ V_a \\ V_x \\ V_y \\ V_s \end{Bmatrix}
=
\begin{Bmatrix} C_p/\mathcal{D}_{po} \\ C_o/\mathcal{D}_{ao} \\ C_x/\mathcal{D}_{xo} \\ C_y/\mathcal{D}_{yo} \\ C_s/\mathcal{D}_{so} \end{Bmatrix} C_o V_o - \frac{C_T}{RT}
\begin{Bmatrix} C_p\nabla\mu_p \\ C_a\nabla\mu_a \\ C_x\nabla\mu_x \\ C_y\nabla\mu_y \\ C_s\nabla\mu_s \end{Bmatrix}
\tag{303}
$$

where α's are revised coefficients (*e.g.*, $\alpha_{pp} = C_p\left(\frac{C_a}{\mathcal{D}_{pa}}+\frac{C_x}{\mathcal{D}_{px}}+\frac{C_y}{\mathcal{D}_{py}}+\frac{C_s}{\mathcal{D}_{ps}}+\frac{C_o}{\mathcal{D}_{po}}\right)$ and $\alpha_{pa} = C_p C_a/\mathcal{D}_{pa}$). This revised system of equation (303) has a symmetric coefficient matrix. The inverse of this matrix is also a symmetric matrix[204, 387], and the solution of (303) can be written as follows:

$$\begin{Bmatrix} V_p \\ V_a \\ V_x \\ V_y \\ V_s \end{Bmatrix} = V_o - \frac{C_T}{RT} \begin{bmatrix} \beta_{pp} & \beta_{pa} & \beta_{px} & \beta_{py} & \beta_{ps} \\ & \beta_{aa} & \beta_{ax} & \beta_{ay} & \beta_{as} \\ & & \beta_{xx} & \beta_{xy} & \beta_{xs} \\ & & & \beta_{yy} & \beta_{ys} \\ & & & & \beta_{ss} \end{bmatrix} \begin{Bmatrix} C_p \nabla \mu_p \\ C_a \nabla \mu_a \\ C_x \nabla \mu_x \\ C_y \nabla \mu_y \\ C_s \nabla \mu_s \end{Bmatrix} \tag{304}$$

where β's are entries in the inverse matrix and given that it is also symmetric, the lower triangular entries are not written. Once these individual species velocities are identified, corresponding flux can be easily written as $N = CV$.

Now that the fluxes are available, total ionic current can be expressed as follows:

$$\frac{I}{F} = z_p N_p + z_a N_a + z_x N_x + z_y N_y \tag{305}$$

which after a few rearrangements and substitutions becomes:

$$I = -\kappa \nabla \phi - \kappa_1 \nabla \ln C_1 - \kappa_2 \nabla \ln C_2 - \kappa_3 \nabla \ln C_3 - \kappa_s \nabla \ln C_s \tag{306}$$

Note that even though the flux of neutral species (dissolved sulfur here) does not appear in the earlier expression (305), it has contributions to the ionic flux in the final form. This dependence stems from inter-species interactions. Also, note that the solvent velocity (bulk flow) has no contribution to the ionic current (as the derivation is carried out in the solvent frame[22]). Note that the electrochemical potentials of each of the anions are expressed in terms of the chemical potential of salt and the Li^+ cation to arrive at the particular form of equation (306). The respective species fluxes can be re-expressed in terms of ionic current and concentration gradients as follows:

$$N_p = -D_{pp} \nabla C_p - D_{px} \nabla C_x - D_{py} \nabla C_y - D_{1s} \nabla C_s + \frac{t_p}{z_p} \cdot \frac{I}{F} + C_p V_o \tag{307}$$

$$N_x = -D_{xp} \nabla C_p - D_{xx} \nabla C_x - D_{xy} \nabla C_y - D_{xs} \nabla C_s + \frac{t_x}{z_x} \cdot \frac{I}{F} + C_x V_o \tag{308}$$

$$N_y = -D_{yp} \nabla C_p - D_{yx} \nabla C_x - D_{yy} \nabla C_y - D_{ys} \nabla C_s + \frac{t_y}{z_y} \cdot \frac{I}{F} + C_y V_o \tag{309}$$

$$N_s = -D_{sp} \nabla C_p - D_{sx} \nabla C_x - D_{sy} \nabla C_y - D_{ss} \nabla C_s + t_s \frac{I}{F} + C_s V_o \tag{310}$$

Equations (306) to (310) form the set of flux relations (species fluxes and ionic current) to describe the electrolyte system at hand. Note that these equations contain 25 transport properties (1 conductivity, 4 diffusional conductivities, 16 diffusivities and 4 transference numbers), out of which only 18 are independent as the original system of equations (303) had 15 independent binary diffusivities and 3 thermodynamic factors). Note that the salt diffusivity tensor D_{ij} is not symmetric while the binary diffusivity tension $\mathcal{D}_{ij}$ is symmetric. Also, the transference numbers add up to unity: $t_p + t_a + t_x + t_y + t_s = 1$. Also, since the sulfur is sparingly soluble in common LiS electrolytes[103, 108], one does not require a thermodynamic factor to quantify its chemical potential[22].

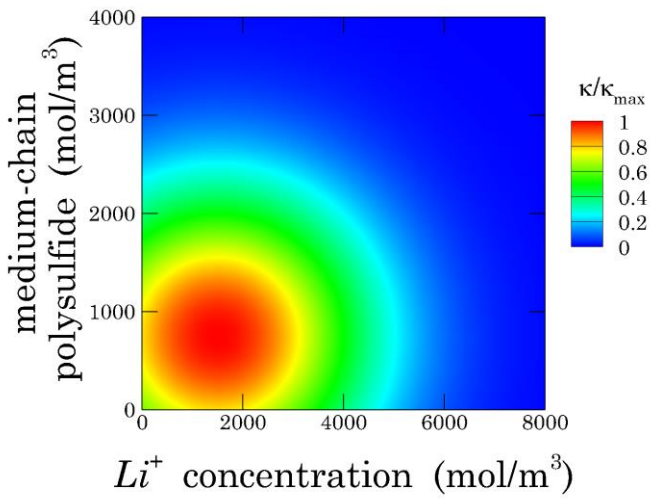

Figure 97. Ionic conductivity, in general, changes with all species concentrations. Here it varies strongly with Li+ and polysulfide concentrations and the corresponding (assumed) dependence is graphically expressed.

Thus, the simplest description of LiS electrolyte requires measurement of 18 different transport properties. This is one of the main reasons why the role of electrolyte transport is so poorly understood in the LiS. Without a proper description of the electrolyte transport, it is also not possible to experimentally estimate these transport coefficient (any electrolyte transport measurements, *e.g.*[24], relies on a specific mathematical form of transport laws). Except for one recent attempt[143], electrolyte transport in the LiS is only characterized in terms of ionic conductivity variations with concentration. The LiS electrolyte transport formulation presented here would be an important step towards characterizing the transport behavior with sufficient rigor.

In the absence of a comprehensive set of measurements, these transport properties (values and/or functional relations) were ascertained in part from available (incomplete) data and in part from intuition. For example, it can be shown that medium-chain polysulfides and lithium-ion are the most dominant ionic species (equivalently the primary salt, LiA, and salt with medium-chain polysulfide, Li_2S_4, both of which are soluble). The ionic conductivity is expected to increase going from zero concentrations to a critical value and later on drop. Such concentrated solution effect commonly observed in electrolytes with a single salt[24] is extended here for two salts exhibiting dominant concentrations (Figure 97). Similarly, it is expected that diffusivity scales with ion size, giving the highest diffusivity to Li^+, and the cross-diffusivities having smaller values than the intra-species diffusivities.

6.11 Electrochemical Dynamics – with Transport Evolution

In line with the electrolyte transport description discussed here, the relevant set of chemical and electrochemical reactions can be assumed as follows:

Chemical:
$$S_{8(l)} \underset{\text{dissolution}}{\overset{\text{precipitation}}{\rightleftharpoons}} S_{8(s)} \tag{311}$$

Electrochemical:
$$\frac{1}{2} S_8^{2-} \underset{\text{reduction}}{\overset{\text{oxidation}}{\rightleftharpoons}} \frac{1}{2} S_{8(l)} + e^- \tag{312}$$

Electrochemical:
$$S_4^{2-} \underset{\text{reduction}}{\overset{\text{oxidation}}{\rightleftharpoons}} \frac{1}{2} S_8^{2-} + e^- \tag{313}$$

Electrochemical:
$$\frac{2}{3} Li_2S_{(s)} \underset{\text{reduction}}{\overset{\text{oxidation}}{\rightleftharpoons}} \frac{4}{3} Li^+ + \frac{1}{6} S_4^{2-} + e^- \tag{314}$$

Here the first reaction (311) represents dissolution of impregnated solid sulfur which is a chemical reaction and depends on the solubility of sulfur in the electrolyte[127, 312]. The remaining three reactions are electrochemical in nature and describe the successive reduction of dissolved sulfur to higher-chain polysulfide (312), high-chain to medium-chain polysulfide (313) and electrodeposition of $Li_2S_{(s)}$ (314). Recent kinetic studies[146, 147] reveal that the electrochemical reduction of medium-chain polysulfides results in electrodeposition of $Li_2S_{(s)}$.

Based on the electrolyte transport description derived here before, the species balance for each individual species forming the electrolyte can be expressed in the form of

$$\frac{\partial}{\partial t}\left(\varepsilon C_i\right) = -\nabla \cdot N_i + \dot{R}_i$$

where ε is local porosity, C_i is species concentration, N_i is species flux and $\dot{R}_i$ is local species generation rate (related to chemical and/or electrochemical reactions (311) - (314)).

<u>*Cation flux*</u>:

$$\frac{\partial}{\partial t}\left(\varepsilon C_p\right) = \nabla \cdot \left(D_{pp}\nabla C_p + D_{px}\nabla C_x + D_{py}\nabla C_y + D_{ps}\nabla C_s\right) - \frac{t_p}{F}\nabla \cdot I + \dot{R}_p \tag{315}$$

<u>*Long-chain polysulfide flux*</u>:

$$\frac{\partial}{\partial t}\left(\varepsilon C_x\right) = \nabla \cdot \left(D_{xp}\nabla C_p + D_{xx}\nabla C_x + D_{xy}\nabla C_y + D_{xs}\nabla C_s\right) + \frac{t_x}{2F}\nabla \cdot I + \dot{R}_x \tag{316}$$

<u>*Medium-chain polysulfide flux*</u>:

$$\frac{\partial}{\partial t}\left(\varepsilon C_y\right) = \nabla \cdot \left(D_{yp}\nabla C_p + D_{yx}\nabla C_x + D_{yy}\nabla C_y + D_{ys}\nabla C_s\right) + \frac{t_y}{2F}\nabla \cdot I + \dot{R}_y \tag{317}$$

<u>*Dissolved sulfur flux*</u>:

$$\frac{\partial}{\partial t}\left(\varepsilon C_s\right) = \nabla \cdot \left(D_{sp}\nabla C_p + D_{sx}\nabla C_x + D_{sy}\nabla C_y + D_{ss}\nabla C_s\right) - \frac{t_s}{F}\nabla \cdot I + \dot{R}_s \tag{318}$$

The transference numbers are often found to demonstrate a weaker spatial dependence and corresponding the $\nabla \cdot t_i$ terms have been omitted from the above set of relations. Appropriate values for charge numbers, z 's, have been substituted as well. The conservation of ionic and electronic charges leads to the following two statements:

<u>*Ionic current*</u>:

$$\nabla \cdot \left(\kappa \nabla \phi_e + \kappa_p \nabla \ln C_p + \kappa_x \nabla \ln C_x + \kappa_y \nabla \ln C_y + \kappa_s \nabla \ln C_s\right) + \dot{J} = 0 \tag{319}$$

<u>*Electronic current*</u>:

$$\nabla \cdot \left(\sigma^{eff} \nabla \phi_s\right) = \dot{J} \tag{320}$$

where the expression (319) follows from (306) after a few rearrangements. ϕ_e is electrolyte phase potential (as defined with respect to an Li / Li^+ electrode) and ϕ_s is solid phase potential. $\dot{J}$ is total volumetric electrochemical reaction rate, defined as:

$$\dot{J} = j_{LS \to S} + j_{MS \to LS} + j_{Li_2S \to MS} \tag{321}$$

where the three terms on the right respectively identify the (volumetric) reaction rates associated with reactions (312) to (314). Note that:

$$\dot{J} = \nabla \cdot I \tag{322}$$

The individual species generation rates, R_i 's, are composed of these reactions as well:

$$\dot{R}_p = \frac{4}{3} \cdot \frac{j_{Li_2S \to MS}}{F} \tag{323}$$

$$\dot{R}_x = -\frac{1}{2} \cdot \frac{j_{LS \to S}}{F} + \frac{1}{2} \cdot \frac{j_{MS \to LS}}{F} \tag{324}$$

$$\dot{R}_y = -\frac{j_{MS \to LS}}{F} + \frac{1}{6} \cdot \frac{j_{Li_2S \to MS}}{F} \tag{325}$$

$$\dot{R}_s = \frac{1}{2} \cdot \frac{j_{LS \to S}}{F} - \dot{R}_{S\uparrow} \tag{326}$$

The reactions (311) and (314) also alter the solid content and in turn porosity as follows:

$$\frac{\partial \varepsilon_s}{\partial t} = \tilde{V}_s \dot{R}_{S\uparrow} \tag{327}$$

$$\frac{\partial \varepsilon_{Li_2S}}{\partial t} = -\tilde{V}_{Li_2S} \dot{R}_{Li_2S \to MS} \tag{328}$$

$$\frac{\partial}{\partial t}\left(\varepsilon + \varepsilon_S + \varepsilon_{Li_2S}\right) = 0 \tag{329}$$

Here ε_S is volume fraction of solid sulfur and ε_{Li_2S} is volume fraction of $Li_2S_{(s)}$.

The capacity of an LiS cathode is correlated to sulfur loading and in turn, the applied current at a prescribed C-rate also relates to volumetric sulfur loading.

$$Q_{capaity} = \frac{16F\varepsilon_S^0 L_{cat}}{3600\tilde{V}_S} \quad \left[\text{Ah/m}^2\right] \tag{330}$$

$$I_{app} = \text{C-rate} \cdot Q_{capacity} \quad \left[\text{A/m}^2\right] \tag{331}$$

The same set of relations (315) to (318) are valid in the separator with no source terms (both $\dot{R}_i$'s as well as $\nabla \cdot I$ vanish in separator). At the separator – anode (Li metal) interface, the electronic current converts to the ionic current in the form of Li^+. Mathematically, this amounts to the following set of boundary conditions:

$$-D_{pp}\nabla C_p - D_{px}\nabla C_x - D_{py}\nabla C_y - D_{ps}\nabla C_s = \left(1-t_p\right)\frac{I_{app}}{F} \tag{332}$$

$$-D_{xp}\nabla C_p - D_{xx}\nabla C_x - D_{xy}\nabla C_y - D_{xs}\nabla C_s = \frac{t_x}{2}\cdot\frac{I_{app}}{F} \tag{333}$$

$$-D_{yp}\nabla C_p - D_{yx}\nabla C_x - D_{yy}\nabla C_y - D_{ys}\nabla C_s = \frac{t_y}{2}\cdot\frac{I_{app}}{F} \tag{334}$$

$$-D_{sp}\nabla C_p - D_{sx}\nabla C_x - D_{sy}\nabla C_y - D_{ss}\nabla C_s = -t_s\frac{I_{app}}{F} \tag{335}$$

The solution of these governing equations with the corresponding boundary conditions is explained earlier[312]. An important fact to keep in mind while solving for these equations is sulfur conservation. The physicochemical changes taking place in the LiS system alter the form of sulfur while keeping the total sulfur content same. As discharge takes place, sulfur successively reduces and in turn reaches the state S^{2-} where it cannot be reduced further. In other words, the total sulfur content:

$$\Sigma S = \int_{L_{cat}}\left(\frac{\varepsilon_S}{\tilde{V}_S} + \varepsilon C_s + \varepsilon C_x + \frac{1}{2}\varepsilon C_y + \frac{1}{8}\cdot\frac{\varepsilon_{Li_2S}}{\tilde{V}_{Li_2S}}\right)\mathrm{d}x = \text{constant} = \frac{\varepsilon_S^0 L_{cat}}{\tilde{V}_S} \tag{336}$$

or,

$$\frac{d}{dt}\left(\Sigma S\right) = \int_{L_{cat}}\left(\frac{1}{\tilde{V}_S}\frac{\partial\varepsilon_S}{\partial t} + \frac{\partial\left(\varepsilon C_s\right)}{\partial t} + \frac{\partial\left(\varepsilon C_x\right)}{\partial t} + \frac{1}{2}\frac{\partial\left(\varepsilon C_y\right)}{\partial t} + \frac{1}{8\tilde{V}_{Li_2S}}\frac{\partial\varepsilon_{Li_2S}}{\partial t}\right)\mathrm{d}x = 0 \tag{337}$$

Note that the various coefficients ensure that the stoichiometrically correct amount of sulfur is accounted for while performing this balance. This also helps identify the (normalized) contributions from various sulfur forms at different instants of electrochemical operation:

$$f_{solid-sulfur} = \frac{1}{\left(\varepsilon_S^0 L_{cat}/\tilde{V}_S\right)}\int_{L_{cat}}\frac{\varepsilon_S}{\tilde{V}_s}\,\mathrm{d}x \tag{338}$$

$$f_{dissolved-sulfur} = \frac{1}{\left(\varepsilon_S^0 L_{cat}/\tilde{V}_S\right)}\int_{L_{cat}}\varepsilon C_s\,\mathrm{d}x \tag{339}$$

$$f_{long-chain-polysulfide} = \frac{1}{\left(\varepsilon_S^0 L_{cat} / \tilde{V}_S\right)} \int_{L_{cat}} \varepsilon C_x \, \mathrm{d}x \tag{340}$$

$$f_{medium-chain-polysulfide} = \frac{1}{\left(\varepsilon_S^0 L_{cat} / \tilde{V}_S\right)} \int_{L_{cat}} \frac{1}{2} \varepsilon C_y \, \mathrm{d}x \tag{341}$$

$$f_{solid-lithium-monosulfide} = \frac{1}{\left(\varepsilon_S^0 L_{cat} / \tilde{V}_S\right)} \int_{L_{cat}} \frac{\varepsilon_{Li_2S}}{8\tilde{V}_{Li_2S}} \, \mathrm{d}x \tag{342}$$

where $f_{solid-sulfur} + f_{dissolved-sulfur} + f_{long-chain-polysulfide} + f_{medium-chain-polysulfide} + f_{solid-lithium-monosulfide} = 1$. Similarly, the electrochemical reaction rates are re-scaled to comparison across different operating conditions.

6.12 Mechanistic Interpretation of Polysulfide Shuttle Effect

The polysulfide shuttle effect, where sulfur species reach the negative electrode surface and undergo chemical reduction, is believed to be a major bottleneck in lithium-sulfur chemistry. The importance of this phenomenon often judged based on phenomenological arguments, does not account for mesoscale complexations. This work presents a comprehensive investigation of the coupled interactions arising from speciation, concentrated electrolyte solution and reaction time scales. Polysulfide transport consists of diffusion and migration, which determines the net flux. This study demonstrates that the polysulfide shuttle effect can be bounded between reaction-limited and shuttle-limited regimes, depending on the operational extremes. At high sulfur to electrolyte ratio (*i.e.*, lean electrolyte condition), the polysulfide shuttle effect may not necessarily attribute to the cell performance limitation, believed contrarily otherwise.

Lithium-sulfur (LiS) chemistry has received a considerable attention of late given its superior theoretical promise as compared to the state of the art energy storage solutions[327, 392, 412-414]. It is a uniquely interesting electrochemical system where electroactive couples are different at anode $\left(Li \mid Li^+\right)$ and cathode $\left(S_8 \mid S_x^{2-}, x \in [1,8]\right)$. Sulfur species translate to the anode and chemically react with Li, thus leading to a reduced electrochemical capacity (in contrast, the Li^+ reaching cathode is already in the highest oxidation state and can only partake in non-redox

interactions of its own, such as Li_2S precipitation). This phenomenon has been termed as polysulfide shuttle effect and is traditionally believed to be the source of irreversibilities associated with the LiS system[148, 386, 404, 415-421]. Surprisingly even if the polysulfide shuttle is one of the most often discussed facet of the LiS, a fundamental understanding is lacking as the detailed mesoscale interactions have never been probed and explicit investigations have either measured cell level observables[130, 131, 393, 394, 422-426] or focused on anode surface[402, 403, 427]. Recent studies identify the presence of multi-modal physicochemical interactions fostering non-ideal response[428], such as precipitation-dissolution dynamics[116, 312, 381], interfacial kinetics[113, 115, 146, 147], concentrated solution effects[143, 361, 429, 430], and poromechanical progression[431, 432] to name a few. The nature of their convolution with the polysulfide shuttle remains unknown.

The polysulfide shuttle is essentially composed of two distinct events: shuttling of (electrolyte-phase) sulfur species and their subsequent chemical reduction at the anode. The species flux (*i.e.*, shuttle) is strongly related to cathode evolution[312] and electrolyte speciation[361]. The present study is aimed at delineating the intricate correlations among polysulfide shuttle and other dynamical progressions present therein. Contributions from responsible chemical reactions vary as sulfur is reduced further. During rest state, the chemical redox is responsible for self-discharge. Capacity defect defines the strength of chemical redox while electrochemical reactions are active (*i.e.*, charge/ discharge). On the other hand, difference potential characterizes the severity of these anode-centric reactions during the rest phase (*i.e.*, self-discharge). The non-monotonic trends resulting from differences in timescales for chemical and electrochemical reactions are analyzed as well. Sulfur and electrolyte contents affect polysulfide shuttle as they affect cathode starvation modes and electrolyte transport dynamics.

Figure 98(a) presents the potential evolution when sulfur impregnated in a mesoporous carbon structure is reduced at a 1C current (corresponding current value is linearly proportional to volumetric sulfur loading; refer to expressions (375) and (376)). The cell is composed of porous carbon cathode with 10 % vol. solid sulfur and 70 % initial porosity. Relevant modeling details are supplied in supporting information. Different forms of sulfur are generated at the cathode in response to physical changes (*e.g.*, dissolution of solid sulfur leading to dissolved sulfur in the electrolyte) and electrochemical reactions (*i.e.*, reduction of sulfur into successively smaller chain polysulfides) and can reach the anode.

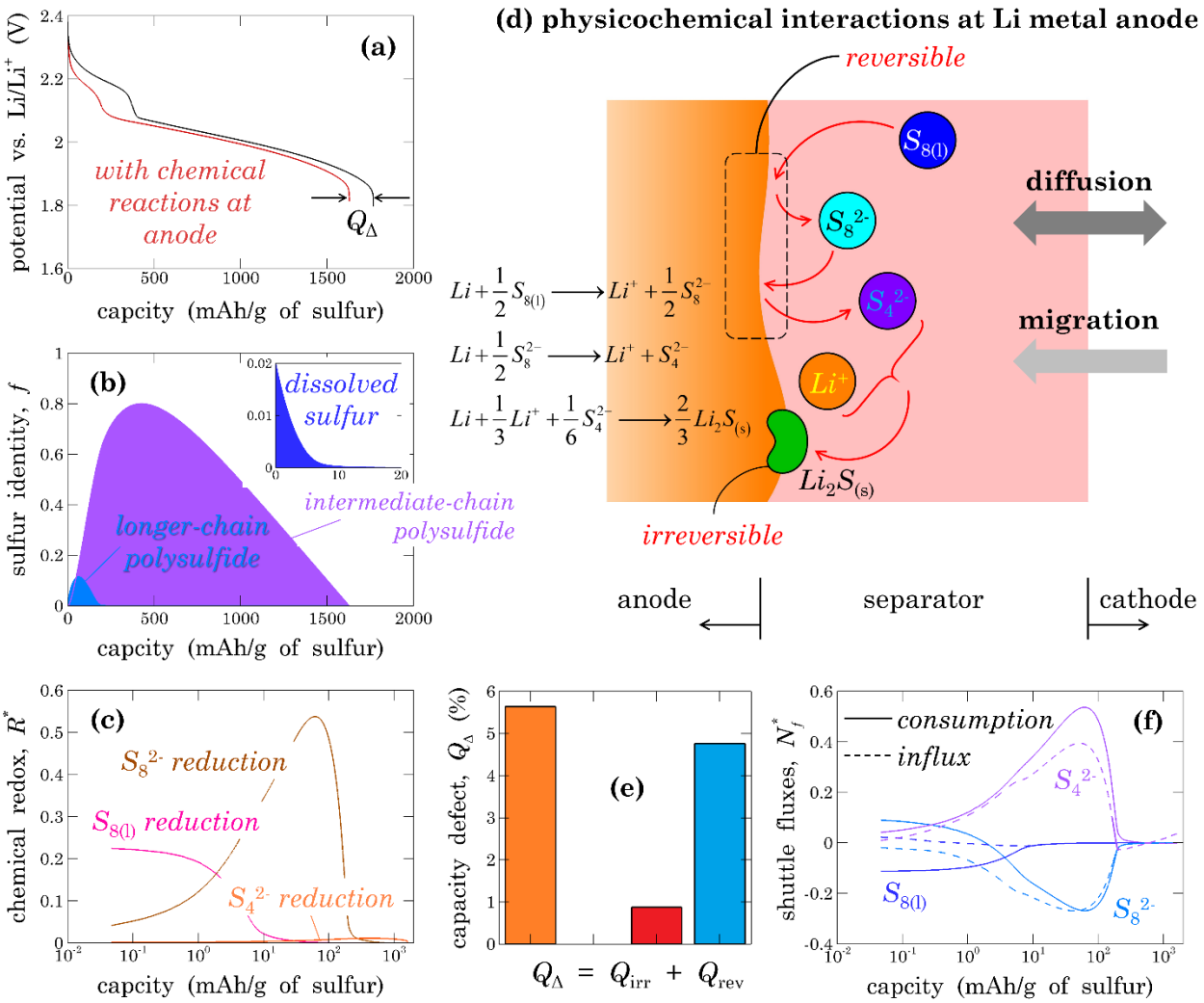

Figure 98. Physicochemical interpretation of polysulfide shuttle effect: (a) effect of chemical redox reactions at anode surface on potential evolution upon sulfur reduction; (b) chemical transitions of sulfur coincide with (c) predominant redox at anode surface; (d) a schematic illustrating the species influx from cathode and subsequent consumption (due to chemical reactions) at anode surface; (e) this chemical reduction of sulfur molecules reduces the achievable capacity that has both reversible and irreversible defects; (f) comparison of influx and consumption of sulfur species reveal that not all that comes in from cathode get reacted at anode and contribute to capacity defect.

The incoming flux of these electrolyte species is composed of two distinct transport modes (i) diffusion – related to concentration gradients and (ii) migration – due to electrolyte phase potential gradient (Figure 98(d)). These sulfur species interact with Li metal anode *via* chemical redox reactions, namely (353) to (355) (Li loses an electron and oxidizes, while sulfur species accept electrons and get reduced further; no electron is exchanged with the external circuit, hence such

reduction is purely chemical in nature). Note that these reactions are different than the electrochemical reduction of sulfur at cathode where electrons are exchanged with the external circuit. Figure 98(a) depicts the effect of sulfur reduction at anode on potential evolution. Quantitatively it manifests as a capacity difference, Q_{Δ}. The capacity defect, Q_{Δ}, is solely the contribution of anode surface reactions (refer to Table 16 for terminology). As authors have recognized earlier[312, 361], there are other possible sources of capacity loss such as surface passivation or transport losses, and all these combined together show a capacity less than 1675.12 mAh/g of solid sulfur.

Table 16. Terminology associated with the physicochemical description of polysulfide shuttle effect.

Terms	***Description***
Capacity defect, Q_{Δ}	is capacity loss due to chemical reduction at anode surface; there are other factors affecting capacity, for example, surface passivation
Reversible capacity defect, Q_{rev}	is a portion of capacity defect caused by chemical reduction where the reduced species returns back to the electrolyte
Irreversible capacity defect, Q_{irr}	is a portion of capacity defect caused by chemical reduction where the reduced species deposits at the anode
Voltage defect, Φ_{Δ}	is the difference between the rest phase voltage and open circuit potential; it is non-zero for a self-discharging cell; if a cell is let to self-discharge, all the sulfur is reduced *via* chemical reactions at anode and $Q_{\Delta} \rightarrow 100\%$
Chemical overpotential, η_{ch}	the reaction rate, *k*, for chemical reduction at the anode is correlated to exchange current density, i_0, for the corresponding reaction at the cathode; $k = \frac{i_0}{F}\exp\left(-\frac{F\eta_{\text{ch}}}{2RT}\right)$ chemical overpotential, η_{ch}, characterizes the reactivity of the anode surface
Influx	the flux of polysulfide species from the cathode to the separator
Consumption flux	the rate of polysulfide chemical reduction at anode – separator interface

Let's deconvolve these chemical interactions at the anode surface. Similar to electrochemical reduction events at the cathode, a commensurate set of reactions at take place at anode surface and exhibit chemical nature (Figure 98(d)). Figure 98(b) sketches the evolution of different sulfur forms in the cell (refer to Sulfur Balance Sheet for specific queries). For the particular rate of sulfur reduction being discussed here (Figure 98; 1C), life-span of various sulfur

species overlap. Given the finite solubility of dissolved sulfur, $S_{8(l)}$, it is never the dominant form of sulfur and coexists with other polysulfides. Longer-chain polysulfide, S_8^{2-}, achieves its highest concentration when the dissolved sulfur is nearly consumed (compare Figure 98(b) and inset). Once the potential drops below that for reduction of longer-chain polysulfide to intermediate-chain, these medium-chain polysulfides start forming. Beyond this point, one observes a continuous dissolution of solid sulfur, its reduction to longer-chain and subsequently intermediate-chain polysulfides. Compare the occurrence of these different sulfur species in the electrolyte (Figure 98(b)) with appropriate chemical reduction rates at anode surface (Figure 98(c)). These reaction rates have been normalized using the applied current density for a consistent interpretation across different operating conditions (note that each of these chemical reactions ((353) to (355)) are written as single electron exchange processes):

$$R^* = \frac{FR}{J_{app}} \tag{343}$$

Figure 98(b) and (c) jointly reveal that the dominant chemical redox closely follows the identity of sulfur species in the electrolyte phase (Figure 98(d)). The rate of each of these reactions depends on two factors: reactivity and reactant concentration. Reactivity is characterized by reaction rate constant (since these reactions are analogous to those taking place at the cathode, one would expect a qualitatively similar order of reactivity). This explains the difference in average reaction rates in Figure 98(c). Temporal variation in local reactant concentration correlates to the reaction rate evolutions for respective reduction events in Figure 98(c). Despite the fact that these reactions are all chemical in nature, their contributions to capacity defect, Q_Δ, are qualitatively different. Reduction of dissolved sulfur (reaction (353)) and longer-chain polysulfide (reaction (354)) release species in the electrolyte phase which in principle can be oxidized back to recover the capacity lost in the respective chemical reactions. On the other hand, the chemical reaction of intermediate-chain polysulfide (reaction (355)) deposits Li_2S at the anode and cannot be oxidized electrochemically. Thus, the total capacity defect (due to chemical redox at the anode) has two types of contributions: reversible, Q_{rev}, and irreversible, Q_{irr}.

$$Q_\Delta = Q_{\text{rev}} + Q_{\text{irr}} \tag{344}$$

$$Q_{\text{rev}} = \int_{T_{\text{operation}}} F\left(R_5 + R_6\right) \mathrm{d}t \tag{345}$$

$$Q_{\text{irr}} = \int_{T_{\text{operation}}} FR_7 \ \mathrm{d}t \tag{346}$$

Figure 98(e) inspects the contributions from these different forms for 1C operation. The values are normalized using the theoretical maximum capacity for a better appreciation. These chemical reactions are sustained based on the availability of sulfur species in the vicinity of the anode, which are primarily replenished due to the incoming flux from the cathode. Since no electrochemical reactions take place in the separator, ionic current at any cross-section along the thickness direction is constant and equal to the applied current density:

$$I = F\left(N_p + z_a N_a - 2N_x - 2N_y\right) = J_{app} \tag{347}$$

Going from anode – to – cathode, the net ionic current remains invariant but the contribution from individual species varies based on local concentration distributions, which are not necessarily monotonic. Take longer-chain polysulfide for instance: at first electrochemical reduction generates a positive slope in S_8^{2-} concentration at the cathode – separator interface which amounts to an influx of S_8^{2-}, while based on relative extents of reduction events at anode surface, its flux at anode (*i.e.*, consumption) changes sign (early on $S_{8(l)}$ reduction generates S_8^{2-} which is a positive flux, later on, reduces to S_4^{2-} and in turn causes a negative flux; Figure 98(f)). Note that at each cross-section, local charge neutrality is ensured. Given the presence of multiple anions, at each location, one has non-trivial profiles for ionic concentrations. Such speciation gives rise to a disparity between the influx of sulfur species at the cathode-separator interface (ions coming from cathode to separator) and subsequent consumption of respective ions at anode-separator interface (related to chemical redox reactions). This mismatch leads to accumulation (or attenuation) of a specific ion in the separator. In other words, even if ions enter separator from the cathode side, the portion that gets reacted at the anode surface relies on the transport effectiveness of electrolyte through the separator pore network. Figure 98(f) sketches these two fluxes for the species of interest: $S_{8(l)}, S_8^{2-}, S_4^{2-}$. At the start of discharge, dissolved sulfur has the same concentration throughout the electrolyte phase (equal to solubility). It starts being consumed (chemically) at anode surface (hence negative flux – solid line) and (electrochemically) inside cathode (*i.e.*, diffuses from the

separator to cathode and the positive influx – dashed line). Later on, once longer-chain polysulfides are generated at the cathode, they start being transported to the anode. Simultaneously, first, the longer-chain polysulfides are generated at the anode and subsequently consumed, which explains the change in sign of the consumption flux. This generation of intermediate-chain polysulfides at anode gives rise to an outflux of the ions to cathode until their concentration due to electrochemical reduction at cathode reverses this gradient and makes it an influx (this inversion is apparent in Figure 98(f)). The direction of this flux might further change if electrodeposition of Li_2S in cathode is sufficient to reduce the intermediate polysulfide concentration at the cathode and in effect cause an inflow. In nutshell, polysulfides do not always move from cathode to anode, even when the net ionic current flows from anode to cathode, since the species flux is composed of diffusion and migration contributions. Their fluxes depend on local concentration gradients which in turn are closely related to the rates of chemical reaction at the anode and electrochemical reactions at the cathode. Diffusion directly involves concentration gradients, while migration indirectly depends on local concentration *via* transference numbers (transference numbers quantify the portion of ionic current being carried by the respective ion).

6.13 Importance of Reaction Timescales

Given the correspondence among the anode and cathode reactions, their rate constants are interrelated. The severity of anode surface reactions can be characterized by chemical overpotential, η_{ch} (expressions (377) to (379)). As chemical overpotential approaches zero, the anode surface reactions are more spontaneous (thermodynamically favored) and in turn faster. These chemical reactions take place even under open circuit conditions (*i.e.*, no passage of current across the cell). After assembly, impregnated solid sulfur dissolves in the electrolyte (finite solubility) and in turn diffuses to the anode and experiences chemical reduction events. This effectively increases the net charge per sulfur atom and equivalently the cell voltage and capacity diminish. This amounts to the self-discharge in LiS and can be quantitatively related to drop in open circuit potential (referred to as the difference potential) $\Phi_\Delta = U - V$, where U is open circuit potential of the pristine cell and $V = V(t)$ (hence $\Phi_\Delta = \Phi_\Delta(t)$), identifies the evolution of electrochemical state given the chemical redox reactions at the anode surface. The capacity defect and difference potential represent two different aspects of these redox interactions at the anode.

Under self-discharge, all the capacity loss is the capacity defect (with different time scales), and difference potential characterizes the severity of these unwanted reactions. On the other hand, during the electrochemical operation, multiple interactions take place simultaneously and Q_Δ is a direct indicator. As the rate of these reactions is increased (*i.e.*, $\eta_{ch} \to 0$), charge accumulation on sulfur is faster and in turn, the difference potential, $\Phi_\Delta(t)$, increases rapidly (Figure 99(a)). In other words, Φ_Δ measurements can shed light on the chemical reactivity of anode. Figure 99(b) correlates the severity of this chemical redox with changes in electrochemical response. As chemical redox becomes severe, capacity defect becomes more prominent.

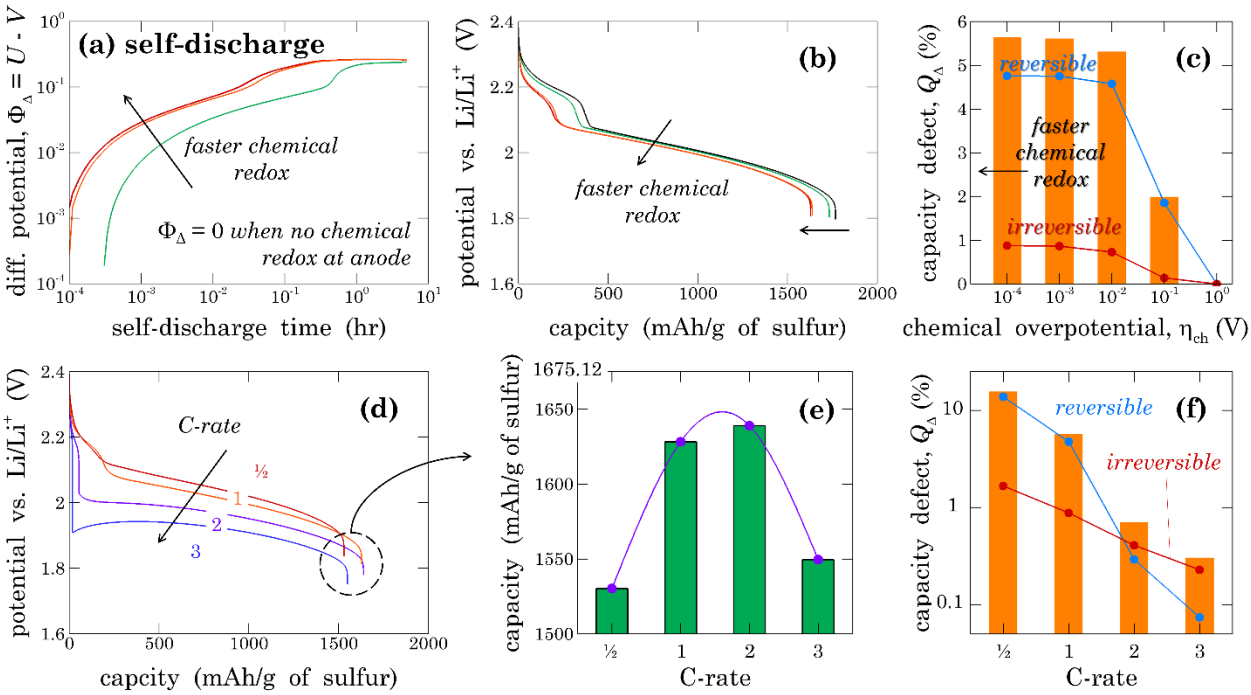

Figure 99. Effect of reaction time scales: (a) anode surface reactions gradually reduce sulfur and in turn limit the cell capacity; the severity of redox reactions is apparent from difference potential evolution during self-discharge; (b-c) at constant C-rate, faster chemical redox means more capacity defect and shortened upper plateau; reversible and irreversible contributions also grow monotonically; (d-f) as C-rate increases, the timescale of electrochemical reactions decreases which reduce the capacity defect but cathode and electrolyte limitations become dominant causing a quadratic capacity trend.

Interestingly, the width of the upper voltage plateau also reduces (1C operation) which effectively relates to the fraction of dissolved sulfur participating in electrochemical reduction at the cathode.

Corresponding capacity defects are sketched in Figure 99(c) along with their reversible and irreversible components. Capacity defect increases monotonically with faster anode reactions.

In contrast, Figure 99(d) – (f) explore the role of cathode electrochemical reactions (at constant polysulfide reactivity). As C-rate is increased, the time scale for electrochemical progression becomes smaller (chemical reaction time scales are rather intrinsically fixed), and one would expect more electrochemical reactions than chemical and subsequently smaller capacity defect (Figure 99(e)). As electrochemical reactions become faster, sulfur species experience faster electrochemical reduction. In fact, going from a low to a high C-rate, cathode reaction order[312] gradually changes from a successive to simultaneous as potential drops below the OCPs for all reactions. This effectively alters the composition of species influx from the cathode to the anode. At higher operating rates, species influx contains a greater amount of reduced sulfur which results in a smaller quantity of chemical interactions at anode surface (Figure 99(f)). There is an additional contribution here. Going towards higher rates, concentration gradients become sharper and in turn, the disparity between the influx and consumption becomes starker (Figure 101) which amounts to the smaller amount of chemical redox at higher rates. This accounts for increased capacity going from low to moderate rates of operation as plotted in Figure 99(e). While at larger rates, physicochemical changes are more drastic at the cathode and lead to inferior performance[312]. These manifest as a nonlinear trend in cell capacity. Figure 99(f) exhibits an interesting trend: relative importance of reversible and irreversible defects qualitatively changes going to higher rates. With increasing rates, the amount of intermediate polysulfide increases in the incoming species flux. This makes the reduction of intermediate polysulfide and irreversible formation of Li_2S at anode the dominant anode reaction and in turn results in a higher irreversible capacity defect. On the other hand, at lower rates, higher order sulfur species do not electrochemically react fast enough, transport towards the anode and participate in reversible chemical reduction. Given the higher reactivity of these higher order sulfur, contributions from the reversible capacity defect are greater when sulfur molecules reaching anode are in low enough reduction state.

6.14 Multimodal Interactions and Competing Limitations

Sulfur-to-electrolyte ratio (S/E) and cathode pristine porosity jointly identify the evolution of cathode microstructure[312] and electrolyte transport. Both these phenomena affect the spatial

distribution of ionic species and consequently the anode surface reactions. Corresponding results are presented in Figure 100. Note that S/E and ε^0 together fix the volumetric sulfur loading:

$$\varepsilon_S^0 = \frac{\varepsilon^0}{\left(1+\frac{\rho_S}{\text{S/E}}\right)} \tag{348}$$

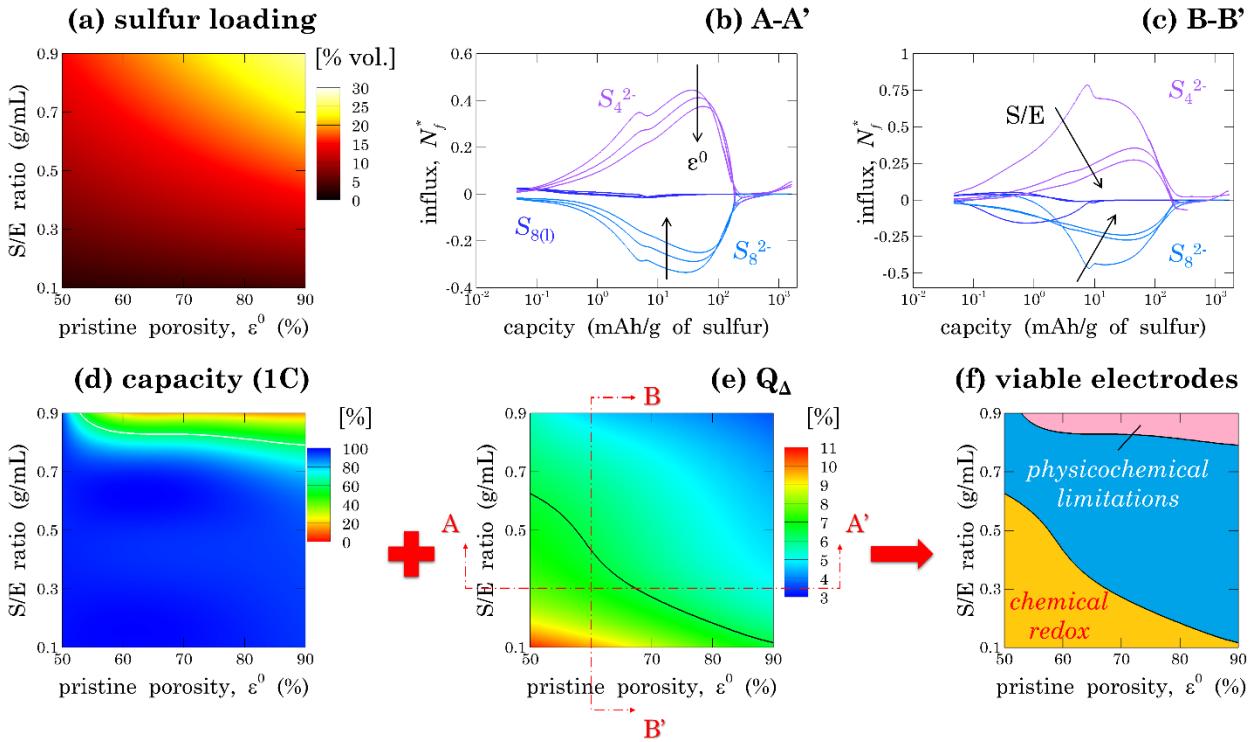

Figure 100. Cathode specifications dictate cell limitations: (a) volumetric sulfur loading as a function of S/E ratio and pristine porosity; (b) electrochemical capacity at 1C and (e) capacity defect maps help identify (f) viable electrodes that have marginal limitations from various interactions; (b) sulfur influx from cathode to anode as cathode porosity is increased and (c) as S/E ratio is increased.

As mentioned earlier, ionic current is proportional to the sulfur loading ((375) and (376)) and consequently, the migration flux increases with increase in either S/E or ε^0 (Figure 100(a)). Curiously, the capacity defect decreases with either of these modifications (Figure 100(e)) because of diffusive transport and faster electrochemical reactions at the cathode. As sulfur loading is increased, operating current increases (at constant C-rate), which results in stronger concentration gradients and in turn diffusive transport is also important. Additionally, the electrochemical reactions become faster and the sulfur species have a greater tendency to get reacted at cathode

rather than to transport to the anode. These two events cooperate with each other and effectively reduce the sulfur transport to the anode. These behavioral transitions are confirmed by the evolution of species influx with pristine porosity (Figure 100(b)) and the sulfur-to-electrolyte ratio (Figure 100(c)). Thus, capacity defect diminishes at higher ε^0 and/or S/E ratio. Figure 102 presents a comparison of consumption and influx for the different conditions along cuts AA' and BB' in Figure 100(e). Study of Figure 102 reveals that higher porosity (at constant S/E) reduces the influx and equivalently the consumption of each of these sulfur molecules. A similar trend is observed when S/E is increased at a constant pristine porosity (Figure 102). Observe that small S/E ratio and high ε^0 both represent more electrolyte, yet their effect on cell response is very different. Smaller S/E leads to more chemical reactions at anode surface as sulfur species are transported to anode more efficiently, while higher ε^0 reduces the reaction rate as more electrolyte volume is available at the cathode to retain more polysulfides.

At higher S/E ratio (*i.e.*, lean electrolyte conditions), cell capacity drops significantly in response to severe physicochemical changes taking place at cathode and electrolyte which comprises of surface passivation, pore blockage and concentrated solution effects (Figure 100(d)). Maps of capacity (Figure 100(d)) and capacity defect (Figure 100(e)) paint a comprehensive picture of limitations in LiS. Figure 100(f) reveals that smaller S/E and electrode porosity result in an enhanced contribution from chemical redox at the anode. On the other hand, with higher sulfur content, a major source of limitation is a physical and chemical progression of cathode and electrolyte. This identifies an intermediate range of cathode specifications where the limitations from each anode, electrolyte, and cathode are marginal.

6.15 Complexations associated with Polysulfide Shuttle

Electrolyte based sulfur species travel to the anode and undergoes chemical reduction given the high reactivity of Li metal. The deleterious effects are caused by the reduction at the anode, while the reactant flux is controlled by a multitude of factors such as cathode evolution, electrolyte transport dynamics and the rate of anode-centric chemical reactions. This transport of species, *i.e.*, shuttling, in itself is not detrimental. For instance, during self-discharge, there is no net current, *i.e.*, no driving force for polysulfides to travel from cathode to anode. However, due to the reaction of sulfur species at the anode, a net flux exists. Thus, it is a reaction-limited extreme of polysulfide shuttle effect. On the other hand, during electrochemical reduction of sulfur at the cathode (i.e.,

discharge), sulfur species travel to the anode in response to concentration and potential gradients. Potential gradients drive transport from cathode to anode, while concentrations evolve non-monotonically and can give rise to fluxes in either direction. This is a shuttle-limited scenario where the extent of chemical reduction depends on the amount of sulfur species coming from cathode to anode. There are various aspects of this extreme. If the electrochemical reactions are carried out faster, the flux reaching anode is in a more reduced state and effectively the severity of anode chemical reactions decreases. If the electrolyte is highly concentrated (*i.e.*, high sulfur – to – electrolyte ratio), its transport effectiveness diminishes and results in smaller polysulfide flux and in turn less detrimental chemical reduction at the anode. In nutshell, the root cause of issues associated with the polysulfide shuttle effect is the anode's ability to reduce incoming sulfur species, and not the species flux (*i.e.*, shuttle). The article title points to this fundamental distinction.

In conclusion, the polysulfide shuttle effect is much more intricate than the phenomenological arguments about its deleterious contributions. Physicochemical investigation reveals that it is composed of two distinct effects: transport of sulfur species to the anode and subsequent chemical reduction at the anode surface. These redox reactions give rise to reversible and irreversible capacity defect. The transport itself is composed of diffusive and migration contributions. Even if the migration flux is always from the cathode to anode, speciation and reaction rates dictate the diffusive fluxes and in turn net transport. Given the multitude of factors affecting transport, the extent of the polysulfide shuttle effect demonstrates a nonlinear dependence on operating conditions. Under lean electrolyte conditions (high S/E ratio), hindered species transport limits the negative contribution of polysulfide shuttle effect and rather cathode and electrolyte phase interactions become performance limiting.

6.16 Chemical Interactions in the Li-sulfur Cell

A major source of complexity in Li-sulfur chemistry is the presence of multiple chemical and electrochemical reactions. Additionally, sulfur exists in different forms – different polysulfide ions in electrolyte phase and solid species. Given the presence of multiple electrolyte species, transport interactions are also closely intertwined.

The following set of reactions are considered at the cathode:

(chemical) dissolution of solid sulfur:

$$S_{8(l)} \underset{\text{dissolution}}{\overset{\text{preccipitation}}{\rightleftharpoons}} S_{8(s)} \tag{349}$$

(electrochemical) dissolved sulfur to higher-chain polysulfide:

$$\frac{1}{2}S_8^{2-} \rightleftharpoons \frac{1}{2}S_{8(l)} + e^- \tag{350}$$

(electrochemical) higher-chain to medium-chain polysulfide:

$$S_4^{2-} \rightleftharpoons \frac{1}{2}S_8^{2-} + e^- \tag{351}$$

(electrochemical) medium-chain polysulfide electrodeposition:

$$\frac{2}{3}Li_2S_{(s)} \rightleftharpoons \frac{4}{3}Li^+ + \frac{1}{6}S_4^{2-} + e^- \tag{352}$$

Note that during discharge operation, reactions (350) to (352)represent a successive electrochemical reduction of sulfur and are the source of electrochemical energy. If any of these molecules (*i.e.*, $S_{8(l)}, S_8^{2-}, S_4^{2-}$) reach anode, high electropositivity of Li metal can chemically reduce. These chemical reduction events represent a direct exchange of electrons from Li to sulfur species in the electrolyte. This is different compared to the electrochemical reduction of sulfur at cathode where (electrochemical) oxidation of lithium at anode $\left(Li \rightleftharpoons Li^+ + e^-\right)$ releases an electron in the external circuit that reaches cathode and partakes in electrochemical reduction of sulfur. Thus, the portion of sulfur reduction that takes place given the direct exchange of electrons at Li metal anode, refers to a defect in electrochemical performance. Appropriate reactions are as follows:

(chemical) reduction of dissolved sulfur:

$$Li + \frac{1}{2}S_{8(l)} \xrightarrow{\text{reduction}} Li^+ + \frac{1}{2}S_8^{2-} \tag{353}$$

(chemical) reduction of higher-chain polysulfide:

$$Li + \frac{1}{2}S_8^{2-} \xrightarrow{\text{reduction}} Li^+ + S_4^{2-} \tag{354}$$

(chemical) reduction of medium-chain polysulfide:

$$Li + \frac{1}{3}Li^+ + \frac{1}{6}S_4^{2-} \xrightarrow{\text{reduction}} \frac{2}{3}Li_2S_{(s)} \tag{355}$$

Thus, the following species (ionic and neutral) coexists in the electrolyte phase. The relative proportions of each will not only depend on the reaction rates but also on the transport interactions. The electrolyte transport for such a multispecies electrolyte is to be described by concentrated solution theory[22, 361] in order to account for the effects arising from interspecies and interspecies interactions. Authors have recently developed a formalism[361] to describe such an interaction. The appropriate forms of transport laws are $\left(p : Li^+ \mid s : S_{8(l)} \mid x : S_8^{2-} \mid y : S_4^{2-}\right)$:

Li^+ *ionic flux*:

$$N_p = -\mathcal{D}_{pp}\nabla C_p - \mathcal{D}_{ps}\nabla C_s - \mathcal{D}_{px}\nabla C_x - \mathcal{D}_{py}\nabla C_y + t_p\frac{I}{F} + C_p V \tag{356}$$

$S_{8(l)}$ <u>*species flux*</u>:

$$N_s = -\mathcal{D}_{sp}\nabla C_p - \mathcal{D}_{ss}\nabla C_s - \mathcal{D}_{sx}\nabla C_x - \mathcal{D}_{sy}\nabla C_y + t_s\frac{I}{F} + C_s V \tag{357}$$

S_8^{2-} <u>*ionic flux*</u>:

$$N_x = -\mathcal{D}_{xp}\nabla C_p - \mathcal{D}_{xs}\nabla C_s - \mathcal{D}_{xx}\nabla C_x - \mathcal{D}_{xy}\nabla C_y - t_x\frac{I}{2F} + C_x V \tag{358}$$

S_4^{2-} <u>*ionic flux*</u>:

$$N_y = -\mathcal{D}_{yp}\nabla C_p - \mathcal{D}_{ys}\nabla C_s - \mathcal{D}_{yx}\nabla C_x - \mathcal{D}_{yy}\nabla C_y - t_y\frac{I}{2F} + C_y V \tag{359}$$

<u>*Ionic current*</u>:

$$I = -\kappa\nabla\phi_e - \kappa_p\nabla\ln C_p - \kappa_s\nabla\ln C_s - \kappa_x\nabla\ln C_x - \kappa_y\nabla\ln C_y \tag{360}$$

Note that the flux of each species is affected by gradients in other species concentrations. Additionally, each of these transport coefficients exhibits dependence on local species concentration. The first term in the ionic current quantifies the migrational current, while the remaining four accounts for the diffusional contributions. Here V is the bulk electrolyte velocity.

Given the local charge neutrality, the concentration of primary salt anion (*e.g.*, *TFSI*$^-$ in *LiTFSI*) is correlated to other concentration and one does not need to track it separately. Here z_a is the charge number of the anion A^{z_a} in primary salt $Li_{\nu_p}A_{\nu_a}$ and ν_p, ν_a are stoichiometric coefficients.

<u>*Local charge neutrality (primary salt anion concentration)*</u>:

$$C_p + z_a C_a - 2C_x - 2C_y = 0 \tag{361}$$

6.17 Electrochemical Description for the Li-sulfur Cell

Following up from the reaction and transport description presented in the previous section, one can identify the appropriate set of governing equations for the Li-S chemistry[312, 381] as follows:

Li^+ <u>*balance*</u>: (362)

$$\frac{\partial(\varepsilon C_p)}{\partial t} = \nabla\cdot\left(\mathcal{D}_{pp}\frac{\varepsilon}{\tau}\nabla C_p\right) + \nabla\cdot\left(\mathcal{D}_{ps}\frac{\varepsilon}{\tau}\nabla C_s\right) + \nabla\cdot\left(\mathcal{D}_{px}\frac{\varepsilon}{\tau}\nabla C_x\right) + \nabla\cdot\left(\mathcal{D}_{py}\frac{\varepsilon}{\tau}\nabla C_y\right) - t_p\frac{J}{F} + R_p$$

$S_{8(l)}$ <u>*balance*</u>: (363)

$$\frac{\partial(\varepsilon C_s)}{\partial t} = \nabla\cdot\left(\mathcal{D}_{sp}\frac{\varepsilon}{\tau}\nabla C_p\right) + \nabla\cdot\left(\mathcal{D}_{ss}\frac{\varepsilon}{\tau}\nabla C_s\right) + \nabla\cdot\left(\mathcal{D}_{sx}\frac{\varepsilon}{\tau}\nabla C_x\right) + \nabla\cdot\left(\mathcal{D}_{sy}\frac{\varepsilon}{\tau}\nabla C_y\right) - t_s\frac{J}{F} + R_s$$

S_8^{2-} <u>*balance*</u>: (364)

$$\frac{\partial\left(\varepsilon C_x\right)}{\partial t}=\nabla\cdot\left(\mathcal{D}_{xp}\frac{\varepsilon}{\tau}\nabla C_p\right)+\nabla\cdot\left(\mathcal{D}_{xs}\frac{\varepsilon}{\tau}\nabla C_s\right)+\nabla\cdot\left(\mathcal{D}_{xx}\frac{\varepsilon}{\tau}\nabla C_x\right)+\nabla\cdot\left(\mathcal{D}_{xy}\frac{\varepsilon}{\tau}\nabla C_y\right)+t_x\frac{J}{2F}+R_x$$

S_4^{2-} <u>*balance*</u>: (365)

$$\frac{\partial\left(\varepsilon C_y\right)}{\partial t}=\nabla\cdot\left(\mathcal{D}_{yp}\frac{\varepsilon}{\tau}\nabla C_p\right)+\nabla\cdot\left(\mathcal{D}_{ys}\frac{\varepsilon}{\tau}\nabla C_s\right)+\nabla\cdot\left(\mathcal{D}_{yx}\frac{\varepsilon}{\tau}\nabla C_x\right)+\nabla\cdot\left(\mathcal{D}_{yy}\frac{\varepsilon}{\tau}\nabla C_y\right)+t_y\frac{J}{2F}+R_y$$

<u>*Ionic current conservation*</u>: (366)

$$\nabla\cdot\left(\kappa\frac{\varepsilon}{\tau}\nabla\phi_e\right)+\nabla\cdot\left(\kappa_p\frac{\varepsilon}{\tau}\nabla\ln C_p\right)+\nabla\cdot\left(\kappa_s\frac{\varepsilon}{\tau}\nabla\ln C_s\right)+\nabla\cdot\left(\kappa_x\frac{\varepsilon}{\tau}\nabla\ln C_x\right)$$
$$+\nabla\cdot\left(\kappa_y\frac{\varepsilon}{\tau}\nabla\ln C_y\right)+J=0$$

<u>*Electronic current conservation*</u>: (367)

$$\nabla\cdot\left(\sigma^{eff}\nabla\phi_s\right)=J$$

$S_{8(s)}$ <u>*evolution*</u>: (368)

$$\frac{\partial\varepsilon_S}{\partial t}=\tilde{V}_S R_1$$

$Li_2S_{(s)}$ <u>*evolution*</u>: (369)

$$\frac{\partial\varepsilon_{Li_2S}}{\partial t}=-\tilde{V}_{Li_2S}\frac{2J_4}{3F}$$

<u>*Porosity evolution*</u>: (370)

$$\frac{\partial}{\partial t}\left(\varepsilon+\varepsilon_S+\varepsilon_{Li_2S}\right)=0$$

Note that net local electrochemical reactions are $J=J_2+J_3+J_4$ where subscripts identify the appropriate reaction prescribed earlier. The generation terms for electrolyte species balance (*i.e.*, *R*'s) are correlated to individual reaction rates (*R*: chemical reaction and *J*: electrochemical reaction) *via* reaction stoichiometry. Cathode microstructure evolves in response to precipitation/dissolution events (reactions (349) and (352)) and this evolution is accounted for by appropriately evolving the relevant effective properties (tortuosity, active area, conductivity) based on pore-scale calculations reported earlier[312].

Note that the chemical reactions at the anode surface appear as interface fluxes and are incorporated in anode-separator boundary conditions:

Li^+ :
$$N_p\big|_{a/s}=\frac{J_{app}}{F}+R_5+R_6-\frac{1}{3}R_7 \tag{371}$$

$S_{8(l)}$:
$$N_s\big|_{a/s}=-\frac{1}{2}R_5 \tag{372}$$

S_8^{2-} :
$$N_x\big|_{a/s}=\frac{1}{2}R_5-\frac{1}{2}R_6 \tag{373}$$

S_4^{2-} :

$$N_y\Big|_{a/s} = R_6 - \frac{1}{6}R_7 \tag{374}$$

Here the applied current density, J_{app} is related to the cell capacity, Q_{cell} *via* C-rate:

$$J_{app} = \text{C-rate} \cdot Q_{cell} \tag{375}$$

$$Q_{cell} = \frac{16F\varepsilon_S^0 L_{cat}}{3600\tilde{V}_S} \qquad [\text{Ah}] \tag{376}$$

It is expected that each sulfur species exhibits different reactivity towards Li metal anode (same as they have different exchange current densities for electrochemical reactions at the cathode). For consistency, reaction rates for chemical reduction at the anode are expressed in terms of corresponding electrochemical reaction at the cathode. For example, reaction current density for reaction (350) is defined as:

$$j_2 = \frac{J_2}{a} = i_2^0 \left\{ \left(\frac{C_x}{C_x^{ref}} \right)^{1/2} e^{\frac{F}{2RT}(\phi_s - \phi_e - U_2)} - \left(\frac{C_s}{C_s^{ref}} \right)^{1/2} e^{-\frac{F}{2RT}(\phi_s - \phi_e - U_2)} \right\} \tag{377}$$

and equivalently the rate of sulfur reduction at anode surface (reaction (353)) is:

$$R_5 = k_5 \left(\frac{C_s}{C_s^{ref}} \right)^{1/2} \tag{378}$$

where the rate constant has been expressed in the form of exchange current density and chemical overpotential:

$$k_5 = \frac{i_2^0}{F} e^{-\frac{F\eta_{ch}}{2RT}} \tag{379}$$

Smaller values of chemical overpotential mean faster kinetics at the anode surface. Here a is a local electrochemically active area (m^2/m^3), j_2 is a reaction rate in A/m^2 of the active surface and R_5 is reaction rate in $mol/m^2/s$.

6.18 Sulfur Balance Sheet

Sulfur is present in various different forms in the Li-sulfur cell, for example, as solid sulfur impregnated in the carbon cathode or as medium-chain polysulfide in the electrolyte. Since sulfur does not leave the system, the net amount of sulfur must stay constant. In other words, sulfur changes the physical form (solid or dissolved) but such that globally total sulfur content is time invariant. Initially sulfur is present as solid impregnated sulfur, hence initial sulfur content is:

$$\$(t=0)=\int_{L_{cat}}\frac{\varepsilon_S}{\tilde{V}_S}\,\mathrm{d}x=\frac{\varepsilon_S^0}{\tilde{V}_s}L_{cat} \tag{380}$$

At any later time, sulfur content can be quantified as:

$$\$(t)=\int_{L_{cat}}\frac{\varepsilon_S}{\tilde{V}_S}\,\mathrm{d}x+\int_{L_{sep}+L_{cat}}\left(\varepsilon C_s+\varepsilon C_x+\frac{1}{2}\varepsilon C_y\right)\mathrm{d}x+\int_{L_{cat}}\frac{\varepsilon_{Li_2S}}{8\tilde{V}_{Li_2S}}\,\mathrm{d}x+\frac{\varphi_{Li_2S}}{8\tilde{V}_{Li_2S}} \tag{381}$$

Here φ_{Li_2S} is the volume of Li_2S deposited on the anode (m^3 of Li_2S/m^2 of anode surface) due to chemical reduction of medium-chain polysulfide (reaction (355)). Except for formation at the anode, all the other interactions return the sulfur back to the reaction zone. In other words, φ_{Li_2S} refers to the irreversible sulfur loss from the inventory.

$$\frac{d\varphi_{Li_2S}}{dt}=\tilde{V}_{Li_2S}\frac{2R_7}{3} \tag{382}$$

Each of these forms of sulfur can be expressed as a fraction of the total sulfur to fix the identity of sulfur at a given stage during electrochemical operation, for example, a fraction of dissolved sulfur is:

$$f_{dissolved-sulfur}=\frac{1}{\left(L_{cat}\varepsilon_S^0\big/\tilde{V}_s\right)}\int_{L_{sep}+L_{cat}}\varepsilon C_s\,\mathrm{d}x \tag{383}$$

6.19 Physicochemical Interactions in the Separator

There are two distinct interactions associated with the polysulfide shuttle effect:

i. transport of sulfur species from the cathode
ii. chemical reduction of sulfur at the anode surface

The transport of these species from the cathode is identified by fluxes at the cathode-separator interface, while the chemical reactions take place at anode-separator interface. Separator behaves as a host space for these interactions. Integrating sulfur species balances (expressions (363) to (365)) over the separator, one arrives at the following set of identities:

$$\frac{\partial}{\partial t}\left(\int_{L_{sep}}\varepsilon C_s\,\mathrm{d}x\right)=N_s\big|_{a/s}-N_s\big|_{c/s} \tag{384}$$

$$\frac{\partial}{\partial t}\left(\int_{L_{sep}}\varepsilon C_x\,\mathrm{d}x\right)=N_x\big|_{a/s}-N_x\big|_{c/s} \tag{385}$$

$$\frac{\partial}{\partial t}\left(\int_{L_{sep}} \varepsilon C_y \, \mathrm{d}x\right) = N_y\Big|_{a/s} - N_y\Big|_{c/s} \tag{386}$$

where the fluxes at the anode – separator interface are related to chemical reaction rates as per equations (372) – (374), while the ones at the cathode – separator interface are quantified from generalized transport laws (357) – (359). Note that the cathode – separator fluxes represent the amount of each of these reactants that are shuttled from cathode to anode. Any mismatch between the two manifests as sulfur accumulation in the separator.

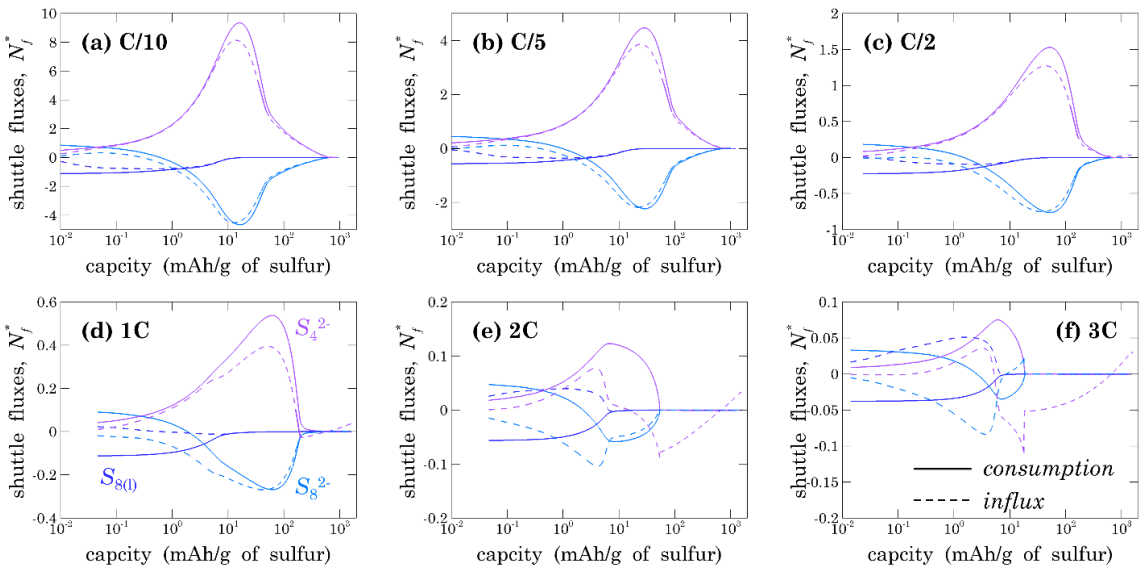

Figure 101. Evolution of sulfur shuttle fluxes changes qualitatively as electrochemical reactions are carried out faster.

Separator species balances (384) – (386) allow a consistent interpretation of the severity of chemical reduction at the anode surface. It also points to the different effects that jointly give rise to a loss in electrochemical performance: shuttling of ions (c/s) and subsequent reactions (a/s). Not necessarily all that shuttles from cathode participate in these side reactions at the anode. For ease of interpretation (across C-rate especially), each of these fluxes is normalized using the applied current density:

$$N_f^* = \frac{FN_f}{J_{app}} \tag{387}$$

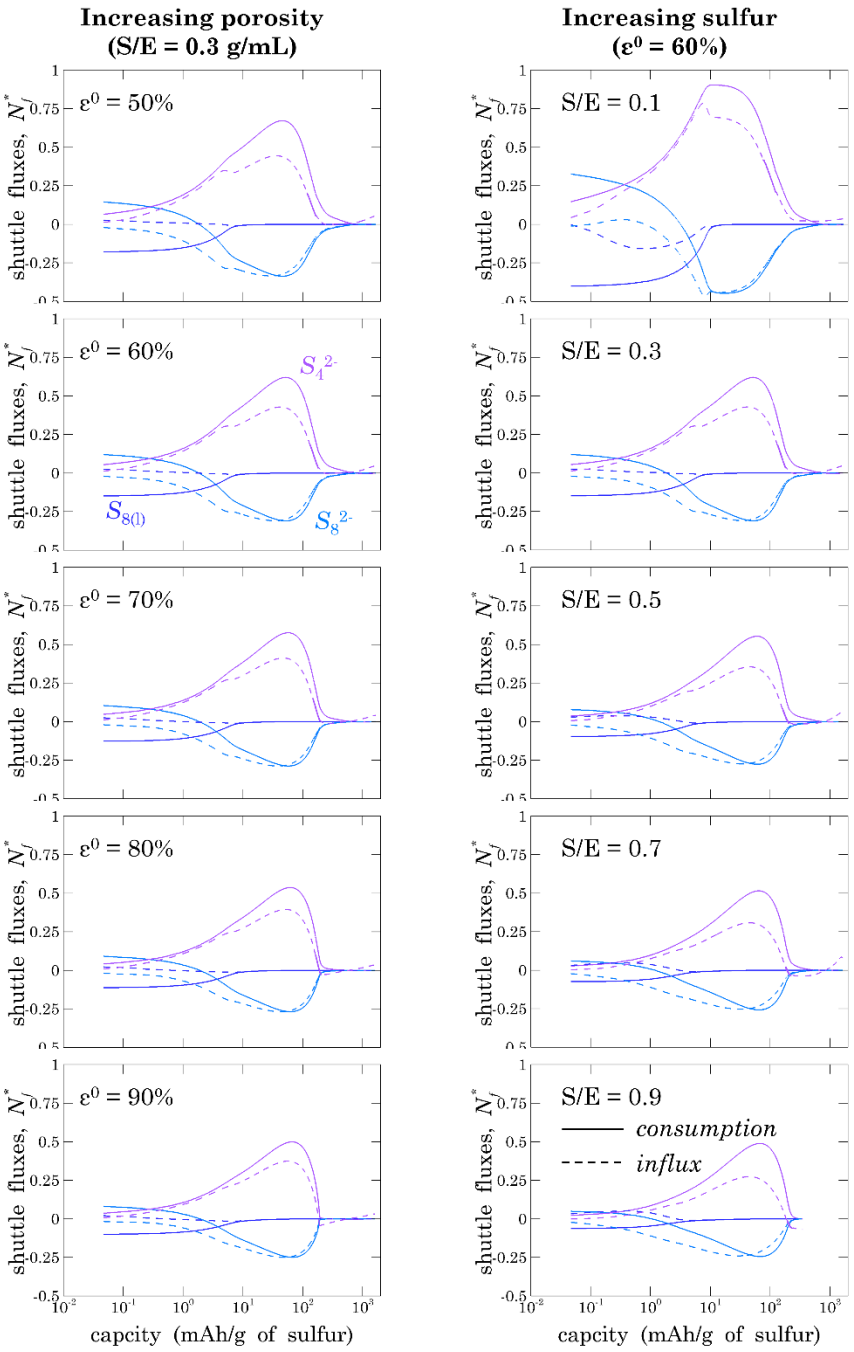

Figure 102. Evolution of polysulfide fluxes is sensitive to cathode specifications, namely, sulfur-to-electrolyte (S/E) ratio and pristine porosity, ε^0.

In response to physicochemical changes taking place inside the cell, sulfur fluxes at anode/separator interface (consumption) and cathode/separator interface (influx) undergo

temporal evolution. Figure 101 investigates such a progression as a function of operating rate, while Figure 102 explores the effect of cathode specifications.

7. SUMMARY AND OUTLOOK

Lack of observability at smaller scales has obscured the progresses in porous electrodes as the associated interactions are not comprehensively understood. Here a unique approach for mechanistic investigation into such mesoscopic complexations has been proposed. It leverages the certainty of physical principles and incomplete experimental probing to synergistically reconstruct aforementioned interactions. The promise of such a philosophy has been shown in three distinct electrochemical systems which non-trivial peculiarities.

The sound physical basis of this investigative approach makes it easily extensible to other complex systems with equivalent mesoscopic interactions. A few immediate science questions that could be answered in the present setting are:

- *Particle-scale Stochasticity*: How particle geometry alters the intercalation response is poorly understood. Since an intercalating particle is the most primary entity in an electrode, particle-scale modifications have the potential to intrinsically tune the electrode response.
- *Conjugate Interactions of Electrode Stochasticity*: Here it was shown that electrode-scale stochasticity brings about intercalation cascade. Equivalently, it is expected to affect conjugate interactions such as thermal safety and chemical degradation.
- *Role of Mechanics in Conversion Electrodes*: Electrodeposition reactions are essential to conversion electrodes. The interfaces grow quite irregularly and cause accelerated decay. Mechanical interactions affect this reaction-transport dynamics, however, the nature of their interplay is unclear.

BIBLIOGRAPHY

1. J. Newman and W. Tiedemann, *AlChE J.*, 1975, **21**, 25-41.
2. D. Bernardi, E. Pawlikowski and J. Newman, *J. Electrochem. Soc.*, 1985, **132**, 5-12.
3. M. Doyle, T. F. Fuller and J. Newman, *J. Electrochem. Soc.*, 1993, **140**, 1526-1533.
4. J. N. Israelachvili, *Intermolecular and surface forces*, Academic press, New York, 2011.
5. A. Mistry and K. Muralidhar, *Phys. Fluids*, 2015, **27**, 092103.
6. A. Mistry and K. Muralidhar, *Phys. Fluids*, 2018, **30**, 042104.
7. L. G. Leal, *Advanced transport phenomena: fluid mechanics and convective transport processes*, Cambridge University Press, 2007.
8. S. R. De Groot and P. Mazur, *Non-equilibrium thermodynamics*, Courier Corporation, 2013.
9. S. Torquato, *Random heterogeneous materials: microstructure and macroscopic properties*, Springer Science & Business Media, 2013.
10. S. Torquato, *Annual review of materials research*, 2002, **32**, 77-111.
11. F. T. Wagner, B. Lakshmanan and M. F. Mathias, *J. Phys. Chem. Lett.*, 2010, **1**, 2204-2219.
12. A. Manthiram, *J. Phys. Chem. Lett.*, 2011, **2**, 176-184.
13. V. Etacheri, R. Marom, R. Elazari, G. Salitra and D. Aurbach, *Energy Environ. Sci.*, 2011, **4**, 3243-3262.
14. K. Xu, *Chem. Rev.*, 2014, **114**, 11503-11618.
15. E. M. Erickson, C. Ghanty and D. Aurbach, *J. Phys. Chem. Lett.*, 2014, **5**, 3313-3324.
16. V. Viswanathan, *J. Phys. Chem. Lett.*, 2015, **6**, 4673-4674.
17. K. Abraham, *J. Phys. Chem. Lett*, 2015, **6**, 830-844.
18. P. P. Mukherjee, A. Mistry and A. Verma, *Modeling Transport Phenomena in Porous Media with Applications*, 93.
19. M. Park, X. Zhang, M. Chung, G. B. Less and A. M. Sastry, *J. Power Sources*, 2010, **195**, 7904-7929.
20. K. Shah, N. Balsara, S. Banerjee, M. Chintapalli, A. Cocco, W. Chiu, I. Lahiri, S. Martha, A. Mistry and P. Mukherjee, *J. Electrochem. Energy Convers. Storage*, 2017, **14**, 020801.
21. P. P. Mukherjee, A. Verma and A. Mistry, *Modeling Transport Phenomena in Porous Media with Applications*, 65.

22. J. Newman and K. E. Thomas-Alyea, *Electrochemical systems*, John Wiley & Sons, New Jersey, 2012.
23. A. M. Bizeray, D. A. Howey and C. W. Monroe, *J. Electrochem. Soc.*, 2016, **163**, E223-E229.
24. L. O. Valøen and J. N. Reimers, *J. Electrochem. Soc.*, 2005, **152**, A882-A891.
25. A. Mistry, D. Juarez-Robles, I. V. M. Stein, K. Smith and P. P. Mukherjee, *J. Electrochem. Energy Convers. Storage*, 2016, **13**, 031006-031006.
26. J. Shim and K. A. Striebel, *J. Power Sources*, 2003, **119**, 934-937.
27. G. Liu, H. Zheng, S. Kim, Y. Deng, A. Minor, X. Song and V. Battaglia, *J. Electrochem. Soc.*, 2008, **155**, A887-A892.
28. J. Chong, S. Xun, H. Zheng, X. Song, G. Liu, P. Ridgway, J. Q. Wang and V. S. Battaglia, *J. Power Sources*, 2011, **196**, 7707-7714.
29. H. Zheng, J. Li, X. Song, G. Liu and V. S. Battaglia, *Electrochim. Acta*, 2012, **71**, 258-265.
30. H. Zheng, R. Yang, G. Liu, X. Song and V. S. Battaglia, *J. Phys. Chem. C*, 2012, **116**, 4875-4882.
31. S. J. Bai and Y. S. Song, *Anal. Chem.*, 2013, **85**, 3918-3925.
32. H. Zheng, L. Zhang, G. Liu, X. Song and V. S. Battaglia, *J. Power Sources*, 2012, **217**, 530-537.
33. G. Liu, H. Zheng, X. Song and V. S. Battaglia, *J. Electrochem. Soc.*, 2012, **159**, A214-A221.
34. C.-C. Li and Y.-W. Wang, *J. Power Sources*, 2013, **227**, 204-210.
35. W. Bauer, D. Nötzel, V. Wenzel and H. Nirschl, *J. Power Sources*, 2015, **288**, 359-367.
36. S. Lim, S. Kim, K. H. Ahn and S. J. Lee, *J. Power Sources*, 2015, **299**, 221-230.
37. H. Bockholt, W. Haselrieder and A. Kwade, *Powder Technol.*, 2016, **297**, 266-274.
38. H. Bockholt, M. Indrikova, A. Netz, F. Golks and A. Kwade, *J. Power Sources*, 2016, **325**, 140-151.
39. A. M. Grillet, T. Humplik, E. K. Stirrup, S. A. Roberts, D. A. Barringer, C. M. Snyder, M. R. Janvrin and C. A. Apblett, *J. Electrochem. Soc.*, 2016, **163**, A1859-A1871.
40. K. G. Gallagher, S. E. Trask, C. Bauer, T. Woehrle, S. F. Lux, M. Tschech, P. Lamp, B. J. Polzin, S. Ha and B. Long, *J. Electrochem. Soc.*, 2016, **163**, A138-A149.
41. M. Indrikova, S. Grunwald, F. Golks, A. Netz, B. Westphal and A. Kwade, *J. Electrochem. Soc.*, 2015, **162**, A2021-A2025.

42. C. Meyer, H. Bockholt, W. Haselrieder and A. Kwade, *J. Mater. Process. Technol.*, 2017.
43. M. Müller, L. Pfaffmann, S. Jaiser, M. Baunach, V. Trouillet, F. Scheiba, P. Scharfer, W. Schabel and W. Bauer, *J. Power Sources*, 2017, **340**, 1-5.
44. S. Jaiser, J. Kumberg, J. Klaver, J. L. Urai, W. Schabel, J. Schmatz and P. Scharfer, *J. Power Sources*, 2017, **345**, 97-107.
45. A. Kraytsberg and Y. Ein-Eli, *Adv. Energy Mater.*, 2016, **6**, 1600655.
46. C.-F. Chen and P. P. Mukherjee, *Phys. Chem. Chem. Phys.*, 2015, **17**, 9812-9827.
47. M. A. Martin, C.-F. Chen, P. P. Mukherjee, S. Pannala, J.-F. Dietiker, J. A. Turner and D. Ranjan, *J. Electrochem. Soc.*, 2015, **162**, A991-A1002.
48. S. Cho, C.-F. Chen and P. P. Mukherjee, *J. Electrochem. Soc.*, 2015, **162**, A1202-A1214.
49. M. Smith, R. E. García and Q. C. Horn, *J. Electrochem. Soc.*, 2009, **156**, A896-A904.
50. B. Yan, C. Lim, L. Yin and L. Zhu, *J. Electrochem. Soc.*, 2012, **159**, A1604-A1614.
51. T. Hutzenlaub, S. Thiele, N. Paust, R. Spotnitz, R. Zengerle and C. Walchshofer, *Electrochim. Acta*, 2014, **115**, 131-139.
52. R. E. Garcıa, Y.-M. Chiang, W. C. Carter, P. Limthongkul and C. M. Bishop, *J. Electrochem. Soc.*, 2005, **152**, A255-A263.
53. C.-W. Wang and A. M. Sastry, *J. Electrochem. Soc.*, 2007, **154**, A1035-A1047.
54. M. Safari and C. Delacourt, *J. Electrochem. Soc.*, 2011, **158**, A63-A73.
55. K. C. Smith, P. P. Mukherjee and T. S. Fisher, *Phys. Chem. Chem. Phys.*, 2012, **14**, 7040-7050.
56. G. M. Goldin, A. M. Colclasure, A. H. Wiedemann and R. J. Kee, *Electrochim. Acta*, 2012, **64**, 118-129.
57. A. H. Wiedemann, G. M. Goldin, S. A. Barnett, H. Zhu and R. J. Kee, *Electrochim. Acta*, 2013, **88**, 580-588.
58. R. García-García and R. E. García, *J. Power Sources*, 2016, **309**, 11-19.
59. H. Mendoza, S. A. Roberts, V. E. Brunini and A. M. Grillet, *Electrochim. Acta*, 2016, **190**, 1-15.
60. V. Malavé, J. Berger, H. Zhu and R. J. Kee, *Electrochim. Acta*, 2014, **130**, 707-717.
61. D.-W. Chung, M. Ebner, D. R. Ely, V. Wood and R. E. García, *Modell. Simul. Mater. Sci. Eng.*, 2013, **21**, 074009.

62. Z. Liu, T. W. Verhallen, D. P. Singh, H. Wang, M. Wagemaker and S. Barnett, *J. Power Sources*, 2016, **324**, 358-367.
63. L. Zielke, T. Hutzenlaub, D. R. Wheeler, C. W. Chao, I. Manke, A. Hilger, N. Paust, R. Zengerle and S. Thiele, *Adv. Energy Mater.*, 2015, **5**, 1401612.
64. M. Ebner, D. W. Chung, R. E. García and V. Wood, *Adv. Energy Mater.*, 2014, **4**, 1301278.
65. L. Zielke, T. Hutzenlaub, D. R. Wheeler, I. Manke, T. Arlt, N. Paust, R. Zengerle and S. Thiele, *Adv. Energy Mater.*, 2014, **4**, 1301617.
66. J. Gelb, D. P. Finegan, D. J. Brett and P. R. Shearing, *J. Power Sources*, 2017, **357**, 77-86.
67. O. O. Taiwo, D. P. Finegan, J. Paz-Garcia, D. S. Eastwood, A. Bodey, C. Rau, S. Hall, D. J. Brett, P. D. Lee and P. R. Shearing, *Phys. Chem. Chem. Phys.*, 2017, **19**, 22111-22120.
68. J. Landesfeind, J. Hattendorff, A. Ehrl, W. A. Wall and H. A. Gasteiger, *J. Electrochem. Soc.*, 2016, **163**, A1373-A1387.
69. O. O. Taiwo, D. P. Finegan, J. Gelb, C. Holzner, D. J. Brett and P. R. Shearing, *Chem. Eng. Sci.*, 2016, **154**, 27-33.
70. M. F. Lagadec, M. Ebner, R. Zahn and V. Wood, *J. Electrochem. Soc.*, 2016, **163**, A992-A994.
71. D. P. Finegan, E. Tudisco, M. Scheel, J. B. Robinson, O. O. Taiwo, D. S. Eastwood, P. D. Lee, M. Di Michiel, B. Bay and S. A. Hall, *Advanced Science*, 2016, **3**.
72. O. O. Taiwo, D. P. Finegan, D. S. Eastwood, J. L. Fife, L. D. Brown, J. A. Darr, P. D. Lee, D. J. Brett and P. R. Shearing, *J. Microsc.*, 2016, **263**, 280-292.
73. D. P. Finegan, S. J. Cooper, B. Tjaden, O. O. Taiwo, J. Gelb, G. Hinds, D. J. Brett and P. R. Shearing, *J. Power Sources*, 2016, **333**, 184-192.
74. J. Paz-Garcia, O. Taiwo, E. Tudisco, D. Finegan, P. Shearing, D. Brett and S. Hall, *J. Power Sources*, 2016, **320**, 196-203.
75. S. Vierrath, L. Zielke, R. Moroni, A. Mondon, D. R. Wheeler, R. Zengerle and S. Thiele, *Electrochem. Commun.*, 2015, **60**, 176-179.
76. F. Tariq, V. Yufit, M. Kishimoto, P. Shearing, S. Menkin, D. Golodnitsky, J. Gelb, E. Peled and N. Brandon, *J. Power Sources*, 2014, **248**, 1014-1020.
77. D. Eastwood, R. Bradley, F. Tariq, S. Cooper, O. Taiwo, J. Gelb, A. Merkle, D. Brett, N. Brandon and P. Withers, *Nuclear Instruments and Methods in Physics Research Section B: Beam Interactions with Materials and Atoms*, 2014, **324**, 118-123.

78. J. B. Robinson, J. A. Darr, D. S. Eastwood, G. Hinds, P. D. Lee, P. R. Shearing, O. O. Taiwo and D. J. Brett, *J. Power Sources*, 2014, **252**, 51-57.

79. D. S. Eastwood, V. Yufit, J. Gelb, A. Gu, R. S. Bradley, S. J. Harris, D. J. Brett, N. P. Brandon, P. D. Lee and P. J. Withers, *Adv. Energy Mater.*, 2014, **4**.

80. M. Ebner, F. Geldmacher, F. Marone, M. Stampanoni and V. Wood, *Adv. Energy Mater.*, 2013, **3**, 845-850.

81. M. Ebner, F. Marone, M. Stampanoni and V. Wood, *Science*, 2013, **342**, 716-720.

82. S. J. Harris and P. Lu, *Journal of Physical Chemistry C*, 2013, **117**, 6481−6492.

83. M. Stein, A. Mistry and P. P. Mukherjee, *J. Electrochem. Soc.*, 2017, **164**, A1616-A1627.

84. M. Ender, J. Joos, T. Carraro and E. Ivers-Tiffée, *J. Electrochem. Soc.*, 2012, **159**, A972-A980.

85. Y.-c. K. Chen-Wiegart, P. Shearing, Q. Yuan, A. Tkachuk and J. Wang, *Electrochem. Commun.*, 2012, **21**, 58-61.

86. P. Shearing, N. Brandon, J. Gelb, R. Bradley, P. Withers, A. Marquis, S. Cooper and S. Harris, *J. Electrochem. Soc.*, 2012, **159**, A1023-A1027.

87. Y.-c. K. Chen-Wiegart, Z. Liu, K. T. Faber, S. A. Barnett and J. Wang, *Electrochem. Commun.*, 2013, **28**, 127-130.

88. S. Cooper, D. Eastwood, J. Gelb, G. Damblanc, D. Brett, R. Bradley, P. Withers, P. Lee, A. Marquis and N. Brandon, *J. Power Sources*, 2014, **247**, 1033-1039.

89. P. Pietsch and V. Wood, *Annual Review of Materials Research*, 2017.

90. D. P. Finegan, M. Scheel, J. B. Robinson, B. Tjaden, M. Di Michiel, G. Hinds, D. J. Brett and P. R. Shearing, *Phys. Chem. Chem. Phys.*, 2016, **18**, 30912-30919.

91. G. J. Nelson, L. J. Ausderau, S. Shin, J. R. Buckley, A. Mistry, P. P. Mukherjee and V. De Andrade, *J. Electrochem. Soc.*, 2017, **164**, A1412-A1424.

92. J. R. Wilson, J. Cronin, S. A. Barnett and S. J. Harris, *J. Power Sources*, 2011, **196**, 3443–3447.

93. J. Joos, T. Carraro, A. Weber and E. Ivers-Tiffée, *J. Power Sources*, 2011, **196**, 7302-7307.

94. M. Ender, J. Joos, T. Carraro and E. Ivers-Tiffée, *Electrochem. Commun.*, 2011, **13**, 166-168.

95. T. Hutzenlaub, S. Thiele, R. Zengerle and C. Ziegler, *Electrochem. Solid-State Lett.*, 2011, **15**, A33-A36.

96. T. Hutzenlaub, A. Asthana, J. Becker, D. Wheeler, R. Zengerle and S. Thiele, *Electrochem. Commun.*, 2013, **27**, 77-80.
97. M. Biton, V. Yufit, F. Tariq, M. Kishimoto and N. Brandon, *J. Electrochem. Soc.*, 2017, **164**, A6032-A6038.
98. G. Less, J. Seo, S. Han, A. Sastry, J. Zausch, A. Latz, S. Schmidt, C. Wieser, D. Kehrwald and S. Fell, *J. Electrochem. Soc.*, 2012, **159**, A697-A704.
99. S. A. Roberts, V. E. Brunini, K. N. Long and A. M. Grillet, *J. Electrochem. Soc.*, 2014, **161**, F3052-F3059.
100. I. V. Thorat, D. E. Stephenson, N. A. Zacharias, K. Zaghib, J. N. Harb and D. R. Wheeler, *J. Power Sources*, 2009, **188**, 592-600.
101. V. D. Bruggeman, *Annalen der physik*, 1935, **416**, 636-664.
102. S. S. Zhang, *J. Power Sources*, 2013, **231**, 153-162.
103. M. Barghamadi, A. S. Best, A. I. Bhatt, A. F. Hollenkamp, M. Musameh, R. J. Rees and T. Rüther, *Energy Environ. Sci.*, 2014, **7**, 3902-3920.
104. X. Fang and H. Peng, *Small*, 2015, **11**, 1488-1511.
105. M. Gauthier, T. J. Carney, A. Grimaud, L. Giordano, N. Pour, H.-H. Chang, D. P. Fenning, S. F. Lux, O. Paschos and C. Bauer, *J. Phys. Chem. Lett.*, 2015, **6**, 4653-4672.
106. M. Wild, L. O'Neill, T. Zhang, R. Purkayastha, G. Minton, M. Marinescu and G. Offer, *Energy Environ. Sci.*, 2015, **8**, 3477-3494.
107. M. Hagen, D. Hanselmann, K. Ahlbrecht, R. Maça, D. Gerber and J. Tübke, *Adv. Energy Mater.*, 2015, **5**, 1401986.
108. S. Zhang, K. Ueno, K. Dokko and M. Watanabe, *Adv. Energy Mater.*, 2015, **5**, 1500117.
109. P. W. Atkins and J. De Paula, 2010.
110. K. Xu, *Chem. Rev.*, 2004, **104**, 4303-4418.
111. F. Wu and G. Yushin, *Energy Environ. Sci.*, 2017, **10**, 435-459.
112. Z. Liu, P. B. Balbuena and P. P. Mukherjee, *J. Phys. Chem. Lett.*, 2017, **8**, 1324-1330.
113. Z. Liu and P. P. Mukherjee, *ACS Appl. Mater. Interfaces*, 2017, **9**, 5263-5271.
114. Z. Liu, D. Hubble, P. B. Balbuena and P. P. Mukherjee, *Phys. Chem. Chem. Phys.*, 2015, **17**, 9032-9039.
115. Z. Liu, P. B. Balbuena and P. P. Mukherjee, *J. Coord. Chem.*, 2016, **69**, 2090-2105.

116. A. Yermukhambetova, C. Tan, S. R. Daemi, Z. Bakenov, J. A. Darr, D. J. Brett and P. R. Shearing, *Sci. Rep.*, 2016, **6**, 35291.
117. C.-F. Chen, A. Verma and P. P. Mukherjee, *J. Electrochem. Soc.*, 2017, **164**, E3146-E3158.
118. L. Yuan, X. Qiu, L. Chen and W. Zhu, *J. Power Sources*, 2009, **189**, 127-132.
119. V. Kolosnitsyn, E. Kuzmina, E. Karaseva and S. Mochalov, *J. Power Sources*, 2011, **196**, 1478-1482.
120. Z. Deng, Z. Zhang, Y. Lai, J. Liu, J. Li and Y. Liu, *J. Electrochem. Soc.*, 2013, **160**, A553-A558.
121. D. N. Fronczek and W. G. Bessler, *J. Power Sources*, 2013, **244**, 183-188.
122. N. A. Canas, K. Hirose, B. Pascucci, N. Wagner, K. A. Friedrich and R. Hiesgen, *Electrochim. Acta*, 2013, **97**, 42-51.
123. J. Conder, C. Villevieille, S. Trabesinger, P. Novák, L. Gubler and R. Bouchet, *Electrochim. Acta*, 2017, **244**, 61-68.
124. T. Zhang, M. Marinescu, S. Walus and G. J. Offer, *Electrochim. Acta*, 2016, **219**, 502-508.
125. Y. Ren, T. Zhao, M. Liu, P. Tan and Y. Zeng, *J. Power Sources*, 2016, **336**, 115-125.
126. V. Thangavel, K.-H. Xue, Y. Mammeri, M. Quiroga, A. Mastouri, C. Guéry, P. Johansson, M. Morcrette and A. A. Franco, *J. Electrochem. Soc.*, 2016, **163**, A2817-A2829.
127. K. Kumaresan, Y. Mikhaylik and R. E. White, *J. Electrochem. Soc.*, 2008, **155**, A576-A582.
128. Y. V. Mikhaylik and J. R. Akridge, *J. Electrochem. Soc.*, 2003, **150**, A306-A311.
129. E. S. Shin, K. Kim, S. H. Oh and W. I. Cho, *Chem. Commun.*, 2013, **49**, 2004-2006.
130. Y. V. Mikhaylik and J. R. Akridge, *J. Electrochem. Soc.*, 2004, **151**, A1969-A1976.
131. D. Moy, A. Manivannan and S. Narayanan, *J. Electrochem. Soc.*, 2015, **162**, A1-A7.
132. M. J. Lacey, A. Yalamanchili, J. Maibach, C. Tengstedt, K. Edström and D. Brandell, *RSC Advances*, 2016, **6**, 3632-3641.
133. Q. Pang, X. Liang, C. Y. Kwok and L. F. Nazar, *Nat. Energy*, 2016, **1**, 16132.
134. Q. Pang, X. Liang, C. Y. Kwok, J. Kulisch and L. F. Nazar, *Adv. Energy Mater.*, 2017, **7**.
135. L. Suo, Y.-S. Hu, H. Li, M. Armand and L. Chen, *Nature communications*, 2013, **4**, 1481.
136. T. A. Pascal, K. H. Wujcik, J. Velasco-Velez, C. Wu, A. A. Teran, M. Kapilashrami, J. Cabana, J. Guo, M. Salmeron and N. Balsara, *J. Phys. Chem. Lett.*, 2014, **5**, 1547-1551.
137. Q. Zou and Y.-C. Lu, *J. Phys. Chem. Lett.*, 2016, **7**, 1518-1525.

138. M. Cuisinier, P.-E. Cabelguen, S. Evers, G. He, M. Kolbeck, A. Garsuch, T. Bolin, M. Balasubramanian and L. F. Nazar, *J. Phys. Chem. Lett.*, 2013, **4**, 3227-3232.
139. A. Kawase, S. Shirai, Y. Yamoto, R. Arakawa and T. Takata, *Phys. Chem. Chem. Phys.*, 2014, **16**, 9344-9350.
140. K. H. Wujcik, J. Velasco-Velez, C. H. Wu, T. Pascal, A. A. Teran, M. A. Marcus, J. Cabana, J. Guo, D. Prendergast and M. Salmeron, *J. Electrochem. Soc.*, 2014, **161**, A1100-A1106.
141. R. Xu, I. Belharouak, X. Zhang, R. Chamoun, C. Yu, Y. Ren, A. Nie, R. Shahbazian-Yassar, J. Lu and J. C. Li, *ACS Appl. Mater. Interfaces*, 2014, **6**, 21938-21945.
142. Y.-C. Lu, Q. He and H. A. Gasteiger, *J. Phys. Chem. C*, 2014, **118**, 5733-5741.
143. M. Safari, C. Kwok and L. Nazar, *ACS Cent. Sci.*, 2016, **2**, 560-568.
144. F. Y. Fan, M. S. Pan, K. C. Lau, R. S. Assary, W. H. Woodford, L. A. Curtiss, W. C. Carter and Y.-M. Chiang, *J. Electrochem. Soc.*, 2016, **163**, A3111-A3116.
145. V. Kolosnitsyn, E. Kuzmina and S. Mochalov, *J. Power Sources*, 2014, **252**, 28-34.
146. F. Y. Fan and Y.-M. Chiang, *J. Electrochem. Soc.*, 2017, **164**, A917-A922.
147. F. Y. Fan, W. C. Carter and Y. M. Chiang, *Adv. Mater.*, 2015, **27**, 5203-5209.
148. T. Poux, P. Novák and S. Trabesinger, *J. Electrochem. Soc.*, 2016, **163**, A1139-A1145.
149. J. Zheng, D. Lv, M. Gu, C. Wang, J.-G. Zhang, J. Liu and J. Xiao, *J. Electrochem. Soc.*, 2013, **160**, A2288-A2292.
150. J. Vetter, P. Novák, M. Wagner, C. Veit, K.-C. Möller, J. Besenhard, M. Winter, M. Wohlfahrt-Mehrens, C. Vogler and A. Hammouche, *J. Power Sources*, 2005, **147**, 269-281.
151. M. Armand and J.-M. Tarascon, *Nature*, 2008, **451**, 652-657.
152. P. Lu, C. Li, E. W. Schneider and S. J. Harris, *J. Phys. Chem. C*, 2014, **118**, 896-903.
153. J.-M. Tarascon and M. Armand, *Nature*, 2001, **414**, 359-367.
154. D. Doughty and E. P. Roth, *Electrochem. Soc. Interface*, 2012, **21**, 37-44.
155. J. B. Goodenough and K.-S. Park, *J. Am. Chem. Soc.*, 2013, **135**, 1167-1176.
156. B. L. Ellis, K. T. Lee and L. F. Nazar, *Chem. Mater.*, 2010, **22**, 691-714.
157. M. Obrovac and V. Chevrier, *Chem. Rev.*, 2014, **114**, 11444-11502.
158. N. Yabuuchi, Y. Kinoshita, K. Misaki, T. Matsuyama and S. Komaba, *J. Electrochem. Soc.*, 2015, **162**, A538-A544.
159. A. P. Cocco, G. J. Nelson, W. M. Harris, A. Nakajo, T. D. Myles, A. M. Kiss, J. J. Lombardo and W. K. Chiu, *Phys. Chem. Chem. Phys.*, 2013, **15**, 16377-16407.

160. P. Shearing, L. Howard, P. S. Jørgensen, N. Brandon and S. Harris, *Electrochem. Commun.*, 2010, **12**, 374-377.

161. T. Danner, M. Singh, S. Hein, J. Kaiser, H. Hahn and A. Latz, *J. Power Sources*, 2016, **334**, 191-201.

162. M. Ebner and V. Wood, *J. Electrochem. Soc.*, 2015, **162**, A3064-A3070.

163. B. L. Trembacki, D. R. Noble, V. E. Brunini, M. E. Ferraro and S. A. Roberts, *J. Electrochem. Soc.*, 2017, **164**, E3613-E3626.

164. Z. Liu, V. Battaglia and P. P. Mukherjee, *Langmuir*, 2014, **30**, 15102-15113.

165. Z. Liu and P. P. Mukherjee, *J. Electrochem. Soc.*, 2014, **161**, E3248-E3258.

166. Y. Saad, *Iterative methods for sparse linear systems*, SIAM, 2003.

167. P. P. Mukherjee, S. Pannala and J. A. Turner, *Handbook of Battery Materials, Second Edition*, 2011, 841-875.

168. E. J. Cairns and P. Albertus, *Annu. Rev. Chem. Biomol. Eng.*, 2010, **1**, 299-320.

169. B. Dunn, H. Kamath and J.-M. Tarascon, *Science*, 2011, **334**, 928-935.

170. S. Ahmed, I. Bloom, A. N. Jansen, T. Tanim, E. J. Dufek, A. Pesaran, A. Burnham, R. B. Carlson, F. Dias and K. Hardy, *J. Power Sources*, 2017, **367**, 250-262.

171. A. Meintz, J. Zhang, R. Vijayagopal, C. Kreutzer, S. Ahmed, I. Bloom, A. Burnham, R. B. Carlson, F. Dias and E. J. Dufek, *J. Power Sources*, 2017, **367**, 216-227.

172. H. Zheng, L. Tan, G. Liu, X. Song and V. S. Battaglia, *J. Power Sources*, 2012, **208**, 52-57.

173. H. Zheng, G. Liu, X. Song, P. Ridgway, S. Xun and V. S. Battaglia, *J. Electrochem. Soc.*, 2010, **157**, A1060-A1066.

174. A. N. Mistry, K. Smith and P. P. Mukherjee, *ACS Appl. Mater. Interfaces*, 2018, **10**, 6317-6326.

175. A. N. Mistry, K. Smith and P. P. Mukherjee, *ACS Appl. Mater. Interfaces*, 2018, **10**, 28644-28655.

176. C. T. Love, M. B. V. Virji, R. E. Rocheleau and K. E. Swider-Lyons, *J. Power Sources*, 2014, **266**, 512-519.

177. GeoDict (http://www.geodict.com/).

178. A. Wiegmann, GEODICT: virtual microstructure simulator and material property predictor (http://www.geodict.com/).

179. P. Atkins, J. De Paula and J. Keeler, *Atkins' physical chemistry*, Oxford university press, 2018.

180. T. Marks, S. Trussler, A. Smith, D. Xiong and J. Dahn, *J. Electrochem. Soc.*, 2011, **158**, A51-A57.

181. C.-J. Bae, C. K. Erdonmez, J. W. Halloran and Y.-M. Chiang, *Adv. Mater.*, 2013, **25**, 1254-1258.

182. Z. Du, D. L. Wood, C. Daniel, S. Kalnaus and J. Li, *J. Appl. Electrochem.*, 2017, **47**, 405-415.

183. Y. Qi, T. Jang, V. Ramadesigan, D. T. Schwartz and V. R. Subramanian, *J. Electrochem. Soc.*, 2017, **164**, A3196-A3207.

184. N. Ogihara, Y. Itou, T. Sasaki and Y. Takeuchi, *J. Phys. Chem. C*, 2015, **119**, 4612-4619.

185. L. R. De Jesus, J. L. Andrews, A. Parija and S. Banerjee, *ACS Energy Lett.*, 2018, **3**, 915-931.

186. J. L. Andrews, A. Mukherjee, H. D. Yoo, A. Parija, P. M. Marley, S. Fakra, D. Prendergast, J. Cabana, R. F. Klie and S. Banerjee, *Chem*, 2018, **4**, 564-585.

187. S. U. Kim and V. Srinivasan, *J. Electrochem. Soc.*, 2016, **163**, A2977-A2980.

188. Z. Feng, K. Higa, K. S. Han and V. Srinivasan, *J. Electrochem. Soc.*, 2017, **164**, A2434-A2440.

189. A. Z. Weber, M. M. Mench, J. P. Meyers, P. N. Ross, J. T. Gostick and Q. Liu, *J. Appl. Electrochem.*, 2011, **41**, 1137.

190. J. Walker, *Halliday & Resnick Fundamentals of Physics*, John Wiley & Sons, Incorporated, 2014.

191. M. Doyle, J. P. Meyers and J. Newman, *J. Electrochem. Soc.*, 2000, **147**, 99-110.

192. J. Lück and A. Latz, *Phys. Chem. Chem. Phys.*, 2016, **18**, 17799-17804.

193. D. Juarez-Robles, C.-F. Chen, Y. Barsukov and P. P. Mukherjee, *J. Electrochem. Soc.*, 2017, **164**, A837-A847.

194. S. Malifarge, B. Delobel and C. Delacourt, *J. Electrochem. Soc.*, 2017, **164**, E3329-E3334.

195. F. P. McGrogan, S. R. Bishop, Y.-M. Chiang and K. J. Van Vliet, *J. Electrochem. Soc.*, 2017, **164**, A3709-A3717.

196. M. Takeno, T. Fukutsuka, K. Miyazaki and T. Abe, *J. Electrochem. Soc.*, 2017, **164**, A3862-A3867.

197. B. Delattre, R. Amin, J. Sander, J. De Coninck, A. P. Tomsia and Y.-M. Chiang, *J. Electrochem. Soc.*, 2018, **165**, A388-A395.
198. J. Landesfeind, M. Ebner, A. Eldiven, V. Wood and H. A. Gasteiger, *J. Electrochem. Soc.*, 2018, **165**, A469-A476.
199. M. D. Murbach and D. T. Schwartz, *J. Electrochem. Soc.*, 2018, **165**, A297-A304.
200. J. Huang, Z. Li, J. Zhang, S. Song, Z. Lou and N. Wu, *J. Electrochem. Soc.*, 2015, **162**, A585-A595.
201. J. P. Meyers, M. Doyle, R. M. Darling and J. Newman, *J. Electrochem. Soc.*, 2000, **147**, 2930-2940.
202. M. D. Murbach and D. T. Schwartz, *J. Electrochem. Soc.*, 2017, **164**, E3311-E3320.
203. J. Huang and J. Zhang, *J. Electrochem. Soc.*, 2016, **163**, A1983-A2000.
204. E. Kreyszig, *Advanced Engineering Mathematics*, John Wiley & Sons, Singapore, 2010.
205. K. M. Diederichsen, E. J. McShane and B. D. McCloskey, *ACS Energy Lett.*, 2017, **2**, 2563-2575.
206. C. D. Rahn and C.-Y. Wang, *Battery systems engineering*, John Wiley & Sons, 2013.
207. B. D. McCloskey, *J. Phys. Chem. Lett*, 2015, **6**, 3592-3593.
208. T. Christen and M. W. Carlen, *J. Power Sources*, 2000, **91**, 210-216.
209. M. S. Whittingham, *Chem. Rev.*, 2004, **104**, 4271-4302.
210. C. M. Hayner, X. Zhao and H. H. Kung, *Annu. Rev. Chem. Biomol. Eng.*, 2012, **3**, 445-471.
211. C.-F. Chen, P. Barai and P. P. Mukherjee, *Current Opinion in Chemical Engineering*, 2016, **13**, 82-90.
212. A. Barré, B. Deguilhem, S. Grolleau, M. Gérard, F. Suard and D. Riu, *J. Power Sources*, 2013, **241**, 680-689.
213. L. Lu, X. Han, J. Li, J. Hua and M. Ouyang, *J. Power Sources*, 2013, **226**, 272-288.
214. C. J. Orendorff, *The Electrochemical society interface*, 2012, **21**, 61-65.
215. J. A. Jeevarajan, *Safety limitations associated with commercial 18650 lithium-ion cells*, H. NASA Johnson Space Center, TX, United States Report JSC-CN-21966, 2010.
216. E. Roth and D. Doughty, *J. Power Sources*, 2004, **128**, 308-318.
217. R. Spotnitz and J. Franklin, *J. Power Sources*, 2003, **113**, 81-100.
218. M. Wohlfahrt-Mehrens, C. Vogler and J. Garche, *J. Power Sources*, 2004, **127**, 58-64.

219. J. Kasnatscheew, M. Evertz, B. Streipert, R. Wagner, S. Nowak, I. Cekic Laskovic and M. Winter, *J. Phys. Chem. C*, 2017, **121**, 1521-1529.
220. D. H. Doughty, E. P. Roth, C. C. Crafts, G. Nagasubramanian, G. Henriksen and K. Amine, *J. Power Sources*, 2005, **146**, 116-120.
221. O. O. Taiwo, M. Loveridge, S. D. Beattie, D. P. Finegan, R. Bhagat, D. J. Brett and P. R. Shearing, *Electrochim. Acta*, 2017, **253**, 85-92.
222. V. Srinivasan and C. Wang, *J. Electrochem. Soc.*, 2003, **150**, A98-A106.
223. C. Wang and V. Srinivasan, *J. Power Sources*, 2002, **110**, 364-376.
224. P. Barai and P. P. Mukherjee, *J. Electrochem. Soc.*, 2013, **160**, A955-A967.
225. X. Zhang, W. Shyy and A. M. Sastry, *J. Electrochem. Soc.*, 2007, **154**, A910-A916.
226. M. W. Verbrugge and B. J. Koch, *J. Electrochem. Soc.*, 2003, **150**, A374-A384.
227. N. Yabuuchi, Y. Makimura and T. Ohzuku, *J. Electrochem. Soc.*, 2007, **154**, A314-A321.
228. Y. Reynier, R. Yazami and B. Fultz, *J. Electrochem. Soc.*, 2004, **151**, A422-A426.
229. W. Lu, I. Belharouak, D. Vissers and K. Amine, *J. Electrochem. Soc.*, 2006, **153**, A2147-A2151.
230. Y. Ji, Y. Zhang and C.-Y. Wang, *J. Electrochem. Soc.*, 2013, **160**, A636-A649.
231. G. Liu, H. Zheng, A. Simens, A. Minor, X. Song and V. Battaglia, *J. Electrochem. Soc.*, 2007, **154**, A1129-A1134.
232. P. Arora, R. E. White and M. Doyle, *J. Electrochem. Soc.*, 1998, **145**, 3647-3667.
233. H. Zheng, Q. Qu, G. Zhu, G. Liu, V. S. Battaglia and H. Zheng, *ACS Appl. Mater. Interfaces*, 2017, **9**, 12445-12452.
234. P. Verma, P. Maire and P. Novák, *Electrochim. Acta*, 2010, **55**, 6332-6341.
235. J. Kasnatscheew, T. Placke, B. Streipert, S. Rothermel, R. Wagner, P. Meister, I. C. Laskovic and M. Winter, *J. Electrochem. Soc.*, 2017, **164**, A2479-A2486.
236. Y. Leng, S. Ge, D. Marple, X.-G. Yang, C. Bauer, P. Lamp and C.-Y. Wang, *J. Electrochem. Soc.*, 2017, **164**, A1037-A1049.
237. M. Singh, J. Kaiser and H. Hahn, *J. Electrochem. Soc.*, 2015, **162**, A1196-A1201.
238. T. Waldmann, B.-I. Hogg and M. Wohlfahrt-Mehrens, *J. Power Sources*, 2018, **384**, 107-124.
239. T. Waldmann, B.-I. Hogg, M. Kasper, S. Grolleau, C. G. Couceiro, K. Trad, B. P. Matadi and M. Wohlfahrt-Mehrens, *J. Electrochem. Soc.*, 2016, **163**, A1232-A1238.

240. T. Waldmann, M. Kasper and M. Wohlfahrt-Mehrens, *Electrochim. Acta*, 2015, **178**, 525-532.
241. J. Billaud, F. Bouville, T. Magrini, C. Villevieille and A. R. Studart, *Nat. Energy*, 2016, **1**, 16097.
242. D. Lisbona and T. Snee, *Process Safety and Environmental Protection*, 2011, **89**, 434-442.
243. T. Hatchard, D. MacNeil, A. Basu and J. Dahn, *J. Electrochem. Soc.*, 2001, **148**, A755-A761.
244. Y. Shi, D. J. Noelle, M. Wang, A. V. Le, H. Yoon, M. Zhang, Y. S. Meng, J. Fan, D. Wu and Y. Qiao, *Appl. Phys. Lett.*, 2017, **110**, 063902.
245. M. Wang, A. V. Le, Y. Shi, D. J. Noelle and Y. Qiao, *Appl. Phys. Lett.*, 2017, **110**, 083902.
246. C. F. Lopez, J. A. Jeevarajan and P. P. Mukherjee, *J. Electrochem. Soc.*, 2015, **162**, A1905-A1915.
247. M. Keyser, A. Pesaran, Q. Li, S. Santhanagopalan, K. Smith, E. Wood, S. Ahmed, I. Bloom, E. Dufek and M. Shirk, *J. Power Sources*, 2017, **367**, 228-236.
248. R. E. Williford, V. V. Viswanathan and J.-G. Zhang, *J. Power Sources*, 2009, **189**, 101-107.
249. M. Balasundaram, V. Ramar, C. Yap, L. Lu, A. A. Tay and B. Palani, *J. Power Sources*, 2016, **328**, 413-421.
250. S. K. Adams, N. W. Piekiel, M. H. Ervin and C. J. Morris, *Appl. Phys. Lett.*, 2018, **112**, 233108.
251. K. Xiao, D. Lee and J. J. Vlassak, *Appl. Phys. Lett.*, 2014, **105**, 171901.
252. J. M. Gregoire, K. Xiao, P. J. McCluskey, D. Dale, G. Cuddalorepatta and J. J. Vlassak, *Appl. Phys. Lett.*, 2013, **102**, 201902.
253. M. N. Ozisik, *Inverse heat transfer: fundamentals and applications*, CRC Press, 2000.
254. J. H. Lienhard, *A heat transfer textbook*, Courier Corporation, 2013.
255. D. Donnelly and B. Rust, *Computing in Science & Engineering*, 2005, **7**, 80-88.
256. J. L. Devore, *Probability and Statistics for Engineering and the Sciences*, Cengage learning, 2011.
257. S. Drake, M. Martin, D. Wetz, J. Ostanek, S. Miller, J. Heinzel and A. Jain, *J. Power Sources*, 2015, **285**, 266-273.
258. S. Sripad and V. Viswanathan, *J. Electrochem. Soc.*, 2017, **164**, E3635-E3646.
259. S. Sripad and V. Viswanathan, *ACS Energy Lett.*, 2017, **2**, 1669-1673.

260. O. Gröger, H. A. Gasteiger and J.-P. Suchsland, *J. Electrochem. Soc.*, 2015, **162**, A2605-A2622.

261. J. Betz, G. Bieker, P. Meister, T. Placke, M. Winter and R. Schmuch, *Adv. Energy Mater.*, 2018, 1803170.

262. U. Eberle and R. Von Helmolt, *Energy Environ. Sci.*, 2010, **3**, 689-699.

263. X.-G. Yang, G. Zhang, S. Ge and C.-Y. Wang, *Proceedings of the National Academy of Sciences*, 2018, **115**, 7266-7271.

264. A. Mistry and P. Mukherjee, *Phys. Chem. Chem. Phys.*, 2018.

265. S. Zhang, K. Xu and T. Jow, *Electrochim. Acta*, 2004, **49**, 1057-1061.

266. E. Plichta, M. Hendrickson, R. Thompson, G. Au, W. Behl, M. Smart, B. Ratnakumar and S. Surampudi, *J. Power Sources*, 2001, **94**, 160-162.

267. S. Zhang, K. Xu and T. Jow, *Electrochem. Commun.*, 2002, **4**, 928-932.

268. Y. Ji and C. Y. Wang, *Electrochim. Acta*, 2013, **107**, 664-674.

269. C.-Y. Wang, G. Zhang, S. Ge, T. Xu, Y. Ji, X.-G. Yang and Y. Leng, *Nature*, 2016, **529**, 515-518.

270. G. Zhang, H. Tian, S. Ge, D. Marple, F. Sun and C.-Y. Wang, *J. Power Sources*, 2018, **376**, 111-116.

271. K. E. Thomas and J. Newman, *J. Power Sources*, 2003, **119**, 844-849.

272. B. L. Trembacki, A. N. Mistry, D. R. Noble, M. E. Ferraro, P. P. Mukherjee and S. A. Roberts, *J. Electrochem. Soc.*, 2018, **165**, E725-E736.

273. F. L. E. Usseglio-Viretta, A. Colclasure, A. N. Mistry, K. P. Y. Claver, F. Pouraghajan, D. P. Finegan, T. M. M. Heenan, D. Abraham, P. P. Mukherjee, D. Wheeler, P. Shearing, S. J. Cooper and K. Smith, *J. Electrochem. Soc.*, 2018, **165**, A3403-A3426.

274. A. Mistry, H. Palle Reddy and P. Mukherjee, *Appl. Phys. Lett.*, 2019, **114**.

275. P. Pietsch, M. Ebner, F. Marone, M. Stampanoni and V. Wood, *Sustainable Energy & Fuels*, 2018, **2**, 598-605.

276. N. Kotak, P. Barai, A. Verma, A. Mistry and P. P. Mukherjee, *J. Electrochem. Soc.*, 2018, **165**, A1064-A1083.

277. A. Mistry, C. Fear, R. Carter, C. T. Love and P. P. Mukherjee, *ACS Energy Lett.*, 2018, DOI: 10.1021/acsenergylett.8b02003, 156-162.

278. P. Bai, J. Li, F. R. Brushett and M. Z. Bazant, *Energy Environ. Sci.*, 2016, **9**, 3221-3229.

279. K.-H. Chen, K. N. Wood, E. Kazyak, W. S. LePage, A. L. Davis, A. J. Sanchez and N. P. Dasgupta, *J. Mater. Chem. A*, 2017, **5**, 11671-11681.
280. D. Aurbach, *J. Power Sources*, 2000, **89**, 206-218.
281. D. Aurbach, E. Zinigrad, Y. Cohen and H. Teller, *Solid State Ionics*, 2002, **148**, 405-416.
282. M. Fleischhammer, T. Waldmann, G. Bisle, B.-I. Hogg and M. Wohlfahrt-Mehrens, *J. Power Sources*, 2015, **274**, 432-439.
283. T. Waldmann and M. Wohlfahrt-Mehrens, *Electrochim. Acta*, 2017, **230**, 454-460.
284. R. Carter and C. T. Love, *ACS Appl. Mater. Interfaces*, 2018, **10**, 26328-26334.
285. R. D. Minter, D. Juarez-Robles, C. Fear, Y. Barsukov and P. P. Mukherjee, *JoVE*, 2018, DOI: doi:10.3791/57735, e57735.
286. X.-G. Yang, S. Ge, T. Liu, Y. Leng and C.-Y. Wang, *J. Power Sources*, 2018, **395**, 251-261.
287. S. Ahmed, I. Bloom, A. N. Jansen, T. Tanim, E. J. Dufek, A. Pesaran, A. Burnham, R. B. Carlson, F. Dias and K. Hardy, *J. Power Sources*, 2017, **367**, 250-262.
288. H. Gao, Q. Wu, Y. Hu, J. P. Zheng, K. Amine and Z. Chen, *J. Phys. Chem. Lett.*, 2018, **9**, 5100-5104.
289. J. Harlow, S. Glazier, J. Li and J. Dahn, *J. Electrochem. Soc.*, 2018, **165**, A3595-A3601.
290. D. Tewari, Z. Liu, P. B. Balbuena and P. P. Mukherjee, *J. Phys. Chem. C*, 2018, **122**, 21097-21107.
291. F. Hao, Z. Liu, P. B. Balbuena and P. P. Mukherjee, *J. Phys. Chem. C*, 2017, **121**, 26233-26240.
292. S. Frisco, D. X. Liu, A. Kumar, J. F. Whitacre, C. T. Love, K. E. Swider-Lyons and S. Litster, *ACS Appl. Mater. Interfaces*, 2017, **9**, 18748-18757.
293. F. L. Usseglio-Viretta, A. Colclasure, A. N. Mistry, K. P. Y. Claver, F. Pouraghajan, D. P. Finegan, T. M. Heenan, D. Abraham, P. P. Mukherjee and D. Wheeler, *J. Electrochem. Soc.*, 2018, **165**.
294. M. Cerbelaud, B. Lestriez, R. Ferrando, A. Videcoq, M. Richard-Plouet, M. Teresa Caldes and D. Guyomard, *Langmuir*, 2014, **30**, 2660-2669.
295. M. M. Forouzan, B. A. Mazzeo and D. R. Wheeler, *J. Electrochem. Soc.*, 2018, **165**, A2127-A2144.
296. S. Müller, J. Eller, M. Ebner, C. Burns, J. Dahn and V. Wood, *J. Electrochem. Soc.*, 2018, **165**, A339-A344.

297. R. Morasch, J. Landesfeind, B. Suthar and H. A. Gasteiger, *J. Electrochem. Soc.*, 2018, **165**, A3459-A3467.

298. Y. Li, F. El Gabaly, T. R. Ferguson, R. B. Smith, N. C. Bartelt, J. D. Sugar, K. R. Fenton, D. A. Cogswell, A. D. Kilcoyne and T. Tyliszczak, *Nat. Mater.*, 2014, **13**, 1149-1156.

299. D. A. Cogswell and M. Z. Bazant, *ACS nano*, 2012, **6**, 2215-2225.

300. P. Bai, D. A. Cogswell and M. Z. Bazant, *Nano Lett.*, 2011, **11**, 4890-4896.

301. C. T. Love and K. Swider-Lyons, *Electrochem. Solid-State Lett.*, 2012, **15**, A53-A56.

302. M. Mühlbauer, A. Schökel, M. Etter, V. Baran and A. Senyshyn, *J. Power Sources*, 2018, **403**, 49-55.

303. D. C. Montgomery and G. C. Runger, *Applied statistics and probability for engineers*, John Wiley & Sons, 2010.

304. M. S. Costanza-Robinson, B. D. Estabrook and D. F. Fouhey, *Water Resour. Res.*, 2011, **47**.

305. J. Bockris, *Journal*.

306. R. G. Carbonell and S. Whitaker, in *Fundamentals of transport phenomena in porous media*, Springer, 1984, pp. 121-198.

307. M. Quintard and S. Whitaker, *Transport in Porous Media*, 1994, **14**, 163-177.

308. M. Quintard and S. Whitaker, *Transport in porous media*, 1994, **14**, 179-206.

309. S. Whitaker, *AlChE J.*, 1967, **13**, 420-427.

310. J. S. Newman and C. W. Tobias, *J. Electrochem. Soc.*, 1962, **109**, 1183-1191.

311. B. Vijayaraghavan, D. R. Ely, Y.-M. Chiang, R. García-García and R. E. García, *J. Electrochem. Soc.*, 2012, **159**, A548-A552.

312. A. Mistry and P. P. Mukherjee, *J. Phys. Chem. C*, 2017, **121**, 26256-26264.

313. D. T. Fullwood, S. R. Niezgoda and S. R. Kalidindi, *Acta Mater.*, 2008, **56**, 942-948.

314. S. Niezgoda, D. Fullwood and S. Kalidindi, *Acta Mater.*, 2008, **56**, 5285-5292.

315. D. Fullwood, S. Kalidindi, S. Niezgoda, A. Fast and N. Hampson, *Materials Science and Engineering: A*, 2008, **494**, 68-72.

316. A. Cecen, T. Fast and S. R. Kalidindi, *Integrating Materials and Manufacturing Innovation*, 2016, **5**, 1.

317. S. R. Niezgoda, A. K. Kanjarla and S. R. Kalidindi, *Integrating Materials and Manufacturing Innovation*, 2013, **2**, 3.

318. P. P. Mukherjee, Q. Kang and C.-Y. Wang, *Energy Environ. Sci.*, 2011, **4**, 346-369.

319. C. Krekeler, A. Agarwal, C. Junghans, M. Praprotnik and L. Delle Site, *The Journal of chemical physics*, 2018, **149**, 024104.
320. S. Torquato, *The Journal of chemical physics*, 2018, **149**, 020901.
321. N. Walker, K.-M. Tam, B. Novak and M. Jarrell, *Phys. Rev. E*, 2018, **98**, 053305.
322. M. Scherbela, L. Hörmann, A. Jeindl, V. Obersteiner and O. T. Hofmann, *Physical Review Materials*, 2018, **2**, 043803.
323. C. Chen, Z. Deng, R. Tran, H. Tang, I.-H. Chu and S. P. Ong, *Physical Review Materials*, 2017, **1**, 043603.
324. A. Talapatra, S. Boluki, T. Duong, X. Qian, E. Dougherty and R. Arróyave, *Physical Review Materials*, 2018, **2**, 113803.
325. P. G. Bruce, S. A. Freunberger, L. J. Hardwick and J.-M. Tarascon, *Nat. Mater.*, 2012, **11**, 19-29.
326. A. C. Luntz and B. D. McCloskey, *Chem. Rev.*, 2014, **114**, 11721-11750.
327. O. Sapunkov, V. Pande, A. Khetan, C. Choomwattana and V. Viswanathan, *Trans. Mater. Res.*, 2015, **2**, 045002.
328. K. G. Gallagher, S. Goebel, T. Greszler, M. Mathias, W. Oelerich, D. Eroglu and V. Srinivasan, *Energy Environ. Sci.*, 2014, **7**, 1555-1563.
329. S.-L. Wu, W. Zhang, X. Song, A. K. Shukla, G. Liu, V. Battaglia and V. Srinivasan, *J. Electrochem. Soc.*, 2012, **159**, A438-A444.
330. L. D. Griffith, A. E. Sleightholme, J. F. Mansfield, D. J. Siegel and C. W. Monroe, *ACS Appl. Mater. Interfaces*, 2015, **7**, 7670-7678.
331. B. D. Adams, C. Radtke, R. Black, M. L. Trudeau, K. Zaghib and L. F. Nazar, *Energy Environ. Sci.*, 2013, **6**, 1772-1778.
332. Y.-C. Lu, D. G. Kwabi, K. P. Yao, J. R. Harding, J. Zhou, L. Zuin and Y. Shao-Horn, *Energy Environ. Sci.*, 2011, **4**, 2999-3007.
333. V. Viswanathan, K. S. Thygesen, J. Hummelshøj, J. K. Nørskov, G. Girishkumar, B. McCloskey and A. Luntz, *The Journal of chemical physics*, 2011, **135**, 214704.
334. A. C. Luntz, V. Viswanathan, J. Voss, J. Varley, J. Nørskov, R. Scheffler and A. Speidel, *J. Phys. Chem. Lett.*, 2013, **4**, 3494-3499.
335. M. D. Radin, C. W. Monroe and D. J. Siegel, *J. Phys. Chem. Lett.*, 2015, **6**, 3017-3022.

336. B. M. Gallant, D. G. Kwabi, R. R. Mitchell, J. Zhou, C. V. Thompson and Y. Shao-Horn, *Energy Environ. Sci.*, 2013, **6**, 2518-2528.

337. R. R. Mitchell, B. M. Gallant, Y. Shao-Horn and C. V. Thompson, *J. Phys. Chem. Lett.*, 2013, **4**, 1060-1064.

338. D. Sharon, D. Hirsberg, M. Afri, F. Chesneau, R. Lavi, A. A. Frimer, Y.-K. Sun and D. Aurbach, *ACS Appl. Mater. Interfaces*, 2015, **7**, 16590-16600.

339. C. M. Burke, V. Pande, A. Khetan, V. Viswanathan and B. D. McCloskey, *Proceedings of the National Academy of Sciences*, 2015, **112**, 9293-9298.

340. Y. Chen, S. A. Freunberger, Z. Peng, O. Fontaine and P. G. Bruce, *Nature chemistry*, 2013, **5**, 489.

341. W.-J. Kwak, H. Kim, H.-G. Jung, D. Aurbach and Y.-K. Sun, *J. Electrochem. Soc.*, 2018, **165**, A2274-A2293.

342. N. B. Aetukuri, B. D. McCloskey, J. M. García, L. E. Krupp, V. Viswanathan and A. C. Luntz, *Nature chemistry*, 2015, **7**, 50.

343. M. D. Radin, C. W. Monroe and D. J. Siegel, *Chem. Mater.*, 2015, **27**, 839-847.

344. Z. Liu, L. R. De Jesus, S. Banerjee and P. P. Mukherjee, *ACS Appl. Mater. Interfaces*, 2016, **8**, 23028-23036.

345. Z. Ma, X. Yuan, L. Li, Z.-F. Ma, D. P. Wilkinson, L. Zhang and J. Zhang, *Energy Environ. Sci.*, 2015, **8**, 2144-2198.

346. N. Mahne, O. Fontaine, M. O. Thotiyl, M. Wilkening and S. A. Freunberger, *Chemical science*, 2017, **8**, 6716-6729.

347. K. He, X. Bi, Y. Yuan, T. Foroozan, B. Song, K. Amine, J. Lu and R. Shahbazian-Yassar, *Nano Energy*, 2018, **49**, 338-345.

348. J. Huang and Z. Peng, *Batteries & Supercaps*, 2019.

349. K. B. Knudsen, T. Vegge, B. D. McCloskey and J. Hjelm, *J. Electrochem. Soc.*, 2016, **163**, A2065-A2071.

350. Y. Yin, C. Gaya, A. Torayev, V. Thangavel and A. A. Franco, *J. Phys. Chem. Lett.*, 2016, **7**, 3897-3902.

351. Y. Yin, A. Torayev, C. Gaya, Y. Mammeri and A. A. Franco, *J. Phys. Chem. C*, 2017, **121**, 19577-19585.

352. C. Shen, J. Xie, T. Liu, M. Zhang, P. Andrei, L. Dong, M. Hendrickson, E. J. Plichta and J. P. Zheng, *J. Electrochem. Soc.*, 2018, **165**, A2833-A2839.
353. L. Li and A. Manthiram, *J. Mater. Chem. A*, 2013, **1**, 5121-5127.
354. W.-J. Kwak, J. W. Park, T. T. Nguyen, H. Kim, H. R. Byon, M. C. Jang and Y.-K. Sun, *J. Mater. Chem. A*, 2019.
355. A. Mistry, C. Fear, R. Carter, C. T. Love and P. P. Mukherjee, *ACS Energy Lett.*, 2019, **4**, 156-162.
356. L. Guo, G. Oskam, A. Radisic, P. M. Hoffmann and P. C. Searson, *J. Phys. D: Appl. Phys.*, 2011, **44**, 443001.
357. M. Paunovic and M. Schlesinger, *Fundamentals of electrochemical deposition*, john wiley & sons, 2006.
358. F. Hao, A. Verma and P. P. Mukherjee, *ACS Appl. Mater. Interfaces*, 2018, **10**, 26320-26327.
359. C. W. Monroe, *J. Electrochem. Soc.*, 2017, **164**, E3547-E3551.
360. B. Balu and A. S. Khair, *Soft matter*, 2018, **14**, 8267-8275.
361. A. N. Mistry and P. P. Mukherjee, *J. Phys. Chem. C*, 2018, **122**, 18329-18335.
362. A. Schürmann, R. Haas, M. Murat, N. Kuritz, M. Balaish, Y. Ein-Eli, J. Janek, A. Natan and D. Schröder, *J. Electrochem. Soc.*, 2018, **165**, A3095-A3099.
363. F. S. Gittleson, R. E. Jones, D. K. Ward and M. E. Foster, *Energy Environ. Sci.*, 2017, **10**, 1167-1179.
364. M. Augustin, P. E. Vullum, F. Vullum-Bruer and A. M. Svensson, *J. Power Sources*, 2019, **414**, 130-140.
365. D. A. Porter, K. E. Easterling and M. Sherif, *Phase Transformations in Metals and Alloys, (Revised Reprint)*, CRC press, 2009.
366. M. Avrami, *J. Chem. Phys*, 1939, **7**, 103.
367. A. Torayev, A. Rucci, P. C. M. M. Magusin, A. Demortière, V. De Andrade, C. P. Grey, C. Merlet and A. A. Franco, *J. Phys. Chem. Lett.*, 2018, **9**, 791-797.
368. K.-H. Xue, E. McTurk, L. Johnson, P. G. Bruce and A. A. Franco, *J. Electrochem. Soc.*, 2015, **162**, A614-A621.
369. J. Bao, W. Xu, P. Bhattacharya, M. Stewart, J.-G. Zhang and W. Pan, *J. Phys. Chem. C*, 2015, **119**, 14851-14860.
370. X. Li, *J. Electrochem. Soc.*, 2015, **162**, A1636-A1645.

371. K. Yoo, S. Banerjee and P. Dutta, *J. Power Sources*, 2014, **258**, 340-350.
372. C. P. Andersen, H. Hu, G. Qiu, V. Kalra and Y. Sun, *J. Electrochem. Soc.*, 2015, **162**, A1135-A1145.
373. Y. Wang, Z. Wang, H. Yuan and T. Li, *Electrochim. Acta*, 2015, **180**, 382-393.
374. U. Sahapatsombut, H. Cheng and K. Scott, *J. Power Sources*, 2013, **227**, 243-253.
375. Y. Wang and S. C. Cho, *J. Electrochem. Soc.*, 2013, **160**, A1847-A1855.
376. M. Mehta, V. Bevara and P. Andrei, *J. Power Sources*, 2015, **286**, 299-308.
377. A. V. Sergeev, A. V. Chertovich, D. M. Itkis, E. A. Goodilin and A. R. Khokhlov, *J. Power Sources*, 2015, **279**, 707-712.
378. K.-H. Xue, T.-K. Nguyen and A. A. Franco, *J. Electrochem. Soc.*, 2014, **161**, E3028-E3035.
379. C. Jung, T. Zhao and L. An, *J. Power Sources*, 2015, **273**, 440-447.
380. V. Bevara and P. Andrei, *J. Electrochem. Soc.*, 2014, **161**, A2068-A2079.
381. C.-F. Chen, A. Mistry and P. P. Mukherjee, *J. Phys. Chem. C*, 2017, **121**, 21206 - 21216.
382. T. Zhang, M. Marinescu, L. O'Neill, M. Wild and G. Offer, *Phys. Chem. Chem. Phys.*, 2015, **17**, 22581-22586.
383. A. D. Dysart, J. C. Burgos, A. Mistry, C.-F. Chen, Z. Liu, C. N. Hong, P. B. Balbuena, P. P. Mukherjee and V. G. Pol, *J. Electrochem. Soc.*, 2016, **163**, A730-A741.
384. J. Zheng, M. Gu, M. J. Wagner, K. A. Hays, X. Li, P. Zuo, C. Wang, J.-G. Zhang, J. Liu and J. Xiao, *J. Electrochem. Soc.*, 2013, **160**, A1624-A1628.
385. S. S. Zhang, *Electrochim. Acta*, 2013, **97**, 226-230.
386. J. Conder, R. Bouchet, S. Trabesinger, C. Marino, L. Gubler and C. Villevieille, *Nat. Energy*, 2017, **2**, 17069.
387. M. D. Greenberg, *Advanced engineering mathematics*, Prentice-Hall, 1988.
388. S. Patankar, *Numerical heat transfer and fluid flow*, CRC press, 1980.
389. J. D. Hoffman and S. Frankel, *Numerical methods for engineers and scientists*, CRC press, 2001.
390. A. Rosenman, E. Markevich, G. Salitra, D. Aurbach, A. Garsuch and F. F. Chesneau, *Adv. Energy Mater.*, 2015, **5**.
391. S. Urbonaite, T. Poux and P. Novák, *Adv. Energy Mater.*, 2015, **5**.
392. G. Li, S. Wang, Y. Zhang, M. Li, Z. Chen and J. Lu, *Adv. Mater.*, 2018.

393. G. Babu, N. Masurkar, H. Al Salem and L. M. R. Arava, *J. Am. Chem. Soc.*, 2017, **139**, 171-178.

394. H. Al Salem, G. Babu, C. V. Rao and L. M. R. Arava, *J. Am. Chem. Soc.*, 2015, **137**, 11542-11545.

395. Z. Liu, P. B. Balbuena and P. P. Mukherjee, *J. Phys. Chem. C*, 2017, **121**, 17169-17175.

396. J. Conder, C. Marino, P. Novak and C. Villevieille, *J. Mater. Chem. A*, 2018.

397. N. A. Cañas, D. N. Fronczek, N. Wagner, A. Latz and K. A. Friedrich, *J. Phys. Chem. C*, 2014, **118**, 12106-12114.

398. K. H. Wujcik, D. R. Wang, A. Raghunathan, M. Drake, T. A. Pascal, D. Prendergast and N. P. Balsara, *J. Phys. Chem. C*, 2016, **120**, 18403-18410.

399. M. Marinescu, L. O'Neill, T. Zhang, S. Walus, T. E. Wilson and G. J. Offer, *J. Electrochem. Soc.*, 2018, **165**, A6107-A6118.

400. F. Sun, M. Osenberg, K. Dong, D. Zhou, A. Hilger, C. J. Jafta, S. Risse, Y. Lu, H. Markötter and I. Manke, *ACS Energy Lett.*, 2018, **3**, 356-365.

401. L. E. Camacho-Forero and P. B. Balbuena, *Phys. Chem. Chem. Phys.*, 2017, **19**, 30861-30873.

402. M. I. Nandasiri, L. E. Camacho-Forero, A. M. Schwarz, V. Shutthanandan, S. Thevuthasan, P. B. Balbuena, K. T. Mueller and V. Murugesan, *Chem. Mater.*, 2017, **29**, 4728-4737.

403. Z. Liu, S. Bertolini, P. B. Balbuena and P. P. Mukherjee, *ACS Appl. Mater. Interfaces*, 2016, **8**, 4700-4708.

404. X. Feng, M.-K. Song, W. C. Stolte, D. Gardenghi, D. Zhang, X. Sun, J. Zhu, E. J. Cairns and J. Guo, *Phys. Chem. Chem. Phys.*, 2014, **16**, 16931-16940.

405. C. Shen, J. Xie, M. Zhang, J. P. Zheng, M. Hendrickson and E. J. Plichta, *J. Electrochem. Soc.*, 2017, **164**, A1220-A1222.

406. R. B. Bird, W. E. Stewart and E. N. Lightfoot, *JohnWiley & Sons, New York*.

407. G. P. Morriss and D. J. Evans, *Statistical Mechanics of Nonequilbrium Liquids*, ANU Press, 2013.

408. A. Einstein, *Ann. der Physik*, 1905, DOI: citeulike-article-id:4036262.

409. Q. Wang, J. Zheng, E. Walter, H. Pan, D. Lv, P. Zuo, H. Chen, Z. D. Deng, B. Y. Liaw and X. Yu, *J. Electrochem. Soc.*, 2015, **162**, A474-A478.

410. J. Newman, *Advances in Electrochemistry and Electrochemical Engineering*, 1967, **5**, 87-136.
411. J. Newman and T. W. Chapman, *AlChE J.*, 1973, **19**, 343-348.
412. J. Conder and C. Villevieille, *Current Opinion in Electrochemistry*, 2018.
413. A. Manthiram, *ACS Cent. Sci.*, 2017, **3**, 1063-1069.
414. E. Zhao, K. Nie, X. Yu, Y. S. Hu, F. Wang, J. Xiao, H. Li and X. Huang, *Adv. Funct. Mater.*, 2018, 1707543.
415. X.-B. Cheng, J.-Q. Huang, H.-J. Peng, J.-Q. Nie, X.-Y. Liu, Q. Zhang and F. Wei, *J. Power Sources*, 2014, **253**, 263-268.
416. X. Yu, H. Pan, Y. Zhou, P. Northrup, J. Xiao, S. Bak, M. Liu, K. W. Nam, D. Qu and J. Liu, *Adv. Energy Mater.*, 2015, **5**.
417. E. Peled, I. Shekhtman, T. Mukra, M. Goor, I. Belenkaya and D. Golodnitsky, *J. Electrochem. Soc.*, 2018, **165**, A6051-A6057.
418. E. J. Berg and S. Trabesinger, *J. Electrochem. Soc.*, 2018, **165**, A5001-A5005.
419. J.-Q. Huang, Q. Zhang, H.-J. Peng, X.-Y. Liu, W.-Z. Qian and F. Wei, *Energy Environ. Sci.*, 2014, **7**, 347-353.
420. M. R. Busche, P. Adelhelm, H. Sommer, H. Schneider, K. Leitner and J. Janek, *J. Power Sources*, 2014, **259**, 289-299.
421. G. Li, X. Wang, M. H. Seo, M. Li, L. Ma, Y. Yuan, T. Wu, A. Yu, S. Wang and J. Lu, *Nature communications*, 2018, **9**, 705.
422. Q. Wang, J. Jin, X. Wu, G. Ma, J. Yang and Z. Wen, *Phys. Chem. Chem. Phys.*, 2014, **16**, 21225-21229.
423. N. Xu, T. Qian, X. Liu, J. Liu, Y. Chen and C. Yan, *Nano Lett.*, 2017, **17**, 538-543.
424. C.-W. Lee, Q. Pang, S. Ha, L. Cheng, S.-D. Han, K. R. Zavadil, K. G. Gallagher, L. F. Nazar and M. Balasubramanian, *ACS Cent. Sci.*, 2017, **3**, 605-613.
425. M. Piwko, C. Weller, F. Hippauf, S. Dörfler, H. Althues and S. Kaskel, *J. Electrochem. Soc.*, 2018, **165**, A1084-A1091.
426. S.-H. Chung, P. Han and A. Manthiram, *ACS Appl. Mater. Interfaces*, 2017, **9**, 20318-20323.
427. L. E. Camacho-Forero, T. W. Smith, S. Bertolini and P. B. Balbuena, *J. Phys. Chem. C*, 2015, **119**, 26828-26839.

428. T. A. Pascal, I. Villaluenga, K. H. Wujcik, D. Devaux, X. Jiang, D. R. Wang, N. Balsara and D. Prendergast, *Nano Lett.*, 2017, **17**, 2517-2523.
429. C. Weller, S. Thieme, P. Härtel, H. Althues and S. Kaskel, *J. Electrochem. Soc.*, 2017, **164**, A3766-A3771.
430. T. A. Pascal, K. H. Wujcik, D. R. Wang, N. P. Balsara and D. Prendergast, *Phys. Chem. Chem. Phys.*, 2017, **19**, 1441-1448.
431. P. Barai, A. Mistry and P. P. Mukherjee, *Extreme Mechanics Letters*, 2016, **9**, 359-370.
432. S. Waluś, G. Offer, I. Hunt, Y. Patel, T. Stockley, J. Williams and R. Purkayastha, *Energy Storage Materials*, 2018, **10**, 233-245.

VITA

Aashutosh N. Mistry

Research Interests

Electrochemical Physics, Kinetic and Transport Interactions, Interfacial Science, Stochastic Complexations in Porous Reactors, Surface tension driven Flow, Computation Analysis, Inverse Problems, Instrumentation, Statistical Learning

Education

Ph.D., Mechanical Engineering

2017 – 2019	Purdue University*	GPA: 4.00/4.00
2015 – 2017	Texas A&M University*	GPA: 4.00/4.00
Advisor:	Prof. Partha Mukherjee	
Dissertation:	*Mesoscale Interactions in Porous Electrodes*	

* Moved from Texas A&M to Purdue in Fall 2017 with Prof. Mukherjee

M.Tech, Mechanical Engineering (Gold Medalist)

2012 – 2014	Indian Institute of Technology, Kanpur	GPA: 10.00/10.00
Advisor:	Prof. Krishnamurthy Muralidhar	
Dissertation:	*Generalized Lagrangian Model for Drop Spreading on Textured Surfaces*	

B.Tech, Mechanical Engineering (Gold Medalist)

2008 – 2012	National Institute of Technology, Surat	GPA: 9.95/10.00
Advisor:	Prof. Jyotirmay Banerjee	
Dissertation:	*Numerical and Experimental Investigation on Heat Transfer in Nanofluids*	

Awards and Honors

2019 Materials Research Society's Graduate Student Award

2019 Hot paper on Engineering porous electrodes for Li-oxygen chemistry in Journal of Materials Chemistry A

2018 Purdue College of Engineering Outstanding Research Award

2018 Edward G. Weston Summer Fellowship, the Electrochemical Society

2018 Lambert Graduate Teaching Fellowship, School of Mechanical Engineering, Purdue University

2018 Invited speaker at Gordon Research Seminar for Batteries (24 – 25th Feb)

2018 Travel Grant, the Electrochemical Society's Spring Meeting

2018 Journal cover art for Secondary-phase Stochasticity research in ACS Applied Materials & Interfaces (https://pubs.acs.org/toc/aamick/10/7)

2018 Editor's choice article on Interfacial modeling of carbon-binder domains

2018 Features news reports on Secondary (inactive) phase stochasticity research – Materials Research Society (MRS) Bulletin, Battery Power: Cambridge EnerTech and Purdue News

2018 Inaugural speaker at Graduate Sandbox Seminar (24th Jan)

2017 Featured news report on Thermal Cross-talk research – Materials Research Society's Fall Meeting

2016 Invited graduate student participant and tutorial lecturer at the College of Multiscale Computational Modeling of Materials for Energy Applications, International Center for Theoretical Physics, Trieste, Italy (4 – 15th Jul)

2016 Invited graduate student participant at Indo-US Workshop on Recent Advances in Multiscale Multiphysics Analysis of Energy Conversion in Li-ion Batteries, IIT-Bombay, India (17 – 19th Jun)

2015 The First prize in a poster presentation at Texas A&M Non-fossil based Technologies for Energy Workshop (24th Jun): "*Investigating Chemical and Electrochemical Interactions during Discharge of a Lithium Sulfur Cell"*

2014 Sashi Pundir Memorial Gold Medal for the best Master's thesis in Fluid Mechanics and Transport Phenomena, IIT-Kanpur

2014 Academic Excellence Award, IIT-Kanpur

2012 Smt. Laxmi Bala Majumdar Gold Medal for securing the 1st merit rank across all disciplines of Bachelor of Technology, NIT-Surat

2012 Siddhartha Gupta Gold Medal for securing the 1st merit rank across all disciplines of Bachelor of Technology, NIT-Surat

2012 Gold Medal for securing the 1st merit rank in Bachelor of Technology, Mechanical Engineering, NIT-Surat

2012 Siddhartha Gupta Gold Medal for securing the 1st merit rank in Bachelor of Technology, Mechanical Engineering, NIT-Surat

Journal Publications (Google Scholar Page)

1. **A. Mistry** *et al*. (2019) *Electrolyte Confinement alters Lithium Electrodeposition* ACS Energy Letters 4 (1) 156
2. **A. Mistry** and P. P. Mukherjee (2019) *Non-equilibrium Thermodynamics in Electrochemical Complexation of Li-oxygen Porous Electrodes* Journal of Materials Chemistry A *in press*
3. **A. Mistry**, H. Reddy Palle and P. P. Mukherjee (2019) *In Operando Thermal Signature Probe for Lithium Ion Cells* Applied Physics Letters 114 (2) 023901
4. (joint first author) R. Adams, **A. Mistry** *et al.*, *Materials by Design: Tailored Morphology and Structures of Carbon Anodes for Enhanced Battery Safety* ACS Applied Materials and Interfaces *in press*
5. **A. Mistry** (2018) *Curvature Effects in Precipitation Dynamics* The Electrochemical Society Interface Winter 27 (4) 80
6. **A. Mistry** and P. P. Mukherjee (2018) *Probing Spatial Coupling of Resistive Modes in Porous Intercalation Electrodes through Impedance Spectroscopy* Physical Chemistry Chemical Physics 21 (7) 3805
7. **A. Mistry** and P. P. Mukherjee (2018) *'Shuttle' in Polysulfide Shuttle: Friend or Foe?* The Journal of Physical Chemistry C 122 (42) 23845
8. **A. Mistry**, K. Smith and P. P. Mukherjee (2018) *Electrochemistry-coupled Mesoscale Complexations in Electrodes Lead to Thermo-electrochemical Extremes* ACS Applied Materials and Interfaces 10 (34) 28644
9. **A. Mistry**, K. Smith, and P. P. Mukherjee (2018) *Secondary Phase Stochastics in Li-ion Battery Cathodes* ACS Applied Materials and Interfaces 10 (7) 6317

10. **A. Mistry** and P. P. Mukherjee (2018) *Electrolyte Transport Evolution Dynamics in Li-sulfur Batteries* The Journal of Physical Chemistry C 122 (32) 18329
11. **A. Mistry** and K. Muralidhar (2018) *Spreading of a Pendant Liquid Drop underneath a Textured Substrate* Physics of Fluids 30 (4) 042104
12. **A. Mistry** and P. P. Mukherjee (2017) *Precipitation – Microstructure Interaction in Li-S Battery Cathode* The Journal of Physical Chemistry C 121 (47) 26256
13. (joint first author) C.-F. Chen, **A. Mistry** and P. P. Mukherjee (2017) *Probing Impedance and Microstructure Evolution in Lithium-sulfur Battery Electrodes* The Journal of Physical Chemistry C 121 (39) 21206
14. **A. Mistry**, D. Juarez-Robles, M. Stein and K. Smith, P. P. Mukherjee (2016) *Analysis of Long-range Interaction in Lithium-ion Battery Electrodes* Journal of Electrochemical Energy Conversion and Storage 13 (3) 031006
15. **A. Mistry** and K. Muralidhar (2015) *Axisymmetric Model of Drop Spreading on a Horizontal Surface* Physics of Fluids 27 (9) 092103
16. J. Grunewald, **A. Mistry**, *et al.* (2019) *Mesoscale Physics in the Catalyst Layer of Proton Exchange Membrane Fuel Cells: a Critical Perspective* Journal of the Electrochemical Society 166 (7) F3089
17. B. Trembacki, **A. Mistry**, *et al.* (2018) *Mesoscale Analysis of Conductive Binder Domain Morphology in Lithium-Ion Battery Electrodes* Journal of the Electrochemical Society 165 (13) E725
18. M. Vasilyeva, **A. Mistry** and P. P. Mukherjee (2018) *Multiscale Model Reduction for Pore-scale Simulation of Li-ion Batteries using GMsFEM* Journal of Computational and Applied Mathematics 344, 73
19. N. Kotak, P. Barai, A. Verma, **A. Mistry** and P. P. Mukherjee (2018) *Electrochemistry-mechanics Coupling in Intercalation Electrodes* Journal of the Electrochemical Society 165 (5) A1064
20. F. Usseglio-Viretta, A. Colclasure, **A. Mistry** *et al.*, (2018) *Resolving the Discrepancy in Tortuosity Factor Estimation for Li-ion Battery Electrodes through Micro-Macro Modeling and Experiment* Journal of the Electrochemical Society 166 (14) A3403
21. Z. Liu, **A. Mistry** and P. P. Mukherjee (2017) *Mesoscale Physicochemical Interactions in Lithium-sulfur Batteries: Progress and Perspective* Journal of Electrochemical Energy Conversion and Storage 15 (1) 010802
22. M. Stein IV, **A. Mistry** and P. P. Mukherjee (2017) *Mechanistic Understanding of the Role of Evaporation in Electrode Processing* Journal of the Electrochemical Society 164 (7) A1616
23. K. Shah, N. Balsara, S. Banerjee, M. Chintapalli, A. P. Cocco, W. K. S. Chiu, I. Lahari, S. Martha, **A. Mistry** *et al.* (2017) *State-of-the-art and Future Research Needs for Multiscale Analysis of Li-ion Cells* Journal of Electrochemical Energy Conversion and Storage 14 (2) 020801
24. G. J. Nelson, L. J. Ausderau, J. R. Buckley, S. Shin, **A. Mistry**, P. P. Mukherjee and V. De Andrade (2017) *Transport-geometry Interactions in Li-ion Cathode Materials Imaged using X-ray Nanotomography* Journal of the Electrochemical Society 164 (7) A1412
25. P. Barai, **A. Mistry** and P. P. Mukherjee (2016) *Poromechanical Effect in the Lithium-sulfur Battery Cathode* Extreme Mechanics Letters 9 (3) 359

26. A. D. Dysart, J. C. Burgos, **A. Mistry** *et al.* (2015) *Towards Next Generation Lithium-sulfur Batteries: Non-conventional Carbon Compartments/ Sulfur Electrodes and Multi-scale Analysis* Journal of the Electrochemical Society 163 (5) A730

Manuscripts under review

27. **A. Mistry** and P. P. Mukherjee, *Stochasticity at Scales Leads to Lithium Intercalation Cascade*
28. **A. Mistry**, A. Verma and P. P. Mukherjee, *Controllable Electrode Stochasticity Self-heats Lithium-ion Batteries at Low Temperatures*
29. **A. Mistry** and P. P. Mukherjee, *Statistical Learning based Abstraction of Pore Network Resistance Descriptor in Porous Electrodes*
30. **A. Mistry**, V. Srinivasan and P. P. Mukherjee, *Interfacial Dynamics in a Concentration-driven Phase Change*
31. **A. Mistry** *et al.*, *Atypical Mechanistics of Electrodeposition in Intercalation Electrodes*
32. **A. Mistry** and P. P. Mukherjee, *Molar Volume Mismatch: a Unified View of Electrodeposition Instability in Solid Ion Conductors*
33. **A. Mistry** and P. P. Mukherjee, *Chemo-mechanical Antimutualism in Porous Conversion Electrodes*
34. **A. Mistry** and P. P. Mukherjee, *Mechanistic Identification of Secondary-phase Morphology in Porous Intercalation Electrodes*

Book Chapters

1. (under review) P. P. Mukherjee and **A. Mistry**, *Basics of Electrochemical Energy Storage*
2. (under review) P. P. Mukherjee, **A. Mistry** and A. Verma, *Lithium-ion Batteries*
3. P. P. Mukherjee, **A. Mistry** and A. Verma (2017) *Porous Media Applications: Electrochemical Systems, in Modeling Transport Phenomena in Porous Media with Applications* eds. M. K. Das, P. P. Mukherjee, K. Muralidhar, Springer
4. P. P. Mukherjee, A. Verma, and **A. Mistry** (2017) *Mesoscale Interactions of Transport Phenomena in Polymer Electrolyte Fuel Cells, in Modeling Transport Phenomena in Porous Media with Applications* eds. M. K. Das, P. P. Mukherjee, K. Muralidhar, Springer

Conference Proceedings

1. **A. Mistry** and K. Muralidhar, *Non-isothermal Spreading of Liquid Drops: Effect of Fluid Convection*, Asian Symposium on Computational Heat Transfer and Fluid Flow, November 2015
2. **A. Mistry** and K. Muralidhar, *Study of Front Tracking Methodology for Simulation of Multiphase Flow*, Proceedings of Fortieth National Conference on Fluid Mechanics and Fluid Power, December 2013
3. **A. Mistry**, A. Verma and M. K. Das, *Modeling of Polymer Electrolyte Membrane (PEM) Fuel Cell Cathode with Agglomerate Catalyst Layer*, Proceedings of Fortieth National Conference on Fluid Mechanics and Fluid Power, December 2013
4. **A. Mistry** and J. Banerjee, *A Comparative Analysis of Single-phase and Two-fluid Model for Nanofluid Heat Transfer in Forced Convection Regime*, Proceedings of Thirty Ninth National Conference on Fluid Mechanics and Fluid Power, December 2012

Oral Presentations and Posters at Conferences

1. **A. Mistry** and P. P. Mukherjee, *Elucidating Electrodeposition Instability at the Solid-solid Interface*, American Physical Society March Meeting, Boston, MA (04 – 08th Mar 2019)

2. **A. Mistry** and P. P. Mukherjee, *Mesoscale Insights into Li-sulfur Battery Charge Transport*, 256th American Chemical Society National Meeting, Boston, MA (19 – 23rd Aug 2018)
3. **A. Mistry** and P. P. Mukherjee, *A Statistical Learning based Characterization of Lithium-ion Battery Electrodes*, 13th World Congress on Computational Mechanics, New York, NY (22 – 27th Jul 2018)
4. **A. Mistry** and P. P. Mukherjee, *Transport and Electrochemical Dynamics in the Li-S Battery Electrolyte*, 233rd Meeting of the Electrochemical Society, Seattle, WA (13 – 17th May 2018)
5. **A. Mistry** and P. P. Mukherjee, *Analyzing the Importance of Particle Morphology and Heterogeneity in Li-ion Battery Electrodes*, 233rd Meeting of the Electrochemical Society, Seattle, WA (13 – 17th May 2018)
6. **A. Mistry** and P. P. Mukherjee, *Analyzing Microstructural and Electrolyte Phase Limitations in Li-air Battery Performance*, 233rd Meeting of the Electrochemical Society, Seattle, WA (13 – 17th May 2018)
7. **A. Mistry** and P. P. Mukherjee, *Mechanistic Understanding of Transport-mechanics Interactions in Li-S Cathodes*, TMS 2018, 147th Annual Meeting and Exhibition, Phoenix, AZ (11 – 15th Mar 2018)
8. **A. Mistry**, *Inverse Formulations for Consistent Thermo-Electro-Chemical Characterization of Li-ion Batteries*, Gordon Research Seminar for Batteries, Ventura, CA (24 – 25th Feb 2018)
9. **A. Mistry**, A. Verma and P. P. Mukherjee, *Electrode Stochastics in Energy Storage*, Gordon Research Conference for Batteries, Ventura, CA (25th Feb – 1st Mar 2018)
10. **A. Mistry** and P. P. Mukherjee, *Mesoscale Physics and Stochastics in Energy Storage and Conversion*, Poster at the Prospective Graduate Student Reception, School of Mechanical Engineering, Purdue University (15th Feb 2018)
11. **A. Mistry**, *Microstructure Mediated Thermo-Electrochemical Interactions in Energy Storage*, Graduate Sandbox Seminar, School of Mechanical Engineering, Purdue University (24th Jan 2018)
12. **A. Mistry** and P. P. Mukherjee, *Thermal Cross-talk in Lithium-ion Battery Safety*, Materials Research Society Fall Meeting, Boston, MA (26th Nov – 1st Dec 2017)
13. **A. Mistry** and P. P. Mukherjee, *Simulated Calorimetry based Thermal Characterization of Lithium-ion Cells*, International Mechanical Engineering Congress & Exposition – IMECE 2017, Tampa, FL (3 – 9th Nov 2017)
14. **A. Mistry** and P. P. Mukherjee, *Hysteresis in Li-S Battery Performance*, Advanced lithium Batteries for Automotive Applications – ABAA 2017, Oakbrook, IL (23 – 25th Oct 2017)
15. **A. Mistry** and P. P. Mukherjee, *Microstructural Limitations in Lithium-sulfur Battery Performance*, 232nd Meeting of Electrochemical Society, National Harbor, MD (1 – 5th Oct 2017)
16. **A. Mistry** and P. P. Mukherjee, *Non-intercalating Phases and Electrochemical Behavior of Lithium-ion Battery Cathode*, 232nd Meeting of the Electrochemical Society, National Harbor, MD (1 – 5th Oct 2017)
17. **A. Mistry**, A. Verma, and P. P. Mukherjee, *Mesoscale Physics and Stochastics in Energy Storage*, Hawkins Lecture Poster Presentation, Purdue Mechanical Engineering, West Lafayette, IN (21st Sep 2017)

18. **A. Mistry** and P. P. Mukherjee, *Virtual Electrode Engineering: From Mesoscale Underpinnings to System Characteristics*, Advanced Automotive Battery Conference – AABC 2017, San Francisco, CA (19 – 22th Jun 2017)
19. **A. Mistry** and P. P. Mukherjee, *Demystifying Microstructure Limitations in Li/S Cells: Surface Passivation vs. Pore Blockage*, Materials Research Society Spring Meeting, Phoenix, AZ (17 – 21th Apr 2017)
20. **A. Mistry** and P. P. Mukherjee, *Mesoscale Probing of Transport-Interface Interaction in Lithium-ion Battery Electrodes*, TMS 2017 146th Annual Meeting and Exhibition, San Diego, CA (26th Feb – 2st Mar 2017)
21. **A. Mistry**, D. Juarez-Robles, and P. P. Mukherjee, *Thermo-electrochemical Analytics in Li-ion Battery Safety*, ESS Safety Forum 2017, Santa Fe, NM (22 – 24th Feb 2017)
22. **A. Mistry**, Z. Liu and P. P. Mukherjee, *Mesoscale Modeling of Transport Limitations during Discharge of a Li-S cell*, 12th Annual Lithium Battery Power Conference, Bethesda, MD (1 – 2nd Nov 2016)
23. **A. Mistry**, *Modeling and Analysis of Electrochemical Performance of Lithium-Sulfur Batteries*, College of Multiscale Computational Modeling of Materials for Energy Applications, International Center for Theoretical Physics, Trieste, Italy (4 – 15th Jul 2016)
24. **A. Mistry** and P. P. Mukherjee, *Improving Discharge Performance of Li-air Batteries with Electrode Microstructural Modifications*, College of Multiscale Computational Modeling of Materials for Energy Applications, International Center for Theoretical Physics, Trieste, Italy (4 – 15th Jul 2016)
25. **A. Mistry**, C.-F. Chen, Z. Liu and P. P. Mukherjee, *Mesoscale Modeling of Transport Limitations during Discharge of a Li-S Cell*, Indo-US Workshop on Recent Advances in Multiscale Multiphysics Analysis of Energy Conversion in Li-ion Batteries, IIT-Bombay, India (17 – 19th Jun 2016)
26. **A. Mistry**, C.-F. Chen, A. Verma and P. P. Mukherjee, *Long Range Interaction in Lithium-Ion Battery Electrodes*, Indo-US Workshop on Recent Advances in Multiscale Multiphysics Analysis of Energy Conversion in Li-ion Batteries, IIT-Bombay, India (17 – 19th Jun 2016)
27. **A. Mistry**, P. Barai, and P. P. Mukherjee, *Precipitation Induced Stress and Degradation in the Lithium-sulfur Battery Cathode*, 229th Meeting of Electrochemical Society, San Diego, CA (29th May – 2nd Jun 2016)
28. **A. Mistry**, A. Verma, R. Mukherjee and P. P. Mukherjee, *Image-based Reconstruction and Statistical Characterization of the Li-ion Battery Electrode Microstructure*, 229th Meeting of Electrochemical Society, San Diego, CA (29th May – 2nd Jun 2016)
29. **A. Mistry**, C.-F. Chen, Z. Liu and P. P. Mukherjee, *Mesoscale Modeling of the Physicochemical Interplay in the Li-sulfur Battery Porous Cathode*, Interpore 2016, Cincinnati, OH (8th May – 12th May 2016)
30. **A. Mistry**, A. Verma, D. Juarez-Robles and P. P. Mukherjee, *How Electrode Processing Affects Li-ion Battery Performance?*, Material Challenges in Alternative and Renewable Energy – MCARE 2016, Clearwater, FL (17 – 21st Apr 2016)
31. **A. Mistry**, A. Verma, D. Juarez-Robles and P. P. Mukherjee, *Physicochemical Evolution Behavior in the Li-air Battery Electrode*, Material Challenges in Alternative and Renewable Energy – MCARE 2016, Clearwater, FL (17 – 21st Apr 2016)
32. **A. Mistry**, P. Barai and P. P. Mukherjee, *A Two-way Coupled Mechano-Electrochemical Model for Estimating Active Material Degradation in Lithium-ion Battery Electrodes*,

International Mechanical Engineering Congress & Exposition – IMECE 2015, Houston, TX (13 – 19th Nov 2015)

33. **A. Mistry**, D. Juarez-Robles, F. Cano-Banda, A. Hernandez-Guerrero and P. P. Mukherjee, *Correlating Precipitation Morphology in the Air Electrode to the Lithium-air Battery Discharge Performance*, 52nd Annual Technical Meeting of Society of Engineering Sciences – SES 2015, Texas A&M (26 – 28th Oct 2015)
34. P. P. Mukherjee, Z. Liu, C.-F. Chen and **A. Mistry**, *Investigating Chemical and Electrochemical Interactions during Discharge of a Lithium Sulfur Cell*, Texas A&M Non-fossil based Technologies for Energy – Research Workshop, Texas A&M (20th Oct 2015)
35. P. P. Mukherjee, A Hernandez-Guerrero, Z. Liu, C.-F. Chen, **A. Mistry**, D. Juarez-Robles and F. Cano-Banda, *High-performance Electrode Architecture for Lithium-Air Batteries*, Texas A&M – CONACyT Symposium 2015, Texas A&M (24th Jun 2015)
36. **A. Mistry** and K. Muralidhar, *Prediction of Drop Spreading in a Lagrangian Framework*, Departmental Poster Presentation, IIT Kanpur (21st Mar 2014)

Undergraduate Research Mentoring

2018 Aug – May	Prathamesh Sankhe (B. S., Purdue University, IN) *Microstructural Analysis of Porous Separators*
2017 Jan – May	Serdar Ozguc (B. S., Texas A&M University, TX) *Identifying Microstructural Signature in Internal Resistance for Porous Intercalation Electrodes*
2016 May – Jul	Akash Verma (B. Tech, IIT-Kanpur, India) *A Reduced-order Model to Quantify Thermal Behavior of Li-ion Cells during Electrochemical Testing*
2015 Sep – Dec	A team of undergrads (Texas A&M University, TX) *AggieChallenge 2015*
2015 May – Jul	Leigha Lewis (B. S., Sam Houston State University, TX) *Data-driven Characterization of Transport Properties for Electrode Microstructure of Lithium Sulfur Batteries*
2015 May – Jul	Mohit Singhal (B. Tech, IIT-Kanpur, India) *Oven Test to Measure Thermal Abuse Tolerance of Li-ion Batteries: A Lumped Model*
2015 May – Jul	Aditya Tiwari (B. Tech., NIT-Surat, India) *Drying of Particulate Slurry: A Model for Preparation of Electrodes*

Other Research Experience

Summer Fellow

Jun 2018 – Aug 2018 Edward G. Weston Summer Fellowship, the Electrochemical Society

Fellowship Mentor: Dr. Venkat Srinivasan, Argonne National Laboratory

Interfacial Effects in Concentration-driven Phase Change

Project Associate

Jun 2014 – Dec 2014 AnuPravaha I

Principal Investigator: Prof. Malay Das, Indian Institute of Technology, Kanpur

Code Parallelization of AnuPravaha I, a general purpose CFD solver

Teaching Activities

Lambert Teaching Fellowship

Fall 2018	Thermodynamics II (ME 30000; 36 students)
Spring 2018	Thermodynamics II (ME 30000; 40 students)
	Exergy Analysis, Ideal Gas Mixtures, Psychrometry

Teaching Assistantships

Spring 2014	Experimental Methods in Thermal Sciences (ME 649; 18 students)
Fall 2013	Programming and Numerical Analysis (ME 685; 22 students)
Spring 2013	Fluid Mechanics (ME 231; 105 students)

Lectures and Workshops

2014, Jul 24-25th	How to generate Technical Diagrams/Figures using Asymptote (IIT-Kanpur)
2014, Jun 30th – Jul 4th	How to become Friends with MATLAB? (IIT-Kanpur)
2013, Aug 27 – 31st	Basics of MATLAB programming (IIT-Kanpur)
2012, Mar 28th	Application of Mathematics in "Real-life Problems" (NIT-Surat)
2010, Sep 15th	Steering and Differential (NIT-Surat)

Peer Reviewer

1. Physics of Fluids (AIP: American Institute of Physics)
2. Journal of the Electrochemical Society (ECS: the Electrochemical Society)
3. RSC Advances (RSC: the Royal Society of Chemistry)
4. Journal of the Electrochemical Energy Storage and Conversion (ASME: American Society of Mechanical Engineers)

Conferences: ASME Power & Energy Conference 2018, IEEE ITherm 2018, IEEE ITherm 2017

Professional Affiliations

1.	American Society of Mechanical Engineering (ASME)	since Nov 2015
2.	The Electrochemical Society (ECS)	since Nov 2015
3.	Materials Research Society (MRS)	since Mar 2017
4.	The Minerals, Metals and Materials Society (TMS)	since Mar 2017
5.	American Chemical Society (ACS)	since Jul 2018
6.	American Physical Society (APS)	since Oct 2018

Scientific Journalism

News reports of invited talks during MRS meetings. Involved attending the talks, understanding the related concepts and reporting them for a broader scientific audience in the written format.

2018	Dislocation Dynamics explain Voltage Fade in Layered-oxide Battery Materials
2017	Asphalt Porous Structure Enables Fast-charging High-capacity Li Metal Anode
2017	Bio-inspired Bistable Shape-changing Displacement Sensors
2017	Data Mining in Small-scale Plasticity
2017	Bio-inspired Anti-fogging Materials: from the Mosquito Effect to the Cicada Effect
2017	Analyzing the Stability and Kinetics of the Li metal – solid electrolyte Interface
2017	Safe, High-energy-density Solid-state Li Batteries

2017 Enhancing Superhydrophobicity and Icephobicity through Surface Flexibility Inspired by Butterfly Wings
2017 Phase Field Models and Interfacial Evolution: a Critical Test of Simulation
2017 Benchmarking Problems for Phase Field Codes
2017 Controlling the Electrical Properties of Organic Electronics: a Path Towards Low-power Printed Electronics
2017 Design of Lubricant Infused Surfaces
2017 Enhancing Understanding of the Solid-electrolyte Interface: Multi-modal Characterization of Battery Systems
2017 Graphene Quantum Dots from Coal
2017 The DAGS chemistry: Droplet Assisted Growth and Shaping for Synthesis of Polymeric Nano- and Microstructures
2017 Special Workshop on Nanomaterials and Their Applications
2017 3D Printing of Transparent and Conductive Heterogeneous Hydrogel-elastomer Systems
2017 Towards Photo-rechargeable Lithium-ion Battery
2017 Garnet-based Li-metal Batteries
2017 X-ray Nanotomography reveals 3D Internal Magnetization Structure
2017 Electrolyte Gating induced Insulator-to-metal Transition in WO_3 Mechanism Identified
2017 Intermolecular Forces for Self-assembly Identified through Simulations
2017 Solar CO_2 Reduction Coupled with Water Oxidation—Semiconductor/Metal-Complex Hybrid System
2017 Photoelectrochemical Solar Energy Storage—Hydrogen Production vs Direct CO2 Reduction and Photoredox Flow Batteries
2017 Nanogenerators for Self-powered Systems and Large-scale Blue Energy
2017 Surface-bound Enzymatic Reactions Organize Microcapsules and Protocells in Solution
2017 Data Analytics for Mining Process-Structure-Property Linkages for Hierarchical Materials
2017 A Multiscale Approach to Cathode Design Based on Mapping Intercalation Gradients within Individual Particles and across Particle Aggregates
2017 Needs and Challenges Associated with High Energy Batteries with an Emphasis on Thermodynamic Underpinnings
2017 Understanding the Nature of Chemical and Electrochemical Stability of Electrolytes at Mg Anode Surfaces

Miscellaneous

2017 Nov Meeting scene reporter at the Materials Research Society's Fall meeting
2017 Apr Meeting scene reporter at the Materials Research Society's Spring meeting
2016 Sep Organizer and judge at Inaugural Texas A&M Energy Conference (~300 participants)
2016 Aug Invited judge at Summer Undergraduate Research Poster Competition, Texas A&M University
2016 May Volunteer at the 229th meeting of the Electrochemical Society

2015 Aug Invited judge at Summer Undergraduate Research Poster Competition, Texas A&M University

2014 Aug Organizer at IITK Student Research Convention (~150 participants)

Conceptualized, planned and organized a two-day conference at IIT-Kanpur for undergraduate and graduate students. The conference had 4 invited lectures by IIT-Kanpur professors, 32 oral presentations (8 sessions), 68 posters, and a small expo by start-ups being supported by IIT-Kanpur.

PUBLICATIONS

The list of publications based on my dissertation research (accepted before Apr 1, 2019) is provided hereafter.

1. **A. Mistry** *et al*. (2019) *Electrolyte Confinement alters Lithium Electrodeposition* ACS Energy Letters 4 (1) 156
2. **A. Mistry** and P. P. Mukherjee (2019) *Non-equilibrium Thermodynamics in Electrochemical Complexation of Li-oxygen Porous Electrodes* Journal of Materials Chemistry A *in press*
3. **A. Mistry**, H. Reddy Palle and P. P. Mukherjee (2019) *In Operando Thermal Signature Probe for Lithium Ion Cells* Applied Physics Letters 114 (2) 023901
4. (joint first author) R. Adams, **A. Mistry** *et al.*, *Materials by Design: Tailored Morphology and Structures of Carbon Anodes for Enhanced Battery Safety* ACS Applied Materials and Interfaces *in press*
5. **A. Mistry** (2018) *Curvature Effects in Precipitation Dynamics* The Electrochemical Society Interface Winter 27 (4) 80
6. **A. Mistry** and P. P. Mukherjee (2018) *Probing Spatial Coupling of Resistive Modes in Porous Intercalation Electrodes through Impedance Spectroscopy* Physical Chemistry Chemical Physics 21 (7) 3805
7. **A. Mistry** and P. P. Mukherjee (2018) *'Shuttle' in Polysulfide Shuttle: Friend or Foe?* The Journal of Physical Chemistry C 122 (42) 23845
8. **A. Mistry**, K. Smith and P. P. Mukherjee (2018) *Electrochemistry-coupled Mesoscale Complexations in Electrodes Lead to Thermo-electrochemical Extremes* ACS Applied Materials and Interfaces 10 (34) 28644
9. **A. Mistry**, K. Smith, and P. P. Mukherjee (2018) *Secondary Phase Stochastics in Li-ion Battery Cathodes* ACS Applied Materials and Interfaces 10 (7) 6317
10. **A. Mistry** and P. P. Mukherjee (2018) *Electrolyte Transport Evolution Dynamics in Li-sulfur Batteries* The Journal of Physical Chemistry C 122 (32) 18329
11. **A. Mistry** and P. P. Mukherjee (2017) *Precipitation – Microstructure Interaction in Li-S Battery Cathode* The Journal of Physical Chemistry C 121 (47) 26256
12. (joint first author) C.-F. Chen, **A. Mistry** and P. P. Mukherjee (2017) *Probing Impedance and Microstructure Evolution in Lithium-sulfur Battery Electrodes* The Journal of Physical Chemistry C 121 (39) 21206
13. **A. Mistry**, D. Juarez-Robles, M. Stein and K. Smith, P. P. Mukherjee (2016) *Analysis of Long-range Interaction in Lithium-ion Battery Electrodes* Journal of Electrochemical Energy Conversion and Storage 13 (3) 031006
14. J. Grunewald, **A. Mistry**, *et al.* (2019) *Mesoscale Physics in the Catalyst Layer of Proton Exchange Membrane Fuel Cells: a Critical Perspective* Journal of the Electrochemical Society 166 (7) F3089
15. B. Trembacki, **A. Mistry**, *et al.* (2018) *Mesoscale Analysis of Conductive Binder Domain Morphology in Lithium-Ion Battery Electrodes* Journal of the Electrochemical Society 165 (13) E725

16. M. Vasilyeva, **A. Mistry** and P. P. Mukherjee (2018) *Multiscale Model Reduction for Pore-scale Simulation of Li-ion Batteries using GMsFEM* Journal of Computational and Applied Mathematics 344, 73
17. N. Kotak, P. Barai, A. Verma, **A. Mistry** and P. P. Mukherjee (2018) *Electrochemistry-mechanics Coupling in Intercalation Electrodes* Journal of the Electrochemical Society 165 (5) A1064
18. F. Usseglio-Viretta, A. Colclasure, **A. Mistry** *et al.*, (2018) *Resolving the Discrepancy in Tortuosity Factor Estimation for Li-ion Battery Electrodes through Micro-Macro Modeling and Experiment* Journal of the Electrochemical Society 166 (14) A3403
19. Z. Liu, **A. Mistry** and P. P. Mukherjee (2017) *Mesoscale Physicochemical Interactions in Lithium-sulfur Batteries: Progress and Perspective* Journal of Electrochemical Energy Conversion and Storage 15 (1) 010802
20. M. Stein IV, **A. Mistry** and P. P. Mukherjee (2017) *Mechanistic Understanding of the Role of Evaporation in Electrode Processing* Journal of the Electrochemical Society 164 (7) A1616
21. K. Shah, N. Balsara, S. Banerjee, M. Chintapalli, A. P. Cocco, W. K. S. Chiu, I. Lahari, S. Martha, **A. Mistry** *et al.* (2017) *State-of-the-art and Future Research Needs for Multiscale Analysis of Li-ion Cells* Journal of Electrochemical Energy Conversion and Storage 14 (2) 020801
22. G. J. Nelson, L. J. Ausderau, J. R. Buckley, S. Shin, **A. Mistry**, P. P. Mukherjee and V. De Andrade (2017) *Transport-geometry Interactions in Li-ion Cathode Materials Imaged using X-ray Nanotomography* Journal of the Electrochemical Society 164 (7) A1412
23. P. Barai, **A. Mistry** and P. P. Mukherjee (2016) *Poromechanical Effect in the Lithium-sulfur Battery Cathode* Extreme Mechanics Letters 9 (3) 359
24. A. D. Dysart, J. C. Burgos, **A. Mistry** *et al.* (2015) *Towards Next Generation Lithium-sulfur Batteries: Non-conventional Carbon Compartments/ Sulfur Electrodes and Multi-scale Analysis* Journal of the Electrochemical Society 163 (5) A730